

N.G.H. Meyendorf  
P.B. Nagy  
S.I. Rokhlin (Eds.)

# Nondestructive Materials Characterization

With Applications  
to Aerospace  
Materials



Springer

**Physics and Astronomy**  **ONLINE LIBRARY**

[springeronline.com](http://springeronline.com)

# Springer Series in MATERIALS SCIENCE

---

*Editors:* R. Hull    R. M. Osgood, Jr.    J. Parisi    H. Warlimont

The Springer Series in Materials Science covers the complete spectrum of materials physics, including fundamental principles, physical properties, materials theory and design. Recognizing the increasing importance of materials science in future device technologies, the book titles in this series reflect the state-of-the-art in understanding and controlling the structure and properties of all important classes of materials.

- |  |   |
|--|---|
| 61 <b>Fatigue in Ferroelectric Ceramics and Related Issues</b><br>By D.C. Lupascu  | 66 <b>Multiphased Ceramic Materials Processing and Potential</b><br>Editors: W.-H. Tuan and J.-K. Guo   |
| 62 <b>Epitaxy</b><br>Physical Foundation and Technical Implementation<br>By M.A. Herman, W. Richter, and H. Sitter                                       | 67 <b>Nondestructive Materials Characterization</b><br>With Applications to Aerospace Materials<br>Editors: N.G.H. Meyendorf, P.B. Nagy, and S.I. Rokhlin |
| 63 <b>Fundamentals of Ion Irradiation of Polymers</b><br>By D. Fink  | 68 <b>Diffraction Analysis of the Microstructure of Materials</b><br>Editors: E.J. Mittemeijer and P. Scardi  |
| 64 <b>Morphology Control of Materials and Nanoparticles</b><br>Advanced Materials Processing and Characterization<br>Editors: Y. Waseda and A. Muramatsu | 69 <b>Chemical–Mechanical Planarization of Semiconductor Materials</b><br>Editor: M.R. Oliver   |
| 65 <b>Transport Processes in Ion Irradiated Polymers</b><br>By D. Fink   | 70 <b>Isotope Effect Applications in Solids</b><br>By G.V. Plekhanov  |

---

Series homepage – <http://www.springer.de/phys/books/ssms/>

---

Volumes 10–60 are listed at the end of the book.

Norbert G.H. Meyendorf  
Peter B. Nagy  
Stanislav I. Rokhlin  
(Eds.)

# **Nondestructive Materials Characterization**

With Applications  
to Aerospace Materials

With 311 Figures and 11 Tables



**Springer**

**Professor Norbert G.H. Meyendorf**  
University of Dayton  
Center for Materials Diagnostics  
300 College Park  
Dayton, OH 45469-0121, USA  
E-mail: meyendorf@udri.udayton.edu

**Professor Peter B. Nagy**  
University of Cincinnati  
Dept. of Aerospace Engineering  
and Engineering Mechanics  
ML0070, Cincinnati, OH 45221, USA  
E-mail: peter.nagy@uc.edu

**Professor Stanislav I. Rokhlin**  
The Ohio State University  
Dept. of Industrial, Welding  
and Systems Engineering  
1248 Arthur E. Adams Drive  
Columbus, OH 43221, USA  
E-mail: rokhlin.2@osu.edu

*Series Editors:*

**Professor Robert Hull**  
University of Virginia  
Dept. of Materials Science and Engineering  
Thornton Hall  
Charlottesville, VA 22903-2442, USA

**Professor Jürgen Parisi**  
Universität Oldenburg, Fachbereich Physik  
Abt. Energie- und Halbleiterforschung  
Carl-von-Ossietzky-Strasse 9-11  
26129 Oldenburg, Germany

**Professor R. M. Osgood, Jr.**  
Microelectronics Science Laboratory  
Department of Electrical Engineering  
Columbia University  
Seeley W. Mudd Building  
New York, NY 10027, USA

**Professor Hans Warlimont**  
Institut für Festkörper-  
und Werkstoffforschung,  
Helmholtzstrasse 20  
01069 Dresden, Germany

ISSN 0933-033X

ISBN 978-3-642-07350-2      ISBN 978-3-662-08988-0 (eBook)  
DOI 10.1007/978-3-662-08988-0

Cataloging-in-Publication Data applied for.

Bibliographic information published by Die Deutsche Bibliothek Die Deutsche Bibliothek lists this publication in the Deutsche Nationalbibliografie; detailed bibliographic data is available in the Internet at <http://dnb.ddb.de>.

This work is subject to copyright. All rights are reserved, whether the whole or part of the material is concerned, specifically the rights of translation, reprinting, reuse of illustrations, recitation, broadcasting, reproduction on microfilm or in any other way, and storage in data banks. Duplication of this publication or parts thereof is permitted only under the provisions of the German Copyright Law of September 9, 1965, in its current version, and permission for use must always be obtained from Springer-Verlag Berlin Heidelberg GmbH Violations are liable for prosecution under the German Copyright Law.

[springeronline.com](http://springeronline.com)

© Springer-Verlag Berlin Heidelberg 2004

Originally published by Springer-Verlag Berlin Heidelberg New York in 2004

Softcover reprint of the hardcover 1st edition 2004

The use of general descriptive names, registered names, trademarks, etc. in this publication does not imply, even in the absence of a specific statement, that such names are exempt from the relevant protective laws and regulations and therefore free for general use.

Typesetting by the authors/editors

Final processing and production: PTP-Berlin Protago-TeX-Production GmbH, Berlin

Cover concept: eStudio Calamar Steinen

Cover production: *design & production* GmbH, Heidelberg

Printed on acid-free paper

SPIN: 10828395

57/3141/YU

5 4 3 2 1 0

## Preface

Nondestructive Evaluation (NDE) becomes a key discipline for modern technology. Information about materials defects and properties is significant to guarantee reliability of a product and avoid fatal accidents. For instance technologies with high safety requirements like aviation, automotive, and energy production are driving forces for NDE. Keeping in mind that aging of the infrastructure is an issue in all industrial countries and that, for example, an aircraft can have a lifetime of several decades poses new challenges for NDE and especially nondestructive materials characterization. Besides the traditional in-field applications, NDE becomes more and more a tool to study materials degradation processes and to provide engineers with input data for sophisticated models describing materials behavior and the life of components. At present, this marriage of NDE and materials modeling shows significant success in predicting damage progression (corrosion, fatigue) and thus an enhancement of availability and reliability of components and complete aircraft.

This book will give a snapshot of the present research in materials characterization of aging aircraft. Methods considered are x-ray, ultrasonic, optical and thermal techniques and in particular techniques with high spatial resolution to detect and quantify early stages of degradation or to characterize materials microstructure. Every chapter briefly describes the basics and the principles of one NDE method under consideration. Discussing recent research results by applying these methods completes the chapters. The readers will get an overview of the present state of the art of materials characterization techniques. The book shows a unique summary of NDE methods applied to similar materials under examination. This allows the reader to understand the advantages and disadvantages of several techniques and will help to find approaches to solve NDE materials characterization problems.

However, the present book can summarize only a limited number of NDE approaches for materials characterization. This overview cannot be complete. For example electromagnetic methods that have significant importance not only for aviation but also in many other industries like automotive, energy, steel making have been completely excluded. The applications discussed in this volume are focused on aluminum and titanium alloys and polymer coatings. The size of the book did not allow the consideration of ferromagnetic materials, ceramic, and composite materials that have high importance for aircraft structures and elsewhere that are challenging for NDE as well. A second volume will be required to complete this overview.

The accomplishments presented in this volume were not possible without strong financial, technical, and administrative support. The editors gratefully acknowledge, The United States Air Force Office of Scientific Research, The State of Ohio, The National Science Foundation, The Air Force Research Laboratory at Wright-Patterson Air Force Base, The Fraunhofer Society, The University of Dayton Research Institute, The University of Dayton, The Ohio State University, and The University of Cincinnati for their support. Lt. Col. Paul Trulove, Dr. Hugh DeLong, Dr. Thomas Moran and Dr. Theodore Matikas are personally acknowledged for their significant impact on the results presented in this book.

Finally we would like to thank Dr. George Y. Baaklini, NASA Glenn Research Center, Dr. Thomas Moran, Air Force Research Laboratories, Wright Patterson Air Force Base, Gerald S. Frankel, The Ohio State University, Robert G. Andrews and Dr. Theodore Nicholas, University of Dayton Research Institute for critical reviewing the manuscripts.

Dayton, Ohio, April 2003

Norbert G.H. Meyendorf  
Peter B. Nagy  
Stanislav I. Rokhlin

# **Contents**

<b>1</b>	<b>Degradation of Aircraft Structures .....</b>	<b>1</b>
1.1	Introduction .....	1
1.2	NDE Methods at a Glance.....	2
1.3	Degradation of Aircraft Materials and NDE .....	5
1.3.1	Corrosion Protective Coatings .....	5
1.3.2	Corrosion.....	9
1.3.3	Fatigue.....	15
1.3.4	Fretting and Fretting Fatigue.....	21
1.4	Introduction to the Next Chapters .....	23
	References .....	24
<b>2</b>	<b>Optical Detection of Surface Damage.....</b>	<b>26</b>
2.1	Introduction .....	26
2.2	Background .....	27
2.3	Instrumentation and Method .....	28
2.4	Applications .....	29
2.4.1	Optical Quantification of Fretting Fatigue Damage.....	30
2.4.2	Characterization of Localized Corrosion Damage and Its Role for Fatigue Crack Initiation.....	37
2.4.3	Characterization of Crack Damage States in Titanium Alloys through Examination of the Surface Deformation Preceding the Crack Front .....	47
2.4	Conclusions .....	55
	References .....	56
<b>3</b>	<b>Microradiographic and Foil Penetration Methods for Quantification of Localized Corrosion.....</b>	<b>58</b>
3.1	Introduction .....	58
3.2	Background .....	59
3.3	Microradiographic System .....	61

<b>3.4</b>	<b>Microradiographic Methods .....</b>	<b>63</b>
3.4.1	Microradiographic Methods Evaluation.....	63
3.4.2	Microradiography of Corrosion Samples .....	74
3.4.3	Microradiographic Methods for Pit Depth Measurement .....	76
3.4.4	Validation of Microradiographic Pit Depth Measurement .....	79
3.4.5	Microradiographic Characterization of Fatigue Cracks Initiated by Corrosion Pits.....	91
3.4.6	Phase-Contrast Image Enhancement with Microradiography .....	95
<b>3.5</b>	<b>Foil Penetration Method.....</b>	<b>99</b>
<b>3.6</b>	<b>Application of Microradiography for Studying Localized Corrosion .....</b>	<b>101</b>
3.6.1	Microradiographic Analysis of Corroded Foil Penetration Samples .....	101
3.6.2	In Situ Microradiography of Localized Corrosion Growth .....	105
<b>3.7</b>	<b>Summary and Conclusions.....</b>	<b>110</b>
	<b>References .....</b>	<b>112</b>

#### **4    Interferometric and Holographic Imaging of Surface Wave Patterns for Characterization of Material Degradation .....** **113**

<b>4.1</b>	<b>Introduction.....</b>	<b>113</b>
<b>4.2</b>	<b>Background .....</b>	<b>114</b>
4.2.1	Ultrasonic Nondestructive Evaluation (NDE).....	114
4.2.2	Surface Acoustic Waves (SAW) .....	116
4.2.3	Ultrasonic Reflection and Scattering from Microcracks .....	119
4.2.4	Local Ultrasonic Scattering from Surface-Breaking Cracks .....	122
4.2.5	Optical Interferometry and Holography .....	125
<b>4.3</b>	<b>Instrumentation and Methods .....</b>	<b>127</b>
4.3.1	Near-Field Scanning Interferometry (NFSI) System .....	127
4.3.2	Frequency Translated Holography (FTH) System .....	128
<b>4.4</b>	<b>Applications .....</b>	<b>128</b>
4.4.1	Interferometric and Holographic Imaging of Surface Waves .....	130
4.4.2	Local Ultrasonic Scattering from Surface-Breaking Cracks .....	131
4.4.3	Crack-Depth Determination .....	133
4.4.4	In Situ Stress-Corrosion Crack (SCC) Growth Measurements .....	136
<b>4.5</b>	<b>Future Trends .....</b>	<b>139</b>
	<b>References .....</b>	<b>140</b>

#### **5    Surface Acoustic Wave Characterization of Pitting Corrosion Damage with Fatigue Crack.....** **142**

<b>5.1</b>	<b>Introduction .....</b>	<b>142</b>
<b>5.2</b>	<b>Background .....</b>	<b>144</b>

---

5.3	Instrumentation and Methods .....	145
5.3.1	Experiments .....	145
5.3.2	Fatigue Crack Growth Analysis .....	147
5.3.3	Analysis of Surface Wave Scattering for Crack Sizing.....	152
5.4	Applications .....	157
5.4.1	Pit Size Measurements .....	157
5.4.2	Ultrasonic Sizing of Crack Initiated from a Pit .....	160
5.4.3	Fatigue Life Prediction.....	172
5.5	Future Trends .....	176
	References .....	177

## **6 Ultrasonic Fatigue Crack Detection in Aluminum and Titanium Alloys.....** 180

6.1	Introduction .....	180
6.2	Background (Crack-Closure) .....	182
6.3	Instrumentation and Methods .....	185
6.3.1	Thermo-Optical Modulation .....	185
6.3.2	The Role of Thermal Diffusivity.....	187
6.4	Applications .....	193
6.4.1	Dynamic Thermo-Optical Modulation in Al-2024.....	193
6.4.2	Quasi-static Thermo-Optical Modulation in Ti-6Al-4V .....	198
6.5	Conclusions .....	204
	References .....	205

## **7 Early Detection of Fatigue Damage in Ti-6Al-4V with Nonlinear Acoustics.....** 206

7.1	Introduction .....	206
7.2	Background .....	207
7.2.1	Linear Acoustic Measurements and Fatigue .....	207
7.2.2	Nonlinear Acoustics in Fatigue Damage Measurement .....	207
7.3	Methods.....	209
7.3.1	General Description .....	209
7.3.2	Capacitive Detector Method.....	210
7.3.3	Piezoelectric Method.....	213
7.3.4	In Situ Measurement .....	214
7.4	Applications .....	216
7.4.1	Material and Sample Description.....	216
7.4.2	Interrupted Fatigue Measurements (Low Cycle Fatigue).....	217
7.4.3	In Situ Measurements.....	220

7.4.4	Discussion of Interrupted and Continuous Measurement Results .....	223
7.4.5	Local Damage Measurements .....	224
7.4.6	Summary and Conclusions.....	230
References.....		232
<b>8</b>	<b>Ultrasonic Absorption Measurements.....</b>	<b>234</b>
8.1	Introduction.....	234
8.2	Background .....	234
8.3	Method .....	237
8.3.1	Laser Ultrasound .....	237
8.3.2	Contact Ultrasound .....	237
8.4	Applications .....	238
8.5	Future Trends .....	242
References .....		244
<b>9</b>	<b>Thermographic Materials Characterization.....</b>	<b>246</b>
9.1	Introduction .....	246
9.2	Background .....	246
9.2.1	Thermal Wave and Thermal Diffusion Techniques .....	246
9.2.2	Mechanically Induced Heat.....	249
9.3	Infrared Cameras for NDE .....	251
9.4	Methods.....	253
9.5	Applications .....	254
9.5.1	Passive Infrared Imaging of Defects through Organic Coating ...	254
9.5.2	Pulsed Thermography for Detection of Subsurface Defects .....	256
9.5.3	Fan Thermography for Imaging of Corrosion under Coatings....	257
9.5.4	Mechanically Induced Dissipated Heat Analysis (MIDA) – High Stress Excitation.....	261
9.5.5	Fatigue Characterization by Mechanically Induced Dissipated Heat Analysis (MIDA) – Ultrasonic Excitation .....	272
9.5.6	Thermographic NDE Based on Heat Dissipation – Summary and Conclusion .....	276
References .....		283
<b>10</b>	<b>Scanning Vibrating Electrode Technique as a Benchmark for NDE of Corrosion .....</b>	<b>286</b>
10.1	Introduction .....	286

---

10.2	Background .....	287
10.3	Instrumentation .....	288
10.4	Applications .....	290
	References .....	292
<b>11</b>	<b>Acoustic Imaging Techniques for Characterization of Corrosion, Corrosion Protective Coatings, and Surface Cracks.....</b>	<b>294</b>
11.1	Introduction .....	294
11.2	Background .....	294
11.3	Instrumentation .....	296
11.3.1	Scanning Acoustic Microscope (SAM).....	297
11.3.2	High Frequency Scanning Acoustic Microscopy (HF-SAM) .....	298
11.4	Methods.....	299
11.4.1	Acoustic Imaging .....	299
11.4.2	Determination of Elastic Properties .....	302
11.5	Applications .....	304
11.5.1	Characterization of Corrosion .....	304
11.5.2	Characterization of Corrosion Protective Coatings .....	313
11.5.3	Microcrack Detection of Fatigued Material Using HF SAM .....	319
	References .....	322
<b>12</b>	<b>Scanning Probe Microscopy: Ultrasonic Force and Scanning Kelvin Probe Force Microscopy.....</b>	<b>323</b>
12.1	Introduction .....	323
12.2	Background and Instrumentation .....	323
12.3	Methods.....	325
12.4	Application of the Methods .....	327
12.4.1	Imaging of Elastic Properties .....	327
12.4.2	Scanning Kelvin Probe Force Microscopy and AFM Scratching for Studies of Corrosion.....	340
	References .....	353
<b>13</b>	<b>High Resolution Microellipsometry .....</b>	<b>356</b>
13.1	Introduction .....	356
13.2	Background .....	356
13.3	Instrumentation .....	358
13.3.1	Imaging Microellipsometer .....	358
13.3.2	Rotationally Symmetric Scanning Microellipsometer .....	360

13.4 Applications .....	363
13.4.1 Measurement of Resolved Features .....	363
13.4.2 Measurement of Surface Features beyond Diffraction Limit .....	366
13.4.3 Measurement of Axial Birefringence .....	368
13.4.4 Measurement of Micro-Optical Components .....	370
13.5 Future Trends .....	371
References .....	372
<b>14 Positron Annihilation Spectroscopy (PAS) .....</b>	<b>374</b>
14.1 Introduction .....	374
14.2 Background and Instrumentation .....	374
14.2.1 Basis of the Method .....	374
14.2.2 Positron Annihilation Lifetime Spectroscopy (PALS).....	376
14.2.3 Doppler-Broadening of Annihilation Radiation (DBAR) .....	379
14.2.4 Slow Positron Beam Techniques.....	381
14.3 Interaction of Positrons with Lattice Defects and Precipitates .....	383
14.3.1 Change of the Annihilation Parameters Due to Positron Trapping at Defects.....	383
14.3.2 Kinetics of Positron Trapping .....	385
14.4 Applications .....	389
14.4.1 Characterization of Plastic Deformation of Stainless Steel.....	389
14.4.2 Characterization of Fatigue in Ti-6Al-4V .....	392
14.4.3 Precipitation Phenomena in Aluminum Alloys.....	395
14.4.4 Characterization of Polymers and Polymer Composites .....	399
14.4.5 Characterization of Polymer Coatings .....	405
References .....	409
<b>Index.....</b>	<b>413</b>

## **List of Contributors**

**Arnold, W.** chapter: 8

Fraunhofer-Institut für zerstörungsfreie Prüfung  
Universität, Gebäude 37, 66123 Saarbrücken  
Germany

**Blackshire, J.L.** chapter: 4

Center for Materials Diagnostics, University of Dayton  
300 College Park, Dayton, OH 45469  
USA

**Buchanan, A.** chapter: 10

Center for Materials Diagnostics, University of Dayton  
300 College Park, Dayton, OH 45469  
USA

**Dlubek, G.** chapter: 14

Institut für innovative Technologien GmbH Köthen  
Außenstelle Halle,  
Wiesenring 4, 06120 Lieskau  
Germany

**Donley, M.** chapter: 2, 10

Air Force Research Laboratories, Wright Patterson Air Force Base  
Dayton, OH 45433  
USA

- Druffner, C. chapter: **12**  
Center for Materials Diagnostics, University of Dayton  
300 College Park, Dayton, OH 45469  
USA
- Eylon, D. chapter: 1, 2  
Graduate Materials Engineering, University of Dayton  
300 College Park, Dayton, OH 45469  
USA
- Fassbender, S. chapter: 11  
Institute for Acoustic Microscopy  
Lerchenweg 16–18, 35729 Herborn  
Germany
- Frankel, G.S. chapter: 1, 3, 12  
The Ohio State University, 477 Watts Hall  
2041 College Rd., Columbus, OH 43210  
USA
- Frouin, J. chapter: 7  
Center for Materials Diagnostics, University of Dayton  
300 College Park, Dayton, OH 45469  
USA
- Hoffmann, J. chapter: 1, 9, **11**  
S&K Technologies, Inc., Georgia Division  
3139 Research Blvd., Suite 101, Dayton, OH 45420  
USA
- Hoying, J. chapter: 2  
Center for Materials Diagnostics, University of Dayton  
300 College Park, Dayton, OH 45469  
USA

Kacmar, C.	chapter: 2
Center for Materials Diagnostics, University of Dayton 300 College Park, Dayton, OH 45469 USA	
Karpen, W.	chapter: 9
Fraunhofer-Institut für zerstörungsfreie Prüfung Universität, Gebäude 37, 66123 Saarbrücken Germany	
Kim, J-Y.	chapter: 5
Department of Industrial, Welding & Systems The Ohio State University 1248 Adams Drive, Columbus, OH 43221 USA	
Khobaib, M.	chapter: 1, 2, <b>10</b>
University of Dayton Research Institute 300 College Park, Dayton, OH 45469 USA	
Kramb, V.	chapter: 2, 9
University of Dayton Research Institute 300 College Park, Dayton, OH 45469 USA	
Leblanc, P.	chapter: 12
The Ohio State University, Fontana Corrosion Center 2041 College Rd., Columbus, OH 43210 USA	
Meyendorf, N.	chapter: <b>1, 9, 11, 14</b>
Center for Materials Diagnostics, University of Dayton 300 College Park, Dayton, OH 45469 USA	

- Na, J.K. chapter: 7  
System Integration Group, Veridian Engineering  
2700 Indian Ripple Road, Dayton, OH 45440  
USA
- Nagy, P.B. chapter: 6  
Department of Aerospace Engineering, University of Cincinnati  
ML 0070, Cincinnati, OH 45221  
USA
- Netzemann, U. chapter: 9  
Fraunhofer-Institut für zerstörungsfreie Prüfverfahren  
Universität, Gebäude 37, 66123 Saarbrücken  
Germany
- Palm, S. chapter: 8  
Fraunhofer-Institut für zerstörungsfreie Prüfverfahren  
Universität, Gebäude 37, 66123 Saarbrücken  
Germany
- Rokhlin, S. I. chapter: 3, 5  
Department of Industrial, Welding & Systems  
The Ohio State University  
1248 Adams Drive, Columbus, OH 43221  
USA
- Rösner, H. chapter: 1, 9  
Fraunhofer-Institut für zerstörungsfreie Prüfverfahren  
Universität, Gebäude 37, 66123 Saarbrücken  
Germany
- Sathish, S. chapter: 1, 7, 11, 12  
University of Dayton Research Institute  
300 College Park, Dayton, OH 45469  
USA

- Shell, E.B. chapter: 1, 2, 11  
Center for Materials Diagnostics, University of Dayton  
300 College Park, Dayton, OH 45469  
USA
- Simon, L. chapter: 2  
Center for Materials Diagnostics, University of Dayton  
300 College Park, Dayton, OH 45469  
USA
- Schumaker, E. chapter: 12  
Center for Materials Diagnostics, University of Dayton  
300 College Park, Dayton, OH 45469  
USA
- Xiao, H. chapter: 6  
Department of Aerospace Engineering, University of Cincinnati  
ML 0070, Cincinnati, OH 45221  
USA
- Yan, Z. chapter: 6  
Department of Aerospace Engineering, University of Cincinnati  
ML 0070, Cincinnati, OH 45221  
USA
- Zhan, Q. chapter: 13  
Graduate Electro-Optics Program, University of Dayton  
300 College Park, Dayton, OH 45469  
USA
- Zoofan, B. chapter: 3  
Department of Industrial, Welding & Systems  
The Ohio State University  
1248 Adams Drive, Columbus, OH 43221  
USA

# 1 Degradation of Aircraft Structures

N. Meyendorf, D. Eylon, G.S. Frankel, J. Hoffmann, M. Khobaib, H. Rösner,  
S. Sathish, E.B. Shell

## 1.1 Introduction

Maintenance and reliability of aircraft is a major safety concern and economical factor. Many civilian and military aircraft have been in service for 35 years or more. Aircrafts that were originally designed for a service life of 20 years are currently considered for life extensions of up to 80 years. The cost of corrosion and fatigue related maintenance on these aging structures has increased dramatically. A study conducted in 1998 showed that the direct costs of corrosion maintenance to the United States Air Force were \$775 million/year [1]. These costs continue to rise in spite of Air Force structure changes resulting in a 20% reduction in the overall fleet. In an effort to reduce these maintenance costs, several programs have been initiated for the development of methods to manage and control corrosion and fatigue damage in aging aircraft.

Nondestructive evaluation (NDE) of materials will undoubtedly play a major role in future maintenance programs. These NDE methods must be able to detect and quantify material defects to prevent catastrophic failure or to provide input data for life prediction models. The NDE methods must have sufficient sensitivity to detect microstructural changes and early stages of damage so that component replacement plans can be implemented prior to failure. As a result of this new maintenance approach, NDE methods will be required to monitor the changes in the material properties that are used to define maintenance cycles.

Typically, NDE is applied to production quality control, periodic systems inspection, and condition monitoring. A new focus that has been developed in the last years is NDE for materials research and development. Such laboratory techniques can help to understand degradation processes, such as the quantification of corrosion kinetics or the degradation of corrosion protective coatings. An understanding of the generation and propagation of defects on a microstructural level will help improve the material properties and develop models for lifetime prediction.

The NDE methods discussed in this book fall into four main categories:

- Detection and characterization of corrosion damage.
- Characterization of polymer-based corrosion protective coatings.
- Characterization of low cycle and high cycle fatigue damage.
- Characterization of fretting and fretting fatigue damage.

Since the earliest stages of damage occur in the material microstructure, NDE techniques for early detection of damage must be sensitive to changes in microstructure. For this reason the book will consider:

- NDE inspection methods that are sensitive to microstructure and intrinsic materials property variations, and
- High-resolution microscopic and imaging techniques.

Detection and quantification of early stages of damage require high resolution, high sensitivity NDE techniques. However, the inspection results must be correlated with the damage states in the material, crack initiation criteria, and relevant mechanical properties in order to predict component life. NDE results have to be compared to benchmark techniques such as destructive fatigue and corrosion tests, as well as scanning and transmission electron microscopy that quantify microstructure states and microstructure variations during materials degradation.

## 1.2 NDE Methods at a Glance

The detection of early stages of degradation, which directly relates to microstructure variations in the material, requires techniques with extremely high resolution or integral characterization methods. Figure 1 shows a chart of appearance of NDE imaging techniques on a time scale compared to the sensitivity or resolution for defects of certain sizes. During the first half of the past century, the conventional NDE techniques like industrial x-ray techniques, magnetic particle techniques, conventional ultrasonics and dye penetrant testing had resolutions of the order of 0.1 mm. This was equal to the measuring accuracy for the mechanical production at that time. The main focus of this book are methods with resolutions of a micrometer or smaller. These methods are able to detect very tiny defects like small corrosion pits, microcracks or even modifications of the microstructure of the material. Figure 2 compares the resolution or detectability of the NDE methods to the typical size of conventional macroscopic defects, to micro-defects like microcracks or corrosion pits, and to microstructure variations, as well as crystal lattice defects.

Very early stages of fatigue (even before microcracks can be detected by NDE) are characterized by defects in the crystal lattice. Non-linear acoustics (Chapter 7) and heat dissipation measurements during mechanical loading (Chapter 9) were found to be sensitive to changes in the dislocation density and modifications of the mechanical properties (elasto-plastic hysteresis) during early stages of degradation. Acoustic absorption (Chapter 8) and positron annihilation (Chapter 13) are sensitive to the very early stages (first 10%) of fatigue life.

Imaging techniques for nanometer size microstructures in materials, scanning electron microscopy and transmission electron microscopy for example, require careful specimen preparation and therefore, are not nondestructive. Scanning Probe Microscopy (SPM) techniques like Atomic Force Microscopy (AFM) or

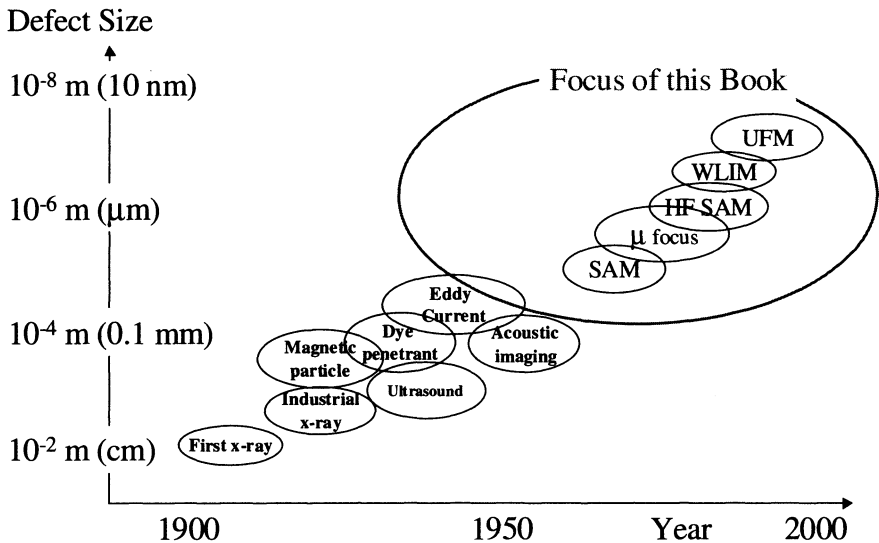


**Fig. 1.** Development of resolution of NDE techniques and resolution of methods discussed in this book (SAM: Scanning Acoustic Microscopy,  $\mu$  focus:  $\mu$  focus x-ray technique, HF SAM: High Frequency Scanning Acoustic Microscopy, WLIM: White Light Interference Microscopy, UFM: Ultrasonic Force Microscopy)

Ultrasonic Force Microscopy (UFM) have been used to image variations in surface elasticity with a resolution down to the atomic scale (Chapter 12). AFM and UFM experiments do not require vacuum and surfaces are easier to prepare, consequently these techniques have numerous advantages over the state-of-the-art transmission electron microscopy.

White light interference microscopy (WLIM) is a non-contact optical method for quantification of the surface topography with a resolution in vertical direction of 3 nanometers or better (Chapter 2). This method was successfully applied to quantify degradation at surfaces due to fretting and to obtain the dimensions of corrosion pits. Another application was the quantification of elastic and plastic deformation fields in front of crack tips. Based on these measurements, criteria for crack stability have been established. Other microscopic NDE techniques like scanning acoustic microscopy (Chapter 11), micro-radiography (Chapter 3), thermal wave microscopy, or thermography with a microscopic lens (Chapter 9) were employed to detect and quantify early stages of degradation and to observe the generation and progression of materials defects. Examples are stress corrosion cracks or corrosion pits. Acoustic and thermal techniques have shown the ability to detect early stages of corrosion underneath intact corrosion protective coatings.

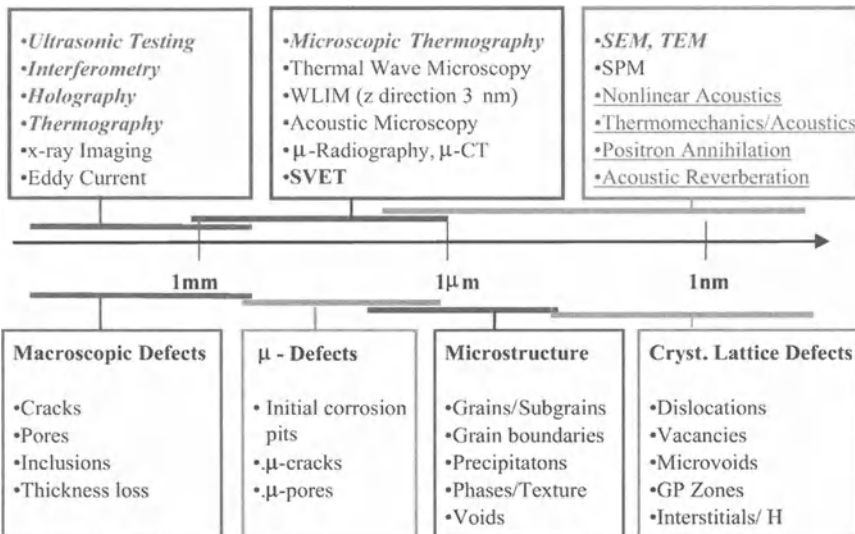


**Fig. 2.** Summary of methods in comparison to typical structures that have to be characterized on a scale of structure size (*Italic*: methods for detection and imaging, standard: methods for metric of local properties, underlined: methods for integral property or structure information)

Scanning vibrating electrode technique (SVET) was employed as a benchmark technique to detect early corrosion defects (Chapter 10).

Ultrasonic, thermal, optical, x-ray, and eddy current methods can be considered to detect and quantify corrosion and fatigue defects and to study and model the generation and progression of cracks (Chapters 3 to 6). Ultrasonic surface waves have been applied to quantify the development of fatigue cracks (Chapter 4 and 5). X-ray micro-focus techniques have been found to be very powerful for investigation of corrosion cracks growing in real time (Chapter 3). Frequency translated holography has been developed as a real time optical method to study the interaction between ultrasonic waves and surface cracks (Chapter 6). This technique allows the real time visualization of progressing cracks and other surface defects.

Approaches for life prediction of components include numerical models for the development and progression of defects and empirical correlation techniques, for example, artificial neural networks [2]. Mechanical or chemical destructive tests are necessary to establish the relations between microstructure variations and mechanical or chemical properties. These property data are necessary to feed the numerical models for lifetime prediction.

In many cases, especially, for corrosion and degradation of corrosion protective coatings, the degradation processes are complex. Therefore, the application of only one NDE technique is not sufficient and it is necessary to combine the information of several techniques in multi-sensor approaches. One possible

solution to relate a set of NDE data to the remaining life of a component is through application of artificial neural networks or multi-parameter regression [2].

## 1.3 Degradation of Aircraft Materials and NDE

Aging aircraft require extensive maintenance to prevent damage leading to failure that may result in a fatal accident. The older the aircraft, the more critical the maintenance of their structural integrity becomes for life sustainment. Hence, increased attention is required for structural damage modeling, repair and life prediction. Some of the common causes of failure of aging aircraft are corrosion damage, fatigue cracking, and their synergistic interactions. Since both corrosion and fatigue are time dependent process, these problems are bound to worsen with the extended service of the aircraft.

### 1.3.1 Corrosion Protective Coatings

The extended use of an aircraft beyond the original design life is limited due to several aging material issues, especially related to corrosion damage. Numerous strategies for corrosion protection exist; the application of multi-functional polymeric coating systems is among the most important. Failure of these coatings leaves the aluminum alloy airframe structures exposed to harmful environmental conditions. However, current practice in aircraft coating maintenance lacks reliable inspection of the coatings themselves. Corrosion inspection of the Al alloy is usually carried out after the coating is removed, which is done at certain time intervals. Replacing the paint (coating) means stripping of the old paint and repainting. These operations generate 70–90% of United States Air Force (USAF) hazardous waste. Corrosion related problems cost over \$1 billion annually; 15% of these costs are paint-related [3].

In order to avoid these procedures, aircraft maintenance must be enabled to monitor the corrosion protection performance of the coating and detect sites of corrosion underneath the coating.

#### ***Degradation of Corrosion Protective Coatings***

Aircraft coatings are multi-functional. They contribute to three important requirements of an aircraft: (1) reduced wind resistance, (2) corrosion protection, and (3) appearance. Only a multi-layer coating-system can satisfy all requirements. Currently used coating systems consist of surface pretreatment, primer layer and topcoat. The primer and topcoat are polymeric [4, 5].

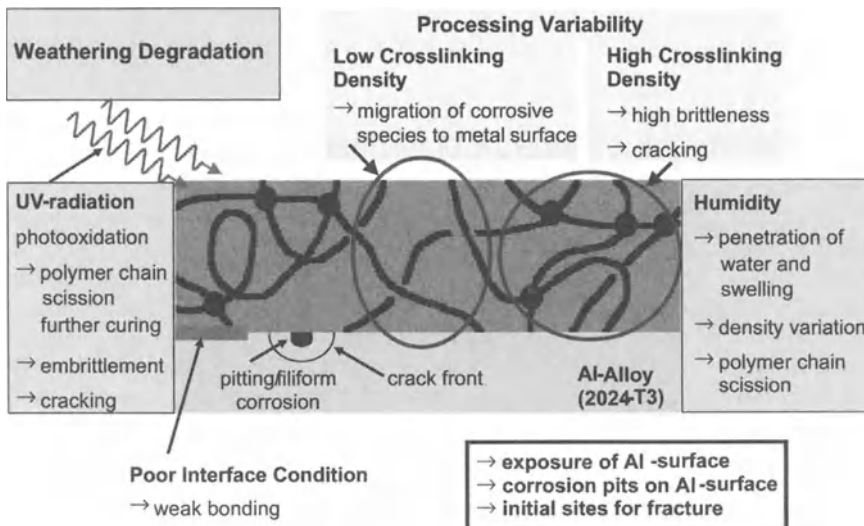


Fig. 3. Degradation processes of organic coatings

Figure 3 summarizes the important degradation mechanisms of corrosion protective aircraft coatings. Several environmental or coating conditions can contribute to coating failure.

**Insufficient Curing:** Insufficient curing is essentially non-uniform distribution of crosslinking agents leading to density variations in the coating; high density regions are brittle and susceptible to cracking, while low density regions may allow migration of environmental particles or interstitials (e.g., oxygen) to the metal substrate.

**Weathering:** Humidity exposure can lead to water penetration in the coating, swelling and polymer chain scission. UV radiation, which is included in sunlight, causes photo-oxidation processes in the coating. The combined and often cyclic exposure to UV/humidity accelerates the coating degradation process. Eventually, the polymer chains are damaged and the coating performance is reduced.

**Weak Bonding and Delamination:** Another problem for coating applications is weak bonding or delamination at the interface. Insufficient bonding results from improper metal surface treatment or insufficient adhesion capability of the polymer. Eventually, these mechanisms lead to an environmentally exposed metal surface, where corrosion can occur. Under mechanical load, these corrosion sites may cause the nucleation of cracks that lead to metal fracture.

### **NDE of Corrosion Protective Coatings**

The most common techniques to characterize coating degradation processes are salt-spray, electrochemical analysis (e.g., Electrochemical Impedance Spectroscopy, EIS), and IR spectroscopy. The latter operates only under laboratory conditions and EIS has not yet gained in-field acceptance. Salt spray tests are destructive, qualitative, and do not necessarily correlate to other environments. There is a need for new methodologies for nondestructive monitoring of aircraft coating performance in service.

Chapter 11 describes the application of scanning acoustic microscopy to study the coating/substrate interface. Using surface waves it is possible to image locations of weak adhesion and corrosion pits underneath coatings. A broadband 50-MHz transducer was applied for time-of-flight techniques. Due to the high time resolution of this transducer, it was possible to separate reflections from the front and backside of a coating. A special data processing technique allows separation of the front and back wall echo amplitude and quantification of the reflectivity coefficient for ultrasonic waves at the coating/surface and the coating/substrate interface. The reflectivity of the coating surface depends on the acoustic impedance. Coating degradation results in a modification of the acoustic impedance at the surface and thus the reflectivity. Acoustic reflectometry is a potential method to quantify coating degradation.

Furthermore, acoustic microscopy was able to detect micro-scale delamination and corrosion defects underneath coatings. Unfortunately, acoustic microscopy requires water as coupling medium to provide acoustic coupling between transducer and specimen. However, the water environment is destructive for both polymer coating and metal substrate. Therefore, the interaction between coating and water was studied extensively. Acoustic image sequences show the degradation of the coating substrate interface and the delamination of the coating for exposure times of several hours. However, no significant damage was found for short testing cycles of several minutes.

A completely nondestructive, non-contact technique for coating characterization with high potential for field application is thermography (Chapter 9). The standard technique for detection of subsurface defects such as delaminations of coatings is Pulsed (or “Flash”) Thermography. A short energy pulse heats the test surface. Defects affect the heat diffusion into the material and are responsible for “thermal contrasts.” An infrared camera images these local temperature inhomogeneities.

Using “Fan Thermography” the coating surface is slowly heated by hot air. An infrared sensitive camera observes the surface temperature. Local corrosion or adhesion failure results in an increased thermal resistivity. This is indicated by a local hot spot in the thermal image. The enhancement of surface temperature is much smaller compared to conventional pulsed thermography. This provides three main advantages:

1. The heating is not harmful for the coating surface.
2. The low temperature dynamics allow a longer measuring time frame that itself enables better image averaging to enhance accuracy.
3. The low temperature dynamics allow the use of cost effective bolometer cameras, which are very robust and easy to handle for in-field application.

Some organic coating systems are semi-transparent to infrared radiation. In these cases, an infrared camera can simply “look through” the coating. As described in Chapter 9, additional heating can be beneficial to enhance the contrast.

Thermal wave techniques use a periodic heat source to stimulate the test surface and measure the amplitude and phase shift of the thermal response. These parameters vary if the thermal pulse frequency is swept. Depth profiling is possible by comparing experimental results and theoretical calculations based on the thermal diffusion equation. This technique is effective to measure the coating thickness or to quantify and distinguish between coating degradation and coating/substrate interface features.

The scanning vibrating electrode technique (SVET) was applied to verify the results obtained by the nondestructive methods (Chapter 10). SVET can detect the small current generated at the onset of corrosion sites in an electrolyte and is able to image corrosion processes underneath intact coatings. Acoustic microscopy, as well as fan thermographic images, showed excellent agreement to SVET results. Locations of high corrosion activity are indicated by both methods as local defects. Recommendations for the applications of NDE methods for coating characterization are given in Table 1.

**Table 1.** Recommendations for Characterization of Organic Corrosion Protective Coatings

Test problem	Recommended method
Polymer degradation	<ul style="list-style-type: none"> <li>• Acoustic reflectivity measurements</li> </ul>
Coating thickness	<ul style="list-style-type: none"> <li>• Thermal wave depth profiling</li> <li>• Acoustic Microscopy with front echo separation</li> </ul>
Coating substrate interface	<ul style="list-style-type: none"> <li>• Acoustic Microscopy</li> <li>• Surface wave techniques</li> </ul>
Delamination and corrosion under coatings	<ul style="list-style-type: none"> <li>• Acoustic Microscopy in the laboratory</li> <li>• Fan Thermography in the field</li> <li>• SVET in the lab</li> </ul>

### 1.3.2 Corrosion

#### ***Corrosion Mechanisms***

Several excellent articles deal with corrosion and its effects on aircraft structural integrity [6–9]. The commonly observed types of corrosion in aging aircraft structures include **general corrosion, crevice corrosion, pitting, exfoliation, intergranular corrosion, corrosion fatigue and stress corrosion cracking**. Each of these corrosion types represents a different problem for NDE requiring different detection tools. While corrosion by itself rarely causes aircraft component failure, corrosion often leads to early crack initiation, which then may cause premature failure. So, from an aircraft maintenance perspective, the most severe corrosion type depends more on the type of stress concentration generated rather than the amount of material corroded.

**General Corrosion:** The most basic form of corrosion is general or uniform corrosion. While uniform corrosion is normally associated with low carbon steels, it is often under this framework that corrosion is investigated in maintenance depots when inspecting aluminum alloy airframe components. Often thinning, or component thickness loss, is the metric that is measured in the field, without regard for localized attack.

General corrosion is a homogeneous attack on the material in which material dissolution is the primary issue. The effect of this attack is to increase the loading upon the component as a smaller cross-section is forced to carry the load. This is probably the least severe form of corrosion that affect airframe structural integrity.

**Crevice Corrosion:** Crevice corrosion is a localized attack in an occluded region of the structure that does not have ready access to the bulk environment. Aircraft are fastened structures, so there is a multitude of sites that can initiate crevice corrosion. In a structure that is fully submerged in an aqueous environment, the crevice becomes depleted in the cathodic reactant, such as dissolved oxygen, because the diffusion barrier associated with the crevice prevents replenishment from the bulk environment. This leads to a physical separation in the location of the anodic and cathodic half reactions, with anodic reactions primarily occurring inside the crevice region and most of the cathodic reaction occurring outside of the crevice. Hydrolysis of the dissolved cations and inward migration of chloride ions lead to a decrease in pH and an increase in the aggressiveness of the environment within the crevice, which stabilizes the corrosion in the crevice. The unfavorable cathode-to-anode area ratio further accelerates the rate of attack within the crevice.

The situation is somewhat different for crevices in aircraft. For the most part, the bulk environment is not an aqueous solution. Some internal environments can be liquid, but the exterior environment is the atmosphere, which can include humidity, precipitation, atmospheric contaminants and salt spray. There is a source of water and aggressive species, but the exposure is usually cyclic in nature. For much of the time in service, the external surface is relatively dry so

that there is no ionic connection between the inside of a crevice and the rest of the structure. Water and other species can enter occluded regions quickly by capillary action when the exterior is wet, but the time for drying of a crevice can be considerably longer because of those same capillary forces. As a result, crevices in aircraft structures are often isolated from the external environment, and both the anodic and cathodic half reactions occur inside of the crevice. The pH within such an isolated crevice tends to be slightly alkaline rather than acidic, and the morphology of attack tends to be different.

Crevice corrosion can occur at locations of naturally high stress concentrations, such as adjacent to rivet holes, fasteners, or lap joints. The localized crevice attack can then lead to crack initiation, which can propagate faster in these locations under high stresses. This form of attack is particularly dangerous as it is often hidden from detection by the surrounding structure.

**Intergranular Corrosion and Exfoliation:** Intergranular corrosion (IGC) is an attack that follows the grain boundaries of the material because of local differences in composition at or near the grain boundaries. In the case of high strength 2xxx and 7xxx series of aluminum alloys, which are widely used in structural applications on aircraft, active grain boundary particles and the copper-depleted region adjacent to the grain boundaries are attacked, leaving room for the electrolyte to enter the material and continue the attack (see Fig. 4). As the corrosive attack grows deeper into the material, the corrosion rate decreases with time because it is controlled by electrolyte transport mechanisms in the narrow grain boundary region. The high strength 2xxx and 7xxx alloys used on aircraft are usually wrought, so they have a microstructure that is elongated in the working direction. The microstructure in a structural component is usually aligned such that the long grain dimension is parallel to the stressing direction. For example, sharp IGC cracks can initiate at fastener through holes where the end grain structure might be exposed to a crevice corrosion solution, and then propagate along the grain boundaries, which are usually in the stressing direction. Such cracks are also difficult to find because, like crevice attack, they are buried in the structure. However, a considerable amount of IGC can be sustained along the stressing direction because there is little net loss in section, and little resultant increase in stress for a given load. On the other hand, any off-axis deviation in the growth direction can lead to the situation where the IGC crack is perpendicular to the loading direction, which can result in the initiation of stress corrosion cracking or corrosion fatigue. If the microstructure in a component is oriented such that the stresses are in the short transverse direction (perpendicular to the elongated grain structure), then the rate of propagation can be quite large.

IGC initiating at or near the working surface of wrought structures can lead to exfoliation corrosion. The product formed when Al corrodes has a greater volume than the metal that was consumed in the corrosion process. When the attack is localized at grain boundaries in an elongated microstructure, and when it occurs near the surface of the structure, the voluminous corrosion product can create forces that wedge open the grains, thereby exposing fresh material to the

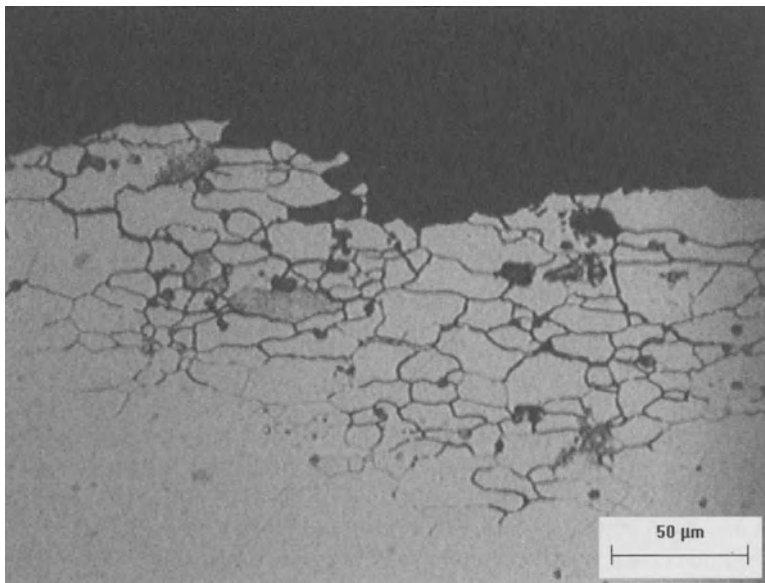


**Fig. 4.** Intergranular corrosion in Al 2024-T3



**Fig. 5.** Exfoliation corrosion in Al 7178 upper wing material (courtesy of S&K Technology)

environment. Because of this, the rate of exfoliation does not decrease with time like it does for the growth of sharp intergranular corrosion. Exfoliated material loses its load-bearing capability, so as the exfoliation propagates from the surface into a component, the load-bearing area decreases and the stress increases. This can lead either to overload failure or crack initiation at the bottom of the exfoliated zone.

**Stress Corrosion Cracking and Corrosion Fatigue:** Stress corrosion cracking (SCC) is cracking that results from the synergistic action of tensile stress and an aggressive environment. The stress can be from either an applied external load or residual stress from finishing operations, shot peening, or other treatments. Crack propagation is typically in a direction perpendicular to the loading axis. SCC in high strength Al alloys is usually intergranular in nature and is associated with Cu-depleted grain boundary regions, like IGC. The tensile stress accelerates the attack by keeping the crack open to allow access of electrolyte and by rupturing protective passive films at the crack tip. Hydrogen generated at the crack tip in Al alloys might also play a role in the embrittlement process.

Many aircraft components are subjected to cyclic rather than constant loading as a result of the vibrations associated with flying and the more traumatic take off and landing events. Crack propagation resulting from the synergistic interaction of a varying stress and an aggressive environment is called corrosion fatigue.

The simultaneous aggressive action of stress and environment required for SCC and corrosion fatigue is not always present for aircraft. Many aircraft spend most of their flight hours at very high altitudes where the temperature is extremely low. Any aqueous environment present in a crevice or pit will freeze at typical cruising altitudes and corrosion will cease. Furthermore, when aircraft are stationary on the ground (which is the case for much more of the service life of a military aircraft compared to a commercial plane), they are exposed to the environment, but the stresses are static and result only from the dead load of the plane itself. Military aircraft can have missions at low altitude and near the aggressive environment of the sea. Furthermore, the stresses exerted during takeoff and landing typically occur at close to ambient temperature. Nonetheless, the mechanical stresses exerted during flight and the environmental stresses exerted on the ground are usual sequential rather than simultaneous.

**Pitting Corrosion:** Pitting corrosion is accelerated attack that occurs at sites of local breakdown of an otherwise protective passive film on a boldly exposed area (i.e. not a creviced area). Pit environments become acidic and rich in chloride for the same reasons that were stated above for crevices. Therefore, pits are autocatalytic and tend to continue to grow once initiated. High strength 2xxx and 7xxx series aluminum alloys are very susceptible to pitting corrosion because of their heterogeneous microstructures. Cu-rich intermetallic particles act as efficient cathodes and Mg- and/or Zn-rich particles can be very reactive and therefore act as sites for initiation of pits [10–12].

Pitting is one of the most destructive forms of corrosion. Although only a small percentage of the metal is dissolved, the result can lead to crack initiation or perforation of the structure in a short time. It is difficult to detect pits due to their small size.

**Corrosion Initiation of Fatigue Cracks:** As mentioned previously, aircraft components rarely fail due to corrosion alone. However, corrosion is often the primary reason for fatigue crack initiation, which does lead to catastrophic failure [13–15]. Corrosion has been recognized as the cause of fatigue crack initiation in many aircraft structural failures. The loss of the upper fuselage section in an Aloha Airlines aircraft during flight and the failure of the trailing edge flap hinge of an Australian F/A-18 are documented failures resulting from fatigue cracks that initiated from corrosion pits [16]. Extensive intergranular cracking has been observed to emanate from severe pitting in the bores and countersink areas of fastener holes in the wing box lower panel of a fighter aircraft [17].

Corrosion and fatigue damage often compete with each other in structures under cyclic loading. When the pit growth rate is smaller than the damage produced under fatigue for crack nucleation, the pit transforms into a crack. The pit creates high stress intensity at its tip. These types of flaws are called stress raisers because of their ability to concentrate the applied stress [18].

### NDE Methods for Detection of Corrosion

Figure 6 summarizes typical corrosion defects (left) and methods for nondestructive detection (right). Surface acoustic waves and x-ray methods have been used to study cracks generated from corrosion sites and to develop a model for fatigue life prediction (Chapter 4 to 6). Chapter 3 will also demonstrate the application of x-ray methods for real-time in situ observations of the progression of corrosion damage. X-rays can be used as a laboratory method to quantify corrosion processes and to determine corrosion kinetics parameters.

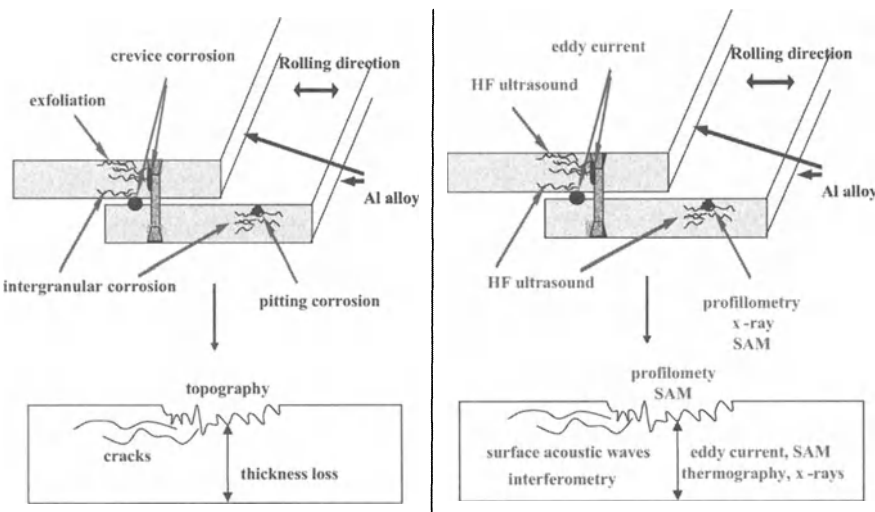


**Fig. 6.** Types of corrosion defects (*left*) and recommended NDE techniques (*right*)

The important material parameters that are discussed for life-prediction models are thickness loss and surface roughness or surface topography at corroded sites. Very precise topographic results are available using white light interference microscopy (WLIM). Chapter 2 will discuss the application of this technique for quantification and evaluation of corrosion defects. Parameters determined by WLIM can be used to calculate the stress intensity factors of corrosion pits, which show an excellent correlation to the fatigue life of corroded test specimens.

Micro-focus x-ray techniques can be employed to quantify hidden corrosion. The gray scale in the x-ray image is analyzed to quantify corrosion depths and thickness loss (Chapter 3). Pixel by pixel comparison between topography calculated from x-ray images and measured by white light interference microscopy indicates that neither technique show the complete damage. White light interference microscopy has better resolution than x-rays and shows smaller details. However, tunnels or holes that are shadowed by other material surfaces, are not visible with this method.

Acoustic microscopy also can be used for quantification of hidden corrosion. Different types of corrosion are indicated by different image structures. Acoustic microscopy may also show additional degradation around the corroded pits, due to exfoliation or intergranular corrosion, which is not visible in x-ray and optical profilometric results.

Chapter 6 presents interferometric and laser optical techniques for the detection of surface defects. A method to enhance the detectability of surface cracks by thermo-optical modulation will be discussed in Chapter 4. Table 2 summarizes recommendations for the application of several NDE techniques for corrosion detection.

**Table 2.** Recommendations for NDE Methods for Corrosion

Test problem	Recommended method
Quantification of corroded surfaces	<ul style="list-style-type: none"> <li>• Optical profilometry</li> </ul>
Thickness loss	<ul style="list-style-type: none"> <li>• Ultrasound (first layer only)</li> <li>• Thermography (first layer only)</li> <li>• Multi frequency or pulsed eddy current</li> </ul>
Exfoliation	<ul style="list-style-type: none"> <li>• HF Ultrasound (with phased array at fasteners)</li> </ul>
Quantification of hidden corrosion (topography and thickness)	<ul style="list-style-type: none"> <li>• Micro-focus x-ray</li> <li>• Acoustic microscopy</li> </ul>
Observation of corrosion processes in the laboratory	<ul style="list-style-type: none"> <li>• Micro-focus x-ray</li> </ul>

### 1.3.3 Fatigue

Fatigue is one of the most important classes of damage leading to crack initiation, propagation and failure in aircraft structures [19–20]. Therefore, aircraft designers are faced with the problem of accurate structural load predictions and reasonable material selection to produce lightweight and damage tolerant components. Despite extensive design efforts, flaw generation in technical components can still occur during service.

In contrast to static mechanical loading, fatigue loading implies repeated application of stresses between maximum and minimum values. The appearance of failures and fracture of technical parts occurring as the consequence of fluctuating loading conditions lower than the breaking strength (maximum strength) of the material is responsible for the usage of the term “fatigue”. The number of loading cycles  $N_f$  required for fracture to take place is usually from  $10^3$  to as much as  $10^9$  depending on the material, its composition, previous history (heat or mechanical treatment, preloading history) and the conditions of the loading (type of stress, frequency of cycling, temperature, nature of the environment). The number of cycles until fracture  $N_f$  in the range below  $10^5$  cycles is usually referred to low cycle fatigue (LCF). When  $N_f$  is higher than  $10^5$ , the fatigue process is referred to high cycle fatigue (HCF). An important factor in fatigue behavior influencing  $N_f$  is the nature of the surface, because the flaw initiation occurs at surfaces, in particular outer surfaces but also internal surfaces [29, 30]. The loading time or loading cycle frequency is also significant. Fatigue damage definitions generally consider a permanent change in material or structure properties due to the exposure to repeated mechanical loading that lead to cracking and eventually to failure [20]. Fatigue failures occur in many different forms due to the various damage mechanisms. Thus, apart from mechanical fatigue, which appears solely due to external stresses or strains, other forms of fatigue are defined. For instance, creep fatigue or thermo-mechanical fatigue occur when additionally high temperature exposure is relevant, corrosion fatigue when chemically aggressive environment contributes to a faster cracking or fretting fatigue occurs when frictional sliding between surfaces is responsible for material damage [20].

A major topic of concern is fatigue of engine components. Aircraft engine failure under high cycle fatigue conditions can result from damage nucleated during processing or by in-service loading and environmental conditions. Additional causes of failure, primarily for titanium-based alloys are listed below:

- Low cycle/ high cycle fatigue loading,
- Fretting,
- Foreign object damage,
- Corrosion,
- Temperature induced microstructural changes,
- Thermal shock and
- Interactions between the above conditions.

Conservative design approaches assume the pre-existence of a crack and examine the behavior of its growth under cyclic loading. This design methodology is based on fracture mechanics and is applied in structural design to predict

component life [21–22]. The success of a fracture mechanics design philosophy relies on the detection of small cracks, and thus, nondestructive inspection methods. Based on the detected defect size, the remaining component lifetime can be predicted under the assumed loading conditions. Such design approaches result in lighter components, but requires periodic inspection.

The titanium alloy containing 6% aluminum and 4% vanadium (Ti-6Al-4V) is commonly used in aircraft engines and structures because of its excellent mechanical strength to density ratio and corrosion resistance. A fracture mechanics life prediction methodology is problematic in such alloys since early detection of very small cracks is difficult. Local microstructural inhomogeneities inhibit generation of reliable crack growth and material property data [22]. Under service conditions, such as high cycle fatigue (HCF), Ti-6Al-4V exhibits low tolerance to small cracks. Very small non-detectable cracks can become unstable and result in catastrophic failure. During in-field inspections, the minimum crack size that can be detected is limited by the nondestructive inspection methodologies [19, 23]. Therefore, the smallest detected crack size can be used to estimate the actual strength of the component. The critical crack length at fracture,  $a_c$ , is related to the applied stress,  $\sigma_{\max}$ , and fracture toughness of the material,  $K_c$ , as defined in the following expression [24]:

$$a_c = \frac{1}{\pi} \cdot \left( \frac{K_c}{Y \cdot \sigma_{\max}} \right)^2 \quad (1)$$

where  $Y$  is a geometry dependent constant.

Aircraft components are designed to provide the most efficient use of the alloy under high loading conditions. The high strength (yield strength approximately 1000 MPa) and low density of titanium alloys make them ideally suited to these high mechanical loading conditions. As shown in (1) however, an increase in the maximum applied stress  $\sigma_{\max}$  reduces the critical crack length  $a_c$  disproportionately. By comparison, many high strength steels exhibit similar values for  $K_c$  but operate at a lower maximum stress level. Thus, the critical crack length  $a_c$  for steel components is significantly larger than for applications employing Ti-6Al-4V.

The detection of such small cracks in titanium components poses a significant problem for nondestructive inspections and ensuring structural integrity. During service, a significant fraction of the fatigue life is spent during the early stages of fatigue prior to the detection of stable crack growth. Especially under high cycle fatigue conditions, more than 90% of lifetime is spent before cracks can be detected by standard techniques. As discussed above, limitations due to the inspection methods and microstructural variability prevent crack detection earlier in the fatigue life. Crack nucleation processes in titanium are further complicated by the generation of subsurface cracks resulting from fatigue induced compressive stresses within the surface region [25].

## Fatigue Damage Mechanisms

Fatigue failures occur in many different forms due to the various damage mechanisms. Thus, apart from mechanical fatigue, which appears solely due to external stresses or strains, other forms of fatigue are defined. For instance, creep fatigue or thermo-mechanical fatigue occurs when high temperature exposure is involved. Temperature oscillations generate thermo-mechanical fatigue due to thermal induced stresses. Corrosion fatigue occurs when chemically aggressive environment contributes to a faster cracking and fretting fatigue occurs when small amplitude relative motion between surfaces is responsible for material damage [20]. This section, however, focuses solely on fatigue caused by cyclic mechanical stressing.

Fatigue in materials is often discussed as a cumulative damage process because of its permanent progressive nature [31]. The internal mechanisms of fatigue can be very complicated, since cyclic hardening, phase transformation, recrystallization, dislocation generation, dislocation migration, dislocation network building, macro shear band formation, and surface slip steps might occur simultaneously. These internal mechanisms generate or at least contribute indirectly to microplastic deformations. First, the accumulation of local plastic deformations leads to crack initiation. When a crack is initiated and can further grow the lifetime is solely determined by the rate of crack growth until the material's static fracture strength is reached and a failure of the entire component appears. It follows that the entire fatigue lifetime can be divided into three characteristic stages: crack initiation, crack propagation and overload fracture.

**Crack Initiation:** The initial stage of fatigue damage is characterized by the absence of cracks. The permanent (sub-) microstructural processes occurring during this stage lead to microcrack initiation due to the accumulation of local microplastic deformations through dislocation motion and restructuring. The crack initiation mechanisms might differ in materials and even vary within a specific material due to varied external loading conditions. The lattice defects (e.g., vacancies, dislocations, grain boundaries) responsible for mechanical properties act as stress concentrators. Thus, the microstructure takes part in the fatigue process. Several micro-fracture mechanical models of crack initiation are discussed in the literature including dislocation cell formation and slip band formation or micro-cracking at grain boundaries due to dislocation pile-ups [29]. Some of these microcracks stop growing, some continue to grow and new ones may be formed. Finally, the dominant crack emerges and become critical for the total lifetime of the component. This crack signifies the change from the initial stage to the following stage of crack growth. This period of fatigue process can be identified with the so called early stages of fatigue. The general definition refers to the initial microstructural process leading to fatigue damage accumulation (lattice defects and slip band formation) and the initiation of fatigue cracks. From the theoretical or scientific point of view when a crack is initiated the early stage is terminated and stable crack growth follows. However, from an engineering point of view, the appearance of fatigue cracks is determined by crack detectability, which depends on the technical sensitivity of the methods used to monitor cracks.

**Crack growth:** After crack initiation occurs and crack growth begins, the crack propagation and its size can then be identified on the fracture surface by beach marks and striations. The fatigue process focuses on the growth of a single dominant crack, which eventually becomes detrimental for the residual life. Thereby, the crack growth dynamics determine the residual lifetime and failure. The relevant fatigue damage accumulates primarily in a local manner within the crack area. However, other microcracks might still be generated during this period with little or no influence on lifetime. During this stage a fracture mechanics approach can satisfy the prediction of the residual lifetime in many cases. Within this stage, the Paris-relation can be employed to predict the residual lifetime until fracture, based on the identified crack length, the mechanical loading conditions and the critical stress intensity factor (critical fracture toughness,  $K_c$ ) of the material [22].

**Unstable crack growth and fracture:** The increase of the crack size leads finally to the exceeding of the critical stress intensity factor  $K_c$  (see (1)). From this follows an unstable crack growth, until the last stress cycle when the cross section is unable to sustain the applied load and structural instability or complete fracture occurs.

**Fatigue life:** The total fatigue life  $N_f$  (number of fatigue cycles until fracture) is the sum of fatigue cycles during the early stages until crack initiation  $N_i$  and the number of fatigue cycles during the stable crack growth until fracture  $N_c$ . The ratio  $N/N_f$  can vary significantly depending to the material, fabrication of the component (surface roughness), the loading and the environmental conditions. In some cases, crack initiation occurs after few cycles, as has been discussed for stainless steel. In contrast titanium alloys can have more than 90% of its lifetime spent on detectable crack initiation under certain loading conditions. Often technical components are already pre-damaged, for instance due to the machining process or significant materials impurities. Thus, no crack initiation period appears and the fatigue process starts practically at the second stage. However, high quality standards of the material and machining processing can prevent the existence of such pre-flaws.

### ***NDE Methods for Characterization of Fatigue Damage in Nonferrous Aircraft Materials***

This section gives a brief overview on currently known NDE principles for fatigue damage characterization. Thereby, the sensitivity of the characterization method to microstructure and defects on the micro scale is highlighted out because it is mandatory for early stage fatigue characterization. The focus is set on methods for non-ferromagnetic materials since the physical principles might be very different in ferromagnetic materials. State-of-the-art in NDE of fatigue for ferromagnetic materials, as well as recent results on new and advanced methods – for instance the SQUID method – are discussed in the literature [26]. The well-known Barkhausen-noise method is very sensitive to microstructure variations in steel during the early stages of fatigue [27, 28].

Due to the late appearance of detectable cracks in titanium structural components, significant improvements in safety cannot rely solely on nondestructive crack inspection. Thus, the challenge is to develop methods for characterizing material degradation caused by fatigue during the early stages of fatigue when no detectable cracks are present. The early stages of fatigue damage are characterized by changes in materials microstructure, especially the accumulation of crystal lattice defects such as dislocations leading to crack initiation [20, 32]. Characterization of crystal lattice defects is possible using transmission electron microscopy [33] or positron annihilation methods [34–35]. These methods, however, are laboratory techniques that are performed on sectioned specimens. At present, there is no reliable technique that can be applied on technical components to detect the onset of failure during the early stages of fatigue. Thus, new nondestructive evaluation (NDE) approaches are required to develop methods capable of nondestructive characterization of fatigue prior to crack nucleation.

The interaction between low cycle and high cycle fatigue can be responsible for catastrophic failure without sufficient warning by generation of visible microcracks. Microstructure variation, particularly changes in the dislocation density and dislocation structure, has to be studied and detected to indicate the degradation of microstructure leading to generation of fatigue cracks.

Nonlinear acoustics is one of the methods that have potential to quantify changes of the dislocation structure (Chapter 7). Materials are inherently elastically nonlinear, but for practical applications, they are treated as linear elastic materials that follow Hooke's law. A pure sinusoidal acoustic wave propagating through a material is distorted due the nonlinear elastic behavior. This gives rise to higher order harmonic signals. The normalized ratio of the absolute amplitude of the second harmonic acoustic signal to the square of the fundamental signals is defined as a dimensionless nonlinear acoustic parameter of the material. The nonlinear acoustic parameter has been found very sensitive to the state of the fatigue damage of the material.

Thermo-mechanical and thermo-acoustic characterization techniques will be discussed in Chapter 9. These techniques have high potential for field applications. The mechanical energy resulting from the stress strain hysteresis is transferred into heat if a test object is cyclically loaded. The heat generated during one cycle varies with fatigue life. The thermo-mechanical fatigue testing makes use of this principle by exposing the test object to several cycles of mechanical load. A thermographic camera observes the process and a sequence of video frames is stored in the computer for a time period of 10 to 20 seconds. The rate of heating of the test specimen is calculated from this sequence. A thermal parameter that describes the heat generated per hysteresis cycle is calculated from the slope of temperature versus time curve. This parameter was found very sensitive to the fatigue state of the material.

The measurement of thermo-electric power of a specimen is a promising technique to characterize the microstructure state and residual stresses [36]. Other techniques of consideration for the characterization of dislocation density and microstructure variations are positron annihilation (Chapter 13), and the acoustic reverberation technique (Chapter 8). Positron annihilation is sensitive to the very

early stages of fatigue. Parameters measured by positron annihilation showed saturation for approximately 20% of fatigue life. A further increase in dislocation density does not result in an increase of the positron lifetime and narrowing the 0.51 MeV positron annihilation line.

Real time holography has been developed to monitor growing cracks during fatigue experiments (Chapter 6). This optical technique images the surface displacement due to surface waves that propagate at the specimen surface. At cracks the displacement amplitude is enhanced and can be imaged in real time using holography.

White light interference microscopy has been applied to characterize the stability of a fatigue crack (Chapter 2). A certain load was applied to the specimen and the displacement field in front of the crack tip was characterized by white light interference microscopy. By characterizing this displacement field a criteria for crack stability had been established.

Figure 7 illustrates the problems for nondestructive fatigue characterization in Ti-6Al-4V. Microcracks are not detectable during the first 90–95% of fatigue life. If they exist, they are below the detectability level of NDE methods (except for high frequency scanning acoustic microscopy). The figure also compares the sensitivity range of several techniques for characterization of fatigue.

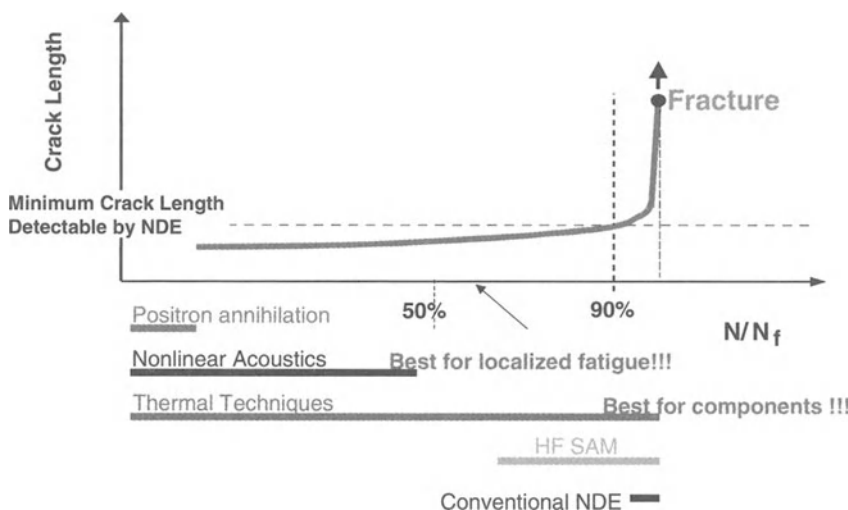


**Fig. 7.** NDE of fatigue damage

### 1.3.4 Fretting and Fretting Fatigue

Fretting fatigue occurs as a result of vibrational loading of two surfaces in contact. The dovetail joint in gas turbine jet engines is one example of a fretting fatigue-prone component. Unexpected life reductions of 70% or more result from early crack initiation in the contact region [37].

#### ***Fretting and Fretting Fatigue Mechanism***

Depending upon the loading conditions, as well as material properties, two surfaces in contact may *slide* against each other, *stick* to each other, or result in a state of *partial slip* or *slip-stick*. It is important to distinguish between ‘sliding’, which is the bulk displacement of one body relative to another resulting in wear and ‘slip’, which occurs at a part of an otherwise adhered interface resulting in fretting fatigue (Fig. 8).

It is important to recognize that the area of contact in the partial slip regime may be composed of a complex pattern of stick regions and slip regions, where relative tangential displacement of corresponding particles on the two contacting bodies occurs, limited only by the coefficient of interfacial friction. It is the elasticity of the bodies that permits them to slip past each other in one region while sticking in another region. In the slip regions, the relative movement causes the expenditure of frictional energy, which provides structural damping, but at the same time causes surface degradation (scar) and the generation of a small amount of heat. The form of the surface degradation varies considerably according to the material combination, the state of stress, the amplitude of the motion, the presence or absence of surface treatment and contaminants, the nature of the surrounding environment, and also the geometry of the contact itself.

The damage associated with each of these regimes is different. Under the stick regime, essentially no damage occurs while wear and particle detachment is the main damage mechanism of sliding surfaces. Under sliding conditions, the material may not be subjected to significant elastic or plastic strains. The amount of surface degradation is often lower than in the partial slip regime. Thus, in the stick and slip regimes, life reduction is minimal [38]. In the partial slip regime of fretting fatigue, however, due to the initiation of cracks, the life expectancy of the material is significantly shortened. Severe surface degradation and the initiation of cracks are characteristics of the partial slip regime [39, 40].

In the partial slip regime of fretting fatigue, the magnitude of normal force is high enough and the amplitude of the oscillatory sliding motion is small enough to significantly restrict the flow of debris away from the originating site [40]. This may affect the nature of the surface damage and the rate of propagation of initiated cracks.

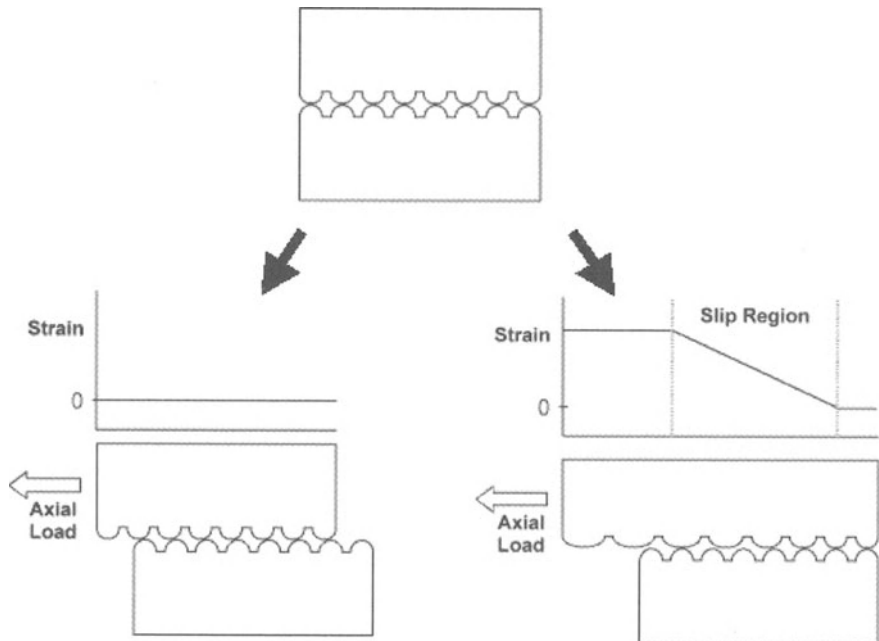


**Fig. 8.** Schematic of the difference between sliding (*left*) and partial slip (*right*)

It has also recently been suggested that the contacting surfaces periodically separate and reengage, resulting in bonding and subsequent shearing or detachment of the surface material [41]. The entrapment of this wear, oxidation, and corrosion debris promotes surface damage while high shear stresses bring about localized plasticity in slip regions.

### **NDE of Fretting Fatigue Damage**

Due to the damage mechanism discussed above, fretting fatigue damage is usually very localized and affects only a surface layer of the material. Characterization of fretting fatigue damage is therefore, one of the most challenging tasks for NDE and a lot of further research will be required. In Chapter 2, an optical technique for the early detection of fretting fatigue damage is presented. This non-contact method is based on profilometric images measured by white light interference microscopy. Image analysis and the determination of the power spectral density give evidence to surface modifications due to fretting. Using this principle, it was possible to determine a damage parameter, which can be correlated to the fretting fatigue damage.

## 1.4 Introduction to the Next Chapters

The following chapters of this book discuss a variety of NDE methods to detect and quantify damage in nonferrous metals, polymer coatings and microelectronic structures. Most of these methods or applications are still in the laboratory stage. So, this book is a “snapshot” of the present state of research and does not claim to give a complete overview over the myriad of different methods and applications of nondestructive materials characterization. Every chapter gives a brief introduction to the method or the methods used. More detailed information about each of these methods can be found in the referenced literature. A major part of each chapter is the discussion of recent applications highlighting the capabilities and limitations of the method in the research laboratory on aircraft materials. The volume of these applications might vary from chapter to chapter. However, the length of the chapter does not reflect the importance of the method presented.

Chapter 2 describes applications of White Light Interference Microscopy (WLIM). This method is only able to analyze surface profiles and required access to the tested surface. In contrast, the x-ray methods discussed in Chapter 3 image internal material flaws. Chapters 4 to 6 present different applications of surface acoustic waves to detect surface cracks initiated by fatigue, corrosion or combinations of both. The following Chapters 7 and 8 present (nonlinear acoustics and acoustic reverberation technique) to characterize microstructure changes of materials respectively. Different microscopy techniques such as Scanning Vibrating Electrode Technique (SVET), Scanning Acoustic Microscopy (SAM), Atomic Force – and Ultrasonic Force Microscopy (AFM/UFM) are presented in Chapters 10 to 12. A potential high-resolution method for evaluation of thin surface layers is microellipsometry. This will be discussed in Chapter 13. Finally, Chapter 14 will introduce positron annihilation as a NDE method that is capable to characterize defects of atomic dimensions in the material.

## References

1. Kinzie R, Cook G (1998) Cost of Corrosion Maintenance. 2nd joint NASA/FAA/DoD Conference on Aging Aircraft
2. Shell EB (2002) Prediction of Residual Fatigue Life from NDE of Corroded Components. PhD. Dissertation, University of Dayton
3. Kinzie R (1994) Proceedings of Tri-Service Corrosion Conference. USA, pp. 3–25
4. Khobaib M (1997) Corrosion Prevention Technology for Advanced Aircraft Coating Systems. Final report for US Air Force, contract-number F 33615-94-C-58-04
5. Jeffcoate CS, Voevodin NN, Khobaib M, Reynolds LB, Kuhn WK, Donley MS (1998) Future trends on non-chromate corrosion inhibitors. 43rd International SAMPE Symposium and Exhibition (Proceedings) 43, pp. 2113–2122
6. Cole GK, Clark G, Sharp PK (1997) The implications of Corrosion with Respect to Aircraft Structural Integrity. Aeronautical and Maritime Research Laboratory, Melbourne, Australia, Research Report DSTO-PR-0102, AR-010-199
7. Chen GS, Gao M, Wei RP (1996) Microconstituent-Induced Pitting Corrosion in Aluminum Alloy 2024-T3. Corrosion Science, vol. 52, No. 1:8
8. Rokhlin SI, Kim JY, Nagy PB, Zoofan B (1999) Effect of pitting corrosion on fatigue crack initiation and fatigue life. Engineering Fracture Mechanics 62:425–444
9. Connolly BJ, Scully JR (2000) Corrosion cracking susceptibility in Al-Li-Cu alloys 2090 and 2096 as a function of isothermal aging time. Scripta Mater 42:1039–1045
10. Goswami, Tarun K, Hoeppner DW (1995) Pitting Corrosion Fatigue of Structural Materials. Structural Integrity in Aging Aircraft, ASME, AD-vol. 47:129–130
11. Frankel GS (1998) Pitting Corrosion of Metals. Journal of the Electrochemical Society, vol. 145:2188–2190
12. Marcus P, Oudar J (eds.) (1995) Corrosion Mechanisms. In: Marcel Dekker Inc. Theory and Practice, New York, pp. 201–237
13. Chen GS, Wan KC, Gao M, Wei RP, Flournoy TH (1996) Transition for Pitting to Fatigue Crack Growth-Modeling of Corrosion Fatigue Crack Nucleation in a 2024-T3 Aluminum Alloy. Materials Science and Engineering A 219:126
14. Piascik RS, Willard SA (1994) The Growth of Small Corrosion Fatigue Cracks in Alloy 2024. Fatigue and Fracture of Engineering Materials and Structures, vol. 17, No. 11:1247–1248
15. Ahn SH, Lawrence Jr. FV, Metzger NM (1992) Fatigue Fracture Eng Mater Struct 15:625
16. Barter S, Sharp PK, Clark G (1994) The Failure of an F/A-18 Trailing Edge Flap Hinge. Engineering Failure Analysis, vol. 1, No. 4: 255
17. Wallace WW, Hoeppner DW (1985) AGARD Corrosion Handbook, vol. 1, Aircraft Corrosion: Causes and Case Histories. AGARDograph No. 278, NATO, p. 101
18. Callister WD Jr. (1994) Materials Science and Engineering: An Introduction, 4th ed. Wiley, New York
19. Cooper DC, Kelto CA (1978) Fatigue in machines and structures—Aircraft. Fatigue and microstructure: Materials science seminar, Proc ASM pp. 29–56
20. Suresh S (1991) Fatigue of Materials. Cambridge University Press, Cambridge, p. 10
21. Finney JM (1994) Fatigue crack growth in metallic military aircraft structures. Handbook of fatigue crack propagation in metallic structures, Elsevier Science B.V., Amsterdam

22. Gregory JK (1994) Fatigue Crack Propagation in Titanium Alloys. *Handbook of fatigue crack propagation in metallic structures I-II*, Elsevier Science B.V., Amsterdam
23. Hagemer DJ (1991) Application of crack detection to aircraft structures. *Fatigue crack measurement: Techniques and applications*. Engineering Materials Advisory Services, London
24. Blumenauer H, Push G (1993) *Technische Bruchmechanik*. Deutscher Verlag für Grundstoffindustrie, Leipzig /Stuttgart
25. Lütjering G, Gysler A (1985) Fatigue in titanium: Science and technology, *Titanium science and technology: Proc 5th Int Con on Titanium*, Deutsche Gesellschaft für Metallkunde DGM, Oberursel
26. Lang M (2001) Ph.D. thesis, University of Saarbrücken, performed at IZFP-FhG
27. Moorthy V, Choudhary BK, Vaidyanathan S, Jayakumar T, Bhanu Sankara Rao K, Raj B (1999) An assessment of low cycle fatigue damage using magnetic Barkhausen emission in 9Cr-1Mo ferritic steel. *International Journal of Fatigue* 21:263–269
28. Dobmann G (1995) Early fatigue damage from the NDE point of view. *Review of Progress in Quantitative Nondestructive Evaluation* 14:2003–2010
29. Schatt W, Worch H (1996) *Werkstoffwissenschaft*. Deutscher Verlag für Grundstoffindustrie, Stuttgart, p. 378, pp. 394–397
30. Zenner WH (1973) Schadensakkumulationshypothesen zur Lebensdauervorhersage bei schwingender Beanspruchung. Teil 1 – Ein kritischer Überblick. *Zeitschrift für Werkstofftechnik / Journal of Materials Technology* 4(1):25
31. Puskar A, Golovin SA (1985) Fatigue in materials: cumulative damage processes. Elsevier, New York, pp. 274–281
32. Xiaoli T, Haicheng G (1996) Fatigue crack initiation in high-purity titanium crystals. *Int J Fatigue* 18:329–333
33. Maurer JL, Frouin J, Sathish S, Matikas TE, Eylon D (1999) Internal damage characterization of cyclically loaded Ti-6Al-4V, using TEM and non linear acoustics. *Proc 9th Titanium World Conference*, St. Petersburg
34. Karjalainen LP, Moilanen M, Myllylä R, Palomäki K (1980) Monotonic and cyclic deformation in mild steel detected by positron annihilation. *Phys stat sol (a)* 62:597–601
35. Uchida M, Yoshida K, Nakagawa YG, Allen AJ, Whapham AD (1992) Application of positron annihilation to fatigue and plastic damage detection in SA508 and type 304 steels. *Nondestr Test Eval* 7:83–91
36. Carreon H, Nagy PB, Blodgett MP (2002) Research in Nondestructive Evaluation 14:59–80
37. Petiot C, Foulquier J, Journet B, Vincent L (1994) In: Waterhouse RB, Lindley TC (eds.) *Fretting Fatigue*. ESIS 18 Mech Eng Pub London, pp. 497–512
38. Vinssbo O, Soderberg S (1988) On Fretting Maps. *Wear* 126:131–147
39. Zhou ZR, Sauger E, Liu JJ, Vincent L (1997) Nucleation and early growth of tribologically transformed structure (TTS) induced by fretting. *Wear* 212:50–58
40. Antoniou RA, Radtke TC (1997) Mechanisms of fretting-fatigue of titanium alloys. *Mat Sci Eng A237:229–240*
41. Fouvry S, Kapsa Ph, Vincent L (1995) Analysis of sliding behavior for fretting loadings: determination of transition criteria. *Wear* 185:35–46

## 2 Optical Detection of Surface Damage

E.B. Shell, M. Khobaib, J. Hoying, L. Simon, C. Kacmar, V. Kramb, M. Donley, D. Eylon

### 2.1 Introduction

In many applications, the onset of damage occurs at the component surface due to plastic deformation, fretting, wear, corrosion, or crack nucleation. One result of these processes is a change in the surface topography. Therefore, the first step in nondestructive evaluation of a component is a thorough evaluation of the surface conditions. Inspection techniques that characterize the damage extent on the surface often present the results as a fraction of the component surface area. For damage originating from environmental or mechanical conditions, the severity of the defect or damage can also be described quantitatively by the three-dimensional surface topography. When using many common inspection methods, information regarding the depth of penetration into the surface layers, or protrusion above the surface is difficult to obtain. In addition, when the defects are of submicron or nanometer scale, high resolution three-dimensional inspection techniques are required.

One method that provides three-dimensional surface profiles with a 3 nm vertical resolution is white light interference microscopy (WLIM) using vertical scanning interferometry. Thus far, white light interferometric methods have been used primarily for production quality control [1] while its use as a nondestructive evaluation (NDE) tool is largely unexplored. When used as an NDE tool, quantitative information can be obtained from the white light interferometry data by statistical analysis of the surface profiles, either directly or from transformations of the data. A quantitative measure of the surface features may then be useful in determining the extent of damage and remaining component life.

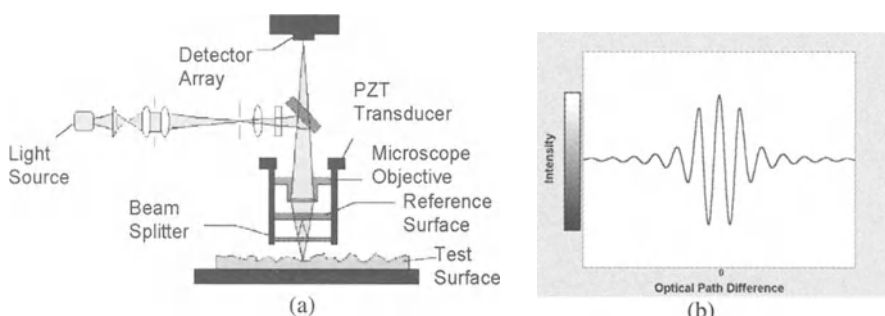


**Fig. 1.** (a) Schematic of a white light interference microscope; (b) Interference of beams from a white light source

The particular instrument used for these studies is the Wyko NT 2000 Optical Profiler [2], which is shown in Fig. 2.

In this section, the applicability of WLIM for the characterization of surface topography is discussed for several different applications, including detecting corrosion initiation and progression, fretting damage characterization, and surface crack characterization. Each of these applications has specific requirements for quantifying damage and establishing a relevant damage metric. The methods used to obtain a quantitative measure of damage and a metric that can be used to determine remaining component life will be discussed for these applications.

## 2.2 Background

White light interference microscopy is a relatively new tool to the NDE field. The technique is capable of height measurements with a resolution of 0.2nm (2Å) and a lateral resolution of 0.2 μm. However, this extreme vertical resolution comes at a high cost. In order to detect extremely small height changes, the instrument must be used in phase shift interferometry (PSI) mode. This limits the vertical range to just a few microns. However, a vertical resolution of about 3nm can still be achieved using vertical scanning interferometry (VSI) as will be described in this section, since this mode of operation is used nearly exclusively in most practical applications. VSI allows for a much larger vertical range, up to a few mm. The lateral resolution is enhanced by the use of optical objectives, as in a light microscope. The tradeoff for a higher lateral resolution is that a smaller field of view is obtained and multiple areas must be collected and merged to examine larger areas.



**Fig. 2.** Instrument used for the experiments

A white light interference microscope works essentially as a Michelson or Mirau-type interferometer that is scanned along the vertical axis to capture quantitative profilometric information about the surface of a specimen [3–5]. The instrument used in this study has an image analysis package that enables automated topographical calculations including height profiles, threshold surface area, surface depression volume, Fourier transforms, and power spectral density calculations.

The principle behind white light interference microscopy is based on the short coherence length of white light. Two beams of white light from one source can be combined to interfere with each other only if their paths are nearly the same distance (Fig. 1). Light beams of a single wavelength, such as from a laser, will interfere with each other over long distances. The short coherence enables a better absolute measurement of height on the specimen surface by only interfering over a short optical path difference.

## 2.3 Instrumentation and Method

White light interference microscopes use a white light source that is split into two beams. One beam is reflected off the surface of the specimen and the other is reflected off a reference mirror (Fig. 1a). The two reflected beams recombine to form interference fringe patterns. Fringe contrast reaches a maximum when the optical path difference between the reference and measurement beams reaches a minimum. At that point, the fringes indicate the surface area of the specimen that is near the calibrated interference height. Since the optical path difference varies from point to point on rough surfaces, vertical scanning is required to map the entire surface. A piezoelectric transducer enables vertical scanning. Typical transducers move the reference mirror in steps of 0.05 to 0.1  $\mu\text{m}$  over a distance of up to a few millimeters. Throughout vertical scanning, a CCD camera captures the fringe modulation. The region of interference is then recorded for each pixel and related to the location of the reference mirror along the z-axis. Digital signal processing hardware then demodulates the fringe data in real time. The result is a fast three-dimensional profile of a surface. White light interference microscopes also enable areas of a surface to be separated by surface height without the complexity and high cost of confocal instruments [5].

Vertical scanning interferometry works by moving the objective, including the beam splitter and reference mirror along the vertical axis. By using a piezoelectric transducer (PZT), the objective is scanned vertically while frames are captured by a CCD camera. When the reference plane (the plane which is the same distance from the beam splitter as the reference surface is) passes through the surface, an envelope of intensity fringes are seen moving across the surface. By recording the location of the PZT at which the primary fringes occur for each pixel location, a height map of the surface can be obtained. The resulting data can then be manipulated by various means.

Quantification of profilometry data can be customized for the particular application. The processing of profilometry data is highly flexible and is based on statistical analysis of the height measurements above or below the focal plane. Several analysis methods are available with the current system. For some applications, a direct three-dimensional topographical representation of the surface features contains the most relevant information. For topographical measurements of surface depressions, the distance below the metal substrate is measured and used to obtain total depression surface area and volume. Similarly, the roughness of the specimen can be evaluated either quantitatively by a roughness calculation or qualitatively by viewing a line scan of the specimen's surface. An evaluation of the surface height maps can also be performed to obtain a Fourier transform of the surface data. The Fourier transform is used to obtain the Power Spectral Density (PSD), which can be plotted against Spatial Frequency. For each application presented, the analysis of the profilometry data and suggested damage metrics will be discussed.

## 2.4 Applications

White light interference microscopy shows promise for the detection and monitoring of surface damage in a variety of applications, including fretting wear, corrosion, and surface cracking. Table 1 shows the application of WLIM for three types of damage that affect the test object in different ways:

**Table 1.** White light interference microscopy for NDE applications

	Fretting Fatigue Damage Detection	Characterization of Corrosion Defects	Deformation Field Ahead of a Crack Tip
Problem to Be Solved	Characterization of damage due to fretting fatigue	Quantitative analysis of corrosion pits and effect on fatigue life	Quantification of deformation at a crack tip
Information from White Light Interferometry	Distinguish between slip, stick and non- contact regions	Corrosion pit topography	Changes in deformation with increasing loads
Data Analysis	Calculation of power spectral density versus spatial frequency	Depth profiles in x- and y-direction of corrosion initiated pits	Two- and three- dimensional analysis of deformation zone
Results	Quantification of degradation and estimation of remaining life	Determination of pit properties affecting fatigue life	Instability criteria for surface cracks

1. Characterization of surface damage due to fretting.
2. Localized characterization of corrosion defects and their relation to the initiation of fatigue cracks.
3. The characterization of the fatigue crack itself by evaluation of the surface displacement field in front of the crack tip either during or after loading.

Analysis of the profilometry data is versatile, and can be customized for the particular application as summarized in Table 1. When used as an NDE tool, quantitative information can be obtained by statistical analysis of the surface data directly or from the Fourier-transformed data. In this study, a quantitative measure of the surface features was used to determine extent of damage and estimates of remaining component life. Each of the applications examined has specific requirements for quantifying damage and establishing a relevant damage metric. The methods used to obtain these quantitative measures of damage and damage metrics can be adapted to other applications to estimate remaining component life and damage progression.

Several example research studies are discussed, showing the potential for the method to be used in a variety of applications.

#### **2.4.1 Optical Quantification of Fretting Fatigue Damage**

##### ***Motivation***

Fretting fatigue has long been recognized as an important mode of failure in the service of mechanical components that are not intended to have a relative motion, but because of vibrational loads or deformations experience minute cyclic relative motions [6]. Such damage can result in a considerably lower component life. Fatigue strength under fretting fatigue conditions may be as low as 30% of the unfretted fatigue strength, depending upon the material and loading conditions [7]. This increased rate of damage accumulation, along with the unpredictability of the actual conditions experienced in use, necessitate a means for nondestructive examination of the surface and prediction of the remaining service life.

Fretting fatigue is a surface and near-surface phenomenon. Thus, surface NDE techniques may be particularly useful in the detection of fretting fatigue damage. However, this may be complicated by the initial surface conditions of the material. Because fretting damage is a very localized phenomenon, techniques developed to detect fretting damage must have a reasonably high spatial resolution. Although much research has been devoted to the understanding of fretting mechanisms, no characterization methodologies have been established for quantifying the level of fretting damage.

Currently, the procedure for the inspection of fretting fatigue critical components (e.g., as turbine engine fan blades and disks) is simply a visual inspection for the presence of any large surface irregularities during depot inspections. This led to the removal of many blades and disks either: (1) before there was a substantial amount of fretting damage, or (2) due to less dangerous surface deformation such as sliding wear.

In addition, this criterion has been proven ineffective when applied to laboratory-tested specimens. In fact, laboratory-testing conditions frequently lead to failure in specimens where the roughness of the surface is less than 3  $\mu\text{m}$ , well below what could be called a “large surface irregularity” during inspection. A new method that would allow for a better understanding of the fretting process is, therefore, needed. This may be achieved through observation of the inherent changes that may be universally observed, leading to the ability to quantify fretting damage and calculate residual component life.

### ***Concept of Precursor Damage Detection***

Because fretting fatigue is a surface and near-surface phenomenon, surface NDE techniques, particularly optical techniques, lend themselves to the detection and characterization of fretting damage. Most surface techniques are specifically designed for the detection of surface cracks. However, because high strength materials, such as titanium and nickel-base alloys, have relatively high crack initiation resistance but lower fracture toughness, methods that are used to detect cracks inherently require frequent inspection since the time from an initiated crack and final failure is short. Most of the lifetime is spent in the crack initiation phase, before cracks of sufficient detectability appear. In fact, some high-strength materials may not form a detectable crack before 95–99% of life has expired. This emphasizes the need for a method that detects damage appearing prior to cracking.

Instead of crack detection, it may be more beneficial to assess the material on the basis of the *likelihood of or potential for* crack initiation. This may be accomplished by evaluating the condition of the surface through such parameters as roughness and asperity spacing. These parameters relate, on a microscopic level, the material surface finish to the very localized stress concentration at the bases of the asperities geometry and spacing.

It is postulated that through fretting action, the morphology of these asperities changes. This change allows, through an analysis of the roughness and the spacing between adjacent asperities, an inference to be made as to the condition of the material and the changes that have occurred due to the vibrational loading of the specimen. The fretting damage level may then be evaluated through profilometric observations and analysis based on the non-destructive characterization of the asperities on the surface.

### ***Advantages of Optical Surface Characterization***

The theoretical basis for a profilometric description of fretting damage accumulation lies in the fracture mechanics that may be used to describe the stress field, on a microscopic level, near the surface of the material. An equation that may be used to describe the stress concentration factor,  $K$ , at the front of a semi-elliptical flaw on the surface of a specimen is

$$K \propto \sqrt{\frac{a}{\rho}}, \quad (1)$$

where  $a$  is the length of flaw, and  $\rho$  is the radius of curvature of the elliptical flaw. In a two-dimensional analysis of asperities on the surface of a specimen this equation may be applicable. In this case, we cannot accurately measure the radius of curvature of the asperity bases. However, we can make an inference into the curvature at the bases of the asperities based upon the spacing between asperities. The average radius of curvature between adjacent asperities is then directly proportional to the average spacing between asperities. For every specimen there will be a continuous range of asperity spacing present on the surface of the material. The range of most interest is that of a low asperity spacing that would lead to a smaller radius of curvature and, thus, higher localized stress intensity near the surface.

Because fretting fatigue is generally associated with failure mechanisms that involve surface-bound crack initiation, surface methods, and in particular optical methods, are ideal for inspection and evaluation of fretted components. White light interference microscopy indirectly gives information about both the height and spacing of asperities on the surface of a component. While WLIM is not sensitive to internal damage suffered during fretting fatigue, much can be learned by measuring changes in the induced surface roughness. A basis for quantifying surface damage may also be attainable based upon the surface topography.

It is assumed that one of the key roots of the fretting fatigue problem is the localized roughening of the surface in the presence of a partial slip situation. As the surface roughens, higher localized stresses are seen at the surface. This is due to the larger depth at the bases of the asperities and the tighter spacing to adjacent asperities. This creates a localized stress concentration for the crack to initiate. It would be prohibitively difficult for a technique to completely measure all the asperities in a given area due to the high resolution that would be required. However, WLIM allows for the measurement of roughness, which is proportional to the mean asperity height, and the power spectral density (PSD), which includes information about the power and population of asperities at a given spatial frequency.

Specimens for this study were obtained from A.L. Hutson at the Air Force Research Laboratory (AFRL). Details of the testing conditions may be found elsewhere [8]. However, specimens from two other experimental set-ups were examined, along with actual roots from a fretted turbine disk. These specimens also were encouraging to the findings of this study.

## **Experiments**

White light interference microscopy was used to measure the surface topography before and after the specimens were subjected to cyclic loads in a fretting fatigue apparatus. From the surface height maps, two evaluations of the data are performed. (a) A Fourier transform of the surface results in the power spectral density (PSD) versus spatial frequency plot. It has been postulated that fretting

fatigue cracks initiate when the surface features reach a critical spatial frequency. As the concentration of high spatial frequencies in the surface increases, cracks are able to initiate easier. (b) The roughness of the specimen is evaluated, either quantitatively by a roughness calculation or qualitatively by viewing a line-scan of the specimen surface.

From the profilometry data, the inherent spatial frequencies of the surface are investigated. Looking at the asperity spacing gives some insight into the likelihood of crack initiation. So, instead of looking at the data in the spatial domain, it would be more useful to investigate the spacing of the surface asperities by transforming the data into the frequency domain. This enables the observation of local decreases in the asperity spacing that are present in the slip region of fretting specimens. The PSD-spatial frequency plot is generated by a Fourier Transform of the three-dimensional height data. This effectively transforms the data from the space domain to the frequency domain, which enables an easier evaluation of the inherent frequencies of the data set. The maximum PSD occurs as the spatial frequency approaches zero, which represents a perfectly flat, smooth surface. The higher range of spatial frequencies corresponds to small, closely spaced asperities. This PSD plot represents a spatial frequency spectrum over the entire field of view of the specimen. So, when using this data to determine the presence of slip regions, care must be taken to ensure that the sampling area and the reference area are uniform. If this is not the case, the PSD levels for the data set will only be an average of the entire field. Likewise, when determining fretting damage levels in a given area, the percentage of slip versus stick regions must be taken into account to determine the true degree of damage.

## Results

White light interference microscopy has been used to obtain profilometric data like that seen in Fig. 3. This data has a high spatial and vertical resolution, which enables small changes in the morphology of the surface to be investigated and quantified through various analysis techniques.

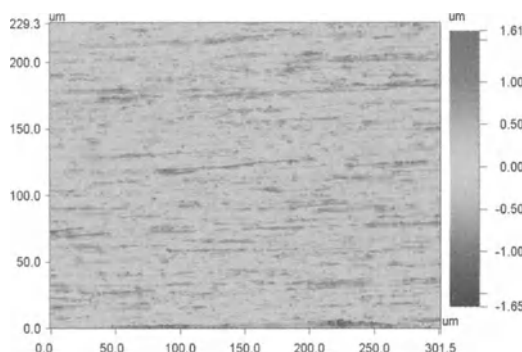


**Fig. 3.** Profilometric data obtained by WLIM

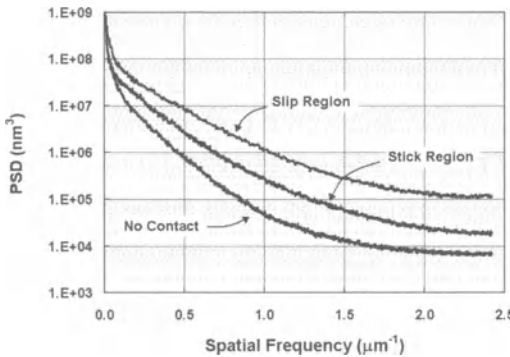


**Fig. 4.** PSD curves for the slip, stick, and non-contact regions

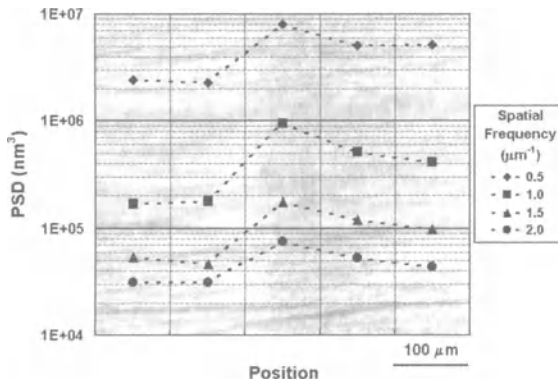


**Fig. 5.** Analysis of five regions on a fretted specimen – the slip line can be seen in the background of the figure

Because we are interested in the frequency of variations on the surface, a Fourier transform is calculated for the data set. This results in curves similar to those in Fig. 4, which give the Power Spectral Density (PSD) over a range of spatial frequencies. This plot basically shows that the population density and height of asperities are high in the low frequency range and decrease at higher frequencies. A spatial frequency of zero represents a completely flat surface.

One strength of Fourier transform analysis of profilometric data is the ability to discern between fretted and non-fretted regions. Even in the absence of an obvious, visible scar, the PSD at higher spatial frequencies is elevated. Relative micro motion tends to break the asperities up through plastic deformation and micro welding [9] thereby creating new, more closely spaced asperities. The end effect can be seen in Fig. 4. Here, a large increase is seen in the PSD level of the slip region. This may be used as a tool to locate damage that should be further investigated.

A second strength of this method is its ability to quantify the damage level of a component relative to the original condition of the surface. For example, in Fig. 5,

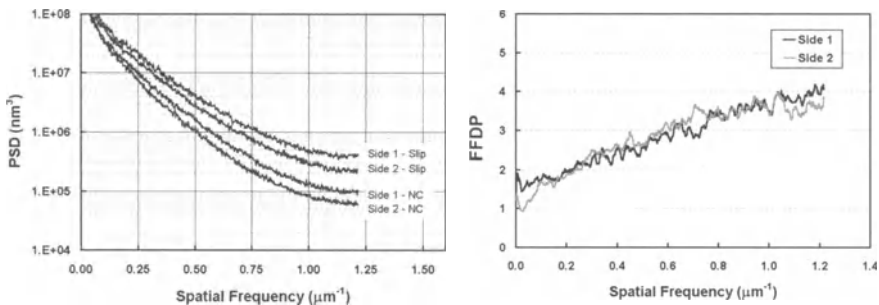


**Fig. 6.** (a) Data taken from the slip and non-contact regions from two sides of a specimen; (b) PSD values from the two sides normalized with respect to the non-contacted surface data

five areas were analyzed. The first two (on the left) were in a non-contact region of a fretted specimen. The slip region started with the middle section and continues towards the stick region to the right. A large increase is seen at the front of the slip region with a gradual decrease towards the stick region. For easy comparison, the PSD is shown only for a few discreet spatial frequencies. The higher spatial frequencies (i.e.  $2 \mu\text{m}^{-1}$ ) may be more relevant to crack initiation, though. This type of analysis enables a relative comparison between adjacent regions in the specimen and illustrates how the slip region might be located on a component.

A quantification of the level of damage may be made by normalizing the PSD of the region of interest with the original state of the material or a non-contact region. In Fig. 6a, one specimen with the same nominal damage state on both sides was scanned. While the initial finish of the surface varies, the increase in the PSD due to the fretting action is the same. Figure 6b shows the normalized curves for the two sides. A fretting fatigue damage parameter (FFDP) is defined as the PSD of the analysis region divided by the PSD of the original surface and is a metric that quantifies the damage to the surface.

Another strength of this technique is the ability to determine the variation of damage level across the test specimen or component. This is illustrated in Fig. 7. This enables the determination of the location at which failure is likely to initiate. In the case of the specimen in Fig. 7 and other tests from the same study, failure initiated within 2 mm of the edge of the sample (either in the 0–2 or 8–10 ranges of “lateral position” of Fig. 7a) [10]. This corresponds well to a sharp increase in the FFDP seen near both edges.

While analysis of fretting-prone components using this technique looks promising, there are still a number of technical challenges that must be addressed before this could be used as a refined field technique.

The primary difficulty in developing a calibrated technique for the prediction of residual life in components is the inability to actually determine the true fractional life of a specific location in a calibration specimen. Because most fretting fatigue experiments do not yield uniform damage across the slip line, there is a question

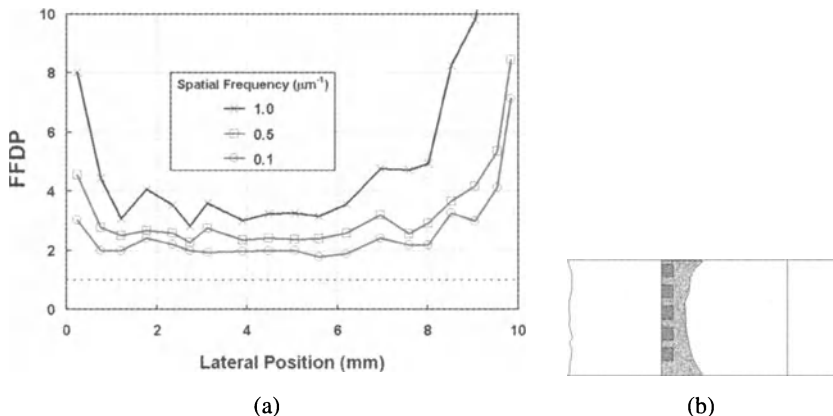


**Fig. 7.** (a) Variation of the FFDP across the slip region of a fretting specimen; (b) Schematic showing the location of the scans in the slip region

as to what damaged area should be considered for determination of the overall sample residual life. In fact, due to non-uniform damage, only the area that is the most damaged will ultimately initiate the final failure and should be considered at the nominal fractional life. This leads to another obstacle to making quantitative measurements for life prediction purposes: the difficulty involved in using an area analysis to search for a relatively localized phenomenon. In any sample or component subjected to fretting fatigue, generally only a small region is subjected to the most severe conditions. As a result, manually searching for this most damaged area is extremely time consuming. However, a methodology based upon these techniques could implement computer analysis of a large image to: first, break up the image into smaller, discrete regions; second, perform a Fourier transform on each of these smaller regions; finally, through comparison of the PSD curves determine the region representative of the highest degree of damage. This type of analysis may be made easier if wavelet transforms were used instead of Fourier transforms.

### Future Trends

This method is currently being evaluated for its ability to benchmark fretting damage in the inspection of gas turbine engine fan blades. While the potential of this method has been shown, a more rigorous parametric study should be conducted to determine the actual capability of the method for fretting damage quantification.

There is potential for Fourier-transformed profilometry data to be used in other applications involving failures that initiate at the surface. These applications include corrosion-initiated fatigue failure and foreign object damage. This technique may also be relevant to problems involving coating degradation or tribological systems.

## 2.4.2 Characterization of Localized Corrosion Damage and Its Role for Fatigue Crack Initiation

### ***Motivation***

Pitting is one of the most dangerous forms of corrosion. Although only a small percentage of metal is dissolved, the result can lead to total failure of the structure in a very short time. Pitting corrosion is commonly observed in high strength aluminum alloys. Research has shown that pits are one of the nucleation sites for fatigue cracks in aluminum alloys [11–13]. It is difficult to detect pits due to their small size and the fact that they may be hidden under a concealed area.

The most practical way of studying the role of pitting on fatigue crack initiation is to conduct fatigue experiments on a specimen containing a pit or a number of pits. Pits on a sample can be created in a number of ways. Some investigators simulate an artificial pit by just drilling a fine depression on the surface, but this does not represent real corrosion damage. In other cases, pits have been grown chemically by immersing or holding the sample in an aggressive environment for a fixed period of time. One of the most common ways is to use salt spray chamber. However, there is no control on the size and distribution of pits in these experiments. For these reasons, pits were electrochemically grown on standard dog bone fatigue specimens. This required the use of a potentiostat to control the electrochemical potential. The CMS 100 Electrochemical Measurement System from Gamry Instruments Inc., Warminster, PA was used for this purpose.

The pits were characterized by a white light interference microscope [14]. The visible surface roughness caused by shallow pitting and line-of-sight pit dimensions were documented in detail. The fracture surface was characterized by Scanning Electron Microscopy (SEM). SEM allowed a comparison of the visible pit dimensions with the actual dimensions, which may include hidden corrosion damage associated with the material microstructure.

### ***Experiments***

A large set of dog–bone fatigue samples of AA2024-T3 were machined with L-T, T-L, S-L, L-S, S-T and T-S orientation (L – longitudinal/rolling direction, T – long transverse direction, S – short transverse direction, ‘L-T’ means sample aligned in the L-direction with crack propagation in the T-direction). The dimensions for the fatigue specimens are shown in Fig. 8. The gage section of the sample was sanded up to 600-grit SiC paper. The sample was then rinsed with distilled water and dried with a stream of air. Most of the specimen’s surface that was to be exposed to the electrochemical environment was covered with a waterproof tape. A small portion in the center of the gage section was initially left exposed as shown in Fig. 8, and covered with a thin coating of micro-stop. Fine hole/holes were created in the coating after the film had dried. This was intentionally done to provide desired site/sites for pit initiation. The sample was then clamped into an electrolytic cell for electrochemically producing pit/pits on the surface.

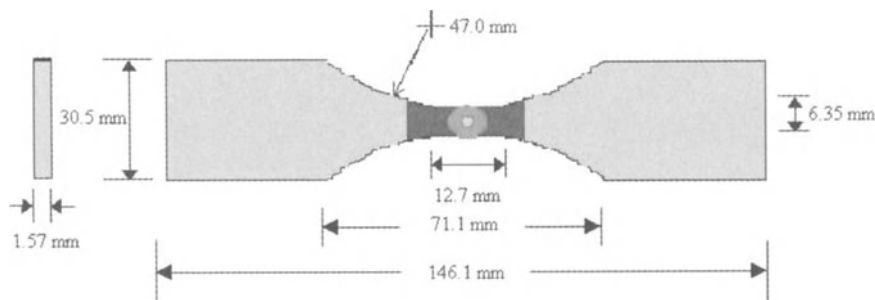


**Fig. 8.** Geometry of dogbone fatigue sample made of AA2024-T3

A solution of 0.1 M NaCl was used as the electrolyte. A Saturated Calomel Electrode (SCE) was used as the reference while a platinum meshed disc served as the counter electrode. The pitting was produced in the area of the exposed gage section using a potentiostatic scan. An initial potential of  $-450$  mV (SCE) was applied for 10 minutes to initiate pitting, and then the potential was lowered to  $-520$  mV (SCE) for the remainder of the scan. Various scan times were used to obtain pits of varying depth. The sample was promptly removed from the cell after the potential scan, cleaned with running distilled water and dried in a stream of air. The pit morphology and depth measurements were determined using optical microscopy, SEM and WLIM. After acquiring pit information, the samples were fatigued. Fatigue tests for all orientations were conducted on a single machine under the same conditions at a stress ratio,  $R = 0.1$ , maximum stress = 256 MPa, and a frequency = 15 Hz. All the samples were analyzed after fracture to determine the exact location of crack initiation from a particular pit. The fracture surface was analyzed to obtain dimensions of the initiated pits and the critical crack dimensions at the onset of fracture.

### ***Optical Characterization of Corrosion Pits***

Optical microscopy, SEM and WLIM were used to characterize the pitted sample surface. Figures 9a, b show optical micrographs of two samples that were pitted using the controlled polarization technique. The sample shown in Fig. 9a was polarized twice over a 24-hour period. The first polarization cycle of one hour and a relatively high potential created several small pits on the surface of the exposed region. A second, longer polarization cycle was used to grow a few of the initiated pits. A lower potential of approximately  $-525$  mV (versus SCE) was used in the second cycle to restrict the initiation of new pits and thus ensure the growth of the pits started in the first polarization cycle.

The sample shown in Fig. 9b was also polarized twice within 24 hours. The first cycle was run for one hour at a single potential. The second cycle differed from that described for the sample in Fig. 9a since the potential was varied within the second cycle. For the first hour of the eleven-hour cycle, the potential was set at  $-450$  mV versus SCE. After this hour, the potential was decreased automatically to  $-475$  mV versus SCE for the remaining 10 hours.

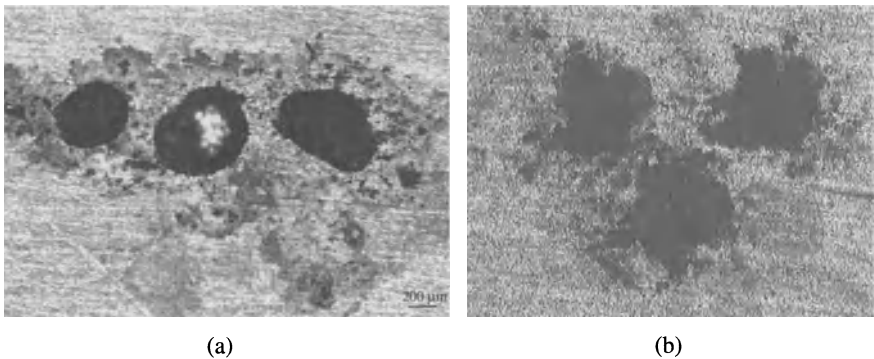


**Fig. 9.** Optical micrographs of two pitted dogbone samples

These optical micrographs only offer qualitative information about the surface features of a pitted sample. No quantitative data, such as pit depth, can be accurately determined from such an optical micrograph. Therefore, white light interference microscopy (WLIM) was used to fully characterize the pitted sample surface. Figure 10 shows WLIM images of Figs. 9a, b, where the details of pits can be more clearly seen [14].

The color scale at the right (shown here in black and white) indicates the various depths of the pits. The WLIM method gives quantitative information, unlike the optical micrograph, because a color scale is used to show depth. Maximum contrast profile and three-dimensional models of pitted surfaces were also generated to obtain detailed information about the pit morphology.

The three-dimensional images corresponding to the samples shown in Fig. 9 are represented in Fig. 11. The data has been inverted, so the pits look like mountains instead of valleys. Only the pit mouth can be seen before the data is inverted. Therefore, inverting the data allows the pit morphology to be viewed more easily. In addition, the software package that runs the equipment provides the means to rotate the three-dimensional image. This allows the shape of each pit to be viewed from any angle.

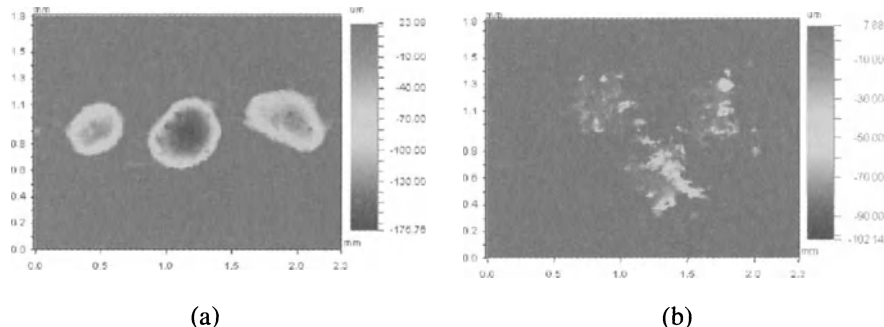


**Fig. 10.** (a) WLIM surface profile of sample shown in Fig. 9a; (b) WLIM surface profile of sample shown in Fig. 9b

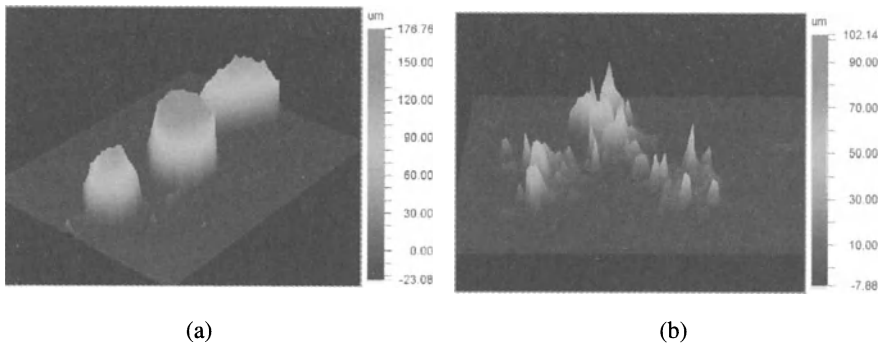


**Fig. 11.** (a) WLIM three-dimensional profile of samples shown in Fig. 9

Specific pit parameters, such as pit depth and diameter, were required in the analysis for the fatigue behavior. All previous WLIM profiles provided only general information about the pitted surface. A two-dimensional analysis was performed to more exactly determine these pit parameters.

Figures 12 and 13 illustrate this two-dimensional analysis. The y-profile shown in Fig. 13a corresponds to the horizontal line shown in Fig. 12. Figure 13a illustrates how the diameter of a pit is accurately determined. One marker is moved to the left side of the pit mouth, and the other marker is moved to the right side of the pit mouth. The distance between these two points is automatically calculated, and in this case is 1279  $\mu\text{m}$ . Similarly, the pit depth can be found as illustrated in Fig. 13b. Here the x-profile, or the vertical line was used. Notice the dark yellow bar around the marker's lines in Fig. 13b. This averages the points contained in that bar, creating a more realistic calculation of the pit depth. Using this accurate WLIM two-dimensional analysis, the pit parameters required for the analysis of fatigue data were determined nondestructively.

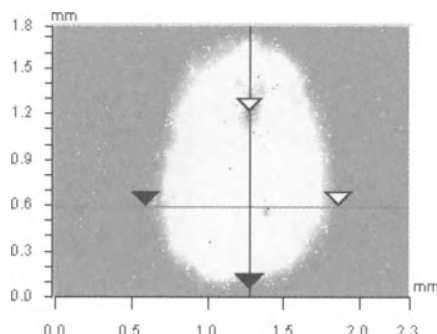


**Fig. 12.** Determination of the surface profile of pits

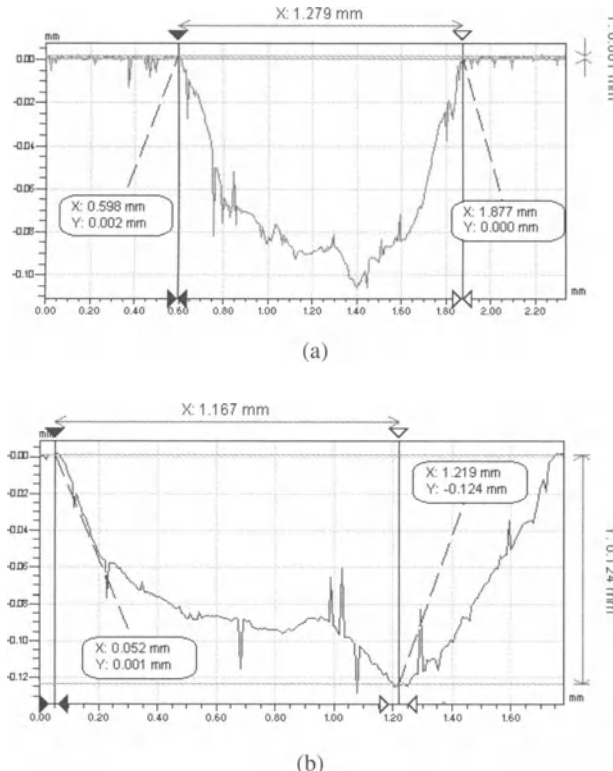


**Fig. 13.** (a) X-profile in two-dimensional analysis illustrating the determination of pit depth; (b) y-profile in two-dimensional analysis illustrating the determination of pit diameter

### **Effect of Pit Size on Fatigue Crack Generation**

The controlled potentiostatic polarization process produced a wide range of pit sizes in a relatively short amount of time. Figure 14 shows examples from six representative samples that were anodically polarized with the substrate coated with the imperfect layer of micro-stop coating. The polarization times range from four hours to twenty-four hours for the six samples shown in Fig. 14. Longer polarization times lead to larger pits. The pit morphology was determined using WLIM. SEM was also used to characterize a few select samples. Since SEM is a well-established method, it was used to mainly compare the qualitative surface features with those shown in the WLIM surface profiles. Figure 15 compares representative optical micrographs and WLIM profiles for one of the samples used in fatigue experiment. These profiles were taken before the samples were fatigued [14].

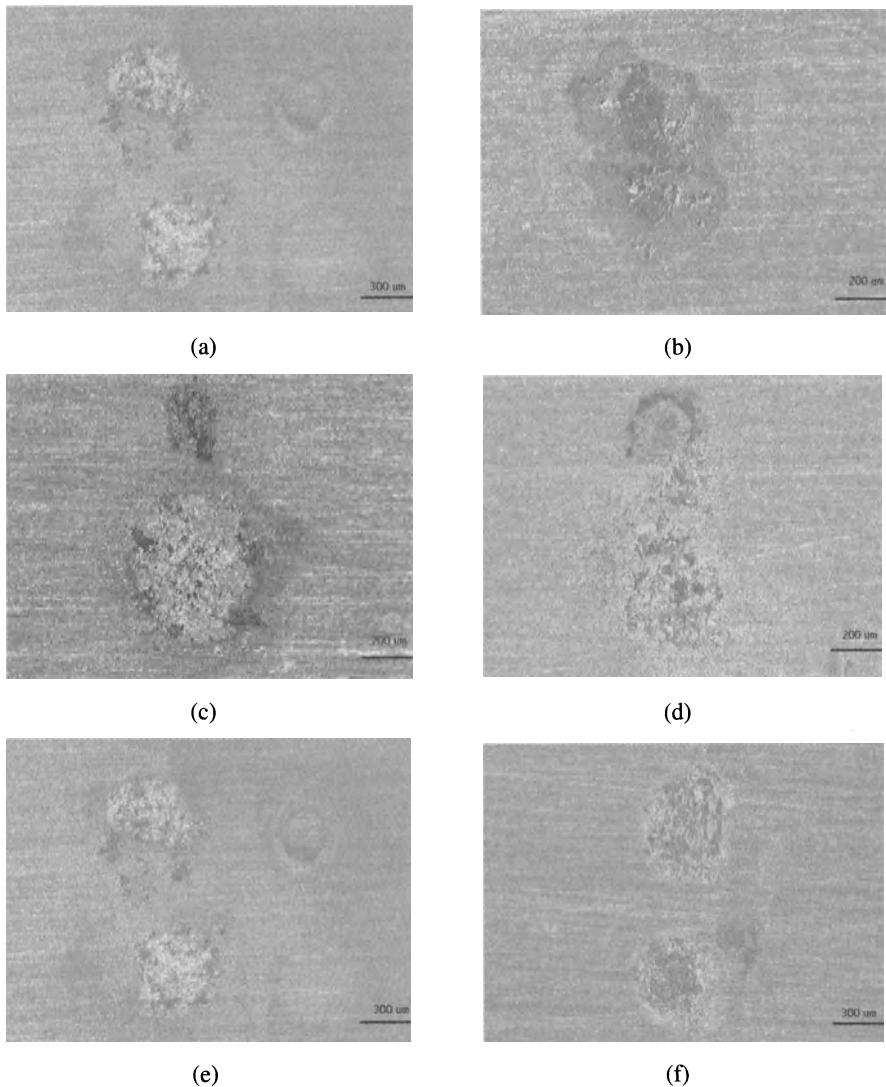


**Fig. 14.** Six examples of dogbone samples coated with the micro-stop and polarized for (a) 4 hours; (b) 8 hours; (c) 12 hours; (d) 16 hours; (e) 20 hour; (f) 24 hours

As expected, the longer polarization times produced larger pits. As the polarization times increased, the pit depths also increased. However, the sample polarized for twenty hours had deeper pits than the sample polarized for twenty-four hours. In this case, instead of growing deeper, the pits expanded during the extra polarization time. This behavior is shown in Fig. 16, which is a plot of surface roughness versus polarization time. All data points were determined to be statistically valid using the average deviation method [15].

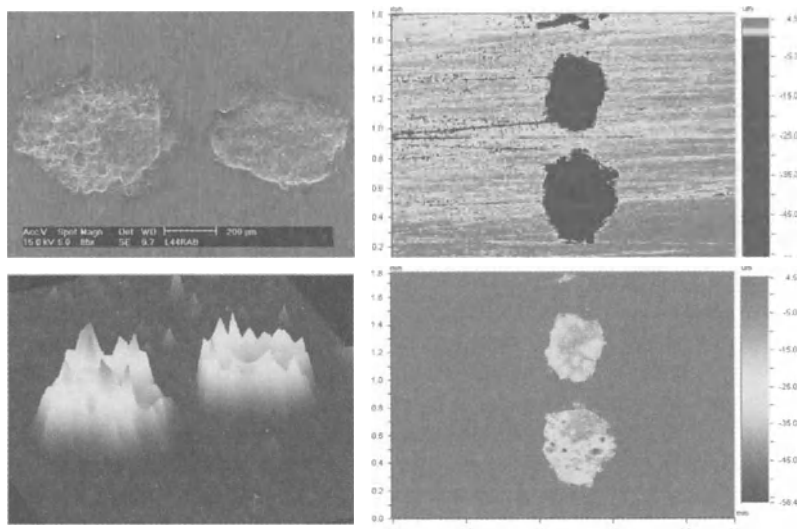


**Fig. 15.** Comparison between different optical analyses

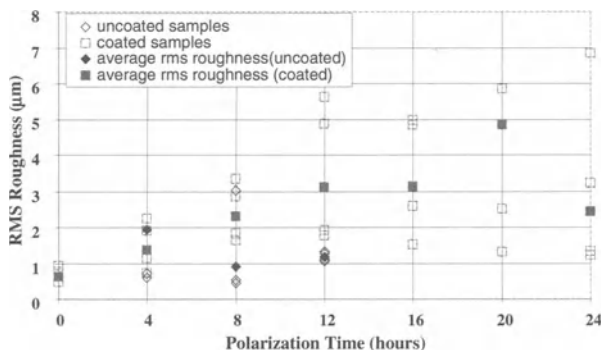


**Fig. 16.** Change in RMS roughness with increasing polarization time

A number of pitting parameters obtained from WLIM analysis for LS orientation were investigated to develop a relationship between these NDE parameters and the electrochemical parameters. For example, the change in RMS roughness with time is shown in Fig. 16. The RMS roughness is an important NDE parameter that can be determined in the field during an inspection. Therefore, a relationship between the RMS roughness and a fatigue parameter can be very useful in predicting the fatigue life of a structure. As seen in Fig. 16, the RMS roughness slowly increases with increasing polarization time, until the last set of data points representing the 24-hour scan. Here, the RMS roughness decreases with increase in polarization time at the highest value for no apparent

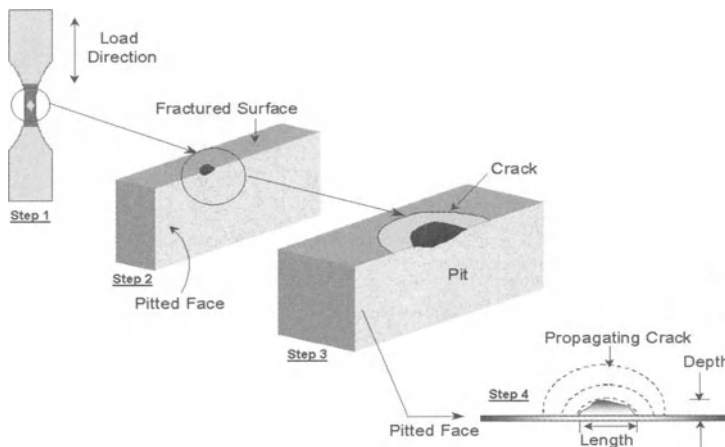


**Fig. 17.** Crack growth schematics

reason. Further investigation of the behavior during long polarization scans is required before any speculation about the cause can be offered, but the pit did grow in width, rather than depth, for the 24-hour scan.

Figure 17 represents a flow chart of the experimental procedure. Step 1 simply shows the dogbone fatigue sample with the load direction and a small area of the gage section where pits are to be initiated. Step 2 shows the pit created by the controlled potentiostatic technique. If the pit initiates a fatigue crack on fatigue loading, a semi-elliptic crack begins to grow. This stage is depicted in Step 3. Step 4 is a two-dimensional scheme of the crack initiation and growth process with the two important parameters of the pit depth and diameter (length) used in stress intensity factor calculation as described below.

The pitted samples were fatigued after the surface pit morphology was characterized completely. The samples were fatigue tested at a stress ratio,  $R = 0.1$  and a frequency,  $f = 15$  Hz. The maximum stress in all cases was 256 MPa. The main goal was to determine a relationship between pit depth and stress intensity factor,  $K$ .

A detailed analysis of the fracture surface indicated that the crack always started from a corrosion pit. In most cases the crack initiated from a single pit and a single semi-elliptical crack grew to a critical size leading to the failure of the specimen. In some cases, the cracks initiated from two or more adjacent pits. In these cases, the cracks linked together to form a single semi-elliptical crack that eventually caused the failure. Figure 18 shows several optical micrographs of a sample before and after it was failed under fatigue. The pitted face was examined first to determine the area in which the crack developed. For the sample in Fig. 18, it appeared that the crack initiated from both of the pits. The fractured surface was then examined for the initiation site of the crack. The crack appeared to be centered on the left pit. The left pit is the crack initiating pit and it corresponds with the top pit shown in Fig. 18a.

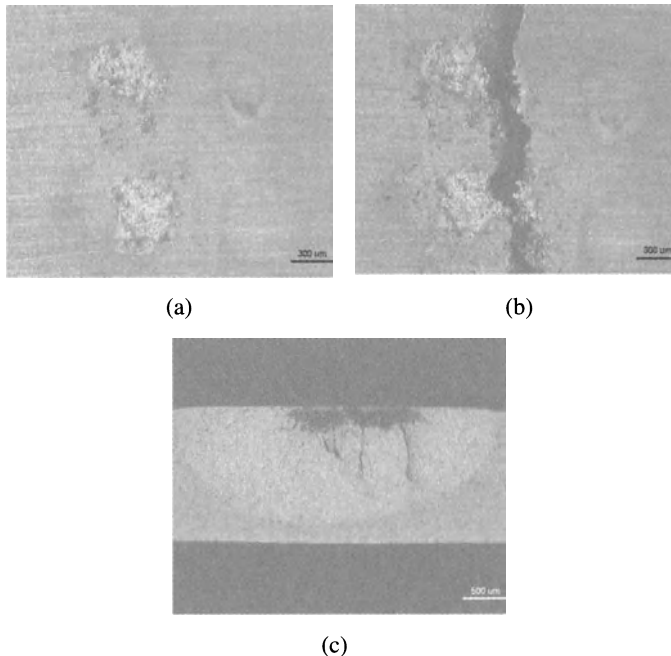


**Fig. 18.** Fractured micro-stop coated dogbone sample polarized for 20 hours (a) Optical micrograph of pitted surface before fracture (b) Optical micrograph of pitted surface after fracture (c) Fractured surface showing semi-elliptic crack

All the samples were examined as described above, and a complete list of the data is available in [14]. Once the parameters of interest were obtained using WLIM, the stress intensity factor for each specimen was calculated using a program developed by Newman and Raju [16].

The stress intensity factor is a strong function of the crack depth (Fig. 19). The scatter increases with increasing pit size. It also is a function of the crack diameter, the dogbone sample geometry and the stresses the sample is undergoing. Using this stress intensity factor, the fatigue life of this sample can be predicted. This data was the main input into the CRACKS model, developed by the University of Dayton Research Institute and used here to predict the crack growth behavior of fatigue cracks initiating from a pit. A single semi-elliptical surface crack is assumed to develop from the critical pit. The model uses the stress intensity factor from previous calculation and the crack growth data is generated from the initial and final crack size measured. Crack growth is assumed to start from the first applied cycle with no crack initiation period. Such an assumption is a reasonable approach because majority of the fatigue life of a pitted aluminum sample is spent in the crack propagation stage [17, 18].

Crack growth data for the LS orientation in the form of  $da/dN$  versus change in stress intensity factor is shown in Fig. 20, where  $a$  is the crack length and  $N$  is the number of fatigue cycles. The data shown with white squares is taken from a notched compact tension specimen representing long crack growth. It appears that

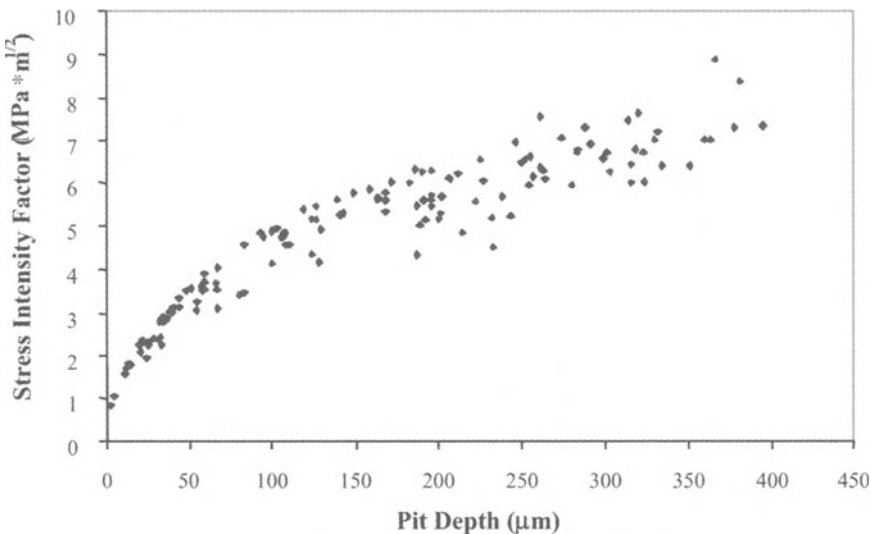


**Fig. 19.** Stress intensity factor calculated from optical NDE data for all pits examined

the crack growth behavior of cracks initiating from the pits, represented as black squares in Fig. 20, is typical of short crack growth behavior. However, a transition to long crack growth behavior is quite evident, suggesting that pits deeper than  $80 \mu\text{m}$  behave similarly to standard notched specimens representing long crack growth data. More tests are required with critical pit depths in the range of  $100\text{--}200 \mu\text{m}$ .

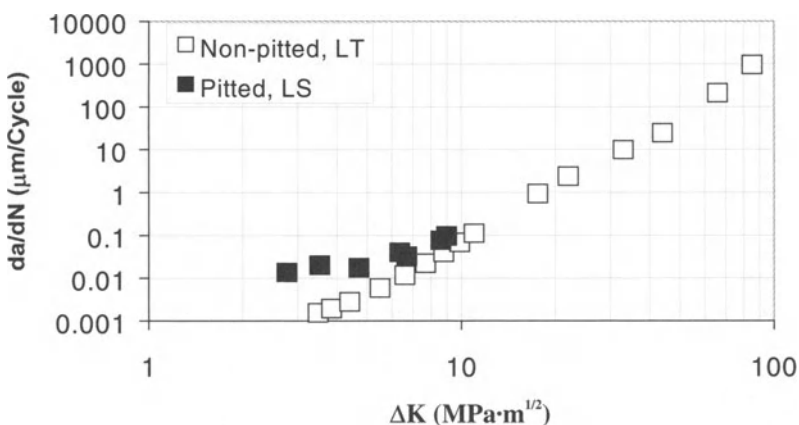


**Fig. 20.** Crack growth  $da/dN$  versus stress intensity factor  $\Delta K$  for AA2024-T3 Fatigue Specimens

### 2.4.3 Characterization of Crack Damage States in Titanium Alloys through Examination of the Surface Deformation Preceding the Crack Front

#### Motivation

Cracks detected through standard NDE methods are currently quantified without regard to the three-dimensional deformation zone ahead of a crack tip. This deformation zone is representative of the stress condition of the crack front [19]. It is believed that this deformation preceding a crack increases the effective length of the crack and must be considered in life prediction models [20]. The deformation is a result of complex stresses and strains at the crack tip. The presence of these stresses and strains is exemplified by necking of the material. The localized necking creates a depressed volume in front of the crack tip as shown in Fig. 21. When the stresses in the deformation area combine to reach a critical level, the conditions for crack advance are satisfied. The crack extends through microcrack coalescence or increased necking, which causes voids to grow larger [20].

The deformation zone is a surface characteristic resulting from the internal stress state of the material ahead of the crack. Thus, it is a perfect candidate for nondestructive measurements of internal damage. In the past, numerous examinations have been performed to measure the stress state at a crack tip. These methods include photoelastic methods [21], moiré interferometry [22–26], holographic interferometry [27] and shearing interferometry [28, 29]. These analysis methods still left a need for a suitable experimental technique providing full-field deformation measurements [30].

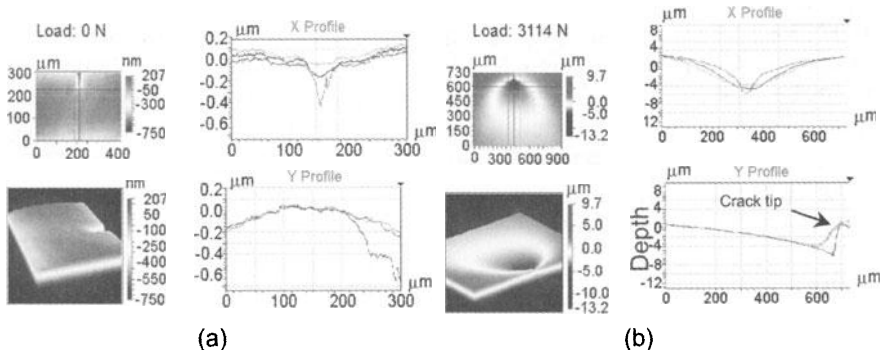


**Fig. 21.** Comparison of the three-dimensional damage zone in front of a crack tip of a mill-annealed Ti-6-4 specimen; (a) directly following fatigue precracking and (b) after application of 3114 N static tensile load (directly prior to failure). These images were taken with white light interference microscopy

## Experiments

Aircraft materials were the focus of this study [31]. Thus, titanium alloys are the first material studied by this method. All samples in this study were Ti-6Al-4V flat 79-mm-long dogbone specimens. A 0.4-mm-long notch was cut into the edge of the center of the gage section of each specimen through electro-discharge machining (EDM). All specimens were polished to a low surface roughness ( $\text{RMS} \approx 250 \text{ nm}$ ). The primary microstructure investigated was a mill-annealed sheet (Fig. 22a). This sheet material was cross-rolled with the final rolling direction indicated. This microstructure had grain sizes of approximately  $5 \mu\text{m}$  in the transverse direction and  $20 \mu\text{m}$  in the longitudinal direction. Both longitudinal and transverse orientation behavior of this material was investigated. The duplex microstructure (Fig. 22b) was obtained from a plate that was forged and solution treated in the  $\alpha + \beta$  phase field. The average grain size was approximately  $10\text{--}20 \mu\text{m}$ . The final microstructure examined was a  $\beta$ -annealed sheet (Fig. 22c). This material began as a mill-annealed sheet that was then vacuum heat-treated above the  $\beta$  transus. All of the  $\beta$ -annealed specimens were chemically etched prior to crack initiation to enable correlation between deformation shape and grain orientation.

Fatigue cracks were initiated from the notch of each specimen by high-cycle fatigue loading. The specimens were subjected to low stress ( $\sim 25\%$  of yield stress) cyclic loading at a stress ratio of 0.1. 10,000 cycles were run during each set to initiate a short crack. Once a visible crack was detected, the stress was reduced by 10% and the specimen was subjected to additional sets of 1000 cycles with stress reductions of 10% after each set. This stress reduction was repeated several times to sharpen the crack front and reduce the initial surface deformation area. The fatigue crack length ranged from 0.05 to 0.25 mm. Including the notch, effective crack length ranged from 0.45 to 0.65 mm.

Following crack initiation, the specimens were loaded in a portable, static, 4500 N load frame. The load frame was placed under a white light interference profilometer for in situ topographical data acquisition. As described above, the instrument used in this study has a data analysis package that enables automated topographical calculations including height profiles, threshold surface area, and surface depression volume analysis, along with other calculable parameters that are not used in this analysis.

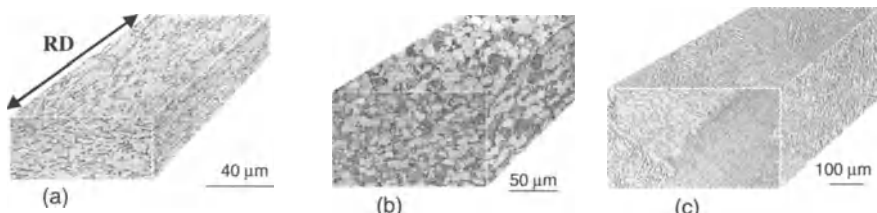


**Fig. 22.** Microstructure of Ti-6Al-4V specimens; (a) mill-annealed sheet; (b) duplex forced plate, and (c)  $\beta$ -annealed sheet material

The threshold analysis method was used to separate surfaces of different heights. This allowed quantification of the volume and surface area of the depressed regions of the sample. In threshold analysis, all pixel points representing regions lower than the threshold value are summed for calculation. Zero is the threshold limit for this data. The zero threshold represents the region level with the bulk sample surface. All regions below this threshold will be summed for deformation calculations. The bulk surface or zero reference was reproduced by focusing the profilometer on the same point of the bulk surface for each measurement.

In early images, it was difficult to identify a specific area of the material surface for focusing and the point of focus varied. This changed the level of the threshold and created error that was corrected by altering the zero-value for images of concern. The desired zero value was chosen through manual masking. The user viewed an image of the area below the new zero threshold. When the desired area was all that remained a new zero value was selected and calculations ensued.

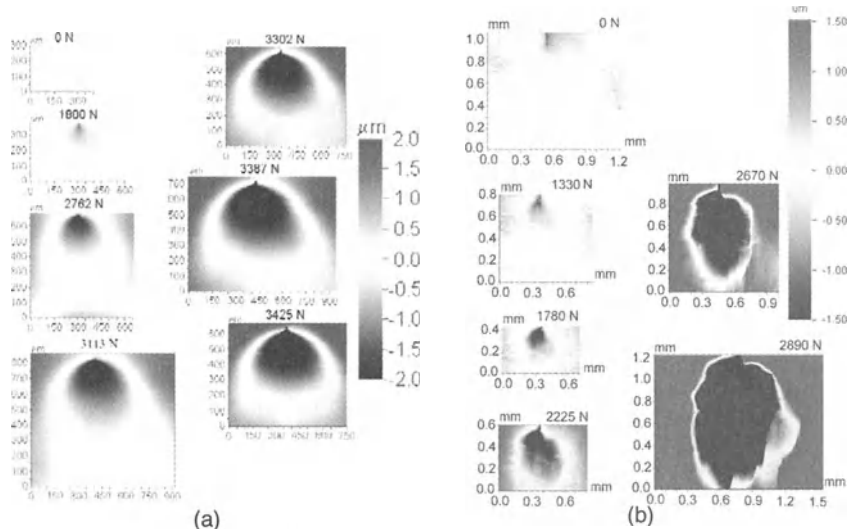
Quantification also required each image examined be of a similar area of the specimen and focused at the same point. Sample images used in deformation quantification calculations are shown in Fig. 23. Images of the duplex microstructure are not included since they resemble the mill-annealed images.

## **Results and Discussion**

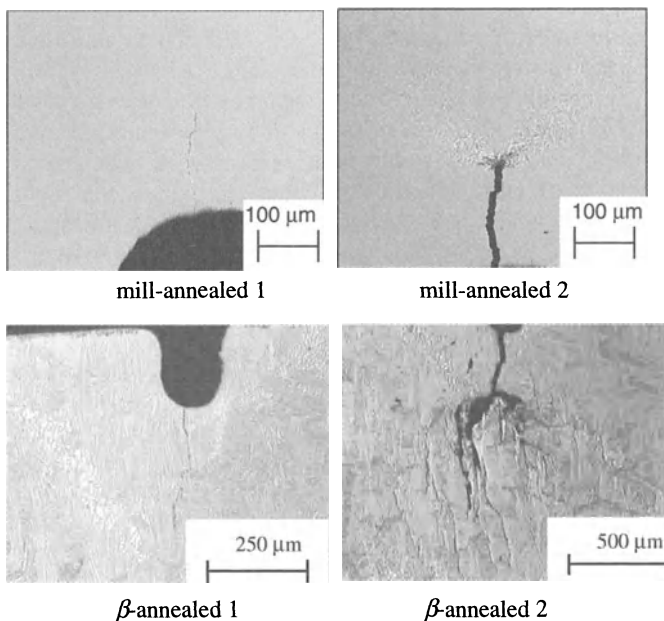
White light interference profilometry has been validated as an efficient means to document the topography of crack tip deformation. Analysis of the documented information reveals relationships enabling the prediction of crack instability.

Figure 24 shows optical images of cracks in both mill-annealed and  $\beta$ -annealed material prior to static loading and after release of a near critical load. The deformation zone of both materials is contained within the area marked by residual shear bands and microcracking (compare Fig. 24 with Fig. 23). The area ahead of the crack front in the  $\beta$ -annealed material contains several small cracks that were created by crack branching. Also note that the crack length of both materials remained constant throughout loading until the point of overload (Fig. 24).

Profilometry images indicate the presence of a distinct region of deformation ahead of the crack in relatively fine-grain materials as shown in Fig. 23a. The deformation in the  $\beta$ -annealed material is uneven and varies from specimen to specimen because the plastic deformation slip activity ahead of the crack tends to follow large grains oriented for easier slip or a preferred crystallographic orientation (Fig. 23b).



**Fig. 23.** Profilometer images of accumulating deformation in front of crack tip with increasing load in (a) a mill-annealed specimen and (b) a  $\beta$ -annealed specimen (images were taken under load)



**Fig. 24.** Optical micrographs of mill-annealed and  $\beta$ -annealed material; (1) directly after fatigue loading and (2) following application of static load directly prior to failure

It was assumed that the deformation zone size would rapidly increase when the applied load developed to stress intensity,  $K$ , levels close to the critical stress intensity factor,  $K_q$ . The stress intensity factor defines the magnitude of the crack-tip stress field. Its value is a function of the stress applied to the component and the crack length. The critical stress intensity factor,  $K_q$ , for plane stress, is referred to in this work instead of  $K_{lc}$ , the critical stress intensity factor for plane strain, because the thickness of the samples used in this work results in a plane stress state.

Quantified data from the incrementally increased static load tests is shown in Fig. 25. Area and volume data was calculated through analysis of images like those contained in Fig. 23. The region of deformation ahead of the crack increased exponentially both in area and volume with increasing stress intensity factor (Fig. 25). Directly prior to failure, the area of deformation retracts for almost all samples. Unlike area, the deformation volume continually increases with  $K$  until the final failure. The consistency of the deformation volume and stress intensity factor relationship makes this comparison a viable tool for failure prediction.

Three microstructures and two material orientations have been tested. Each different microstructure results in a slight change in the magnitude of the relationship between the deformation size and the stress intensity factor, but all materials tested behave similarly. The difference in deformation volume between materials can both be anticipated and explained. The slope of the deformation versus  $K$  curve approaches infinity at the  $K_q$  of each material. The microstructure effect is eliminated by normalizing the stress intensity factor with respect to  $K_q$  and comparing the change in deformation to  $K/K_q$  (Fig. 25c). In this study, the  $K_q$  of the  $\beta$ -annealed material is much lower than expected [32]. This discrepancy may be the result of oxygen embrittlement that occurred when the sheet material was exposed to air during heat treatment.

A correlation between the observed surface deformation and plastic deformation is beneficial for stress field and damage analysis. A rough comparison of theoretical plastic deformation and surface deformation was created by plotting the theoretical radius of plastic deformation for a  $K$  level equivalent to that documented for a surface deformation image. The theoretical equation plotted ((2)) describes the radius of plastic deformation of a material in the plane stress condition and is based on an in-plane two-dimensional model [33]. This equation is only a broad comparison since the surface deformations represent out-of-plane displacement or displacement perpendicular to the theoretical modeling plane.

$$r_y = \frac{K^2}{2\pi\sigma_{ys}^2} \cos^2 \frac{\theta}{2} \left(1 + 3 \sin^2 \frac{\theta}{2}\right) \quad (2)$$

The theoretical radius was calculated, plotted as a function of  $\theta$ , the angle from the crack tip mouth, and  $\sigma_{ys}$ , the yield strength, and then sized to correlate to the figure over which it was overlaid. The theoretical plastic deformation shape did not represent the surface deformation (Fig. 26). The difference in shape was justified because the kidney shape represents the in-plane material behavior and the shape seen on the surface is the result of out of plane displacement.

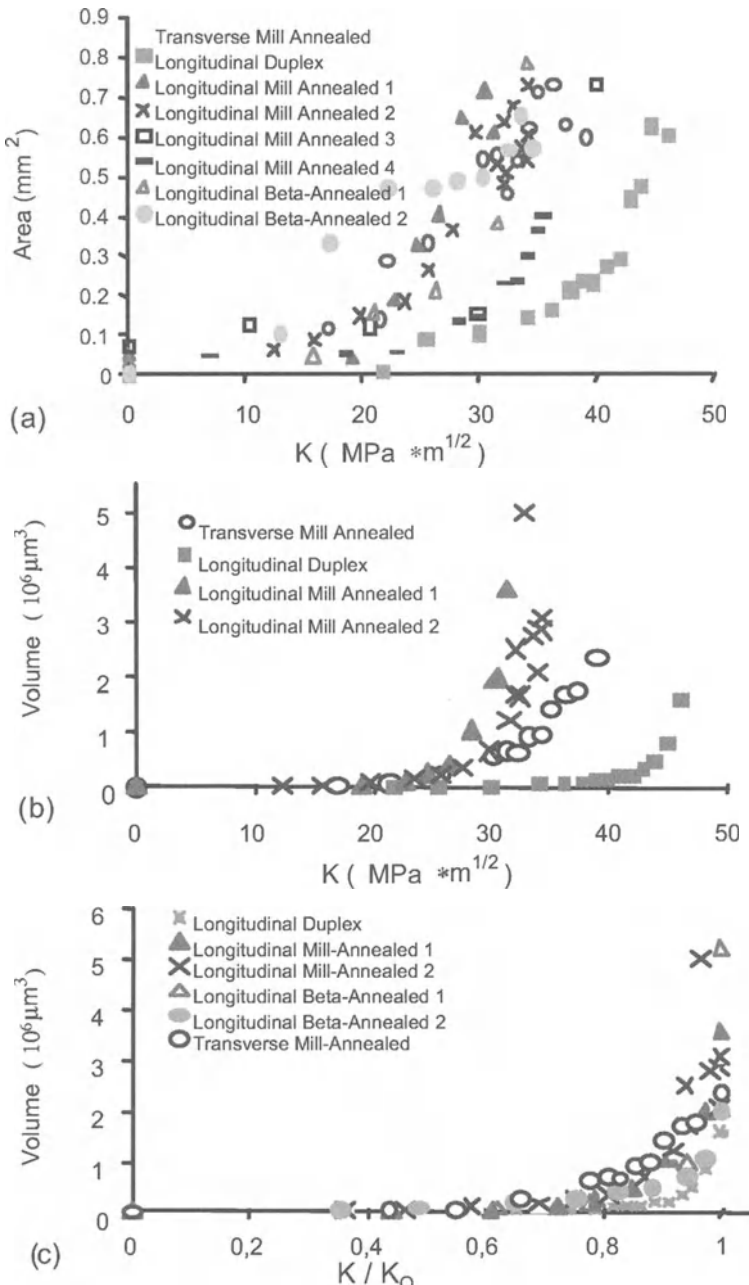


**Fig. 25.** Deformation and stress factor relationship of Ti-6Al-4V for (a) area of deformation and (b) volume of depression for a variety of microstructures and test orientations. The same volume data is normalized by  $K/K_Q$  in (c).

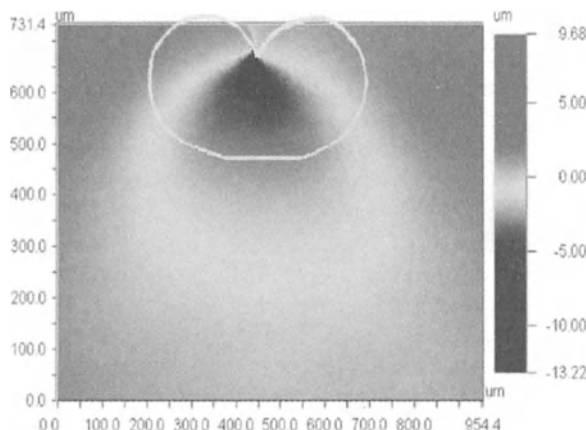


**Fig. 26.** In-plane theoretical plastic zone compared to surface deformation at 3114 N load (image is of mill-annealed material)

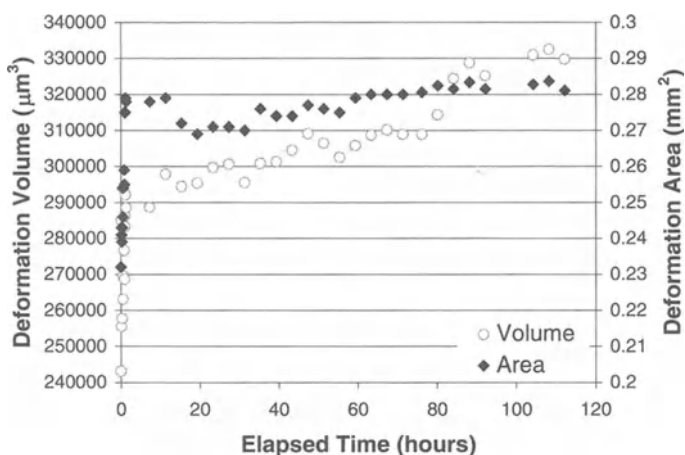


**Fig. 27.** Deformation area and depression volume as a function of time (under static load of 3000 N, duplex material)

Finite element modeling of out-of-plane displacements reveals a shape similar to the surface deformation shape seen in fine grained materials. Deformation accumulation under a maintained load was also investigated in this work. This was done by taking multiple images of a loaded specimen over an extended period of time. Examination of the data revealed that the deformation zone expands under static loading. During the initial hour of loading, the increase in deformation size is substantial. After a few hours, the rate of increase in the deformation zone size drops considerably (Fig. 27). This decrease in rate may be partially related to a negligible release of load that occurs as the deformation increases. This load release was less than 1% of the total load.

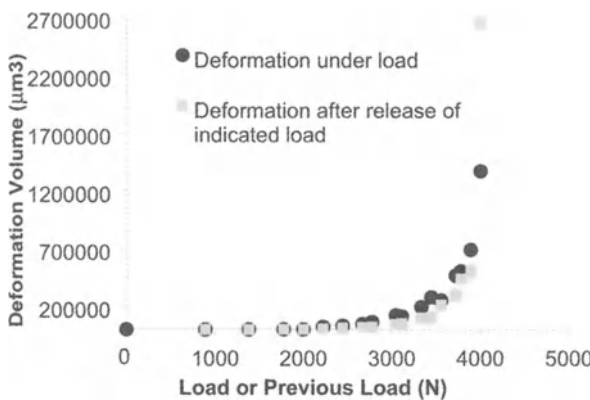


**Fig. 28.** Deformation relaxation after release of load for mill-annealed material

The surface deformation investigated throughout this work includes both plastic and elastic contributions. A substantial amount of the deformation was expected to relax upon release of the static load. The relationship between elastic and plastic deformation was tracked by loading a specimen to a specific load, imaging the sample under load, releasing the load, and immediately imaging the sample without load. The result of this test is presented in Fig. 28. The duration of time the sample was under load was relatively constant for all load steps. Note that after deformation relaxation, the relationship between the deformation size and the stress intensity factor remains similar to that seen in images taken under load.

Examination of the common relationship between deformation zone size and the stress intensity factor indicates that criteria for failure may be extracted from surface deformation data. The suggested criterion for failure is a critical rate of change ( $r_c$ ). This rate is equal to the change in the size of deformation over the change in the stress intensity factor at a determined point prior to failure. A schematic of this rate is shown in Fig. 29.

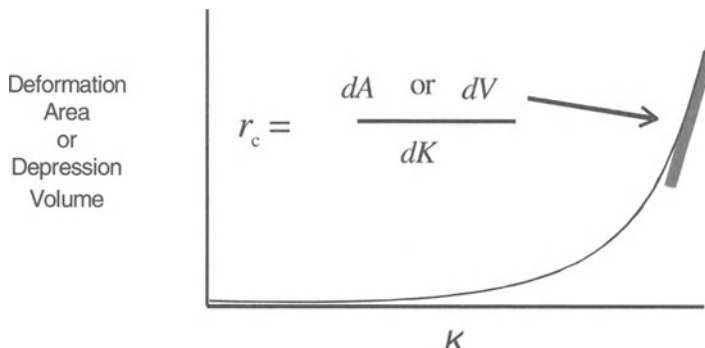


**Fig. 29.** Criteria for failure: critical rate of deformation growth with respect to change in stress intensity factor (a schematic)

## 2.5 Conclusions

WLIM has proven to be a valuable tool in nondestructive characterization of the surface topography of samples. In addition:

- WLIM data has proven effective in quantifying surface damage associated with fretting fatigue loading.
- WLIM can be used to measure line-of-sight corrosion pit dimensions, which are useful for structural integrity calculations.
- A comparison of the change in the volume of the depression measured by WLIM with the change in the stress intensity factor can be the basis for a nondestructive method to predict oncoming crack instability of visible flaws.

## References

1. WYKO (1996) Surface profilers technical reference manual. WYKO Corporation, Tuscon AZ
2. Veeco Instruments, 10/2/2002, <<http://www.veeco.com>>
3. Caber P (1997) Interferometer characterizes laser-textured steel. *Laser Focus World*: 157–158
4. Bowe B, Toal V (1998) White light interferometric surface profiler. *Opt Engn* 37(6):1796–1799
5. Raz E (1996) A multiple white light interferometer. *Rev Sci Instrum.* 67(10):3416–3419
6. Wallace WW, Hoeppner DW (1985) AGARD Corrosion Handbook. Vol. 1, Aircraft Corrosion: Causes and Case Histories. AGARDograph No.278, NATO p. 101
7. Collins JA (1981) Failure of Materials. In: John Wiley & Sons Mechanical Design, New York
8. Antoniou RA, Radtke TC (1997) *Mat Sci Eng* A237:229–240
9. Hutson AL, Nicholas T (1999) *Int J of Fatigue* 21:663–669
10. Hutson A (1999) unpublished research conducted at Wright-Patterson Air Force Base
11. Chen GS, Wan KC, Gao M, Wei RP, Flournoy TH (1996) Transition for Pitting to Fatigue Crack Growth-Modeling of Corrosion Fatigue Crack Nucleation in a 2024-T3 Aluminum Alloy. *Materials Science and Engineering* A219:126
12. Piascik RS, Willard SA (1994) The Growth of Small Corrosion Fatigue Cracks in Alloy 2024. *Fatigue and Fracture of Engineering Materials and Structures* 17(11):1247–1248
13. Ahn SH, Lawrence FV, Metzger NM (1992) Fatigue Fracture. *Eng Mater Struct* 15:625
14. Simon LB (1999) Influence of Pitting Corrosion on the Loss of Structural Integrity in Aluminum Alloy 2024-T3. Master's Thesis, University of Dayton, Dayton, OH
15. Wilson L (1995) Quantitative Analysis: Gravimetric, Volumetric and Instrumental Analysis. 3rd edn. Mohican Textbook Publishing Co. Loudonville, Ohio, pp. 50–58
16. Newman JC, Raju JIS (1983) Stress-Intensity Factor Equations for Cracks in Three-Dimensional Finite Bodies. *Fracture Mechanics: Fourteenth Symposium-Volume 1: Theory and Analysis*. ASM STP 791 pp. I-238–I-265
17. Shankaran K (1998) Validation of Accelerated Corrosion Tests for Aging Aircraft Life Prediction: Effects of Pitting Corrosion on the Mechanical Behavior of 7075-T6 Aluminum Alloy. Final Report, F33615-96-D-5835, Delivery Order: 0026–02, AFRL, Wright-Patterson AFB, OH
18. Bray GH, Bucci RJ, Colvin EL, Kulak M (1997) Effect of Prior Corrosion on the S/N Fatigue Performance of Aluminum Alloys 2024-T3 and 2524-T3, Effects of the Environment on the Initiation of Crack Growth. *ASTM STP 1298*, p. 8
19. Shimojo M, Chujo M, Higo Y, Shigetomo (1998) *Int J Fatigue* 20(5):365–371
20. Harmain GA, Provan JW (1997) *Theoretical and Applied Fracture Mechanics* 26:63–79
21. Sanford RJ, Daily JW (1979) *Eng Fract Mech* 11:621–633
22. Smith CW, Post D, Hiatt G, Nicoletto G (1983) *Experimental Mechanics* 23(1):15–20
23. Kang BSJ, Zhuang YN, Liu YK (1992) *Experimental Mechanics*:309–315
24. Krishnamoorthy H, Tippur HV (1999) *Experimental Techniques*:22–25

25. Dadkhah MS, Kobayashi AS, Wang FX, Grasser DL (1998) Proc. VI Int. Congr. Exp. Mech., pp. 227
26. Bastawros AF, Kim KS (2000) Journal of the Mechanics and Physics of Solids 48:67–98
27. Dudderar TD, Gorman HJ (1973) Experimental Mechanics 13 (4):145–149
28. Krishnaswamy S, Hareesh V, Tippur HV, Roaskis AJ (1992) J Mech Phys Solids 40(2):339–372
29. Ramaswamy S, Tippur HV, Xu L (1993) Experimental Mechanics:218–227
30. Sanford RJ (1993) Experimental Mechanics:241–247
31. Schroeder J, Shell EB, Matikas T, Eylon D (1999) Development of methods to observe fatigue damage through surface characteristics. SPIE Conference on Nondestructive Evaluation of Aging Materials and Composites, volume 3585, Paper No. 15
32. Eylon D, Bania PJ (1978) Metallurgical Transactions A9:1273–1279
33. Hertzberg RW (1983) Deformation and Fracture Mechanics of Engineering Materials. In: John Wiley & Sons, New York, pp. 279–280

### 3 Microradiographic and Foil Penetration Methods for Quantification of Localized Corrosion

S.I. Rokhlin, B. Zoofan, G.S. Frankel

#### 3.1 Introduction

Early detection of corrosion is important to prevent fatigue crack initiation and to decrease the cost of aircraft repair. It is well known that the depth of pitting corrosion plays an important role in fatigue crack initiation and fatigue life. Figure 1 illustrates a significant reduction of fatigue life versus pit depth in Al 2024-T3 alloy [1]. Therefore, it is important to have nondestructive means for detecting corrosion pitting and measuring of its depth.

In this chapter, we discuss a quantitative microradiographic method for detecting of critical corrosion pitting associated with fatigue crack initiation, which is particularly accurate in pit depth determining, a critical parameter in determining fatigue life.

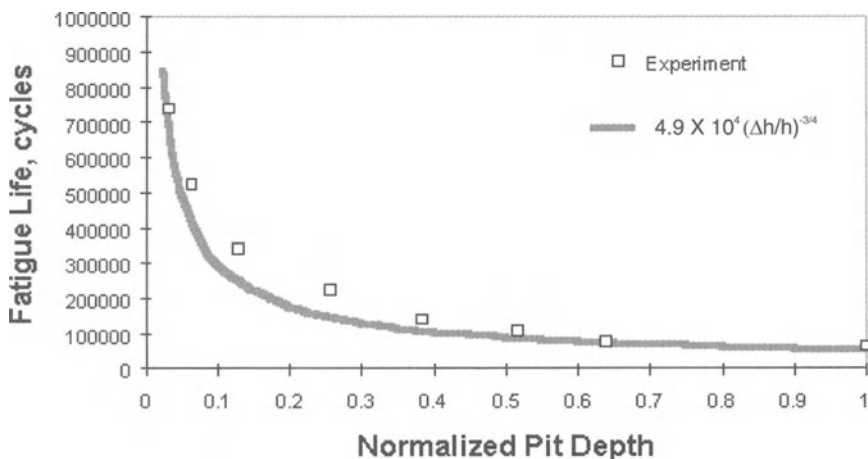


**Fig. 1.** Variation of fatigue life with normalized pit depth. D is pit depth, H is plate thickness

We used different techniques to compare the microradiographic depth measurement. These comparisons help point out some of the advantages and disadvantages of different techniques, and also demonstrate the advantages of a multi-sensory approach to NDE of airframe components.

The other technique described here for pitting corrosion study is the foil penetration method. The foil penetration method has been used to investigate the growth kinetics of localized corrosion in Al 2024-T3. In this method, the deepest pit is detected electrically when it just penetrates through the sample thickness. By varying the foil thickness, pit growth kinetics can be determined. Microradiography helps to quantify the pit depth distribution in the foil.

## 3.2 Background

The essence of radiography is modulation of x-ray intensity due to discontinuities or thickness change. One or two percent sensitivity to thickness change is achievable in conventional radiography. Unfortunately, the system's unsharpness reduces the radiographic resolution and detectability of small flaws such as pitting corrosion. This issue is of major importance for radiographic detection of early corrosion and forms the topic of our research and development.

The geometrical unsharpness can be reduced by using x-ray microfocal tubes. Microfocal radiography has negligible geometric unsharpness and therefore the system unsharpness is dominated by the unsharpness of the recording medium. By using projection magnification, it is possible to overcome the recording medium's unsharpness [2]. However, geometrical unsharpness increases with magnification, and thus optimum magnification exists where the effect of geometrical unsharpness balances the recording medium's unsharpness. To take full advantage of microradiography, one should optimize magnification and other system parameters by reducing overall system unsharpness, thus improving the radiographic system's detectability. The microradiographic technique is distinguished by the capability of producing images with high projection magnifications. The high-resolution images enabled us to develop quantitative NDE techniques to characterize corrosion microdamage and fine fatigue cracks in Al 2024-T3 alloys. Since we have shown that the size and the normalized depth of a pit have a critical effect on the fatigue life of a sample, the early detection of a microdamage site is an important task for any NDE technique. This necessitates a quantitative assessment of radiographic detectability. In characterizing the system's detectability, the question of optimum magnification and a suitable x-ray system for field inspection can be addressed. The detectability of a radiographic system depends on contrast sensitivity and the system's unsharpness. In a microradiographic system, the focal size of the x-ray source, projection magnification, and unsharpness of the imaging chain play important roles in detectability. The characteristics of the fluorescent screen in an image intensifier, the performances of the optical lenses, the CCD camera, and of the image display all have their own effect on the overall detectability of a radiographic system. The

development of general concepts of microradiographic system characterization is very important.

Probably one of the most challenging problems in the NDE of pitting corrosion is hidden corrosion. As far as radiographic techniques are concerned, hidden corrosion is not different from visible corrosion if two principal conditions are met. First, no obstacle should lie in the direction of the x-ray and the detector. Second, the thickness reduction due to corrosion damage should produce enough contrast sensitivity for the detecting medium. In radiography, the orientation angle between object and x-ray beam plays a vital role in the detectability of the image produced. Therefore, the radiographer should be aware of the viewing condition of the job under test.

The magnified images provided by the projection magnification technique enable us to use direct gray level reading in the pit area of the image. This is possible when the magnification is such that the pit image size is larger than the pixel size or the optical beam size of the densitometer. This allows us to measure the pit depth  $\Delta h$  by approximating the film characteristic curve with a gradient G.

One can obtain the change in film density D for a pit with depth  $\Delta h$ :

$$D = G \log(It) + K, \quad (1)$$

$$\Delta D = D_p - D_b = 0.43G\mu\Delta h, \quad (2)$$

where  $(It)$  is the radiographic exposure ( $t$  is time and  $I$  is x-ray intensity),  $K$  is a constant,  $\mu$  is linear radiographic attenuation,  $D_p$  is the optical density of images for different pits, and  $D_b$  is the optical density of the base metal. The accuracy of pit depth determination depends on several factors:

The main axis of each pit is perpendicular to the surface of the metal. Therefore, any change in the optical density in the pit image corresponds directly to the depth (thickness) change along the x-ray beam.

The influence of scattered radiation is considered negligible, which is satisfied at larger projective magnifications.

The method should be applied differently to small pits if their images after projection magnification are smaller than the densitometer beam size. For these small indications, a calibrated density strip should be used, and the gray level of the pitting should be compared by eye with the related gray level in the strip. It is reported that the smallest optical density difference that can be distinguished by eye is around  $\pm 0.02$  for normal eyes [2]. When the pit size image is smaller than the densitometer beam diameter, one should prefer the histogram method for pit depth measurement, which will be discussed below. The calibration curves for pit depth measurements were produced using samples with artificial pits and film microfocal radiography with projective magnifications of 10 and 40 times. The radiographs were digitized using a TV camera and a PC frame grabber for further analysis.

The images obtained from pits with known depths are used to set a reference curve for finding the unknown depth of pitting in the aluminum specimens. Two methods are used for this purpose, the densitometer and histogram methods.

### 3.3 Microradiographic System

In the beginning of this study, we designed, installed, and integrated an advanced microradiographic system. It includes a state-of-the-art imaging chain with a microfocal tube and a dedicated high precision micropositioning system. A FeinFocus® 225 kV x-ray unit with a 3–5  $\mu\text{m}$  (0.0002 in.) focal size is used as an x-ray source. The maximum output of the tube (tube current) is 3mA. The beam of electrons is focused by coils on the tungsten target similarly to an electron microscope. The cathode inside the x-ray tube is a point head filament to generate a fine, focused beam of electrons. The other feature in a microfocal system compared to a conventional one is that the tube is demountable so that the filament or anode assembly can be replaced easily. The vacuum inside the tube is maintained continuously by roughing and turbomolecular vacuum pumps. The tube has a 0.5 mm beryllium window to minimize filtering of the soft x-ray beam. The tube head is water-cooled and it is designed so that a specimen can be placed 5 mm from the target to allow for the highest projection magnification. The tube has a continuously variable focal spot size. The focal spot size, when adjusted to its smallest size, has a maximum diameter less than 5  $\mu\text{m}$ . During our experiment,

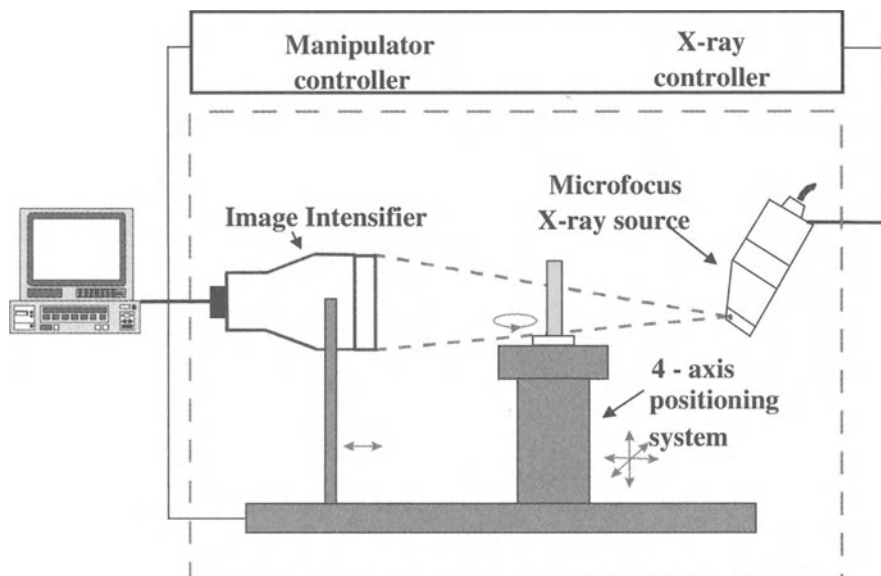


**Fig. 2.** Schematic of the microradiographic system

the exposure parameters are carefully selected so that the focal spot size for each exposure remains in the microfocal region of the tube to get the optimum resolution. The voltage, current, time, beam focus, and beam steering are controllable through fiber optic cables between the microprocessor based control unit, the generator and the tube. The accuracy of the voltage control is  $\pm 2\%$ , and of the current control is  $\pm 1\%$ . An image intensifier integrated with a Sony CCD camera (XC-75) with a standard frame rate of 30 frames/s is used for real-time radiography and also for aligning of the samples prior to film microradiography. Two additional TV cameras are used to monitor the exposure room and the position of the sample during the experiment inside the control room. To control the position of the sample, we designed a precise inspection positioning system, which has three linear (with  $2\mu$  resolution) and one rotational (with  $0.01^\circ$  resolution) computer controlled axis. One additional high-resolution linear axis is used for translation of the image intensifier. In addition, a separate x-y manipulator is used for positioning the x-ray source. The x-axis of the system is designed for 60 sec travel length with 30 lb. capacity, and the micron resolution movement of the sample provides accurate projection magnification of the image.

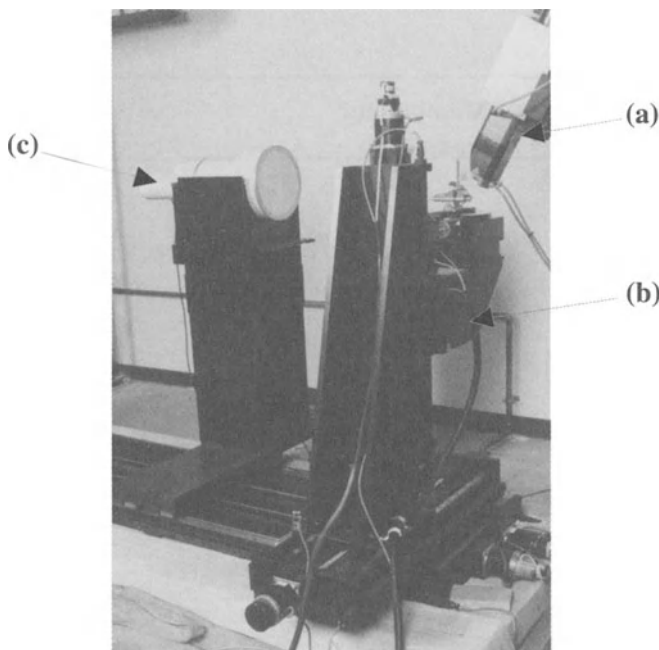


**Fig. 3.** General view of the microradiographic system. (a) x-ray tube; (b) mechanical positioning system; (c) image intensifier

To prevent any vibration of the specimen that could generate unwanted image smearing, the whole system is placed on a 4-inch thick 8 ft x 4 ft solid stone, which is placed on 0.5-inch thick strong rubber pad. The schematic of the developed microradiographic experimental setup for evaluating microdamage in different samples is shown in Fig. 2 and its photograph in Fig. 3. For film microradiography, the film can be placed in front of the image intensifier, which is in this case used for mechanical support of the film. Kodak AA film, a fast and high contrast film, was used to reduce the exposure time (due to the use of projection magnification, there is no need for higher resolution films). The exposed and processed films are digitized by illuminating them in front of a Hitachi® KP-M2 CCD camera. A monochromatic PCI-bus frame grabber board PCVision® (from Imaging Technology) with 2MB of onboard memory installed in a PC computer was used for real-time microradiography and digitization of x-ray films. The sharp images obtained during microradiography enable further magnification by the film digitization camera. This optical magnification improves the pixel resolution of the digitized images.

## 3.4 Microradiographic Methods

### 3.4.1 Microradiographic Methods Evaluation

#### *Three-Dimensional Simulation of Radiographic Images*

A technical problem inherent in radiography of complex objects is selection of radiographic views. Simulation of radiographs can provide significant help in optimizing selection of such views, can help in radiograph interpretation, and can serve as a useful training tool. As an aid to understanding the simulation method, let us first refer to Fig. 4, where a sample with pitting is shown. The x-ray is attenuated as it passes through the material. The attenuation depends on the linear attenuation coefficient and the distance  $x$  in the material along the x-ray path.

For example, the intensity of an x-ray with initial intensity  $I_0$  passing a distance  $l$  through a specimen (path  $L_0$  in Fig. 4) is

$$I = I_0 e^{-\mu l}. \quad (3)$$

To simulate radiographic images of a complicated nonhomogeneous object, one must calculate the attenuation along the x-ray path for each pixel (picture element) in the display. The straightforward technique for these calculations is ray tracing. In this method, the attenuation along path  $L$  in (1) is approximated by

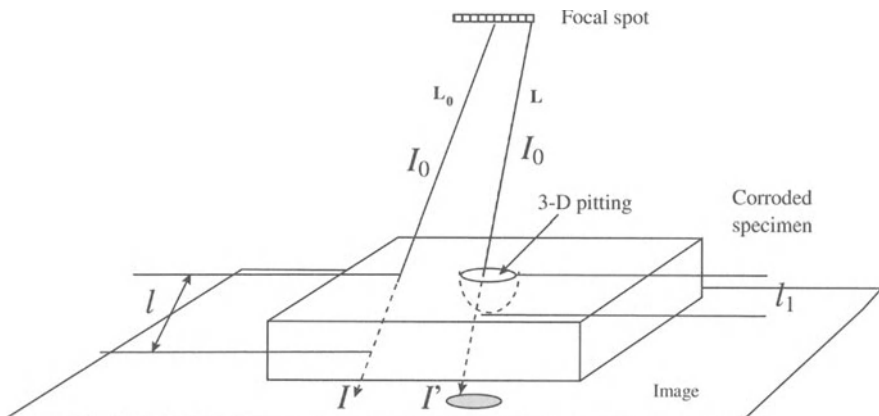


**Fig. 4.** Radiographic image formation of a specimen with a pit

$$I' \approx I_0 \exp \left[ - \sum_k \mu(x_k) \Delta x \right], \quad (4)$$

where  $x_k$  is a point along path  $L$  and  $\mu(x_k)$  is the attenuation coefficient at  $x_k$ . For reasonable accuracy, the step size  $\Delta x$  must be made small for inhomogeneous objects ( $\mu$  depends on  $x$ ). When one takes into account the fact that this calculation must be made for each pixel and the number of pixels is large, one sees that the computational requirements for this approach are monumental. Suppose, however, that the object is composed of several homogeneous pieces. Then the linear attenuation can be calculated for each piece. The resulting linear attenuation for the entire object is given via the principle of superposition. In particular, if the object is composed of  $n$  homogeneous pieces with linear attenuation coefficients ( $\mu_1, \mu_2, \dots, \mu_n$ ) and intersection lengths ( $l_1, l_2, \dots, l_n$ ) for a given x-ray path with the pieces, then by this method, only the intersection length  $l_k$  must be calculated for each path. If these lengths can be computed for an entire radiographic object,

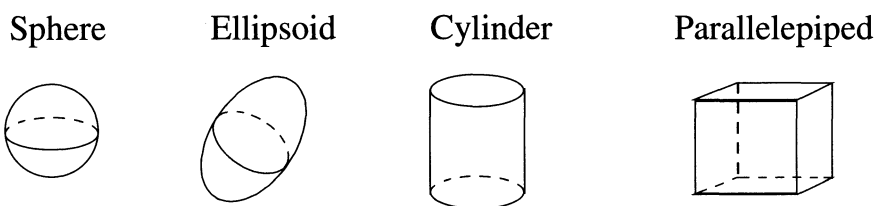


**Fig. 5.** Base elements for simulation of radiographs

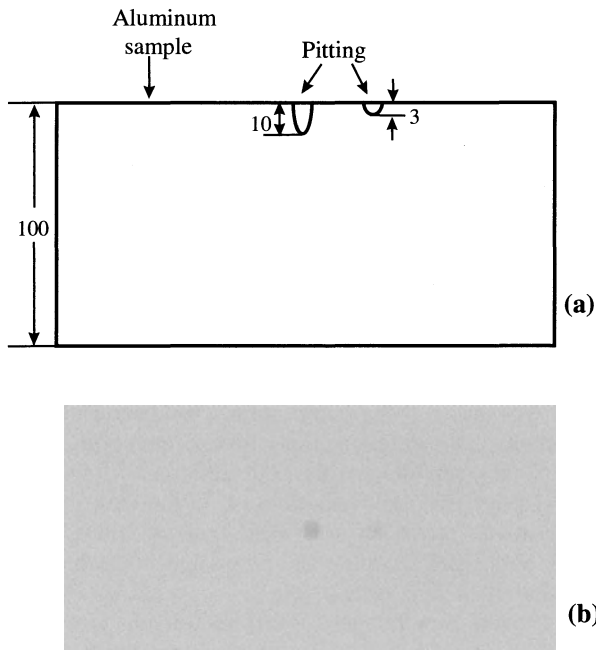


**Fig. 6.** Simulation of corrosion pitting

computational requirements can be reduced by a factor of several hundred. The method developed uses this approach. A number of base elements (spheres, rectangles, cylinders, etc.) are introduced, which may be combined in arbitrary orientations to form more complex objects (Fig. 5).

The process of radiographic simulation is to decompose the object into a collection of basic elements. We have derived analytical expressions for the length of intersection of arbitrary lines for the base elements. The positions and orientations of these elements must be stored in a data file, called the object description data file. The user should provide the object description data file and the location and beam geometry of the x-ray source. Once this data file is prepared, the simulation can be performed. Then the attenuation is calculated, and the image is automatically displayed on the display monitor. This method allows near real-time radiographic simulation on a PC platform. The actual simulation time depends on object complexity and size. For example, Fig. 6a shows a specimen with two different pits corroded to different depths and Fig. 6b shows the simulation results. To simulate pitting corrosion, two base elements are used: a finite cylinder and a semisphere attached to its end. The base element for the sample is a parallelepiped.

### **Microradiographic Detectability**

**Sample Preparation:** To find the detectability (the minimum visible depth  $\Delta h$  of a pit for a given pit diameter  $\phi$ ), we developed 1.6 mm Al 2024-T3 dogbone samples with artificial pits produced by electrodisscharge machining (EDM) with precise depth control. The samples are standard fatigue samples. The geometry and sizes of the pits are shown in Fig. 7a, b.

**Detectability Results:** The image of each artificial pit is captured at different projection magnifications in the range from 1X to 150X. The exposure parameters, tube voltage: 46 kV, current: 158  $\mu$ A, were constant for all magnifications. Figure 8a, b shows different samples and the radiographic setup. For each magnification, the source-to-detector distance ( $f_s$ ) (Fig. 9) is kept constant and the object-to-source distance  $f_o$  was varied to give appropriate projection magnifications. A 9-inch, HX series Thomson image intensifier with a  $\frac{1}{2}$ -inch Sony CCD camera and a high-resolution, 17-inch monitor with 800 horizontal lines were used as a receiving device. To decrease the random noise in the real-time images, a DVS-3000 Hamamatsu image processor was used for fast frame averaging for 252 frames. After averaging 252 frames, the pit image at each magnification was judged as visible, barely visible, or invisible.

Some examples of real-time images for different depths and different projection magnifications are shown in Fig. 10. Figure 11 shows the typical dependence of the image brightness  $\Delta B$  normalized to the background brightness  $B_0$ , on magnification. The data are collected for 12 pit depths at different magnifications. As an example, the curves are plotted for just two pit depths (shallow: 40  $\mu$ m deep,  $\Delta h/h=2.5\%$  and deep: 120  $\mu$ m deep,  $\Delta h/h=7.5\%$ ). The data shows that the

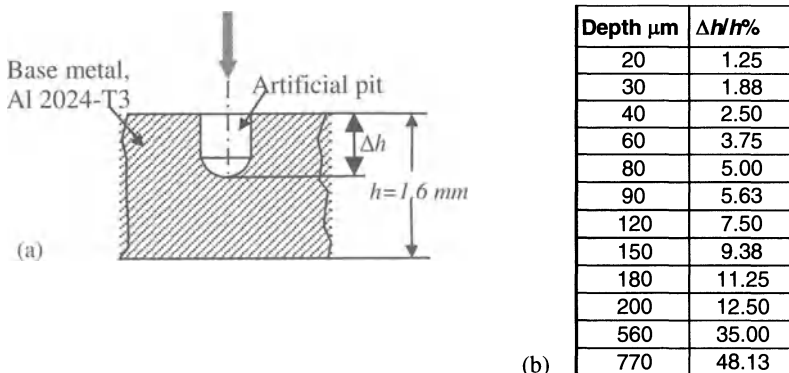


**Fig. 7.** (a) The profile of an artificial pit introduced by EDM. (b) The actual and normalized depths of artificial pits

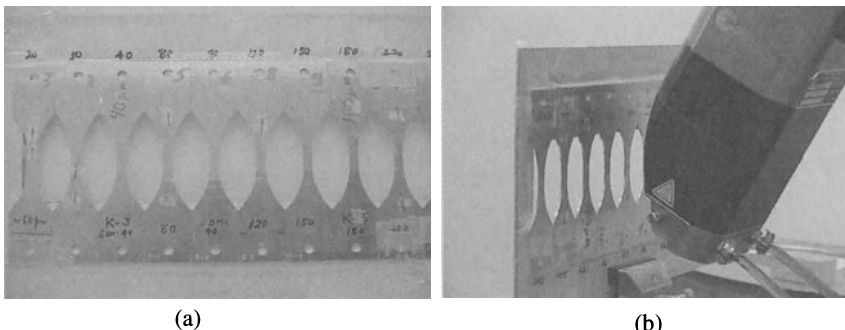


**Fig. 8.** (a) Al 2024-T3 dogbone samples with artificial pits of different depths. (b) The samples are held in front of the fine focus tube head. Projection magnification was varied from 1X to 150X for each sample (pit depth)

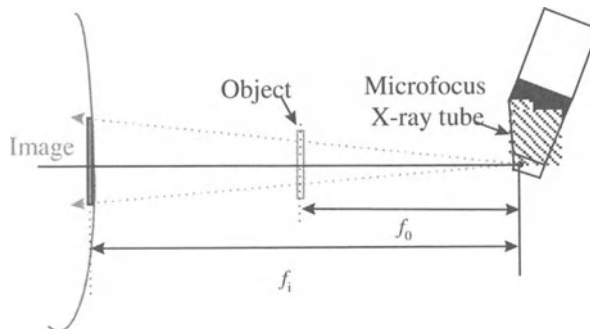


**Fig. 9.** Experimental setup for taking exposure at different projection magnification ( $f_i = 30$  inches for all cases)

normalized brightness of the image for each pit reaches a maximum versus magnification and the image of the pit becomes invisible for small or very large magnifications.

The data for visible, invisible, and barely visible pits are collected in Fig. 12, where normalized pit depths are shown versus projection magnification. The dashed line indicates the boundary between visible and invisible regions. From this curve, it is obvious that in order to detect a single pit at very low magnification, the pit should be considerably deep. The curves are formed by two different curve branches; in the left branch, the system detectability increases with magnification, (pit threshold visibility contrast  $\Delta h/h$  decreases) until it reaches the inherent contrast limitation of the radiographic system. The magnification at the curve dip represents the optimum projection magnification. In the left branch of the magnification range, the effect of the detector unsharpness on the contrast versus magnification is the dominant factor. The effect of receiving chain

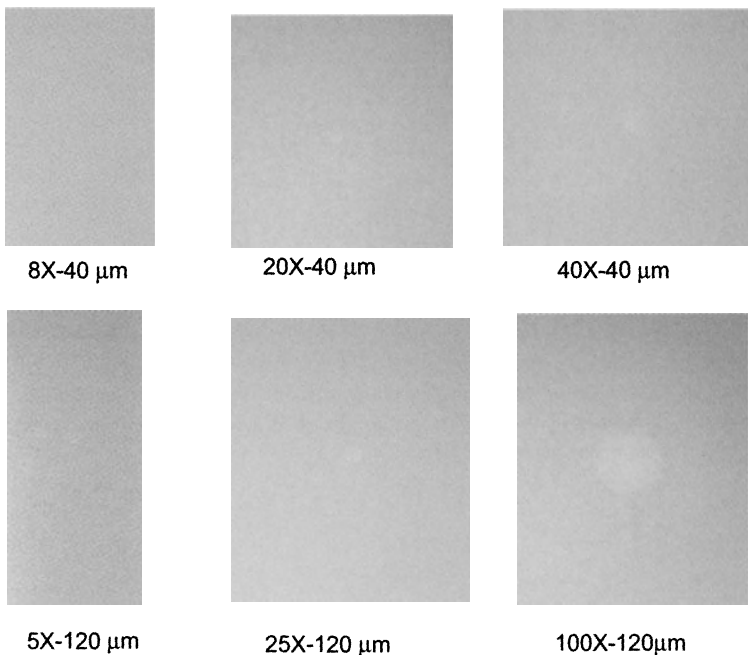


**Fig. 10.** Examples of a few pit images of different depths in  $\mu\text{m}$  at different projection magnifications

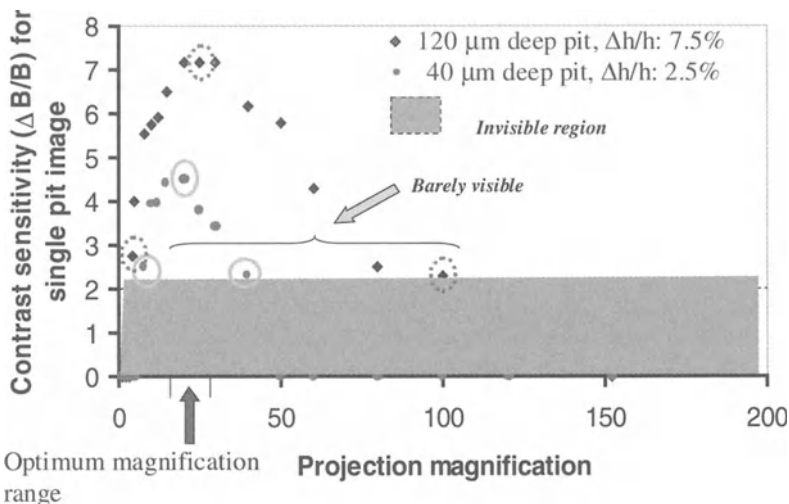


**Fig. 11.** The effect of projection magnification on pit detectability. The marks **O** and **C** indicate the magnification for images shown previously in Fig. 10

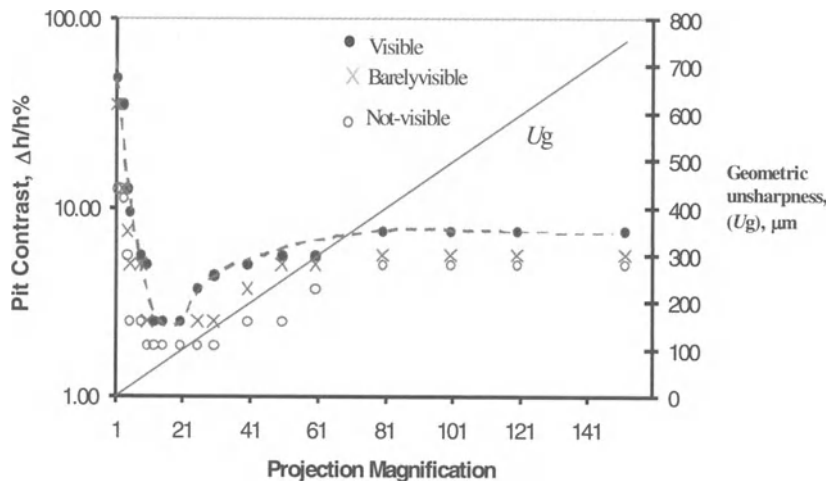


**Fig. 12.** The detectability curve of different normalized pit depths at different projection magnifications

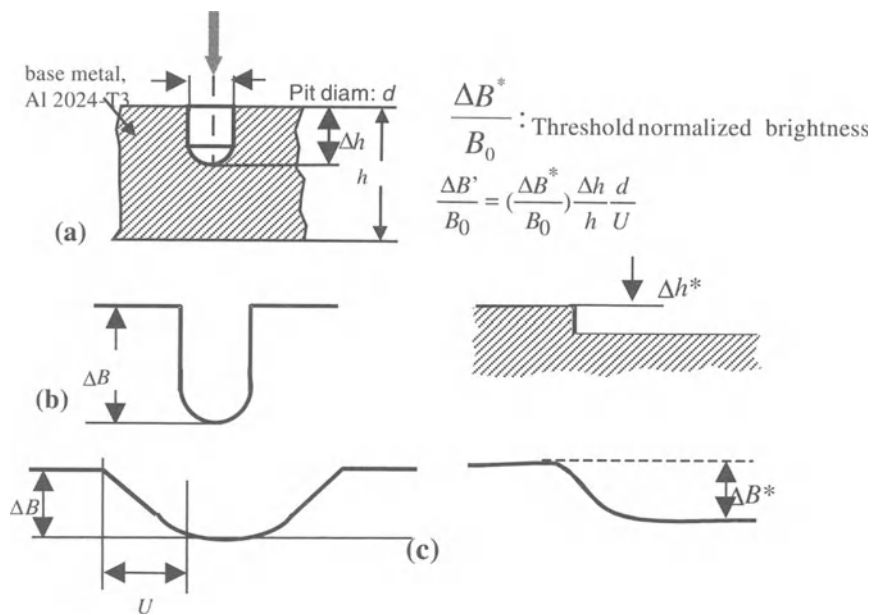


**Fig. 13.** Illustration of the effect of unsharpness on the normalized brightness of a pit image. (a) The profile of a pit. (b) Brightness of a pit in the absence of unsharpness. (c) Reduction in brightness due to the system unsharpness

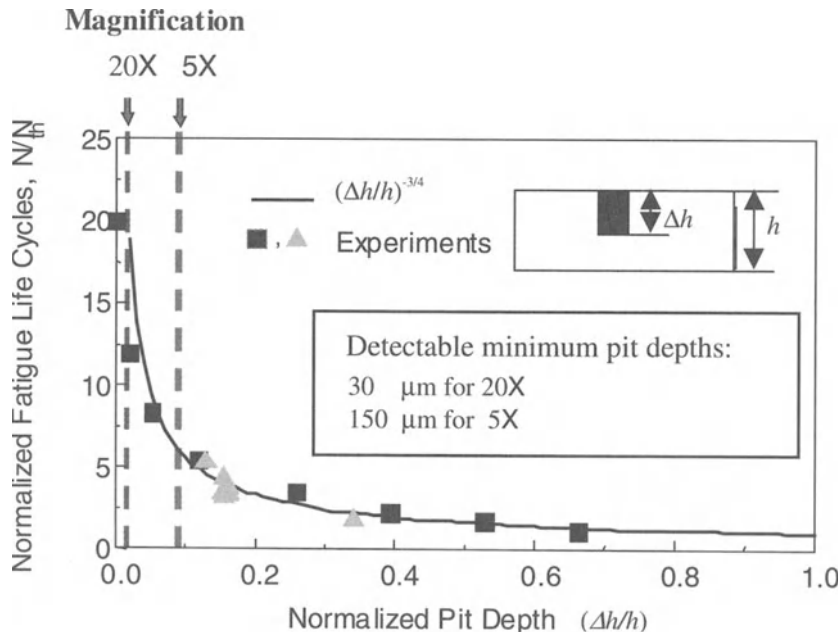


**Fig. 14.** Variation of fatigue life with normalized pit depth. (The proposed model for the fatigue life with a single pit in an Al 2024-T3 sample 1.6 mm thick)

unsharpness decreases due to the geometrical magnification of the pit image size relative to the pixel size of the receiver. On the right branch of the curve (after passing the dip), the system detectability gradually decreases. The detectability curve shows the strong effect of the system's geometric unsharpness that increases with magnification and becomes a dominant factor. The solid line labeled  $U_g$  shows the variation of geometric unsharpness versus projection magnification  $M$ ,  $U_g = F(M-1)$ , where  $F$  is the focal spot size. Thus, the dip in the contrast threshold (maximum detectability) is formed by competition between the decrease in the receiver unsharpness and the increase in the geometric unsharpness versus magnification.

The effect of geometric unsharpness on image contrast is explained in Fig. 13. The reduction in image contrast is a function of the system threshold brightness, the diameter of the pit (constant at this case), the normalized pit depth, and the system unsharpness. The increase in the total unsharpness gradually decreases the image contrast and the system detectability. The importance of the system detectability for detecting corrosion damage is illustrated in Fig. 14. As an example, the smallest detectable pit at a projection magnification of 5X reduces the fatigue life of the sample approximately four times (based on the single pit fatigue life model [1]). With a system capable of projection magnification by 20X, the smallest detectable pit will reduce the fatigue life about 20%.

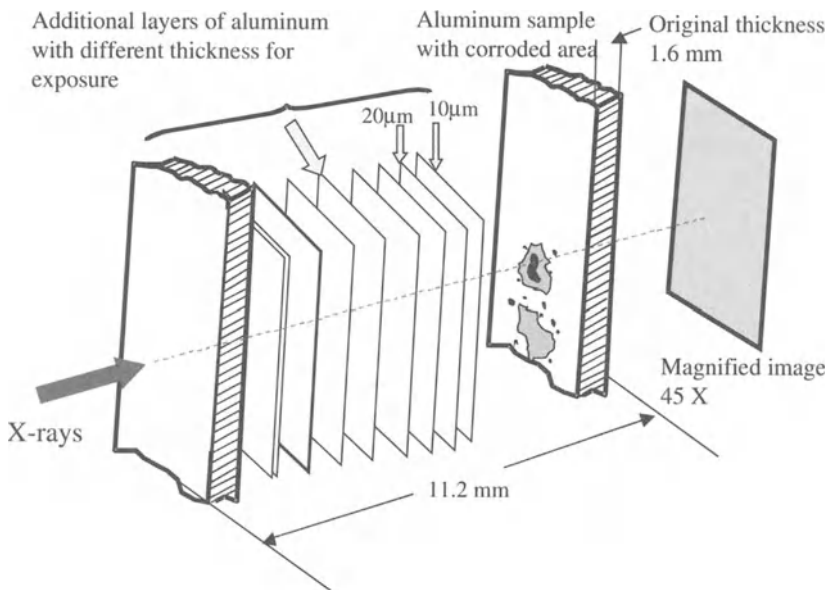


**Fig. 15.** Experimental setup for microradiography of hidden corrosion

### **Microradiographic Characterization of Hidden Corrosion**

**Sample Preparation:** To simulate the effect of hidden corrosion, different aluminum layers with thicknesses varying from 10 μm up to 9.6 mm are added to a 1.6 mm Al 2024-T3 sample with a corrosion site (Fig. 15). The experimental conditions were set up so that in all cases the same projection magnification was applied to the corrosion area and the films or real-time microradiographic images have the same gray level as the background area.

**Results:** Figure 16a, b shows several corrosion images for film and real-time microradiography after adding different thicknesses of aluminum. The contrast sensitivity of the image of the deepest pit is measured and plotted versus the total thickness. For film microradiography, the difference in the film optical densities of the corroded area and the base metal were used for contrast measurement, and for real-time microradiography, the difference in brightness for these areas. The theoretical contrast sensitivity for film microradiography is calculated from the following formula:

$$\frac{\Delta h}{h} = \frac{2.3 \Delta D}{\mu G h} \left( 1 + \frac{I_s}{I_D} \right) \quad (5)$$

where  $\Delta D$  is the measured optical density difference,  $G$  the average gradient of the film characteristic curve,  $\mu$  the linear absorption coefficient of aluminum for applied tube voltages for each thickness, and  $I_s$  the scattered radiation.  $\Delta h$  is the depth of the corroded area and is constant for all cases.

For real-time microradiography, the theoretical contrast sensitivity is calculated based on

$$\frac{\Delta h}{h} = \frac{\Delta B}{B\mu\gamma_s} \times 100, \quad (6)$$

where  $\Delta B$  is the measured brightness difference,  $\gamma_s$  is a screen characteristic. Note that for all cases,  $\Delta h$  is constant and  $I_s/I_D$  is negligible due to projection magnification.

The measured contrast sensitivities for each case are compared with the theoretical in Fig. 17.

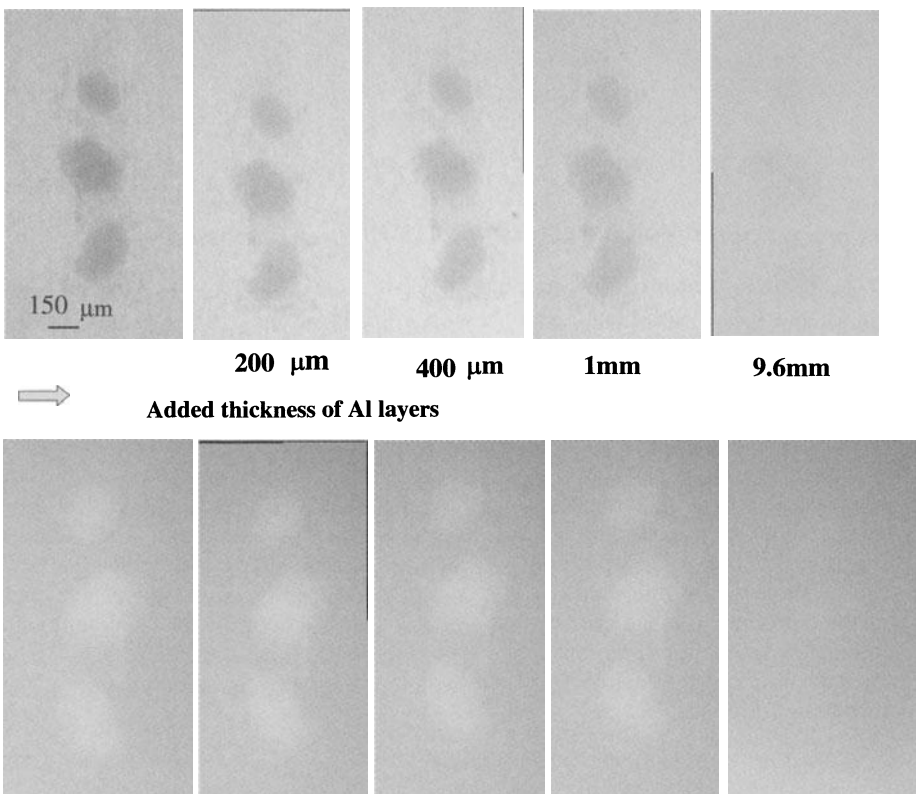


**Fig. 16.** Typical examples of hidden corrosion images after adding different thicknesses of Al. *Top row:* film microradiography; *bottom row:* real-time microradiography

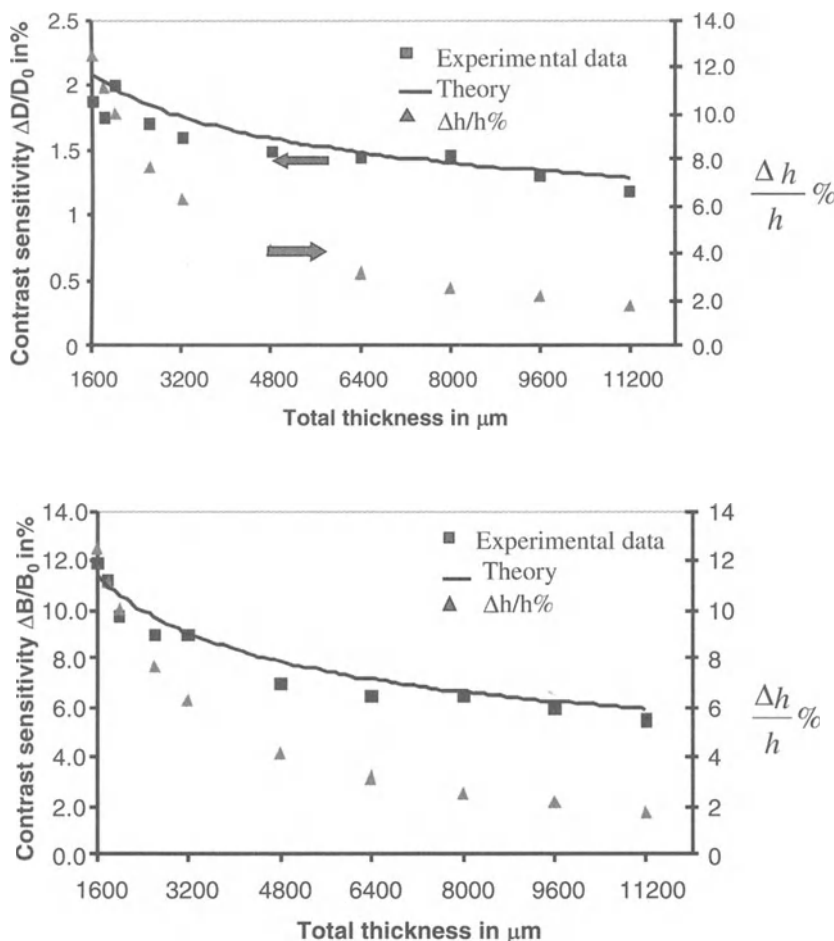


**Fig. 17.** Contrast sensitivity measurements for the corroded sample covered by different aluminum layers. *Top*: film microradiography; *bottom*: real-time microradiography

Film and real-time microradiographic evaluation of hidden corrosion show a reduction in the overall contrast sensitivity of images as thickness increases. Since the pitted area is larger than the total unsharpness of the system, this reduction is due to the increase in the total penetrating thickness of the corroded sample that causes a reduction in overall image contrast. The linear attenuation coefficients  $\mu$  obtained from reference [4] are corrected for the applied tube voltages. Note that the linear attenuation coefficients given in the reference are for pure aluminum (with  $Z=13$ ) whereas the samples in our experiment were Al 2024-T3 with 4.4% Cu, 0.6% Mn, 1.5% Mg, and the rest Al with a physical density of  $2.77 \times 10^3 \text{ kg/m}^3$  ( $0.100 \text{ lb/in}^3$ ) for a monochromatic source, whereas our x-ray source had a wide

spectrum. This may explain differences between theoretical and experimental results.

### **3.4.2 Microradiography of Corrosion Samples**

#### ***Methodology***

To compare microradiography and conventional radiography, images were obtained for the same sample by both techniques. A tube with 0.4 mm (0.016 inch) focal size was used for conventional radiography.

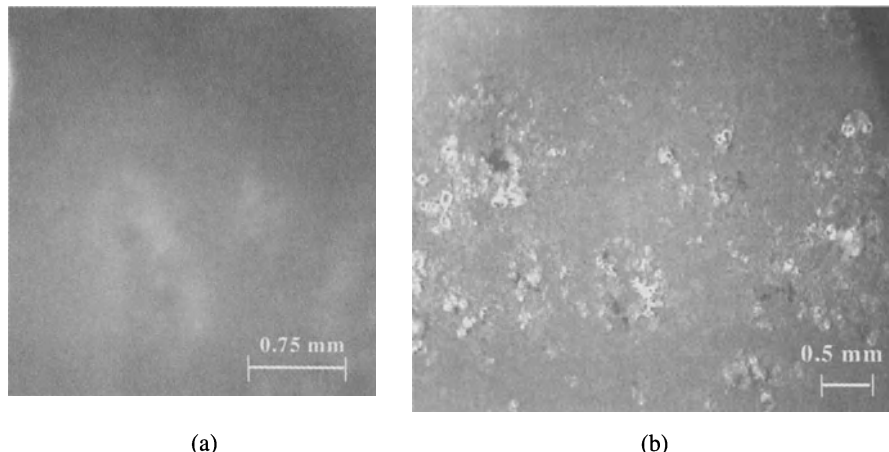
#### ***Preparation of the Samples with Corrosion***

Al 2024-T3 was selected as a model material system in this study. For this group of experiments, pitting corrosion was produced by exposure in a bath containing about 21 g per liter (0.175 lb. per gal.) NaCl solution for different periods starting from 4 hours to 4 days. Two types of specimens were corroded using this method: Al foil specimens 0.016 mm (0.0006 inch) thick and Al 2024-T3 fatigue specimens 1.6 mm (0.06 inch) thick. In addition, the corroded samples which were used for microradiographic evaluation and comparison of different NDE methods were produced by the University of Dayton and Wright Patterson Laboratories. A different group of corroded samples discussed in Sects. 3.5 and 3.6 was produced at the OSU Fontana Corrosion Center.

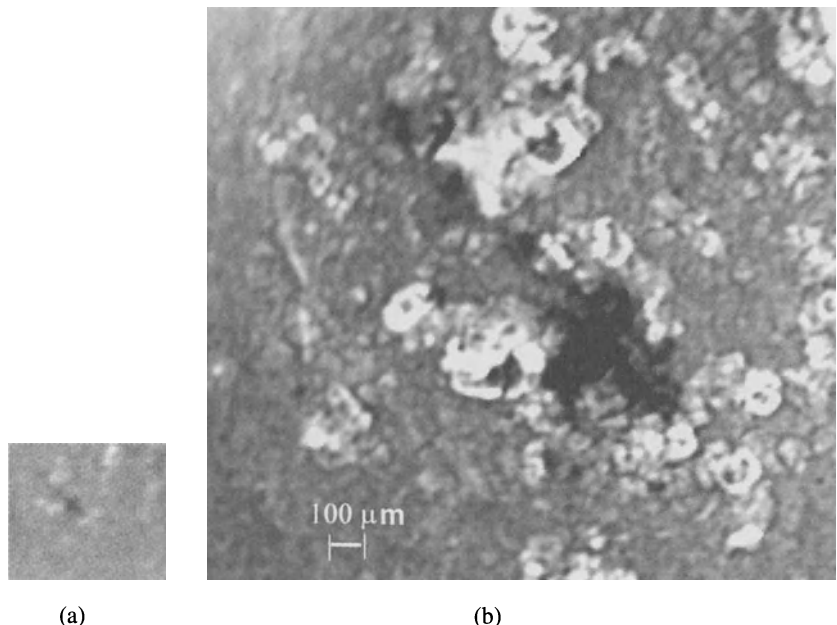
#### ***Results***

Figure 18a shows the results indicating that geometric unsharpness completely destroys the image in conventional radiography if one uses projection magnification.

Projection magnification is the key to sharp radiographic imaging of fine details in an object. This is illustrated in Fig. 19a where a conventional radiograph (with no projection magnification) is compared with a microradiographic image in Fig. 19b. The same optical magnification is used for image digitization in both cases. The advantage of microradiography with projection magnification is obvious here. The corrosion products are clearly seen as white areas in Fig. 20a. The effect of corrosion products on the radiographic image requires careful study. Also, one can see that 10  $\mu\text{m}$  (0.0004 inch) size pitting is detectable in the image. Figure 20b shows the initiation of very fine cracks in the vicinity of a pit.



**Fig. 18.** Comparison of conventional radiography with microradiography; the projection magnification is equal to 10. (a) Radiograph taken with a small focal x-ray source 0.4 mm; (b) Radiograph of the same sample with a microfocal x-ray source



**Fig. 19.** (a) Conventional radiograph with no projection magnification but with optical magnification; (b) Microradiograph of the same area with 10X projection magnification

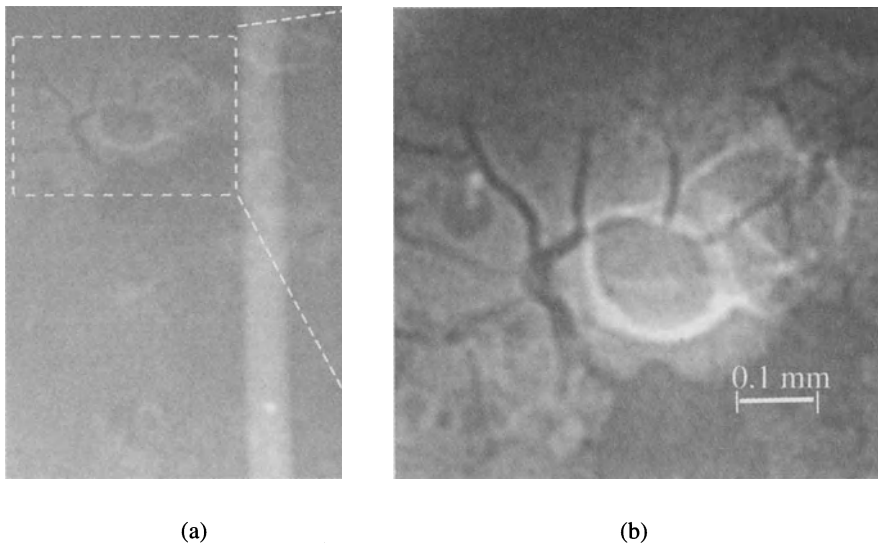


**Fig. 20.** Microradiograph of the corroded sample with 25X projection magnification. The bright strip on the image is the image of a wire for calibrating the magnification of the image (a) without any optical magnification; (b) with optical magnification in the selected area

### 3.4.3 Microradiographic Methods for Pit Depth Measurement

#### ***Methodology***

Two methods are used for this purpose, the densitometer and histogram methods. The densitometry method is based on finding the difference between the direct reading of the optical density on the image of the pit and the optical density of the adjacent area of the base metal with a densitometer. After projection magnification, it is possible to use a direct densitometer reading in the pit images when the pit image size is larger than the optical beam size of the densitometer.

The second method is based on finding the mean values of the gray level distribution (histograms) of the digitized images in the pit area and comparing them to the histogram of the adjoining base metal area of the radiograph.

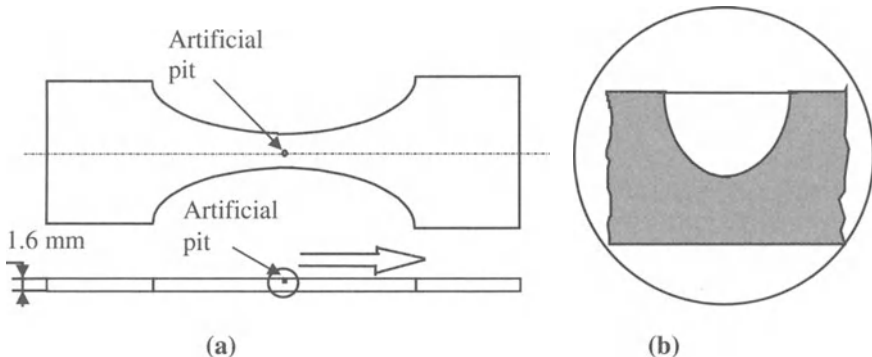


**Fig. 21.** (a) Schematic of an aluminum sample with artificial pit; (b) Approximate profile of the pit

### Samples for Radiographic Depth Measurement

To calibrate microradiographic measurements of corrosion pit depths, we prepared samples with artificial pits produced by spark erosion, as shown in Fig. 21. The samples have pits with 200  $\mu\text{m}$  (0.008 inch) diameters and depths ranging from 50 to 250  $\mu\text{m}$  (0.002 to 0.01 inch). The shape of the pits can be considered part of an ellipsoid, as shown in Fig. 21b.

### Results

The calibration curves for pit depth measurements were produced using samples with artificial pits and film microfocal radiography with projective magnifications of 10 and 40X. The radiographs were digitized using a CCD camera and a PC frame grabber for further analysis. As an example, Fig. 22 shows the digitized images with 40X projection magnification. The images obtained from the artificial pits with known depths are used to set a reference curve for finding the unknown depth of pitting in the aluminum specimens.

As an example, Fig. 23 shows the shift in the histogram mean of the image of a 50- $\mu\text{m}$  deep pit from the mean value of the image grayness in the base metal area. Figure 24 shows the developed calibration curve. The pitting depths are determined in the radiographic image shown in Fig. 25, which are measured by the calibration curve. Pits with diameters of about 10  $\mu\text{m}$  are detectable in the image.

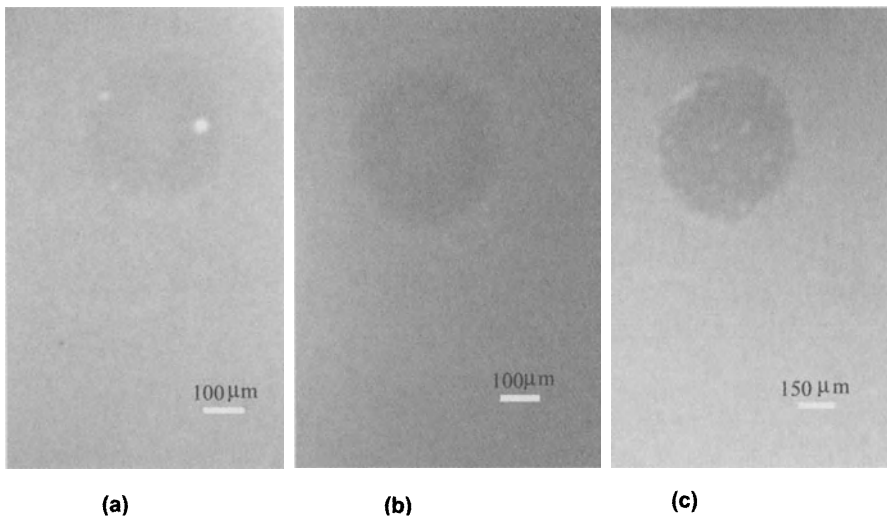


**Fig. 22.** Digitized radiographs of artificial pits of different depths; (a) 50  $\mu\text{m}$ , (b) 100  $\mu\text{m}$ , (c) 150  $\mu\text{m}$ . The projection magnification is 40X for all images. The optical magnification is 1.5X. The darker areas show the pits; the bright spots in the pits show impurities trapped inside the pit during spark erosion

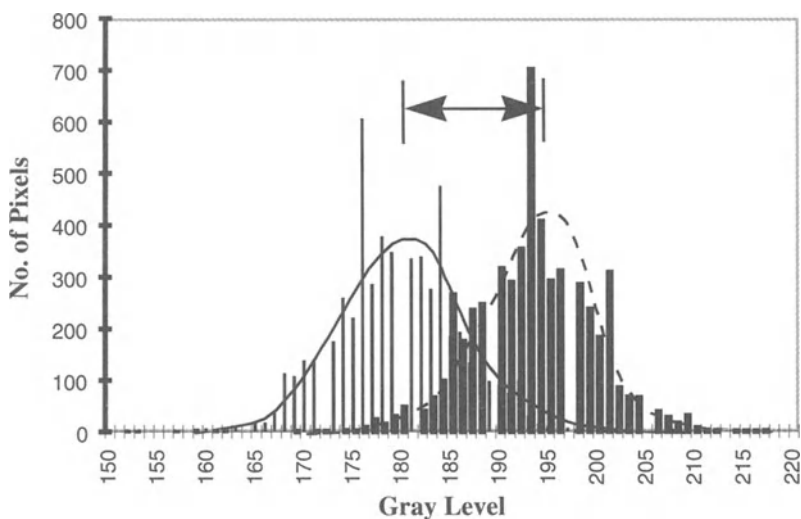


**Fig. 23.** Shift in the mean value of the histogram of images of the pit and base metal

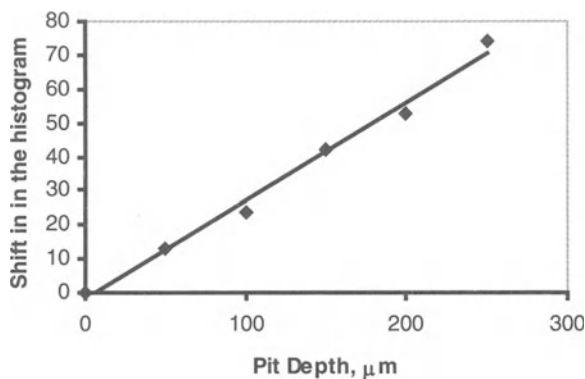


**Fig. 24.** Variation of shift in the histogram versus pit depth

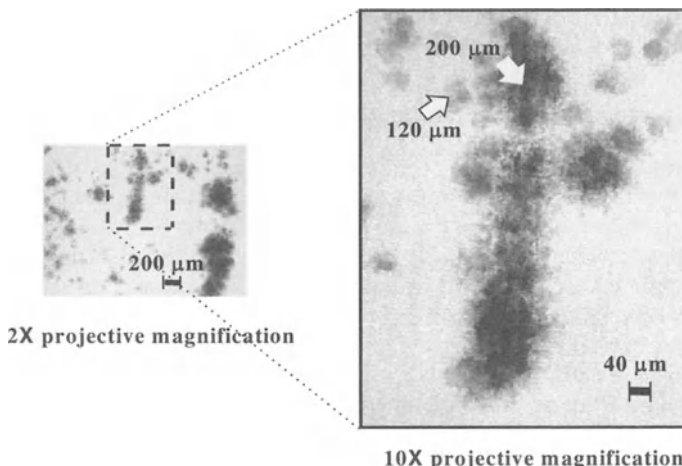


**Fig. 25.** Microradiography of 0.8 mm aluminum sample with different projection magnifications and with 4.5X optical magnification. Signs indicate the calculated depth of the corrosion area

### 3.4.4 Validation of Microradiographic Pit Depth Measurement

The accuracy of the developed technique has been validated using different alternative methods: optical microscopy of the corroded samples, metallographic cross sectioning, x-ray exposure at different angles, three-dimensional optical

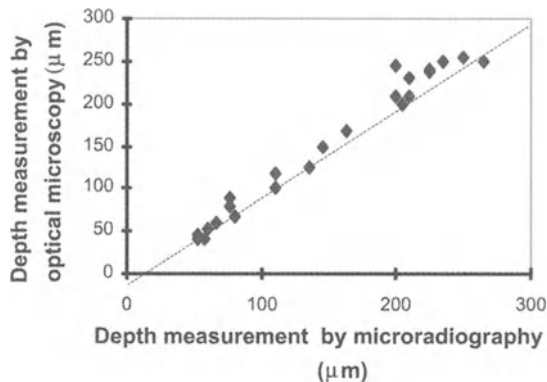


**Fig. 26.** Comparison between artificial pit depth measurement by optical microscopy and by microradiography

profilometry, and finally pixel-by-pixel comparison between microradiography and profilometry data for corroded samples.

#### ***Comparison with Optical Measurement***

The calibration curve (Fig. 24) for pit depth measurement has been used for a large number of Al 2024-T3 samples with artificial pits produced by EDM. Microradiographs with 20X projection magnification and 2X optical magnification were digitized, and pit depths were measured. The pit depths were also measured by optical microscopy by image focusing on the pit bottoms and sample surface. Figure 26 compares the microradiographic depth measurement with those measured by optical microscopy.

One can see that there is good agreement between the two techniques. In some cases, the optical microscope measurement may be affected by an obstacle inside the pit.

#### ***Comparison of Microradiographic Depth Measurement Method with Mechanically Sliced Corroded Samples***

Al 2024-T3 standard dogbone fatigue test samples 1.6 mm thick and corrosion pits introduced on one surface are used for this comparison. The desired directions for the sample slicing are marked on them with 20  $\mu\text{m}$  diameter 4% gold wire (see Fig. 27). Before cutting the samples, microradiographs are taken on high-contrast

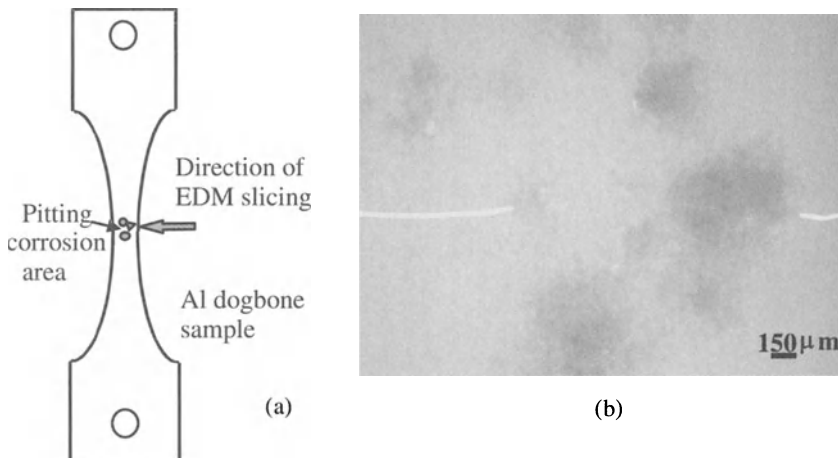


**Fig. 27.** (a) Example of an Al dogbone sample with pitting corrosion and indicated direction of slicing; (b) Digitized microradiograph (40X) of the corroded sample to be sliced along the line marked with two 20  $\mu\text{m}$  wires (white lines at the *left* and *right* sides of the image (b))

and high-speed films with 40X projection magnification. The cutting directions are indicated by the wire images in the radiographs. The samples are then precisely sliced in the indicated directions by EDM to save as much as possible of the corroded area. In each case, the line to be cut is selected so that it contains both shallow and deep pitting corrosion areas. The gray levels of pitting corrosion along the slice are obtained by line profiling exactly in the direction indicated in the microradiographs. The gray level of the image of the base metal as background is taken by a free-hand histogram on the corrosion-free area next to the corroded area. The shifts in the histogram of each pixel compared to that of the base metal are then converted to depth (in  $\mu\text{m}$ ) by using the calibrated line developed for the same types of aluminum samples and with the same projection magnifications.

The radiographic data are compared to direct pit depth measurement taken from the cross section of the sliced samples. Optical microscope images were used with the same magnifications as the radiographic images to find the boundaries of the corroded area in the cross section of the sample (Fig. 28). The image of a corrosion-free cross section is subtracted from the sliced surface to find the boundary of the corroded area. Microscope scaling and pixel calibrations are used to find the depth of each point on the corrosion boundary at the cross section. The surface line of the sample is considered zero height, and the beginning and ending of the pitting corrosion area are the two extreme points of the cross section to be compared. Exactly the same number of pixels is selected on both the optical images of the cross section and the microradiographic images.

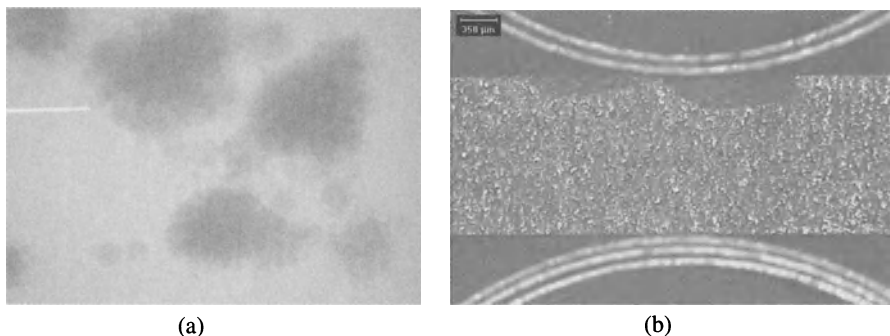


**Fig. 28.** (a) Example of microradiograph (40X) of an aluminum sample before slicing on the indicated path; (b) The optical microscopic image (40X) of the same sample after slicing showing the cross section of pitting corrosion as a dark area. The white curved lines are the image of the special fixture for holding the sample

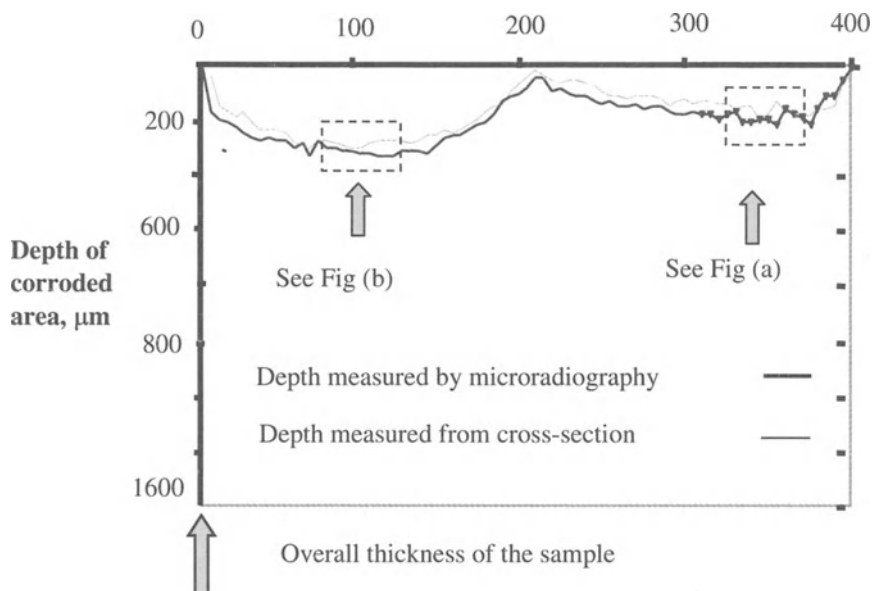


**Fig. 29.** One example of the comparison between optical and microradiographic depth measurement

Figure 29 shows this comparison for one of the corroded aluminum samples. The vertical axis, which shows the depth of the pitting corrosion inside the sample, is extended to 1600  $\mu\text{m}$ , the thickness of the sample. The area below the two curves represents the undamaged area inside the sample.

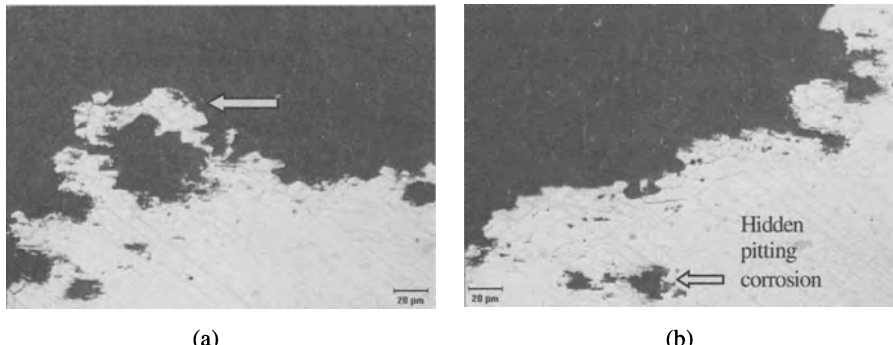


**Fig. 30.** (a and b) Optical microscopy images with 400X magnification of two cross sections indicated by boxes in Fig. 29, which show chipped out corrosion products and hidden pitting corrosion contributing to discrepancies in the results of the two methods of measurement

The overall profiles of the corroded area obtained by each method show similar patterns. To investigate the area of unmatched depths measured by the two methods, further investigation is done by optical microscopy with higher magnification (400X) on the sliced pitting corrosion cross section. Figure 30 shows two examples from two different areas. An average of 45 μm difference in depths can be observed between the two measurement methods. The depths measured from the cross section by the direct optical method are higher in some areas since during cross sectioning, some of the corrosion products could have chipped from the pit surface and thus do not appear in the optical images. An example of chipped out corrosion product can be observed at higher optical magnifications in Fig. 30a. The pit depths measured in these areas along the path of the x-ray are less since the corrosion products have absorption comparable to that of the Al, contribute to x-ray attenuation, and as a consequence, to the x-ray image. On the other hand, the presence of any hidden corrosion areas leads to a larger depth measurement by microradiography than by optical measurement. Two examples are highlighted in Fig. 29.

#### ***Comparison of Microradiographic Depth Measurement Method with Data Obtained from a 90° Shot***

The 90° exposures show the detectability of hidden pitting and can also provide useful data for evaluating the microradiographic depth measurement. By its through-transmission nature, a radiographic image provides two-dimensional information about the sample under test without providing depth information. Two shots of a sample at perpendicular angles can provide direct information about the depths of internal structures or discontinuities. This can be done only if the geometric configuration of an object and the energy of the radiation allow one to carry out such an evaluation. This is another way to evaluate the

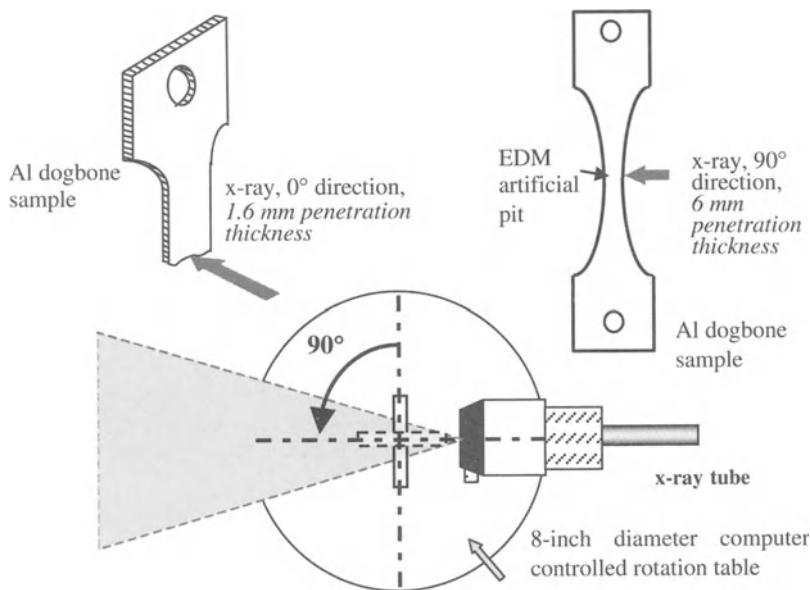


**Fig. 31.** The experimental setup for longitudinal and transverse magnifications of artificial pits

microradiographic depth measurement. Two perpendicular shots are taken of samples with artificial pits of controlled depths, and data obtained from these shots are compared.

Artificial pits with controlled depths produced by EDM are used for evaluating the microradiographic depth measurement by two perpendicular shots. Figure 31 shows the radiographic setup of the experiment. The longitudinal images or 0° shots (the angle between the axis of an artificial pit and the x-ray direction is 0°) are used for microradiographic depth measurement by shifting the gray level of the image. The transverse images or 90° shots (the angle between the axis of an artificial pit and the x-ray direction is 90°) are used to measure the depth of each pit directly by pixel calibration. A precise computer controlled 8-inch rotating table (with 0.01° resolution) is used to rotate the sample 90°. Due to the dogbone shape of the samples, further adjustment is done to get the same projection magnification as the 0° shot. The thickness of aluminum to be penetrated by the 0° shot is 1.6mm; for the 90°, it is 6mm. In each case, the exposure parameters are carefully selected, so that the focal spot size stays in the microfocal range.

Figure 32 shows two examples of 0° and 90° shots. The microradiograph at 90° shows the profile of the artificial pits produced by EDM, as well as the location of the microinclusions trapped during the EDM process (Fig. 32c, d).

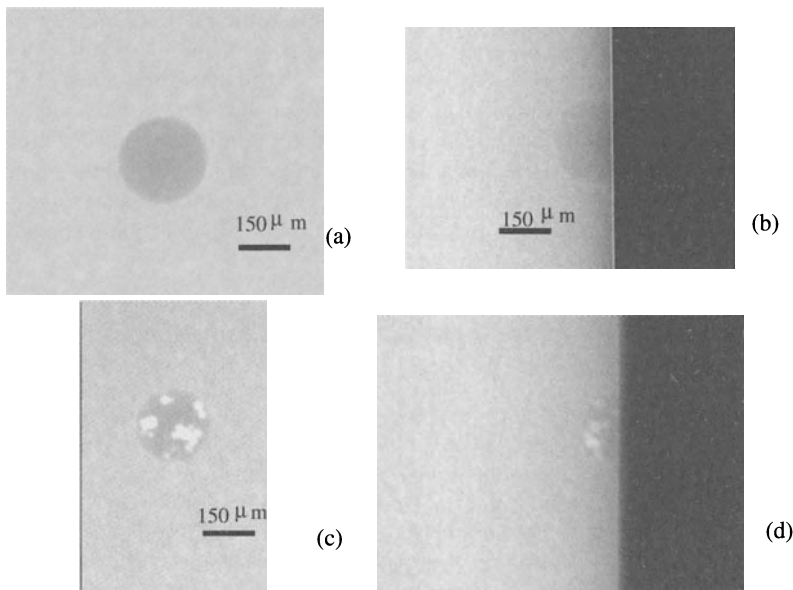


**Fig. 32.** Two examples of  $0^\circ$  and  $90^\circ$  microradiographs on film from artificial pits in dogbone aluminum samples; (a) and (c) are  $0^\circ$  shots; (b) and (d) are the corresponding  $90^\circ$ . White spots in the image (c) and (d) are microinclusions developed during the EDM process

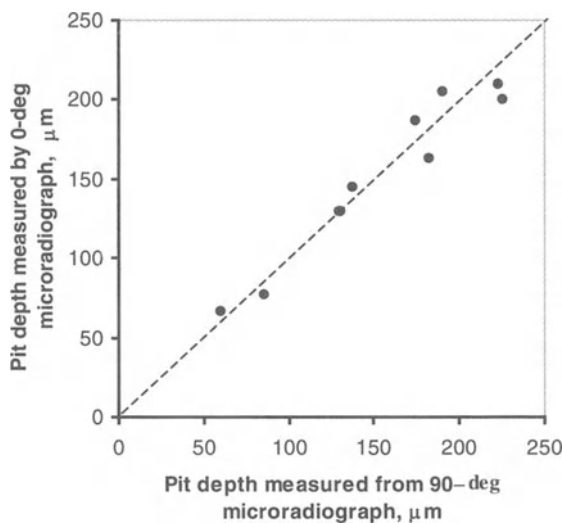


**Fig. 33.** Comparison between microradiographic depth measurements for the  $0^\circ$  and the  $90^\circ$  microradiographs

For pixel calibration at the 90° exposure, an additional microradiograph is taken (with the same projection magnification as for the samples) from a precise Micro-Etch 316 stainless steel screen with 0.005 inch thickness and holes of 0.006 inch diameter and 0.112 inch pitch distance. Figure 33 shows the comparison between the depths measured by the shift in the histogram of the gray level of the artificial pit images in 0° and the direct depth readings from the 90° shots.

The comparison shows consistency between the two methods, particularly up to about 150 μm depth. Deviation of the angle from 90° can contribute some error in direct depth reading for 90° exposures.

### ***Comparison of Microradiographic Corrosion Depth Measurement with WLIM Surface Profiles***

Images are taken from the same corroded aluminum samples with SEM, white light interference microscopy (WLIM), and microradiography to compare the images obtained by these different imaging techniques. Figure 34b, c shows the white light surface profile and a reconstructed color image from the microradiograph of the same sample to show the overall indication of each technique on the corroded surface. Comparing images from profilometry, SEM, and microradiography of this sample shows the limitations and capabilities of each technique for characterizing a corroded surface. It seems that the images obtained show very similar profiles of the corrosion-damaged area. Microradiography seems to pick up more fine and deep pitting than the WLIM surface profile.

Samples with artificial pits were scanned by optical profilometry and their depths were determined across the entire image of each artificial pit. The depths of the same pits were measured by the microradiographic method, and these depths are compared with each other. For most points, the measured depths are close, but there is a detectable difference in the depths of the deeper pits probably because, by microradiography, the average of the histogram is considered, and in profilometry, the deepest point of each pit is measured.

The most relevant comparison is to quantitatively compare the pixel-by-pixel data from microradiographic and profilometric methods from an actual corroded sample. This comparison was done in cooperation with the University of Dayton. To match the images taken by each method, two EDM holes of approximately 200 μm diameter and 200 μm deep are introduced in both sides of the corroded site. These two holes serve as our pivot point to fit the images (see Fig. 35a). The microradiographic image is taken with 23X projection magnification, and then it is digitized with 2X optical magnification (an overall magnification of 46X). Then the optical profilometry image is taken from the sample with exactly the same overall magnification (see Fig. 35b). The profilometric image is converted to a semitransparency and overlapped on the microradiographic image. The two pivot points are used to match the two images together to eliminate any distortion or odd pixel ratio.

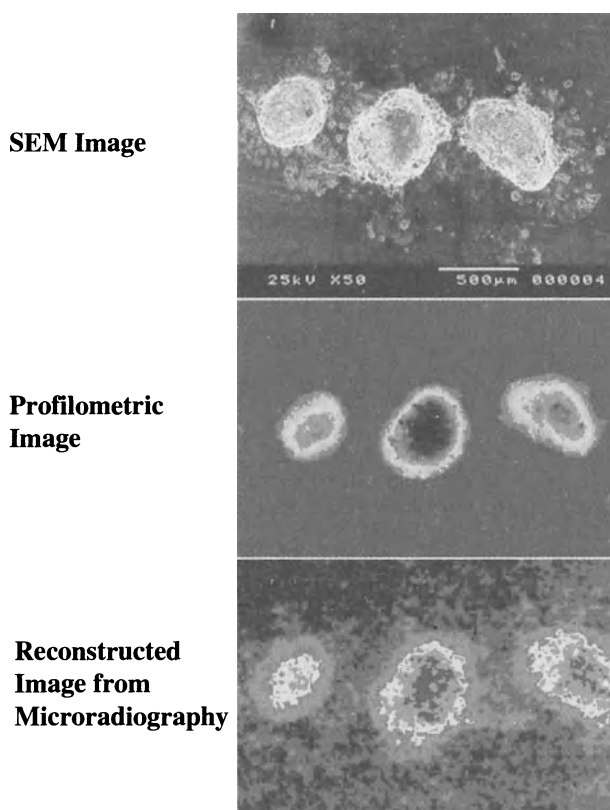


**Fig. 34.** Comparison of different surface images; (*top*) SEM image of the corroded surface with 50X magnification; (*middle*) Surface profile taken by WLIM with approximately 50X magnification; (*bottom*) Reconstructed image of the same aluminum sample from the microradiograph (20X projection magnification, 2.5X optical magnification).

Optical profilometry has almost twice the number of pixels as microradiography. The pixel number in profilometry is reduced by half to achieve the same pixel number in each image. The digitized radiographic images in general have two artifacts that should be corrected before any comparison. The first is the background noise due to the graininess of the film; the second is the uneven intensity of the illuminator during film digitization. A five-point smoothing filter is used to eliminate the background noise in the microradiographic image. It involves averaging the 24 pixels that are within two places next to a given pixel. The correction has been done by subtracting the background gray level for the uneven light source during film digitization. A least squares quadratic surface fit of the background gray level (excluding the corroded

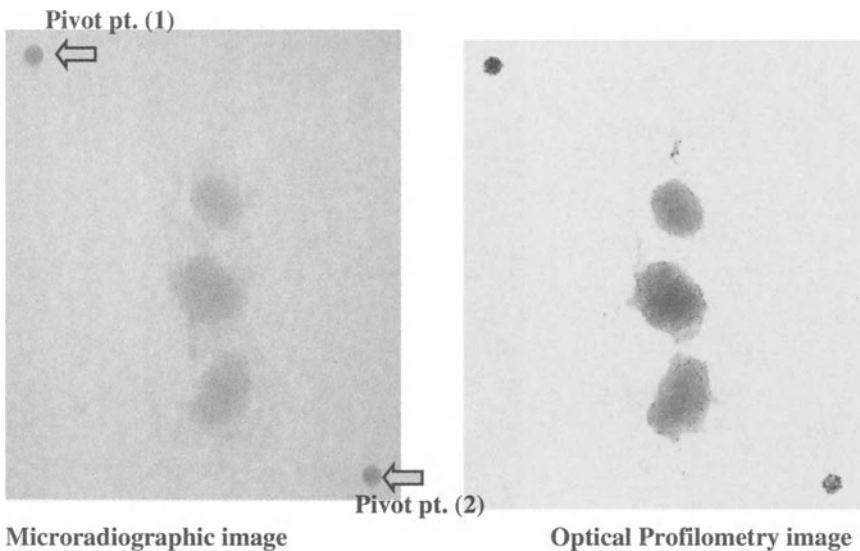


**Fig. 35.** Microradiography and optical profilometry images are taken with the same overall magnification

sites) is done and then subtracted from the image, resulting in a nearly even background. For profilometry, there are discrete pixels that have gross errors in the height measurement. These pixels are corrected for by a DESPECKLE routine of the optical profilometry software. The DESPECKLE routine inspects each point in the image and determines if that pixel's height differs from the mean height of the surrounding eight pixels by more than some fixed multiple of the standard deviation (typically 1.5 to 3 $\times$ ); that pixel is replaced by the mean value of the eight pixels. This routine is extremely successful in correcting for “specks” or discrete noise in the data without affecting the bulk of the data at all. This process does result in the loss of the perimeter pixels in the image.

Figure 36 shows a line scan comparison between the depth data measured by two different techniques along the width of two images (x-axis). The space between each successive scan line is 2.5  $\mu\text{m}$ .

Profilometry has difficulty with edges due to the low angle relative to the light beam. Light is reflected primarily down into the pit, rather than back to the detector, leaving little means of measurement. Radiography is slightly better but still has problems detecting sharp, shallow features due to the small depth change of the pits near the edges and the inherent limitation of radiographic contrast.

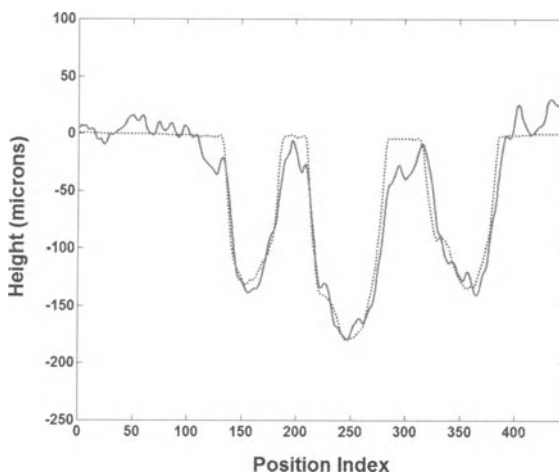


**Fig. 36.** Line scan comparison between depths measured with profilometry (*dashed line*) and microradiography (*solid line*)

As we can see, each method has its own weaknesses and strengths. Optical profilometry is an excellent technique for determining the topology of smooth to moderately rough surfaces. In these cases, the surface height can be measured with a vertical resolution of 3 nm. However, when examining samples with very deep or steep-walled pits, profilometry cannot accurately measure the height of the surface that is parallel to the light beam, as we could see in the two deep EDM holes that were our pivot points.

Because the images obtained by the radiographic technique are based on through transmission data, the contrast sensitivity of the recording medium is a limiting factor for recording a thickness change in the material under test in the x-ray direction. In the 1.6 mm Al 2024-T3 aluminum samples with the high-contrast films that are used, 30  $\mu\text{m}$  (related to 1.9% contrast sensitivity) is the minimum thickness change that can be recorded. Also for any pit with a diameter size smaller than the system unsharpness, there will be a reduction in contrast due to the induced unsharpness. This can happen especially at higher projection magnifications. Any two pits, which are located at a distance much smaller than the system unsharpness, can be recorded as a single pit in a radiographic image due to the system resolution. Any distortion in the image obtained due to the orientation of the corroded surface with respect to the x-ray direction can lead to a false depth measurement. For hidden corrosion areas, for example, for samples with paint or samples with side pitted areas, radiography is probably one of the best NDT methods for corrosion detection and measurement.

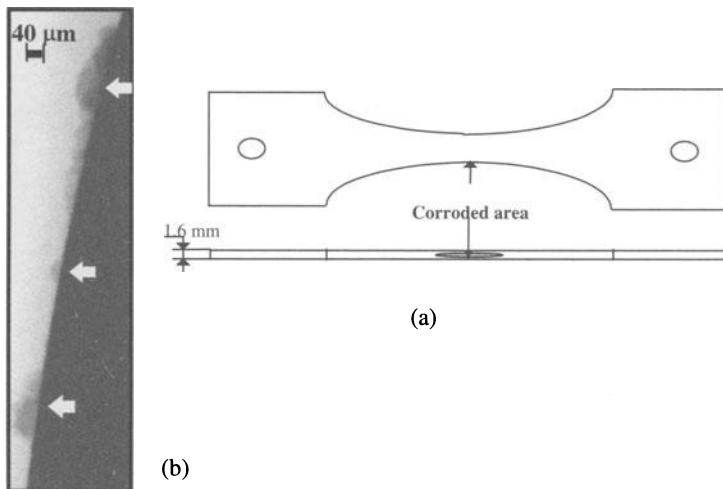


**Fig. 37.** (a) Al 2024-T3 aluminum alloy dogbone sample with the indicated side pitted area.  
(b) Microradiograph of the pitted area with 30X projection magnification

As an example, Fig. 37 shows a microradiograph of the indicated side pitted area in an aluminum dogbone sample, which is easily detected by microradiography and can be completely hidden by any visual method. Hidden pitted areas along the grain boundary of materials can be detected easily by microradiography, whereas they can be partially detected by microscopic techniques based on light reflection. Figure 38 represents a case in which a pitting area can be fully detected by microradiography with a correct thickness loss measurement, but partially detected by an optical microscope with a wrong depth measurement (smaller than its actual thickness loss).

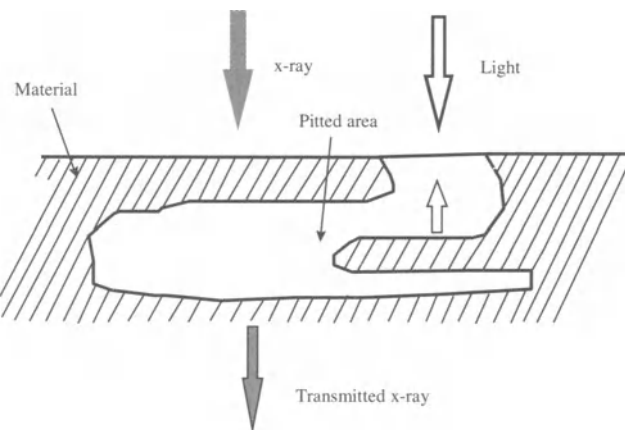


**Fig. 38.** A hidden pitting corrosion area that leads to a wrong depth measurement based on the surface profile by reflected light

### 3.4.5 Microradiographic Characterization of Fatigue Cracks Initiated by Corrosion Pits

#### **Methodology**

Dogbone fatigue samples with induced artificial pits are used to detect fatigue cracks at different fatigue stages. After a certain number of fatigue cycles and before sample failure, they are tested by microradiography to get an image of the crack and to determine the microradiographic crack detectability. A more realistic time for inspecting a fatigue crack is when the sample is under its designed load. In these cases, the crack initiation and its propagation are in their actual working conditions, and the detectability of the crack by radiography also increases. A stress fixture is used to apply a controlled load on the sample during microradiography. The elongation of the stress fixture is calibrated based on the applied force. The necessary load to open the crack is calculated from the ultrasonic amplitude-load curves for different specific fatigue cycles. The fixture with the sample inside is positioned in front of the microfocal tube for exposure at different projection magnifications.

#### **Results**

At the beginning stage, the initiated crack is a surface crack, which does not produce sufficient contrast to form a detectable image, although it can be detected by ultrasound and seen by an optical microscope with at least 50X magnification. In crack detection by radiography, the angle between the x-ray direction and the crack plane is a vital factor.

Tight fatigue cracks can easily be detected in the latest stage of the fatigue life of a sample. Figure 39 shows a strong, clear indication of a fatigue crack after 60,000 fatigue cycles.

One can use radiographic exposures from different directions to produce a three-dimensional reconstruction of the crack geometry. Figure 39 shows film microradiography of a dogbone sample with an artificial pit after a fatigue test of 60,101 cycles. In Fig. 39a, the 0° exposure (in which the direction of the x-ray beam and the pit axis are aligned) shows the initiated cracks around the pit. Figure 39b shows the same cracks in the 90° exposure (in which the direction of x-ray beam and the pit axis are perpendicular). To increase the detectability of the details in the 90° shot, zinc iodide as an x-ray dye was applied to the sample for 10 minutes prior to the microradiography. The outline of the pit and the cracks are in white due to the high radiation absorption of the x-ray dye. Before carrying out microradiography, the sample is marked with lead to ensure its exact orientation during the 0° and 90° exposures; therefore, the crack in the right branch in Fig. 39a appears at the top of the other branch in Fig. 39b. Exact pixel calibration

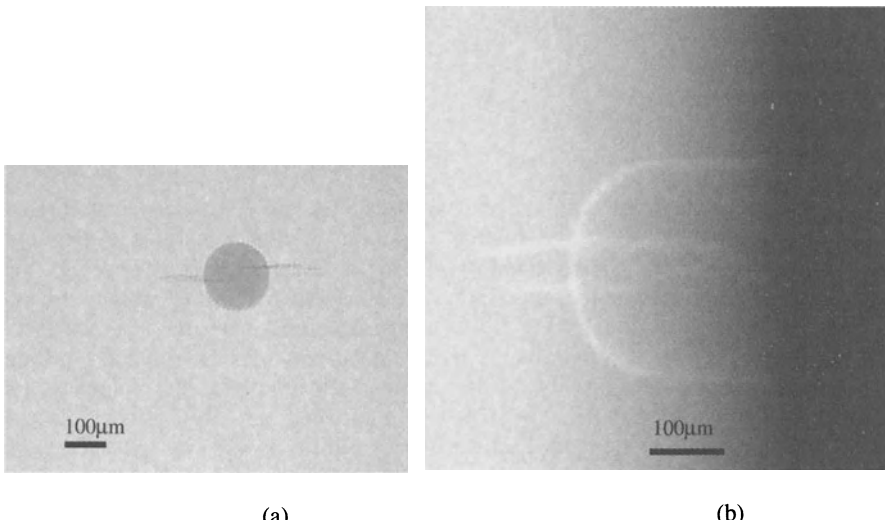


**Fig. 39.** Microradiographs at  $0^\circ$  (a) and  $90^\circ$  (b) from an aluminum dogbone sample with an artificial pit after a fatigue test with 60,000 cycles; (b) is taken after applying x-ray dye to the sample

allows one to measure the length of each crack from Fig. 39a and the depths from Fig. 39b. As one can see, the longer crack is deeper. Based on the two radiographs at perpendicular exposures (Fig. 39), the three-dimensional view of the cracks emanating from the pit is depicted schematically in Fig. 40. The method of two perpendicular microradiographic projections with large magnifications provides valuable data for fracture mechanics study. This technique serves as a valuable addition to the ultrasonic evaluation of crack depth.

Figure 41 shows a stress fixture for opening crack by applying tensile force prior to microradiographic exposure. Figure 42 shows the microradiographs of a dogbone sample with an artificial pit after 60,000 cycles while applying different loads along the longer axis of the sample. No indication of the initiated crack can be seen on the radiograph without load (a), although there was a strong ultrasonic indication during the fatigue test at this stage. After loading (150-lb stretching force), the initiated cracks are opened and start to show on the microradiograph on both sides of the artificial pit (b). Starting at a 350-lb load, the cracks are more visible (c) and show their profiles under the pit where the two cracks connect with each other. At a 550-lb load, the crack has its highest detectability, and the developed branches can be seen clearly (c). At this stage, the sample is taken off the fixture, and a microradiograph of the sample is taken without applying more load. The microradiograph (d) still shows the presence of the crack, indicating the residual plastic deformation that leads to crack opening.

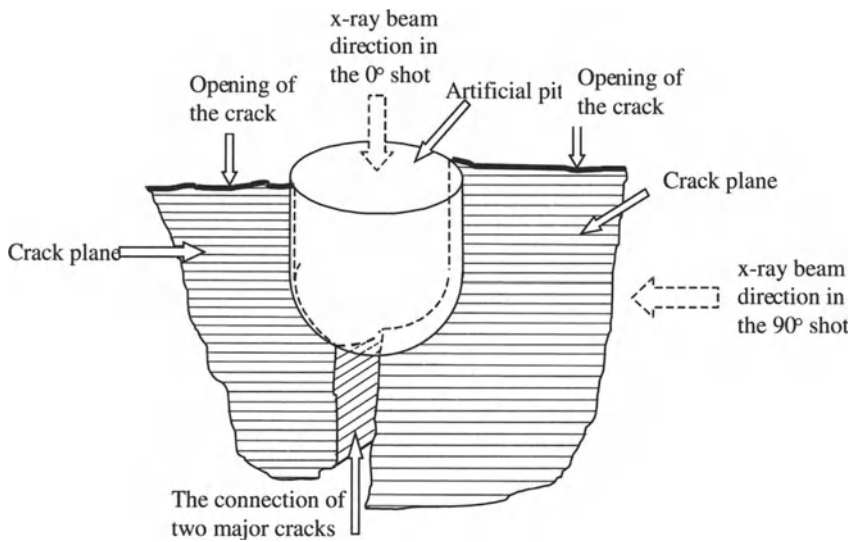


**Fig. 40.** Three-dimensional representation of crack branching based on two perpendicular exposures in Fig. 36a, b

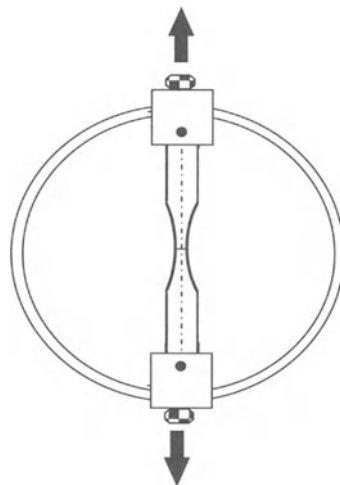


**Fig. 41.** Stress fixture for opening a crack by applying tensile force during microradiography

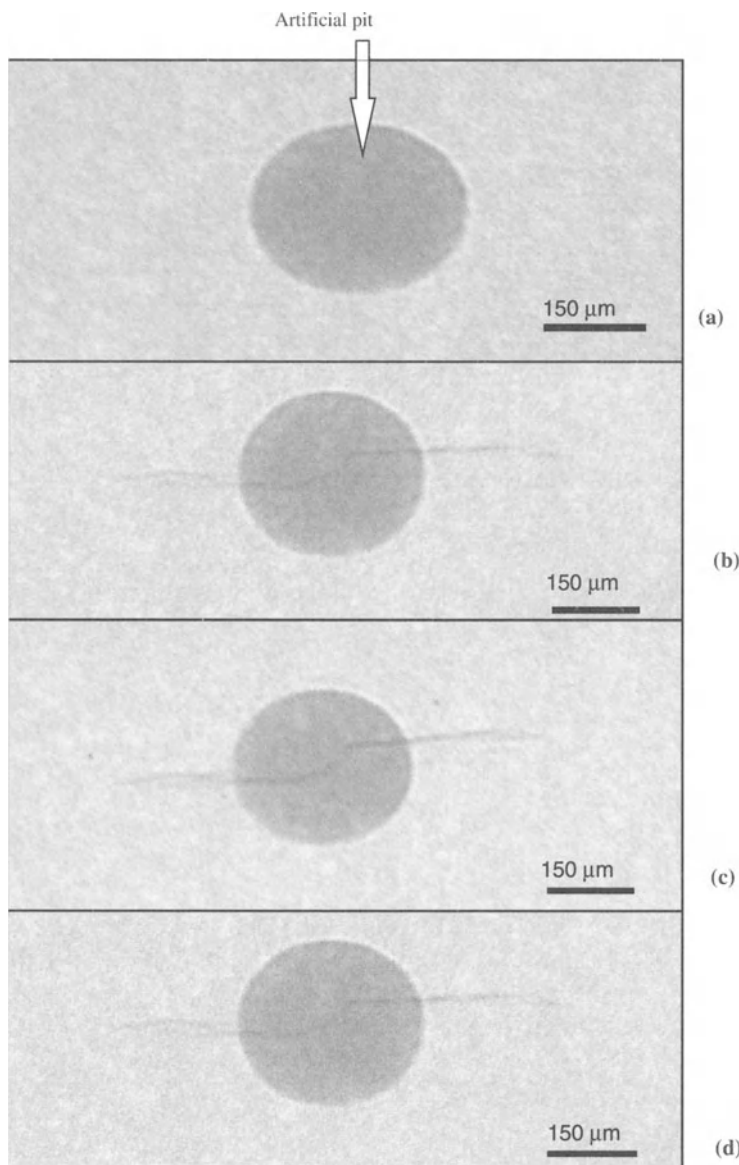


**Fig. 42.** Microphotographs of an aluminum dogbone sample after 60,000-cycle fatigue test. In all cases, the projection magnification is 20X; optical magnification is 5X. (a) Microradiographs of the sample without applied load. (b) Under 150-lb load. (c) Under 550-lb load. (d) Microradiograph of the sample after removing the applied load

### 3.4.6 Phase-Contrast Image Enhancement with Microradiography

In conventional radiography, x-ray beams, that penetrate through a specimen are partially absorbed based on the object's thickness or the attenuation by the inside structures. The pattern of the transmitted beams with different intensity then can be recorded on film or any recording medium to produce a two-dimensional image of the object. The technique is limited to small thickness or density changes due to the inherent contrast limitation in conventional radiography. An alternative approach to overcome this limitation is phase-contrast imaging. In this technique, one records on film the interference pattern due to variation in the phase of the passing x-ray beam. This is similar to the optical refraction and interference in materials due to a change in the refractive index [5–7]. For a sample with low attenuation, this approach can significantly improve the contrast sensitivity of the image [5–10]. Most phase-contrast imaging techniques require highly monochromatic x-ray beams and expensive x-ray optics. However, microfocal x-ray tubes that have high spatial coherence can also be used for phase-contrast enhancement [5].

Here we illustrate the application of this new imaging technique for characterizing of microdamage in materials. The results are compared with through-contrast microradiography; we also describe optimization of the conditions for phase-contrast imaging.

## Experiments

To demonstrate the ability of the technique and study the effects of different radiographic parameters, a simple specimen is made by putting a small amount of transparent epoxy with porosity on thin Plexiglas. Microradiography is used to obtain images with through-contrast and phase-contrast techniques. To get a through-contrast image, a very short object-to-film distance (OFD) (182 mm) is selected, and for a phase-contrast image, a long OFD (1m) is applied. The projection magnification is kept at 2.5 $\times$  for both. Radiographic exposures are selected so that both images have the same optical density. For the phase-contrast technique, a long 11 minute exposure is used.

Figure 43 shows the comparison of images obtained by the two techniques. In the phase-contrast image, the white rings indicate that the contrast sensitivity of the image is improved significantly. The line profiles across the cavities in the image are given in the bottom part of the image.

To show that the spatial coherency of x-ray beams is the key factor in producing phase contrast in a radiographic image, different magnifications are applied to the same sample to introduce higher geometric unsharpness of the image. Figure 44 shows the effect of projection magnification on phase contrast. In all cases, the source-to-film distance (SFD) is kept constant to have the same amount of exposure and optical density on the image obtained. The difference in the brightness of the white ring around the image of the cavity, which is produced by phase contrast, with the gray level of the image background, is plotted versus

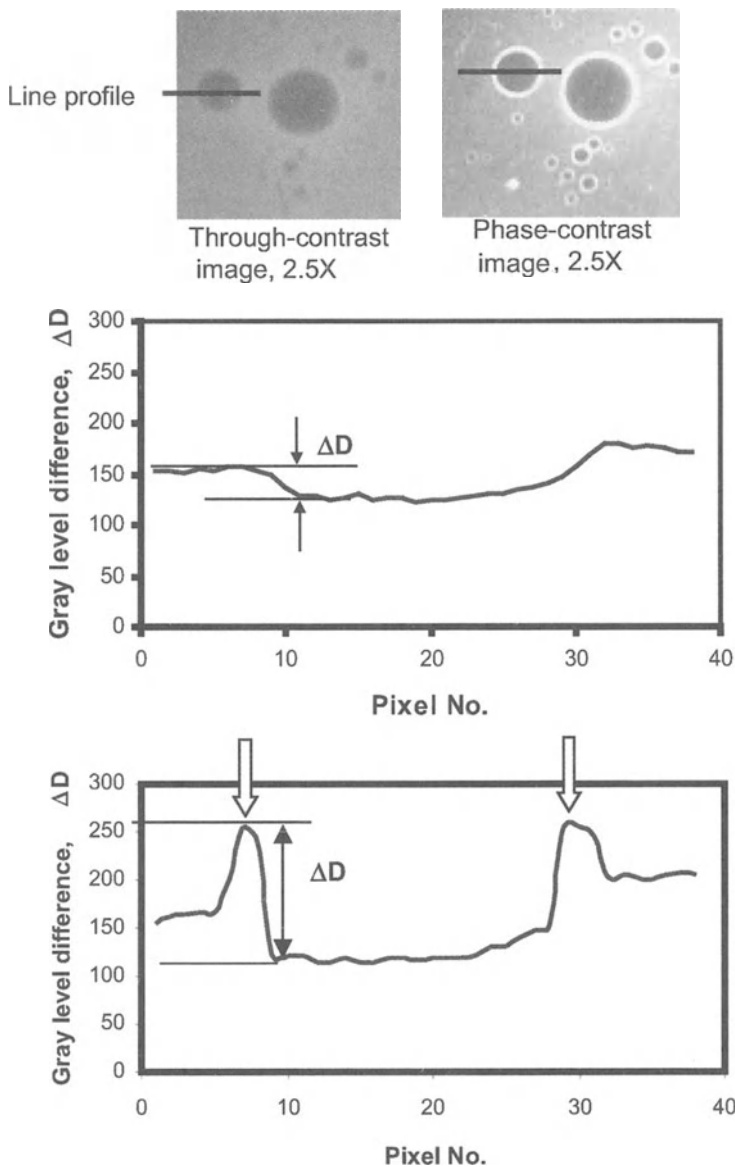


**Fig. 43.** Comparison of phase-contrast enhancement with through-contrast imaging on a cavity in an epoxy sample

projection magnification in Fig. 44b. One can see that there is an optimum projection magnification at which the images are enhanced by the phase contrast and after passing that point, the quality of the image degrades.

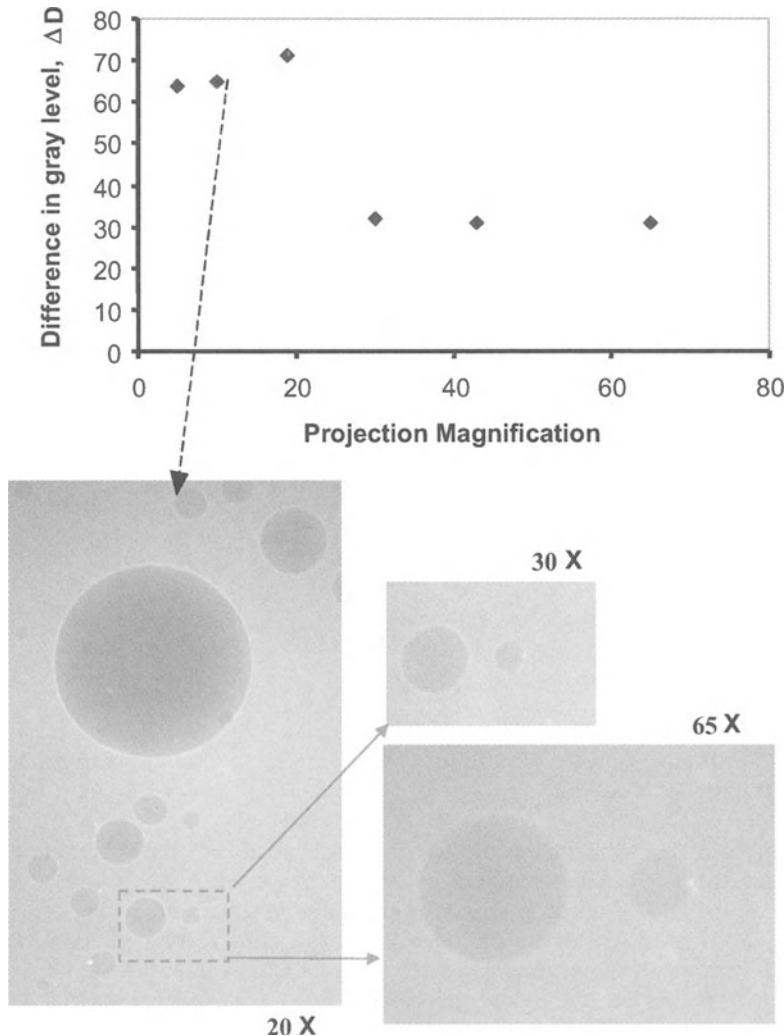


**Fig. 44.** Effect of projection magnification on phase contrast

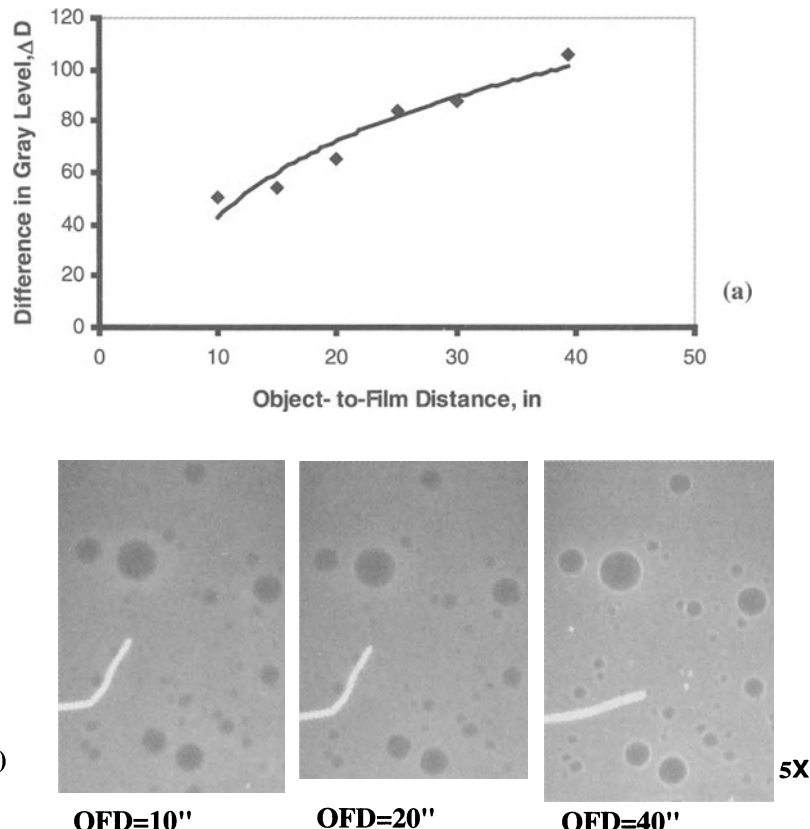


**Fig. 45.** Effect of object-to-film distance on phase contrast. The image magnification is kept constant at 5X in all cases

In the above experiment, the OFD is changed to get the desired projection magnification. To see the effect of the changing OFD on the phase-contrast images, the OFD is changed while the projection magnification is kept constant at all times. Figure 45a shows the improvement in phase contrast with an increase OFD. Figure 45b shows the images for different OFDs. In each case the exposure is corrected so that the same optical density is achieved for each radiograph. Although a larger OFD seems to improve the phase contrast significantly, a very large OFD is not practical due to the necessity of increasing the exposure by the inverse-square law. The low current in the microfocal tubes leads to a very long exposure time.

To demonstrate the method and its application to corrosion detection, we applied the technique to a very thin corroded aluminum foil (15  $\mu\text{m}$  thick). The

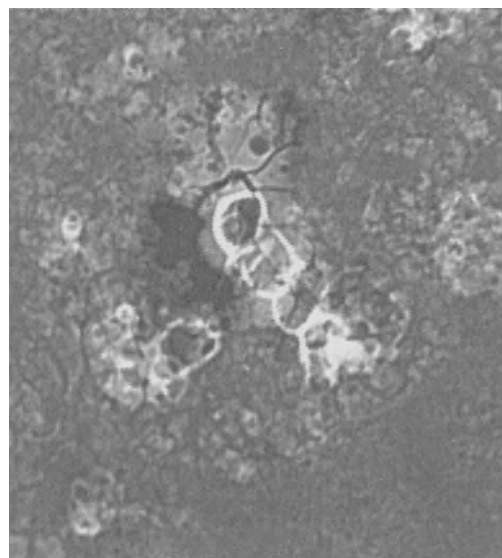


**Fig. 46.** Microradiographic image of a corroded aluminum foil sample (15  $\mu\text{m}$  thick) with 20X magnification and a long OFD

technique was applied by using a relatively large OFD and low voltage, and the tube was in the microfocal state with the smallest focal spot size of 5  $\mu\text{m}$ . The optimum OFD in this case let the phase change recorded on film significantly increase the contrast sensitivity (Fig. 46). The enhanced image shows the details of corrosion products and ultrafine initiated cracks. We attribute the white rings surrounding the dark area of the image (pits) to this effect.

Phase-contrast enhancement for microradiography shows a lot of potential for studying microdamage in materials; further evolution of this new technique is needed in the future.

### 3.5 Foil Penetration Method

Details of the foil penetration method have been presented elsewhere [11–13]. As schematically shown in Fig. 47, a foil sample is attached to the bottom of an electrochemical cell by pressing it against an O-ring. Sandwiched between the foil sample and the backing plate are a piece of filter paper and a Cu foil. A detection circuit is used to sense the resistance between the sample foil and the Cu foil. As long as the sample is unpenetrated, the filter paper remains dry and the resistance is high. However, as soon as a corrosion site penetrates from the top surface and reaches the back of the foil, the filter paper is wetted by the solution at the corrosion site, and the resistance between the Al and Cu foils drops rapidly. This resistance decrease trips the detection circuit, which shuts off a timer and

disconnects the counterelectrode, thereby removing the applied potential if the sample is under potentiostatic control. The system can measure eight samples simultaneously and is under computer control. If a series of experiments is performed on samples having a range of thicknesses, a relationship between penetration time and sample thickness is determined. This relationship can be inverted to determine the depth of the fastest growing corrosion site as a function of time. Note that the potential of the samples was stepped to a high value for one second at the start of the experiment to initiate the attack. Following the initiation treatment, the potential was reduced to the growth value.

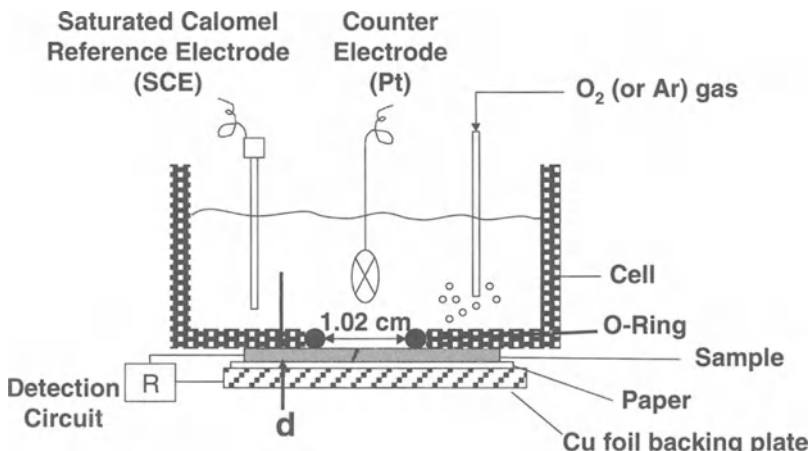


**Fig. 47.** Schematic setup of foil penetration cell

Foil penetration experiments were performed on Al 2024-T3 samples under a range of conditions. Foil samples with different orientations relative to the rolling direction were taken from plate material. The orientations of the samples were noted by the orientation of the perpendicular direction: L (longitudinal, in the rolling direction), LT (long transverse), or ST (short transverse, through thickness). Some samples were stressed in tension using an ASTM G49 constant extension jig that was modified to handle dogbone foil samples. Such samples were noted by a set of orientations, first the perpendicular plane and then the stressing direction. For example, an ST-L sample had an orientation such that its thickness (and thus, the nominal direction of penetration) was in the ST or plate through-thickness direction, and it was stressed in the L or rolling direction. Details of the stressing jig are provided in [14].

## 3.6 Application of Microradiography for Studying Localized Corrosion

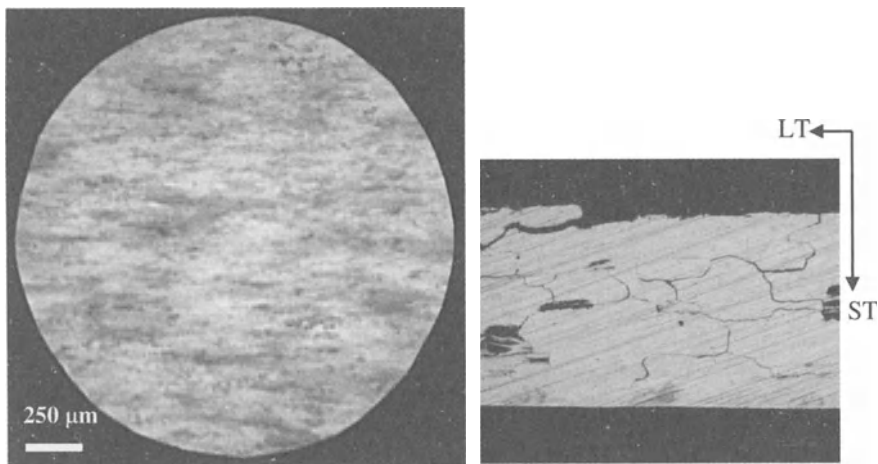
### 3.6.1 Microradiographic Analysis of Corroded Foil Penetration Samples

Microradiography was used to characterize foil penetration samples that were exposed to a range of conditions and therefore, exhibited a range of attack morphologies. It is possible to characterize corrosion morphologies using metallographic sectioning. However, sectioning provides only an image of the sectioned plane. As will be shown, microradiography provides a more complete description of the corrosion site's morphology.

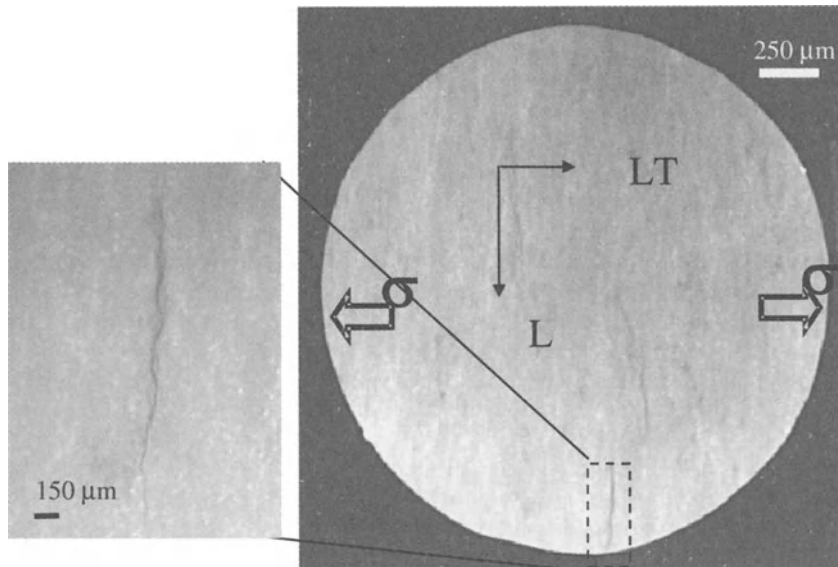
Foil penetration samples were analyzed by microradiography. This technique provides a description of the corrosion attack morphology through the thickness of the sample in a nondestructive manner [15]. It combines the sensitivity of x-rays to discontinuities and/or thickness change with a microfocal x-ray source to increase resolution. With this technique, very small ( $<10 \mu\text{m}$ ) pits have been detected. Standard metallographic sectioning was performed on some samples to assist in interpreting of the radiographs.

Figure 48 shows a microradiograph and metallographic cross section of an Al 2024-T3 ST sample exposed to 1 M (mole/liter) NaCl at a potential of  $-580 \text{ mV}$  versus the SCE reference electrode. The attack is intergranular, as clearly seen by the optical micrograph of the foil cross section. This sample was taken from a rolled plate that had an elongated microstructure. As intergranular corrosion proceeded through the thickness of this microstructure, it followed a circuitous path around the elongated grain structure. The corrosion sites are seen as dark features in the radiograph. The corroded features in the sample consisted of electrolyte and corrosion product; both have a lower density than the alloy itself. The lower density associated with the corrosion sites resulted in a lesser attenuation of the x-rays as they passed through the sample. The image is a negative because the regions of lower attenuation and higher x-ray intensity are dark. Such contrast provides the best resolution of the features. The microradiograph of this sample shows lots of broad and diffuse corrosion sites. The radiograph has this nature because it is a summation of the attack through the thickness of the sample and the attack spreads laterally in the foil in this orientation.

Figure 49 shows the microradiograph of an ST-LT sample that was penetrated at the same potential in the same solution during the application of stress. The foil perpendicular direction was the same as that in Fig. 48, but a stress was applied in the LT direction. The radiograph of this sample has several differences compared to that of the unstressed sample. The lower density of features indicates that there was much less attack on the stressed sample than on unstressed sample. This is



**Fig. 48.** Al 2024-T3 ST sample, 0.22 mm thick, polarized at -580 mV SCE in 1 M NaCl, and penetrated in 8.2 h, unstressed. *Left:* microradiograph; *right:* optical cross section [14]



**Fig. 49.** Al 2024-T3 ST-LT sample, 0.2 mm thick, polarized at -580 mV SCE in 1 M NaCl, stressed. *Right:* microradiograph; *left:* magnified view of crack [14]

partly the result of the faster penetration time of the stressed sample. The stress concentrated the attack at cracks that were perpendicular to the direction of the applied stress.

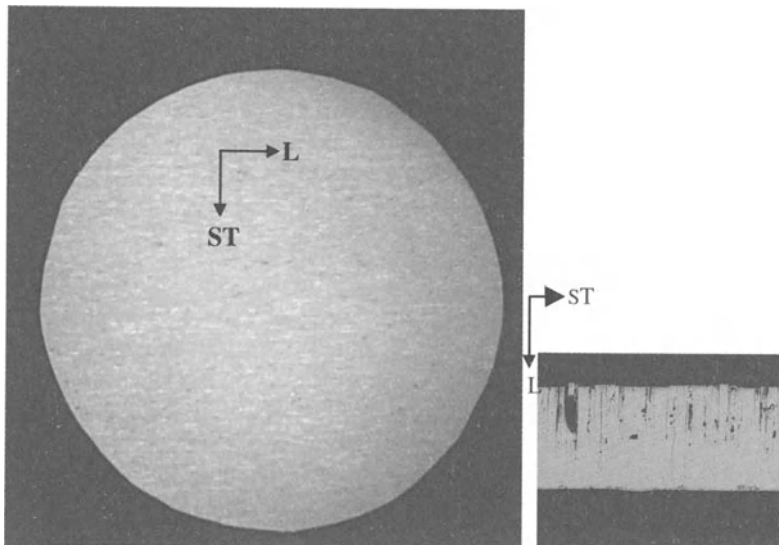
The higher magnification microradiograph in Fig. 49 shows that the cracks are wavy and not perfectly perpendicular to the stress. As will be shown below, this waviness occurred because the intergranular nature of the attack forced the cracks to propagate around the pancake-shaped grains, while still generally maintaining a direction perpendicular to the applied stress.

A microradiograph and optical cross section of an L-oriented sample exposed unstressed to the same 1 M NaCl solution at -580 mV SCE are shown in Fig. 50. The corrosion sites were much more focused than in the ST sample, showing assharp spots or lines in the radiograph. The cross section shows that the corrosion path was essentially straight through the foil. Because of the orientation of the elongated grains, the grain boundaries go almost straight through L-oriented foils. The white spots in the microradiograph are higher density regions associated with intermetallic particles. The particle number is very high because the radiograph senses all of the particles through the whole cross section. These particles are not evident in Fig. 48 because the extensive corrosion damage spread through the cross section of that sample masked the particles. Samples oriented in the LT direction had an appearance similar to the L samples.

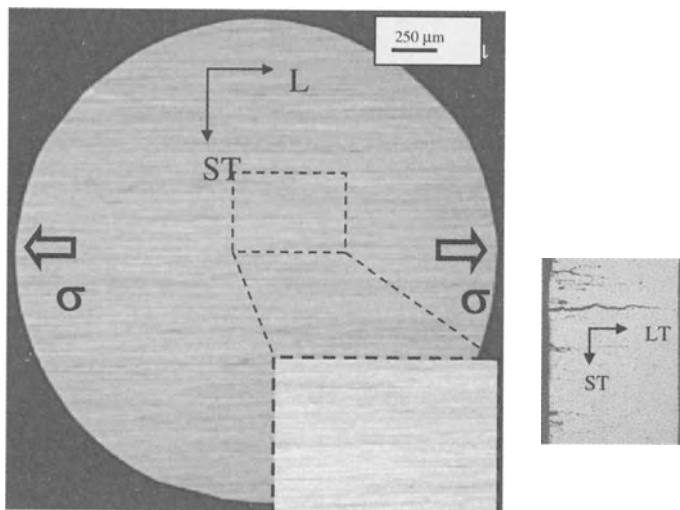
The results for an LT-L sample exposed under the same conditions but with an applied stress are given in Fig. 51. Careful examination of the defects in the microradiographs shows that they are short straight cracks that appear to be oriented in the stressing direction. It is quite interesting to have cracks oriented in the stressing direction. However, the optical micrograph of the cross section shows that the cracks went through the thickness in the LT direction. (Actually, only one of them went all the way through.) This direction of propagation was perpendicular to the applied stress. The cracks were about 50–100  $\mu\text{m}$  wide in the L direction but propagated through the 550  $\mu\text{m}$  thick sample in the LT direction. They were constrained to the LT-L plane because they were intergranular.

Figure 52 gives a summary of the stressed samples used for microradiography. It shows a schematic three-dimensional view of the pancake grain structure. For the ST-LT sample, the crack was perpendicular to the stress, but wavy and broad, since it had to find its way between the elongated grains. The LT-L sample exhibited straight cracks whose long axes were perpendicular to the stress. However, the microradiograph showed a projection of those cracks on the LT plane. In that projection, they appeared to be parallel to the stress. The crack faces, which were ST faces, were parallel to the applied stress, even though the long axis was perpendicular to the stress. It is not clear how the stress enhanced the penetration rate, given the orientation of the crack in the stressing plane.

It is clear that the combination of microradiography and cross-sectional microscopy give a complete picture of cracks.



**Fig. 50.** Al 2024-T3 L sample, polarized at  $-580$  mV SCE in  $1\text{ M}$  NaCl, unstressed. *Left:* microradiograph; *right:* optical cross section [14]



**Fig. 51.** Al 2024-T3 LT-L sample,  $0.55\text{ mm}$  thick polarized at  $-580$  mV SCE in  $1\text{ M}$  NaCl, penetrated in  $2.6\text{ h}$ , stressed. *Left:* microradiographs, *right:* optical section [14]

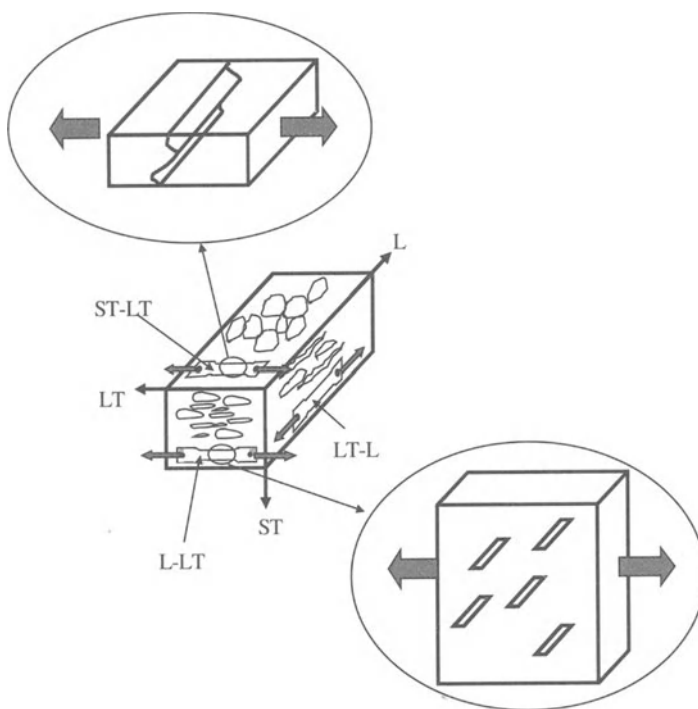


**Fig. 52.** Schematic representation of three-dimensional nature of the cracks in stressed foil penetration samples (not drawn to scale) [14]

### 3.6.2 In Situ Microradiography of Localized Corrosion Growth

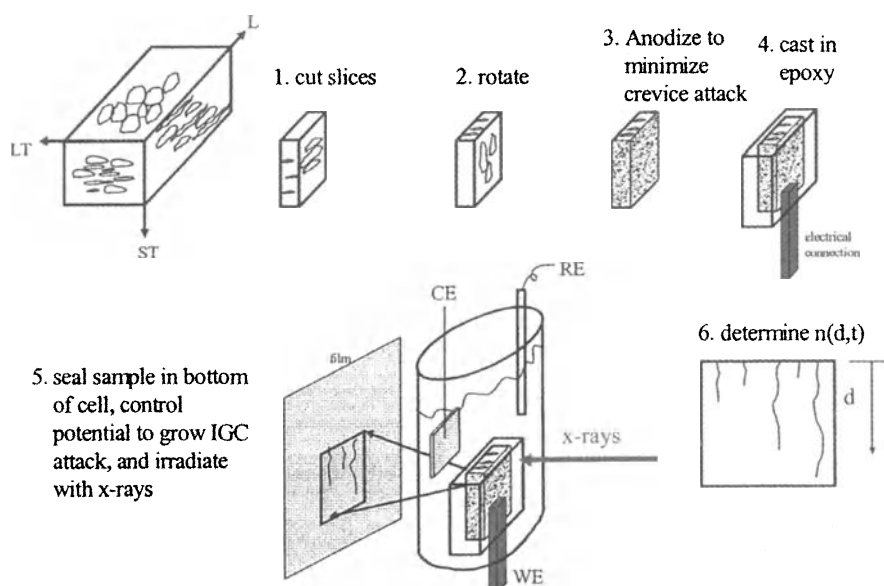
Foil penetration experiments determine the time for the fastest growing defect to penetrate a foil. When performed on foils with a range of thicknesses, these experiments provide the growth kinetics of the fastest growing localized corrosion sites. However, there were many other sites in such samples that did not penetrate, and those sites had a set of different growth kinetics. It is possible that many sites simply grew more slowly than the fastest sites. Others might have repassivated and stopped growing before they penetrated the foil. Still other sites might have started growing after the high potential initiation treatment at the beginning of the experiment. The latter two types of sites could have had faster growth kinetics than that is determined by the foil penetration technique. It is clearly of interest to obtain information regarding the full population of corrosion sites, not just the fastest growing sites.

Figure 53 shows a schematic of the approach that was used for the in situ microradiography [16]. A 2-mm thick sample was cut from a 19.05 mm (0.75 inch) thick plate of Al 2024-T3 such that the L direction was along the length of the sample and the thin dimension was along the LT direction. Some samples were machined to have a square 2 mm × 2 mm cross section rather than a rectangular section. When turned 90°, the L orientation faced upward, and localized corrosion should grow straight down the grain boundaries in the L direction. Some samples were sealed in epoxy, except for the L edge, which was polished clean. Prior to casting in epoxy, the surface was anodized to prevent crevice corrosion at the epoxy/metal interface. The anodized sample, cast in epoxy and polished to expose an edge, was placed in a small cell that was filled with 1 M NaCl solution. As has been shown before, intergranular corrosion will occur in Al 2024-T3 in this solution at a potential of -580 mV SCE.

Other samples were exposed freely to the solution with no epoxy encasement to eliminate the physical constraints and allow exfoliation corrosion to occur. These samples were either cylinders or had square cross sections with their long axis oriented either in the L or ST direction.

Before showing the results of the in situ microradiography, an example of metallographic sectioning results will be given. Figure 54 shows an example of a metallographic section for a 3-mm thick cylindrical Al 2024-T3 sample with axial orientation in the ST direction after a 4-hour exposure at -580 mV SCE in 1 M NaCl. The attack was in the L-LT plane of the sample, i.e. along the grain boundaries. Samples were exposed for different times and sectioned. The kinetics determined from the longest site in each section was slower than that found for L or LT oriented samples determined by the foil penetration technique, which measures the fastest growing site. This proves that metallographic sectioning does not determine the kinetics of the fastest growing sites. The section reveals only a fraction of the sites in a sample.

Figure 55 shows an in situ microradiograph of a 2-mm thick sample oriented so that the L direction was down. The sample was encased in epoxy with one face, the L face, exposed to the solution. This sample was exposed for 19 h to the same conditions as the last sample. The dark lines in the image are corroded grain boundaries. Analysis of a series of images taken from this sample at varying exposure times resulted in the data shown in Fig. 56. The depth of specific IG sites is shown as a function of time in that figure. The rates comprise a band that falls just beneath the line representing an extrapolation of the data from foil penetration experiments [17]. These results show that in situ microradiography provides information on the full range of growth kinetics, including that for the fastest growing sites.



**Fig. 53.** Schematic representation of approach for in situ microradiography of localized corrosion sites

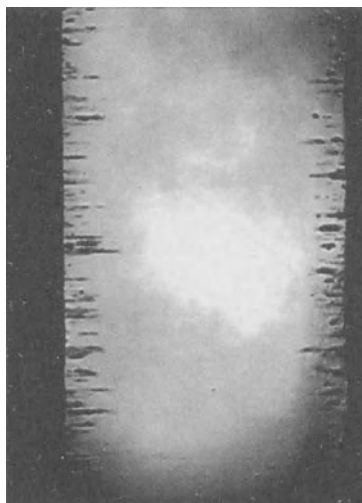


**Fig. 54.** Metallographic cross section of ST oriented 3-mm wide Al 2024-T3 cylinder exposed to 1.0 M NaCl at  $-580$  mV SCE for 4 hr [16]

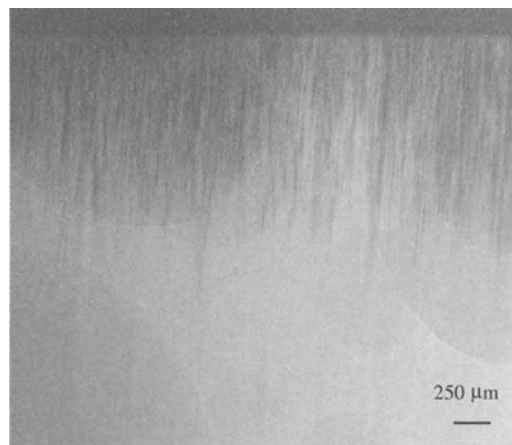


**Fig. 55.** In situ microradiograph of L-oriented Al 2024-T3 sample exposed to 1.0 M NaCl at -580 mV SCE for 19 hr [16]

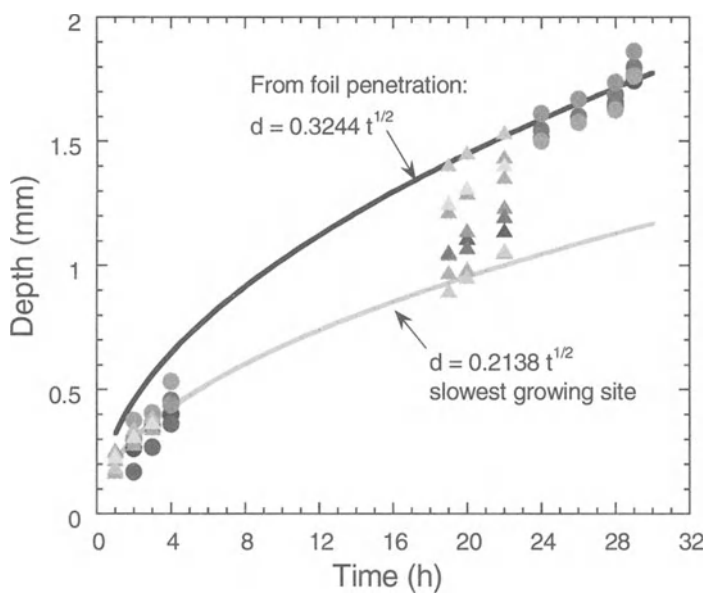


**Fig. 56.** Plot of the depth of various specific sites for an L-oriented Al 2024-T3 sample as a function of time. Also shown is the curve for L-oriented foil penetration samples [16]

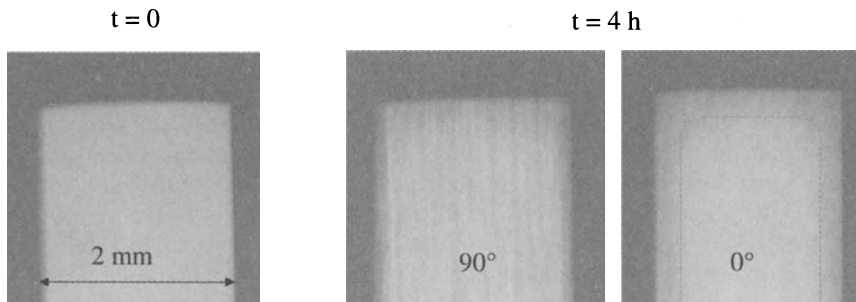


**Fig. 57.** Microradiographs of  $2 \times 2$  mm sample of Al 2024-T3 exposed to 1.0 M NaCl at  $-580$  mV SCE. Sample was not encased in epoxy. Image at left taken before exposure, image at right taken after 4 h. Long axis (vertical orientation) of sample L direction.  $90^\circ$  image taken in LT direction;  $0^\circ$  image taken in ST direction [16]

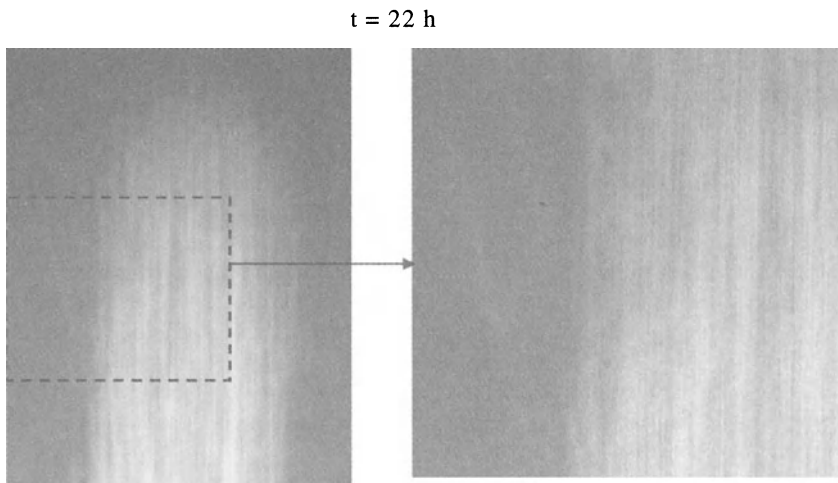


**Fig. 58.** Same sample as Fig. 6–10, taken in LT direction. Exfoliation is evident

Figures 57 and 58 show microradiographs of a similarly oriented sample with no epoxy encasement exposed under the same conditions. This sample had a square  $2 \times 2$  mm cross section. After 4 hours, the attack is apparent in the microradiographs. Since the sample was freestanding with no epoxy encasement, attack proceeded from both the L face on the top and the free LT faces on the sides. The orthogonal views in Fig. 57 show the morphology of attack. Very little attack was evident from the microradiograph taken in the ST direction, but clear evidence of the attack was visible in the LT direction. The front of the attack from all faces of the sample was evident and is highlighted in Fig. 57 by the dotted lines. With time, the attack developed into exfoliation, as seen in Fig. 58.

### 3.7 Summary and Conclusions

We have demonstrated the capabilities of microradiography for characterizing pitting and intergranular corrosion. The microradiographic system has a few micron focal size and therefore allows higher projection magnifications and micron range image resolution. Thus it has inspection capabilities comparable to that of optical microscopy and it is used in this work to detect corrosion pitting. The methodology is developed for determining the detectability of pitting corrosion by real-time microradiography. The existence of an optimum projection magnification has been shown. The value of this optimum depends on the focal size of the x-ray source, geometrical unsharpness, and the unsharpness of the recording chain. This allows one to make recommendations for optimized system parameters.

High-resolution images with large magnifications let us develop a microradiographic method to measure the pitting depth in 2024-T3 aluminum alloy samples. Pitting depth measurement was quantified, and calibration curves were obtained. High-resolution white light interference microscopy (profilometry) was used to validate the radiographic metrics of the pitting corrosion. Direct optical microscopy methods were also employed for pit depth measurements. The quantitative comparison between microradiography and the optical technique shows that radiography may serve as a quantitative tool for surface mapping of corroded areas. Samples with controlled artificial pits were used to establish this technique. Real-time microradiography is used as a fast and practical technique for inspecting hidden corrosion. Artificial pits and corroded aluminum samples are used for developing depth measurement by real-time imaging. The results are compared to those taken from digitized films. Three-dimensional reconstructed images from digitized films and real-time radiography are compared with optical profilometry images. The microradiographic characterization of hidden corrosion is studied on Al 2024-T3 samples with corroded areas covered by different thicknesses of overlaying aluminum foils. The variation of image-contrast sensitivity at different thicknesses for film and real-time microradiography are measured and compared with the theory.

The capability and limitation of microradiography for detecting fine fatigue cracks in aluminum alloys with artificial pits is also demonstrated. It was shown that it depends on crack closure. Three-dimensional visualizations of fine fatigue cracks from microradiographs at different angles are a useful tool for determining crack depth and characterizing its morphology. The phase-contrast microradiographic imaging technique is explored to enhance low-contrast images. Its potential and applications have been demonstrated for evaluating fine microdamage in thin and low-attenuation materials. The results are compared with through-contrast microradiography. The effects of projection magnification and object-to-film distance are studied to determine the optimum conditions for the phase-contrast imaging technique.

We also have demonstrated new applications of microradiography:

1. Penetrated foil samples such as are generated by the foil penetration technique are ideal for use with the microradiographic technique because the deepest corrosion site just penetrated the samples prior to removal from the solution.

2. The intergranular nature of the attack on Al 2024-T3 presented different microradiographs depending on the orientation of the sample and microradiography relative to that of the elongated microstructure.
3. Microradiography shows that IGC appears as broad and diffuse features when looking in the ST direction, and as focused sharp features in the L or LT direction.
4. Novel cells that used samples with specific size, shape, and orientation were used to perform *in situ* microradiographic measurements.
5. *In situ* microradiography of such samples generated information about the growth kinetics of a large number of sites with a range of penetration rates, not just the fastest sites.

## References

1. Rokhlin SI, Nagy PB, Zoofan B (1997) Effect of Corrosion Pitting on Fatigue Crack Initiation and Fatigue Life. Proceedings of An International Symposium on Fatigue of Materials, TMS
2. Halmshaw R (1988) Magnified Radiographic Images. *Bri J NDT* 30 (2):106
3. Becker L (1990) (ed.) Radiographic NDT. Du Pont de Nemours & Co.
4. NDT Handbook, vol. 3, Radiography and Radiation Testing. 2nd ed. 1986, ASNT, Columbus, OH
5. Davis TJ, Gao D, Gureyev TE, Stevenson AW, Wilkins SW (1995) Phase-Contrast Imaging of Weakly Absorbing Materials Using Hard X-rays. *Nature* 373:595–598
6. Wilkins SW, Gureyev TE, Gao D, Pogany A, Stevenson AW (1996) Phase-Contrast Imaging Using Polychromatic Hard X-rays. *Nature* 384:335–338
7. Fitzgerald R (2000) Phase-Sensitive X-ray Imaging. *Physics Today*:23–26
8. Singirev A, Snigireva I (1995) On the Possibilities of X-ray Phase Contrast Micro-imaging by Coherent High-Energy Synchrotron Radiation. *Rev Sci Instrum* 66 (12):5486–5492
9. Ingal VN, Beliaevskaya EA (1995) X-ray Plane-Wave Topography Observation of the Phase Contrast from a Non-Crystalline Object. *J Phys D Appl Phys* 285:2313–2317
10. Spanne P, Raven C, Snigireva I, Singirev A (1999) In-line Holography and Phase-Contrast Micro-tomography with High Energy-X-rays. *Phys Med Biol* 44:741–749
11. Hunkeler F, Bohni H (1981) Corrosion 37 (11): 645–650
12. Hunkeler F, Bohni H (1984) Corrosion, 40 (10):534–540
13. Sehgal A, Frankel GS, Zoofan B, Rokhlin SI (2000) *J Electrochem Soc* 147 (1):140–148
14. Liu X, Frankel GS, Zoofan B, Rokhlin SI submitted for publication to Corrosion.
15. Zoofan B, Rokhlin SI (1998) *Materials Evaluation* 52:191
16. Zhao X, Frankel GS, Zoofan B, Rokhlin SI submitted for publication to Corrosion.
17. Zhang W, Frankel GS (2000) *Electrochem Solid-State Lett* 3 (6):268–270

# **4 Interferometric and Holographic Imaging of Surface Wave Patterns for Characterization of Material Degradation**

J.L. Blackshire

## **4.1 Introduction**

Optical interferometry and holography systems provide an effective means for measuring surface motions and vibrations on nanometer scales, and have been used extensively in the past in a number of different applications [1–4]. For nondestructive evaluation (NDE) of material degradation, both techniques can be combined with classical ultrasonic testing methods to provide non-contact measurement capabilities for evaluating important parameters such as fatigue state [5], and the existence of microcracks [6] and corrosion [7]. Here we describe two advanced NDE systems capable of ‘visualizing’ ultrasonic fields on material surfaces with high sensitivity and spatial resolution. The systems use heterodyne interferometry and frequency-translated holography concepts to create detailed two-dimensional displacement-field images, which provide quantitative measurements of ultrasonic field parameters related to ultrasonic wave dispersion, phase velocity, attenuation, and localized scattering. Each of these parameters, in turn, can be used to assess the underlying material structure. Local ultrasonic scattering, for example, can be used to detect and characterize surface-breaking cracks [8–11]. As a limiting factor Hassan and Nagy have studied the effect of grain noise in detail [12].

In this chapter, two aspects of crack ‘imaging’ using interferometric/holographic NDE are discussed and experimentally studied. The first aspect involves an intensification of the ultrasonic displacement field in the immediate vicinity of the crack, which provides a means for easily detecting cracks relative to the background ultrasonic displacement field levels. The second aspect involves the detailed characterization capabilities of the techniques, which provide comprehensive *images* of the surface-breaking cracks that actually follow the intricate contours of the crack with microscopic precision. This microscopic imaging precision, in turn, provides for dramatically improved crack-detection capabilities, which are fundamentally limited by optical diffraction-limited spatial resolution levels of 1 micron. In addition, the possibility of acquiring crack-depth information based on local displacement levels was studied in detail. Preliminary results indicate that it may be possible to image cracks in full, three-dimensional detail using either of these two new NDE techniques.

The organization of this chapter first provides background information on ultrasonic NDE, optical interferometry and holography, and ultrasonic scattering by surface-breaking cracks. The importance of local ultrasonic scattering is

emphasized, where the implications of free-boundary reflection from surface-breaking cracks is highlighted. A description of the two NDE systems is then given, followed by a number of measurement examples showing the displacement field imaging capabilities of the two techniques. The application of the two techniques to crack measurements is then covered, where a number of realistic surface-breaking cracks are imaged and studied. The possibility of obtaining crack-depth information based on local displacement level is then described, where the results of a set of measurements using precision-milled ledges are presented. A final measurement example involving an *in situ*, stress-corrosion crack (SCC) growth study is then provided, where crack-initiation and crack-growth measurements were conducted.

## 4.2 Background

The advanced interferometric and holographic NDE systems discussed in this chapter are based primarily on laser-ultrasound concepts originally pioneered in the 1960s and early 1970s. Because traditional ultrasonic NDE and ultrasonic scattering processes are such a major part of these systems, a brief theoretical description of ultrasonic NDE and elastic wave propagation in materials is provided. In particular, the generation, propagation, and scattering of surface acoustic waves (SAW) is covered in some detail. The elastic scattering of ultrasonic energy from surface breaking cracks is then described, with emphasis being placed on local scattering effects, and free-boundary reflection. The basic principles behind interferometric and holographic measurements of dynamic motions are then briefly covered, with focus being placed on the heterodyne interferometry and frequency-translated holography concepts. A much more comprehensive description of elastic scattering processes can be found in references [13–17], while additional information on interferometry and holography can be found in references [18–21].

### 4.2.1 Ultrasonic Nondestructive Evaluation (NDE)

Ultrasonic inspection methods are one of the most widely used for the nondestructive examination of engineering materials and structures. This is primarily due to the advantages of simplicity, low cost, high signal-to-noise ratio, and good detection sensitivity. Because the ultrasonic energy is intimately coupled to the underlying material substrate, measurements of ultrasonic attenuation, phase velocity, reflectance, and frequency provide a wealth of information regarding the state of the material being evaluated. An excellent survey of modern applications of ultra-sound in nondestructive evaluation is given by Thompson and Thompson (1985) in reference [22].

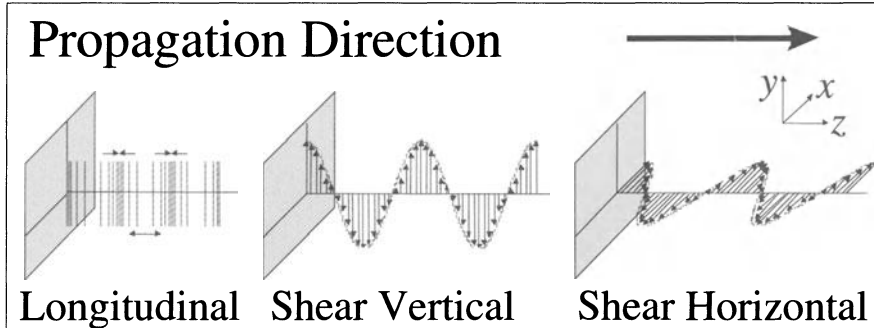


**Fig. 1.** Ultrasonic wave propagation in an elastic solid. Shear vertical and shear horizontal are identical for an isotropic medium.

In general, ultrasonic energy propagates as a combination of longitudinal and transverse waves in an elastic solid (Fig. 1). For an anisotropic medium particle motions can be resolved into three perpendicular components; two transverse/shear and one longitudinal, which are referred to as SV (shear vertical), SH (shear horizontal) and P (longitudinal). The longitudinal wave involves displacements parallel to the direction of propagation, and propagates through the material as a series of alternating compressions and rarefactions of the underlying material. The transverse waves involve displacement perpendicular to the direction of propagation, with particle displacements in the vertical (SV) and horizontal (SH) directions as shown in Fig. 1. Each of the three modes has its own characteristic velocity, which impact the dispersion, diffraction, reflection, and scattering properties of the waves.

For simplicity the discussion below will consider only isotropic media. Only one shear wave mode exists for isotropic media. The velocities of shear waves of all polarization directions are identical in this case.

For NDE applications, ultrasonic waves are introduced into a material, and cracks, boundaries, inclusions, etc., are detected primarily through ultrasonic reflection and scattering processes. In reflection measurements, information regarding the location and basic size of the defect site is obtained through the time-of-flight and amplitude signatures of the reflected ultrasonic signal, respectively [13–17, 22]. This situation is depicted schematically in Fig. 2, where traditional pulse-echo and pitch-catch ultrasonic methods are depicted.

NDE measurements based on the *scattering* of ultrasonic energy from a defect site have also been used very successfully in identifying and sizing defects [22–27]. Although the amplitudes of scattered waves are quite small when compared to specular reflection amplitudes, much more information is typically available for the basic analysis of defect depth, width, and length. In ultrasonic scattering measurements, the diffraction, mode conversion, and scattering of energy from sharp discontinuities is used to discriminate the various features of a particular defect site, as shown in Fig. 3.

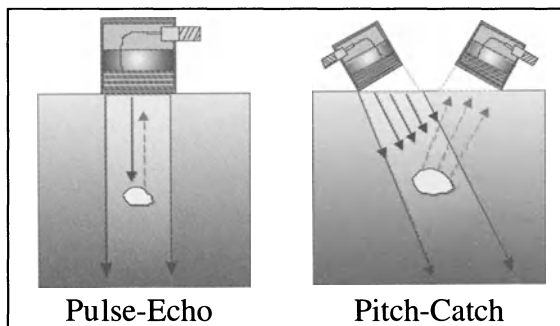


**Fig. 2.** Traditional ultrasonic NDE using pulse-echo and pitch-catch methods

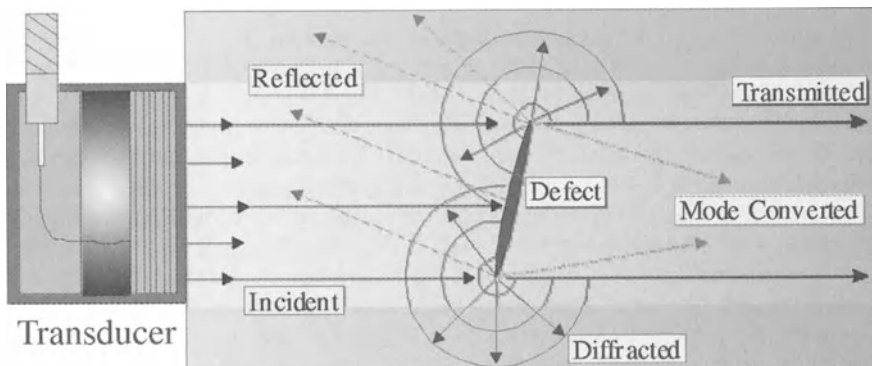


**Fig. 3.** Ultrasonic scattering from a defect with sharp features

#### 4.2.2 Surface Acoustic Waves (SAW)

Surface acoustic waves (SAW) have been used in a wide variety of NDE applications, and are particularly well suited to detecting and characterizing surface-breaking defects. The SAW energy distribution decays away substantially into the depth of the material. The level and rate of decay is frequency dependent, which potentially allows different depths in the material to be probed by simply adjusting the SAW frequency. These and other important features of SAW make them perfectly suited for measuring and characterizing surface-breaking defects such as cracks.

Physically, surface acoustic waves (Rayleigh waves) involve elastic perturbations propagating along the stress free boundary of a solid that decay with depth [28, 29]. The particle displacements associated with a SAW have two components, one in the direction of propagation and one perpendicular to it. These correspond to a combination of motions associated with the longitudinal, P, and

shear vertical, SV, modes of propagation. The components  $U_R$  and  $W_R$  of the particle displacement along the x and z axes, respectively, are

$$U_R = k_R (e^{-q_R z} - \frac{2q_R s_R}{k_R^2 + s_R^2} e^{-s_R z}) \sin(k_R x - \omega t) \quad \text{tangential} \quad (1)$$

$$W_R = q_R (e^{-q_R z} - \frac{2k_R^2}{k_R^2 + s_R^2} e^{-s_R z}) \cos(k_R x - \omega t) \quad \text{normal}$$

where  $q_R = \sqrt{k_R^2 - k_t^2}$ ,  $s_R = \sqrt{k_R^2 - k_l^2}$ ;  $k_l = \omega\sqrt{\rho/(\zeta + 2\mu)}$ ,  $k_t = \omega\sqrt{\rho/\mu}$ , and  $k_R$  are the wave numbers of the longitudinal, shear (transverse), and Rayleigh modes respectively;  $\omega$  is the angular frequency;  $\zeta$  and  $\mu$  are elastic Lame constants; and  $\rho$  is the density of the medium.

Figure 4 provides plots of  $U_R$ , the tangential particle displacements in the x-direction (parallel to the surface), and  $W_R$ , the normal particle displacement in the z-direction (normal to the surface). The  $U_R$  displacement amplitude is seen to decrease with depth, and at a depth of approximately  $z/\lambda_R = -1.1$ , the displacement amplitude actually changes phase by  $180^\circ$ . The normal displacement  $W_R$  increases at first, then falls off monotonically with depth, and does not undergo a phase change at any depth. The amplitude of  $W_R$  at the surface is greater than that of  $U_R$  by a factor of about 1.56. The SAW displacement levels are ultimately localized within a thin surface layer of thickness between  $\lambda_R$  to  $2\lambda_R$ .

The linear combination of the normal and tangential particle displacement components is also plotted in Fig. 4 (right). A phase shift of  $\pi/2$  between the  $U_R$  and  $W_R$  components results in particle motion trajectories in the wave that are elliptical in nature. The ellipsoidal rotation of the particles near the surface

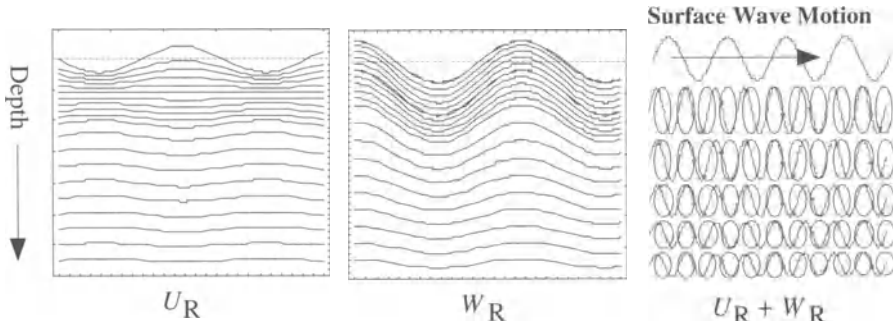


**Fig. 4.** Surface acoustic wave motions fields versus depth into the material surface calculated from (1)

proceed counter-clockwise, while at a depth,  $z > 0.2\lambda_R$ , the direction of rotation reverses. The aspect ratio of the elliptical motions varies with depth, with the semi-major axes of the ellipses oriented normal to the boundary of the half-space, and the semi-minor axes oriented parallel to the direction of wave propagation. This particular feature of SAW is particularly beneficial for interferometric and holographic NDE techniques because they are primarily sensitive to the **out-of-plane**, SV-wave, displacement component.

With regard to surface-breaking defect measurements, the combination of tangential and normal displacement components in a SAW provides a very efficient and effective means for coupling energy into *complicated* defect features through ultrasonic reflection, transmission, and scattering processes. This topic will be covered in more detail in the next section, but it is worth mentioning that the propagation of both longitudinal and shear components in a SAW permits defects with sharp, angled, and curves features to be evaluated in detail. A simple shear-wave by itself, for example, would not provide the same interaction capability.

The limited and structured depth profile of SAW also provides a very important characterization NDE tool with regard to characterizing the depth characteristics of a surface-breaking defect site. As shown in Fig. 5, the P- and SV-wave depth profiles (left plot) can be used independently, or in combination, to evaluate local depth information through reflected ultrasonic energy levels based on the cross-sectional area of the defect site. A deep, half-penny shaped crack, for example, will interact with, and reflect much more of the available incident SAW energy than will a very shallow crack. Although the situation is somewhat complicated because 1) the SAW depth profiles are not simple linear relationships, and 2) there are two separate depth profiles (P- and SV-components) to consider, the potential does exist for making accurate assessments of crack-depth based on reflected energy levels.

It should also be possible to adjust the SAW frequency as a means for characterizing defect depth profiles. This situation is depicted in Fig. 5 (right plot), where the depth characteristics of three SAW of different frequencies is plotted. The 10 MHz SAW has a maximum depth profile of ~200 microns, while the 5 MHz SAW has a maximum depth profile of ~400 microns.

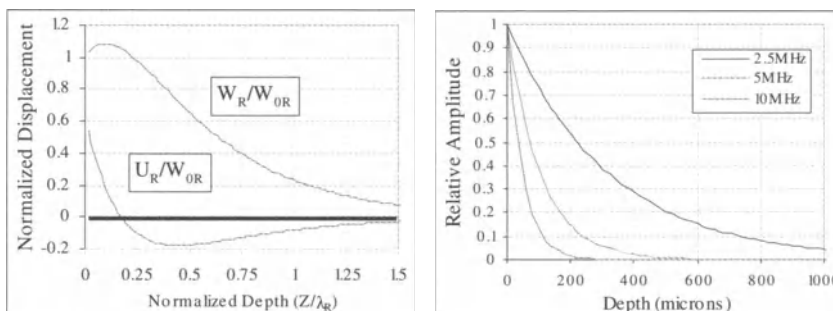


**Fig. 5.** Rayleigh wave displacement components as a function of depth

### 4.2.3 Ultrasonic Reflection and Scattering from Microcracks

For surface-breaking cracks, the primary mechanism for ultrasonic reflection processes is due to a substantial mismatch between the acoustic impedance of the substrate material and an air-gap that exists between the two crack-faces (see Fig. 6).

As with other wave-boundary interactions, the specular reflection of ultrasonic energy from a crack obeys the normal laws of reflection [25]. A determination of the angle and amplitude of the reflected signal simply requires an evaluation of the various wave components so as to satisfy the appropriate boundary conditions – namely, continuity of displacements and stresses across the interface [15,17]. The preferred geometry for crack detection and characterization purposes is a normally-incident ultrasonic wave relative to the crack direction. This allows the ultrasonic wave to hit the crack broadside, and results in a maximum reflectance. For obliquely incident angles, the reflected wave is redirected away from the incident direction, and a reduction in the reflected waves amplitude is observed. For crack measurements this can be problematic in that the reflectance level changes based on the geometry of the measurement setup.

Another important process referred to as ‘mode-conversion’ also occurs for ultrasonic waves incident at oblique angles relative to the surface normal [25]. This situation is depicted schematically in Fig. 6b, where a longitudinal P-wave is directed towards a material-air interface at an angle,  $\alpha_1$ . As depicted in the figure, a partial wave or mode conversion takes place at the boundary, creating an additional SV-wave that reflects and propagates into the material substrate. The SV-wave is reflected at a different angle relative to the P-wave reflection angle, and take energy away from the receiving transducer, and complicate the measurement process. The extent of the mode conversion depends on the angle of incidence of the P-wave, and Poisson’s ratio of the material substrate. The various angles of incidence and reflection are related to one another through the wave velocities in the substrate material according to the expression

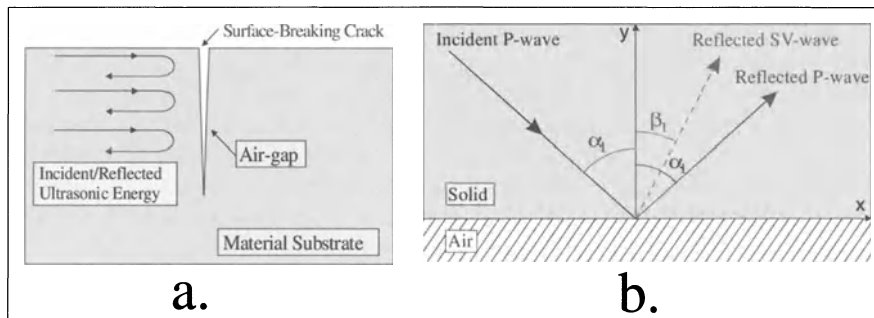


**Fig. 6.** Reflection of a P-wave at a boundary between a solid material and air

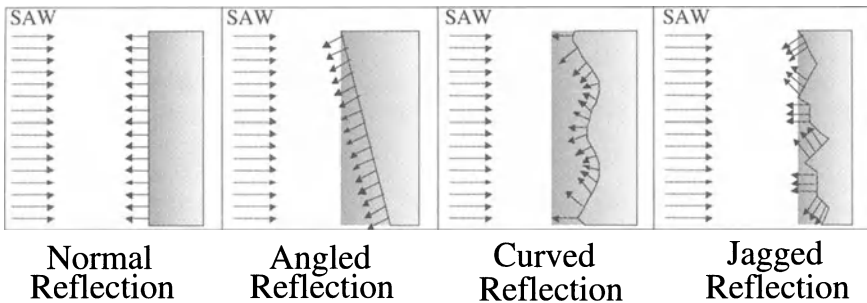


**Fig. 7.** Ultrasonic reflections from various types of crack faces if the wavelength is short compared to the crack surface roughness

$$\frac{\sin \alpha_i}{\sin \alpha_j} = \frac{V_i}{V_j} \quad (2)$$

where i and j correspond to the P- and SV-waves properties in air and the substrate material, respectively.

Realistic cracks are often very irregular in their shape and three-dimensional structure, and this will tend to reflect ultrasonic energy in very complicated manners. Several examples of this are presented schematically in Fig. 7, where the interaction of a SAW with 1) a normal-incidence planar crack, 2) an oblique-incidence planar crack, 3) a normal-incidence curved crack, and 4) a normal-incidence jagged crack are depicted. The normal-incidence, planar crack (infinite lateral and depth extent), in particular, is often used in analytical models and experimentally studies because it is the simplest case. The curved- and jagged-crack cases are more typical of realistic cracks, and as shown in the figure, result in energy being reflected into very complicated directions and patterns. Figure 8 provides a y-z plane perspective of the SAW-crack interaction process (cross-section through the material depicting the depth of the crack). The y-axis is perpendicular to the boundary of the half-space, and the z-axis is parallel to the direction of wave propagation. A ray-description is used in the figure to simplify the explanation. As shown in the figure, the incident SAW first interacts with the front crack mouth, resulting in a primary reflected wave, an initial transmitted wave around the first corner, and bulk-wave scattering by the corner. The primary reflected wave amplitude is often used for detecting/sizing cracks in pulse-echo NDE measurements, and is 0% to ~40% of the incident amplitude. The transmitted wave continues propagating as a SAW down the front crack-face until it encounters the crack-tip. A second bulk-wave scattering event occurs at the crack-tip, leaving a small portion of the transmitted energy to continue propagating up the back crack face. Upon reaching the back crack mouth, the transmitted wave again reflects a small portion of its energy, and mode-converts energy at the corner though a final bulk-wave scattering event. Bulk wave

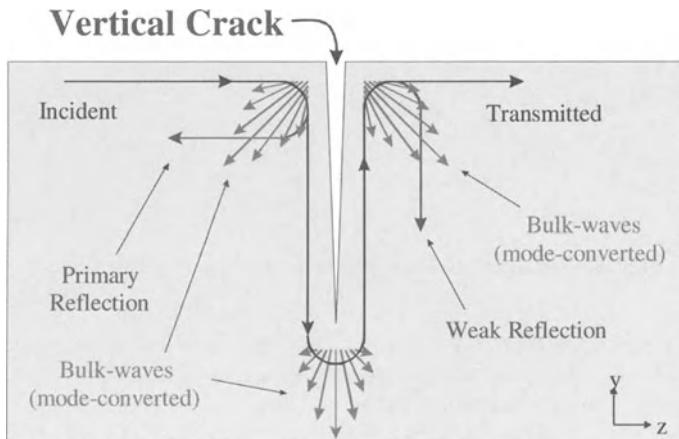


**Fig. 8.** SAW-crack interaction process

conversion processes scatter the majority of available energy (~80%) away from the crack site, leaving very little energy to be transmitted completely around the crack (1–10%).

Several important points can, therefore, be made regarding the simple reflection (and/or transmission) of SAW for crack detection and sizing measurements. First, the maximum available reflected signal levels are on the order of 40% of the incident SAW amplitude. This is under optimum conditions, with additional effects such as absorption losses and geometric beam spreading being neglected. Second, the bulk-wave scattering and mode-conversion of SAW by crack-tips and crack-roots is significant, and not only takes ultrasonic energy away from the reflected/transmitted SAW, but redirects energy in very complicated ways. And finally, the SAW reflection process is optimum for a planar crack at normal incidence. If there is any structure to the crack as depicted in Fig. 7, or if the crack as a whole is oblique relative to the incoming SAW direction, the energy distribution will redirect and spread, reducing the available signal level for the detecting transducer. All of these effects will ultimately reduce signal-to-noise ratios (SNR), and will add unwanted complexity to the measurement process and results.

In addition to the basic reflection, transmission, and bulk-wave conversion processes just mentioned, a crack can also scatter, radiate, and diffract the ultrasonic energy that is incident upon it. This becomes particularly important when the crack is small relative to the ultrasonic wavelength (i.e., long-wavelength regime,  $ka \gg 1$ , where  $k$  is the ultrasonic wavenumber, and  $a$  is the crack length or radius). Because most surface-breaking fatigue cracks fall into this category, a number of researchers have studied and modeled the scattering of elastic waves from three-dimensional, surface-breaking cracks [31–36]. A typical surface-breaking fatigue crack has a ‘half-penny’ shaped cross-section, with a nominal radius of 10 microns to 1 mm in size. A typical NDE measurement utilizes a SAW with a frequency of 1–10 MHz, which corresponds to wavelengths

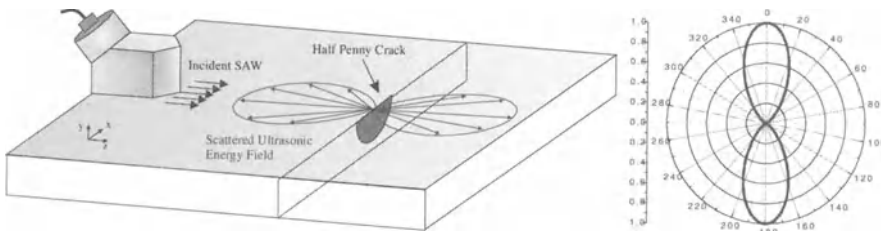


**Fig. 9.** Ultrasonic scattering pattern for half-penny shaped crack

of 300 microns to 3 mm (for aluminum and titanium substrate materials). For these conditions, ultrasonic scattering and diffraction can be significant, resulting in very distinct radial scattering patterns. A numerical example of this is depicted in Fig. 9, where a 5 MHz SAW has been incident normal to a 300 micron, half-penny shaped crack. A distinct radially-symmetric scattering pattern is observed, with the majority of energy being directed in the backward and forward scattering directions. It should be noted that the scattering pattern will change considerably for minor changes in the defect shape or the SAW frequency, which again would add complexity and ambiguity to the measurement process using traditional ultrasonic approaches.

#### 4.2.4 Local Ultrasonic Scattering from Surface-Breaking Cracks

It would, therefore, be very beneficial to have an NDE technique that could take advantage of the positive aspects of a traditional ultrasonic approach, but would not be limited by many of the pitfalls of such systems. The use of laser detection of near-field ultrasonic scattering processes for example from surface-breaking cracks provides one such way of accomplishing this.

The near-field scattering of ultrasonic energy from surface-breaking cracks has only recently been utilized as a detection and characterization tool [10,11]. A number of researchers realized the advantages of using laser interferometry systems to probe ultrasonic fields with high resolution and sensitivity [2–8,27]. The two key aspects of laser ultrasonic NDE that make near-field measurements possible include: 1) probing without perturbing the ultrasonic field, and 2) micron resolution capabilities.

Local crack scattering effects are based on free-boundary reflection processes, that result in a local intensification of the ultrasonic displacement field level in the immediate vicinity of the defect site. The key aspect of this free-boundary reflection process takes advantage of the *free surfaces* that are present in many defect sites (corrosion pits, surface-breaking cracks). As shown in Fig. 10, a surface-breaking crack has two potential free-boundaries represented by the opposing crack faces (right). In a simple spring-mass analysis, the top surface of the material and both crack faces represent tension-free, uncoupled spring systems

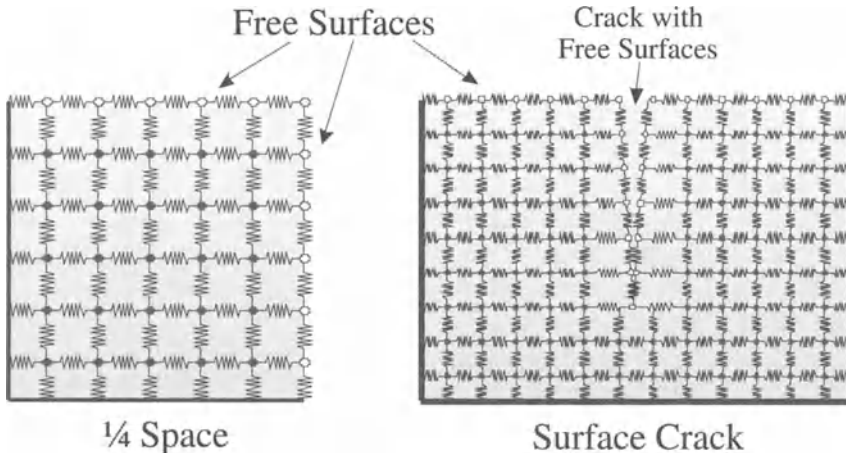


**Fig. 10.** Quarter-space corner and surface-breaking crack as free surfaces

to the areas just above the material surface, and within the crack opening. The  $\frac{1}{4}$ -space diagram on the left, for example, has two free surfaces (top and right edges), while the surface-breaking crack (right diagram) has three free surfaces (top, left crack face, and right crack face). The free-surfaces oscillate differently than the bulk material, and also support the propagation of ultrasonic energy differently. In simplest terms, the free-boundary reflection process involves a *constructive superposition* of incident and reflected waveforms. This situation is depicted graphically in Fig. 11, where the incident, reflected, and superposition waves of a pulse interacting with a free-boundary surface are depicted at different times during the propagation cycle. When the incident pulse arrives at the free-boundary, the particles are *free* to move, because of the lack of material (and resistive forces) further upstream. In a spring-mass sense (as depicted in Fig. 10), the particles respond to the tension/compression forces imposed by the incoming wave without restrictions. As the particles along the free-boundary move, however, they pull on the particles they are connected to, stretching the spring-mass bonds. This ultimately produces a reflected pulse with the same sign and amplitude as the incident pulse. The incident and reflected pulses reinforce each other, creating an antinode at the free boundary that has a nominal peak displacement that is twice the amplitude of either of the individual pulses (for 100% reflection).

The free-boundary ‘constructive superposition’ process is very localized spatially, leading to an increase in the displacement level **only** within an approximate distance of  $\frac{1}{4} \lambda_r$ . Because of this fact, we term the detection process as a ‘near-field’ measurement. This does not correspond to the same nomenclature typically used to describe near-field wave scattering effects (e.g. Fresnel zone;  $z < \frac{1}{4} L^2/\lambda_r$ ), which include a parameter, L, for the geometric size of the scattering site.

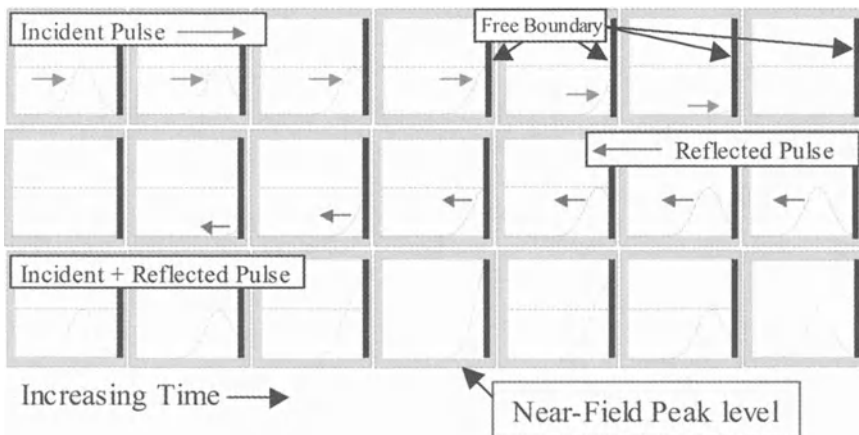


**Fig. 11.** Free-boundary reflection for a pulse incident on a crack-like boundary

With regard to SAW, both the longitudinal and shear components take part in the free-boundary reflection process. A nominal 2-fold displacement increase occurs for both P- and SV-wave components, in the longitudinal and transverse directions. This is usually an advantage for surface-breaking crack measurements, where the interaction of the SAW with a complicated crack structure often involves oblique reflection features, which couple with both longitudinal and shear components.

Conceptually, the free-boundary reflection process is simple to understand, analyze, and model. This is in contrast to traditional ultrasonic reflection/scattering measurements, which require very sophisticated reflection and scattering theories to understand or interpret measurement results. The free-boundary reflection process is also very localized around the defect site. This is very important, because it allows extremely small defects to be measured and discriminated from the background material. In addition, surface-breaking defects can actually be ‘imaged’ based on the contours of the local displacement-field intensity increase. The local ultrasonic intensification is much less susceptible to variations in the propagation, diffraction, and scattering of ultrasonic energy far from the crack site. This is primarily due to the fact that the free-boundary reflection process depends almost exclusively on the incident waveform just prior to it hitting the free-surface and the reflected wave from the boundary interaction. Many of these advantages will be highlighted using examples in the measurement results section.

The only requirements for making measurements in the “near-field” are 1) and adequate spatial resolution that can probe effectively very close to the defect site, and 2) the ability to probe the local displacement field without changing its characteristics. Laser ultrasonic techniques using optical interferometry and holography systems adhere to both of these requirements, as described in the next section.

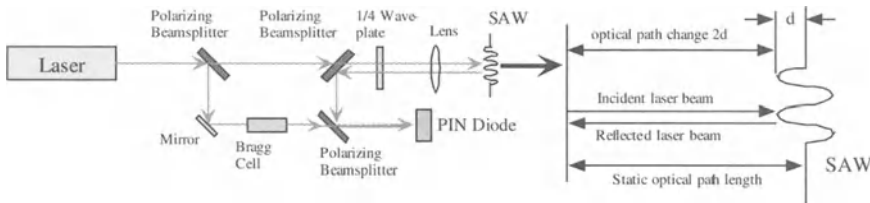


**Fig. 12.** Heterodyne interferometry system for surface displacement measurements

#### 4.2.5 Optical Interferometry and Holography

A typical heterodyne interferometry system provides an output electrical signal that is proportional to the instantaneous displacement of a vibrating surface at a single point [8]. As shown in Fig. 12, the light from a low-powered laser is separated into reference and signal beams. The signal beam is directed towards the material surface and is focused down to a small spot. This focused spot determines the lateral spatial resolution of the system, and is typically between 1–10 microns in diameter. The vibrating material surface modulates the phase of the reflected signal beam, and when the reference and signal beams are recombined, a modulated beam intensity is created that can be used to precisely track the out-of-plane motions of the surface.

Optical heterodyning is often used to enhance the sensitivity and performance of an interferometry system. This is typically accomplished by placing an acoustic Bragg cell in the reference beam as shown in Fig. 12. The Bragg cell frequency shifts the reference beam, which results in a modulation of the detected intensity that acts as an RF carrier. Every movement of the target specimen then turns into a direction dependent deviation of the output modulated frequency from its steady-state value. Phase demodulation of the detected electronic signal then provides an accurate and direction-sensitive measure of the surface displacement that is less sensitive to environmental noise. The three primary advantages of optical heterodyning include: 1) environmental noise reduction, 2) discrimination between forward or backward moving surface motions, and 3) absolute calibration of the displacements.

Frequency-translated holography provides an additional capability for visualizing surface displacement patterns as full-field images [9]. As shown in Fig. 13, a typical system uses a Leith-Upatniek off-axis holographic setup for recording a hologram, where the light from a moderate-power laser is split into signal and reference beams. The signal beam is expanded and collimated, and is directed towards the material surface. Light scattered from the surface is collected, spatially-filtered, and relay-imaged to the holographic film using a series of lenses. The reference beam is also directed towards the holographic film, after a

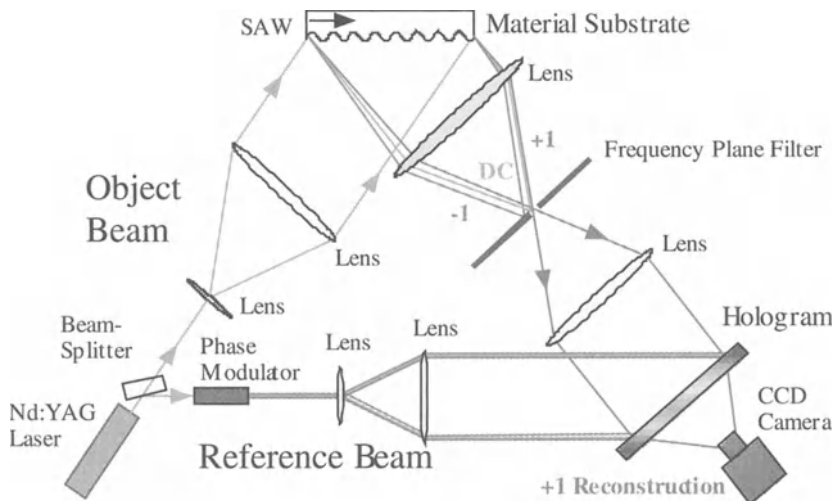


**Fig. 13.** Frequency translated holography system for surface displacement measurements

phase modulator has been used to frequency-shift its optical frequency. A holographic record of the surface motions is created when the signal and reference beams are made to interfere in the holographic film. An accurate representation of the surface motions can be reconstructed and viewed by a CCD camera when the stored hologram is illuminated by the original reference beam.

Direct visualization of surface wave patterns is made possible through two key features of the frequency-translation measurement process. The first feature involves the Surface Acoustic Wave (SAW) pattern induced on the material surface, which acts as a traveling phase-grating structure. The phase-grating causes light to be diffracted into separate orders, and at different angles relative to the surface normal. The local surface wave amplitude information is carried in the  $+/-1$  orders, which as depicted in Fig. 13, can be filtered using a series of lenses and frequency plane filter. In addition, the SAW imparts a frequency shift in the  $+/-1$  orders because it is a traveling wave. If the object and reference beams are in phase, and are modulated at the same frequency, the hologram acts as a narrow bandpass filter, and a direct visualization of the SAW becomes possible during reconstruction.

For real-time holographic measurements, a photochromic film called Bacteriorhodopsin (bR) was used [37]. Holograms are recorded in bR films as a local concentration/population difference between the film's B- and M-state molecules. The local population difference between the two states, in turn, causes local variations in absorption and index of refraction to occur, which results in a periodic modulation of the local refractive index and absorption coefficient in the film, which constitutes the hologram recording. Real-time holographic readout is accomplished by recording the hologram with frequency-doubled light from a Nd:YAG laser at 532 nm, and reconstructing/reading the hologram in real-time with a Bragg-matched HeNe laser at 632 nm.

## 4.3 Instrumentation and Methods

The near-field scanning interferometry (NFSI), and real-time, frequency-translated holography (FTH) systems described in this section provide a capability for measuring out-of-plane displacements on a material surface with high sensitivity and spatial resolution. The basic interferometry system provides a measurement of the displacement level at a single point as a ‘displacement versus time’ signal output. A complete, two-dimensional displacement-field image is created by raster scanning the position of the probe beam relative to the sample surface. The holography system, in contrast, provides a complete, full-field image of the displacement-field in a single exposure ( $\mu\text{s} - \text{ms}$  timescales). This is similar to taking a picture with a traditional camera. The two systems are complementary in nature, however. The interferometry system, for example, provides much more information in a given measurement (a complete time-versus displacement history) than the holography system (a single ‘snapshot’ of the SAW displacement at a single instant in time). The holography system does, however, provide a complete measurement in a very short time, while the interferometry system takes minutes to hours to complete its raster-scan process. The interferometry system also has a significant advantage with respect to signal-to-noise, when signal isolation, in-line averaging, and time-gating was applied to the signal. Both systems did, however, prove to be very capable of imaging SAW, and detecting/characterizing cracks on a material surface.

### 4.3.1 Near-Field Scanning Interferometry (NFSI) System

A schematic diagram of the near-field scanning interferometry (NFSI) system is presented in Fig. 14. The system is built around a Polytec OFV 301 vibrometer, which uses heterodyne interferometry principles to measure out-of-plane displacements at a single point on a material surface. The system uses a 1 mW HeNe laser, and a variable-focus lens, to provide spatial resolutions between 5–10 microns, and standoff distances from 10 cm to  $>1$  meter. Optical heterodyning is provided by a 40 MHz acousto-optic Bragg cell placed in the reference beam path. The resulting instrument is capable of making sensitive displacement measurements in the frequency band 25 kHz to 20 MHz, with sub-nanometer sensitivities.

A computer-controlled x-y scanning system was integrated into the basic system to allow two-dimensional displacement field images to be obtained. At each scan position, the computer provides a trigger signal to a toneburst generator, which in turn, supplies a sinusoidal, AC voltage toneburst to drive the SAW transducer. The interferometry system then senses the out-of-plane motion at the focused spot position, and provides an displacement vs. time signal to the control software. The detected signal is time-gated and phase-locked to the original drive signal, providing a measure of the absolute amplitude and phase at each measurement point. The system has a scan precision in excess of 1  $\mu\text{m}$ , and can scan at speeds of three data points per second. A typical measurement of 100 by 100 points takes approximately one hour.

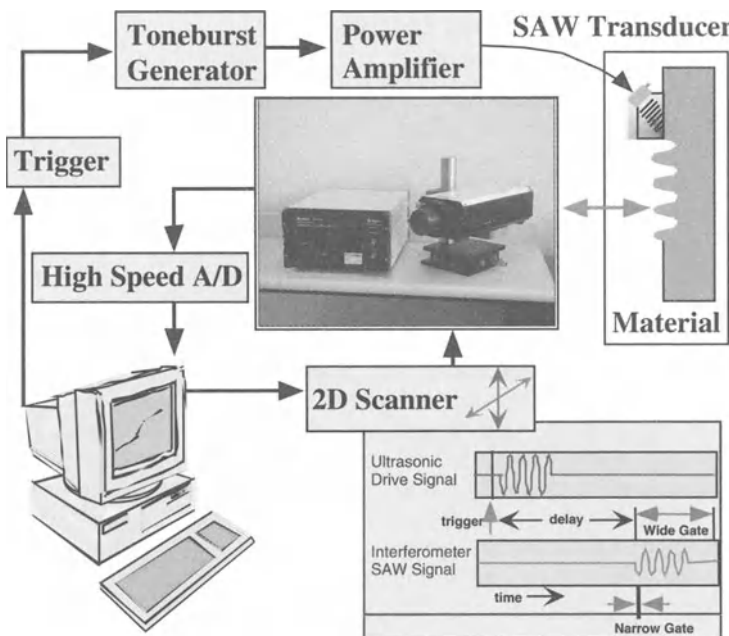


**Fig. 14.** Near-Field Scanning Interferometry (NFSI) system

### 4.3.2 Frequency Translated Holography (FTH) System

A schematic diagram of the frequency-translated holography (FTH) system is provided in Fig. 15. The hologram is written to the bacteriorhodopsin (bR) film using a 100 mW Nd:YAG laser. Frequency shifting of the reference beam is accomplished using a tunable acousto-optic modulator, which is phase-locked to the SAW driver. The hologram is read-out to the CCD camera in real-time using a 35 mW HeNe laser. The frequency-plane filter consists of an opaque vertical slit, 1mm wide, positioned at the back focal plane of the 1st imaging lens. A color filter blocks the Nd:YAG (532 nm) light, and passes the HeNe (632 nm) light.

## 4.4 Applications

The interferometry and holography systems provide a capability for imaging displacement fields on a material surface as false-color images. In effect, large displacement levels show up as bright regions in the image field, while zero displacement levels appear as dark regions. The surface displacements can originate from a number of sources including bulk waves that work their way to the surface level, generic vibrations of the entire material, or in most of the cases

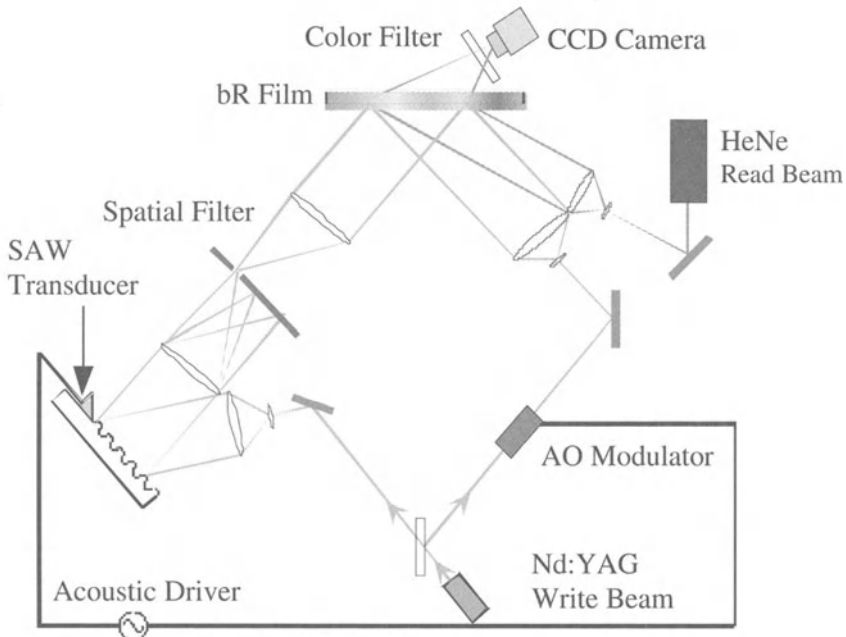


**Fig. 15.** Frequency-Translated Holography (FTH) system

that will be presented in this section – surface acoustic waves traveling along the material surface. As a precursor to ‘defect imaging’, a number of surface wave visualization examples will be presented, showing some of the key aspects of the displacement-field imaging techniques. Several crack imaging examples will then be presented, showing the versatility, and detailed characterization capabilities, of the local crack imaging approach. A final experimental measurement involving the *in situ* detection and characterization of a stress-corrosion crack will then be presented.

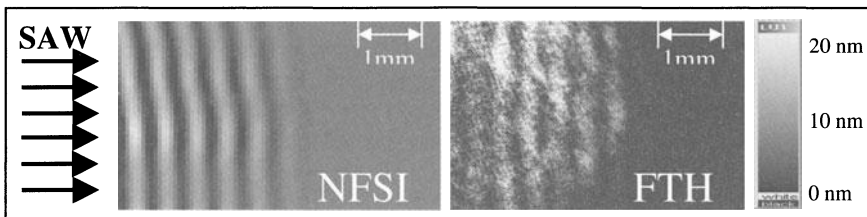


**Fig. 16.** Displacement-field images of 5 MHz SAW taken with the NFSI and FTH systems

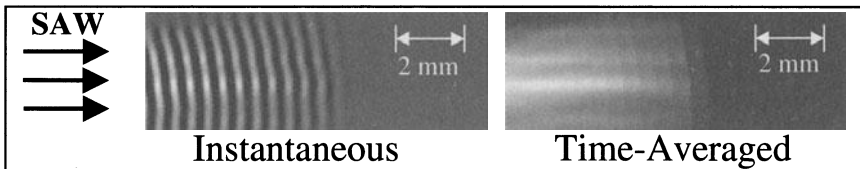


**Fig. 17.** Instantaneous and time-averaged displacement field images using NFSI

#### 4.4.1 Interferometric and Holographic Imaging of Surface Waves

Figure 16 provides a comparison of the displacement-field imaging capabilities of the scanning interferometry and real-time holography measurement systems. The images depict the instantaneous displacement field of a 5 MHz SAW propagating from left to right in the image fields. The peak out-of-plane displacement levels were 17 nanometers. The significant improvement in SNR for the NFSI image is very evident when comparing the two images. The NFSI image took approximately 40 minutes to acquire (80x60 image points), while the FTH image was taken in real-time.

In addition to taking instantaneous images, the NFSI system can take time-averaged, peak-displacement measurements. A comparison of a SAW waveform taken using the instantaneous and time-averaged measurement schemes is depicted in Fig. 17. The basic difference in the measurements involves the use of a narrow- versus wide-detection gate. When a narrow-gate is used, the time-resolved, instantaneous displacement field can be resolved. When a wide-gate is used, the entire temporal waveform is considered in the measurement process, where the peak displacement is extracted. The time-averaged, wide-gate measurement scheme is far superior in the way it represents crack interactions when local crack scattering effects are being evaluated. This will be highlighted in the next section.

One of the biggest problems with making crack-scattering measurements far from the crack site is depicted in the set of images in Fig. 18. The NFSI system in this case was used to image the scattering of ultrasonic waves from a series of complicated crack systems (the crack positions have been highlighted in each image). Each image depicts the instantaneous, out-of-plane displacement field one microsecond after the wave has interacted with the crack site. The 5 MHz SAW was propagated from the top-down, and reflected/scattered waves propagated primarily bottom-up in the figure. In a traditional ultrasonic NDE measurement, the piezoelectric receiver transducer would acquire a complicated displacement-versus-time signal in the far-field. As shown in the figure, this signal would be made of the various waves as they propagate, reflect, scatter, diffract, geometrically spread, and attenuate. The characterization of crack lengths and depths would most likely be difficult in these three cases using traditional ultrasonic NDE approaches.

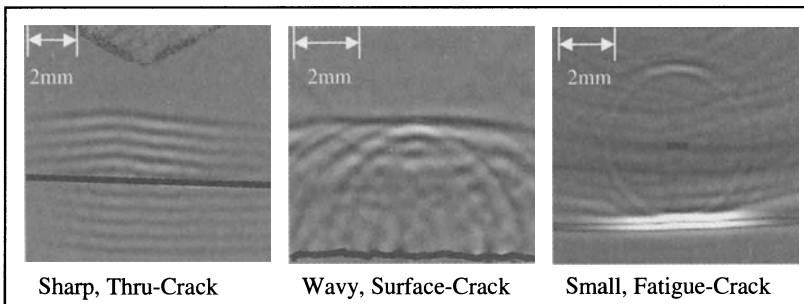


**Fig. 18.** Far-field, instantaneous scattering from complicated crack structures

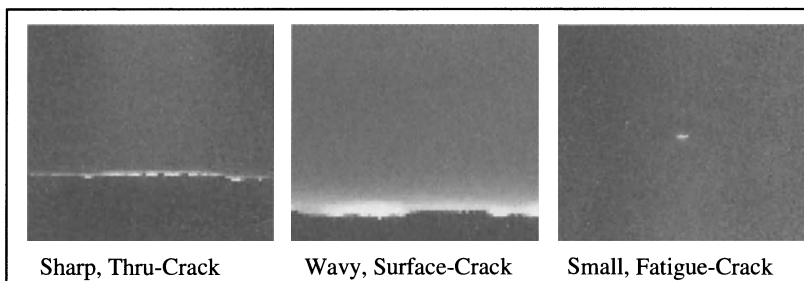


**Fig. 19.** Displacement-field images of complicated crack structures

#### 4.4.2 Local Ultrasonic Scattering from Surface-Breaking Cracks

Figure 19 depicts the same cracks shown in Fig. 18, however, in this case the displacement-field images were taken in such a way as to highlight ultrasonic scattering processes very near the crack sites. In effect, a time-average, displacement-field image has been obtained that shows an enhancement of the out-of-plane motion field in the immediate vicinity of the cracks. The positions and basic structure of the cracks are easily seen in each case. The displacements in each case were 1.5 to 2.0 times greater than incident displacement levels (versus 40% for a traditional ultrasonic reflection measurement).

Figure 20 shows a comparison of the scanning interferometry and real-time holography NDE systems for measurements of the same three crack defects. The 5 MHz SAW is again propagating from the top-down as in the previous measurements. The local crack scattering patterns follow the crack contours very closely in both cases, and a good comparison between the two image fields is evident. Peak displacement levels were 7 nanometers for the incident field, and 14–20 nanometers for the near-field displacement levels. The small fatigue crack

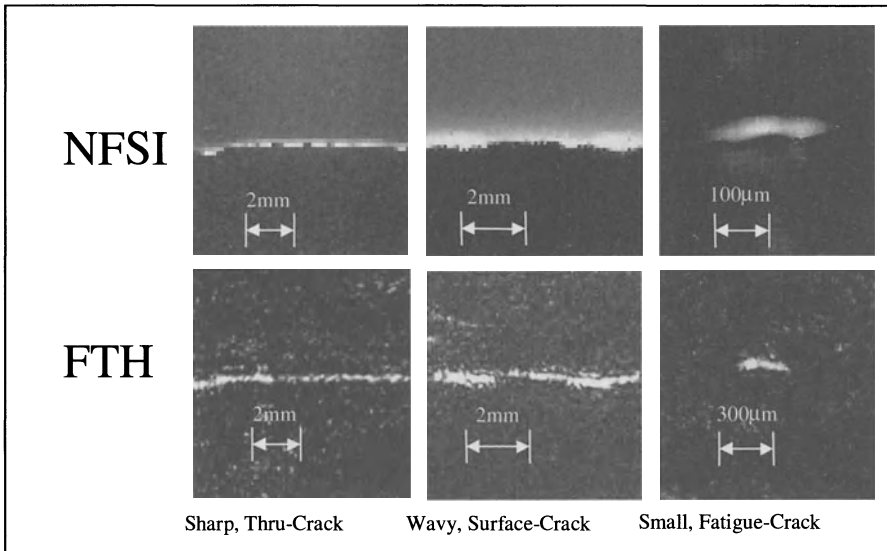


**Fig. 20.** Comparison of scanning interferometry and real time holography images

in the right set of images was 250 microns in length. The detection of a 75 micron-long by 4 micron-deep laser-etched notch defect was also successfully imaged using the NFSI system, providing a nominal measure of the detection limits of the technique.

An interesting, and potentially very important feature of the local crack scattering effect is depicted in Figs. 21 and 22, where the local scattering pattern of a small surface notch (1mm long x 25 μm wide x 100 μm deep) was studied for various angles of incidence. As described in the ultrasonic reflection and scattering section of this chapter, the angle of incidence is a critical aspect of the measurement process for traditional NDE approaches. This is because the ultrasonic energy is 1) reflected at a skewed angle for oblique incidence angles, and 2) is scattered in distinct radially-symmetric scattering patterns for small localized defects. This has two severe consequences for traditional measurement approaches. First, the receiver must be placed very precisely in order to optimize the signal and measurement, and second, any given measurement can vary significantly for angular and symmetric beam alignment variations. As shown in Figs. 21 and 22, however, the scattering pattern is observed through the entire range of angles of incidence (0 to 90 degrees). There is some variation observed in the maximum level of displacement as seen in Fig. 21, but a nominal increase in the near-field displacement level is still evident between 1.5x to 2.0x. The ‘imaging’ characteristics of the technique are also still preserved in all cases, even at 0-degree incidence levels as shown in Fig. 21.

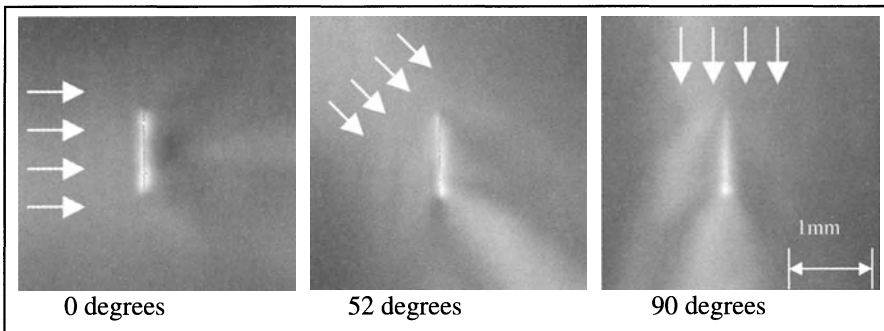


**Fig. 21.** Intensity patterns for variations of incident angle

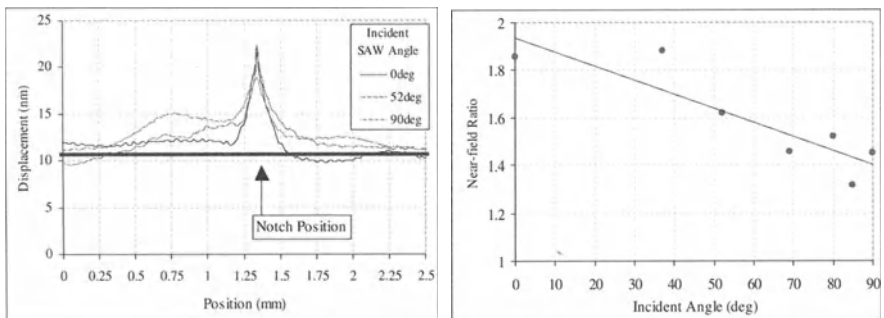


**Fig. 22.** Intensity patterns for variations of incident angle

#### 4.4.3 Crack-Depth Determination

One of the most interesting aspects of the above discussed technique involves the possibility of acquiring local depth information for the surface-breaking crack based on the local displacement level. As described in the surface acoustic wave section of this chapter, the SAW has a very important depth profile that limits its penetration depth into the material. Several researchers have used this SAW feature to extract information related to crack depths in the past based on reflected and transmitted energy levels [22, 27, 30].

As shown in Fig. 23, the depth of a crack, and its interaction with a SAW of a given depth will reflect and transmit different levels of ultrasonic energy depending on relative depth levels of each. The SAW penetration depth is dependent on its frequency (see Fig. 5), and therefore, the frequency can be swept from high to low frequencies to provide an increased depth penetration level for the SAW.

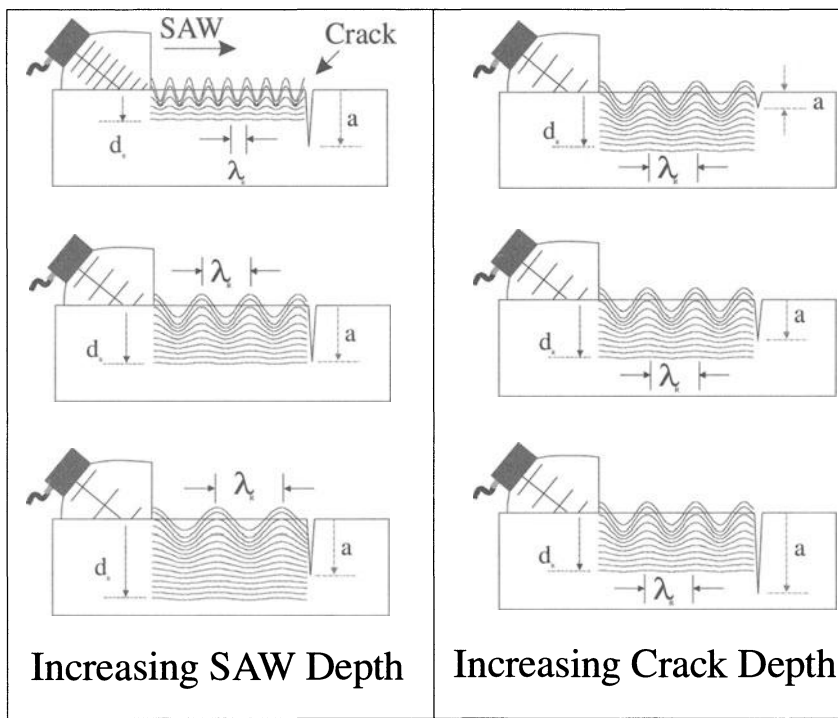


**Fig. 23.** Surface acoustic wave penetration depth versus crack depth

At one specific frequency, the depth of the crack will match the depth of the SAW, and a maximum reflection will occur, along with a minimum transmittance of energy beyond the crack site. Beyond this SAW frequency (i.e. at lower frequencies), the transmitted energy level will increase as the SAW propagates under the crack, and reflected energy levels will reduce. For ultrasonic scattering processes, the same basic effect can be used to extract local depth information based on the level of free-boundary reflection that has occurred at a particular crack-depth versus SAW-depth match.

In order to test this, a series of precision ledges were cut in an aluminum block at various depths ranging from 75 to 800 microns. The intensity level was then measured for normal-incident SAW at different frequencies ranging from 2.5 MHz to 10 MHz. The topographic features of one such ledge are depicted in Fig. 24, where a profilometry system was used to accurately measure and characterize the precision and orthogonality of the depth cut. The ledge in Fig. 24 was the second shallowest available, and had a nominal depth of 127 microns  $\pm 5$  microns.

Figure 25 provides the major results of the study for three drive frequencies of 2.5 MHz, 5 MHz, and 10MHz (right). The displacement field images for two of the ledges (800  $\mu\text{m}$  and 127  $\mu\text{m}$ ) are provided on the left. A 5 MHz SAW pulse

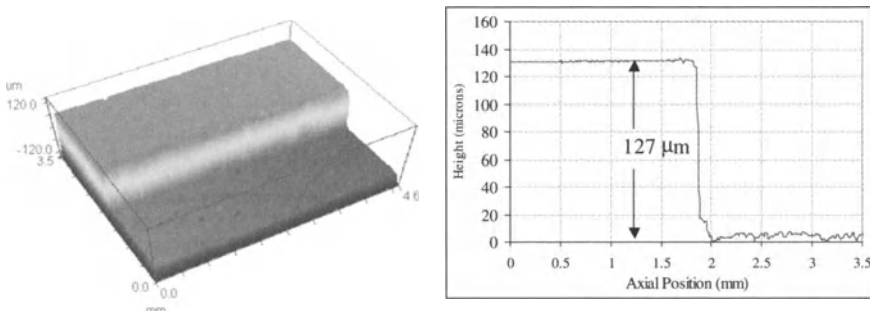


**Fig. 24.** Surface acoustic wave penetration depth versus crack depth

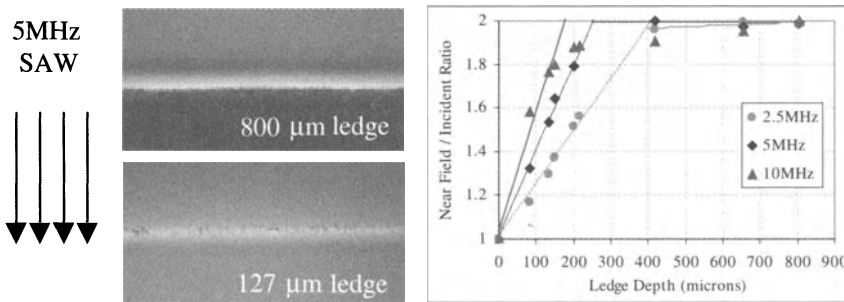


**Fig. 25.** Local ultrasonic displacement level versus ledge depths

was incident from the top-down in the images. The 800 micron ledge is seen to have a darker region at the lower step height indicating that the SAW energy was not able to travel beyond that ledge depth (the nominal depth of a 5 MHz SAW in aluminum is 300 microns). The energy was able to propagate past the shallow 127  $\mu\text{m}$  ledge, however, and resulted in a noticeable SAW amplitude in the lower step region. Although a more sophisticated model and analysis is needed, the plot on the right does show very good indications that there is a definite correlation between the depth of the ledge and the local SAW displacement level. A linear fit was applied to the data to show basic trends, but as described in the surface acoustic wave theory section, the SAW displacement level at a given depth actually shows more of an exponential trend for the transverse, SV-wave component (Fig. 5). A distinct saturation point for each of the three frequencies is also observed in the plot, which is likely the depth level at which the SAW penetration and ledge depths match.

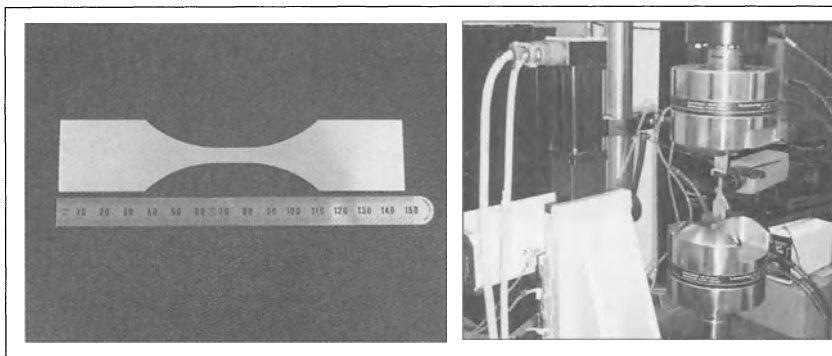
#### 4.4.4 In Situ Stress-Corrosion Crack (SCC) Growth Measurements

A number of researchers have shown the importance of understanding stress-corrosion crack (SCC) processes, which in general, initiate cracks earlier and have significantly higher crack growth rates than that of uncorroded surfaces [38–39]. The possibility of *imaging* a SCC growth process *in situ* was, therefore, thought to be a very good match for the new capabilities of the crack-imaging system. The goal of the study was to image the detailed structure of a stress-corrosion crack as fatigue cycles increased, and to determine the crack initiation site if possible. It was anticipated that the ultrasonic displacement field image would provide evidence of crack initiation before visual evidence was observed. In addition, an evaluation of the local displacement level was characterized at increasing fatigue cycles to determine if local crack-depth information could be extracted.

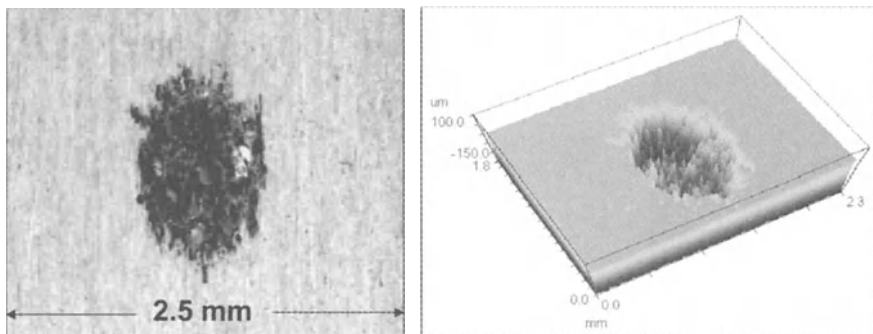
Figure 26 provides an image of the Al2024-T3 aluminum dogbone sample before pitting, and a picture of the experimental setup during the fatigue process. The dogbone sample was 146.1 mm long, 1.57 mm thick, and had a gauge section length of 12.7 mm and width of 6.35 mm. The sample was fatigued at 15 Hz, with  $\sigma_{max} = 286$  MPa, and an R-ratio = 0.1. A single corrosion pit was introduced into the center of the gauge region using an electrochemical pitting system.

Figure 27 provides a digital and topographic image of the resulting pit. The pit was nominally 0.83 mm x 1.28 mm in size, was elliptically-shaped (major axis oriented along the long axis of the dogbone), and had a peak depth of -280  $\mu$ m, an average depth of -150  $\mu$ m, and had a general inverted-bowl depth profile.

The displacement field measurements were made using the NFSI Interferometry system, which required the fatigue cycling to be interrupted periodically to build up the displacement field image through raster scanning of the probe beam relative to the dogbone surface. A 5 MHz,  $\frac{1}{4}$ " diameter SAW transducer was attached to the top grip section of the aluminum sample, so that the SAW propagated through the grip region of the test specimen. An impulse excitation was applied to the



**Fig. 26.** Stress-corrosion crack dog bone (*left*) and experimental setup (*right*)



**Fig. 27.** Digital (left) and topographic (right) images of the corrosion pit

transducer, which resulted in a SAW displacement level propagating along the material surface of 10 nm. Time-gating of the detected signal levels allowed ultrasonic reflections to be minimized.

Figure 28 depicts a series of 8 displacement-field images taken at various stages of fatigue cycling. Crack initiation at the surface was first observed at 28,000 cycles based on a relative increase in the displacement-field intensity levels. This corresponded to a first observance of crack initiation at 49.6% of life, given a final fracture event at 56,400 cycles. By comparison, the first visual evidence of crack initiation (using an in situ digital microscope system) was observed at 51,000 cycles or 90.4% of life.

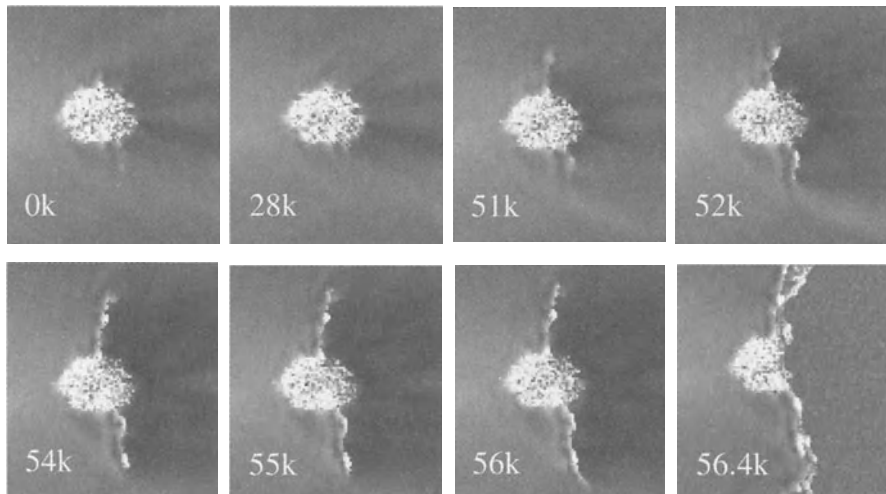


**Fig. 28.** Displacement-field images showing stress-corrosion crack growth

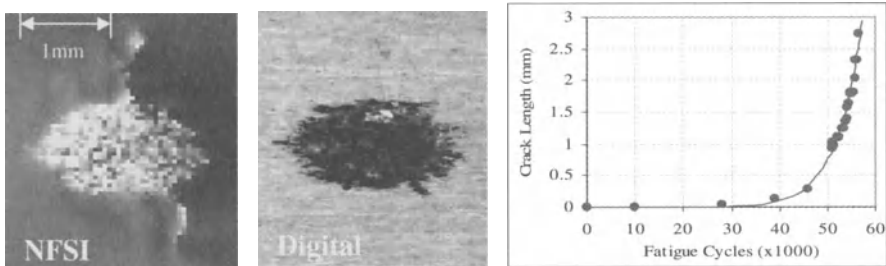


**Fig. 29.** Digital and NFSI images taken at 51,000 cycles (*left images*), and a plot of the stress-corrosion crack lengths versus fatigue cycles

Figure 29 provides a comparison of the digital and NFSI images at 51,000 cycles along with a crack-growth curve based on the maximum length of the crack at a given cycle number. The crack grew symmetrically, with 1st observance occurring almost simultaneously on either side of the the pit, normal to the forcing direction. It is interesting to note that the cracks on either side of the pit emanated from distinct protrusions, which represented sharp, irregular features of the pitting surface, and likely acted as stress-concentration regions. Various image subtraction and enhancement techniques were used in an attempt to follow crack-growth activity inside the pit itself, but strong vibrations within the pit region resulted in out-of-plane motions that masked the crack position. Measurements were conducted with, and without ultrasonic energy present so that surface-roughness effects could be isolated from vibrational energy levels present inside the pit. The results of these measurements showed that the surface roughness levels inside the pit region accounted for only 0.51–1.53% of the observed noise levels within the pit. Further investigation studies are underway to understand this phenomenon.

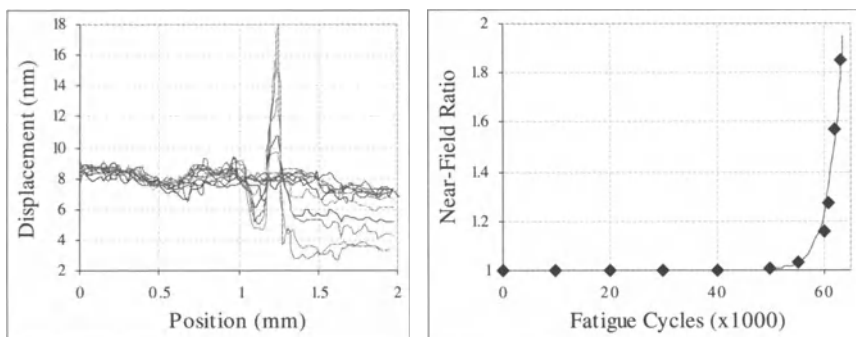


**Fig. 30.** Displacement field intensity vs axial position (*left*), and peak displacement versus cycle number (*right*)

The possibility of obtaining local crack depth information versus fatigue cycle number was also studied. The results of this effort are presented in Fig. 30, where cross-sectional cuts taken from the NFSI image data are presented for increasing fatigue cycles (left plot). The cuts were taken in the axial direction (oriented along the length of the dogbone, thru the crack, and normal to the crack) at a position 1.99 mm from the corrosion pit center in the transverse direction. A general increase in the peak displacement level close to the crack (near-field displacement) is seen as the fatigue cycles are increased, which would indicate that the crack is deepening and reflecting more SAW energy as the fatigue cycles increase. A plot of the near-field ratio (near-field displacement versus incident displacement) shows further evidence of this (right plot).

## 4.5 Future Trends

The combination of interferometric and holographic displacement measurements with classical ultrasonic testing methods provides a powerful NDE method for microcrack detection and characterization. In this effort, advanced holographic and scanning interferometric systems were developed and used to image surface wave patterns, and to characterize microcracks through near-field ultrasonic scattering processes. The techniques provide non-contact and remote measurement capabilities with high resolution and sensitivity. The crack imaging concept is new, and provides a powerful NDE capability for detecting and characterizing surface-breaking microcracks. The near-field scattering displacement was found to be much less sensitive to oblique-incidence SAW, which can be problematic in traditional ultrasonic measurements. The local displacement level was also found to be sensitive to crack-depth, which may provide a means for *imaging* surface-breaking crack features if full three-dimensions in the near future.

## References

1. Morre P, McIntire P (1995) Nondestructive Testing Handbook, vol. 9, Special Nondestructive Testing Methods, ASNT, New York
2. Doyle J (1999) The Expanding Use of Lasers in Nondestructive Testing. Materials Evaluation
3. Stegeman G (1976) Optical Probing of Surface Waves and Surface Wave Devices, IEEE Trans. On Sonics and Ultrasonics, vol. 23, No. 1
4. Erf R (1974) Holographic Nondestructive Testing. Academic Press, New York
5. Hurley D, Fortunko C (1997) Determination of the Nonlinear Ultrasonic Parameter  $\beta$  using a Michelson Interferometer. Meas Sci Technol 8
6. Xiao H, Nagy PB (1998) Enhanced Ultrasonic Detection of Fatigue Cracks by Laser-Induced Crack Closure. Journal of Applied Physics, vol. 83, No. 12
7. Choquet M, Neron C, Reid B, Viens M, Monchalin JP, Komorowski JP, Gould R (1998) Corrosion detection in aircraft structures using laser-ultrasonics. SPIE Conference on NDE of Aging Aircraft
8. Scruby C, Drain L (1990) Laser Ultrasonics – Techniques and Applications. Adam Hilger Publishing Ltd, Bristol, England
9. Shiokawa S, Moriizumi T, Yasuda T (1975) Study of SAW Propagation Characteristics by Frequency-Translated Holography. Applied Physics Letters, vol. 27, No. 8
10. Blackshire JL, Sathish S (2002) Near-field ultrasonic scattering from surface-breaking cracks. Applied Physics Letters, vol. 80, No. 18
11. Blackshire JL, Sathish S, Duncan B, Millard M (2002) Real-time, frequency-translated holographic visualization of surface acoustic wave interactions with surface-breaking defects. Optics Letters, vol. 27, No. 12
12. Hassan W, Nagy PB, (1999) Experimental Investigation of the Grain Noise in Interferometric Detection of Ultrasonic Waves. J. of Nondestructive Evaluation 18(4):139–147
13. Reinhart H, Dally J (1970) Materials Evaluation, vol. 30
14. Buck O, Frandsen J, Marcus H (1976) Fatigue Crack Growth Under Spectrum Loads. ASTM Publishing, Philadelphia
15. Auld B (1990) Acoustic Fields and Waves in Solids, vols. I and II, Robert E. Krieger Publishing Company, Malabar, Florida
16. Varadan VK, Varadan VV (1982) Elastic Wave Scattering and Propagation. Ann Arbor Science Publishers, Ann Arbor, Michigan
17. Achenbach J (1980) Wave Propagation in Elastic Solids. North-Holland Publishing Company, New York
18. Hecht E (1987) Optics. Addison-Wesley Publishing Company
19. Hariharan P (1991) Optical Holography. Cambridge University Press
20. Korpel A (ed) (1990) Selected Papers on Acousto-Optics. SPIE Optical Engineering Press
21. Goodman J (1968) Introduction to Fourier Optics. McGraw-Hill, New York
22. Thompson R, Thompson D (1985) Ultrasonics in Nondestructive Evaluation. Proc IEEE 73, pp. 1716
23. Her S, Lu S (2002) The Diffraction of Elastic Waves on the Tip of Slots. Journal of Nondestructive Evaluation vol.20, 4:133–143

24. Dai W, Kim J, Rokhlin SI (1999) In-Situ Surface Wave Monitoring of Fatigue Crack Initiation and Propagation. Review of Progress in Quantitative Nondestructive Evaluation, vol. 18
25. Harker A (1988) Elastic Waves in Solids. Adam Hilger Publishing, Philadelphia
26. Bruttomesso D, Jacobs L, Fiedler C (1997) Experimental and Numerical Investigation of the Interaction of Rayleigh Surface Waves with Corners. Journal of Nondestructive Evaluation
27. Cooper J, Crosbie R, Dewhurst R, McKie A, Palmer S (1986) Surface Acoustic Wave Interactions with Cracks and Slots: A Noncontacting Study using Lasers. IEEE Transactions on Sonics and Ultrasonics, vol. 33, No. 5
28. Viktorov I (1967) Rayleigh and Lamb Waves. Plenum Press, New York
29. Oliner A (1978) Acoustic Surface Waves. Springer-Verlag, New York
30. Cheng A (1994) Evaluation of Surface Fatigue Cracks using Rayleigh Waves. PhD Thesis, Univ. of Nebraska
31. Achenbach J, Fine M, Komsky I, McGuire S (1992) Ultrasonic Wave Technique to Assess Cyclic-Load Fatigue Damage in Silicon Carbide Whisker Reinforced 2124 Aluminum Alloy Composites. Cyclic Deformation, Fracture, and Nondestructive Evaluation in Advanced Materials, ASTM STP 1157, Philadelphia, pp. 241–250.
32. Tittmann B, Buck O, Ahlberg L (1980) Surface Wave Scattering from Elliptical Cracks for Failure Prediction. J Appl Phys, vol. 51, No. 1
33. Tittmann B, Ahlberg L (1986) Rayleigh Wave Diffraction from Surface-Breaking Discontinuities. Appl Phys Lett, vol. 49, No. 20
34. Lin W, Keer L (1987) Scattering by a Planar Three-Dimensional Crack. J Acoust Soc Am, vol. 82, No. 4
35. Burdeck D, Achenbach J (1989) Three-Dimensional Elastic Wave Scattering from Surface-Breaking Cracks. J Acoust Soc Am, vol. 86, No. 1
36. Her S, Lu S (2001) The Diffraction of Elastic Waves on the Tip of Slots. J of NDE, vol. 20, No. 4
37. Fitzpatrick C (1992) The Erasable Material Bacteria Rhodopsin: Its Characteristics and Uses in Holographic Applications. Practical Holography VI, SPIE, vol. 1667
38. Ma L (1994) Pitting Effects on the Corrosion Fatigue Life of 7075-T6 Aluminum Alloy. Ph.D. thesis, Univ. of Utah
39. Kim J, Rokhlin SI (2001) Surface Acoustic Wave Measurements of Small Fatigue Crack Initiated from a Pit. Int J Solids and Structs

## **5 Surface Acoustic Wave Characterization of Pitting Corrosion Damage with Fatigue Cracks**

S.I. Rokhlin, J.-Y. Kim

### **5.1 Introduction**

The design goals for length of operation of the present aircraft generation will be exceeded by most operators of jet-powered airplanes and turboprops [1]. The design was performed for fatigue life related to total flight hours or total number of cycles depending on aircraft type, and did not usually consider different in-service degradation and damage mechanisms such as environmental (corrosion) damage. Among the different types of corrosion damage, pitting has been known to be one mechanism triggering widespread fatigue crack initiation and reducing fatigue life of aging aircraft [2]. Therefore, it is important to detect surface flaws and associated cracks and to determine their sizes early in fatigue life in order to prevent catastrophic failure. The effect of pitting on fatigue is not yet well understood. This may be due to the lack of understanding of the inter-action between defects and electrochemical reactions in pitting [3]. It is shown in [4] and our own experiments [5] that the crack is usually initiated from the largest pit assuming homogeneous stress distribution in an unpitted sample. Thus it is important to understand the effect of a single pit on fatigue life.

Surface flaws resulting from corrosion or other types of surface damage induce plastic deformation even under a moderate level of applied stress due to high stress concentration. The fatigue crack emanating from a surface flaw grows, in general, with a higher growth rate than that of a flawless surface. However, according to experimental observations [6], crack growth is retarded, while the crack tip lies in the notch plastic zone. The commonly-used linear fracture mechanics (LEFM) fails to predict this phenomenon presumably because of the formation of a relatively large plastic yielding zone that in fact violates the small-yielding assumption of LEFM. When a small fatigue crack initiates from a notch, two opposite effects work together: the notch effect, which raises the level of driving stress for crack extension, and the effect of plasticity-induced compressive stress that tends to close the crack. The compressive stress due to unrestored plastic deformation and crack closure is known to be responsible for the growth retardation of small cracks emanating from the notch. To account for the effects of crack closure on the fatigue crack growth rate, the effective stress intensity factor range is used in Paris' law for fatigue life prediction [7,8]. Therefore, the determination of crack closure (opening) stresses becomes very important. For this reason numerous techniques have been developed for the measurement of crack closure to date [9].

Most of the previous works on ultrasonic characterization of surface breaking cracks have been concerned with a crack on a flawless surface or an artificial saw-cut as a simulated crack. However, actual cracks often initiate from surface flaws (foreign object impact damage, corrosion pit, etc.). The additional interaction of scattered waves with the surface flaw complicates crack detection and prevents an immediate application of existing methods for small crack evaluation. Also, these surface flaws serve as stress risers and, as discussed above, lead to plasticity-induced crack closure, which can affect the crack detectability. The adverse effect of crack closure on nondestructive detection of fatigue cracks has been recognized in the past. When a fatigue crack is under compressive stress it may be tightly closed and may be undetectable by non-destructive means.

The objective of this work is to develop a systematic experimental/model-based method to predict the remaining fatigue life of a sample with corrosion damage. To this end, nondestructive techniques to measure parameters of the existing damage and a fatigue life prediction model are developed. The damage parameters such as pit depth/diameter, crack depth and crack closure stresses are obtained from the measured surface wave reflection signals. The model utilizes these parameters as input for predicting the remaining fatigue life.

An experimental ultrasonic method is developed for in situ monitoring of fatigue crack initiation and measuring crack opening/closure stress with data acquired during fatigue cycling as a function of cycling load. The method is demonstrated for two widely used aerospace materials: Al 2024-T3 alloy and Ni-base superalloy (Inconel 718). A small artificial pit is produced to simulate the surface flaws caused by the pitting corrosion or the foreign object impact damages. The microradiographic and ultrasonic methods for pit depth measurement are presented. Surface acoustic wave reflections from the crack have been obtained as functions of fatigue load and number of cycles and from them the crack opening/closure loads have been determined.

A model for surface acoustic wave scattering from cracks initiated from a surface pit is developed. It makes use of a stress intensity factor calculated using an approximate fracture mechanics model for a pit with a corner crack. Pit depths and diameters are determined by analyzing the ultrasonic reflection signals. Calculated time domain reflection signals and spectra are compared with experimental results. The depths of the fully and partially open cracks are determined.

Fatigue experiments and analysis for the fatigue crack initiation and propagation from a single artificial pit in Al 2024-T3 alloy are described to investigate the effect of pit depth on fatigue life. To predict the remaining fatigue life of the sample using measured damage parameters a fracture-mechanical model is developed.

## 5.2 Background

Due to the lack of understanding of the interaction between defects and electrochemical reactions on pitting [4], the effect of pitting on fatigue is not yet well understood. Several authors have studied the effect of microstructural defects on fatigue life [10–12]. Nakajima and Tokaji [13] have found that a crack emanates from a pit during simultaneous corrosion fatigue only if the pit grows to such a level that the stress-intensity factor reaches a certain threshold value. Becker et al. [14] reported the effect of pitting corrosion on fatigue and fracture behavior of 13% Cr stainless steel. Chen et al. [4] also studied interactive effects of corrosion fatigue. To account for the pit effect on crack nucleation and propagation in a rivet hole they used an elliptical surface crack model accounting for a circular hole stress concentration. The problem is complicated by different fatigue behaviors of short and long cracks. Phillips and Newman [15] demonstrated that the fracture mechanics of long crack fatigue growth in Al 2024-T3 alloy leads to substantial exaggeration of fatigue life for very small initial flaw sizes. They established the importance of short crack analysis and experimentally found Paris power law constants for short and long crack growth in Al 2024-T3 alloy.

Numerous techniques have been developed for the measurement of crack closure stress [9], including the thickness-averaging compliance method [16], potential drop [17] and laser interferometry [18]. The ultrasonic bulk wave [19] and surface acoustic wave [20–24] methods have also been used for this purpose. Recently, Rokhlin and Kim [24] determined opening (closure) stresses of a crack initiated in the pit-induced plastic yielding zone by means of surface acoustic waves.

The ultrasonic surface wave method can be a valuable technique, especially for measuring surface and sub-surface cracks. Resch and Nelson [20] and Yuce et al. [21] demonstrated the feasibility of ultrasonic surface wave measurements of the depth of small fatigue cracks and crack opening load. Tittman and Buck [22] performed experiments to determine size and closure loads of a surface fatigue crack in a titanium alloy. Tien et al. [23] studied the effect of indentation-induced residual stress on crack extension by comparing results for heat-treated and as-indented samples. Rokhlin and Kim [25] performed ultrasonic surface wave experiments for monitoring surface fatigue crack initiation and growth from a surface flaw and also investigated opening/closure behaviors. Also, they developed a model for surface wave scattering from corner cracks initiated from a pit and determined the depths of the cracks [26].

## 5.3 Instrumentation and Methods

### 5.3.1 Experiments

#### Fatigue Tests

Materials used in our fatigue experiments were Al 2024-T3 alloy and Ni-base superalloy (Inconel 718). The thickness of the Al 2024-T3 alloy fatigue sample was 1.6 mm, yield stress ( $\sigma_y$ ) 340 MPa, ultimate tensile stress ( $\sigma_u$ ) 483 MPa, and elongation 17.5%. The Ni-base superalloy fatigue sample was 1.97 mm thick, the yield stress 1100 MPa, ultimate tensile stress 1310 MPa and elongation 17.0%. The specimens were machined according to the ASTM standard (ASTM E-466-96). Controlled-size small pits with depths in the range from 30  $\mu\text{m}$  to through-the-thickness and diameter 250  $\mu\text{m}$  were produced by an electrical discharge machine (EDM) in the center of the surface. Also, samples having pits with 250  $\mu\text{m}$  depth were used for *in situ* ultrasonic fatigue crack measurement while samples having pits with 250–970  $\mu\text{m}$  depth were used for ultrasonic pit depth measurements.

Fatigue tests were carried out on the servo-hydraulic MTS (mechanical testing system) in the load-controlled mode with the following parameters: the frequency of cyclic loading=15 Hz, the maximum stress level=76 % of the yield stress, stress ratio  $R=0.1$  and 0.2 (for the fatigue life test) and the stress range  $\Delta\sigma=206$  MPa (for the fatigue life test) and 231 MPa. The stress ratios were selected to avoid thin specimens undergoing compressive stresses. The high stress from stress concentration leads to the development of a plastic zone around the pit. Considering that the onset of the long crack regime for this material is about 650  $\mu\text{m}$  [5], the measurements performed in this study are during and immediately after the short-crack regime of the fatigue life cycle. Post-fracture surfaces were examined with SEM fractographs and actual sizes of crack and pit were measured.

The fatigue crack growth rate was determined for specimens with a central pit of nominal depth 170  $\mu\text{m}$  and diameter 240  $\mu\text{m}$ . After a predetermined number of fatigue cycles the test was stopped, the load was released to zero and then a monotonic tensile load was applied until failure under displacement control at a rate of 0.22  $\mu\text{m}$  per second. The fracture surfaces of the broken samples were examined to measure the fatigue crack dimensions using an optical microscope with a fillar (graded) lens and the SEM. Overall 10 specimens were tested to determine the fatigue crack growth rate for samples with different pit depths, which was compared with the model prediction using the Paris law. The objective of these experiments was to understand the effects of a pit on the fatigue life and to verify the fatigue life prediction model presented in the next section. The microradiographic technique described in [27] is also used to determine depths of pit and crack.

### In Situ Ultrasonic Measurement

In order to monitor crack initiation and propagation during the fatigue cycle, ultrasonic surface wave reflections from the pit and the crack were measured. A commercial wide band longitudinal wave transducer with center frequency 5 MHz was assembled on the specially designed polystyrene wedge and used for generating and receiving the surface wave signals as shown in Fig. 1. The shape of the wedge was designed to increase the signal-to-noise ratio by eliminating multiple ultrasonic reflections. For an in situ measurement, the transducer assembly is attached on the sample undergoing the fatigue test so that the ultrasonic signals are collected during fatigue cycling and at different load levels. The experimental system includes ultrasonic pulser/receiver, digital oscilloscope, control computer for MTS and ultrasonic data collection. At a predetermined number of cycles, the computer controlled fatigue load was changed to a step-up (10 steps) load (Fig. 1b) with recording of ultrasonic reflections at each step-load level. At each load level, the ultrasonic measurements were repeated with a 2 kHz rate and the reflected signals were averaged in time using the digital oscilloscope to suppress random noise and then fed to the computer in digital form.

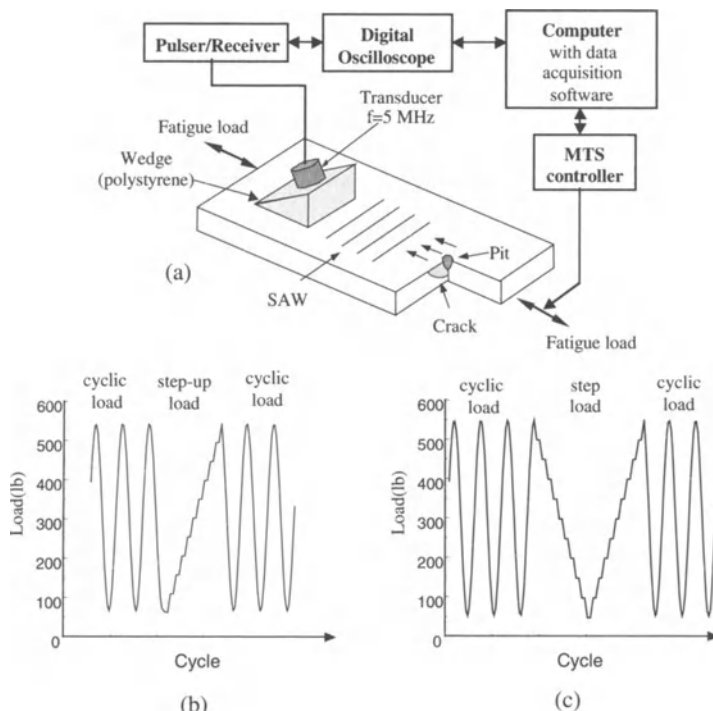


**Fig. 1.** Surface acoustic wave monitoring of a crack initiated from a pit. (a) Experimental setup; (b) and (c) Load profiles to perform in situ ultrasonic measurements during fatigue test [26]

### 5.3.2 Fatigue Crack Growth Analysis

#### **Paris Law**

Crack growth during fatigue life can be described by the well-known Paris law

$$\frac{da}{dN} = C [\Delta K(a)]^m, \quad (1)$$

where  $a$  is the crack length,  $N$  is the number of cycles,  $\Delta K$  is the range of the stress-intensity factor for the cyclic loading, and  $C$  and  $m$  are the material constants for the crack growth rate. For the Al 2024-T3 alloy and the fatigue parameters selected in the present study the Paris constants  $C$  and  $m$  of were taken to be  $1.86 \times 10^{-11}$  and 4.06 for the long crack [28] and  $1.092 \times 10^{-9}$  and 1.55 for the short crack based on the experimental results of Phillips and Newman [5]. The stress-intensity factors for the crack configurations considered in this study are analyzed in the following sections. The number of cycles required for an initial crack size  $a_i$  to grow to a final size  $a_f$  is determined by integrating (1)

$$N = \int_{a_i}^{a_f} \frac{da}{C [\Delta K(a)]^m}. \quad (2)$$

#### **Crack Growth Stages**

Fractographic images in Fig. 2 show that the fatigue cracks initiate at the edges of the pit with the highest stress concentration to form two corner cracks. These cracks grow [5] separately on both sides of the pit, with shapes approximately a quarter circle, until their depth reaches that of the pit as shown in Figs. 2a and b. As these cracks grow further beyond the root of the pit, they combine into a single semi-elliptical crack whose initial aspect ratio ( $a/2c$ ) is dependent on the ratio of depth to diameter of the pit. The period to this time we define as the first stage of the fatigue life and the remaining period to sample failure as the second stage. For the deep pit ( $d > 2R$ ), the initial crack of the second stage is almost semicircular ( $a/2c = 0.5$ ). For the shallow pit ( $d < 2R$ ), the initial crack has a long elliptical shape whose aspect ratio is much smaller than 0.5. First it grows to a semicircular shape and then further in the second stage, the initial shape of the crack changes gradually into a final semielliptical shape as shown in Fig. 2c. Therefore, the entire fatigue life can be divided into two different main stages with cracks of different geometry. Accordingly, the stress-intensity factors for a crack growing from a pit can be approximated with different models for each stage.

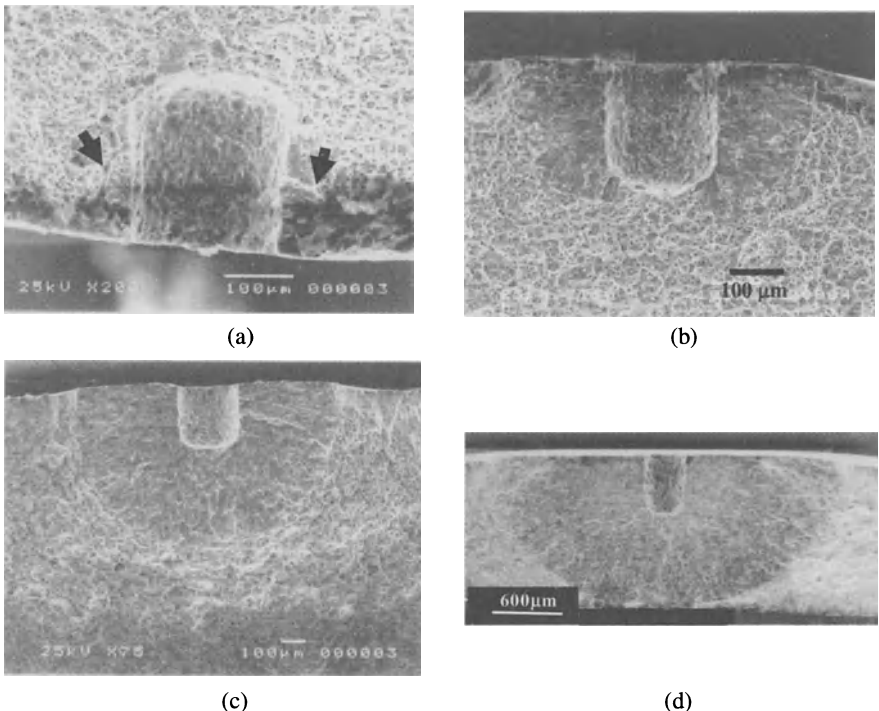


**Fig. 2.** Fractography of Al-2024-T3 fatigue samples [5] (a) At 25,000 cycles, fatigue crack just initiated near the sample surface. Cracks about 42  $\mu\text{m}$  and 54  $\mu\text{m}$  width are indicated on two sides of the pit; (b) At 65,000 cycles, the crack reached the depth of the pit; (c) At 104,000 cycles, the crack forms a single semicircular crack; (d) The crack initiated from the pit with depth 570 mm. At 140,000 cycles, the crack depth is near the plate thickness

### The First Stage

**(A) Corner Crack Model:** To approximate the problem, we first carried out a finite element analysis (FEA) to simulate the stress distribution around pits with different depths. The FEA results showed that the stress concentration factors at the edges do not change significantly from that of the through-thickness hole. Based on this analysis, crack growth during the first stage is modeled as the corner crack growth (Fig. 3a) at the edges of the through-thickness hole in a plate. The thickness of the plate is assumed to be equal to the pit depth as shown in Fig. 3. The stress-intensity factor for the corner crack at the through-thickness hole has been analyzed by Raju and Newman [29] using the finite element method. For a remote tensile stress ( $\sigma$ ), the stress-intensity factor at any point along the tip of the corner crack in a finite thickness plate is represented as

$$K_1 = \sigma \sqrt{\frac{\pi a}{Q}} F_c \left( \frac{a}{h}, \frac{R}{h}, \theta \right), \quad (3)$$

where  $Q$  is the shape factor of the crack on the circular hole. The boundary correction factor  $F_c$  is a function of crack depth  $a$ , hole radius  $R$ , plate thickness  $h$ , and the angle  $\theta$  on the crack edge as shown in Fig. 3b. To account for the finite width of the sample ( $2b$ ), we use the standard correction factor [30],

$$f_b = \sqrt{\sec(\pi c / 2b)}. \quad (4)$$

The effect of crack closure on fatigue life is accounted for by the correction factor for Al 2024-T3 alloy [31]

$$f_c = 0.5 + 0.4R_s \quad (5)$$

where  $R_s$  is the  $R$  ratio of fatigue load. Therefore, the resulting stress-intensity factor range is

$$\Delta K_1 = \Delta\sigma \sqrt{\frac{\pi a}{Q}} F_c f_b f_c. \quad (6)$$

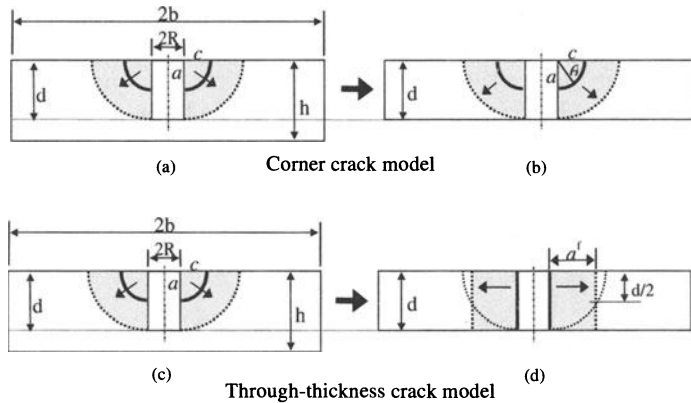
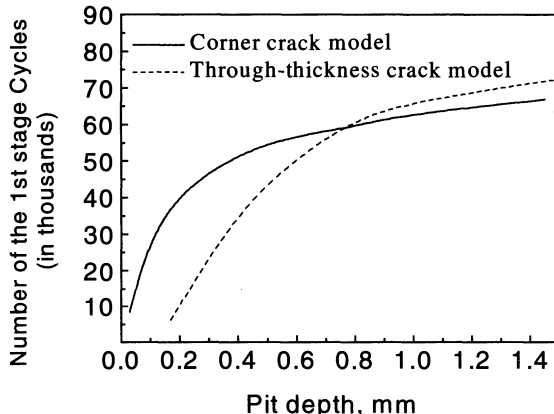
**(B) Equivalent Through-Thickness Crack Model:** The corner crack model, described in the previous section, requires considering the detailed geometric configuration of the pit and the two growing cracks, and depends on many parameters. Since crack growth is significantly affected by the stress riser (pit), one may simplify the actual shape of the crack and consider a simplified model for the crack growth in the first stage. As in the corner crack model we consider a plate having thickness equal to the pit depth and a through-thickness crack emanating from the through-thickness hole, serving as an equivalent stress concentrator in the plate. During this stage, the effective crack length changes from the radius of the pit  $R$  to the final crack size  $a_f^*$  as shown in Fig. 3d. The effective crack length  $a^*$  is less than the actual crack radius  $a$  and is determined as an equivalent through-thickness crack with depth equal to that of the quarter-circular crack at half of the pit depth:  $a_f^* = 0.866d$  [5]. The stress-intensity factor for this geometry has been analyzed by Newman [32] and expressed as

$$K_1 = \sigma \sqrt{\pi a^*} F_t \left( \frac{a^*}{R + a^*} \right), \quad (7)$$

where  $F_t$  denotes the boundary correction factor [32, 33]. Taking into account the effects of the finite sample width and crack closure ((4) and (5)), the stress-intensity factor range is given by

$$\Delta K_1 = \Delta\sigma \sqrt{\pi a^*} F_t f_b f_c \quad (8)$$

In Fig. 4, the number of fatigue cycles of the first stage versus pit depth predicted by the corner crack model and the through-thickness crack model are compared. It is noted that the result of the through-thickness crack model shows good agreement with that of the corner crack model except for shallow pits.

**Fig. 3.** Crack propagation models for the first stage [5]**Fig. 4.** Comparison of number of cycles predicted by two crack growth models for the 1st stage [5]

### The Second Stage

In the second stage, since the crack tip is away from the pit, the effect of the pit on the crack growth rate may be neglected. Thus, the crack with pit is approximated with a surface-breaking crack on a flawless flat surface as shown in Fig. 5. The stress-intensity factor for the surface crack can be expressed as [34]

$$K_2 = \sigma \sqrt{\pi} \frac{a}{Q} F_s \left( \frac{a}{h}, \frac{a}{c}, \frac{c}{b}, \theta \right), \quad (9)$$

where  $c$  is surface crack length and  $F_s$  is the boundary correction factor. Newman and Raju [34] provided an interpolation formula for the boundary correction factor. The stress-intensity factor range for the second stage is

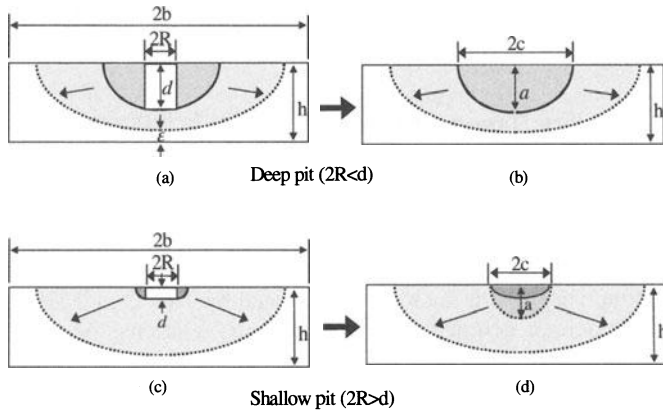


**Fig. 5.** Crack propagation model for the second stage [5]

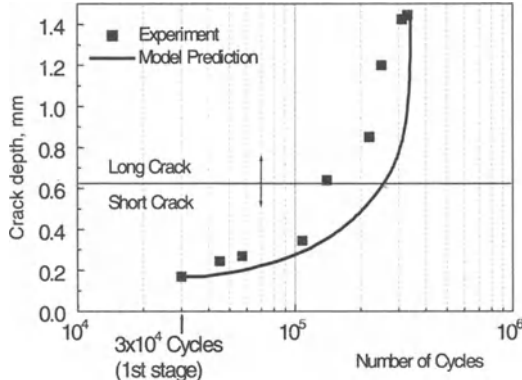


**Fig. 6.** Growth of crack in the 2nd stage. Comparison of experimental data with prediction of surface crack model for samples having pits with average depth 170  $\mu\text{m}$  and diameter 240  $\mu\text{m}$  [5]

$$\Delta K_2 = \Delta \sigma \sqrt{\frac{\pi a}{Q}} F_s f_b f_c . \quad (10)$$

In Fig. 6, the model prediction is compared with the experimental data for the sample with a pit of 170  $\mu\text{m}$  average depth and 240  $\mu\text{m}$  average diameter. The change of crack aspect ratio ( $a/2c$ ) is considered in numerical calculation [5]. The number of cycles of the first stage is taken into account by adding the experimentally determined nominal number of cycles of the first stage,  $3 \times 10^4$ . The model prediction shows reasonable agreement with the experimental data.

For a crack initiated from a shallow pit ( $d < 2R$ ), the initial elliptical crack with depth  $d$  is assumed to be a semicircular shape crack ( $a=c$ ), and then the semicircular crack grows into a final elliptical one (Fig. 5d).

### 5.3.3 Analysis of Surface Wave Scattering for Crack Sizing

#### **Scattering Theory Based on the Reciprocity Principle**

In this section, we develop a scattering model to determine ultrasonically the depth of a small fatigue crack. The crack size to be considered is up to the depth of the pit ( $\sim 250 \mu\text{m}$ ). As discussed in the previous section, the size of the crack considered in this paper is short in the context of fatigue.

The low frequency scattering theory described by Tien et al. [23] is extended to consider the pit/crack geometry. The reciprocity relations for the elastic wave scattering from a flaw derived by Kino [35] and Auld [36] are applied. Assuming that there is no acoustic source within the volume of interest, the following two states are considered. In state (I) the system is excited by the incident power from a transducer, while another transducer receives the response of the system containing the flaw. In state (II) transducers are placed at the same positions as in state (I) but the flaw is absent and the system is excited by the same amount of incident power from the second transducer, while the first transducer acts as the receiver. When the second transducer is identical to the first, according to the reciprocity relation [36] the normalized backscattering output in the receiver is

$$R_{11}(\omega) = \frac{i\omega}{4P} \int_S (u_i^{(I)} \sigma_{ij}^{(II)} - u_j^{(II)} \sigma_{ij}^{(I)}) n_j dS, \quad (11)$$

where  $\omega$  is the angular frequency,  $S$  is the surface of the flaw,  $u_i^{(I)}$  and  $\sigma_{ij}^{(I)}$  are the displacement and stress fields in state (I),  $u_j^{(II)}$  and  $\sigma_{ij}^{(II)}$  are those in state (II),  $n_j$  means the inward normal vector of the flaw surface and  $P$  is the input power to the transmitting transducer. If the internal surface of the flaw is free, that is,  $\sigma_{ij}^{(I)} = 0$ , (11) becomes

$$R_{11}(\omega) = \frac{i\omega}{4P} \int_S u_i^{(I)} \sigma_{ij}^{(II)} n_j dS. \quad (12)$$

Consider corner cracks developed at the two sides of the pit as shown in Fig. 7 and the surface wave normally incident on the crack surface. The normalized backscattering output defined above can be separated into two terms: those with integration over the pit surface ( $S_p$ ) and over the crack surface ( $S_c = S_c^+ + S_c^-$ )

$$\begin{aligned} R_{11}(\omega) &= \frac{i\omega}{4P} \int_{S_p} u_i^{(I)} \sigma_{ij}^{(II)} n_j dS + \frac{i\omega}{4P} \int_{S_c} u_i^{(I)} \sigma_{ij}^{(II)} n_j dS, \\ &= R_{11}^p(\omega) + R_{11}^c(\omega) \end{aligned} \quad (13)$$

where  $S_c^+$  and  $S_c^-$  are the front and back surfaces of the crack. This separation is exact and corresponds physically to the separation of the reflection field into two parts: one mainly from the pit and the second from the crack.

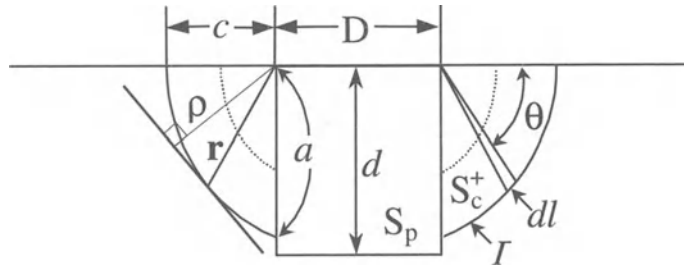


**Fig. 7.** Geometry of a pit with corner cracks

Since the stress  $\sigma_{ij}^{(II)}$  is continuous across the crack faces, the second integral in (13) can be expressed as an integral over only the front face

$$R_{11}^c(\omega) = \frac{i\omega}{4P} \int_{S_c} u_i^{(I)} \sigma_{ij}^{(II)} n_j dS = \frac{i\omega}{4P} \int_{S_c^+} \Delta u_i^{(I)} \sigma_{ij}^{(II)} n_j dS, \quad (14)$$

where  $\Delta u_i^{(I)}$  is the displacement jump across the crack. Accounting for only the normal stress  $\sigma_{zz}$  of the incident wave, which is dominant at shallow depths, the normalized backscattering output from the crack is approximated as

$$R_{11}^c(\omega) = \frac{i\omega}{4P} \int_{S_c^+} \Delta u_z^{(I)} \sigma_{zz}^{(II)} dS. \quad (15)$$

Using the results of Budiansky and O'Connell [37], the crack backscattering output can be represented as a contour integral along the crack tip ( $\Gamma$ )

$$R_{11}^c(\omega) = \frac{i\omega(1-\nu^2)}{3EP} \int_{\Gamma} \rho(\mathbf{r}) K_I^2 dl \quad (16)$$

where  $\nu$  is Poisson's ratio,  $E$  is Young's modulus,  $K_I$  is the mode-I stress intensity factor of the corner crack,  $\rho(\mathbf{r})$  is the perpendicular distance from the coordinate origin to the tangential line to the crack tip  $\Gamma$  at the given point  $\mathbf{r}$  and  $dl$  is the line element on  $\Gamma$  as shown in Fig. 7. Therefore, the normalized backscattering coefficient from the crack can be calculated using (16) if the stress intensity factor for the crack emanating from the pit is known.

The time domain reflection signal is represented using (14) [26],

$$r(t, a) = \int_{-\infty}^{\infty} [R_{11}^p(\omega) + R_{11}^c(\omega)] V_i(\omega) e^{i\omega t} d\omega, \quad (17)$$

where  $V_i(\omega)$  is the frequency characteristic of the measurement system.

### **Calculation of Crack Reflection**

In our experiments, ultrasonic measurements are performed at  $f h = 8$  MHz-mm, where  $f$  is frequency and  $h$  sample thickness. At the Rayleigh incident angle, both the lowest order symmetric ( $S_0$ ) and antisymmetric ( $A_0$ ) Lamb waves are excited with approximately equal amplitudes and phases (see, for example, Viktorov [38]). Since the stress field of the  $S_0$  mode is symmetrical with respect to the median plane, whereas that of the  $A_0$  mode is antisymmetrical, the stresses below the median plane are cancelled resulting in a stress distribution very similar to that of a pure Rayleigh wave [38], and the incident stress field can be approximated by that of the pure Rayleigh wave.

To calculate the backscattering coefficient  $R_{11}^c$  in the low frequency approximation the static stress intensity factor due to the stress generated by the incident surface wave is utilized. To obtain the stress intensity factor for this complicated geometry (Fig. 7) we approximate the stress ( $\sigma_{zz}$ ) of the incident surface wave as a bending stress in a plate with effective thickness  $h^*$  [23]. Considering that the SAW stress  $\sigma_{zz}$  changes its sign for aluminum at the depth  $x/\lambda_k \approx 0.225$  [38], we take  $h^* = 0.45\lambda_k$  and the bending stress dependence as  $\sigma_{zz} = \sigma_0(1 - 2x/h^*)$ , where  $\sigma_0$  is the stress at the surface of the plate. In our experiment the ratio of pit depth  $d$  to the effective thickness  $h^*$  is  $d/h^* \approx 1$ . To calculate the stress intensity factor, we consider the  $h^*$  thick plate with a through-thickness hole as shown in Fig. 8. Note that this approximation is similar to that presented in Section 6.3.2 for fatigue crack initiation from the pit.

The mode I stress intensity factor for symmetric corner cracks at a through-thickness hole in a plate subject to bending has been calculated numerically by Raju and Newman [29].

$$K_I = \sigma_0 \sqrt{\frac{\pi a}{Q}} F_b \left( \frac{a}{h^*}, \frac{a}{c}, \frac{D}{h^*}, \theta \right), \quad (18)$$

where  $a$  is crack depth,  $c$  is surface crack length,  $D$  is hole diameter, and  $Q$  is the shape factor of the crack. The boundary correction factor  $F_b$  is a function of the crack-and-hole geometries and the angle  $\theta$  shown in Fig. 9. Raju and Newman [29] calculated the boundary correction factors for various combinations of geometric parameters. We use their data to calculate interpolated curves for the stress intensity factor of different crack configurations. Fig. 9 shows the boundary correction factor as a function of the angle  $\theta$ . Note the stress intensity factor is always highest at  $\theta=0^\circ$  for different crack sizes and aspect ratios shown.

To calculate the backscattering output of the crack using the stress intensity factor, one should first know the shape of the crack. From the SEM pictures of fracture surfaces for samples broken in tension at different fatigue cycles, it is found that the crack aspect ratio changes in the range of 0.6–1.65 [5] as the crack grows (see Fig. 2).

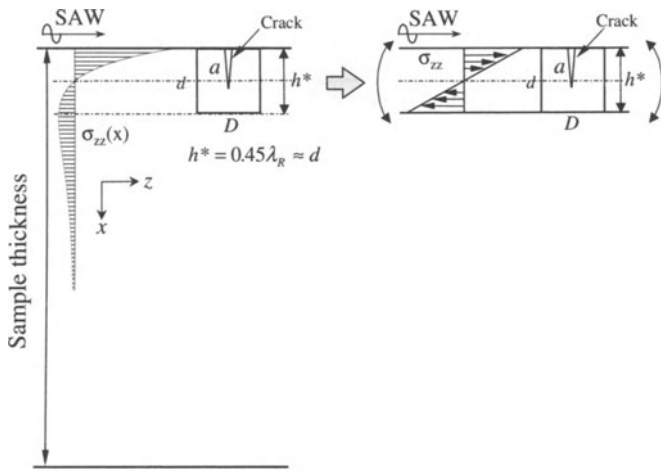


**Fig. 8.** Effective plate thickness for calculating the stress intensity factor of two corner cracks [26]

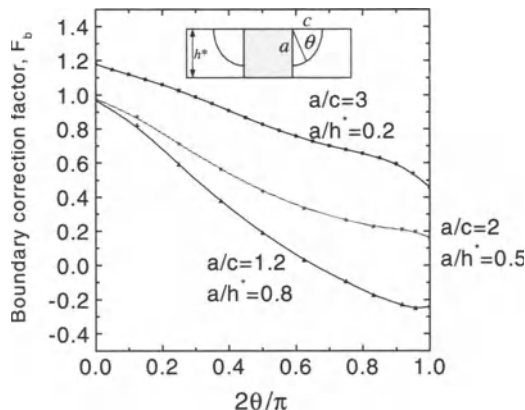


**Fig. 9.** Boundary correction factor versus angle  $\theta$ . Curves in this form are used for calculating normalized backscattering coefficient [26]

From (16) and (18) the normalized backscattering output is expressed as the line integral of the boundary correction factor along the front of the two corner cracks,

$$R_{11}^c(\omega) = \frac{i\omega(1-\nu^2)\pi a \eta_T}{3EQ} \int_{\Gamma} \rho(\mathbf{r}) F_b^2 \left( \frac{a}{h^*}, \theta \right) dl , \quad (19)$$

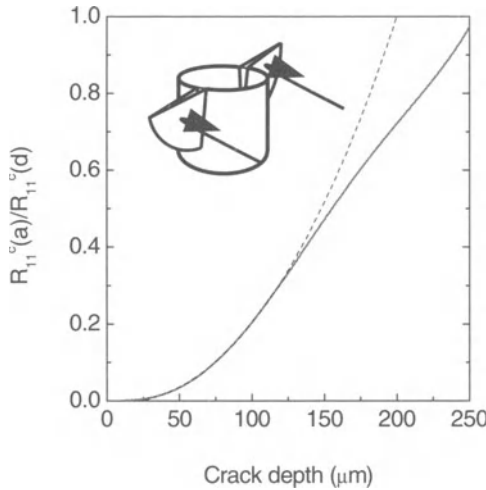


**Fig. 10.** Reflection from two corner cracks emanating from a cylindrical pit. Normalization is done with reflection from the crack whose depth is equal to the pit depth. Dashed line is the long wavelength approximation ( $R_{11}^c \sim a^3$ )

where  $\eta_r = \sigma_o^2 / P$  is the factor related to the electromechanical efficiency of the transducer [20]. The line integral is calculated numerically as a function of the crack size with a known boundary correction factor and with the geometric parameters presented above. The normalized crack backscattering coefficient ( $R_{11}^c(a) / R_{11}^c(d)$ ) is shown in Fig. 10, where  $R_{11}^c(d)$  is the backscattering coefficient at the crack depth equal to the pit depth ( $a=d$ ). For small cracks, the reflection amplitude depends on the third power of crack depth  $R_{11}^c \sim a^3$  (dashed line in Fig. 10), which is common to long wavelength scattering [23].

### Determination of Pit Backscattering

The backscattering coefficient  $R_{11}^p(\omega)$  in (14) corresponds physically to the wave reflection from the pit front surface and the contribution from the corner creeping wave propagating around the front half of the pit (see Fig. 11). Although this creeping wave is not fully investigated in the present work, we suspect it is associated with a wave propagating on the 90° pit corner in the form of a corner wave [39, 40]. Due to the cylindrical curvature of the edge the corner wave is coupled with the surface wave. This creeping wave is excited by the surface wave incident at the pit/crack corners. The effect of the corner creeping wave on the reflection from a pit with crack has been analyzed and it was understood from the time domain signals that the cracks shield the creeping wave traveling around the

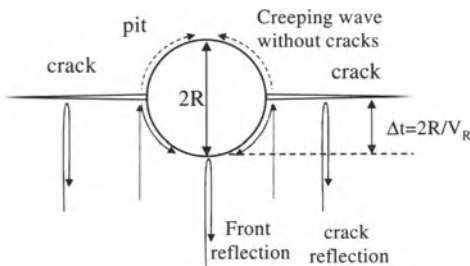


**Fig. 11.** Creeping wave shielded by cracks. Difference of path lengths for signals reflected from pit front and crack surfaces

pit and diminishing its effect. For this reason we neglect the creeping wave contribution to the pit backscattering output  $R_{11}^p(\omega)$  and use the pit front backscattering amplitude measured prior to fatigue (the pit without fatigue crack). Thus, considering only the pit front reflection, the time domain pit reflected signal is

$$\int_{-\infty}^{\infty} R_{11}^p(\omega) V_i(\omega) e^{i\omega t} d\omega \approx r(t, a = 0), \quad (20)$$

where  $R_{11}^p(\omega)$  is the experimental spectrum of the reflection signal in Gate-1 [26]. The total reflected signal is calculated as

$$r(t, a) = r(t, a = 0) + \int_{-\infty}^{\infty} R_{11}^c(\omega) V_i(\omega) e^{i\omega(t - D/V_R)} d\omega. \quad (21)$$

## 5.4 Applications

### 5.4.1 Pit Size Measurements

#### *Microradiographic Measurement*

The microradiographic measurement of pit size was performed as described in Chapter 3 [27] of this book. The calibration curves for pit depth measurements were produced using samples with artificial pits and film microfocal radiography with projective magnifications of 10 and 40X. The radiographs were digitized using a TV camera and a PC frame grabber for further analysis. As an example, Fig. 12 shows the digitized images with 40X projection magnification.

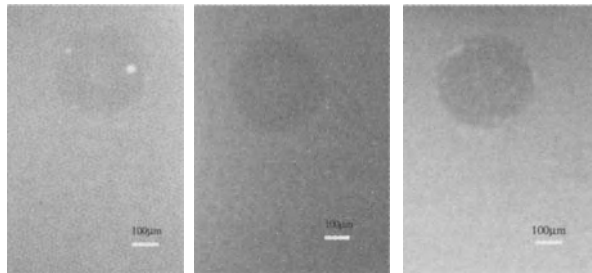


**Fig. 12.** Examples of digitized radiographs of artificial pits in 1.6 mm thick 2024T3 Al samples with (a) 50  $\mu\text{m}$ , (b) 100  $\mu\text{m}$  and (c) 150  $\mu\text{m}$  depths. The projection magnification is 40X

The images obtained from the artificial pits with known depths are used to set a reference curve for finding the unknown depth of pitting in the aluminum specimens. Two methods are used for this purpose, the densitometer and histogram methods. The densitometry method is based on finding the difference between the direct reading of the optical density on the image of the pit and the optical density of the adjacent area of the base metal with a densitometer. After projection magnification, it is possible to use a direct densitometer reading in the pit images when the pit image size is larger than the optical beam size of the densitometer. One can obtain the change in film density  $\Delta D$  for a pit with depth  $d$  as

$$\Delta D = D_p - D_b = 0.43G\mu d, \quad (22)$$

where  $\mu$  is linear radiographic attenuation,  $G$  is the gradient of the film characteristic film,  $D_p$  is the optical density of images for different pits, and  $D_b$  is the optical density of the base metal. For images of pits, which are smaller than the densitometer beam size, the calibrated density strip is used, and the gray level of the pitting is compared with that of the strip by eye. The second method is based on finding the mean values of the gray level distribution (histograms) of the digitized images in the pit area and comparing to the histogram of the adjoining base metal area of the radiograph. The histogram is taken from the image of the pit avoiding the lighter spots (Fig. 12) which are micro-inclusions produced during the spark erosion process.

### ***Ultrasonic Measurements***

In this section, we show that the surface pit can be sized by analyzing reflected ultrasonic signals. A typical reflected ultrasonic signal from a pit is shown in Fig. 13. The surface acoustic wave reflection from a pit is composed of waves reflecting from different corners of the pit, followed by the plate bottom reflections of a mode-converted shear wave. The first group consists of the specular reflection from the front of the pit (1), the corner creeping wave on the edge of the pit (2) and the reflection signal going down around the pit and reflected from the pit opposite corner (3). The second signal is the bottom

reflection (4) of the shear wave that is mode-converted at the bottom of the pit (and the crack tip when a crack exists). This signal is separated from the pit reflected signals in the time domain.

Although the signals in the first group are not well separated, the time delay between the signals can be calculated from the frequency spectrum of the gated signal [26]. From the time delays, the diameter and depth of the pit are estimated. In Fig. 14, the pit size determined from the spectrum of reflection signals is compared with those measured from fractographs taken by SEM for different pit depths. The result shows an acceptable accuracy of the present ultrasonic measurement using a 5 MHz transducer for determining the size of the pits. The ultrasonic signature was repeatable for different samples.

The mode-converted shear wave ((4) in Fig. 13) is launched on the bottom of the pit and propagates down toward the bottom of the plate where it is reflected, mode-converted back to the surface wave at the bottom of the pit, and returned to and received by the surface wave transducer. One can get the depth of the surface discontinuity by analyzing the time delay and amplitude of the bottom reflection signal. As one can see in Fig. 13b, the plate bottom reflection signal is narrower and better defined than that of the pit reflection. As will be shown next, the bottom reflection provides useful information on fatigue crack depth and crack closure behavior.

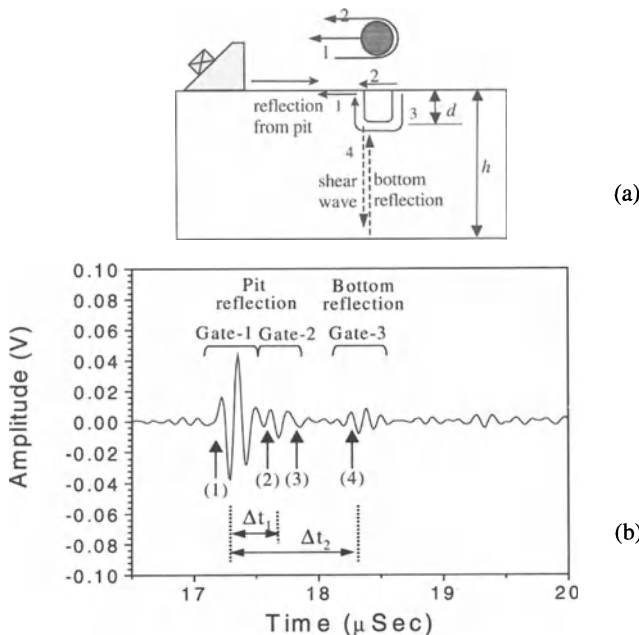


**Fig. 13.** Reflection surface wave signal from a pit with 280  $\mu\text{m}$  diameter and 230  $\mu\text{m}$  depth [26] (a) Different paths of reflected waves; (b) Reflections from different corners are marked. The gates for determining time delays are shown

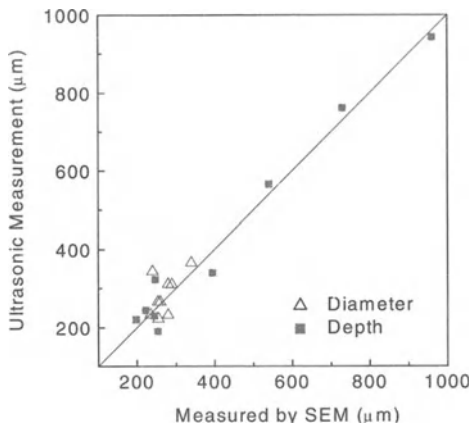


**Fig. 14.** Comparison of pit dimensions measured from SEM microfractographs and calculated from ultrasonic signatures [26]

#### 5.4.2 Ultrasonic Sizing of Crack Initiated from a Pit

##### **Reflection of Surface Wave from Surface Pit with Crack in Al 2024-T3 and Ni-Base Superalloy Samples**

As an example, Fig. 15 shows surface wave reflection signals taken for two load levels (100 lbs on the left (a) and 400 lbs on the right (b)) at different fatigue cycles for the Al 2024-T3 sample. The depth and diameter of the pit were 252  $\mu\text{m}$  and 246  $\mu\text{m}$ , respectively. The fatigue life was 142,856 cycles. As a result of the crack initiation and growth during the fatigue test the amplitudes of both the first ( $A^{(1)}$ ) and plate bottom ( $A^{(2)}$ ) reflections change continuously. It is interesting to compare the signals (Fig. 15a, b) taken from the same sample at the same number of cycles but only under different load levels. While the reflection signal recorded at the load level 400 lb changes significantly as the number of cycle increases, no change is observed until 52% of the fatigue life when the signal is recorded at 100 lb load.

Figure 16 shows peak-to-peak amplitudes of the first and plate bottom reflections normalized by those before the fatigue test ( $A_o^{(1)}$  and  $A_o^{(2)}$  in Fig. 15) at different levels of fatigue cyclic load as a function of number of fatigue cycles. It is noted that the first reflection has minima near the number of cycles 60,000 and 130,000 as marked in Fig. 16a whereas the second reflection shows a monotonic increase. Since the crack emanates approximately in the mid-plane of the pit as shown in Fig. 11, the path difference ( $2R$ ) of reflected waves from the pit front and crack surface is about half of the surface wave wavelength ( $\lambda_R$ ) at

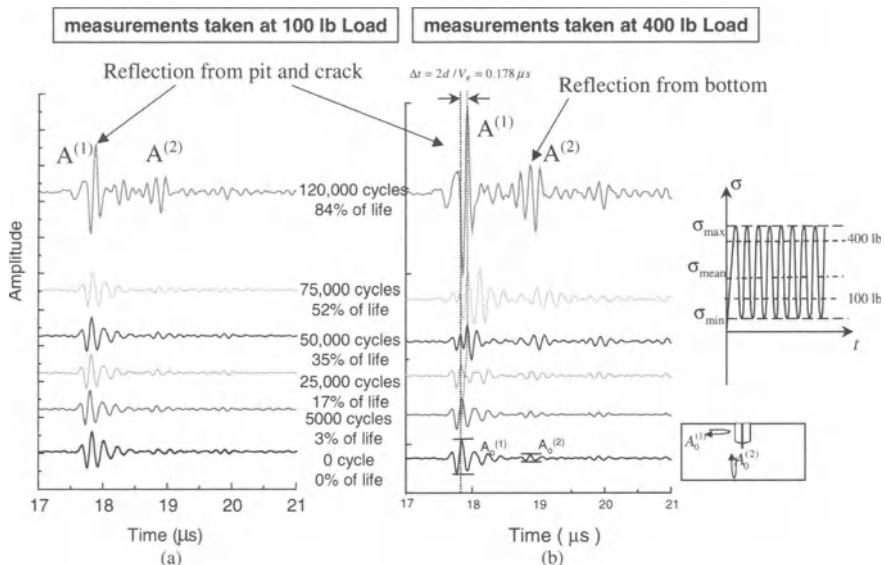


**Fig. 15.** Change of reflection signal at different fatigue cycles at two different loads (a) 100 lb, (b) 400 lb during fatigue test for an Al 2024-T3 sample. The fatigue life of the sample is 142,856 cycles

5 MHz:  $2R/\lambda_R \approx 0.5$ . Hence, the interference of reflected waves from pit front and crack surfaces becomes destructive resulting in decrease of the first reflection amplitude. The first reflection starts to decrease at around 20,000 cycles and has minimum at 60,000 cycles as marked in Fig. 16a. This effect is also observed in the time signals for the number of cycles higher than 25,000 as shown in Fig. 15b.

As the crack grows further, the reflection from the crack eventually becomes dominant in forming a reflection signal and thus the peak amplitude of the reflection signal shifts by  $\Delta t = 0.178 \mu\text{sec}$ , which corresponds to the time for the surface wave to travel twice the distance of the pit radius ( $2R/v_R$ ) as indicated by the dashed line in Fig. 15b.

In Fig. 16a, the first reflections show dips at about 130,000 cycles. This may be attributed to the lowest order resonance of surface waves on the crack surface excited when the crack grows to half the wavelength of the surface wave [41]. However, it is known that the surface wave forms a weak resonance on the crack surface because of low reflection coefficient (~0.2) from the crack tip [42]. The dips in reflection signal amplitudes can, therefore, result from the surface wave resonance reinforced by constructive interference of corner creeping waves that are reflecting back and forth on the front half of the pit between the two crack surfaces. From the fractograph for this sample shown in Fig. 2c, the crack length on the surface from the edge of the pit is about 356 μm, just above half a surface wavelength, 300 μm.

The amplitude of the plate bottom reflection (Fig. 16b) increases with the number of cycles, since it is not affected by wave interference. In Fig. 16b at around 60,000 cycles, the second reflection starts to increase with higher slope. This happens when the crack becomes deeper than the pit, thus substantially more bottom reflection energy can be captured by the crack surface. Therefore, one may expect that crack depth equals pit depth at around 60,000 cycles. The fractograph at 65,000 cycles shows the actual crack depth to be 265  $\mu\text{m}$  and half-width 200  $\mu\text{m}$  as shown in Fig. 2c, which is slightly larger than the pit depth 250  $\mu\text{m}$ . As observed in Figs. 15 and 16, ultrasonic signatures are sensitive to the load level at which they are measured. At this stage of fatigue, the signal does not change up to 200 lb. This is related to the crack opening-closure behavior as discussed below.

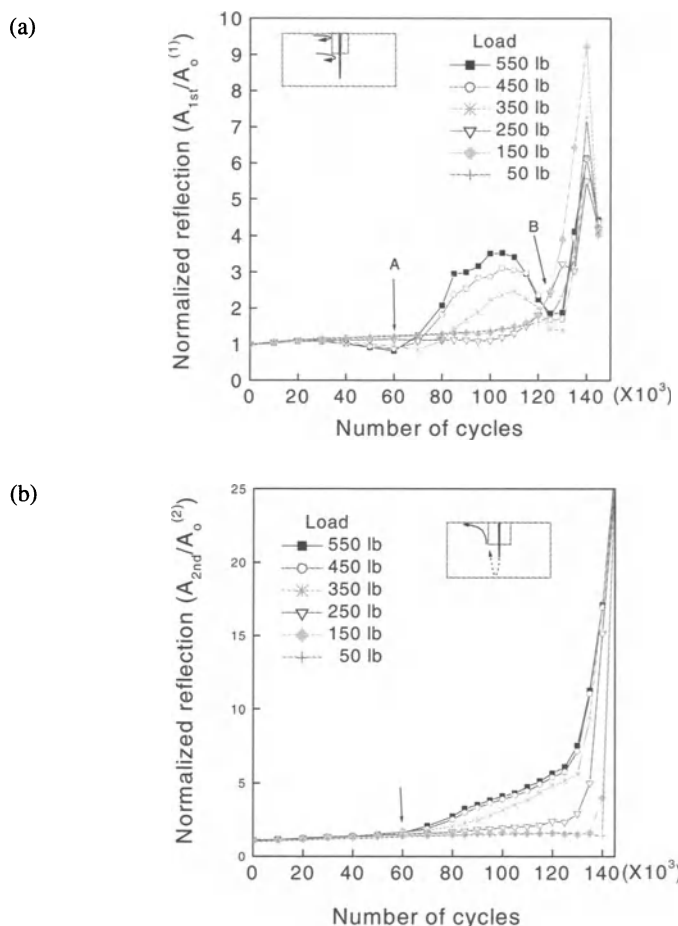


**Fig. 16.** Change of normalized reflection signal amplitude during fatigue life of Al 2024-T3 sample. (a) First reflection; (b) Plate bottom reflection

In Fig. 17, the normalized first and plate bottom reflections versus the cyclic load are shown at different numbers of cycles. As can be seen in Fig. 17a, the reflected signal amplitude passes through a minimum with increase of load, which is due to the interference between the pit and the crack reflected signals as discussed in [26]. The signal interferences enhance sensitivity to crack initiation and crack mouth opening; however, this complicates the determination of the crack-fully-opening loads. The crack-mouth-opening load can be determined, as marked by the arrow in Fig. 17a, below 60,000 cycles.

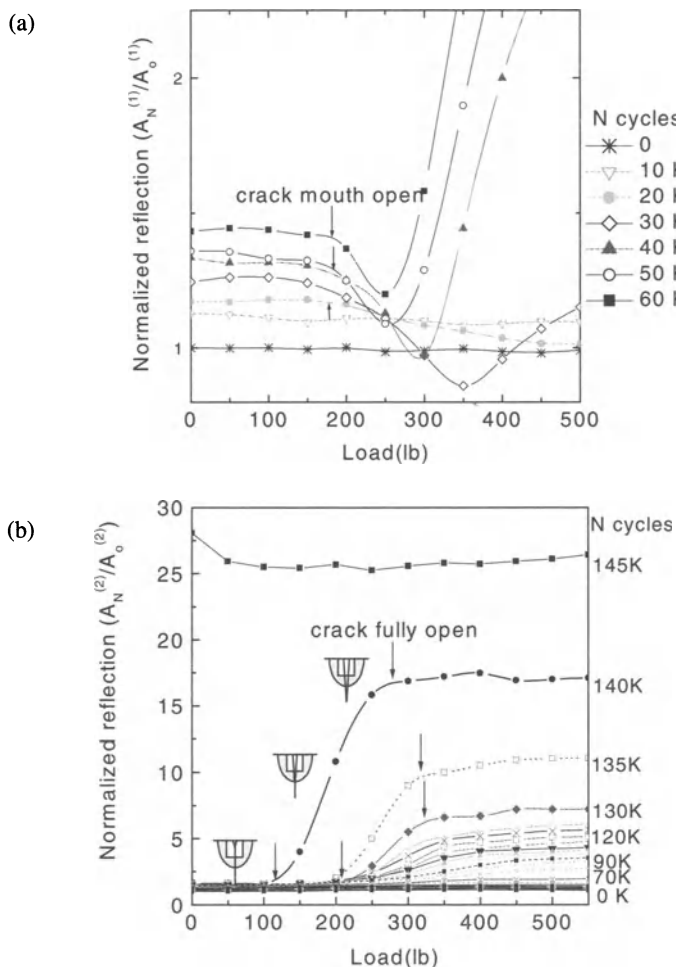


**Fig. 17.** Normalized reflections vs. load at different number of fatigue cycles for Al2024-T3 sample [24]. (a) First reflection; (b) Plate bottom reflection

The plate bottom reflections versus cyclic load at different fatigue cycles are shown in Fig. 17b. The behavior has a common trend: each curve after a plateau begins to bend upward at a certain load level and saturates at some higher load. The bend-up load level occurs when the crack opening/closure boundary reaches the pit depth; it is slightly above the crack-mouth-opening load. The saturation of the reflection-versus-load curve occurs at a fully open crack. The behavior changes significantly at the end of fatigue life; for example, at 145,000 cycles, just before sample failure, the reflection amplitude does not change with varying load level since the crack tip deforms as a plastic hinge and the crack remains open during the whole loading cycle. The plate bottom reflection is useful in determining the crack-fully-open load and, for high numbers of cycles, the load slightly above the mouth-opening-load.

### ***Reflection of Surface Wave from Pit with Crack in Ni-Base Superalloy Sample***

Similar surface acoustic wave measurements were performed for a Ni-base superalloy sample (Inconel 718). The depth and diameter of the pit were 182  $\mu\text{m}$  and 254  $\mu\text{m}$ , respectively. The fatigue life of the sample was 147,346 cycles. The peak-to-peak amplitude of the plate bottom reflection is illustrated in Fig. 18 as a function of number of cycles at different load levels (Fig. 18a) and as a function of load at different number of cycles (Fig. 18b). Since the signal does not show any change before 113,000 cycles, the reflection amplitudes after 110,000 cycles are shown in Fig. 18a. The change of ultrasonic signal amplitude due to crack initiation and evolution is similar to that for Al alloy samples. However, one should note that the crack initiation in the Inconel-718 sample occurs in much later stages of fatigue life (113,000 cycles, 76% of the fatigue life) than that for aluminum samples (17% of the fatigue life). The similarity between these figures and Fig. 16b and Fig. 17 is obvious, indicating similar effect of crack closure due to the plastic zone. This is expected since we selected the same normalized (to the yield stress) fatigue load parameters for both the aluminum and the Inconel samples.

### ***Measurement of Crack Closure Loads***

Figure 19 summarizes the crack-mouth-opening and crack-fully-open loads (or stresses) versus number of fatigue cycles determined from Fig. 17a (open squares), 17b (solid circles). The crack-opening-loads determined applying our ultrasonic scattering model [26] is also shown. The crack-mouth-opening load is constant until around 100,000 cycles and then decreases, while the complete-opening load has its maximum at around 80,000 cycles. The results from the first reflection based on the model [26] coincide with those obtained from the plate-bottom-reflection versus load curves (Fig. 17b). The change of the opening loads is explained with a simple mechanical model in the next section.

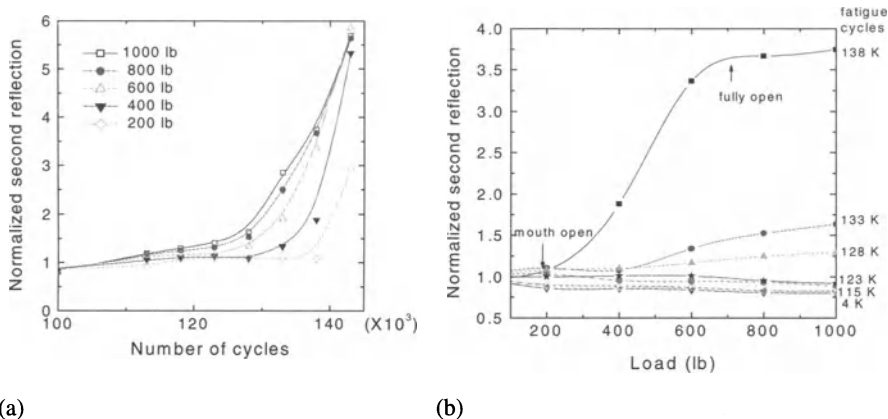


**Fig. 18.** Change of (a) first reflection vs. number of cycles at different load levels and (b) plate bottom reflections vs. load at different number of fatigue cycles. (Inconel 718) [25].

In these experiments, the increment of the step load (Fig. 1c) for ultrasonic measurements was 50 lb, limiting the resolution of opening loads which appeared to be constant in some ranges of Fig. 19 (correspondingly the stress intensity ratios in Fig. 21). This limited resolution is not a conceptual limitation of the method and can be improved by decreasing the load step; we have currently modified our data acquisition, reading ultrasonic data practically continuously during loading cycles.

To understand the open load behavior as a function of number of cycles, we need to consider the effect of the pit-induced plastic zone (Fig. 20). The effect of a notch on fatigue crack closure has been reported [6, 7, 43, 44]. When a crack grows at the root of the notch the notch plasticity is dominant over the crack-tip plasticity and is the main reason for crack closure in the small crack regime. Thus, for interpretation of the present results, one should consider the size of the plastic zone caused by a pit under stress versus the emerging fatigue crack size. The pit-induced plastic yielding zone is constrained by the surrounding elastic medium, thus during crack growth in the plastic zone compressive closure force is applied to the crack surface as shown in Fig. 20a.

Let us consider, for example, three different crack sizes at different stages of fatigue life as marked by dotted lines 1, 2 and 3 in Fig. 19. As shown in Fig. 20b, when the crack is short ( $a = a_1$ , curves 1 and 2) the stress required to open the crack completely  $\sigma_{FO}^{(1)}$  is just slightly higher than the stress for crack mouth opening  $\sigma_{MO}^{(1)}$ , which is constant at this stage of crack growth. With growth in the pit-induced plasticity zone, the crack-fully-open stress increases from  $\sigma_{FO}^{(1)}$  to  $\sigma_{FO}^{(2)}$ .

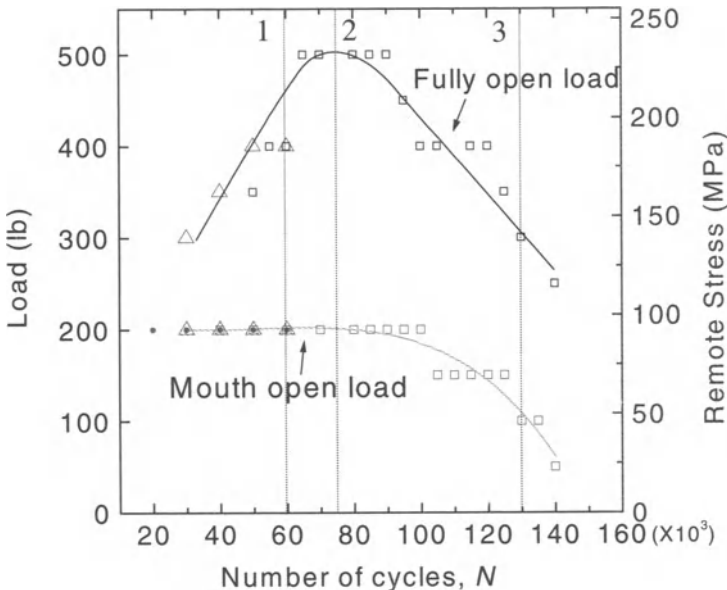


**Fig. 19.** Crack opening load versus number of cycles obtained during fatigue test of Al 2024-T3 sample [24]. Points were determined from Fig. 17a (open squares), 17b (solid circles). Triangles correspond to points indicated in Fig. 27b

When the crack grows out of the pit-induced plastic zone ( $a > l_p$ ), part of the crack surface is unloaded and due to the reduction of the sample cross section the sample becomes more compliant and thus the constraint and the compressive stresses decrease leading to reduction of the crack opening stresses (curve 3 in Fig. 19b). For the same reason, when the crack tip lies outside the pit-induced plastic zone, the crack-fully-opening load decreases from  $\sigma_O^{(2)}$  to  $\sigma_O^{(3)}$  and the crack-mouth-opening load decreases from  $\sigma_{MO}^{(2)}$  to  $\sigma_{MO}^{(3)}$  (Fig. 20c).

The above hypothesis can be evaluated by comparing the actual crack sizes with the estimated size of the pit-induced plastic zone. According to our finite element analysis of the stress distribution around a pit, the maximum stress occurs slightly below the sample surface in the pit mid-plane perpendicular to the loading direction; the stress concentration factor was  $k_c = 3.2$  for the 250-μm-depth pit in the 1600-μm-thickness plate (the stress concentration on the surface was very close to  $k_c = 3.0$ ). To calculate the length of the plastic zone ( $l_p$ ), the near-surface stress distribution around the pit was approximated with the stress distribution around a through-thickness hole [45] and the contour, where the stress level equals the yield stress is assumed to be the boundary of the plastic zone. The increase of the stress concentration ( $k_c = 3.2$ ) from that of the through-thickness hole ( $k_c = 3.0$ ) was taken into account assuming 1.07 (=3.2/3) times higher applied stress. The estimated length of the pit plastic zone  $l_p$  near the sample surface where the stress concentration is maximum is 290 μm. The ultrasonically estimated crack length at

60,000 cycles is 252  $\mu\text{m}$  [25]. The crack length measured from the SEM [24] is 356  $\mu\text{m}$  at 130,000 cycles. Therefore, the peak of the fully opening load (Fig. 19) at around 70,000 cycles corresponds reasonably well to the crack length approaching the size (290  $\mu\text{m}$ ) of the pit-induced plastic zone.

The fatigue life of a sample with a pit can be predicted using the model developed in [26] in which the effective stress intensity factor range  $\Delta K_{\text{eff}} = K_{\max} - K_{\text{op}}$  [7] is used in the Paris law  $da/dN = C(\Delta K_{\text{eff}})^m$ . Recently, various forms of  $\Delta K_{\text{eff}}$  have been proposed [46,47] to take the effects of partial crack closure into account. These models may be more relevant to the cracks considered in the present paper that exhibit partial closure. Fig. 21 shows the stress intensity ratios  $U = \Delta K_{\text{eff}} / \Delta K$  obtained based on the measured crack-fully-opening stress  $\sigma_{\text{FO}}$  without  $(\Delta K_{\text{FO}} / \Delta K)$  and with  $(\Delta K_{2/\pi} / \Delta K)$  the  $2/\pi$ -correction [46,47]; and those based on the measured crack-mouth-opening stress  $\sigma_{\text{MO}}$  ( $\Delta K_{\text{MO}} / \Delta K$ ). They are shown together with the calculated stress intensity factor ratios based on the applied maximum stress  $\Delta K_{\max} / \Delta K$  and Elber's [7] empirical formula. In concurrence with the discussion in references [46,47] the stress intensity ratio based on the fully-opening load underestimates the stress intensity factor ratio. It is interesting to note that Elber's empirical effective stress intensity ratio is close to the average of the ratios predicted based on the corrected opening load [7]. Other authors have observed a similar behavior for the measured [6] and numerically predicted [44] stress intensity ratios for fatigue crack growth in notched specimens.

To investigate the existence of crack opening-closure hysteresis, we performed measurements for an Al 2024-T3 sample using the load schedule shown in Fig. 1c. The sample had the same dimensions, 230  $\mu\text{m}$  pit depth and 269  $\mu\text{m}$  pit diameter. The fatigue load conditions were the same and the fatigue life of this sample was 129,843 cycles. The change of the plate bottom reflection versus step-up and step-down loads is shown in Fig. 22. A small, but ultrasonically detectable, irreversibility during crack opening-closure is observed.

It is interesting that the surface wave reflection amplitude, which increases with the length of the open part of the crack, has a reversal point in its hysteresis loop. At the same load level of a loading-unloading cycle at the lower loads, the reflection amplitude (open crack length) is higher when the crack is unloaded than when the crack is loaded; with increase of the load level a transition occurs when the length of the open part of the crack is larger at loading than for the same load at unloading as marked in Fig. 22.

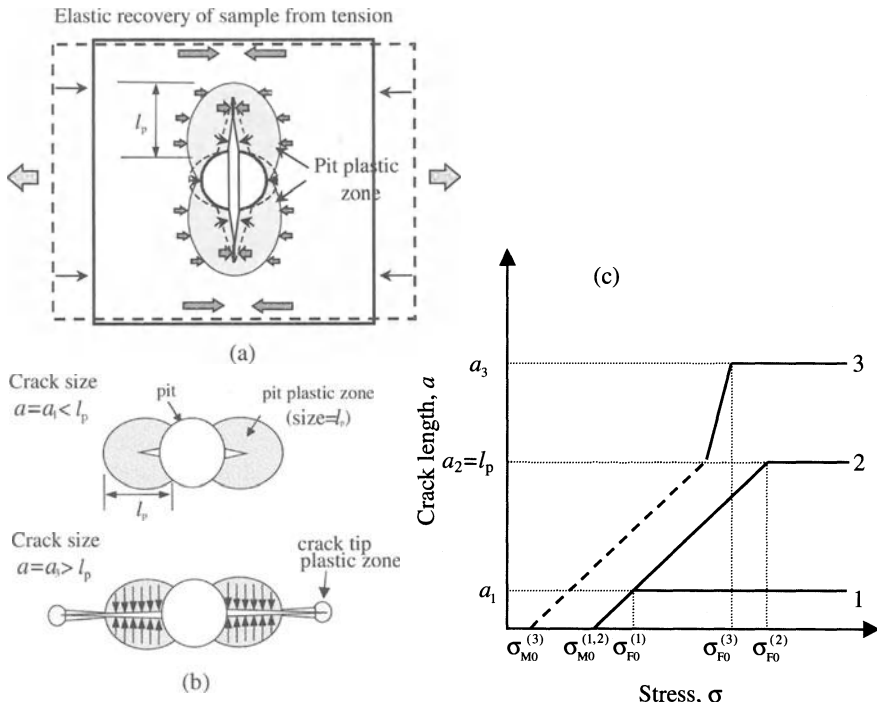


**Fig. 20.** Illustrations of effect of pit plastic zone on crack growth from pit [24]. (a) Crack closure stress due to pit plastic deformation; (b) Crack closure stress at different stages of crack growth; (c) Diagram illustrating crack length versus crack opening stresses

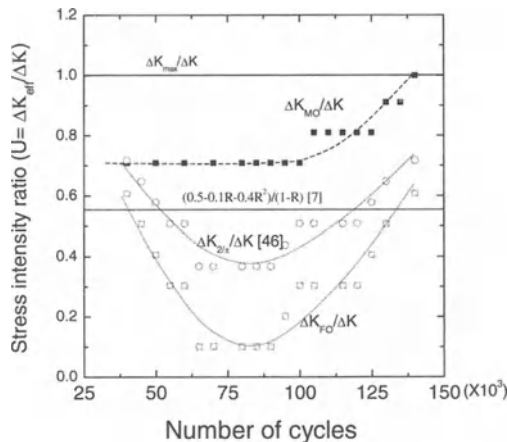


**Fig. 21.** Stress intensity factor ratios calculated based on measured crack mouth opening stress ( $\sigma_{MO}$ ), crack fully opening stress ( $\sigma_{FO}$ ) without and with  $2/\pi$  correction [46]. Also Elber's empirical stress intensity ratio for Al 2024-T3 [7] and the ratio calculated based on the maximum applied stress are shown by solid lines [24]

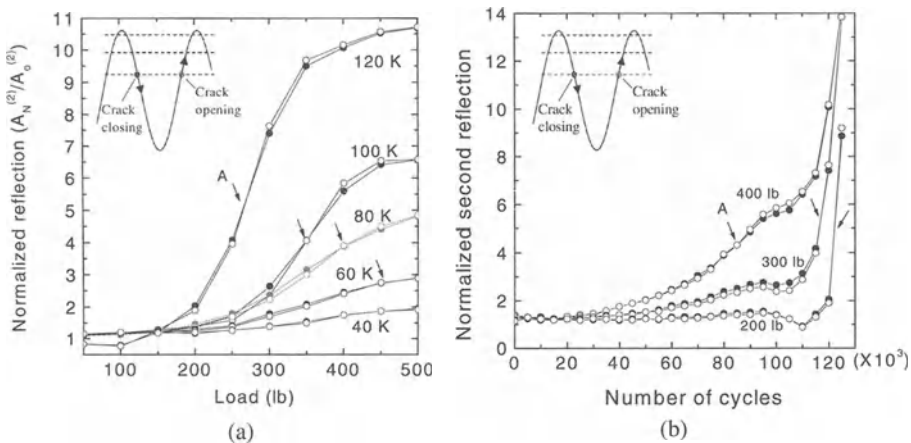


**Fig. 22.** Change of reflection amplitude during crack opening (open circles) and closing (solid circles) phases [24]. (a) reflection vs. load; (b) reflection vs. number of cycles

The load transition point decreases with increase of number of cycles. The transition seems to be associated with the movement of the crack opening/closure boundary through the edge of the plastic zone. Figure 23 summarizes the crack opening/closure behaviors and the reversal of the hysteresis loop appearing in surface wave reflection versus load curves during fatigue cycles.

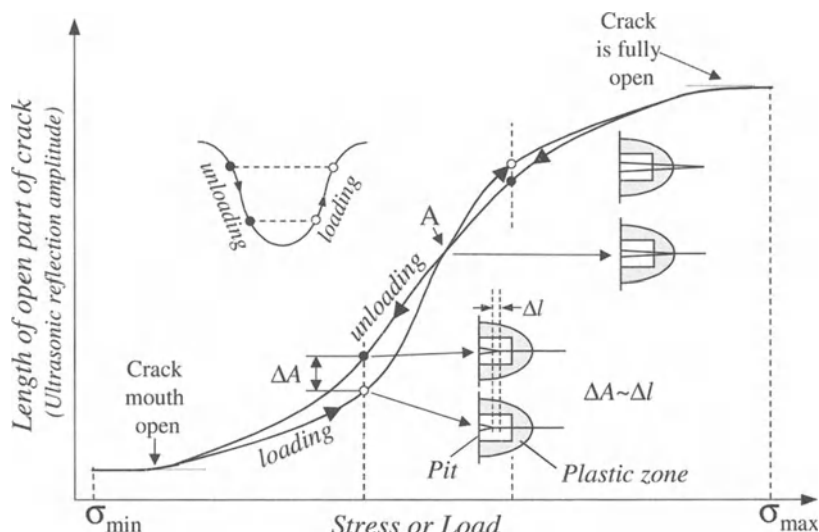


**Fig. 23.** Schematic illustrating crack opening/closure and reversal of hysteresis loop during loading-unloading cycle

### **Crack Size Determination**

To compare the model prediction with experiment, the time domain signals of the reflected surface wave were calculated using (17) as a function of the crack depth. The actual crack and pit geometries were determined from SEM fractographs for four samples fractured in tension at the following numbers of fatigue cycles: 25,000, 37,500, 60,000 and 65,000 (Table 1). These measured sizes of the pits and cracks are used for calculating the reflection signals. Figures 24 and 25 show calculated time domain signals and their spectra for two cases (2 and 3 Table 2) along with the experimental signatures obtained from the same samples. The results are in excellent agreement in both frequency and time domains. A stronger interference appears in the time domain signal at 60,000 cycles than at 37,500 cycles, due to stronger reflection from the crack.

Figure 26 shows the normalized reflection amplitude versus crack depth for different pit diameters (the amplitude determination was done as indicated on the time domain signals in Figs. 24 and 25). At small crack depths the pit diameter significantly affects the dependence of reflected amplitude on crack size: from monotonic decrease to increase of the signal. The range of crack depths calculated in Fig. 26 is up to the pit depth. To compare with calculations, we plotted the measured reflection amplitudes (solid squares) for the samples in Table 1. The results indicate good agreement between calculations and experiment. This illustrates that the present model can be applied for determination of the sizes of cracks emanating from pits if the pit diameter is known. The pit parameters should be determined from ultrasonic measurements prior to crack formation or at minimum fatigue load during the fatigue cycling when the crack is closed. If the crack is open, the pit size can be determined using microradiographic means [5] or using the ultrasonic wave technique with application of a compressional stress to close the crack.

The depth of the crack at different numbers of cycles can be determined by comparing computed reflection amplitudes versus crack depth ( $A^{(1)}$  in Figs. 24 and 25) with experimental reflection signatures obtained at different levels of fatigue

**Table 1.** Dimension of pit and crack determined from SEM fractographs ( $\mu\text{m}$ )

Sample	# of cycles at sample fracture	Pit		Crack		
		Depth	Diameter	Depth (a)	Surface length (c)	Aspect ratio (c/a)
1	25,000	256	231	123.5*	53*	0.43
2	37,500	257	253	197	102	0.52
3	60,000	260	262	259	196	0.75
4	65,000	259	230	265	202	0.76

\* Average values of two cracks

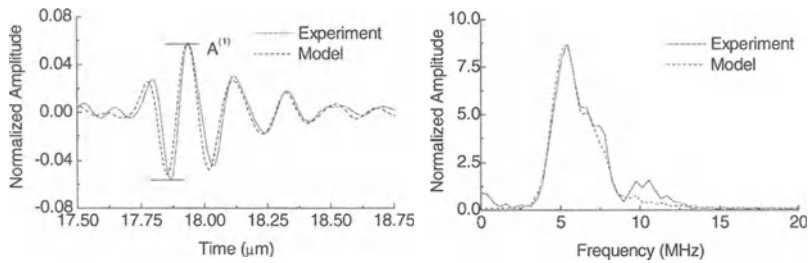


**Fig. 24.** Comparison of time domain signals and frequency spectra from experiment [26] (a) and model (b). The model used the measured sizes of pit and crack from fractograph at 37,500 cycles: crack depth is determined to be 197 μm; pit depth 257 μm; pit diameter 253 μm

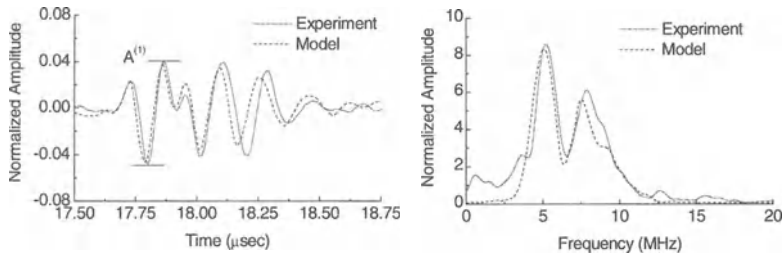


**Fig. 25.** Comparison of time domain signals and frequency spectra from experiment [26] (a) and model (b). The model used the measured sizes of pit and crack from fractograph at 60,000 cycles: crack depth is determined to be 259 μm; pit depth 262 μm; pit diameter 258 μm

load. In this way, the dependences of effective depths of fully and partially open cracks versus number of cycles (Fig. 27) are obtained for a sample at different levels of cycling load showing the dependences of the ultrasonically detectable crack depth ( $a_{\text{eff}}$ ): for example, at around 20,000 fatigue cycles, the actual crack depth determined at the load level 238 MPa (500 lb) is 110 μm whereas the detectable crack depth at the load level 95 MPa (200 lb) is 80 μm.

Rapid crack growth is observed in the beginning of the fatigue cycle: that is, the crack depth determined at 4600 cycles is already about 70 μm. Thereafter, the crack grows with a lower growth rate until 16,000 cycles, and then with a higher but relatively constant growth rate. This is due to a small crack growth behavior in the residual plastic zone. Due to the high stress concentration at the pit the maximum stress level near the pit is 2.6 times the yield stress. Therefore, the plastic deformation caused by the first half cycle of loading results in compressive residual stresses that retard crack growth (Fig. 27).

The present method allows monitoring the opening/closure behavior of a small fatigue crack [26]; this is difficult to do for small cracks by other methods.

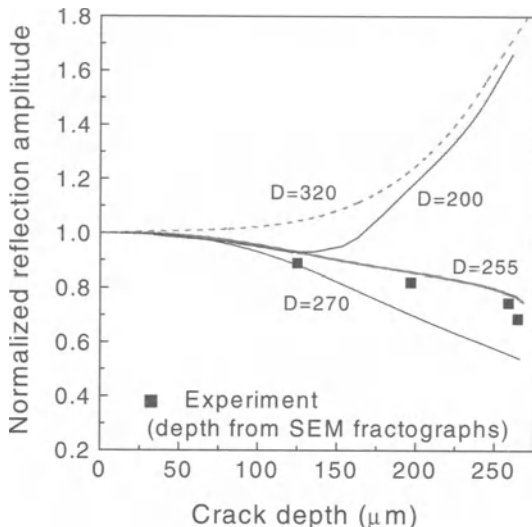


**Fig. 26.** Normalized reflection amplitude from the corner cracks on the pit for different pit diameters (D) [26]. Normalization is performed with the reflection amplitude from the pit prior to fatigue. Solid squares are measurements

### 5.4.3 Fatigue Life Prediction

Based on the stress-intensity factors obtained in Section 3.2 and the measured pit and crack sizes, the total fatigue life can be predicted as the sum of the life in each stage as follows,

$$N = \int_{a_{th}}^{a_f} \frac{da}{C[(\Delta K_1(a))]^m} + \int_a^{t-\varepsilon} \frac{da}{C[(\Delta K_2(a))]^m}. \quad (23)$$

The lower limit  $a_{th}$  in the integration for the first stage is the threshold crack length with the stress-intensity factor range,  $\Delta K_{th}(a_{th}) = 1.0 \text{ MPa } \sqrt{m}$  for Al 2024-T3 [15]. The upper limit in the integration for the first stage is  $a_f = d$  for the corner crack model (Fig. 3b) and  $a_f = a_f^*$  for the through-thickness crack model (Fig. 3d).

The number of cycles for the second stage was calculated by using the second integral in (23) with upper limit of integration  $t - \varepsilon$ , where  $\varepsilon$  is determined from the fractograph for each sample. The onset of long crack behavior is determined by the point of intersection of  $da/dN$  for short and long cracks as shown in Fig. 28.

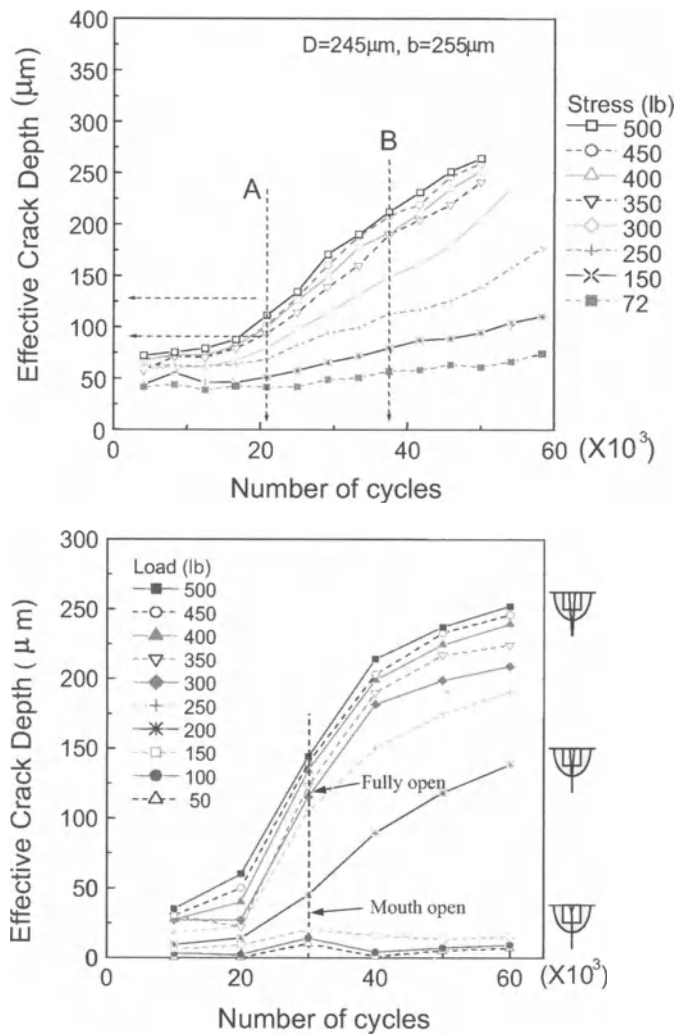


**Fig. 27.** Effective crack depths calculated using model and ultrasonic signatures for partially open cracks at different load levels during fatigue cycle. (top) Al 2024-T3 sample with pit depth of 245  $\mu\text{m}$  and diameter of 255  $\mu\text{m}$ ; (bottom) Al 2024-T3 sample with pit depth of 252  $\mu\text{m}$  and diameter of 246  $\mu\text{m}$

The same approach is used to determine the remaining life of the sample if the size of the fatigue crack initiated from the pit is measured ultrasonically as discussed above.

The experimental and calculated fatigue lives for samples with different pit depths are shown in Fig. 29 and listed in Table 2, where the calculated number of cycles for each stage of the fatigue life is also given. It should be noted that the

number of cycles of the first stage predicted by the simplified model agrees quite

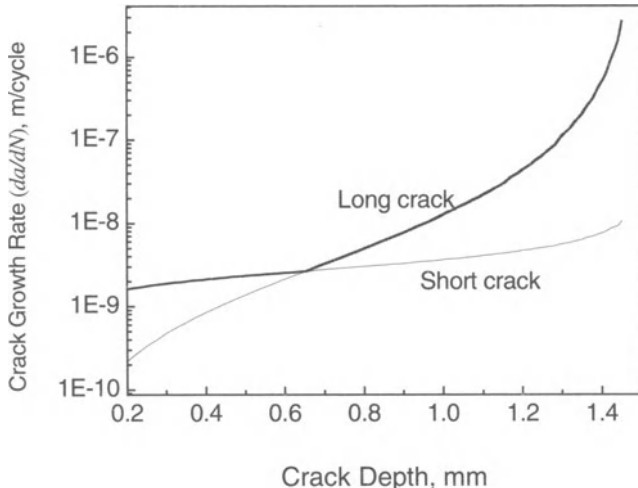


**Fig. 28.** Crack growth rates for short and long cracks

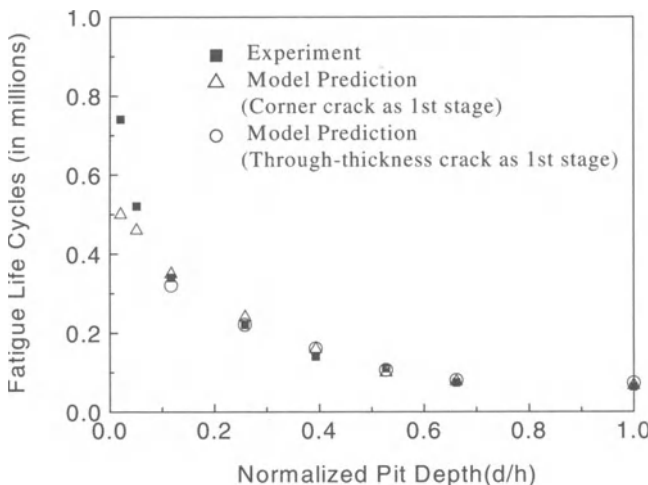
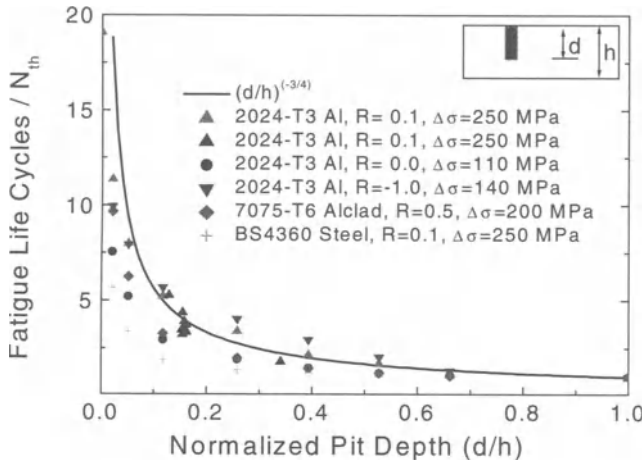


**Fig. 29.** Measured and predicted fatigue lives versus normalized pit depth [5]

well with that predicted by the corner crack model up to normalized pit depth  $d/h = 0.1$ . The model predictions for total lifetimes for the samples with different pit depths are also in good agreement with the experimental data.

For shallow pits, as was discussed in Sec. 5.3.2 an additional crack growth period has been taken into account in the beginning of the second stage, that is, the

period from a semi-elliptical crack with small aspect ratio ( $a/2c$ ) to the semicircular one. The deviation of the model predictions from the experimental



ones for shallow pits can be attributed to the approximate replacement in the

**Fig. 30.** Comparison of experiment and empirical relation for normalized fatigue life vs. normalized pit depth. The normalization factor  $N_{th}$  for fatigue life  $N$ , is the fatigue life of the sample with through-thickness hole for the same material and fatigue conditions

model of the inhomogeneous stress distribution of a finite depth pit by the homogeneous stress distribution of a through-thickness hole of equal depth, and the time taken to initiate a crack at a low stress concentrator. This lifetime includes the period required to nucleate a microcrack and for the microcrack to grow over the small crack threshold length. For the samples with deep pits ( $d > 2R$ ), the crack initiates very quickly, several thousand cycles after applying the fatigue load.

The prediction of crack initiation and growth from a pit presented in the previous sections requires significant effort to account for the different fracture mechanical behavior of the growing crack in each stage. Moreover, for the fatigue life prediction, many reliable experiments should be done to determine the Paris constants for the material of interest. Therefore, a simple empirical equation [5] for the fatigue life  $N$  of a sample with an arbitrary pit depth based on an experimental fatigue life for the reference standard sample geometry can reduce those efforts for field applications. The fit of experimental data shown in Fig. 30 with

$$\frac{N}{N_{th}} = \left(\frac{d}{h}\right)^{-3/4} \quad (24)$$

shows reasonable results. Here,  $N_{th}$  is the fatigue life of the sample with through-thickness hole, which is selected as an experimentally determined normalization

parameter for the fatigue life of the sample with arbitrary pit depth. Such a representation factorizes the fatigue life problem by accounting for one normalization parameter depending on material fatigue properties, and the dependence on pit depth by one geometrical parameter ( $d/h$ ). The normalized fatigue life cycles versus the normalized pit depth is shown in Fig. 30 for different materials at different fatigue conditions together with approximation. The solid squares and hollow triangles are experimental data; other symbols are calculations using the model described above. The Paris constants for Al 2024-T3 alloy at different loads can be found in [28] and those for Alclad 7075-T6 alloy and BS4360 steel are presented in [48, 49].

As we can see the dependence of fatigue life on the pit depth is fitted well by the proposed equation for data under different fatigue conditions. The simplicity of (14) should be noted in that the fatigue life of a sample with arbitrary pit depth can be predicted once the fatigue life of the sample with through-thickness hole has been obtained experimentally.

**Table 2.** Predicted and experimental fatigue lives

Dimension ( $\mu\text{m}$ )	Model Prediction					Experiment- total life
	D / d / t	1st stage (through- crack)	1st stage (Corner crack)	2nd stage	total life (through- crack model for 1st stage )	
30/230/1550	–	$0.9 \times 10^4$	$4.9 \times 10^5$	–	$5.0 \times 10^5$	$7.4 \times 10^5$
75/240/1560	–	$2.3 \times 10^4$	$4.2 \times 10^5$	–	$4.6 \times 10^5$	$5.2 \times 10^5$
170/240/1540	$0.6 \times 10^4$	$3.9 \times 10^4$	$3.1 \times 10^5$	$3.2 \times 10^5$	$3.5 \times 10^5$	$3.4 \times 10^5$
375/250/1560	$3.4 \times 10^4$	$5.1 \times 10^4$	$1.9 \times 10^5$	$2.2 \times 10^5$	$2.4 \times 10^5$	$2.2 \times 10^5$
570/245/1565	$4.9 \times 10^4$	$5.6 \times 10^4$	$1.1 \times 10^5$	$1.6 \times 10^5$	$1.6 \times 10^5$	$1.4 \times 10^5$
765/250/1550	$6.0 \times 10^4$	$5.9 \times 10^4$	$4.5 \times 10^4$	$1.1 \times 10^5$	$1.0 \times 10^4$	$1.1 \times 10^5$
960/230/1565	$6.5 \times 10^4$	$6.2 \times 10^4$	$1.5 \times 10^4$	$8.0 \times 10^4$	$7.7 \times 10^4$	$7.3 \times 10^4$
1550/200/1550	$7.2 \times 10^4$	$6.7 \times 10^4$	–	$7.2 \times 10^4$	$6.7 \times 10^4$	$6.2 \times 10^4$

## 5.5 Future Trends

In this work, we describe an ultrasonic method for characterization of a single pit with an emanating fatigue crack. This is the first step in addressing an important problem in maintenance of aging aircraft: the characterization of multiple corrosion pitting and widespread fatigue damage. This problem can be dealt with by combining surface acoustic wave interrogation with microradiography [27]. The surface acoustic wave method is significantly complicated due to shielding of the propagating surface wave by multiple pits and cracks. This may be addressed by localized excitation of surface waves utilizing ultrasonic angle beam scanning.

## References

1. Schmidt HJ, Brandecker B (1996) Corrosion fatigue data and design from an aircraft manufacturer's point of view. *Fatigue '96, Proceedings of The Sixth International Fatigue Congress*, Berlin, Germany, pp. 643–654
2. Chang JCI (1995) Aging aircraft science and technology issues and challenge and USAF aging aircraft program. *Structural integrity of aging aircraft*, AD-vol.47, ASME, pp.1–7
3. Scheuring JN, Grandt AF (1996) A fracture mechanics based approach for quantifying corrosion damage. *Structural Integrity in Aging Aircraft*, AD-vol.48, ASME, pp. A7-1–A7-7
4. Chen GS, Wan KC, Gao M, Wei RP, Flournoy TH (1996) Transition from Pitting to Fatigue Crack Growth-Modeling of Corrosion Fatigue Crack Nucleation in a 2024-T3 Aluminum Alloy. *Mater Sci and Eng A* 219:126–132
5. Rokhlin SI, Kim J-Y, Nagy PB, Zoofan B (1999) Effect of pitting corrosion on the fatigue crack initiation and fatigue life. *Eng Fract Mech* 62:425–444
6. Shin CS, Smith RA (1988) Fatigue crack growth at stress concentrations-The role of notch plasticity and crack closure. *Eng Fract Mech* 29:301–315
7. Elber W (1971) The significance of fatigue crack closure. *Damage tolerance in aircraft structures*, ASTM STP 486, pp. 230–242
8. McEvily AJ (1988) On crack closure in fatigue crack growth. In: Newman JC Jr., Elber W (eds.) *Mechanics of Fatigue Crack Closure*. ASTM STP 982, pp. 35–43
9. McClung RC, Newman JC Jr. (1999) Advances in fatigue crack closure measurement and analysis. *ASTM STP-143*, W. Conshocken, PA
10. Laz PJ, Hillberry BM (1995) A probabilistic approach to the generation of EIFS distributions derived from inclusion characteristics. *Structural Integrity in Aging Aircraft*, AD-47, ASME, pp. 81–85
11. Laz PJ, Hillberry BM (1996) The role of inclusions in fatigue crack formation in aluminum 2024-T3. *Fatigue '96, Proceedings of The Sixth International Fatigue Congress*, Berlin, Germany, pp. 1293–1298
12. Piascik RS, Willard SA (1994) The growth of small corrosion fatigue cracks in alloy Al-2024. *Fatigue Fract Eng Mater Struct* 17(11):1247–1259
13. Nakajima M, Tokaji K (1996) A mechanical condition of fatigue crack initiation from corrosion pits. *Fatigue '96, Proceedings of The Sixth International Fatigue Congress*, Berlin, Germany, pp. 697–702
14. Becker K, Rukwied A, Allen, D, Knosp B, Saisse H, Brondsted P, Bridge M, Lyon M (1994) The effect of surface degradation on fatigue and fracture behaviour. *Mater and Design* 14(3):175–182
15. Philips EP, Neuman JC (1989) Impact of small crack effect on design life calculations. *Exp Mech*:221–225
16. Irving PE, Robinson JL, Beevers CJ (1975) *Eng Fract Mech* 7(2):619–630
17. Van Stone RH, Richardson TL (1985) Automated test methods for fracture and fatigue crack growth. *ASTM STP 877*:148–159
18. Sharpe WN Jr, Grandt AF Jr. (1976) A preliminary study of fatigue crack retardation using laser interferometry to measure crack surface displacement. *Mechanics of Crack Growth*, ASTM STP 590:302–320

19. Buck O, Thompson RB, Rehbein DK (1988) Using acoustic waves for the characterization of closed fatigue cracks. In: Newman, JC Jr., Elber W (eds) Mechanics of Fatigue Crack Closure, ASTM STP 982,) pp. 536–547
20. Resch MT, Nelson DV (1992) An ultrasonic method for measurement of size and opening behavior of small fatigue cracks. In: Larsen JM, Allison JE (eds) Small-crack test methods, ASTM STP 1149, pp. 169–196
21. Yuce HH, Nelson DV, Resch MT (1985) The use of surface acoustic waves to study small fatigue cracks in 7075-T651 aluminum and 4340 steel. In: Thompson DO, Chimenti DE (eds) Review of Progress in Quantitative Nondestructive Evaluation, Plenum Press, New York, 3A, pp. 105–113
22. Tittman BR, Buck O (1980) Fatigue lifetime prediction with the aid of SAW NDE." Proceedings of the DARPA/AFML Review of Progress in Quantitative Nondestructive Evaluation, pp. 411–421
23. Tien JJW, Khuri-Yakub BT, Kino G.S, Marshall DB, Evans AG (1981) Surface acoustic wave measurement of surface cracks in ceramics. J Nondestr Eval 2(3,4):219–229
24. Rokhlin SI, Kim JY (2003) In-situ ultrasonic measurement of crack closure. Int J Fatigue 25:41–49
25. Rokhlin SI, Kim JY (2003) In-situ ultrasonic monitoring of surface fatigue crack initiation and growth from surface cavity. Int J Fatigue 25:51–58
26. Kim JY, Rokhlin SI (2002), Surface acoustic wave measurements of small fatigue crack initiated from a pit. Int J Solids and Structs 39:1487–1504
27. Rokhlin SI, Zoofan B, Frankel GS (2003) Microradiographic and foil penetration methods for quantification of localized corrosion. Chap.3
28. Phillips EP (1988) The influence of crack closure on fatigue crack growth thresholds in 2024-T3 aluminum alloy. In: Newman JC Jr., Elber W (eds) Mechanics of Fatigue Crack Closure, ASTM STP 982, pp. 505–515
29. Raju IS, Newman JC Jr. (1979) Stress-intensity factors for two symmetric corner cracks. In Smith CW (ed): Fracture Mechanics, ASTM STP 677, pp. 411–430
30. Tada H, Paris PC, Irwin GR (1973) The Stress Analysis of Crack Handbook. Del Research Corporation, Hellertown, PA., pp. 122–126
31. Elber W (1970) Fatigue crack closure under cyclic tension. Eng Fract Mech 12(1):37–45
32. Newman Jr. JC (1971) An improved method of collocation for the stress analysis of cracked plates with various shaped boundaries. NASA Technical Note, NASA TN D-6376
33. Rolfe ST, Barsom JM (1987) Fracture and Fatigue Control in Structures Applications of Fracture Mechanics. Prentice Hall, NJ, pp. 42
34. Newman JC, Raju IS (1981) An Empirical Stress-Intensity Factor Equation for the Surface Crack. Eng Fract Mech 40:185–192
35. Kino GS (1978) The application of reciprocity theory to scattering of acoustic waves by flaws. J Appl Phys 49 (6):3190–3199
36. Auld BA (1979) General electromechanical reciprocity theory relations applied to the calculation of elastic wave scattering coefficients. Wave Motion 1:3–10
37. Budiansky B, O'Connell RJ (1976) Elastic moduli of a cracked solid. Int J of Solids Struct 12:81–97
38. Viktorov IA (1967) Rayleigh and Lamb Waves-Physical Theory and Application. Plenum, New York

39. Datta S Hunsinger BJ (1977) Analysis of line acoustical waves in general piezoelectric crystals. *Phys Rev B*16:4224–4229
40. Lagasse PE, Mason IM, Ash EA (1973) Acoustic surface waveguide-analysis and assessment. *IEEE, Trans Microwave Theory and Tech MTT*-21:225–236
41. Ayter S, Auld BA (1980) On the resonances of surface breaking cracks. *Proceedings of the DARPA/AFML Review of Progress in Quantitative Nondestructive Evaluation*, pp. 394–402
42. Freund LB (1971) The oblique reflection of a Rayleigh wave from a crack tip. *Int J Solids Struct* 12:1192–1210
43. Dowling NE (1979) Fatigue at notched and local strain and fracture mechanics approaches. In: Smith CW (ed) *Fracture Mechanics*, ASTM STP 677 pp. 247–273
44. Hou CY, Charng JJ (1996) Estimation of plasticity-induced crack closure in a pre-existing plastic zone. *Int J Fatigue* 18:463–474
45. Pilkey WD (1999) *Peterson's Stress Concentration Factors*. Wiley, New York 1997
46. Donald K, Paris PC (1999) An evaluation of  $\Delta K_{\text{eff}}$  estimation procedures on 6061-T6 and 2024-T3 aluminum alloys. *Int J Fatigue* 21:S47–S57
47. Kujawski D (2001) Enhanced model of partial crack closure for correlation of R-ratio effects in aluminum alloys. *Int J Fatigue* 22:95–102.
48. de Koning AU (1981) A simple crack closure model for prediction of fatigue crack growth rates under variable-amplitude loading. In: Roberts R (ed) *Fracture Mechanics ASTM STP 743*, pp. 63–85
49. Ewalds HL, Wanhill RJH (1984) *Fracture Mechanics*. Edward Arnold and Delftse Uitgevers Maatschappij, MD, pp. 173

## **6 Ultrasonic Fatigue Crack Detection in Aluminum and Titanium Alloys**

P.B. Nagy, H. Xiao, Z. Yan

The well-known thermo-elastic effect of laser irradiation can be exploited to generate strong localized stresses when an expanded, long-pulse, low-intensity laser beam is used to irradiate the specimen. These stresses will produce a parametric modulation of the received ultrasonic signals, which is somewhat similar to the acousto-elastic effect often used in nonlinear ultrasonic studies. Otherwise hidden small cracks in fatigue-damaged aluminum and titanium specimens can be readily detected by exploiting this optically induced thermo-elastic modulation during ultrasonic surface wave inspection since they are susceptible to crack-closure and therefore exhibit strong parametric modulation. The temporal and spatial variations of the ultrasonic signals due to laser irradiation were studied experimentally. Based on these results, the direct temperature modulation of the ultrasonic velocity can be separated from the thermo-elastic stress modulation present only in cracked specimens. It has been found that this method can be used to selectively increase the sensitivity of ultrasonic flaw detection to small fatigue cracks by more than one order of magnitude.

### **6.1 Introduction**

Positive identification of small fatigue cracks presents a challenging problem during nondestructive testing of fatigue damaged structures. First, it is important to distinguish fatigue cracks from primary geometrical features (e.g., nearby holes, corners, and edges) and secondary irregularities (e.g., uneven machining, mechanical wear, corrosion, fretting, etc.). Second, it is important to distinguish small fatigue cracks as early as possible after crack initiation from intrinsic material inhomogeneities such as coarse grains, anomalous microstructure, second phases, precipitates, porosity, various types of reinforcement, etc. The detection threshold of any given nondestructive inspection system together with the crack growth rate and the critical crack size determine the minimum frequency of inspection necessary to prevent structural failure. An ever increasing demand for earlier detection of fatigue damage is fueled by the fact that small cracks have been found to grow at unexpectedly high growth rates well below the large-crack threshold in aluminum, aluminum-lithium, and titanium alloys [1]. For example, extensive multiple-site fatigue cracking may develop in airframe structures before it can be reliably detected by any of the currently available nondestructive evaluation techniques [2]. Under laboratory conditions, a great variety of Nondestructive Evaluation (NDE) techniques are available for early fatigue

damage detection and characterization. These techniques include acoustic emission, linear and nonlinear ultrasonics, vibration analysis, eddy current inspection, magnetics, thermal imaging, x-ray, etc. Three novel NDE techniques, namely holographic interferometry, structural integrity monitoring, and laser ultrasonic inspection, which allow simultaneous detection of numerous small (less than 1 mm) cracks over a large area, have been reviewed recently [3]. Laser-ultrasonics in particular has been recognized as one of the most promising ways for future applications due to its noncontacting and remote nature [4]. Unfortunately, these techniques tend to lose sensitivity when adapted to in-field inspection of large, complex structures or in situ monitoring of a fatigue test.

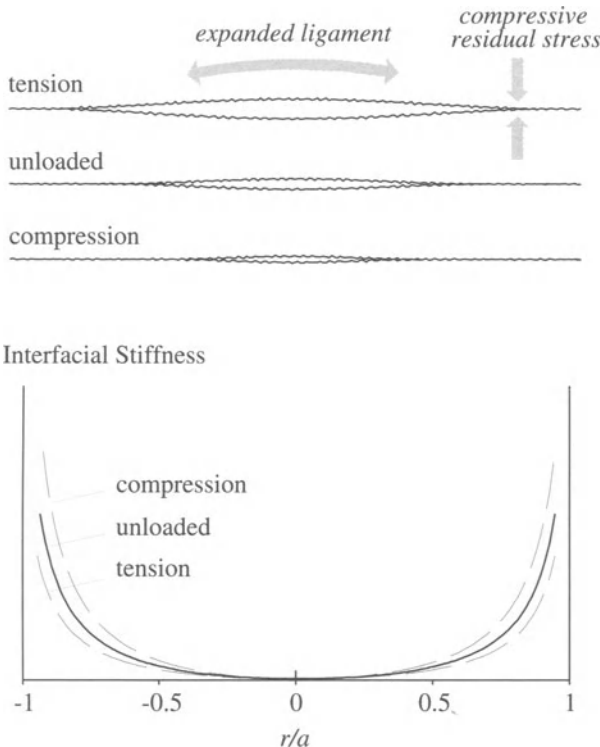
To a large degree, this insensitivity is due to the fact that fatigue cracks are usually initiated by small geometrical irregularities or material inhomogeneities that give rise to sharp local stress concentrations. In the early stages of fatigue, small cracks often are hidden from ultrasonic detection by stronger scattering from the very same structural imperfection that produced them in the first place. In other words, small fatigue cracks are undetectable not necessarily because the scattered wave they produce is weak in an absolute sense, but because it is weak relative to other signals produced by inherent inhomogeneities such as the coarse grain structure. Various signal processing techniques have been studied in order to reduce this inherent material noise, including Split Spectrum Processing [5], cut Spectrum Processing [6], Wavelet Transform Technique [7], etc. However, since these techniques are all based upon the nonspecular properties of grain scattering, they can only be used efficiently when the grain size, or more generally the characteristic dimension of the competing microstructural feature, is orders of magnitude smaller than the targeted fatigue crack, which is not the case in many aerospace materials with relatively coarse grain structure like titanium alloys. Furthermore, in most practical applications the weak fatigue crack signal competes with a single, large artifact when the anomalous reflector is comparable or larger than the acoustic wavelength. It should be mentioned that the more recently developed Neural Network technique provides another way to identify fatigue cracks [8]. It is actually another kind of signal processing technique using flaw classification algorithms instead of direct filtering at the cost of much more intensive computations.

## 6.2 Background (Crack-Closure)

Generally, linear acoustic characteristics (attenuation, velocity, backscattering, etc.) are not sufficiently sensitive to very small fatigue cracks. On the other hand, it has been noticed that in a great variety of structural materials even very small fatigue damage can produce very significant excess nonlinearity, which can be orders of magnitude higher than the intrinsic nonlinearity of the intact material [9].

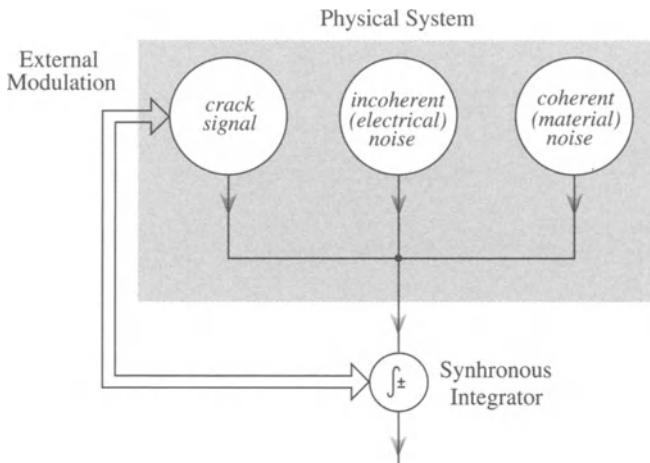
The excess nonlinearity is produced by the strong local nonlinearity of a microcrack whose opening is smaller than the particle displacement. There are two basic types of nonlinear phenomena that can be exploited for enhanced crack detection. In the so-called harmonic generation method a narrow-band, high-amplitude ultrasonic vibration itself produces sufficient particle displacements on the surface of the crack, that results in partial temporal crack-closure which in turn exhibits itself in the generation of second, third, and higher harmonics of the fundamental ultrasonic frequency in the reflected and transmitted waves [10, 11]. In the so-called acousto-elastic method the low-amplitude ultrasonic vibration itself produces but negligible particle displacements on the surface of the crack while a static or very slow quasi-static external load is applied to produce the high-amplitude elastic deformation required for partial crack-closure [9]. In this study, we will consider a variation of this acousto-elastic technique, when the partial crack-closure is conveniently produced by localized thermal stresses.

Figure 1 shows a schematic diagram of a partially closed fatigue crack under varying normal stress. The center of the fatigue crack is usually open due to the plastic elongation of the ligament connecting the tips, that occurs during the nucleation and growth of the crack. At the same time, the tips of the same crack are usually tightly closed by compressive residual stresses resulting from the same plastic deformation. The temporal modulation of the ultrasonic scattering from such a partially closed fatigue crack under varying normal stress can be interpreted in two ways. According to the simpler approach, it is only the size of the open part of the crack that increases and decreases under tensile and compressive normal stresses, respectively. Actually, the transition between the open and closed parts is more continuous. According to more realistic models of crack-closure, the stiffness of the interface contact between the opposite surfaces of the crack undergoes a parametric modulation by the changing normal stress, as it is shown in Fig. 1. In the compression phase, the interfacial stiffness becomes increasingly high as the crack becomes tightly closed. In contrast, in the tension phase, the interfacial stiffness approaches zero as the crack becomes fully open. The parametric modulation of the ultrasonic scattering from the crack is caused by the stress-dependence of the interfacial stiffness between the opposite faces of the fatigue crack. The resulting nonlinearity is zero for both entirely open and entirely closed cracks. Due to local residual stresses in the material, typical fatigue cracks are partially closed when the external load is removed and generate strong excess nonlinearity via crack-closure. This effect can be exploited through different ways to significantly improve the detectability of small cracks.



**Fig. 1.** Schematic illustration of crack-closure as parametric modulation of the interfacial stiffness by the changing normal stress

Perhaps the simplest way to observe crack-closure under laboratory conditions is to ultrasonically monitor the opening and closing of fatigue cracks when subjecting the specimen to static or quasi-static external loading. The technical realization of the acousto-elastic method must incorporate two tasks. One is to find an effective way to generate crack-closure in the specimen, i.e., the “elastic” problem. The other is to find a way to monitor the resulting parametric modulation by ultrasonic means, i.e., the “acoustic” problem. The modulation stress may be generated in different ways such as external cyclic loading in a typical fatigue test [9], static loading during breaks between periods of cyclic loading [12], or exploiting the inherent vibration of the structure itself during operation [13]. The main disadvantage of using external mechanical loading is that usually the whole structure must be loaded, which requires very substantial forces and might cause additional damage in certain parts of the structure. More localized temporary stresses can be produced by simply cooling or warming the specimen to be tested [14].



**Fig. 2.** A schematic diagram of phase-locked synchronous detection of crack closure

In order to detect and quantitatively measure the resulting parametric modulation, the detected ultrasonic wave form can be processed and analyzed by different methods depending on the degree of modulation. The simplest asynchronous method is based on signal differentiation achieved by continuously subtracting from the detected wave its most recent running average taken over a few seconds [14]. Such simple signal processing is readily available on most state-of-the-art digital flaw detectors. However, the asynchronous method cannot distinguish between the periodic modulation caused by cyclic loading and the essentially random extraneous modulation caused by artifacts such as thermal drift or material creep. Much better selectivity can be achieved by phase-sensitive synchronous detection when only variations maintaining a constant phase relation with the excitation signal over a long integration period are measured. A schematic diagram of phase-locked synchronous detection of crack closure is shown in Fig. 2. As an example, Fig. 3 shows the effects of ordinary asynchronous time-averaging and synchronous (phase-locked) time-averaging on the detected signal [14]. Ordinary time-averaging routinely used in digital ultrasonic flaw detectors eliminates only the truly incoherent electrical noise without discriminating between fatigue cracks and artifacts. In comparison, synchronous detection also eliminates time-invariant artifacts by alternating the sign associated with the detected signal before averaging depending on whether it was taken during crack opening or closure. The only retained phase-locked dynamic component is the difference of the reflected echoes from the tip of a fatigue crack in its closing and opening states. This signal is mainly caused by the nonlinear effect of tension and compression stresses on the interfacial stiffness between the opposite faces of the partially closed fatigue crack, while other scatterers, including fully open large cracks, are eliminated.

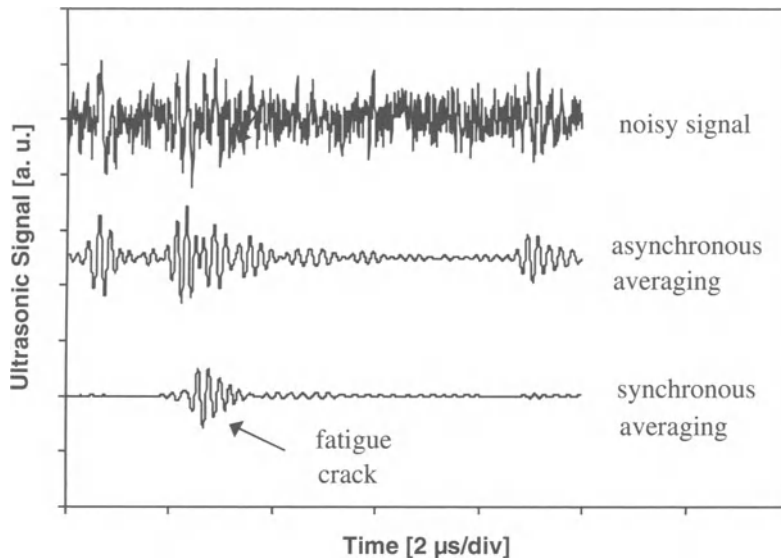


**Fig. 3.** The effects of ordinary asynchronous time-averaging and synchronous (phase-locked) time-averaging on the detected signal

It should be mentioned that this kind of synchronous modulation has also been used successfully in some other kinds of nondestructive testing techniques such as eddy current inspection [14] and acoustic emission [15]. Furthermore, the nonlinear effect of crack-closure could also be exploited through some other ways to increase the detectability of fatigue cracks, such as measurement of “harmonic mode shapes” during vibration [16] and monitoring of strain wave functions under a random load [17]. In fact, any significant change in structural and material characteristics under external deformation can be a telltale indication of fatigue crack somewhere in the structure.

## 6.3 Instrumentation and Method

### 6.3.1 Thermo-Optical Modulation

As we have mentioned in the previous section, an alternative way of producing dynamic crack-closure is by cooling or warming. It is well known that temperature variations can lead to high levels of internal stresses in materials having constituents of different thermal expansion coefficients. For example, in a metal matrix composite strong static stresses can be produced just by slowly cooling or warming the specimen. Of course, the same approach would not work in

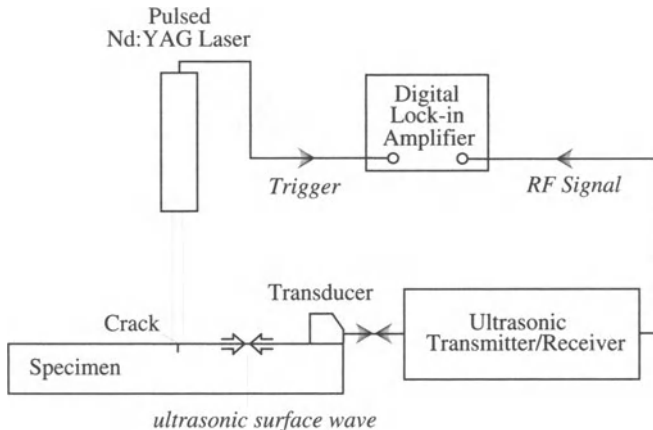


**Fig. 4.** A schematic diagram of the experimental arrangement with thermo-optical modulation

essentially homogeneous materials such as an aluminum airframe part or a titanium alloy engine component. However, dynamic thermal stresses can be still produced by rapid and concentrated cooling and heating. These stresses are temporary only as they disappear when the temperature gradients vanish due to the thermal conductivity of the material.

In the following we investigate the possibility of using laser irradiation to produce dynamic crack-closure. Laser-ultrasonics is a new nondestructive materials characterization technology, which combines the ability of ultrasonic inspection with the flexibility of optical methods [4]. This method has already shown its potential in numerous applications for the aerospace industry and other demanding applications. When relatively low-intensity ( $<10^6 \text{ W/cm}^2$ ) radiation is incident on a metal surface, some of the light energy is absorbed via electrons in the conduction band and converted into heat, while the rest is reflected. The absorbed energy is dissipated within a few nanometers of the surface, producing a rapid rise in temperature. The thickness of the heated layer increases with time as heat is conducted into the bulk of the material. In the case of a short pulse of less than  $1\mu\text{s}$  in duration, the sudden rise in the surface layer's temperature causes ultrasonic radiation via thermal expansion. By increasing the length of the optical pulse to approximately  $100\mu\text{s}$ , this direct generation of ultrasound can be eliminated and the resulting thermal stresses can be exploited to produce parametric modulation by dynamic crack-closure. Laser irradiation is a rather efficient way to generate crack-closure since it is very easy to control and operate while maintaining the noncontact, remote nature of laser ultrasonics. Since it does not produce acoustic loading on the free surface of the specimen, it can be directly applied at the spot to be inspected. Furthermore, the short duration of the heating laser pulse allows us to produce higher temperature gradients, and consequently higher thermal stresses, without significantly warming the specimen.

Figure 4 shows a schematic diagram of the experimental arrangement with thermo-optical modulation [18–21]. The crack is located at the surface of the specimen. The region of interest is continuously monitored by an ultrasonic flaw detector emitting a surface acoustic wave and operating in pulse-echo mode. Surface waves carry most of their energy in a shallow layer of less than one wavelength below the surface therefore they offer unique sensitivity to near-surface variations in material properties. However, weak reflected signals from small cracks cannot be unequivocally distinguished from scattering from intrinsic inhomogeneities and surface irregularities. Such hidden cracks can be revealed by monitoring the variation of the detected ultrasonic signal as the surface temperature is abruptly increased. The sharp temperature rise produced by laser irradiation is accomplished by a strong temporal compressive stress as the extending “skin” becomes too large for the bulk of the material.

### 6.3.2 The Role of Thermal Diffusivity

We will see in the following discussion that, depending on the repetition frequency of the pulsed laser and the thermal diffusion time in the material, we can distinguish between two types of modulation. First, there is an essentially instantaneous “dynamic” modulation, which is in phase with the repetition frequency of the laser therefore, can be most easily detected by synchronous demodulation of the received ultrasonic signal. This type of modulation is characteristic to materials of high thermal diffusivity, such as aluminum, in which the temperature gradients and the resulting thermo-elastic stresses quickly disappear after the termination of the laser pulse. Second, there is a much slower “quasi-static” modulation which is an integrated effect of many individual pulses when the laser is turned on for a few seconds or longer therefore can be most easily detected by asynchronous demodulation of the received ultrasonic signal. This type of modulation is characteristic to materials of low thermal diffusivity, such as titanium, in which the temperature gradients and the resulting thermo-

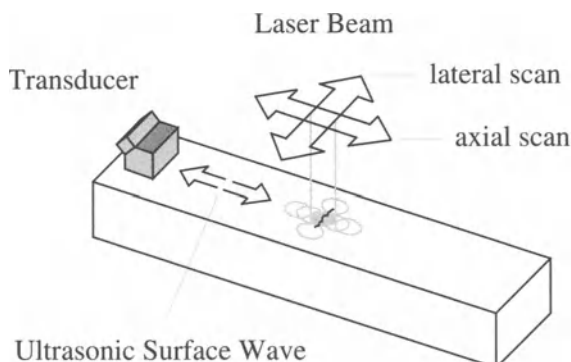


**Fig. 5.** Scanning of the area to be inspected by the pulsed laser beam

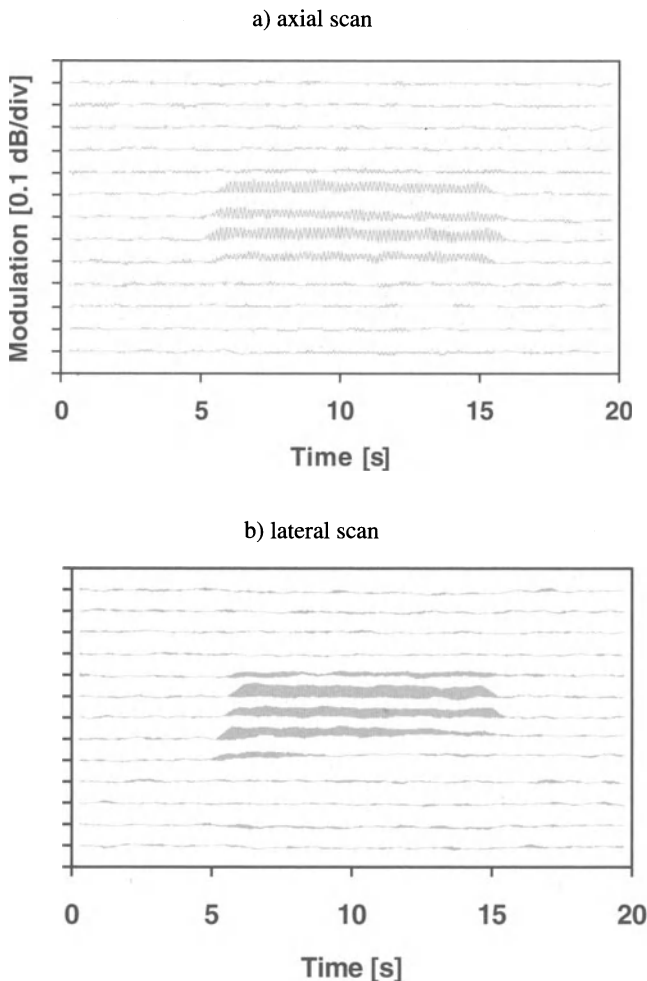


**Fig. 6.** Time dependence of the observed thermo-optical modulation of a small fatigue crack at 13 different axial (a) and radial (b) irradiation positions (2024 Aluminum, 5 MHz, scanning over a 0.600"-by-0.600" area in 0.050"-steps)

elastic stresses linger long after the termination of the individual laser pulses and the modulation is greatly amplified by the cumulative effect of subsequent pulses.

One obvious disadvantage of the suggested thermo-optical modulation method is that either the whole inspected area must be irradiated by sufficiently high intensity laser light in one shot, or, when this is not feasible because of the limited available laser power, a smaller irradiated spot has to be scanned over the interrogated area as shown in Fig. 5. As an example, Fig. 6 shows the time dependence of the observed thermo-optical modulation of a small fatigue crack in aluminum at 13 different axial (a) and radial (b) irradiation positions. During the

20 seconds shown in this figure, the laser was turned on for approximately 10 seconds and fired roughly 500 pulses. The 2024 Aluminum specimen contained a 0.025"-long fatigue crack, the Rayleigh wave inspection was made at 5 MHz, the laser beam diameter was approximately 0.160" and the 0.600"-by-0.600" area was scanned in 0.050"-steps. The previously described dynamic thermo-optical modulation becomes strong only (i) when the laser is on and (ii) when the irradiated spot lies directly over the crack to be detected. Although the fine structure of the modulation cannot be seen at this scale, the periodicity of this so-called dynamic modulation is 50 Hz, i.e., it is synchronous with the pulsing laser.

In theory, the dynamic thermo-optical technique should provide increased sensitivity over the conventional ultrasonic flaw detection approach in titanium alloys just as well as in aluminum. The actual sensitivity of the technique, however, depends on a great variety of material parameters, which should be all considered carefully and incorporated into the optimization of the procedure. Table 1 lists the relevant material properties of Aluminum alloy 2024 and Titanium alloy Ti-6Al-4V. Due to its low thermal conductivity, the thermal diffusivity is approximately one order of magnitude lower in Ti-6Al-4V than in 2024Al, which increases the optically induced temperature gradients since the heat cannot spread out in the short time of illumination in titanium as much as it does in aluminum. Other parameters, however, favor aluminum. For example, the thermal expansion coefficient is higher and the stiffness is lower in aluminum. In addition to the significant differences in mechanical and thermal properties, there is a substantial difference between aluminum and titanium in optical absorption as shown in Fig. 7.

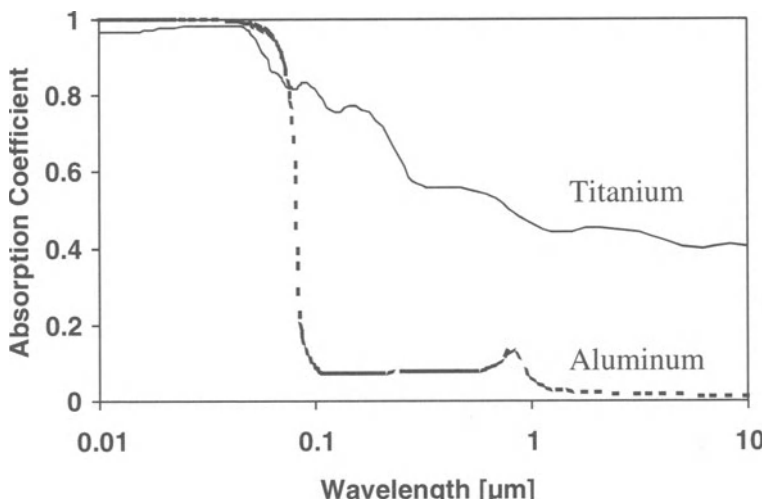


Fig. 7. Optical absorption spectra for aluminum and titanium

In the near infrared region, where the Nd:YAG pulsed laser operates ( $\approx 1.06 \mu\text{m}$ ), the optical absorption coefficient in titanium is as much as 50% versus the meager 5% in aluminum, i.e., the same irradiating power produces one order of magnitude stronger heating in the specimen. Unfortunately, the most crucial parameter, namely the interfacial stiffness of typical fatigue cracks is the most difficult to quantify. Generally, the tips of small fatigue cracks in ductile aluminum alloys are tightly closed and consequently significant crack closure can be achieved at modest compressive stress levels. In comparison, the tips of even relatively small fatigue cracks in less ductile titanium alloys can be fairly open and consequently significant crack closure requires very high compressive stress levels. In conclusion, a direct comparison between Al 2024 and Ti-6Al-4V is all but impossible and additional experiments are necessary to establish the feasibility of the thermo-optical modulation technique in Ti-6Al-4V and other titanium alloys.

**Table 1.** Material Properties of Aluminum Alloy 2024 and Titanium Alloy Ti-6Al-4V.

	2024 Aluminum	Ti-6Al-4V
thermal expansion coefficient[ $10^{-6}/^\circ\text{C}$ ]	23	9.5
thermal conductivity[ $\text{W} / \text{m}^\circ\text{C}$ ]	190	7.3
specific heat[ $\text{J} / \text{kg}^\circ\text{C}$ ]	895	565
density[ $\text{kg} / \text{m}^3$ ]	2,710	4,430
thermal diffusivity [ $10^{-6} \text{ m}^2 / \text{s}$ ]	78	2.9
Young's modulus[ $10^9 \text{ N} / \text{m}^2$ ]	72	114
Poisson's ratio	0.33	0.33

Figure 8 shows the temperature and normal stress distributions in a plane normal to the surface produced by a 4-mm-diameter Gaussian laser beam in titanium at two different delays after the incidence of a 150- $\mu\text{s}$ -long infrared laser pulse of 300 mJ total energy [21]. The surface region is in compression (light area with negative normal stress), while below the surface there is a region of somewhat weaker tension (dark area with positive normal stress). It should be mentioned that in aluminum both the temperature and stress disturbances are completely gone in 10 ms, therefore there is no cumulative effect to speak of.

Since the modulation does not entirely disappear by the beginning of the next laser pulse, a very significant cumulative effect occurs in titanium. Figure 9 shows a typical thermo-optical modulation pattern observed in titanium. The laser is turned on for approximately 8 seconds and then the specimen is left to cool for as long as 2 minutes to eliminate all thermal stresses. The repetition frequency of the ultrasonic pulse was increased to 500 Hz in order to better resolve the details of the modulation pattern which is very complex compared to the case of aluminum where the modulation is mainly due to synchronous dynamic crack-closure. The

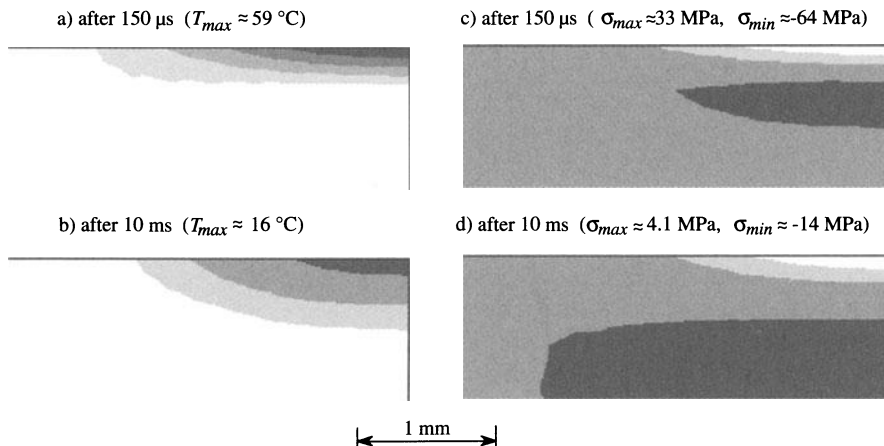


**Fig. 8.** Temperature distribution produced by a 4-mm-diameter Gaussian laser beam 150  $\mu\text{s}$  (a) and 10 ms (b) after the start of a 150- $\mu\text{s}$ -long infrared laser pulse of 300 mJ total energy in titanium. Optically induced normal stress distributions in the plane normal to the surface for the same delay times (c and d)

overall pattern can be separated into a slow quasi-static and a synchronous dynamic modulation. However, the superposition of the two effects is highly nonlinear as indicated by the continuously changing amplitude of the dynamic modulation during laser irradiation. The rather complex quasi-static modulation dominates the observed long-term behavior (Fig. 9a) and it lingers long after the termination of the laser irradiation. During laser illumination (Fig. 9b) the periodic dynamic modulation is also detectable but it disappears immediately when the laser is turned off.

The role of different physical mechanisms in the evolution of the rather complex thermo-optical modulation pattern shown in Fig. 9 have been investigated by theoretical, numerical, and experimental means. Finite element simulations indicated that in low-diffusivity titanium alloys three typical situations can occur. First, shallow crack tips (less than 0.010" deep) are always in compression, which tends to reduce the ultrasonic scattering via crack closure. Second, crack tips at moderate depth (between 0.010" and 0.040") are initially in tension, but subsequently go into compression when the local temperature starts to rise as the thermal energy diffuses to larger depths. Finally, deep crack tips (more than 0.040") are always in tension, which tends to increase the ultrasonic scattering via crack opening.

The above described behavior is further complicated by the fact that crack opening and closure usually, but not always, increases and decreases, respectively, the detected ultrasonic echo. The non-monotonous dependence of the ultrasonic echo on the effective crack length is mainly due to two different effects. First, the

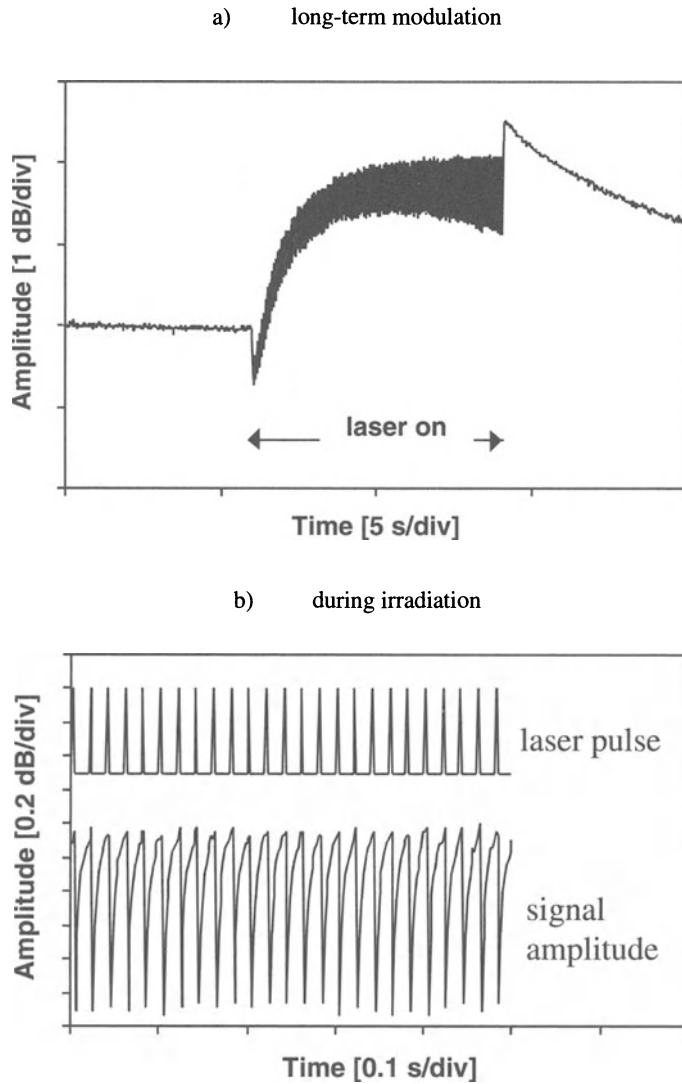


**Fig. 9.** Typical thermo-optical modulation in titanium. The complex quasi-static modulation dominates the long-term behavior (*top*) while the periodic dynamic modulation is detectable only during laser illumination (*bottom*)

Rayleigh wave reflection coefficient of cracks deeper than approximately 20% of the acoustic wavelength exhibits very significant oscillations as the depth-to-wavelength ratio increases [22]. In Ti-6Al-4V at 5 MHz, this non-monotonous behavior occurs above 0.005" crack depth, i.e., in most cases of practical importance. Second, the detected ultrasonic signal containing the hidden echo

from the fatigue crack is usually the result of either constructive or destructive interference. Fatigue cracks are often hidden by larger scattering from the material inhomogeneity or geometrical irregularity, in our case the artificial starter notch, which produced the stress concentration that in turn led to crack initiation. Because of this and additional interference with grain scattering, even an increasing fatigue crack signal can very well reduce the detected ultrasonic echo if phase cancellation occurs. Under these conditions, it is clear that the magnitude of the observed thermo-optical modulation can be exploited for detection of otherwise hidden fatigue cracks, but quantitative evaluation of the measured modulation in terms of crack size or other crack parameters is all but impossible.

## 6.4 Applications

### 6.4.1 Dynamic Thermo-Optical Modulation in Al-2024

The dynamic modulation of the measured signal is caused by the alternating variation of the detected ultrasonic echo between cold and hot states. This modulation is partly caused by direct thermal modulation of the sound velocity in the material and partly by thermal stresses via crack-closure. It has been demonstrated that in aluminum alloys the modulation is mainly due to the second effect, therefore it can be exploited for discriminating fatigue cracks against other artifacts which are much less affected by thermal stresses [18].

In order to optimize the sensitivity of the thermo-optical modulation technique, we have to maximize the temperature gradients causing the thermal stress. This can be achieved by either increasing the total optical power or by reducing the length of the irradiation period, but certain limitations have to be complied with in order to avoid permanent surface damage on the specimen and direct ultrasonic surface wave generation by the induced thermal stresses. We have used a long-pulse Brilliant Nd:YAG laser without Q-switching that produces 120- $\mu$ s-long pulses of 360-mJ total energy at 1.06- $\mu$ m near-infrared wavelength at 50 Hz repetition frequency. The detected ultrasonic signal was analyzed by a programmable digital peak detector that assures excellent accuracy and repeatability. The ultrasonic pulser is synchronized to the laser to produce two pulses for each irradiation; one directly following the laser pulse with an adjustable delay of up to 300  $\mu$ s and the other delayed by a fixed amount of 10 ms. The first pulse interrogates the crack when it is “hot” while the second one provides a “cold” reference. Figure 10 shows the sequential diagram of the synchronized optical and ultrasonic pulses. Only the hot ultrasonic pulse is shown which reaches the location of inspection when the compressive thermal stress is maximum. The cold ultrasonic pulse is launched 10 ms later when the compressive stress has already diminished and it is not shown in Fig. 10. It should be mentioned that the actual delay between the start of the laser

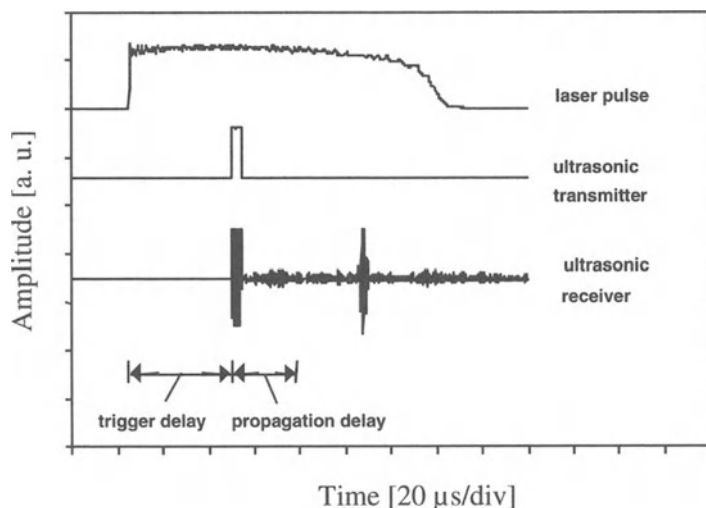


**Fig. 10.** Sequential diagram of the synchronized optical and ultrasonic pulses

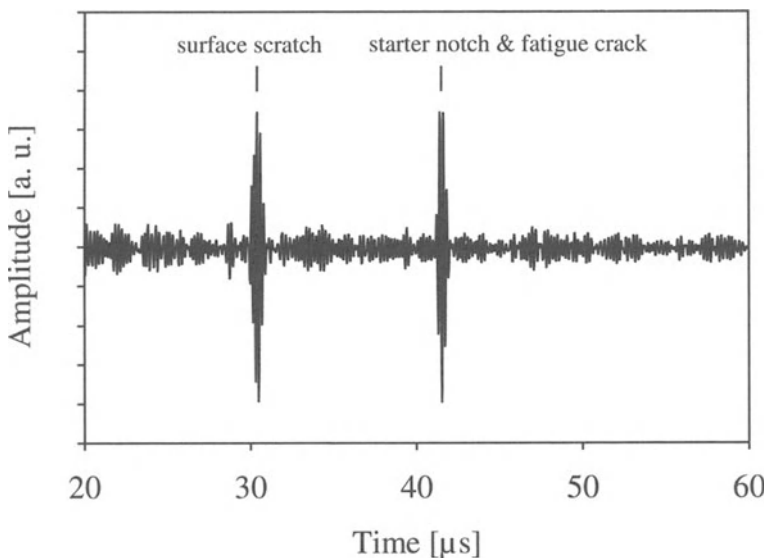


**Fig. 11.** The backscattered ultrasonic echo received from a specimen which contains a starter notch that is hiding a small fatigue crack of 1.7 mm length and an additional surface scratch made after fatigue cycling

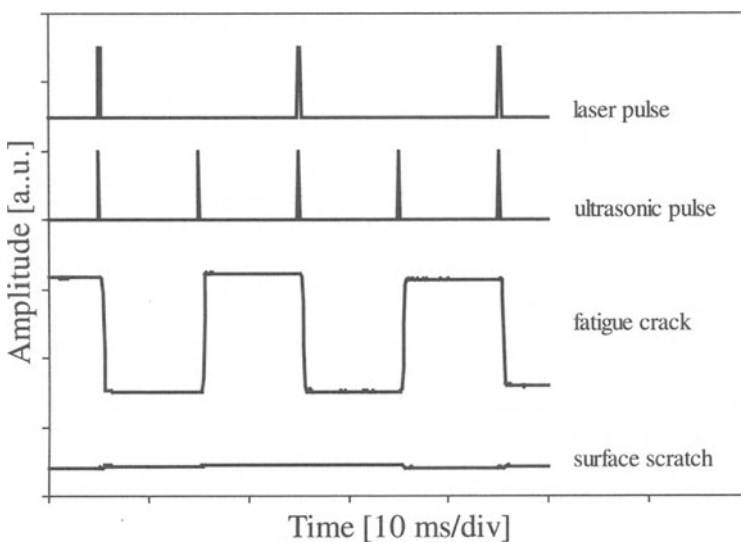


**Fig. 12.** Identification of a fatigue crack by laser-induced crack-closure

irradiation and the arrival of the ultrasonic pulse at the location of inspection includes not only the adjustable synchronization delay between the laser and the ultrasonic transmitter but also the approximately 20  $\mu$ s one-way propagation delay from the transducer to the crack.

Figure 11 shows the backscattered ultrasonic echo received from a specimen which contains a starter notch that is hiding a small fatigue crack and an additional surface scratch made after the fatigue cycling. This measurement was taken at 5 MHz, when both the real and artifact signals were approximately 18 dB above the grain noise. Our main goal here is to demonstrate the ability of the thermo-optical crack-closure technique to unequivocally distinguish real fatigue cracks from comparable artifacts. From this figure, we can see that the echo reflected from the surface scratch has almost the same amplitude as the one from the fatigue crack and thus may cause false alarms in conventional inspection. Furthermore, the fatigue crack is partially hidden by the edm starter notch itself that is necessary to initiate the crack. It is rather typical that the geometrical feature or material imperfection that produces the stress concentration, which will ultimately start the fatigue crack, itself produces an ultrasonic echo that is difficult to distinguish from the initially weaker scattering of the fatigue crack.

By applying dynamic crack-closure modulation via pulsed-laser irradiation, the fatigue crack can be identified very easily. Figure 12 shows the different

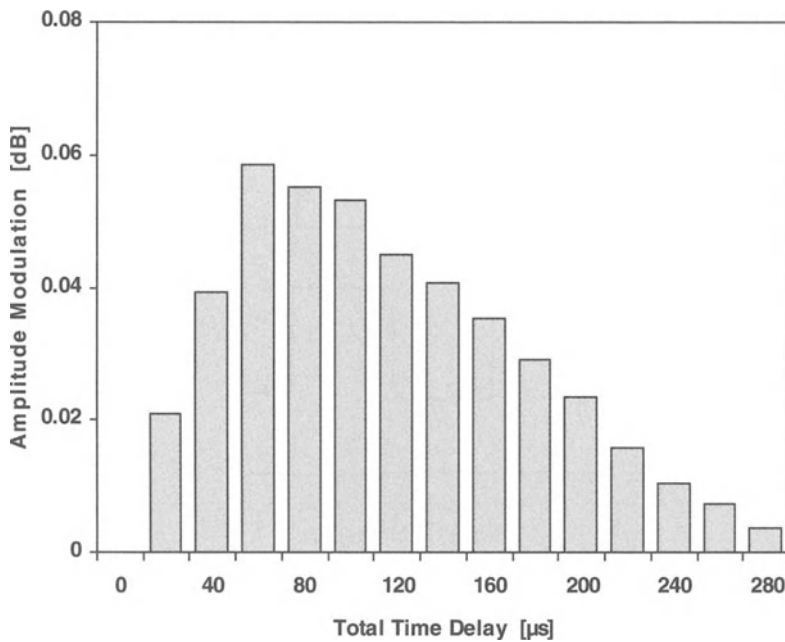


**Fig. 13.** Measured amplitude modulation from the fatigue crack of 1.7 mm length as a function of synchronization delay

modulation levels for the surface scratch and the fatigue crack. The two traces on the top show that every second ultrasonic signal reaches the inspected area just after laser irradiation, i.e., when the area is hot and any possible fatigue crack is slightly closed by the resulting compressive thermal stress. The lower two traces show the output of the digital sample-hold unit that measures the peak of the ultrasonic backreflection for every ultrasonic transmission. Clearly, the reflections from the hot fatigue crack are lower than those from the cold one. This strong thermo-optical modulation of the ultrasonic signal is uniquely characteristic to partially closed fatigue cracks. In comparison, the modulation associated with the surface scratch is negligible since it lacks those characteristic features that render a real fatigue crack particularly sensitive to dynamic crack-closure.

Figure 13 shows the measured amplitude modulation from the same specimen as a function of synchronization delay. Strong crack-closure occurs between 40 and 160  $\mu$ s after the beginning of the laser irradiation. The maximum modulation is approximately 0.06 dB, roughly six times higher than the 0.01-dB standard deviation of individual amplitude measurements done by our digital data acquisition and processing system. Since both hot and cold measurements are continuously refreshed at the 50-Hz repetition frequency of the pulsed laser, the

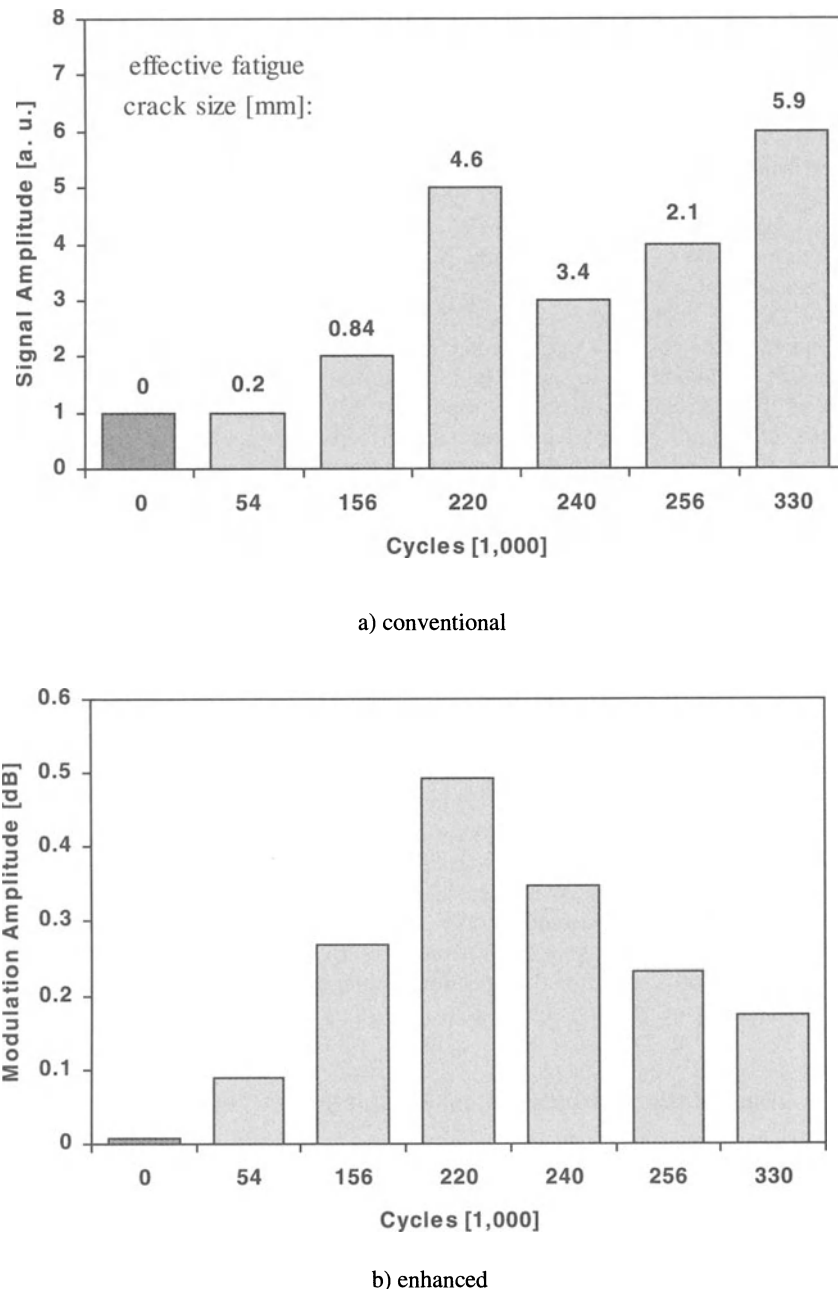


**Fig. 14.** The measured flaw signal (a) and modulation (b) amplitudes in a reference specimen containing an intact edm starter notch only (darker first column) and six fatigue-damaged Al-2024 specimens at 2.25 MHz

accuracy of the phase-locked synchronous demodulator over a 1-s integration time is as good as 0.0015 dB. It should be mentioned that these measurements were done at 5 MHz and the crack-closure modulation is approximately 60% higher at 2.25 MHz. Furthermore, the modulation can be easily increased by a factor of four via blackening the surface with a permanent marker, which increases the otherwise rather low absorption of laser power in aluminum. Measurements were carried out on a series of specimens to establish the threshold sensitivity of the thermo-optical modulation technique in aluminum at 2.25 MHz. Figure 14a shows the measured flaw signal amplitude in an intact reference specimen and six fatigue-damaged specimens. The Al-2024 specimens were fatigued at a maximum load of 28.6 ksi, load ratio of 0.9, and frequency of 29 Hz. For each specimen we also indicated the effective fatigue crack size, which was calculated by subtracting the length of the edm starter notch (0.43 mm) from the total length of the fatigue crack on the surface as measured by optical microscopy. Generally, the higher the number of fatigue cycles, the higher the effective fatigue crack size and the detected flaw signal amplitude, however the relationship is somewhat random. Slightly better, although still less than perfect, correlation can be observed between the actual crack size and the amplitude of the scattered flaw signal. The most important conclusion one can draw from these results is that the smallest 0.2-mm-long fatigue crack does not perceptibly increase the flaw signal compared to the 0.43-mm-long edm notch and would certainly remain undetected by conventional ultrasonic inspection.

Figure 14b shows the measured modulation amplitude in the same specimens. Owing to the selective sensitivity of the thermo-optical crack-closure technique to partially closed fatigue cracks, even the smallest fatigue crack can be easily distinguished from the intact edm notch since it produces one order of magnitude larger modulation. As one would expect, after going through a maximum, the modulation amplitude actually decreases for large cracks since the relatively weak thermal stresses produced by laser irradiation are not sufficient to close large, widely open cracks. This is acceptable since our main goal is to improve the detection threshold of ultrasonic inspection so that very small fatigue cracks could be detected shortly after crack nucleation. Larger cracks well above the detection threshold level of conventional inspection techniques can be readily found based on the amplitude of the flaw signal alone.

#### 6.4.2 Quasi-static Thermo-Optical Modulation in Ti-6Al-4V

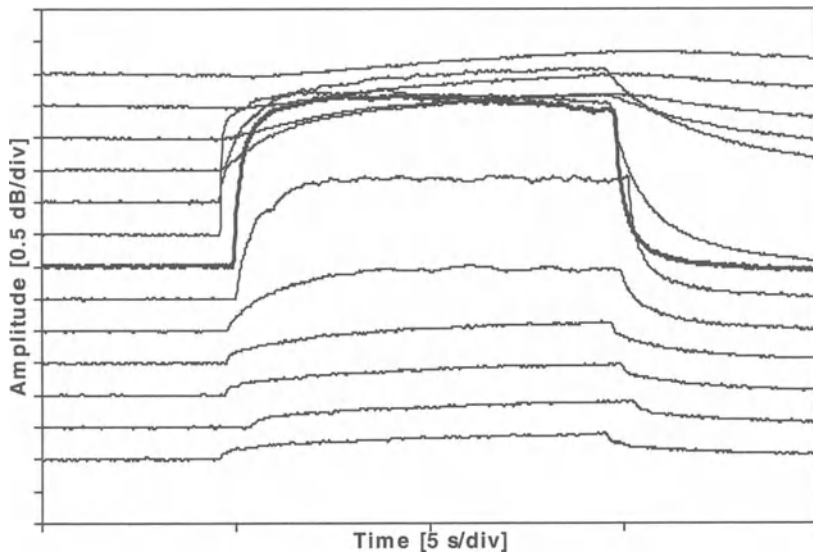
In order to study the thermo-optical modulation in Ti-6Al-4V alloy we prepared a total of 16 specimens. Eight of them ("c1" through "c8") contained starter notches and fatigue cracks between 0.5 mm and 1 mm in length. The other eight ("n1" through "n8") contained only intact starter notches. In the following experimental results, unless otherwise indicated, the center frequency of the Rayleigh wave transducer is 5 MHz, the total time delay between the laser pulse and the arrival of the surface wave at the notch is 130  $\mu$ s, and the repetition rate of the ultrasonic pulser is 100 Hz (twice the repetition rate of the laser). It was found that on the average the magnitude of the dynamic thermo-optical modulation in titanium

specimens is 2.5 times larger from fatigue-damaged edm notches than from intact ones. However, there is a large scatter in the modulation data, therefore the dynamic modulation itself cannot be used to positively distinguish fatigue cracks from artifact signals as it could be done in aluminum. The main reason for this is the relatively large modulation exhibited by intact specimens. The thermo-elastic deformation itself is clearly insufficient to produce closure in 75- $\mu\text{m}$ -wide edm notches, therefore the observed modulation must be directly related to the temperature variation in the specimen. The heated low-velocity spot acts like a lens bending and focusing the transmitted surface wave thereby slightly changing the reflected echo from the scatterer [20]. We used the reflection from a straight normal corner, which is obviously not affected by thermal stresses, to assess the spurious modulation caused by direct temperature variations. When the ultrasonic path between the surface wave transducer and the corner was scanned over in the lateral direction by our laser, we observed as much as 0.3 dB loss in the reflected amplitude.

The overall thermo-optical modulation in titanium is partly due to direct temperature modulation and partly due to thermal stresses. Only the latter can be exploited for enhanced fatigue crack detection, therefore we have to consider possible differences between the two contributions so that they can be distinguished from each other. Such differences include variations in spatial distribution and time-dependence. First, we studied the effect of the relative position of the heated spot with respect to the damage site. It is expected that, when the damaged area is scanned by the pulsed laser beam in the axial direction, the direct temperature effect is asymmetric with respect to the scatterer, i.e., it occurs only when the irradiated spot is between the transducer and the scatterer, but not when it is on the other side of the scatterer. In comparison, the thermal stress induced modulation of partially closed fatigue cracks is expected to be symmetric to the scatterer since the resulting closure is essentially the same regardless whether the thermal expansion occurs on one side of the scatterer or on the other. There is also a substantial difference between the direct temperature and thermal stress effects when the scatterer is scanned over in the lateral direction, i.e., normal to the sound propagation and parallel to the potential crack. In most cases the direct temperature effect is expected to exhibit odd symmetry with respect to the scatterer since bending the wave in opposite directions usually produces opposite changes in the echo amplitude, unless the beam is perfectly aligned, in which case there is a symmetric, but very small modulation [19]. In comparison, the thermal stress induced modulation of partially closed fatigue cracks exhibits even symmetry with respect to the scatterer since the resulting closure is essentially the same regardless whether the thermal expansion occurs at one end of the crack or at the other.

These expectations were qualitatively verified by our experimental results. Figure 15 shows the typical time dependence of the observed thermo-optical modulation from a fatigue crack (a) and an intact edm notch (b) at 13 different axial positions. For simplicity, only the low-frequency quasi-static modulation is shown while the high-frequency dynamic modulation was suppressed by low-pass filtering. The measurements were made at 5 MHz in 1.25-mm-steps over a

a) c8



b) n1

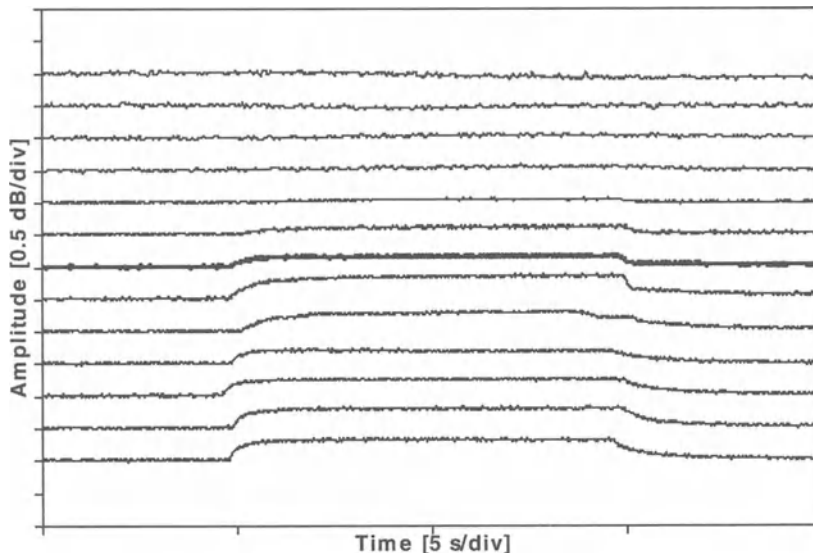


**Fig. 15.** Typical time dependence of the observed thermo-optical modulation from a fatigue crack (a) and an intact edm notch (b) at 13 different axial positions

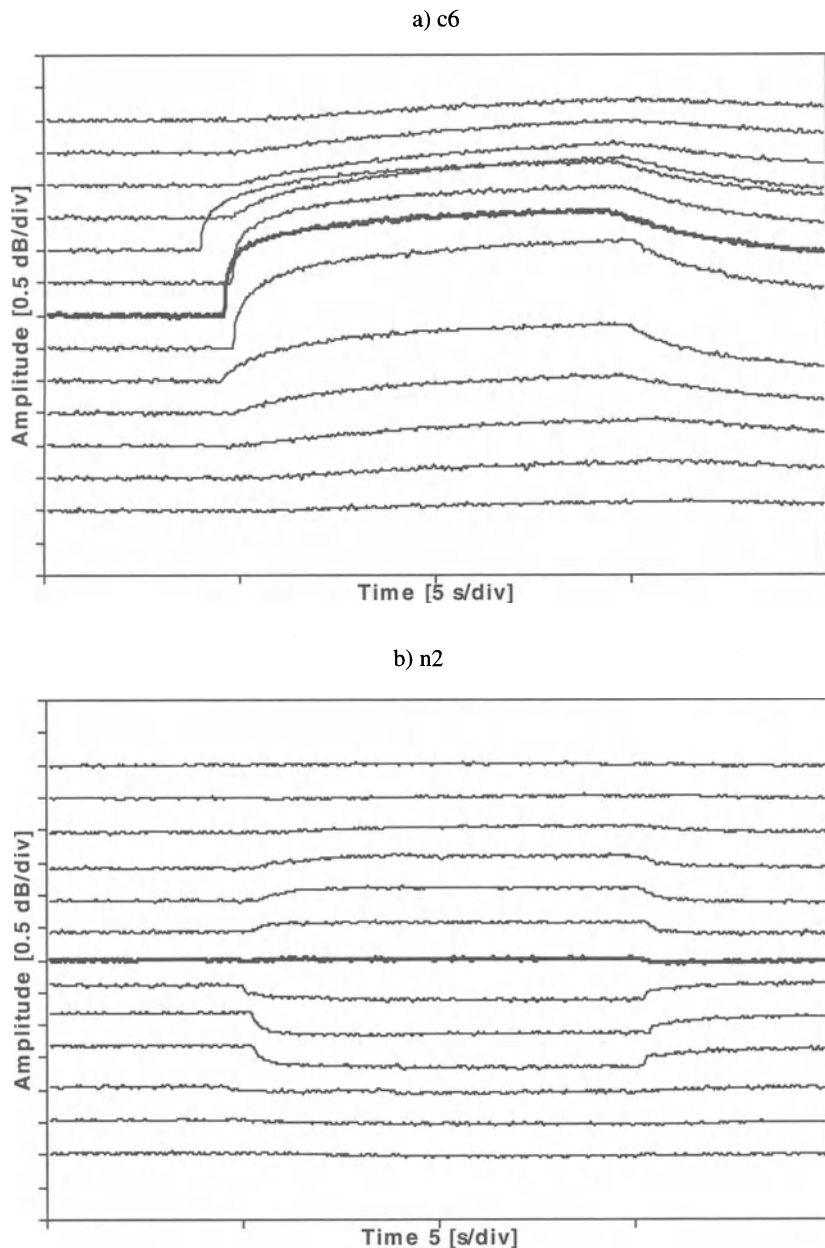


**Fig. 16.** Typical time dependence of the observed thermo-optical modulation from a fatigue crack (a) and an intact edm notch (b) at 13 different lateral positions

scanning range of  $\pm 7.5$  mm relative to the position of the scatterer. In each case the center wave form recorded directly above the scatterer is shown in thicker line for convenience. It is clear that the substantially stronger modulation observed from the fatigue crack is more-or-less symmetric to the scatterer, although it does not completely disappear when the irradiated spot is in front of the crack. On the otherhand, in the case of the intact edm notch the modulation becomes negligible when the irradiated spot is behind the scatterer, which demonstrates that the small modulation observed when the irradiated spot is in front of the scatterer, i.e., in the line of the interrogating surface wave, is entirely due to the direct temperature effect. Figure 16 shows the typical time dependence of the observed thermo-optical modulation from a fatigue crack (a) and an intact edm notch (b) at 13 different lateral positions. The modulation observed from fatigue cracks is not only substantially stronger than the modulation exhibited by undamaged edm notches, but it also reveals different symmetry with respect the scatterer's position. In the case of fatigue cracks the modulation is mainly due to thermal stresses therefore it possesses even symmetry as both ends of the crack exhibit roughly the same closure behavior. In contrast, the modulation produced by an intact edm notch is mainly due to the direct temperature effect therefore it exhibits dominantly odd symmetry. This is because in cases when perceptible modulation occurs the alignment between the scatterer and the interrogating beam is less than perfect consequently bending of the beam in opposite directions results in opposite changes in the scattered amplitude.

Figures 15 and 16 suggest that the symmetry of the observed thermo-optical modulation with respect to the position of the scatterer is strongly dependent on whether the modulation is caused by thermal stresses via crack-closure or directly by the temperature variation via the inherent temperature dependence of the intact material. However, discrimination between small fatigue cracks and other artifacts based on this difference is rendered extremely cumbersome by the need to scan the area by the laser beam after a suspected area has been identified. A simpler approach can be based on the also significant differences between the temporal modulations caused by crack-closure and direct temperature variations. Beside the difference in magnitude, the most obvious difference between the measured modulation from fatigue cracks and intact edm notches is the much slower decay of the modulation from fatigue cracks after terminating the laser irradiation [19]. The reason for this is that the direct temperature effect is a highly localized phenomenon which promptly disappears as the dissipated heat diffuses from the shallow surface layer into the interior of the specimen. In comparison, the thermal stress effect is more of a long-range phenomenon that lingers on as the dissipated heat becomes distributed over a larger depth. In order to demonstrate the sensitivity of this technique for fatigue crack identification, Fig. 17 shows the measured echo amplitudes and quasi-static thermo-optical modulation from eight fatigue cracks and eight intact edm notches at the center of the irradiated spot 2 s after the end of a 10-s-long laser pulse at 5 MHz. The weakest modulation from a fatigue crack (c7) is approximately 13 times larger than the strongest modulation from an intact edm notch (n2). Clearly, no reliable detection can be achieved based on the amplitude of the ultrasonic scattering itself, while the thermo-optical modulation clearly identifies all of the otherwise hidden fatigue cracks.

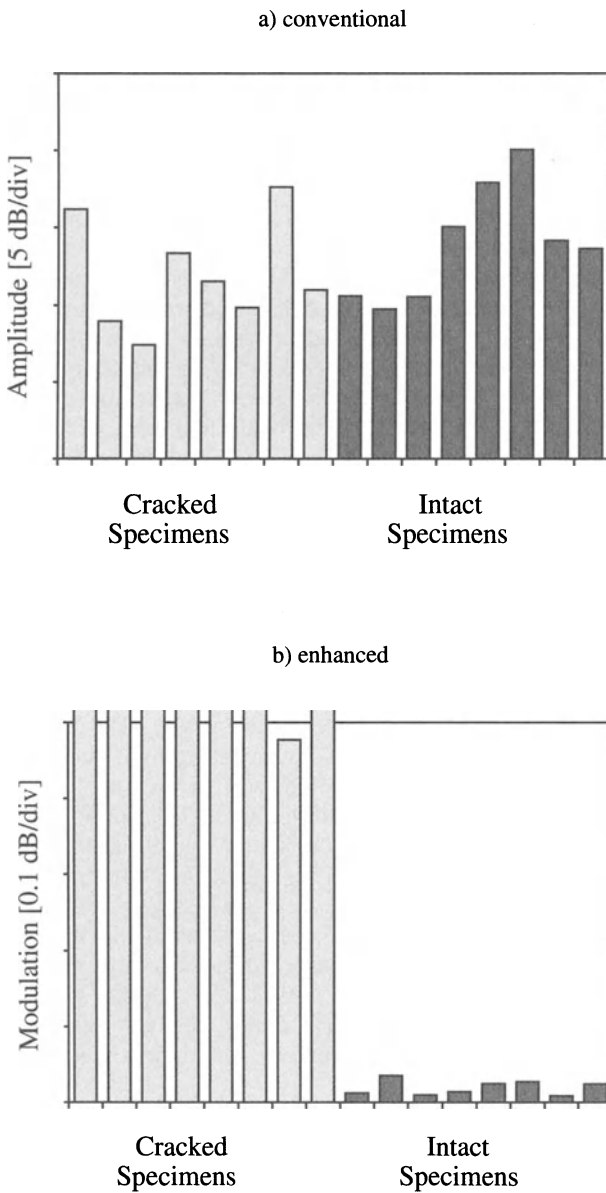


**Fig. 17.** Comparison of the absolute amplitude and thermo-optical modulation from eight cracked and eight intact Ti-6Al-4V specimens

## 6.5 Conclusions

We have investigated the feasibility of unequivocal discrimination of real fatigue cracks from spurious artifact signals produced by other scattering sources. The suggested method is based on the susceptibility of partially closed fatigue cracks to parametric modulation by normal stresses. Direct mechanical deformation of the whole structure is usually not practical except during real-time monitoring of fatigue cycling. Even then, the overall mechanical deformation and vibration of the specimen often causes instability and artifacts might be mistakenly identified as fatigue cracks. Alternatively, localized dynamic thermal stresses produced by laser irradiation can be used to produce crack-closure without adverse deformations and vibrations in the specimen as a whole. Infrared laser irradiation offers an attractive way to produce the necessary compressive stresses as the suspected area can be optically scanned while the ultrasonic scattering is monitored by either conventional contact or more sophisticated laser-ultrasonic means. The resulting transient thermo-elastic deformation perceptibly changes the opening of partially closed surface cracks without affecting other scatterers, such as surface grooves, corrosion pits, coarse grains, etc., that might hide the fatigue crack from ultrasonic detection.

The dynamic thermo-optical modulation method has been shown to be capable of identifying small fatigue cracks in aluminum alloys, where the high thermal diffusivity of the material results in a strong synchronous modulation. Unfortunately, the same technique was found to be much less effective in titanium alloys because of their much lower thermal diffusivity. The high temperature coefficient of the sound velocity in titanium further complicated the problem by introducing a direct temperature modulation even in the case of scatterers that would not exhibit stress induced crack-closure at all. This spurious modulation is caused by direct thermal modulation of the sound velocity in the material rather than thermal stresses via crack-closure. These difficulties prompted us to modify the thermo-optical method and rely on the slow quasi-static modulation for fatigue crack detection instead of the previously used fast dynamic modulation. With this modification we have successfully demonstrated the feasibility of thermo-optical fatigue crack identification in Ti-6Al-4V. We found that the suggested thermo-optical modulation method can increase the detectability of hidden fatigue cracks in both aluminum and titanium alloy specimens by approximately one order of magnitude.

## Acknowledgments

This research was sponsored by the Defense Advanced Research Project Agency (DARPA) Multidisciplinary University Research Initiative (MURI), under Air Force Office of Scientific Research Grant No. F49620-96-1-0442.

## References

1. Gangloff RP, Piascik RS, Dicus DL, Newman JC Jr. (1994) *J Aircraft* 31:720
2. Moukawsher EJ, Grandt AF, Neussl MA (1996) *J Aircraft* 33:1003
3. Sharp PK, Rowlands DE, Clark G (1996) Technical Report DSTO-TR-0366 Defense Science and Technology Organization, Melbourne
4. Scruby CB (1993) In: Achenbach JD (ed) *Evaluation of Materials and Structures by Quantitative Ultrasonics*, Springer Verlag, New York, pp. 223–237
5. Resch MT, Karpur P (1992) In: Mitchell MR, Buck O (eds) *Cyclic Deformation, Fracture and Nondestructive Evaluation of Advanced Materials*. American Society for Testing and Materials, Philadelphia, pp. 323–333
6. Ericsson L, Stepinski T (1993) In: Thompson DO, Chimenti DE (eds) *Review of Progress in Quantitative Nondestructive Evaluation*, Plenum, New York, vol. 12A, pp. 695–702
7. Abbate A, Frankel J, Das P (1996) In: Thompson DO, Chimenti DE (eds) *Review of Progress in Quantitative Nondestructive Evaluation*, Plenum, New York, vol. 15A, pp. 741–748
8. Chiou CP, Schmerr LW, Thompson RB (1993) In: Thompson DO, Chimenti DE (eds) *Review of Progress in Quantitative Nondestructive Evaluation*, Plenum, New York, vol. 12A, pp. 789–795
9. Nagy PB, Blaho G, Adler L (1994) In: Thompson DO, Chimenti DE (eds) *Review of Progress in Quantitative Nondestructive Evaluation*, Plenum, New York, vol. 13B, pp. 1987–1994
10. Buck O, Morris WL, Richardson JM (1978) *Appl Phys Lett* 33:371
11. Morris WL, Buck O, Inman RV (1979) *J Appl Phys* 50:6737
12. Dai W, Kim JY, Rokhlin SI (1999) In: Thompson DO, Chimenti DE (eds) *Review of Progress in Quantitative Nondestructive Evaluation*, Plenum, New York, vol. 18B, pp. 2225–2233
13. Bucher I, Seibold S (1997) In: *Proceedings of the 15th International Modal Analysis Conference* Society for Experimental Mechanics, Bethel, vol. 1, pp. 870–876
14. Nagy PB, Blaho G (1995) In: Thompson DO, Chimenti DE (eds) *Review of Progress in Quantitative Nondestructive Evaluation*, Plenum, New York, vol. 14B, pp. 1979–1986
15. Uchida Y, Ono M, Higo Y, Nunomura S (1998) In: *Progress in Acoustic Emission IV*, Kobe, Japan, pp. 491–498
16. Shen MHH, Chu YC (1992) *Comp Struct* 45:79
17. Makabe C, Kaneshiro H (1996) In: *Localized Damage IV – Computer-aided assessment and control*, Proceedings of the 4th International Conference Computational Mechanics Publications, Billerica, pp. 841–847
18. Xiao H, Nagy PB (1998) *J Appl Phys* 83:7453
19. Yan Z, Nagy PB (2000) *NDT &E International* 33:213
20. Yan Z, Nagy PB (2001) In: Thompson DO, Chimenti DE (eds) *Review of Progress in Quantitative Nondestructive Evaluation*, AIP, New York, vol. 20A, pp. 1650–1657
21. Yan Z, Nagy PB (2002) *Ultrasonics* 40:689.
22. Li ZL, Achenbach JD (1991) *J Appl Mech* 58:688

# **7 Early Detection of Fatigue Damage in Ti-6Al-4V with Nonlinear Acoustics**

S. Sathish, J. Frouin, J.K. Na

## **7.1 Introduction**

Metallic materials undergo fatigue under cyclic mechanical loading. During loading, the microstructure of the material changes continuously. Dislocations build up that lead to the formation of slip bands that appear on the surface of the material. These slip bands act as stress concentrators for the origination of micro-cracks, which can grow under fatigue loading and lead to a catastrophic fracture of the material [1]. In the last few decades, major efforts in life prediction methodology have been based on fracture mechanics. Usually, the predicted crack length under cyclic loading is related to the number of loading cycles. Thus, crack growth rate has been used to predict the life of the material [2,3]. A systematic study of the fracture mechanics of materials has been the main source for life prediction and design of components. Two types of fatigue have been studied in the last few decades; (i) the traditional low cycle fatigue (LCF), in which the applied loads are fairly large and close to yield strength; (ii) high cycle fatigue (HCF), where the applied loads are well below the yield stress in the elastic regime. In LCF, the damage produced per cycle is significantly larger and hence damage is initiated early in the first few cycles of loading. Damage accumulates quickly and drives the material to fail at a low number of cycles. In contrast, under high cycle fatigue (HCF), the damage produced during the first few fatigue cycles is very small, and it takes a significantly longer time to accumulate enough damage to initiate a crack. It is believed that it takes 90% of the life of the material to initiate a crack in HCF loading conditions (for titanium alloys). Once crack initiation occurs, it has been observed that under HCF conditions, rapid crack growth quickly results in catastrophic failure.

Since the rate of crack growth is the critical parameter in failure prediction, it is extremely important to detect the crack at its early stages. Several nondestructive evaluation techniques such as ultrasonics, eddy current, thermographic, X-ray, and dye penetrant [4] have been developed for this purpose. It has been a challenge in the development of NDE techniques to detect cracks that are smaller than 25 to 50  $\mu\text{m}$ . In spite of the need to detect small cracks, not as much attention has been paid to nondestructive techniques to detect changes in material microstructure that lead to crack initiation. At present, only microscopic techniques are used to observe such changes, but these methods are not nondestructive tools. The emphasis of this chapter is to discuss a nondestructive technique based on nonlinear acoustics that can detect changes at the microstructural level during

early stages of fatigue. This nondestructive technique can lead to detection of damage accumulation in the material that leads to the initiation of microcracks.

The following article is organized to present first the state of the art of both linear and nonlinear acoustic techniques used to study microstructural degradation due to fatigue. Second, a three-step experimental approach of measurements with interrupted fatigue, continuous fatigue measurements, and finally local measurements will be discussed. Third, the results of the acoustic experiments will be correlated with measurements of dislocation density on similar samples by transmission electron microscopy (TEM).

## 7.2 Background

### 7.2.1 Linear Acoustic Measurements and Fatigue

Propagation of acoustic waves through a material provides two fundamental material properties, velocity of sound and attenuation in the material. The velocity of sound is related to the elastic modulus and the attenuation to the damping capacity of the material; they can be measured by different techniques [5]. Both elastic modulus and damping are expected to change, as the material is fatigued. Several researchers have used acoustic wave propagation to investigate fatigue in materials [6–9]. An examination of these results for several different materials indicates that the change in the velocity of sound is less than 1% over the entire fatigue life. Since the change in the density of the material during fatigue is insignificant and the velocity is proportional to the square root of the elastic modulus, the elastic modulus is expected to change by about 2%. Thus, to use sound velocity measurement as a tool for fatigue damage characterization, it is necessary to measure the sound velocity with very high precision. From an experimental standpoint, this would require special surface preparation and specialized instrumentation. On the other hand, changes in attenuation are small in the early stages of fatigue and increase by a few percent as final fracture is approached. Although attenuation changes are measurable, correlating with the changes in microstructure can be difficult due to other effects. Attenuation is affected by material absorption, diffraction, and geometric effects.

### 7.2.2 Nonlinear Acoustics in Fatigue Damage Measurement

Nonlinear acoustic measurements were used as early as 1950 to study the nature of interatomic potential in single crystalline materials [10]. In a series of experiments on deformed aluminum single crystals, it was observed that the nonlinear acoustic parameter (NAP),  $\beta$ , was much larger than that due to the lattice [11–15]. To explain the extra contribution to the nonlinear parameter, Suzuki et al. [15] developed a theoretical model based on the interaction of

acoustic waves with dislocations. The dislocations are held or anchored by point defects and other dislocations and vibrate under the influence of a passing acoustic wave. Suzuki et al. [15] extended the Granato-Lucke vibrating string model [16] and showed that by the contribution of dislocation vibration to the nonlinear acoustic behavior of the material, the increase in nonlinearity due to dislocations is much higher than the lattice contribution. Studies by Hikata et al. [14] and theoretical developments by Suzuki et al. [15] have been the starting points for acoustic nonlinearity in the study of material fatigue.

Later, several other researchers [6, 17–24, 34] following similar models extended the use of nonlinear acoustic property to investigate fatigue. As a direct application of acoustic nonlinearity measurement to characterize fatigue, Morris et al. [20] measured the nonlinearity parameter in single crystal aluminum as a function of the number of fatigue loading cycles. It has been observed that the nonlinear acoustic parameter increases as the number of fatigue cycles increased. Morris et al. [17] used a modified version of the Suzuki [15] theory to explain the increase in nonlinearity due to fatigue. Both models are suitable for single crystal materials where the dislocation loop lengths are significantly large. In most polycrystalline materials, the dislocation loop length is very short, and their contribution is significantly reduced.

In a more recent study, Cantrell and Yost [21] investigated the variation of the nonlinear acoustic parameter as a function of fatigue in the polycrystalline aluminum alloy 2024-T4. A series of Al 2024-T4 alloy dogbone samples were cut out from the same stock. Each of them was fatigued to a certain number of cycles. The gauge section was cut from the dogbone sample and the nonlinear acoustic parameter was measured. Nonlinear acoustic parameter measurements showed a large increase as the number of fatigue cycles was increased. A large increase in the nonlinear acoustic parameter wasn't possible to explain [15] with the existing Suzuki et al. model. Cantrell and Yost [19] proposed a new model based on the interaction of acoustic waves with the dislocation dipoles and their contribution to the nonlinear acoustic property. According to this model, the nonlinear acoustic parameter is proportional to the dislocation dipole distance and density. Not only the dislocation dipoles but also the networks and vein structures have been shown to contribute to the total nonlinear acoustic parameter. The total nonlinearity can be evaluated using the rule of mixtures by knowing the dislocation density and the volume fraction of each type of dislocation structure. They obtained a good comparison between experimental measurement and theory in Al 2024-T3 samples.

A similar experimental approach has been used in the study of degradation of steel specimens due to fatigue [21–23, 35]. Most of the experiments that have used the nonlinear acoustic parameter to study fatigue are conducted on specimens obtained from the same bar stock or similar material. It is well known that small variations in microstructure can play an extremely important role in the number of cycles to fracture in fatigue. The assumption that all samples have the same microstructure introduces variability into the fatigue results, which is already known to be loaded with statistically varying parameters. To conduct a more meaningful study, it would be highly advantageous to perform measurements on the same sample from an initial virgin state to fatigue. The measurements on

single specimens would eliminate variability in the results due to geometry, microstructure, and other external conditions. Based on this approach, Nagy [6] has studied nonlinear acoustic properties in the bending fatigue of polymers, composites, and aluminum 7076. In these measurements, a piezoelectric transducer was bonded to the specimen at the position of maximum stress. The amplitude of the reflected signal from the opposite face of the sample was recorded as the bending force was increased. Measurements of linear elastic properties, as well as nonlinearity data, were recorded. The results clearly showed that the linear elastic properties did not show appreciable changes due to fatigue, whereas the nonlinearity increased dramatically. These measurements however, were only qualitative.

Experimental investigations of the linear elastic properties in fatigued metallic samples (aluminum, aluminum alloys, and steel) clearly show that the changes are very small and difficult to attribute to microstructural changes. On the other hand, the nonlinear behavior shows a dramatic increase. This article presents the development of an experimental approach to investigate fatigue damage in Ti-6Al-4V in a systematic way. The approach has been to conduct all tests on a single microstructure and to monitor the change in the nonlinear parameter on the same specimen throughout the fatigue life until fracture. The measurements were preformed on three different levels. In the first stage, measurements of the linear and nonlinear acoustic properties were performed on the same dogbone sample during fatigue test interruptions. Second, an experimental setup was designed to perform in situ measurements on a dogbone sample while it is mounted inside a fatigue test machine. Third, an experimental methodology was developed to examine the changes in acoustic parameters locally so that the accumulated damage along the length of the fractured sample could be examined after fatigue. The fatigue damage in the samples was examined using transmission electron microscopy. The changes in sound velocity, attenuation and the nonlinear acoustic parameter are presented, and the results are discussed with the background of the microstructural changes occurring during fatigue [25, 26].

## 7.3 Methods

### 7.3.1 General Description

In general, nonlinear acoustic measurements are performed by propagating a fundamental frequency acoustic signal through a sample and then measuring the harmonic signals generated by the sample. Nonlinear acoustic measurements at ultrasonic frequencies require significant experimental care at each step. The input fundamental signal should have a very narrow frequency band to eliminate the introduction of other frequency components. This is usually achieved by using single crystal piezoelectric plate transducers ( $\text{LiNbO}_3$ , quartz, etc.) that resonate with a narrowband fundamental frequency. The amplitude of the higher order

harmonic signals generated by the material is inversely proportional to the power of the fundamental harmonic. The amplitude of the harmonic signals is orders of magnitude smaller than the fundamental signal. In the research presented here, we limit the measurements to second harmonic signals. Since the amplitudes are very small, the signals are amplified by a low-noise amplifier. Although, we have developed three different techniques for nonlinear acoustic measurements, the general structure of the instrumentation is similar for all techniques. A tone burst (5 to 10 cycles) signal generated by a signal generator is amplified using a high-power amplifier. The output signal is filtered using a narrowband high-power filter to eliminate any harmonics generated by the amplifier and fed to the piezoelectric transducer bonded to the sample. The signal appearing on the other end of the sample contains both the fundamental and the second harmonic frequency signals. Usually the signal is split into two parts for measuring fundamental and second harmonic frequencies. These signals are filtered with corresponding narrowband filters and amplified using low-noise narrowband amplifiers. The amplitude of the signals is recorded and measured using a digital oscilloscope.

To determine the nonlinear acoustic parameter (relative or absolute), the amplitude of the second harmonic frequency signal ( $A_2$ ) and the amplitude of the fundamental frequency signal ( $A_1$ ) are measured for different input amplitudes. The nonlinear acoustic parameter is determined using the equation [27]

$$\beta = \frac{2}{L} \left( \frac{V_L}{\pi f} \right)^2 \left( \frac{A_2}{A_1^2} \right) , \quad (1)$$

where  $L$  is the length of the sample,  $f$  is the frequency, and  $V_L$  is the longitudinal wave velocity.

We have developed two different methods to detect and measure the amplitude of the fundamental and second harmonic signals through the sample. The capacitive detector method allows determining the absolute acoustic displacements and hence the absolute nonlinearity parameter. The piezoelectric method has been developed for relative measurements.

### 7.3.2 Capacitive Detector Method

The capacitive detector is a simple but unique apparatus capable of measuring absolute displacements of the order of  $10^{-10}$  m [28] that are common in nonlinear acoustic measurements. In principle, the sample forms one plate of a parallel plate capacitor, and a detector button placed a few microns away from the sample face forms the second parallel plate. A longitudinal acoustic wave propagating through the sample produces a sinusoidal variation in the gap spacing. A measure of the voltage across the capacitor will produce a sinusoidal voltage corresponding to the input amplitude. This amplitude can be used to measure the absolute displacement

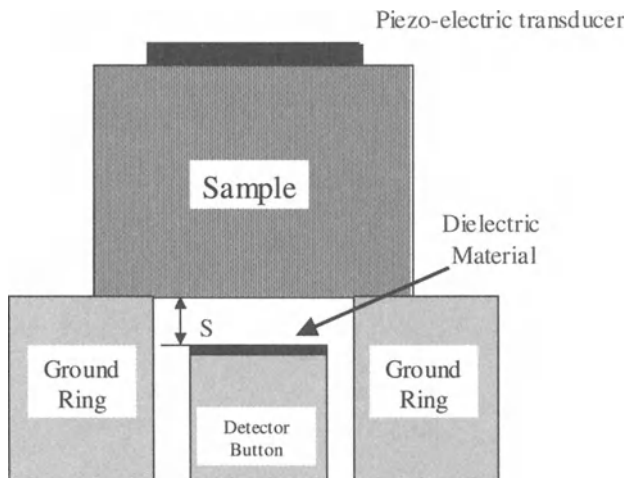


**Fig. 1.** Cross-sectional view of an dielectric capacitive detector

of the acoustic signal. A simplified diagram of the capacitive receiver assembly is shown in Fig.1. The assembly consists of a detecting electrode held in place by a fused silica optical flat so that it is insulated from the outer ground ring, which forms the ground of the electrical system. The detector and ground ring are made optically flat to an accuracy of half a wavelength of light. The detector electrode is positioned at the center of the ground ring and is recessed slightly with respect to the ground ring so that the distance between the surfaces of the detector button and ground ring is of the order of  $10\text{ }\mu\text{m}$ . The sample faces are polished optically flat to the same accuracy. The sample rests on the outer ground ring, and the assembly is aligned carefully so that the sample face and the electrode surface form a parallel-plate capacitor with air as a dielectric. Typical gap spacing between the sample face and the electrode surface is of the order of  $5\text{--}10\text{ }\mu\text{m}$ . A bias voltage of the order of  $100\text{ V}$  is applied to the detector electrode producing a high electric field in the detector gap. When a plane longitudinal wave impinges on the sample face, causing it to vibrate, the gap spacing varies correspondingly, and an alternating voltage is induced between the electrode and the ground. The sample surface, the electrode surface, and the ground ring have to be carefully aligned to avoid shorting. A picture of an assembled capacitive detector is shown in Fig. 2.

If the end of the sample vibrates sinusoidally at an angular frequency  $\omega$  with amplitude  $2A$ , where  $A$  is the acoustical wave amplitude (the factor 2 is due to free surface reflections) in the sample, the gap spacing changes with time according to the relation

$$S = S_0 - 2A \sin(\omega t), \quad (2)$$

where  $S_0$  is the static gap spacing. The capacitance of the detector changes as

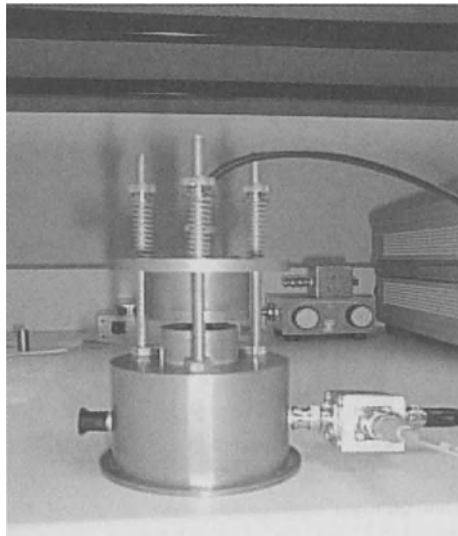


**Fig. 2.** Photograph of the assembled capacitive detector

$$\frac{1}{C} = \frac{1}{C_0} \left( 1 + \frac{2A}{S_0} \sin \omega t \right), \quad (3)$$

$$C_0 = \frac{\epsilon \alpha}{S_0}, \quad (4)$$

where  $C_0$  is the static capacitance of the receiver,  $\alpha$  is the cross sectional area of the receiver, and  $\epsilon$  is the permittivity of the medium (air in this case).

If  $U_b$  is the bias voltage applied to the detector, the equivalent ac voltage induced by the acoustic signal on the detector is given as

$$U = \frac{2A U_b}{S_0}. \quad (5)$$

To determine the absolute amplitude, the capacitive detector is replaced by an equivalent capacitance, and the source of the ultrasonic signal by a substitution current generator. The substitution current generator is adjusted to give the same output from the amplifier as the acoustic signal. Using this approach, the absolute amplitude of the acoustic signal is determined.

To increase the sensitivity to detect small displacements caused by harmonic signals, a thin dielectric layer was used on top of the capacitive detector button. A thin plastic film (approximately 4  $\mu\text{m}$  thick) with a dielectric constant 2.5 was used in this work to provide enhanced sensitivity [36].

One of the characteristics of the capacitive detector is its flat frequency response. Thus, it is very useful for measuring both fundamental and second harmonic frequency signal amplitudes. In our experimental measurements, the signal detected by the capacitive detector is split into two parts. One part is sent through a narrow band-pass filter centered on the fundamental frequency. The other part is sent through another filter centered on the second harmonic frequency. The signals are amplified further by narrowband, low-noise amplifiers, and the amplitudes are measured with a digital oscilloscope. By calibrating the capacitive detector, the absolute amplitudes of both fundamental and second harmonic signals are determined. The absolute amplitude of the second harmonic signal is measured for various absolute amplitudes of the fundamental signal. The absolute nonlinear acoustic parameter is determined using (1).

### 7.3.3 Piezoelectric Method

In the piezoelectric method, ultrasonic signals of the fundamental frequency are generated by a piezoelectric transducer attached to one end of the sample, and a similar second transducer operating at frequency  $2f$  is used to detect the second harmonic signal. To measure the nonlinearity parameter, the amplitude of the fundamental signal after propagating through the sample is necessary. It is not possible to detect the signal at the other end because a  $2f$ -frequency transducer is already attached. For this purpose, we use the transmitting transducer to detect the reflected signal [31]. The nonlinear acoustic parameter is determined using (1). A block diagram of the experimental measurement setup is shown in Fig. 3. Since two piezoelectric transducers are used in this technique, sometimes it is also called the “ $f$ - $2f$ ” method. The transducers used in these measurements have very narrow band frequencies with high  $Q$  values. Since they are only sensitive to their respective frequencies, they further act as filters and thus, improve sensitivity to nonlinear signals.

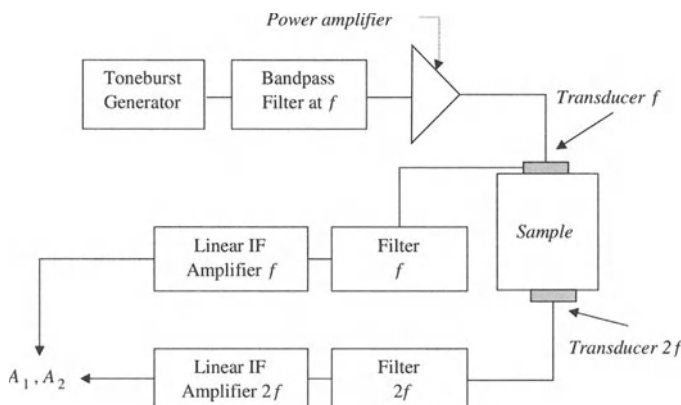


**Fig. 3.** Block diagram of the experimental setup used for nonlinear acoustic measurements using the  $f$ - $2f$  piezoelectric method

In the piezoelectric method, the amplitudes of both fundamental and second harmonic signals are measured as voltages. Hence, the nonlinear acoustic parameter determined is not an absolute parameter, as in the capacitive detector method. Dace et al. [30] have developed a calibration procedure to convert the amplitude voltages into absolute displacements and used it for determining the absolute nonlinear acoustic parameter. Since we are more interested in relative measurements, we have not developed calibration procedures to determine absolute values using this method.

One of the advantages of the piezoelectric method is that it can be adapted to measurement *in situ* during fatigue testing of samples.

#### 7.3.4 In Situ Measurement

Designing an experimental arrangement for nonlinear acoustic measurements during fatigue involves integrating the ultrasonic measurement system, the servo-hydraulic fatigue machine, and an automatic data collection system. One of the difficulties for *in situ* ultrasonic measurement during a fatigue experiment is that the dogbone sample must be placed in grips along with the transducers. The pressure exerted by the grips on the sample should not adversely affect the bonding of the transducer, and the bond should remain intact throughout the measurement. Keeping these facts in mind, we have designed a new transducer holder and grips for the fatigue machine load frame. To reduce the deformation caused by conventional grips, modifications were also made to the grips. Figures 4 and 5 show a digital photograph of the transducer holder and a test specimen with the holders attached, respectively.

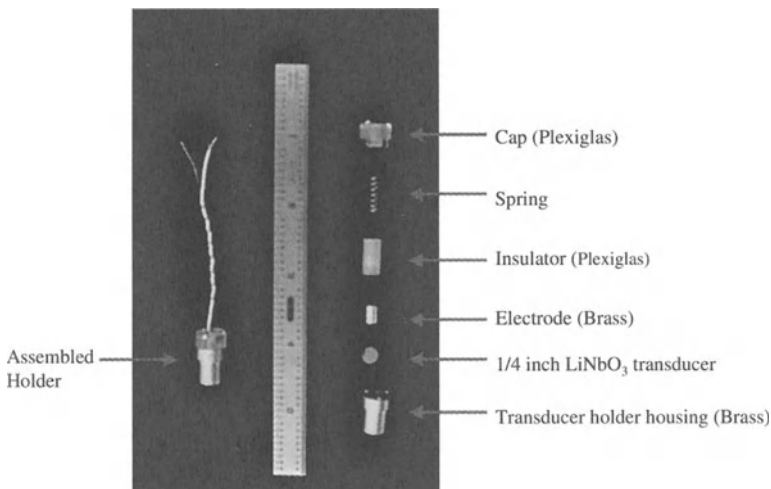


**Fig. 4.** Parts of the transducer assembly going into the grips for continuous fatigue measurements

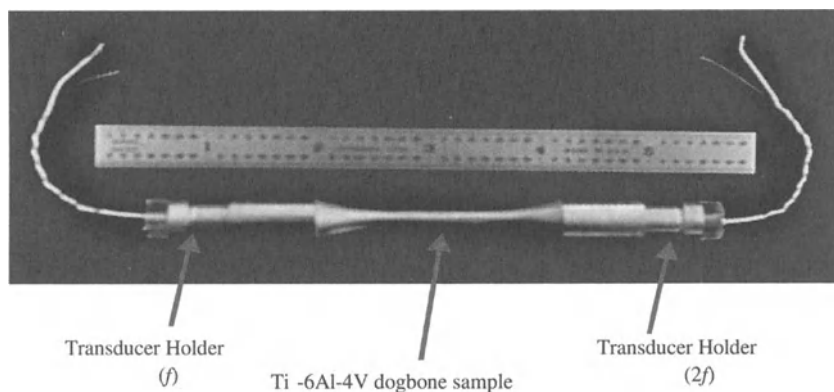


**Fig. 5.** Sample with attached transducers for continuous fatigue measurements

Figure 6 shows a block diagram of the main system components, their interconnections, and subcomponents. The fatigue machine loads the specimen with a certain number of fatigue cycles. The interlocking signal output by the servohydraulic fatigue machine indicates this fatigue state. When the number of cycles in the set reaches the programmed value, the interlocking signal output triggers the start of the measurement. At this point, the fatigue machine sets the load on the specimen to zero. The ultrasonic measurement system becomes

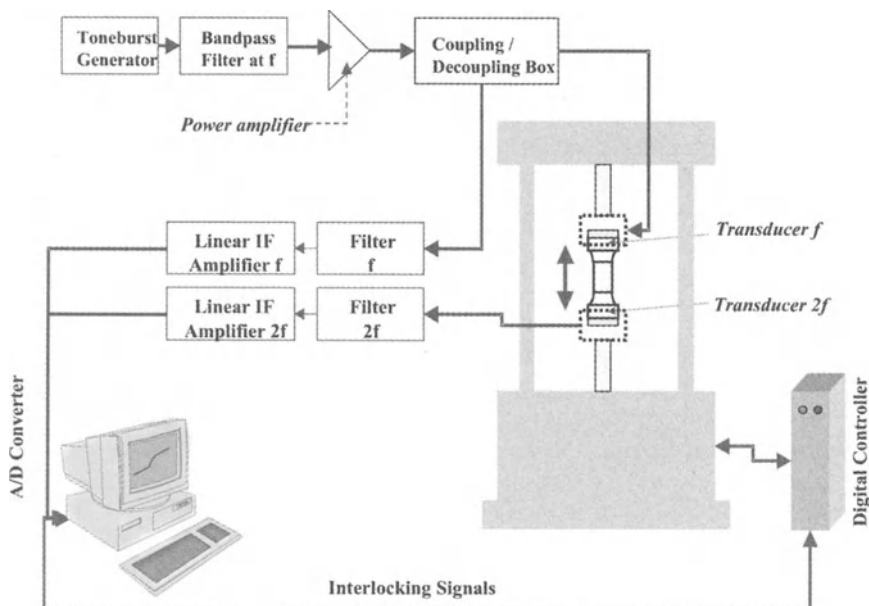


**Fig. 6.** Block diagram of instrumentation used for continuous fatigue measurements

active, the entire waveforms of the transmitted second harmonic signal and the reflected fundamental signal are acquired by the data acquisition system, and the data are stored in the computer. After the measurement is completed, the state of the interlocking signal input changes and initiates the next set of fatigue cycles. This handshaking and data acquisition will continue until the sample fractures.

Software has been developed to evaluate the sound velocity, attenuation, and nonlinear acoustic parameter from the acquired waveform data. The sound velocity is determined by measuring the time elapsed between the first reflected echo and the second reflected echo and the input parameter of the length. A threshold level was used to detect the signals. The amplitude of the reflected fundamental signal and the transmitted second harmonic signal were measured to evaluate the nonlinear acoustic parameter. More extensive details about the entire procedure can be found elsewhere [31–33].

## 7.4 Applications

### 7.4.1 Material and Sample Description

The samples used in this study were obtained from a single plate of Ti-6Al-4V. The titanium alloy has two phases; the alpha (HCP) phase is more than 95% and the beta phase (BCC) is approximately 5%. The average grain size of the material is in the range of 25–50  $\mu\text{m}$  [25]. Cylindrical dogbone specimens (see Fig. 7) were prepared using electroerosion. The specimen surface was low-stress ground to produce a smooth surface finish. For ultrasonic measurements, the specimen faces to which the transducers were attached were polished flat and parallel. The flatness of the polished surface was examined using an optical flat with green light interference fringes. The parallelism was examined using a dial indicator. Lithium niobate 36 y-cut, 6 mm diameter, piezoelectric longitudinal wave transducers were mounted on the specimen surface using Salol (phenyl salicylate).

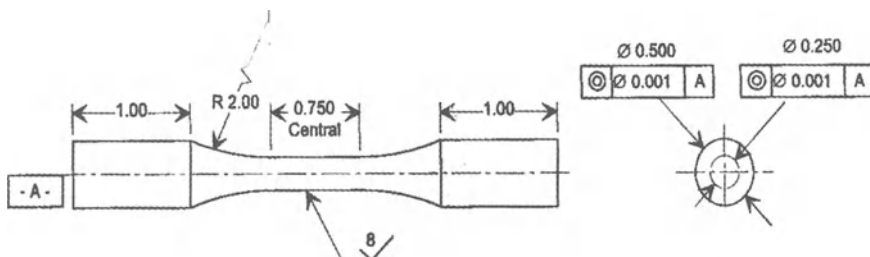


**Fig. 7.** Ti-6Al-4V dogbone specimen

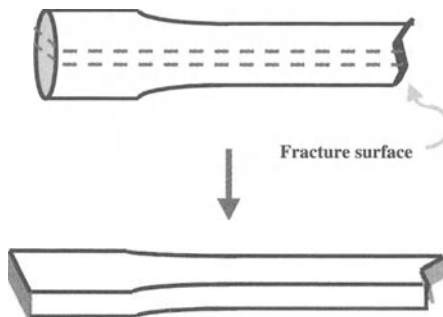


**Fig. 8.** A 1.5-mm thick slice cut from the central region of the fatigue fractured Ti-6Al-4V cylindrical fatigue sample

The specimen used for interrupted and in situ fatigue measurements shown in Fig. 7 had a total length of 90 mm, a grip section diameter of 12.5 mm, and a gauge section diameter of 6.25 mm. The length of the grip section was 25 mm, and the gauge section had a length of 50 mm. The two circular ends on the grip section were polished flat (2 micron variation across the diameter) and parallel to better than a half wavelength of green light. For local measurements, slices from the central section of the fractured samples along the length were obtained (1.5 mm thick) (Fig. 8). The flat faces of the slices were polished flat and parallel for ultrasonic measurements.

#### 7.4.2 Interrupted Fatigue Measurements (Low Cycle Fatigue)

Linear and nonlinear acoustic measurements were performed under interrupted fatigue conditions. The dogbone sample was placed in a fatigue machine and fatigued to a fixed number of cycles. The specimens were fatigued under stress controlled loading with  $R=0.1$  at a frequency of 1 Hz on a servohydraulic load frame. The specimen was removed from the load frame to measure the acoustic parameters at equal intervals of fatigue life. A series of specimens was fatigued until failure under the same conditions, and the average fatigue life was estimated at 35,000 cycles. The sample was taken out of the machine, and using the piezoelectric method, the sound velocity, attenuation, and nonlinear acoustic parameter were measured. After the measurements, the sample was placed back in the fatigue machine and fatigued further. The results of sound velocity, attenuation, and nonlinear acoustic parameter will be presented below. A transducer operating at 10 MHz was used to transmit the signal and to measure the amplitude of the fundamental signal. Another transducer operating at 20 MHz was used to detect the second harmonic signal.

**Linear Acoustic Measurements:  
Attenuation and Longitudinal Sound Velocity**

Attenuation and velocity of longitudinal sound wave were measured at a frequency of 10 MHz at various stages of fatigue. The results of the variation of attenuation for different stages of fatigue are shown in Fig. 9. The error in the measurement is 0.5 dB/cm (standard deviation). It is clear from the measurements that the attenuation increases significantly in the initial stages of fatigue. It shows a further increase up to about 50% until the fatigue life reaches 20% of the entire

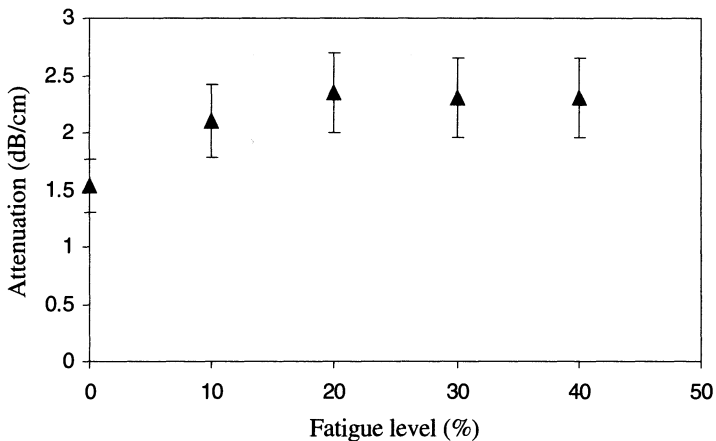


**Fig. 9.** Attenuation as a function of fatigue level for Ti-6Al-4V with a duplex microstructure at 10 MHz frequency

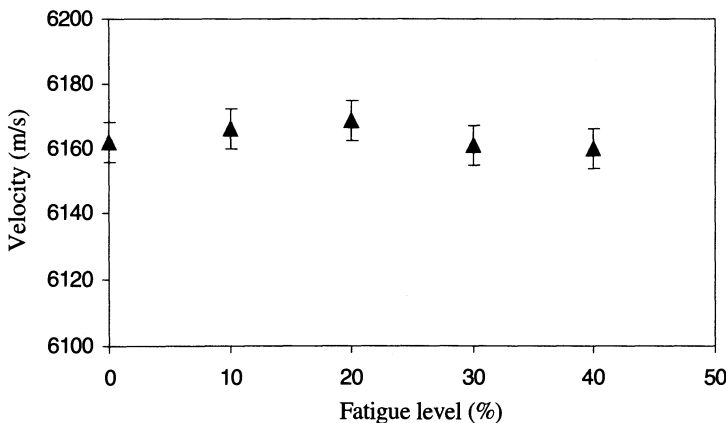


**Fig. 10.** Longitudinal velocity of sound as a function of fatigue level for a Ti-6Al-4V

lifetime and then remains fairly constant up to 40% of lifetime. The initial increase of 50% is quite significant, however, it is less sensitive to the fatigue process beyond 20% of the fatigue life.

The longitudinal velocity changes for different stages of fatigue are shown in Fig. 10. It is observed that the longitudinal velocity of sound has a measurable change in the beginning of the fatigue process. As the fatigue process continues, there is an indication of reduction in the sound velocity beyond 20% of the fatigue lifetime. During the processes of fatigue, there may be a small increase in the specimen length. For an accurate determination of the velocity of sound, it is necessary to incorporate the changes in the specimen length. Since length changes were not monitored during fatigue, no attempt has been made to correct the sound velocity changes.

### **Nonlinear Acoustic Measurements**

Variation in the amplitude of the second harmonic signal, as the amplitude of the fundamental signal is changed, is used to measure the nonlinear acoustic behavior in the material. Figure 11 shows a plot of the variation of the amplitude of the second harmonic signal as a function of the square of the fundamental signal at each stage of fatigue. At each fatigue level, the curve is a straight line, and the slope is a measure of acoustic nonlinearity. The changes in the slope for different fatigue levels are shown in Fig. 12. As the material is fatigued, the amplitude of the second harmonic signal increases. The slope determined by  $U_2$  versus  $U_1^2$

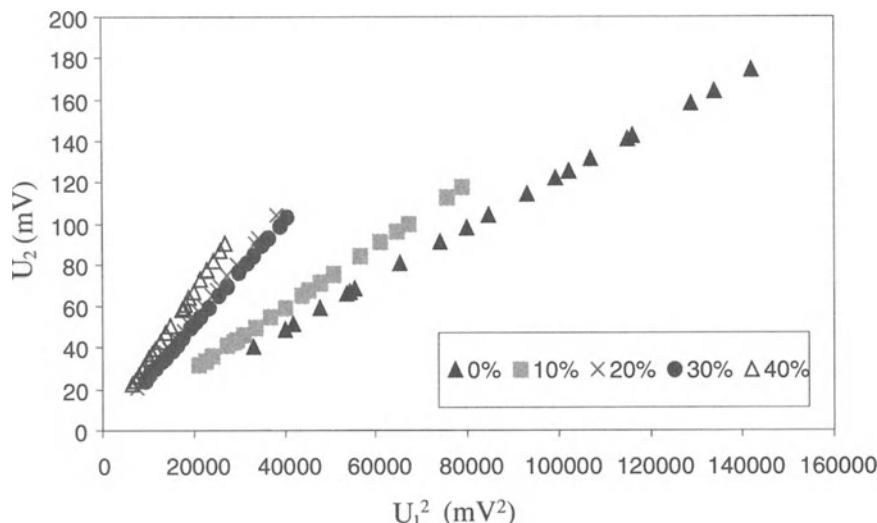


**Fig. 11.** Amplitude of the second harmonic signal versus the square of the fundamental signal for various stages of fatigue in Ti-6Al-4V

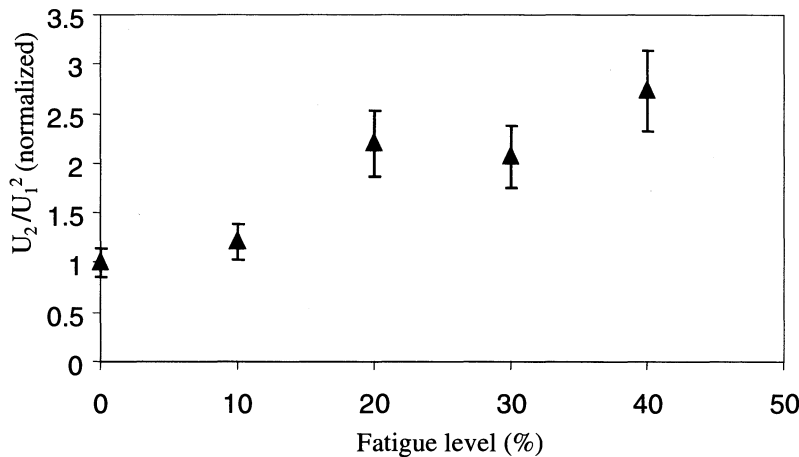


**Fig. 12.** The amplitude ratio  $U_2/U_1^2$  of acoustic signals (normalized to the value for the virgin specimen) as a function of fatigue level for Ti-6Al-4V

shows a significant change in the material during the process of fatigue. As the material is fatigued, the amplitude of the second harmonic signal increases to give a steeper slope. In these measurements,  $U_1$  and  $U_2$  are measured in terms of voltages rather than absolute displacements. Figure 12 shows an approximately 180% increase in the amplitude ratio during the 40% increase in fatigue life. There is an indication of continuous increase in its value, as the fatigue level increases beyond 40% of the lifetime. This result is in contrast with the results of attenuation and elastic constant. For the latter case, the majority of the change occurred before the fatigue lifetime reached 20%; however, the amplitude of the second harmonic signal keeps growing up to 40% of the life, and probably it continues the trend all the way to the fracture point.

An increase of 180% in the amplitude ratio  $U_2/U_1^2$  is a substantial change. The second harmonic signal generated during the fatigue process is sensitive to the early stage of the process. This indicates that it is very sensitive to microstructural changes in the material [31, 32].

#### 7.4.3 In Situ Measurements

The results of acoustic measurements made on interrupted fatigue test specimens showed that the acoustic nonlinearity increases significantly as the fatigue damage progresses. These measurements are tedious, however, because after each step in fatigue cycles, the specimen must be removed from the test machine for the acoustic measurements, then replaced for continued cycling. The time required for each measurement makes acquiring data over a small number of fatigue cycles prohibitive. Moreover, acoustics must be measured after fixed stages of fatigue. A

continuous measuring capability would allow monitoring the fatigue behavior after each cycle or at a fixed number of cycles.

In the continuous fatigue measurements, the sample was subjected to cyclic loading at the frequency of 1 Hz under loading conditions of  $\sigma_{\max} = 850$  MPa and  $R = 0.1$ . The ultrasonic velocity and nonlinear acoustic parameter were measured at zero loads on the sample at an interval of 100 cycles of fatigue.

### **Longitudinal Sound Velocity and Nonlinear Acoustic Parameter**

The changes in the longitudinal sound velocity as a function of fatigue cycles are shown in Fig. 13. It can be observed that the change in the longitudinal sound velocity over the entire fatigue life of the sample is less than 1%. These changes are similar to the results observed in the interrupted measurements.

The amplitude measurements were used to examine the nonlinear acoustic parameter variation. Since the measurements are voltages rather than displacements, the absolute parameter was not determined. The emphasis of the measurements is to investigate the changes rather than absolute values. Thus, the estimated values are normalized to the initial nonlinear acoustic parameter in the virgin state of the sample. The variation in the normalized nonlinear acoustic parameter ( $\Delta\beta/\beta_0$ ) during the fatigue of the same sample is shown in Fig. 14. The variations in the normalized nonlinear acoustic parameter over the entire life of the material can be generally separated into three regions, and the following inferences can be drawn [31, 32]:

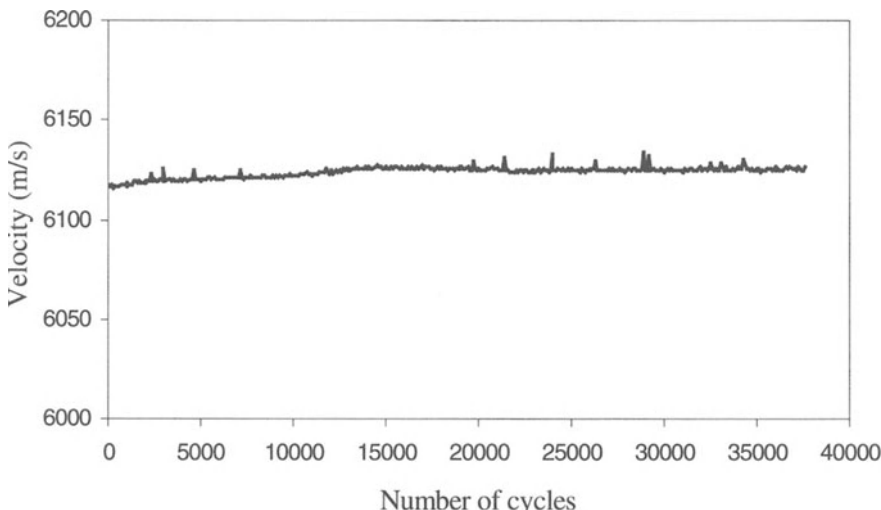


**Fig. 13.** Ultrasonic sound velocity as a function of the number of cycles monitored in real-time under LCF1 fatigue test condition

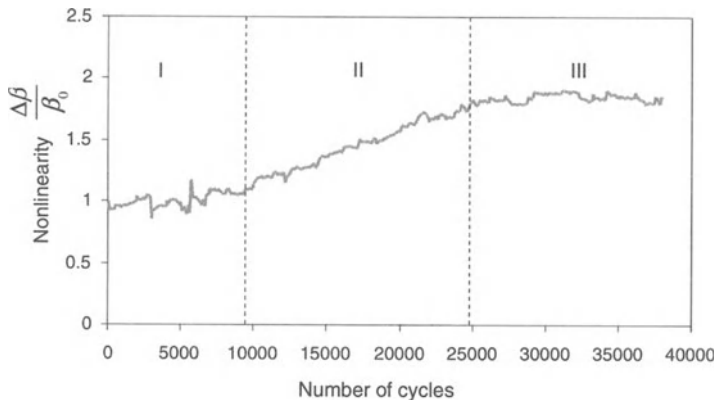


**Fig. 14.** Normalized nonlinear parameter as a function of the number of cycles monitored in real-time under LCF1 fatigue test condition

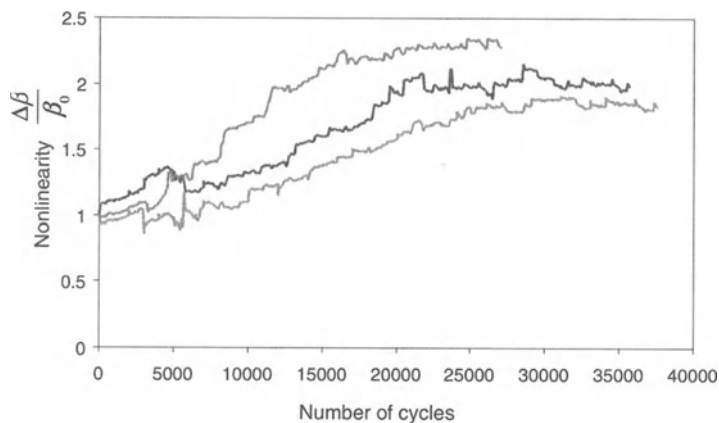


**Fig. 15.** Normalized nonlinear parameter for three different specimens as a function of the number of cycles monitored in real-time under LCF1 fatigue test condition

1. During the early stages of fatigue (10–20% of fatigue life) (region I), the parameter increases, on average, by about 30%. The parameter exhibits significant scatter in this region.
2. After this first region, the parameter increases linearly for about 40 to 50% of fatigue life cycles (region II). At the end of this period, the total increase in material nonlinearity from the virgin state corresponds to about 100%.
3. At about 50 to 60% of the fatigue life and up to the final fracture, the parameter exhibits a plateau (region III).

Measurements on several specimens under the same fatigue conditions showed a similar trend indicating consistency and the possibility of a “signature” in the relation between fatigue and acoustic nonlinearity. Figure 15 shows the material nonlinearity as a function of fatigue cycles for different specimens. The general trend remains the same for all specimens tested, and only regions I, II, and III that are characteristic of the curve, change from specimen to specimen.

The results obtained from the continuous measurements are consistent with the observations of the interrupted measurements. The average increase in the nonlinear acoustic parameter in both measurements is of the order of 150–180%.

#### **7.4.4 Discussion of Interrupted and Continuous Measurement Results**

The results for longitudinal sound velocity obtained from both the interrupted and the continuous measurements show that the change in the velocity of sound over the entire fatigue life is less than 2%. Assuming that the material density remains constant, the changes in elastic modulus are very small. Measurements of elastic modulus by several researchers have indicated that the changes are very small and in many cases are not detectable. On the other hand, from a theoretical perspective, a change in the velocity is expected as the dislocation density is increased. The vibrating string dislocation model of Granato and Lucke predicts a small increase in the velocity of sound. This may be comparable to the accuracy in time delay measurements.

The precision in velocity measurements should be much higher than this to detect the changes in velocity due to fatigue. Unfortunately, this level of precision would require much more careful specimen preparation and the application of corrections to the measurements. Another factor that is much more important is that the velocity measurement is an average over the entire length of the specimen. Although the dislocation density varies across the length, the maximum variation occurs at the highest stress concentration. Thus, the average measurement might mask a localized increase. In conclusion, it can be assumed that the average velocity changes in sound or elastic modulus cannot be used as good indicators for characterizing fatigue damage.

The measurements of attenuation and longitudinal sound velocity show results that generally would be expected in progressively fatigued specimens. The higher attenuation from higher fatigue cycles may indicate an increase in the scattering of sound waves due to the increased dislocation dipole density from fatigue. As the increase in dislocation density saturates, the level of scattering of sound waves within the material becomes stable. It should be pointed out, however, that the general tendency of dislocation movement is to migrate to the surface of the material. This could mean that the attenuation measurement in the bulk is less meaningful throughout the entire lifetime of the material.

### 7.4.5 Local Damage Measurements

Local damage was evaluated in four specimens that were fractured under low cycle fatigue conditions ( $\sigma_{\max} = 850$  MPa,  $f = 1.0$  Hz, and  $R = 0.1$ ). All specimens were machined from the fractured specimens used in the continuous measurements previously discussed. The specimens used for continuous measurements fractured very close to the center of the gauge section. Using EDM wire cutting, longitudinal slices 1.5 mm thick were obtained from the two separated portions of the sample. Both sides of the flat dogbone sample were polished to the flatness and parallelism described before (see Fig. 8).

The longitudinal velocity of sound, attenuation, and nonlinear acoustic parameter were measured at eight different locations along the length of the sample, from the fractured edge to the grip section. Six mm diameter, 36° y-cut lithium niobate transducers operating at 10 MHz were used to propagate longitudinal ultrasonic waves through the specimen. The diameter of the transducer chosen was smaller than the width of the gauge section. The capacitive detector was used to detect and measure the fundamental and second harmonic signals.

The longitudinal velocity of sound through the thickness of the sample was measured using the pulse-echo overlap technique. The velocity of sound measured using this technique has a precision of 1 part in 10,000. Attenuation was determined by measuring the amplitude of several echoes and generating an exponential fit to the measured amplitude.

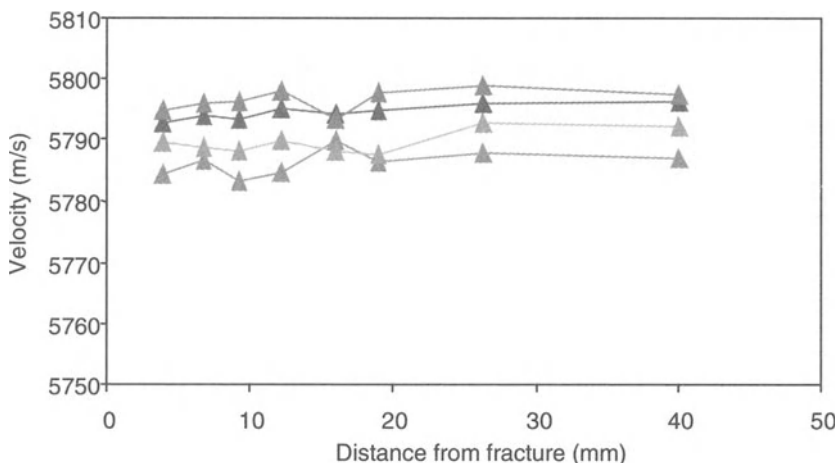


**Fig. 16.** Variation in the longitudinal velocity of sound as a function of the distance from the fracture edge in LCF samples

### **Longitudinal Sound Velocity**

The longitudinal velocity of sound measured at 10 MHz is shown in Fig. 16 for all four samples. In each of the samples, a 0.1% decrease in the sound velocity has been observed as the fracture edge is approached from the grip section side. The observed change in the velocity of sound is essentially buried in the error. Although the damage in the central portion of the sample is higher than the damage in the grip section, there is a very small difference in the velocity of sound. This is consistent with several measurements reported in the literature through direct measurement of the elastic modulus. These measurements indicate very small changes as the fatigue damage increases. The results are also consistent with interrupted measurements, as well as with continuous measurements discussed earlier.

### **Attenuation**

Attenuation measurements at 10 MHz for four samples at eight different locations along the length of the sample are shown in Fig. 17. In all samples, a significant increase in attenuation is observed as the fracture edge is approached. The average change in attenuation at 10 MHz for all samples is 1.7 dB/cm. As expected, attenuation increases with frequency. Measurements at 20 MHz show that the attenuation increases to 4.4 dB/cm. It has been observed in general that the attenuation/damping in the material increases as the number of fatigue cycles increases.

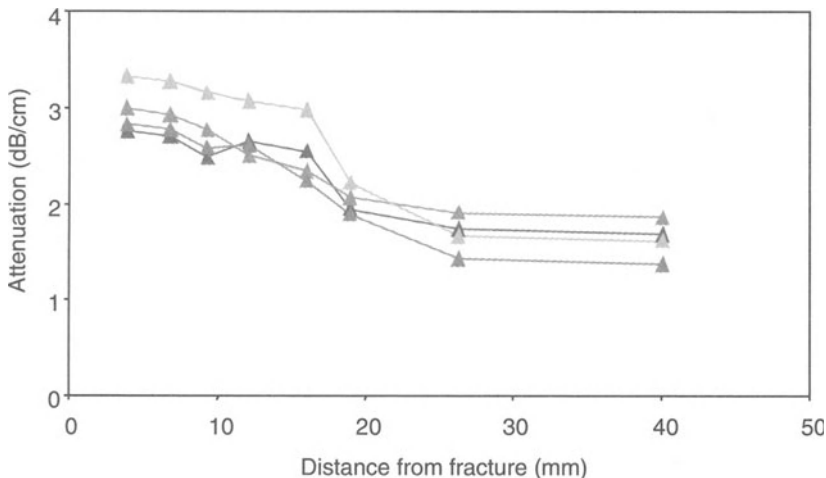


**Fig. 17.** Changes in attenuation as a function of the distance from the fracture edge in LCF samples

### **Nonlinear Acoustic Parameter**

Figure 18 shows the variation in the nonlinearity acoustic parameter for all four samples measured at eight different locations between the fractured edge and the grip section. The absolute nonlinearity parameter is corrected for attenuation of the fundamental and second harmonic signals. The nonlinear acoustic parameter in the grip section for all four samples is approximately 5 and the spread is very small. On the other hand, near the fracture section, it varies between 14 and 17. The difference might be due to the positioning of the transducer close to the edge. Although care has been taken to perform measurements at the same distance from the fracture edge of the sample, there could be some uncertainty in the positioning of the transducer. A large increase of 320% relative to the grip is observed as the fracture edge is approached. As the distance from the grip section increases, the nonlinear acoustic parameter increases almost exponentially for each of the samples. In contrast with the measurements of the velocity of sound and attenuation, the changes observed in the nonlinear parameter are very dramatic.

In a fatigue test, the sample is designed such that the stress and strain experienced by the sample in the gauge section are uniform. Fracture could be expected within the gauge section and most often very near the center of the sample. Though the properties of the material in the gauge section are expected to be uniform, the nonlinear acoustic parameter increases dramatically close to the fracture location. Therefore, the damage developed from cyclic loading is distributed over the entire gauge section of the sample, however, the fatigue damage is highest at the center of the sample and decreases on either side within the gauge section.

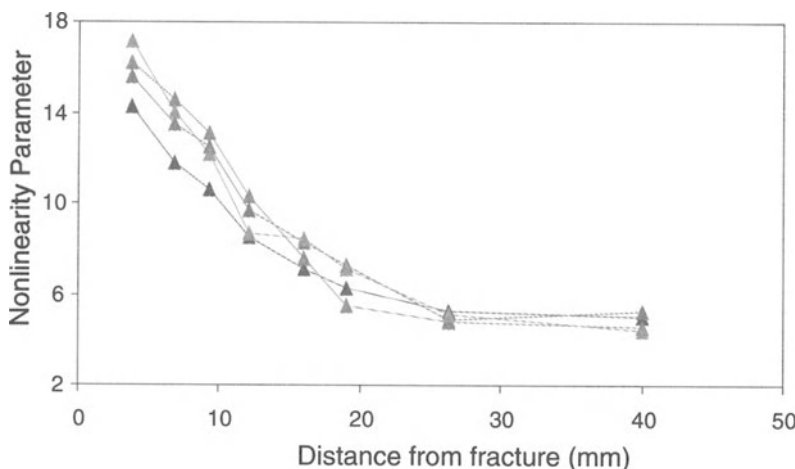


**Fig. 18.** Variations in the nonlinear acoustic parameter as a function of the distance from the fracture edge in LCF samples

### High Cycle Fatigue

Local damage was measured in a specimen subjected to high cycle fatigue loading conditions where  $\sigma_{\max} = 620$  MPa,  $R = 0.1$ ,  $F = 10$  Hz. A slice of the central portion was prepared as described earlier and shown in Fig. 8. The longitudinal velocity of sound, attenuation, and nonlinear acoustic parameter were measured at eight different locations along the length of the sample using a capacitive detector. The variations in longitudinal velocity along the length of the sample are shown in Fig. 19. The change in sound velocity is less than 0.01%. This is similar to the results observed in low cycle fatigue measurements. The attenuation measurements at a frequency of 10 MHz are shown in comparison to the low cycle fatigue specimen in Fig. 20. The attenuation increases by 1.0 dB/cm as the fracture edge is approached.

Figure 21 shows the variation in the nonlinear acoustic parameter along the length of the sample. The figure also shows the nonlinear acoustic parameter measured on one of the low cycle fatigue fractured samples. The nonlinear acoustic parameter for the HCF specimen in the grip section is 5 and increases to 14 as the fracture edge is approached. A dramatic increase of 200% is observed. In between the two ends of the sample, the nonlinear acoustic parameter remains the same as that of the grip section for nearly 80% of the length of the sample. It dramatically increases to a maximum only in the remaining 20% of the length closer to the fracture region.

Figures 22 and 23 show the variation in nonlinear acoustic parameters along with the dislocation density (determined from TEM measurements, [25]) in

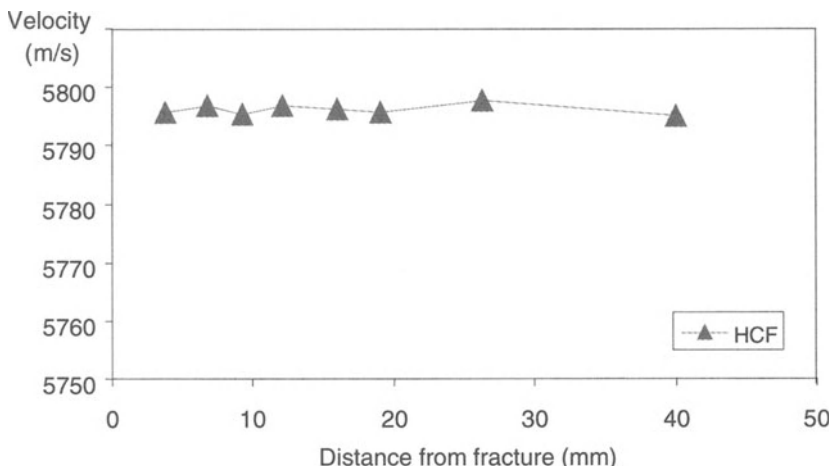


**Fig. 19.** Longitudinal velocity of sound changes as a function of the distance from the fracture edge in the HCF sample

samples fatigued under LCF and HCF conditions, respectively. It is clearly shown that the nonlinear acoustic parameter follows the dislocation density variations in both samples. These variations indicate that the nonlinear acoustic parameter is very sensitive to local microstructural changes. According to the Cantrell and Yost model, the nonlinear acoustic parameter depends on the dislocation density and the distance between the dislocation dipoles. If we assume that fatigue creates only dislocation dipoles and that dipole distance is constant, it is expected that the nonlinear acoustic parameter will vary as the dislocation density.

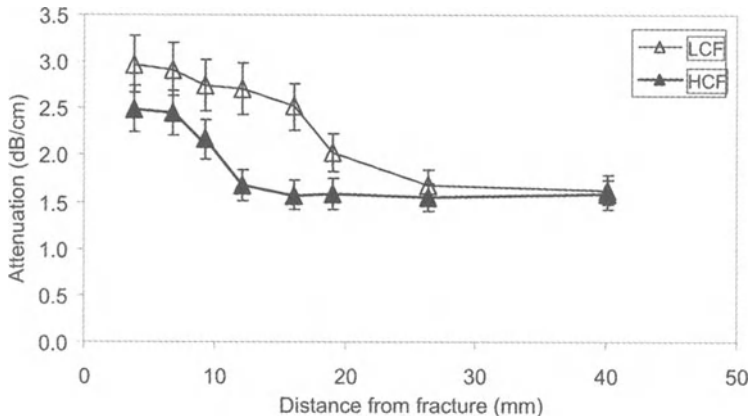


**Fig. 20.** Attenuation changes as a function of distance from the fracture edge for HCF and LCF samples

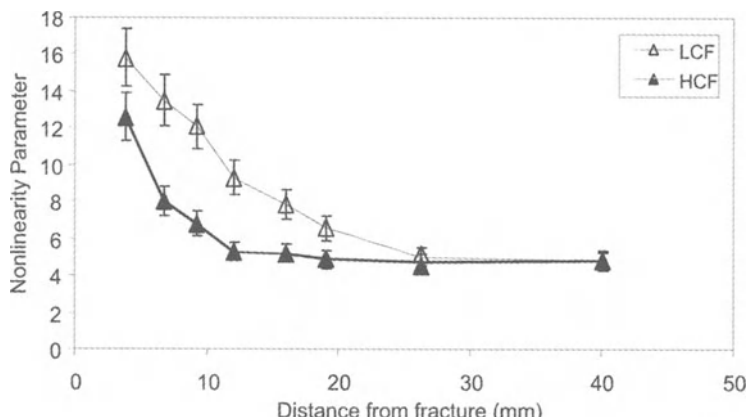


**Fig. 21.** Variation of the nonlinear acoustic parameter as a function of the distance from the fracture edge for samples fatigued under LCF and HCF conditions

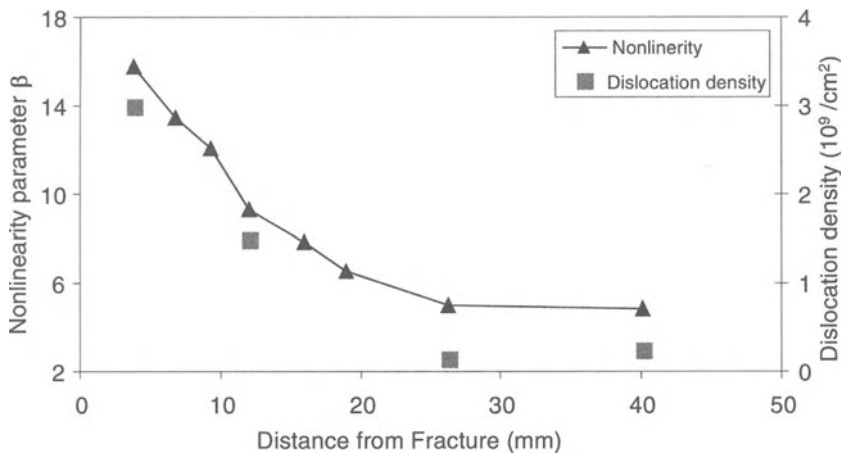


**Fig. 22.** Absolute nonlinearity parameter and dislocation density as a function of the distance from the fracture surface for samples fatigued under LCF

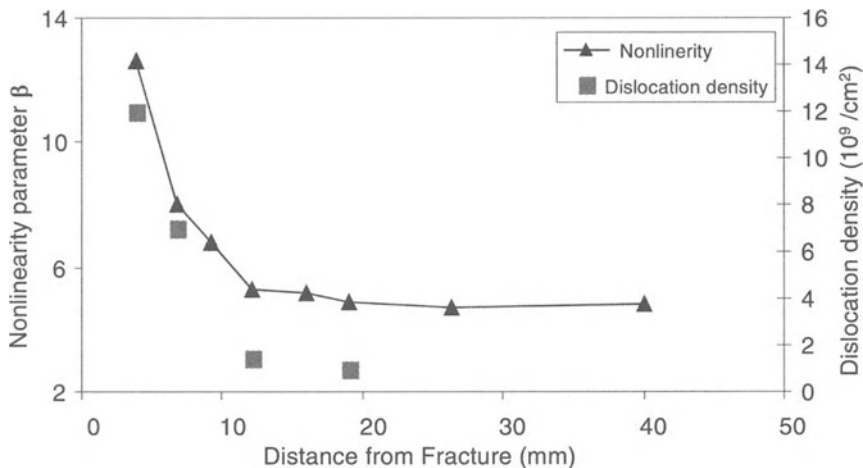


**Fig. 23.** Absolute nonlinearity parameter and dislocation density as a function of the distance from the fracture surface for samples fatigued under HCF

### **Comparison between Low Cycle Fatigue and High Cycle Fatigue**

Measurements of linear and nonlinear acoustic behavior of low cycle and high cycle fatigue fractured specimens show some clear distinctions in their properties. All results presented show that the sound velocity in the material does not change appreciably as a function of fatigue cycles under both LCF and HCF conditions.

On the other hand, the attenuation measured at 10 MHz exhibited measurable differences. Figure 20 shows a direct comparison of attenuation measurements obtained on the LCF and HCF samples. The attenuation in the grip section of the two samples is the same. As the distance from the grip section increases, in the region of the specimen taper, the attenuation curves begin to separate. In the LCF specimen, the attenuation increases gradually before saturating. The attenuation in the HCF specimen remains constant from the grip section to about 75% of the length of the specimen before increasing. Within a short distance from the point of increase, the attenuation saturates.

The nonlinear acoustic parameter for the same specimens is shown in Fig. 21. The parameter is almost the same in the grip section for both samples. As the distance increases from the grip section the parameter increases almost exponentially. The rate at which it increases for LCF and HCF are different. In the HCF sample, the nonlinearity remains at the virgin material level for nearly 75% of the length. From then on, it increases dramatically to a high value of 12. On the other hand, the parameter in the LCF specimen starts to increase just after the grip section. The steepness in the curve is much lower than that of the HCF specimen.

An increase in fatigue damage is related to an increase in the nonlinearity parameter. In LCF, the damage is distributed over the entire length of the gauge section. In the HCF sample, the nonlinearity variation is observed very close to the fractured region, and the damage is distributed over a small region. It is believed that low cycle fatigue produces distributed damage and high cycle fatigue gives rise to local damage, and the nonlinear acoustic parameter provides experimental confirmation of this fact. Thus, the nonlinear acoustic behavior can be used to estimate the level of damage and the volumetric distribution of damage.

#### 7.4.6 Summary and Conclusions

The fatigue behavior of Ti-6Al-4V has been observed using an ultrasonic technique. The linear properties, velocity, attenuation and the nonlinear properties have been measured. It is found that the material nonlinearity is very sensitive to fatigue mechanisms. The contribution of dislocations to the second harmonic and the overall material nonlinearity is confirmed by the experiment on fatigued Ti-6Al-4V samples, which is consistent with the results of other authors. Fatigue damage mechanisms, it was found, have a greater effect on the nonlinearity parameter than on the velocity and attenuation.

Continuous monitoring of the material nonlinearity during fatigue has been observed for the first time on Ti-6Al-4V. A new methodology has been developed for measuring the nonlinearity parameter in real time during the fatigue test. Low cycle fatigue experiments on Ti-6Al-4V specimens with a duplex microstructure show a large increase of the nonlinearity parameter due to the accumulation of damage in the material. A good correlation between material nonlinearity and dislocation density has been found. Different regions in the nonlinearity parameter's behavior during fatigue life has been observed, indicating different fatigue mechanisms. The first two regions show a slow increase followed by a quasi-linear increase; then after 50% of the fatigue life saturation, is reached until

the final fracture. The same trend in the nonlinearity parameter during fatigue indicated consistency, and the possibility of a “signature” in the relation between fatigue and acoustic nonlinearity was observed.

Local measurements of attenuation show saturation behavior close to the fracture section. This can be qualitatively explained using the dislocation damping theory of Granato and Lucke. The spatial distribution of excess attenuation is different under LCF and HCF conditions. Local evaluation of the nonlinearity parameter as a function of the distance from the fracture section has been done for samples fatigued under LCF and HCF condition. An exponential increase in the nonlinearity parameter from the grip section to the fracture section has been observed. The damage zone measured using the nonlinear acoustic parameter in the HCF sample is confined to a small area near the fracture, whereas in the LCF sample, it is spread over the entire gauge section.

### Acknowledgements

The authors acknowledge Mr. Tim Campbell for help with specimen preparation and Mr. Edward Klosterman for help in the operation and maintenance of the MTS fatigue machine. Dr. Gabor Blaho is acknowledged for his help in developing the interface for continuous fatigue measurements. Julie Maurer is acknowledged for her help with the fatigue measurement experimental setup and providing transmission electron microscope microstructural information. Prof. D. Eylon is acknowledged for helpful discussions.

## References

1. Suresh S (1998) Fatigue of Materials. Cambridge University Press, New York
2. Paris PC, Gomez MP, Anderson WP (1961) A Rational Analytical Theory of Fatigue, the Trend in Engineering 13:9–14
3. Bolingbroke RK, King JE (1986) In: Riche RO, Lankford J (eds) Small Fatigue Cracks. TMS, Warrendale, PA
4. McIntire P (ed) Nondestructive Testing Handbook vol. 1–6, American Society for Nondestructive Testing
5. Puskar A, Golovin SA (1985) Fatigue in Materials: Cumulative Damage Processes. Materials Science Monographs 24, Elsevier, New York
6. Nagy PB (1988) Fatigue Damage Assessment by Nonlinear Ultrasonic Materials Characterization. Ultrasonics 36:375–381
7. Na JK (1991) Ultrasonic Measurement of the Linear and the Nonlinear Elastic Properties of PZT Ceramics. Ph. D. thesis, University of Tennessee
8. Frouin J, Sathish S, Matikas TE, Na JK (1999) Ultrasonic Linear and Nonlinear Behavior of Fatigued Ti-6Al-4V. J Materials Res 14
9. Ogi H, Hirao M, Aoki S (2001) Noncontact Monitoring of Surface-Wave Nonlinearity for Predicting the Remaining Life of Fatigued Steels. J Appl Phys 90:438–442
10. Philip J, Breazeale MA (1984) in Physical Acoustics, Mason WP, Thurston RN, vol. XVII, Academic Press, New York
11. Hikata A, Chick BB, Elbaum C (1963) Effect of Dislocations on Finite Amplitude Ultrasonic Waves in Aluminum. Appl Phys Lett 3:195–197
12. Hikata A, Chick BB, Elbaum C (1965) Dislocation Contribution to the Second Harmonic Generation of Ultrasonic Waves. J Appl Phys 36:229–236
13. Hikata A, Sewell FA Jr., Elbaum C (1965) Phys Rev 151:442
14. Hikata A, Elbaum C (1966) Generation of Ultrasonic Second and Third Harmonics Due to Dislocations. Phys Rev 144:469
15. Suzuki T, Hikata A, Elbaum C (1964) Anharmonicity Due to Glide Motion of Dislocations. J Appl Phys 9:2761
16. Granato AV, Lucke K (1956) Theory of Mechanical Damping Due to Dislocations. J Appl Phys 27:583
17. Buck O (1976) Harmonic Generation for Measurement of Internal Stresses as produced by Dislocations. IEEE Trans Sonics Ultrasonics, SU-23, 346–350
18. Thompson A, Buck O, Thompson DO (1976) J Acoust Soc Am 59:1087–1097
19. Cantrell JH, Yost WT (1994) Acoustic Harmonic Generation from Fatigue-Induced Dislocation Dipoles. Philos Mag A 69:315–326
20. Morris WL, Buck O, Inman RV (1979) Acoustic Harmonic Generation Due to Fatigue Damage in High Strength Aluminum. J Appl Phys 50:6737–6741
21. Na JK, Cantrell JH, Yost WT (1996) Linear and Nonlinear Ultrasonic Properties of Fatigued 410Cb Stainless Steel. Rev Prog QNDE 15:1347–1351
22. Jhang KY, Kim KJ (1999) Evaluation of Material Degradation Using Nonlinear Acoustic Effect. Ultrasonics 37:39–44
23. Jhang KY (2000) Application of Ultrasonic Nonlinear Ultrasonics to the NDE of Material Degradation. IEEE Trans UFFC 47:540–548
24. Nazarov VE, Ostrovskii LA, Soustova IA, Sutin AM (1988) Anomalous Acoustic Nonlinearity in Metals. Sov Phys Acoust 34:284–289

25. Maurer J, Frouin J, Sathish S, Eylon D, Matikas TE (1999) Characterization of Accumulated Fatigue Damage in Ti-6Al-4V Plate Material. 9th World titanium Conference, St. Petersburg, Russia
26. Maurer J (2001) Characterization of Accumulated Fatigue Damage in Ti-6Al-4V Plate Material Using Transmission Electron Microscopy and Nonlinear Acoustics. Ph. D Thesis, University of Dayton
27. Cantrell JH, Salama K (1991) Acoustoelastic Characterization of Materials. *Int Mater Rev* 36:125–145
28. Gauster WB, Breazeale MA (1966) *Rev Sci Instrum* 37:1544
29. Dace GE, Thompson RB, Brasche LJH, Rehbein DK, Buck O (1991) Nonlinear Acoustics, A Technique to Determine Microstructural Changes in Materials. In Thompson DO, Chimenti DE (eds) *Rev. Progress in QNDE*, vol. 10 b, Plenum Press, New York, pp. 1685–1692
30. Dace GE, Thompson RB, Buck O (1991) Measurement of the Acoustic Harmonic Generation for Materials Characterization Using Contact Transducers. In Thompson DO, Chimenti DE (eds) *Rev. Progress in QNDE*, Vol.11, Plenum Press, New York, pp. 2069–2076
31. Frouin J, Sathish S, Na JK, Matikas TE (1999) Ultrasonic Linear and Nonlinear Behavior of Fatigued Ti-6Al-4V. *J Mater Res* 14(4)
32. Frouin J, Matikas TE, Na JK, Sathish S (1999) In-situ Monitoring of Acoustic Linear and Nonlinear Behavior of Titanium Alloys During Cyclic Loading. Proc. SPIE; NDE of Aging Materials and Composites
33. Frouin J (2001) Linear and Nonlinear Acoustic Behavior of Titanium Alloys under Cyclic Loading. Ph.D. Thesis, University of Dayton
34. Zaremba LK, Krasilnikov VA, Shkolnik IE (1989) Nonlinear Acoustics in a Problem of Diagnosing the Strength of Solids. *Strength Mater* 21:1544–1551
35. Ogi H, Minami, Y, Aoki M, Hirao M (2000) Noncontact Monitoring of Surface-Wave Attenuation and Nonlinearity for Evaluating Remaining Life of Fatigued Steels. Proc. 15th World Conf Non-destructive Testing, 337
36. Na, JK (1986) Ultrasonic Measurements of the Linear and the Nonlinear Elastic Properties of PZT Ceramics. Ph.D. Thesis, The University of Tennessee

# **8 Ultrasonic Absorption Measurement**

S. Palm, W. Arnold

## **8.1 Introduction**

For materials used under extreme conditions, the recognition of damage caused by materials aging is of great importance. In order to avoid failure of components during operation, many parts are replaced earlier than necessary, i.e., while they are still intact, leading to higher costs that could be reduced if the degree of damage in the component material could be determined nondestructively.

Any changes in the microstructure of a material resulting from the fatigue process affect the absorption of ultrasonic waves in the material. Thus, quantitative measurement of ultrasonic absorption could allow an indirect measurement of fatigue damage, and therefore be of interest to NDE applications. The aim of our research is to study the influence of fatigue damage on ultrasonic absorption in order to identify the mechanisms responsible for the increase of absorption with increasing degree of damage. This information may then be used to develop NDE techniques for detection of fatigue damage.

In section 8.2, we describe the basic concept for measurement of ultrasonic absorption in metals; section 8.3 gives an overview of the experimental techniques and instruments used for the applications presented in section 8.4. In the last section, 8.5, results are summarized and suggestions for future research are given.

## **8.2 Background**

Ultrasonic absorption is that part of the total attenuation of ultrasound in a material caused by energy dissipation in irreversible processes. This includes several effects, such as thermoelastic losses, phonon-electron interaction, interaction with the dislocation structure, and magnetoelastic effects. With conventional measurements of attenuation using pulse-echo techniques, it is difficult to distinguish between attenuation caused by scattering and attenuation caused by absorption. In a metallic material, scattering by the grain structure is the dominant contribution to the total attenuation measured in the frequency range of a few hundred kHz to about 10 MHz [1]. Attenuation due to absorption, however, is typically too small to be measured using this technique.

A method for direct measurement of ultrasonic absorption is the so-called reverberation technique [2, 3]. This technique uses the fact that an incident ultrasonic beam loses coherence when it is scattered at grain and phase boundaries

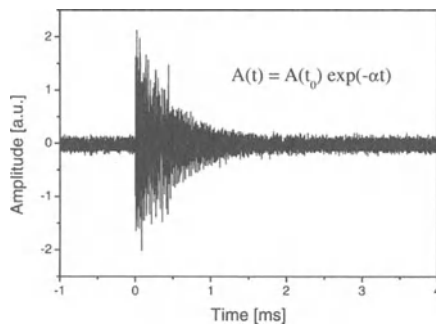


**Fig. 1.** Typical time signal (A-scan) of a reverberation experiment

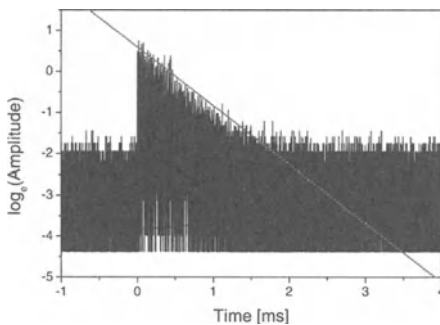


**Fig. 2.** Logarithmic A-Scan with fit function

and reflected at the sample surfaces. After a few microseconds, the elastic energy is distributed over the whole sample volume creating a diffuse sound field, the decay of which is determined only by absorption – no losses due to scattering or diffraction play a role. The distribution of energy among the various modes (longitudinal, shear, and surface waves) depends on the size and shape of the specimen and on the wave speeds of the material.

Figure 1 shows a typical time signal of a reverberation experiment. The ultrasonic absorption coefficient  $\alpha$  can be extracted directly from the fitted function approximating the decay of the signal (Fig. 2). The major limitation of the technique is the fact that its application is restricted to samples of relatively small size, depending on the type of material and the ultrasonic transducer. In larger samples, the sound signals will decay to noise level before the formation of the diffuse sound field is completed.

For generation and detection of ultrasound, any type of ultrasonic transducer can be used. In order to reduce additional losses due to coupling of a contact

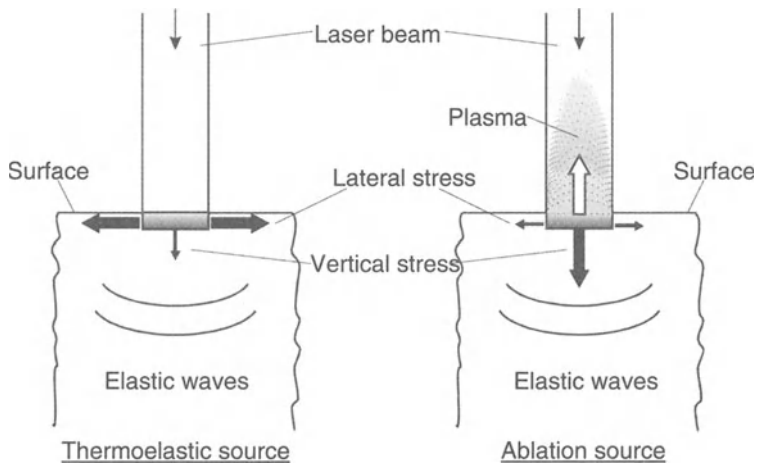


**Fig. 3.** Principle for laser-generation of ultrasound

transducer, a non-contact technique would be the preferable solution. Additional losses due to the physical support of the sample can be minimized by keeping the contact area small.

One possible non-contact method is the so-called laser ultrasound technique [4, 5], which was used for the majority of the applications presented here. The expression “laser ultrasound” is used for ultrasonic signals generated with a pulsed laser and detected with a laser probe. Depending on the laser power, the two principal mechanisms for the generation of ultrasound by laser pulses are the thermoelastic effect and material ablation [6] (Fig. 3). In the thermoelastic regime, where the laser power density is below the material ablation threshold, the thermal expansion of the irradiated volume induces stresses, which propagate as sound waves through the sample. At higher laser power, material is vaporized and ejected at the sample surface and the momentum transfer causes an increase of the pressure wave amplitude [7]. The generated ultrasonic signal has a large frequency bandwidth, ranging from a few kHz up to several tens of MHz.

For optical detection of the surface displacement caused by sound waves, different types of laser interferometers can be used as well as the so-called photo-EMF detectors [8]. A detailed review of techniques for optical detection of ultrasound is given in [9].

It is assumed that the reader is familiar with the piezoelectric effect and its application in ultrasonic transducers. Therefore, principles of piezoelectric generation and detection of ultrasound will not be discussed here.

## 8.3 Method

### 8.3.1 Laser Ultrasound

The experimental set-up for the laser ultrasonic absorption measurements presented in Section 8.4 is shown schematically in Fig. 4. The ultrasonic signals were generated using a Q-switched Nd:YAG laser with a pulse duration of 10 ns and variable pulse energy of 70–450 mJ. The surface displacement caused by the ultrasound was detected with a heterodyne interferometer [10]. The detected signals were recorded using a digital oscilloscope for further analysis. To determine the frequency dependence of the absorption, the digital signals were analyzed with a computer program which calculates the FFT of the time signal and filters the signals with respect to a certain bandwidth – either around a chosen set of frequencies or around the peak frequencies in the Fourier spectrum. For each time signal (A-scan), an average over several single laser shots was performed. The absorption coefficient  $\alpha$  was obtained from the exponential decay by taking the logarithm of the averaged A-scans and fitting the result with a linear function.

In general, the accuracy with which the ultrasonic absorption coefficient can be determined depends on the quality of the signal. If the signal-to-noise ratio is very low, a reliable fit of the data is difficult to achieve.

### 8.3.2 Contact Ultrasound

For the measurements using ultrasonic contact transducers, two identical piezoelectric transducers of a resonance frequency of 10 MHz were attached to the specimens (Fig. 5). Generation and detection of the signals was done with an ultrasonic pulser/receiver. A large number of received signals were averaged using a digital oscilloscope, and the averaged signals were sent to a computer for analysis. A joint time-frequency analysis – developed in a research group at the University of Nebraska-Lincoln, Department of Engineering Mechanics, where these experiments were done – yielded the ultrasonic amplitude as a function of time in the frequency range of 1–20 MHz [11].

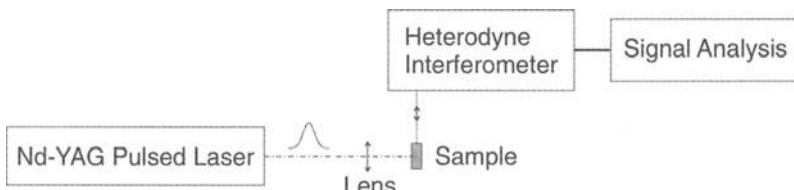


**Fig. 4.** Set-up for laser-ultrasonic measurement

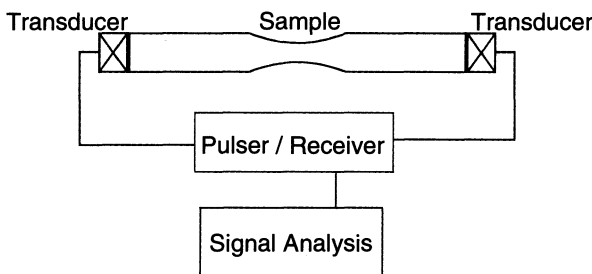


**Fig. 5.** Set-up for absorption measurement using a contact technique

## 8.4 Applications

The application of the reverberation and ultrasonic diffusion techniques for ultrasonic absorption measurements has a long tradition at the Fraunhofer Institute for Nondestructive Testing (IZFP) [2, 12]. Various different materials, mostly metals, have been studied during the last 15 years, not only with respect to fatigue damage. For some of these studies, the non-contact laser ultrasonic technique was applied [4, 13].

Several studies of ultrasonic absorption in metals have shown that the absorption coefficient varies with increasing level of fatigue damage. In steels, however, magnetic techniques have proven to be more sensitive for the detection of damage [14]. Therefore, our recent studies of fatigue have focused on materials in which the effect of damage on ultrasonic absorption is much larger, and/or for which magnetic techniques cannot be applied.

The experimental results presented here show applications of the reverberation technique, in combination with laser ultrasound as well as conventional piezoelectric ultrasonic transducers, to determine the ultrasonic absorption coefficient in a titanium alloy (Ti-6Al-4V).

The first set of samples, set 1, consisted of 4 specimens loaded in a rotating-bending mode (Fig. 6). The number of rotations was varied from  $10^4$  to  $10^7$  cycles to achieve different levels of damage between specimens. The ultrasonic absorption coefficients were obtained by generating and detecting the ultrasonic reverberation with conventional piezoelectric transducers.

Set 2 consisted of a specimen that had undergone cyclic axial loading up to failure. One half of the specimen was cut into slices, and the single pieces were assigned numbers from 1 up to 20, beginning with that piece which contained the broken area (Fig. 7). It was thus assumed that the degree of damage decreases with increasing specimen number. This set of specimens was studied using the laser ultrasound technique [13].

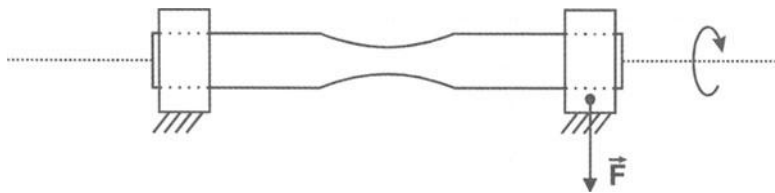


**Fig. 6.** Rotating-bending specimens (set 1)

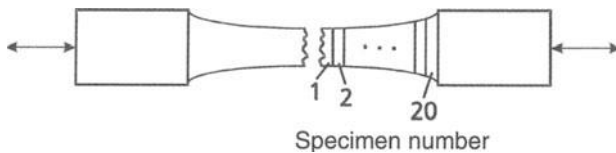


**Fig. 7.** Set of small specimens (set 2), obtained from a larger, broken specimen, which had been loaded up to failure. (Slice thickness 2 mm, low cycle fatigue conditions  $\sigma_{\max} = 850$  MPa,  $f = 1.0$  Hz and  $R = 0.1$ )

The experimental results for both studies show a considerable increase of the ultrasonic absorption coefficient with increasing degree of damage (Figs. 8–11). However, close to the failure point for set 1 ( $10^7$  cycles), and near the fracture surface for Set 2, the absorption coefficients decrease – almost to the value for the undamaged material (Figs. 8, 9). This behavior could be used as an indicator that the specimen is approaching the end of its fatigue life.

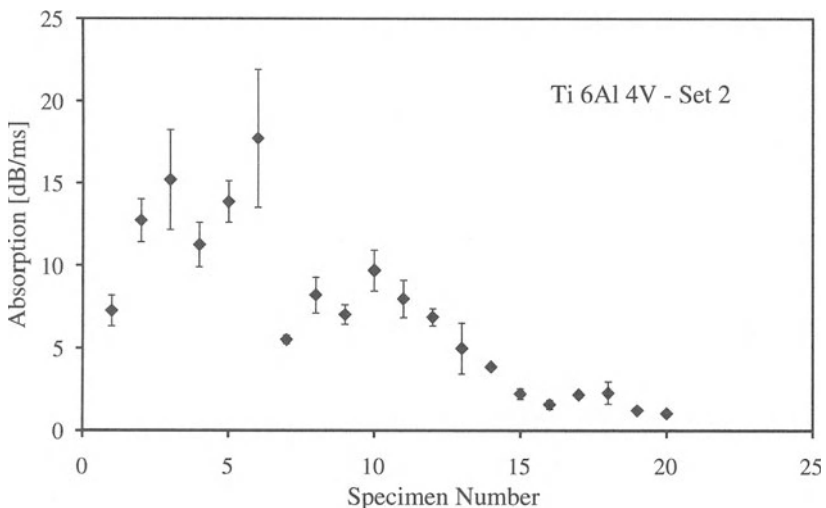


**Fig. 8.** Ultrasonic absorption as a function of specimen number for set 2 [13]

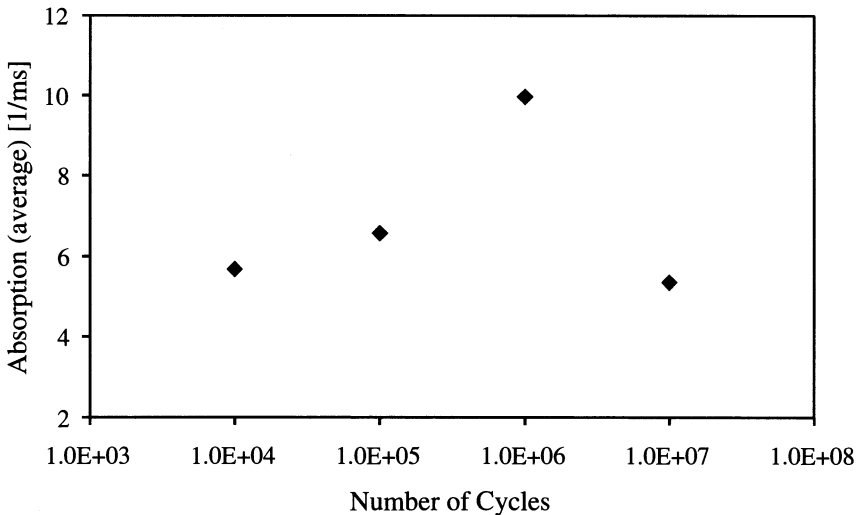


**Fig. 9.** Average ultrasonic absorption in rotating-bending specimens as a function of fatigue cycles for set 1

In many materials used for technological applications, such as steels [1], polymers [15, 16], aluminum alloys [4], and nano-crystalline materials [17], a linear increase of ultrasonic absorption with frequency is observed. The same behavior of the absorption coefficient for elastic waves is predicted for materials with micro-scale damage by several theories [18–20]. Whether these theories can be applied to describe the absorption mechanisms in the above-mentioned materials, as well as in fatigue-damaged metals, is still uncertain.

The experimental results from the study of ultrasonic absorption as a function of frequency in the titanium alloy Ti-6Al-4V do not show this linear increase of the absorption coefficient with frequency over the entire frequency range (Figs. 10, 11).

As a comparison, results obtained on a set of steel fatigue specimens are shown in Fig. 12. This set consisted of 5 specimens of low-carbon steel. Four of the specimens were subjected to constant-amplitude axial fatigue tests of 20, 40, 60, and 80% of the approximate fatigue life. The approximate value for the fatigue life was estimated from additional fatigue tests on the same material. One specimen remained unloaded. For this set of specimens, the same technique as for set 1 of the titanium alloy Ti-6Al-4V was applied.

The results confirm earlier observations on steels: the absorption coefficient shows a linear increase with frequency, and a reliable distinction between specimens with different levels of fatigue damage is not possible in the low MHz range. Only at higher frequencies is there a noticeable difference in the absorption coefficient between the unloaded specimen and the damaged specimens.

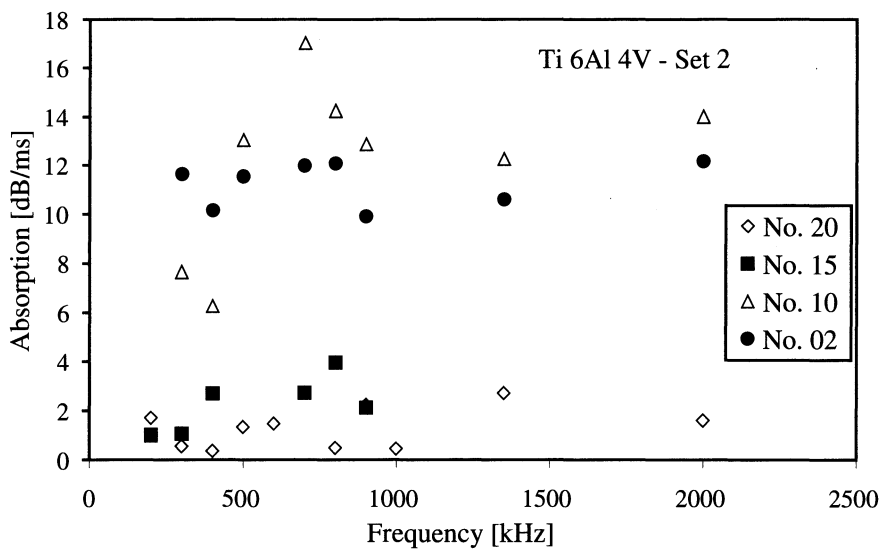


**Fig. 10.** Ultrasonic absorption as a function of frequency for set 2. For clarity, only four sets of data are shown [13]

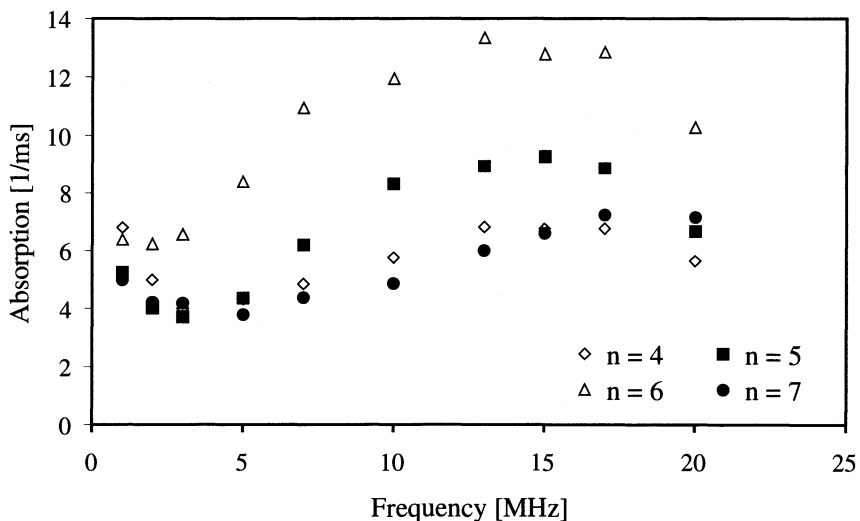


**Fig. 11.** Ultrasonic absorption as a function of frequency in set 1 with  $10^n$  fatigue cycles,  $n = 4 \dots 7$

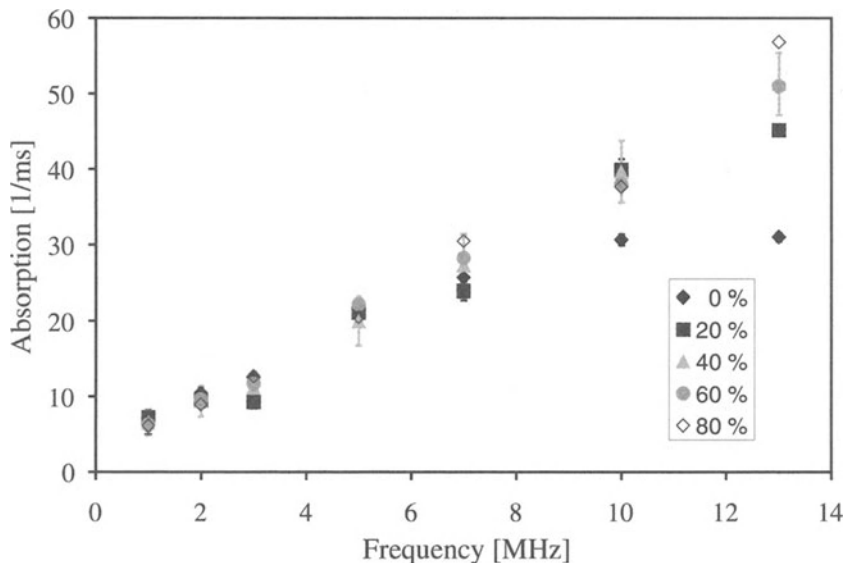


**Fig. 12.** Ultrasonic absorption as a function of frequency in steel at 0, 20, 40, 60, and 80% of the estimated fatigue life

## 8.5 Future Trends

The experiments have shown that the reverberation technique is well suited for the measurement of ultrasonic absorption in small samples. We will continue to use this technique in our study of absorption mechanisms in materials with nano- and micro-scale inhomogeneities.

In order to relate the observed absorption behavior to the physical properties of the material, analysis of experimental data from a large number of test specimens with well-characterized microstructure will be necessary.

For the application to larger components, a modification of the reverberation technique is required. For example, Guo et al. [12] suggested extracting the absorption coefficient from data from ultrasonic scattering experiments using a diffusion model. A verification of the applicability of this technique for the determination of fatigue damage is still required, and will be a subject of ongoing studies.

## Acknowledgements

We gratefully acknowledge the support of the German Research Foundation DFG for research within the graduate college “Neue Hochleistungswerkstoffe für effiziente Energienutzung” at the University Saarbrücken, as well as the support of the German Academic Exchange Service DAAD for sponsoring our exchange program with the University of Nebraska-Lincoln.

## References

1. Goebbel K (1980) Structure analysis by scattered ultrasonic radiation. Research in Ed. R. Sharpe Non-destructive Testing, Academic, London, pp. 87–157
2. Willems H (1987) A new method for the measurement of ultrasonic absorption in polycrystalline materials. In: Thompson DO, Chimenti DE (eds) Review of Progress in Quantitative NDE, 6th ed. Plenum Press, New York, pp. 473–481
3. Weaver RL (1987) Diffuse field decay rates for material characterization. In: Achenbach JD, Rajapakse Y (eds.) Solid Mechanics Research for Quantitative Nondestructive Evaluation, Matinus Nijhoff, Dordrecht pp. 425–433
4. Haberer B, Paul M, Willems H, Arnold W (1994) Measurement of internal friction in polycrystalline materials using laser-generated ultrasound. *J Alloys and Comp* 211/212:636–639
5. Moreau A, Lord M, Lévesque D, Dubois M, Bussière JF (2000) Laser-ultrasonic absorption measurements in low carbon steel. *J Alloys and Comp* 310:427–431
6. C.B. Scruby CB, Drain LE (1990) Laser Ultrasonics – Techniques and Applications. Adam Hilger, Bristol, 1990
7. Hoffmann A, Arnold W (2000) Modeling of the ablation source in laser ultrasonics. In: Chimenti DE (ed.) Review of Progress in Quantitative NDE 19 A, Melville, New York: American Institute of Physics (AIP), 279–286 AIP Conference Proceedings 509
8. Klein MB, Bacher GD (1998) Robust laser-based detection of lamb waves by photo-EMF sensors. *Proc SPIE* 3399:12–17
9. Dewhurst RJ, Shan Q (1999) Optical remote measurement of ultrasound. *Meas Sci Technol* 10:R139–R168
10. Paul M (1987) Breitbandiger Nachweis von Ultraschall mittels Interferometrie und kapazitiven Aufnehmern. Diploma Thesis, Physics Department, Universität des Saarlandes, Saarbrücken and IZFP Saarbrücken, unpublished
11. Anugonda P, Wiehn JS, Turner JA (2001) Diffusion of ultrasound in concrete. *Ultrasonics* 39:429–435
12. Guo CB, Höller P, Goebbel K (1985) Scattering of ultrasonic waves in anisotropic polycrystalline metals. *Acustica* 59:112–120
13. Luxenburger S, Arnold W (2001) Laser ultrasonic absorption measurement in fatigue-damaged materials. *Ultrasonics* 40:797–801
14. Lang MA, Bassler HJ, Dobmann G, Eifler D (1998) Characterization of the fatigue behaviour of austenitic steel using HTSL-SQUID. *Review of Progress in Quantitative NDE* 17B:1597–1604
15. Hartmann B, Jarzynski J (1972) Ultrasonic hysteresis absorption in polymers. *J Appl Phys* 43 No. 11:4304–4312
16. Unwin ME Challis RE Modelling ultrasonic wave propagation in curing thermosets. *Proceedings of the IEEE International Ultrasonics Symposium 2002*, to be published
17. Lang MJ, Duarte-Dominguez M, Birringer R, Hempelmann R, Natter H, Arnold W (1999) Measurement of elastic and anelastic properties of nanocrystalline metals. *NanoStructured Materials* 12:811–816
18. Gremaud G (2001) Dislocation-Point Defect Interaction. In: Schaller R, Fantozzi G, Gremaud G (eds) Mechanical Spectroscopy  $Q^1$  2001 with Application to Material Science, Trans Tech Publications

19. Van Den Abeele KE, Johnson PA, Guyer RA, McCall KR (1997) On the quasi-analytic treatment of hysteretic nonlinear response in elastic wave propagation. *J Acoust Soc Am* 101:1885–1898
20. Zaitsev V, Sas P (2000) Dissipation in microinhomogeneous solids: inherent amplitude-dependent losses of a non-hysteretical and non-frictional type. *Acustica* 86:429–445

# 9 Thermographic Materials Characterization

H. Rösner, U. Netzelmann, J. Hoffmann, W. Karpen, V. Kramb, N. Meyendorf

## 9.1 Introduction

Thermal techniques are attractive for materials characterization. They provide sophisticated contrast mechanisms and fast, non-contact investigation of large inspection areas. Recent progress in the development of infrared cameras is the key for a wide variety of new applications. In particular, active thermal techniques provide useful information about thermal properties and related quantities as well as geometrical and structural information. “Active” thermography means that, for the purpose of testing, heat is deposited at the surface of the test object or generated within the test object. The surface temperature is monitored as a function of time during or after stimulation. Thermal quantities are determined from the infrared frame sequence. With “Passive” thermography, the temperature of an object is imaged without additional thermal stimulation.

The current chapter presents thermographic NDE methods for detection of delaminations, cracks and corrosion damage. Particular focus is set on the new thermographic NDE method called **Mechanically Induced Dissipated Heat Analysis – MIDA**. This method is employed for fatigue damage characterization.

## 9.2 Background

### 9.2.1 Thermal Wave and Thermal Diffusion Techniques

Thermal imaging techniques are based on the fact that every object emits electromagnetic waves. For wavelengths between 350 nm and 750 nm, this radiation is visible light. Red light has the longest wavelength (600–750 nm). Electromagnetic radiation with longer wavelength (up to approximately 10  $\mu\text{m}$ ) is called “infrared” (IR) and is invisible for the human eye. However, “infrared cameras” can detect this radiation. The spectral distribution and intensity of the radiation that is emitted by objects depends on the object temperature. The spectral radiation density can be calculated using Plank’s radiation formula, which is valid for an object with the highest possible emissivity, the black body. A correction for the spectral radiation density of real objects is obtained by multiplication with an emissivity coefficient  $\varepsilon_r$ . The wavelength dependent emissivity coefficient  $\varepsilon_r$  describes the fraction of emitted radiation intensity from the real object compared to the black body, and is always a value smaller than 1. Unfortunately,  $\varepsilon_r$  becomes very small for metals in the infrared range (0.1 or even

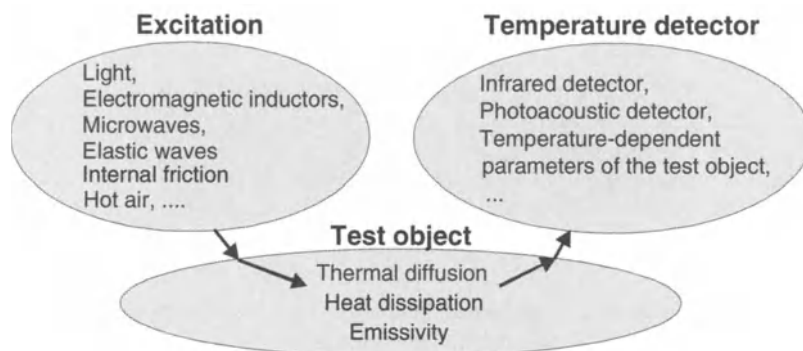


**Fig. 1.** General scheme for active thermal NDE using external heat sources

less for aluminum surfaces at a wavelength of  $10 \mu\text{m}$ ). The sum of emissivity ( $\varepsilon$ ) that is identical to absorbency, transmissivity ( $\tau$ ) and reflectivity ( $r$ ) must be 1 for a selected material ( $\varepsilon + \tau + r = 1$ ). Most metal surfaces are excellent infrared reflectors, therefore, thermographic NDE of metallic parts usually requires the application of a black IR absorptive coating which must then be removed after the inspection. For testing of ceramics or plastics, it must be considered that these materials might be transparent or opaque to infrared radiation.

Active thermal techniques require a time-dependent heat source. Using an external heat source, a thermal diffusion process in the test object is responsible for the development of the thermal contrast to be detected (Fig. 1). Heat is deposited at the surface or generated within the material. The thermal diffusion process is the key to the image contrast obtainable by the techniques. It is governed by the differential equation for thermal conduction for the temperature  $T(x,y,z,t)$  (Fourier equation)

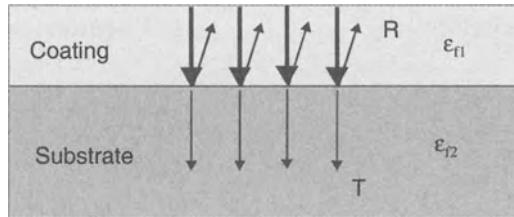
$$\frac{\partial T}{\partial t} - \alpha \nabla^2 T = \frac{q}{\rho c_p} . \quad (1)$$

Here,  $\alpha = \lambda / (\rho c_p)$  is the thermal diffusivity,  $\lambda$  the thermal conductivity,  $\rho$  the density and  $c_p$  the specific heat capacity at constant pressure of a homogeneous material.  $q$ , the absorbed power density in  $\text{W/m}^3$ , gives the heat source.

A solution to the temperature equation for heat sources, where the absorbed power density is periodic with a modulation frequency  $\omega$ , is given by

$$T(\vec{r}, t) = T_0 + T_{dc}(\vec{r}) + \vartheta(\vec{r}) \exp(i\omega t + \varphi) , \quad (2)$$

where  $T_0$  is the ambient temperature,  $T_{dc}$  the static temperature rise,  $\varphi$  the phase and  $\vartheta$  the complex amplitude of a temperature oscillation. The last term describes the temperature variation due to a thermal wave and is the most interesting for coating characterization.

**Fig. 2.** Reflection of thermal waves at interfaces

If one restricts to one-dimensional heat-flow in test objects with an optical surface absorption  $q'$  (in  $\text{W/m}^2$ ) at  $z=0$ , the solution for  $\vartheta$  is given by

$$\vartheta(z) = \frac{q'}{\varepsilon_f} \cdot \frac{1}{\sqrt{\omega}} \cdot e^{-\frac{i\pi}{4}} \cdot e^{-\frac{z}{\mu}} \cdot e^{-\frac{i z}{\mu}}. \quad (3)$$

where  $\mu=(2\alpha/\omega)^{1/2}$  is the thermal diffusion length and  $\varepsilon_f=(\lambda\rho c_p)^{1/2}$  is the effusivity of the material. The exponential damping with depth  $z$  and the corresponding phase delay is characteristic of thermal wave diffusion.

Another important case is pulsed heating, where an energy density of  $q'_p$  is deposited in the surface at a time  $t=0$ . In this case, the solution for the dynamic temperature change  $\Delta T=T(z,t)-T_0$  is given by

$$\Delta T(z,t) = \frac{q'_p}{2\varepsilon_f \sqrt{\pi} \sqrt{t}} \exp\left(-\frac{z^2}{4\alpha t}\right). \quad (4)$$

Here, one can recognize the diffusion of a heat pulse into the depth. At the sample surface ( $z=0$ ), the temperature decay shows a characteristic  $1/t^{1/2}$  dependence. In both cases of sinusoidal and pulsed excitation, the thermal contrast for a given energy input is determined by the effusivity and the spatial/temporal behavior of the thermal process is controlled by the thermal diffusivity of the test object. Table 1 lists these thermal properties for various materials.

**Table 1.** Thermophysical parameters of selected materials

Material	Thermal Diffusivity $\alpha [10^{-6} \text{ m}^2/\text{s}]$	Effusivity $\varepsilon_f$ [ $\text{Ws}^{1/2}/(\text{Km}^2)$ ]	Thermal Diffusion Length $\mu$ at 1 Hz [mm]	Thermal Diffusion Length $\mu$ at 1 kHz [ $\mu\text{m}$ ]
Aluminum 2024	73.0	20710	4.8	153
Titanium	6.6	6037	1.5	46
Glass	0.35	1280	0.34	10.6
Polyethylene	0.165	860	0.23	7.3
Air	18.5	5.6	2.43	76.8

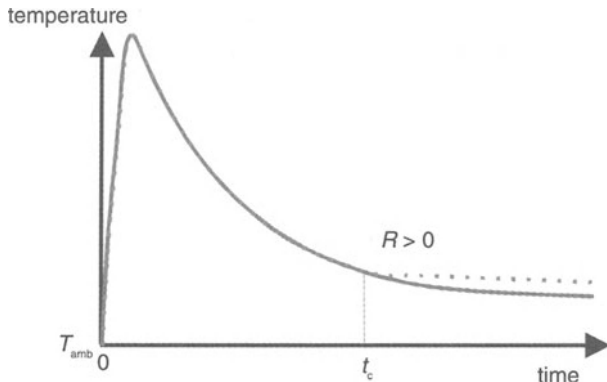


**Fig. 3.** Typical temperature decay curve of a homogeneous body (*solid line*) and a coated sample (*dashed line*) after pulsed heating

At the interface between two materials, a fraction of the thermal wave (or the thermal pulse) is transmitted, another fraction is reflected and interferes with the incoming wave (Fig. 2). These processes can be described by a thermal reflection coefficient  $R=(\varepsilon_{n1}-\varepsilon_{n2})/(\varepsilon_{n1}+\varepsilon_{n2})$  and a transmission coefficient  $T=2\varepsilon_{n1}/(\varepsilon_{n1}+\varepsilon_{n2})$ . Here,  $\varepsilon_{n1}$  and  $\varepsilon_{n2}$  are the effusivities of the coating and the substrate, respectively. Coating or defect characterization requires a significant difference in the effusivities of the tested materials.

In addition, the thermal transfer at the interface between coating and substrate may be described by a thermal resistance [1]. The effect of the coating is to generate additional amplitude changes and phase shifts of the surface temperature  $T(0,t)$  when the coating thickness equals 0.2 to 1.5 thermal diffusion lengths [2]. When using a thermal pulse excitation, deviations from the  $1/t^{1/2}$  temperature decay are observed after a time of about  $t_c \equiv 0.25 d^2/\alpha$ , where  $d$  is the coating thickness (Fig. 3) [3].

### 9.2.2 Mechanically Induced Heat

Dynamic mechanical loading of a material stimulates thermal effects that are related to the mechanical properties. The total temperature change,  $\Delta T$ , of a material due to cyclic mechanical loading is a superposition of the thermoelastic temperature variation,  $\Delta T_{el}$ , the temperature due to heat dissipation,  $\Delta T_{diss}$ , and the temperature variation,  $\Delta T_{loss}$ , due to heat exchange with the environment (energy losses controlled by the specific thermal boundary conditions for instance)

$$\Delta T(t) = T(t) - T_0 = \Delta T_{el}(t) + \Delta T_{diss}(t) + \Delta T_{loss}(t) \quad (5)$$

Here,  $T_0$  is the absolute reference temperature corresponding to the temperature at time  $t = 0$ . In the following discussion, adiabatic conditions are assumed, thus,  $\Delta T_{loss}$ , is neglected.

The thermoelastic temperature change, under adiabatic conditions, is a reversible thermodynamic effect caused by a change in the material's free energy due to elastic deformation. The thermoelastic temperature change due to a sinusoidal mechanical loading at the frequency  $f$  ( $\text{s}^{-1}$ ) can be expressed as [4]

$$\Delta T_{\text{el}}(t) = -\frac{a \cdot T_0 \cdot \sigma_a}{\rho \cdot c_p} \cdot \sin(2\pi f \cdot t). \quad (6)$$

Here,  $\sigma_a$  (Pa) is the amplitude of the mechanical stress,  $a$  ( $\text{K}^{-1}$ ) is the coefficient of thermal expansion,  $\rho$  ( $\text{kgm}^{-3}$ ) is the density and  $c_p$  ( $\text{J kg}^{-1} \text{K}^{-1}$ ) is the specific heat at constant pressure. This temperature change is directly related to the applied mechanical stress, thus, it can be utilized for stress characterization.

Dynamic elastic deformations may also be accompanied by reversible anelastic deformations, or at higher stress levels by irreversible plastic deformations. A result of the non-elastic deformation is mechanical damping, whereby, the mechanical energy is transformed into dissipated heat energy. The dissipated heat produces a secondary mechanically induced temperature effect, which superimposes on the thermoelastic temperature change [5–6]. In contrast to the thermoelastic effect under adiabatic conditions, the generation of the dissipated heat is a thermodynamically irreversible process. The temperature change  $\Delta T_{\text{diss}}$  is directly related to the generated and accumulated dissipated heat  $Q_{\text{diss}}$  ( $\text{J m}^{-3}$ ) in the material and it can be described as follows [7]

$$\Delta T_{\text{diss}}(t) = \frac{Q_{\text{diss}}(t)}{\rho \cdot c_p} \quad (7)$$

This effect is exhibited during cyclic periodic loading by the mechanical hysteresis. Mechanical hysteresis is the result of a phase shift between the stress,  $\sigma$ , and strain,  $\varepsilon$ , during a mechanical loading cycle. A phase shift always appears when the strain amplitude,  $\varepsilon_a$ , consists of anelastic strain (strain due to reversible microstructure changes),  $\varepsilon_{\text{anel}}$ , or plastic strain,  $\varepsilon_p$ , in addition to the elastic deformation. Figure 4 shows schematically a typical mechanical hysteresis loop with mean stress,  $\sigma_m$ , equal to zero. As shown in the figure, stress amplitudes,  $\sigma_a$ , above the yield strength of the material result in significant plastic strain,  $\varepsilon_p$ , apart from the anelastic strain,  $\varepsilon_{\text{anel}}$ . The area encircled by the hysteresis loop corresponds to the total mechanical energy loss,  $w_{\text{mech}}$ , during a single loading cycle [7].

Even at very small stresses, e.g., during ultrasonic loading, dissipated heat is generated that can be measured experimentally [5]. Under these very low stress conditions, reversible time dependent anelastic deformations are responsible for the mechanical damping. Very small mechanical hysteresis loops are generated. The entire mechanical energy loss per single mechanical loading cycle,  $w_{\text{mech}}$ , is transformed into heat energy  $q_{\text{diss}}$  (lower case will be used to indicate quantities for one loading cycle). Some of the mechanisms activated under these low stress conditions have been described for example as Granato-Lücke damping, ferromagnetic damping or thermoelastic damping [9,10]. These effects are considered to be non elastic.

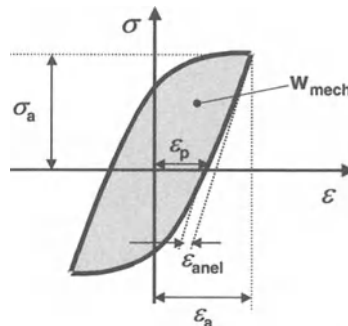


**Fig. 4.** Mechanical hysteresis ( $\varepsilon$ : mechanical strain,  $\sigma$ : mechanical stress)

However, if the mechanical loading is significantly higher local (micro-) plastic deformations dominates the mechanical damping mechanisms. In addition to reversible anelastic strains, irreversible plastic deformations appear, which are responsible for a significantly larger hysteresis area. For this case,  $w_{\text{mech}}$  is not identical to  $q_{\text{diss}}$ , because a small fraction of  $w_{\text{mech}}$  (approximately 5%) is consumed as deformation energy (microscopic elastic strains, crystal lattice defects). The consumed (stored) energy increases the internal energy of the crystal. When the plastic deformation is the dominant mechanism for mechanical damping, the temperature due to heat dissipation can be expressed for sinusoidal loading as

$$\Delta T_{\text{diss}}(t) = N \cdot \Delta \tau_{\text{diss}} = \frac{N}{\rho \cdot c_p} \int_0^{\varepsilon_p(t)} \sigma_a \cdot \sin(2\pi f \cdot t) \cdot d\varepsilon_p, \quad (8)$$

where  $N$  is the number of loading cycles and  $\Delta \tau_{\text{diss}}$  is the temperature increment per loading cycle [6,11].

Although mechanical damping depends on the microstructure, the mechanisms causing mechanical damping are diverse and their activation is affected by external factors, as temperature and type of mechanical loading (stress amplitude, mean stress, loading frequency). From the literature, it is well known that both the mechanical damping due to anelasticity and plasticity undergo changes when the material is exposed to fatigue damage [11–13]. The microstructure and mechanical properties undergo changes due to fatigue, causing a corresponding change in the mechanical damping properties and mechanical hysteresis of the material.

### 9.3 Infrared Cameras for NDE

Infrared cameras are available for either short wavelengths (3 to 5  $\mu\text{m}$ ) or long wavelengths (8 to 12  $\mu\text{m}$ ). These wavelength ranges are the “atmospheric windows”, where normal, clean air has the highest transparency. Molecular gases absorb and emit infrared radiation at certain wavelength above 1  $\mu\text{m}$  (absorption bands). No major absorption bands for gases that form clean air are in the wavelength range of the atmospheric windows. However, this can be different in

industrial atmospheres, where effects of other gas impurities must be considered for thermal NDE.

Older IR cameras are scanner systems. They have only one infrared detector. The sensitive spot is scanned across the test surface by means of mirror systems to generate a single frame. For NDE tasks with high temperature dynamics, such as testing of thin coatings or metallic objects it has to be considered that each pixel in a thermographic image represents another testing time.

Focal Plane Array (FPA) cameras employ multi-sensor arrays. These cameras capture the thermal image in one shot. These cameras are available with different sensor types, different pixel sizes and different frame rates (Table 2).

**Table 2.** Infrared cameras available for NDE (Numbers for 50/60Hz frame rate)

Detector Material	Si	Micro bolometer	HgCdTe	PtSi	HgCdTe	QWIP
Detector Type	CCD array	Array	Scanner	FPA	FPA	FPA
Noise Equivalent (white noise)		80 mK	150 mK	75 mK	25 mK	down to 7mK
Lowest Detectable Temperature	400°C	-20°C	-30°C	-30°C	-30°C	-50°C

For most NDE applications, cameras with as high as possible temperature resolution are required. Cameras based on Quantum Well Infrared Photon detectors (QWIP) are available with excellent temperature resolution (noise equivalent temperature difference of a few mK) and high pixel resolution. Testing very thin or high thermal conducting films require high temperature dynamics. Therefore, frame rates higher than video standard (USA: 60 half frames per second) are used. Some of these “high-end” cameras generate frame rates of up to 7000 frames per second. Unfortunately, the high price of these cameras is a limiting factor for a wide variety of applications.

Micro bolometer cameras are a cost efficient alternative for many NDE applications. An important advantage of these systems is that the detector does not require a liquid coolant or a mechanical cooling system (Stirling motor) with limited lifetime. These systems are low priced and have low service and maintenance requirements. Unfortunately, these cameras have poor temperature sensitivity (high noise) compared to QWIP systems.

Averaging of a high number of video frames during the inspection can reduce thermal noise. Assuming random noise, an average of 100 frames will increase the temperature resolution by a factor of 10. However, frame averaging requires NDE test procedures with low temperature dynamics, or quasi-static images such as fan thermography (see below).

Conventional CCD cameras based on silicon detectors are available for a few hundred dollars. If the infrared filters are removed from the CCD-chip near infrared radiation from 0.8 to 1.1  $\mu\text{m}$  wavelength can be detected. This is sufficient for imaging of temperatures above 400 °C. These CCD cameras can be

used for several applications and have been successfully applied to control of a welding process [14].

## 9.4 Methods

Techniques that detect heat radiation emitted from a test object without external heating are called passive thermal NDE. An example is the control of welding processes. Another interesting application is the inspection of internal structures of semiconductors. Silicon and Germanium are transparent to infrared radiation. Therefore, infrared cameras can detect internal structures of microelectronic chips. Also, military aircraft coatings are semitransparent in a wavelength range between 3 and 5.5  $\mu\text{m}$ . Infrared cameras that are sensitive in this wavelength range are able to detect defects underneath the coating without additional heating [15].

Most thermal NDE techniques are based on active heating and are called active thermal NDE. The test object is stimulated by external heat sources, such as light or thermal radiation, electric current, microwaves, or mechanical loads. The thermal camera detects the surface temperature variations, due to these effects [16, 17].

At present, the most widely used thermal NDE technique is flash or pulsed thermography. An energy pulse (usually light) heats the surface of the test object and the cooling process is observed by an infrared camera. Subsurface defects disturb the cooling process and result in a temperature contrast after a certain response time. This technique is useful for characterization of coatings and detection of subsurface defects, such as corrosion or detection of defects in adhesive bonds [18]. A modification of flash thermography is line-scanning thermography, where a heat line is scanned across the surface. The temperature field behind the heat line represents the cooling process [19]. The distance between heat generation and detection determines the response time  $t_r = s/v$  where “s” is generation to detection distance and “v” is scanning speed.

Lock-in thermography detects similar types of defects like pulsed thermography. An unsteady thermal diffusion process is generated by a sinusoidal heat source. It follows from (2), that the unsteady or “thermal wave” part of the temperature in the test object is described by

$$T(\vec{r}, t) = \vartheta(\vec{r}) \exp(i\omega t) \quad (9)$$

Amplitude and phase images are calculated from thermography frame sequences. The phase is sensitive to the defect depths. Local emissivity variations do not affect the phase image significantly. Some authors report higher depth sensitivity for the phase signal. However, this method requires significantly more testing time [20].

Temperature oscillations ( $\Delta T_{\text{el}}$ ) which occur under the application of a cyclic load ( $\sigma_a$ ) are known as the thermoelastic effect, and are described by Joule Thomson Law (see (6)). The thermoelastic principle is the basis for imaging techniques used for detecting local stress concentrations where fatigue cracks might appear first [4].

As described above, cyclic loading results in the generation of dissipated heat due to the mechanical hysteresis. By averaging thermal images for a large number of mechanical loading cycles, the temperature enhancement due to dissipated heat can be separated from thermoelastic effects. The application of these effects will be described in detail below (see Section 9.5.4).

Table 3 summarizes different thermographic techniques. These methods vary with regard to the mechanism of heat generation and the time dependence of the temperature measurement.

**Table 3.** Thermographic Techniques

Temperature Measurement	Physical Mechanisms Used for Heat Generation
<ul style="list-style-type: none"> <li>• During periodical modulation (Lock-in Thermography)</li> <li>• During cooling phase after an heat pulse (Flash Thermography)</li> <li>• Behind a heating line scanned across the surface (Line Scanning Thermography)</li> <li>• During the heating process (Thermosonics, Fan Thermography)</li> </ul>	<ul style="list-style-type: none"> <li>• Absorption of light</li> <li>• Absorption of infrared radiation</li> <li>• Absorption of microwave radiation</li> <li>• Inductive heating</li> <li>• High power ultrasound</li> <li>• Hot air</li> <li>• Mechanical loading cycles</li> </ul>

## 9.5 Applications

### 9.5.1 Passive Infrared Imaging of Defects through Organic Coatings

A high-performance focal plane array camera was used to evaluate the detectability of corrosion defects under paint. To prepare test specimens, perfectly shaped triangle patterns were cut into Aluminum alloy Al 2024-T3 panels using laser ablation. The triangles simulate corrosion pits. The pits were then filled with an epoxy/alumina-composite to simulate corrosion byproducts. After careful polishing, the panels were coated with a typical aircraft coating system: a double-layer system consisting of an epoxy primer and a polyurethane topcoat.

The specimens had one row of triangles etched in the Al 2024-T3 substrate, each triangle had a base line length of 1 mm and a depth of 0.5 mm. The coating thicknesses were 60 µm and 145 µm, respectively. The camera (Indigo Merlin) used was a short wavelength system with a sensitivity range between 3 µm and 5 µm. The camera has a temperature resolution of 20 mK. Thermal imaging in the 3–5 µm waveband yields two important advantages: (i) the camera operates within the ‘atmospheric window’, i.e., air absorption of the thermal energy is minimal; (ii) the polymeric coating system is semitransparent for the infrared waves within this waveband.

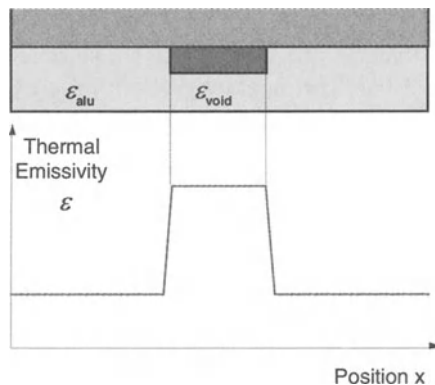


**Fig. 5.** Principle of infrared imaging of metal substrates under polymeric coatings (coatings transparent for infrared light up to certain thickness)

The latter advantage enabled infrared imaging of the Al-alloy substrate without heating (passive thermography) [14]. As previously discussed, the corrosion pit on the metal/coating interface was filled with a corrosion byproduct. Since the byproduct material has a different thermal emissivity than the metal substrate, the IR-camera could distinguish between regions of different emissivity, thus clearly imaging the corrosion pit (Fig. 5). Results obtained on these specimens are shown in Fig. 6. In Fig. 6a, the artificial defects under the coating are clearly visible. This picture was taken without additional thermal stimulation of the specimen. However, this technique can be used to inspect under coatings up to a certain maximum coating thickness, since most of the infrared light is absorbed during transmission through the coating.

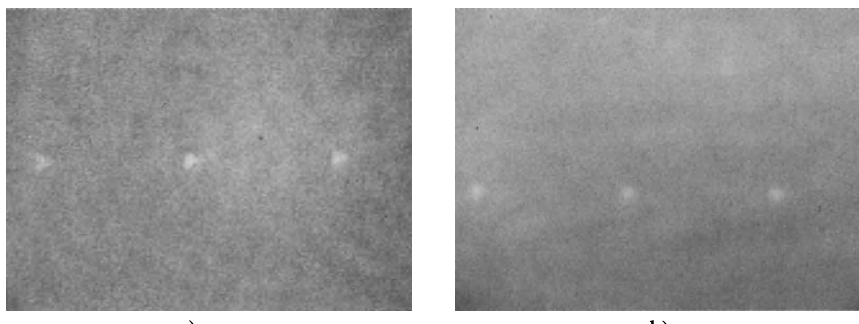


**Fig. 6.** a) Infrared imaging of triangle shaped artificial corrosion pits under 60  $\mu\text{m}$  thick coating  $\mu\text{m}$ ; b) hot air heating of triangle shaped artificial corrosion pits under 145  $\mu\text{m}$  thick coating

Hot air heating was required to enhance the thermal contrast for the specimen with 145 µm coating thickness because it was not sufficiently transparent for IR light (see Section 9.5.3 Fan Thermography). Both infrared images (Fig. 6a) and (Fig. 6b) clearly identify the triangles under the coating.

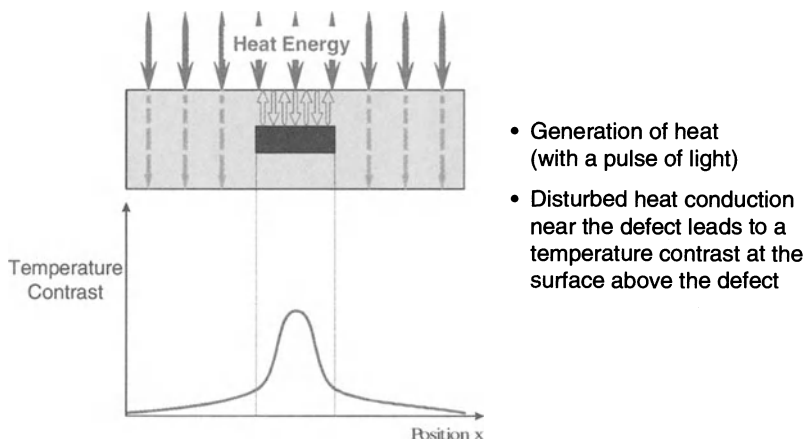
Typical aircraft coating systems have a thickness between 60–80 µm. Thus, infrared imaging without heating has high potential for in-field aircraft inspection of corrosion under paint [14].

### 9.5.2 Pulsed Thermography for Detection of Subsurface Defects

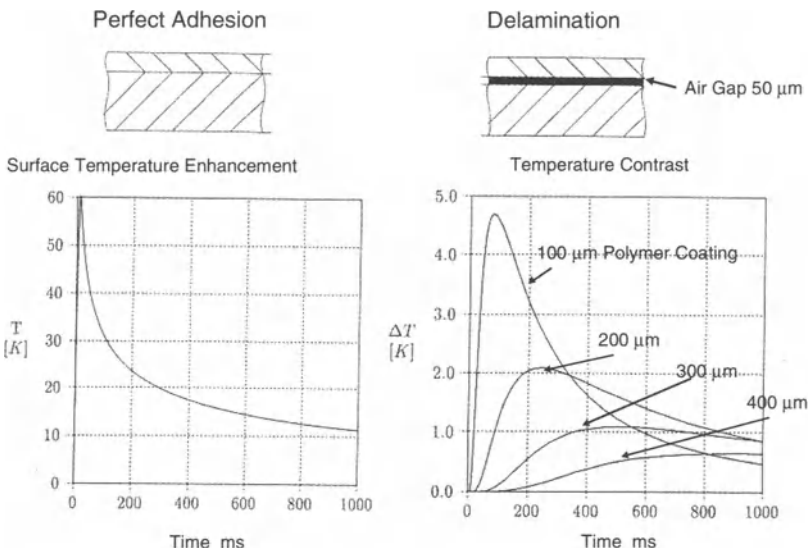
Thermal wave techniques and pulsed thermography are sensitive to defects below the surface. These defects disturb the diffusion of heat deposited at the surface into the bulk (Fig. 7). Therefore these techniques are excellent tools for the detection of coating delaminations and corrosion defects under coatings. The difficulty with most of these thermal NDE techniques is the high temperature dynamics. The testing of thin layers requires highly sensitive, high-speed thermal cameras. A model simulation for testing of a polymer coating using flash thermography illustrates the problem. This simulation is based on the thermal diffusion equation ( $c_p$ : specific heat;  $\lambda$ : heat conductivity,  $\rho$ : density,  $\gamma$ : absorption coefficient,  $I_0(t)$ : intensity of absorbed radiation).

$$c_p \rho \frac{\partial T}{\partial t} = \lambda \frac{\partial^2 T}{\partial x^2} + I_0(t) \gamma e^{-rx} \quad (10)$$

The heat generated by a short pulse at the surface is assumed to diffuse into the structure. Layers that consist of a polymer and air (for the assumed delamination) of different thickness modify the cooling process.



**Fig. 7.** Principle of pulsed thermography



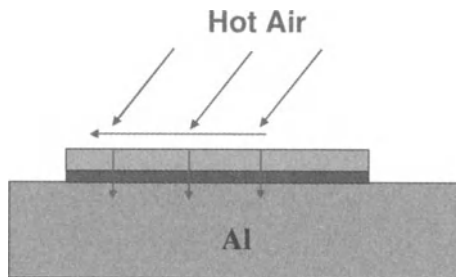
**Fig. 8.** Simulation of surface temperature for flash thermography testing: *Left:* Surface temperature/ time diagram; *Right:* Temperature contrast due to a delamination [21]

Figure 8 shows the simulated temperature dynamics during pulsed thermography. A temperature dynamics of 50 K is required to achieve a temperature contrast of approximately 0.5 K for a 50  $\mu\text{m}$  delamination between the aluminum substrate and a 400  $\mu\text{m}$  coating. For thinner coatings the contrast increases, but the corresponding response time decreases. The maximum contrast for a delamination of a 100  $\mu\text{m}$  coating is significant higher. Even the remaining contrast after 800 ms is as high as the maximum contrast for the 400  $\mu\text{m}$  coating. However, the maximum contrast appears only for the time of one video frame (30ms). Therefore, image averaging to enhance temperature resolution can not be used efficiently for cameras with standard video frame rate.

### 9.5.3 Fan Thermography for Imaging of Corrosion under Coatings

#### **Principle**

A possible way to avoid this problem is to measure the temperature contrast during a slow heating process or in a quasi-static equilibrium between the absorbed heat energy and the heat energy losses. Unfortunately, light or heat radiation can not be used simultaneously for stimulation and detection from the same side of the test object because reflected heat radiation and emitted radiation will interfere. A very simple application of this principle was based on detecting



**Fig. 9.** Principle of Fan Thermography

the surface temperature by liquid crystals [22]. A different approach is to use hot air from a fan for heating and (cost-effective) micro-bolometer infrared camera for detection. Since IR-cameras are sensitive in the atmospheric windows, hot air will not affect the infrared image (Fig. 9). Heating and temperature measurement can then occur on the same side of the object. In this case, a constant heat current  $H=Q/t$  ( $Q$ : heat energy) through the coating (quasi-static conditions) is assumed. The assumption includes constant temperature at the metal substrate. If the surface temperature ( $T_{\text{surface}}$ ) enhancement is small compared to the air temperature ( $T_{\text{air}}$ ), the heat current is determined by the heat transition from air to coating:  $H = Q/t = \beta_t A (T_{\text{air}} - T_{\text{surface}})$ .  $\beta_t$  is the heat transfer coefficient and is approximately 15 W/m<sup>2</sup>K for an air velocity of 5m/s [23]. For heat conduction through coating and air gap, the heat conductivity equation  $H = Q/t = \Delta T/R$  is valid.  $R = d/(\lambda A)$  is the heat resistance where  $\lambda$  is the heat conduction coefficient for the layer material,  $d$  is the layer thickness and  $A$  is the area where heat conductivity appears. For the assumed test procedure,  $A$  is the same for heat transition from air to surface and heat conduction into the test object. Due to the analogy to Ohm's law, a series circuit of (thermal) resistivities can be considered for a multi-layer problem such as coating and air gap. From the formulas above, the surface temperature enhancement for quasi-static conditions can be calculated for an n-layer system

$$\Delta T = \beta_t (T_{\text{air}} - T_{\text{surface}}) \cdot \sum_{i=1}^n (d_i / \lambda_i). \quad (11)$$

Table 4 shows the results for equal geometrical and thermal parameters as assumed for pulsed thermography in Fig. 8 ( $\lambda_{\text{coating}}=0.17$  W/mK;  $\lambda_{\text{air}}=0.025$  W/Km).

Even for the thinnest coating, the contrast is in the same range as for flash thermography, but for fan thermography, a stable contrast for a longer time period allows image averaging to reduce quantum noise. Both quasi-static conditions and image averaging should allow testing of thin coatings with high thermal conductivity by using uncooled bolometer cameras. These cameras have a rather poor signal/noise-ratio, however, image averaging reduces the noise drastically. As discussed above for comparison, pulsed (flash) thermography requires high-speed cameras because of the short time period for thermal exchange processes in this case.

**Table 4.** Temperature Contrast for Fan Thermography (Air Velocity = 5m/s,  $\alpha_t$  = 15W/m<sup>2</sup>K; Air Temperature = 150°C)

Coating Thickness	100 µm	200 µm	300 µm	400 µm
$\Delta T$ without air gap	1.15 K	2.30 K	3.45 K	4.60 K
$\Delta T$ with air gap 50 µm	5.05 K	6.25 K	7.35 K	8.50 K
Temperature contrast	3.9 K	3.9 K	3.9 K	3.9 K

### Evaluation of Fan Thermography

Test specimens to quantify corrosion detectability were prepared using the procedure described above in Section 9.5.1. Triangle shaped patterns have been cut into Aluminum alloy Al 2024-T3 panels using laser ablation and were filled with an epoxy/alumina-composite to simulate corrosion byproducts. A double-layer system consisting of an epoxy primer and a polyurethane topcoat was used for this experiment. The overall coating thickness was approximately 120 µm.

Two triangle arrays were prepared, each row with 4 triangles with decreasing size (triangle base length: 4 mm, 3 mm, 2 mm, 1 mm). The upper triangle row is shallower (approximately 0.5 mm compared to 1 mm of the row below). The triangles are easily detected, as demonstrated in Fig. 10. Furthermore, one can observe the increased thermal contrast for the deeper row.

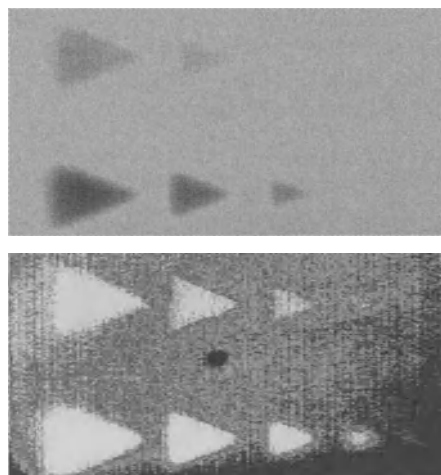


**Fig. 10.** Detection of standardized defects under intact coating; *top*: linear contrast; *bottom*: enhanced contrast

Instead of triangles, Al 2024-T3 panels with artificially generated corrosion pits were used to quantify the Fan Thermography results. Corrosion pits of different sizes were generated electrochemically. The exact pit topography was evaluated using White Light Interference Microscopy before the panels were coated. Since no coating defects were involved, the measured thermal contrast was due solely to the corrosion pits. The temperature measurements on these samples yielded a correlation between thermal contrast and pit size especially, pit depth. Results obtained so far indicate a pit depth of approximately 110 µm to be the threshold for detection. However, since the pits were filled with corrosion byproducts and polymer, the contrast is significantly smaller than that estimated from Table 4 for a delamination (air gap).

### **Detection of Subsurface Corrosion**

Figure 11 compares consecutive Scanning Vibrating Electrode Technique (SVET), Fan Thermography and Scanning Acoustic Microscope (SAM) images taken from the exact same area of an actual coated corrosion panel. The SVET and SAM technique will be described in the following Chapters 10 and 11. The Al 2024-T3 panel was coated with 50 µm thick epoxy coating, then exposed for 125 hours at open circuit potential in Harrison's solution. SVET measurements were carried out first. Figure 11a shows a vector overlay mapping of electrochemical current density superimposed over a video image. There are indications of delamination in the SVET video image. The longer vectors indicate increased corrosion activity underneath these delaminated regions.

Coating delamination or sites of corrosion are thermal barriers. If the test object surface is heated, the heat diffusion into the aluminum plate is inhibited in the delaminated or corroded region. This causes a change in the thermal response. Figure 11b shows the thermal contrast for corrosion below this coating. The spatial resolution was improved with a microscopic lens used with the IR camera. The bright spots (higher surface temperature) indicate regions of reduced heat diffusion and correlate well with the SVET image.

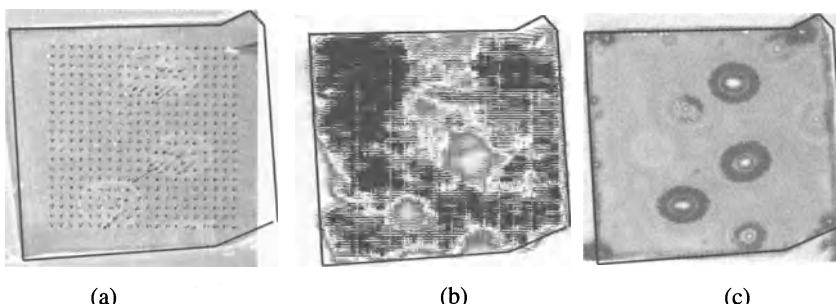


**Fig. 11.** 50-µm-thick artificially damaged epoxy coating on Al 2024 substrate a) SVET video image + current density vector overlay: vector area: 4x4 mm<sup>2</sup>; b) Fan Thermography image (gray scale reproduction) area: 6x6 mm<sup>2</sup>; c) SAM C-scan: scan area: 6x6 mm<sup>2</sup>

The sample was then scanned with SAM (Fig. 11c). The SAM scan clearly identifies the same three spots indicated by SVET and Fan Thermography. Some additional spots are visible by SAM. This could be due to the rather poor performance of this coating and the fact that repeated heating and additional exposure in a water bath has a deteriorating effect on the sample.

These results demonstrate that the electrochemical and NDE techniques provide complimentary information about the state of the coating. This information can provide the details of the health of the substrate beneath a coating exposed to corroding environment.

### ***Summary/Conclusions***

Fan Thermography is a modified thermal NDE technique that has a high sensitivity for detection of corrosion below intact aircraft coatings. The surface temperature is measured while the surface is heated with hot air. Delamination and corrosion size with corrosion byproducts is indicated by local hotspots. Model simulations show the advantages of this technique: high temperature contrast, high accuracy due to averaging of a large amount of video frames, low energy input to the surface, and simple application for in-field inspection. The strengths and limitations of this technique have been discussed by evaluating results obtained with corrosion standard samples.

#### **9.5.4 Mechanically Induced Dissipated Heat Analysis (MIDA) – High Stress Excitation**

##### ***Introduction***

Thermographic methods offer in general the capability for rapid, non-contact, high-resolution material inspection and characterization, applicable for technical components. The following paragraph describes a nondestructive method for monitoring fatigue damage progression in the Ti-6Al-4V alloy as a result of cyclic mechanical loading. The method is based on the physical effect of dissipated heat generation due to mechanical damping. The methodology was inspired from investigations of the characteristic temperature change due to dissipated heat measured in situ during fatigue experiments mainly performed on steel materials [12, 24, 25]. Recently, such temperature effects were also found to be exceptionally sensitive to fatigue damage accumulation in Ti-6Al-4V during continuous fatigue testing [26]. The new method discussed in this paragraph is called (M)echanically (I)nduced (D)issipated Heat (A)nalysis – MIDA, since it is based on a defined short-term mechanical loading to induce heat dissipation and appropriate analysis of the captured thermographic data.

### **Principle of the Method**

Figure 12 shows a schematic of the experimental set-up. Heat is generated within the tested material through application of short term, cyclic, mechanical excitation. The corresponding temperature increase in the specimen is measured using an infrared camera. Analysis of the temperature increase as a function of excitation cycles is performed off line. The short-term excitation consists of several defined mechanical loading cycles. In general, any mechanical loading induces thermal effects, however the temperature resolution that can be achieved using the available thermal detection system is the limiting factor for practical application. Therefore, optimization of both the excitation methodology and the measurement of the thermal effects is important.

The required number of loading cycles for the short-term excitation is determined by the accumulation of the dissipated heat,  $Q_{\text{diss}}$ , in the tested material. Two important factors that affect the dissipated heat accumulation are the energy loss, as determined by the thermal boundary conditions, and the heat power rate,  $P_{\text{diss}}$  ( $\text{J s}^{-1}$ ), of the mechanical excitation. The power rate depends on the loading frequency,  $f(\text{s}^{-1})$ , and the dissipated heat per cycle,  $q_{\text{diss}}(\text{J m}^{-3})$  according to

$$P_{\text{diss}} = q_{\text{diss}} \cdot f. \quad (12)$$

The dissipated heat per cycle,  $q_{\text{diss}}$ , is determined by the mechanical hysteresis loop area. The hysteresis area can be increased by cycling at a higher mean stress or by increasing the stress amplitude of the cyclic loading. Cycling at a higher frequency is also advantageous because a lower mechanical excitation stress is required. Optimization of the excitation frequency and loading conditions is necessary to generate sufficient dissipated heat,  $Q_{\text{diss}}$ , in the tested material and to produce a measurable increase in temperature,  $\Delta T_{\text{diss}}$ .

### **Experimental Setup**

Assessment of the thermal NDE method was performed using titanium cylindrical dogbone specimens (ASTM-standard, diameter 6.35 mm). The Ti-6Al-4V alloy used in the experiments is the same as described in Chapter 7 and consisted of a duplex microstructure with grain sizes of approximately 25–50  $\mu\text{m}$ . The grain structure was equi-axed and no perceivable mechanical anisotropy was found. The yield strength and maximum tensile strength were determined to be  $951 \pm 32$  MPa and  $1000 \pm 32$  MPa, respectively. Excitation of the thermal effect within the specimen was performed using sinusoidal cyclic loading in a servo-hydraulic fatigue machine. Excitation frequencies examined were in the 1–40 Hz range. The effect of excitation stress level was examined by measuring the thermal effects over a range of maximum stress levels ranging from low stress levels below the endurance limit, up to higher stress levels near the low cycle fatigue (LCF) regime. In all cases, the applied stresses were lower than the yield strength of the titanium alloy. An infrared camera, operating in the long wavelength range (8–12  $\mu\text{m}$ ; Hg-Cd-Te detector) with a relatively poor temperature resolution of approximately 0.2 K and a frame rate of 30 Hz was used for these experiments.

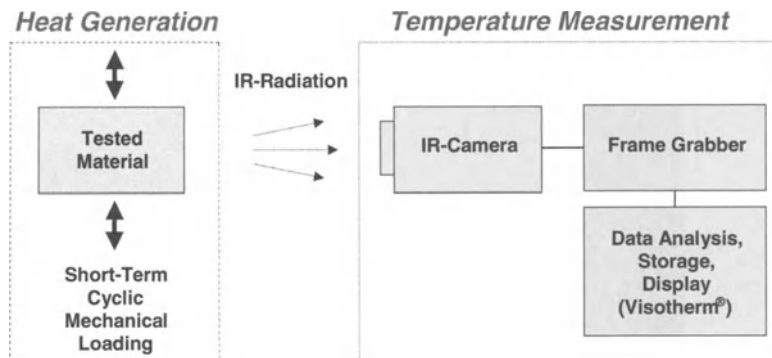


**Fig. 12.** Experimental set-up for the measurement of mechanically induced temperature effects

The camera was placed in front of the specimen at a distance of less than 1 m. The specimen was coated with a black polymer coating to increase the emissivity of the metallic surface and to ensure accurate temperature measurements. The Visotherm<sup>®</sup> data acquisition software allowed automated, time dependent measurements and storage of frame sequences in real time. Thus, the thermographic frame sequences were available for later analysis and evaluation of the thermal NDE parameters. To enhance the temperature resolution of the system, time averaging over several mechanical loading cycles and averaging of the temperature distribution over a region containing approximately 100 pixels was performed. Use of carefully selected spatial and time sequence averaging improved the temperature resolution by at least a factor of 10. Fast, high performance cameras with enhanced temperature resolution would be advantageous because it would allow measurement and analysis of temperature effects generated with lower heat power rate  $P_{\text{diss}}$  (see (12)).

### Evaluation of the Thermal NDE Parameter

Figure 13 shows a thermograph of a dogbone specimen during mechanical excitation. Also shown is a schematic of the change in temperature ( $\Delta T$ ) averaged over the middle (gage) section of the specimen as a function of time during the sinusoidal mechanical excitation cycles. Mechanical excitation was conducted at a constant heat power rating  $P_{\text{diss}}$ . Since  $\Delta T_{\text{el}}$  is a reversible temperature change that depends on the instantaneous loading, the thermoelastic effects can be measured if the frame rate of the infrared camera system is significantly higher than that of the cyclic mechanical loading. However, the scanner camera used in this study generated thermal images line by line. Therefore, temperature oscillations caused by thermoelasticity affected the image content for single frames (frame frequency of 30 Hz). Averaging of the temperature (gray value) over an area of interest that contains several lines, plus averaging of several frames (time averaging) eliminated the periodic temperature variation. Thus, the quasi-static temperature

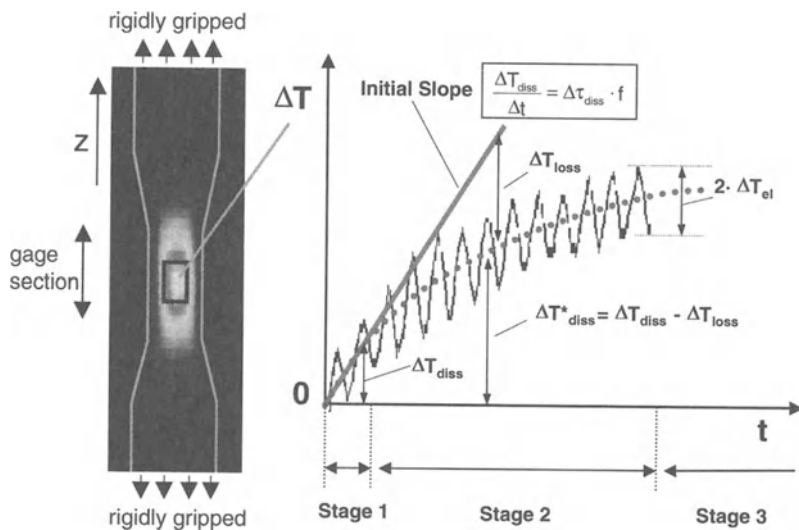


**Fig. 13.** Infrared thermograph of a dogbone specimen; Temperature change  $\Delta T$  after the start of a cyclic loading and evaluation of the thermal NDE parameter  $\Delta \tau_{diss}$  from the initial slope

increase due to heat dissipation solely influenced by heat losses,  $\Delta T^*_{diss}$ , was extracted from the measured thermal effects.

The time dependent quasi-static temperature increase  $\Delta T^*_{diss}$  due to heat dissipation depends upon the thermal boundary conditions.  $\Delta T^*_{diss} = \Delta T_{diss} - \Delta T_{loss}$  is shown by the dotted line in Fig. 13. It was examined by dividing the heat dissipation process into three characteristic stages:

**Stage 1:** The initial increase in  $\Delta T^*_{diss}$  with time ( $t$ ) is approximately linear. During an initial short time interval the amount of heat energy loss is extremely small. Thus, nearly all the heat energy,  $Q_{diss}$ , generated contributes to an increase in  $\Delta T^*_{diss}$ . In this case  $\Delta T^*_{diss}$  equals  $\Delta T_{diss}$  due to the negligible influence of the thermal boundary conditions (quasi-adiabatic conditions).

**Stage 2:** After the initial short time period, the slope ( $\Delta T^*_{diss}/\Delta t$ ) decreases although  $P_{diss}$  is constant. During this stage, the loss of heat due to radiation, convection and mainly heat conductivity is no longer negligible. The slope ( $\Delta T^*_{diss}/\Delta t$ ) decreases as  $\Delta T_{loss}$  increases.

**Stage 3:** Finally, the slope ( $\Delta T^*_{diss}/\Delta t$ ) approaches zero as equilibrium between the generated heat energy due to the mechanical loading and the heat losses to the environment is reached.  $\Delta T_{loss}$  increases linearly with the same slope as  $\Delta T_{diss}$  during the stage 1.

Characterization of the material microstructure based on thermal effects measured during stage 1 shows important advantages. Since the tested material is loaded for a very short period of time the testing conditions are nondestructive or quasi-nondestructive. As previously discussed, the thermodynamic conditions are also quasi-adiabatic (negligible energy losses) during this period. Thus, the

influence of variable thermal boundary conditions (geometry of the tested component, environmental temperature) is extremely small. These simplifications allow us to define the thermal NDE parameter  $\Delta\tau_{\text{diss}}$  based on the increase  $\Delta T_{\text{diss}}$  during stage 1 as

$$\Delta\tau_{\text{diss}} = \frac{\Delta T_{\text{diss}}}{\Delta t \cdot f}. \quad (13)$$

This parameter corresponds to  $\Delta T_{\text{diss}}$  during a time interval  $\Delta t$  normalized to loading frequency  $f$ .

The quantity  $\Delta\tau_{\text{diss}}$  is identical with the temperature change per loading cycle for adiabatic conditions previously defined in (8). It is now possible to calculate the dissipated heat energy,  $q_{\text{diss}}$ , corresponding to the enclosed area of the mechanical hysteresis,  $w_{\text{mech}}$ , (see Fig. 4).

### ***Discussion of the Quasi-adiabatic Conditions***

Although true adiabatic conditions cannot be precisely attained even under laboratory conditions, the effects of heat flow can be greatly reduced by applying two different principles. One is the thermal isolation of the specimen, which will reduce the heat energy exchange with the environment. Similarly, minimizing the time interval for a temperature measurement can result in negligible energy exchange therefore approaching quasi-adiabatic conditions. In the following discussion, the effect of the loading frequency as an experimental parameter on the adiabatic assumption will be discussed. Also, a theoretical model will validate and quantify the quasi-adiabatic conditions during the initial stage of the mechanical loading (stage 1 in Fig.13).

**Effect of the Loading Frequency on  $\Delta\tau_{\text{diss}}$ :** In the case of thermoelastic stress measurements, maintaining quasi-adiabatic conditions is critical. Prior studies have shown that for frequencies above 1 Hz the thermoelastic stress amplitude is frequency independent. Thus, for time periods less than 1 second no significant heat flow occurs and the thermoelastic temperature amplitude,  $\Delta T_{\text{el}}$ , is constant. These results indicate that for metals a frequency above 1 Hz should be adequate to insure quasi-adiabatic conditions. For each experimental set-up however, the minimum frequency to insure adiabatic conditions depends on the specific boundary conditions, thermal conductivity ( $\lambda$ ), and test object geometry. Harwood and Cummings [4] discussed the effect of loading frequency on thermoelastic stress analysis. From this technological experience follows that an independence to the frequency of the mechanical loading indicates quasi-adiabatic conditions.

The temperature change due to heat dissipation per mechanical loading cycle  $\Delta\tau_{\text{diss}}$  should not be influenced by the mechanical loading frequency under adiabatic conditions. In the case of negligible heat energy losses the accumulation of the dissipated heat energy per loading cycle in the tested material is independent of the frequency of the loading. Under quasi-adiabatic conditions an

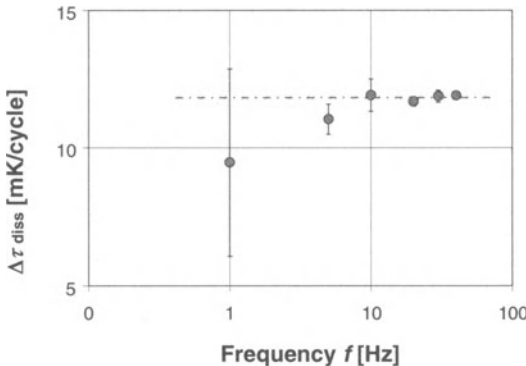


**Fig. 14.** Effect of excitation loading frequency on the thermal NDE parameter  $\Delta\tau_{\text{diss}}$

increase in frequency results in an increase in the accumulated heat energy,  $Q_{\text{diss}}$ . The corresponding increase in  $\Delta T_{\text{diss}}$  exhibits a nearly linear dependence on excitation frequency. According to (13) the thermal NDE parameter,  $\Delta\tau_{\text{diss}}$ , remains independent of frequency. The independence of  $\Delta\tau_{\text{diss}}$  on frequency was demonstrated in the current study by measuring  $\Delta\tau_{\text{diss}}$  at various excitation frequencies in a fatigue-damaged Ti-4Al-6V specimen. Figure 14 shows that at frequencies higher than 10 Hz,  $\Delta\tau_{\text{diss}}$  was nearly constant. High excitation frequencies allowed for a larger increase in temperature, and thus the accuracy of the  $\Delta\tau_{\text{diss}}$  measurements was enhanced. At lower frequencies however,  $\Delta\tau_{\text{diss}}$  measurements exhibited a lower accuracy. Very low excitation frequencies resulted in a temperature increase below the temperature resolution of the infrared camera, thus it was difficult to extract an accurate measurement of  $\Delta T_{\text{diss}}$  from the background noise.

In certain cases however  $\Delta\tau_{\text{diss}}$  is influenced by the loading frequency in stage 1, although the quasi-adiabatic conditions are practically assured. The reason is a change in the mechanical damping due to the dynamics of material loading. At higher frequencies the dynamic yield strength of materials increases, thus the microscopic deformations and the hysteresis area decrease significantly [11]. Within the frequency range investigated in the current study (1–100 Hz), for low frequency loading these effects of dynamic loading were not observed.

**Theoretical Model:** The duration of loading time where quasi-adiabatic conditions are valid,  $\Delta t_{\text{ad}}$ , (during the stage 1 in Fig. 13) was estimated theoretically by developing and applying a mathematical model that described the heat losses in a cylindrical dogbone specimen. In the model, the mechanical hysteresis was related to heat sources,  $Q_{\text{diss}}(x,y,z,t)$ , that produce a temperature variation,  $T^*_{\text{diss}}(x,y,z,t)$ , as a function of time,  $t$  and position  $r(x,y,z)$  within the specimen.  $T^*_{\text{diss}}(x,y,z,t)$  is defined as the temperature change in the center of the gage section of the fatigue specimen that is detected by the infrared camera during the experiment. It corresponds to the dotted line in Fig. 13 and includes heat dissipation and heat loss due to energy exchange with the environment. Heat loss

is assumed to be primarily due to thermal conductivity as described by the heat diffusion equation [28],

$$Q(\underline{r}, t) = \rho c_p \frac{\partial T_{\text{diss}}^*(\underline{r}, t)}{\partial t} - \nabla(\lambda \nabla T_{\text{diss}}^*(\underline{r}, t)), \quad (14)$$

where  $\lambda$  ( $\text{W m}^{-1} \text{K}^{-1}$ ) is the thermal conductivity of the tested material. The cylindrical geometry of a dogbone specimen results in mechanical stresses primarily in the longitudinal direction, and therefore the mechanical damping and the activation of the heat sources  $Q_{\text{diss}}(\underline{r}, t)$  occur in the middle section of the specimen (Fig. 13). The dogbone specimen geometry used in the experiments resulted in a mechanical stress concentration in the gage section by a factor of 4 compared to the specimen mounting area. In the following discussion, it will be shown that  $Q_{\text{diss}}(\underline{r}, t)$  is approximately proportional to  $\sigma_a^3$ . Therefore, the heat sources due to heat dissipation within the mounting area can be assumed lower by a factor of 64.

A closed form solution of the heat conduction processes, heat losses by convection and radiation on dogbone specimens for realistic experimental conditions is not feasible. Therefore, several simplifications of the model were implemented to obtain an analytical solution for  $T_{\text{diss}}^*(\underline{r}, t)$ . An analytical solution of (14) is already possible assuming the geometry of the specimen as cylindrical and restricting the heat flow solely to the mounting section of the fatigue machine. However, it was found that further simplification of the model was possible by assuming a one-dimensional model:

- one-dimensional heat flow in the z-direction
- an idealized heat source located in the center of the gage section
- the heat source extends infinitely perpendicular to the z-direction
- the constant heat source  $Q_{\text{diss}}$  is activated at time  $t = 0$

For this case the open space Green's function  $G(z, z', t, t')$  is valid [28], which enables the calculation of the temperature variation  $T_{\text{diss}}^*$  as a convolution integral along the heat flow axis  $z$  as a function of time  $t$

$$T_{\text{diss}}^*(z, t) = \int_0^\infty \int_{-\infty}^\infty G(z, z', t, t') Q(z', t') dz' dt' \quad (15)$$

with

$$G(z, z', t, t') = \begin{cases} \frac{\alpha/\lambda}{\sqrt{4\pi\alpha(t-t')}} \exp\left(\frac{(z-z')^2}{4\alpha(t-t')}\right) & , \text{ for } t' \leq t \\ 0 & , \text{ for } t' > t \end{cases} \quad (16)$$

and the thermal diffusivity

$$\alpha = \frac{\lambda}{\rho c_p} . \quad (17)$$

The material parameters were assumed to be constant throughout the sample for the mathematical simulation purposes. Values for the material density ( $\rho = 4.47 \cdot 10^3 \text{ kg m}^{-3}$ ) and heat capacity ( $c_p = 523 \text{ J kg}^{-1} \text{ K}^{-1}$ ) were obtained from

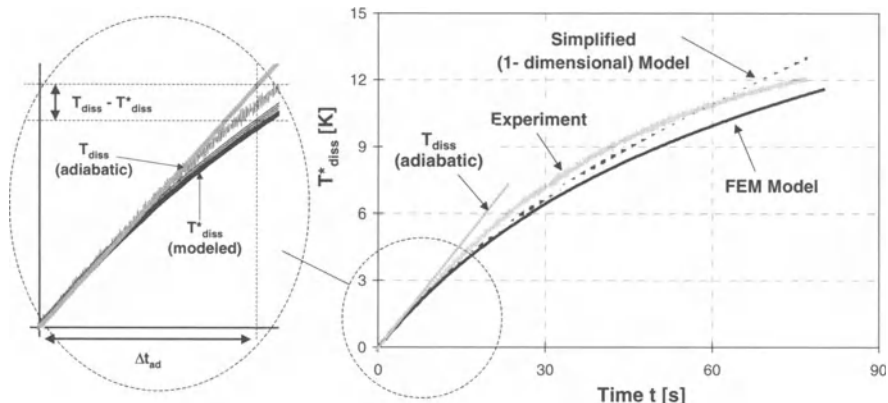


**Fig. 15.** Temperature variation  $T^*_{\text{diss}}(t)$  after the start of a cyclic mechanical loading: Experimental result in comparison to the mathematical model

the open literature. However, thermal conductivity,  $\lambda$ , for Ti-6Al-4V can vary significantly with chemical composition, heat treatment and mechanical treatment.

Therefore, the thermal conductivity was determined for the current Ti-6Al-4V alloy from the electrical conductivity by applicability of the Wiedemann-Franz-Lorenz law. Electrical conductivity measurements were performed to estimate  $\lambda$ . The value obtained from this experiment was  $\lambda=5 \text{ W m}^{-1}\text{K}^{-1}$ . (For comparison, the value for pure titanium in the open literature was  $\lambda=22 \text{ W m}^{-1}\text{K}^{-1}$ ). This is also lower than the value of  $7.2 \text{ W m}^{-1}\text{K}^{-1}$  given in Chapter 4 for a similar alloy. Figure 15 shows a comparison between the predicted and experimental results for  $T^*_{\text{diss}}(t)$  in the center of the gage section of the specimen using the simplified one-dimensional model. The thermal excitation loading parameters were:  $f=30 \text{ Hz}$ ,  $\sigma_a = 467.5 \text{ MPa}$  and  $\sigma_m = 400 \text{ MPa}$ . The figure shows good agreement between the predicted and experimental results during the initial increase in  $T^*_{\text{diss}}(t)$ . Beyond the initial increase however, the predicted values deviate significantly from the experiment.

To enable an improved matching of the model to the experiment Finite Element Modeling (FEM) was performed for the  $T^*_{\text{diss}}(r, t)$  calculation. Figure 15 compares the predicted temperature variation from the FEM simulation to the measured temperature variation in the center of the gage section of the dogbone specimen. As can be seen from Fig. 15, the FEM-simulated temperature increase matches the experimental result particularly well at the start of the mechanical excitation. After more than 10 seconds the FEM-model underestimates the temperature increase,  $T^*_{\text{diss}}$ . However, qualitatively it provides a better matching to the experiment than the one-dimensional analytical model.

The simplified one-dimensional model matches the experimental result during the initial period of temperature increase after the start of the heat source activation. The assumption of one-dimensional heat flow (along the dogbone specimen to the mounting section) matches the actual experimental conditions during a short time interval.

Based on the results of the simulations in Fig. 15, the following conclusions can be drawn:

- Stage 1 (as defined in Fig. 13) is characterized by a small temperature increase and short time period,  $\Delta t_{ad}$ . The nearly linear increase in  $T^*_{diss}(t)$  was predicted theoretically, and observed experimentally. Nearly the entire generated dissipated heat energy results in an increase of  $T^*_{diss}(t)$  during the period  $\Delta t_{ad}$ . The heat loss due to thermal boundary conditions is negligible for this period.
- The deviation from linearity for longer loading times (stage 2 in Fig. 13) indicates the loss of the quasi-adiabatic conditions. The deviation of  $T^*_{diss}(t)$  from the linear increase that is assumed to determine  $\Delta T_{diss}$  was set to 2% to define a period  $\Delta t_{ad}$ , which ensures quasi-adiabatic conditions (see Fig. 15).
- The time period  $\Delta t_{ad}$  depends on the thermal diffusivity,  $\alpha$ , whereby a low value for  $\alpha$  results in an increase in  $\Delta t_{ad}$  and lowers the performance requirements for the heat energy rating,  $P_{diss}$ , and infrared camera. For the titanium alloy investigated the value obtained for  $\Delta t_{ad}$  was 7.14 sec. By comparison, the time period obtained for high conductivity pure copper material decreases to  $\Delta t_{ad} = 0.14$  sec.

### **Fatigue Characterization Using $\Delta\tau_{diss}$**

Applicability of heat dissipation measurements for fatigue damage characterization was investigated using the same Ti-6Al-4V alloy and dogbone geometry discussed above. The specimens were subjected to interrupted fatigue tests so that the thermal NDE parameter,  $\Delta\tau_{diss}$  could be measured after each predetermined block of fatigue loading cycles. The testing procedure is illustrated schematically in Fig. 16.

The fatigue tests were conducted under low cycle fatigue (LCF) conditions with  $f=30$  Hz,  $\sigma_a=382.5$  MPa,  $\sigma_m=467.5$  MPa. For these test conditions the maximum stress is 850 MPa. By comparison, the yield strength of the alloy ( $\sigma_{ys}$ ) is  $951 \pm 32$  MPa. Figure 17 shows the change in  $\Delta\tau_{diss}$  after every cycle block of approximately 6,500 cycles. For this fatigue test, the total number of fatigue

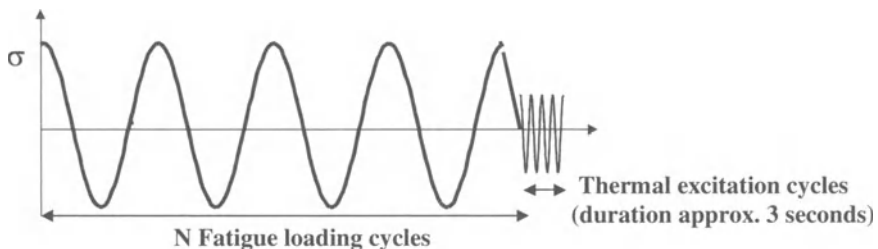


**Fig. 16.** Schematic loading sequence. Fatigue loading interrupted by short-term thermal excitation loading cycles

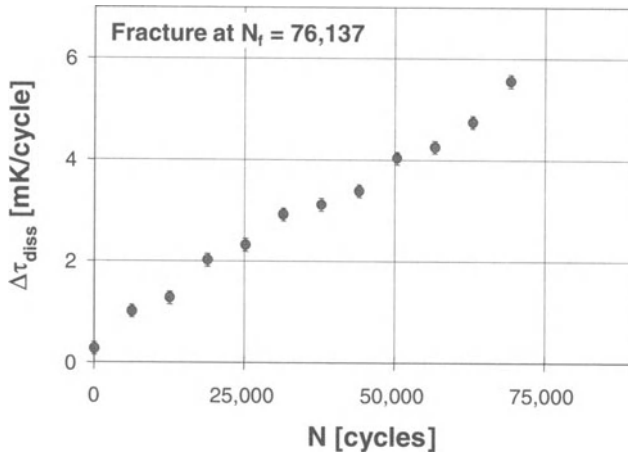


**Fig. 17.**  $\Delta\tau_{\text{diss}}$  after each block of 6500 fatigue cycles. Fatigue and thermal excitation loading parameters:  $f=30$  Hz,  $\sigma_a=382.5$  MPa,  $\sigma_m=467.5$  MPa

cycles to fracture was  $N_f=76,137$ . Excitation of the dissipated heat was conducted by subjecting the specimen to short-term mechanical loading of approximately 90 cycles during each thermal measurement. The excitation loading parameters used in this experiment were the same as the fatigue conditions, namely  $f=30$  Hz,  $\sigma_a=382.5$  MPa,  $\sigma_m=467.5$  MPa. However, different mechanical excitation parameters can be used as schematically shown in Fig. 16. During each fatigue test interruption,  $\Delta T_{\text{diss}}(t)$  was measured three times and an average standard deviation was evaluated.

The experimental results in Fig. 17 show that  $\Delta\tau_{\text{diss}}$  increases continuously up to specimen fracture. Thus, the thermal NDE parameter,  $\Delta\tau_{\text{diss}}$ , exhibits high sensitivity for fatigue damage characterization. The LCF damage caused an increase of  $\Delta\tau_{\text{diss}}$  from 0.28 to 5.55 mK/cycle, whereas the averaged standard deviation was  $\pm 0.23$  mK/cycle. The nearly linear increase during the entire lifetime until fracture, indicates a definite correlation between the NDE parameter and the fatigue damage accumulation. In fact, during the early stages of fatigue, prior to crack detection, a significant increase of  $\Delta\tau_{\text{diss}}$  was measured. Therefore, the use of  $\Delta\tau_{\text{diss}}$  as a fatigue damage metric was examined.

### ***Discussion of the Thermal NDE Parameter $\Delta\tau_{\text{diss}}$***

**Excitation of  $\Delta\tau_{\text{diss}}$ :** Excitation of  $\Delta\tau_{\text{diss}}$  was performed using cyclic loading with stress amplitudes in the LCF-regime. Excitation with high stress amplitudes such as these, results in testing that is quasi-nondestructive, since the excitation loading cycles consume a small fraction of the fatigue lifetime (approximately 0.1%). Therefore, the use of lower excitation stresses for measurement of  $\Delta\tau_{\text{diss}}$  was also examined. Excitation of  $\Delta\tau_{\text{diss}}$  was generated by cycling at stress amplitudes,  $\sigma_a$ , between 100 and 400MPa, after each block of  $\approx 6,500$  fatigue cycles. Figure 18

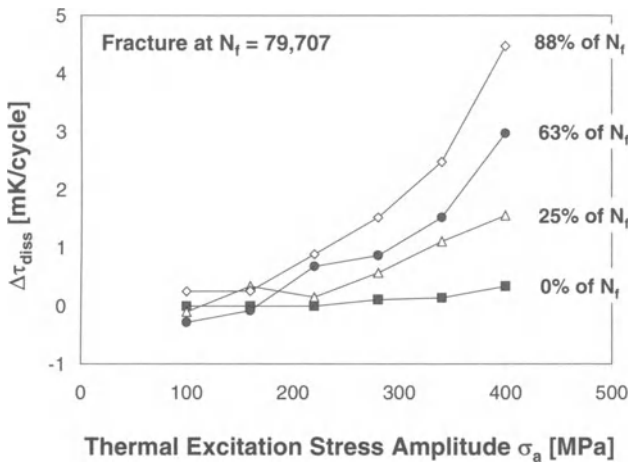


**Fig. 18.**  $\Delta\tau_{\text{diss}}$  excited at varied stress amplitude  $\sigma_a = 100\text{--}400 \text{ MPa}$  ( $f=30 \text{ Hz}$ ,  $\sigma_m=467.5 \text{ MPa}$ ) at various stages of fatigue life

shows the variation of  $\Delta\tau_{\text{diss}}$  as function of  $\sigma_a$ . When  $\sigma_a < 200 \text{ MPa}$  the virgin material (0% of  $N_f$ , where  $N_f$  is the number of cycles until fracture) shows significantly less heat dissipation than the fatigued material (25, 63, and 88% of  $N_f$ ). The accuracy of the  $\Delta\tau_{\text{diss}}$  measurement is poor for lower stress amplitudes due to the lower heat energy rating,  $P_{\text{diss}}$ . However, the accuracy of the temperature measurements can be enhanced by frame averaging, use of high sensitivity infrared cameras, or by use of high frequency loading to increase  $P_{\text{diss}}$ .

**Interpretation of  $\Delta\tau_{\text{diss}}$  Based on Microplasticity:** In the case of plastic deformations the mechanical energy  $w_{\text{mech}}$  for one hysteresis cycle (hysteresis area) that is transferred into heat,  $q_{\text{diss}}$ , can be described as follows

$$w_{\text{mech}} = \int_0^{\varepsilon_p(t)} \sigma_a \cdot \sin(2\pi f \cdot t) \cdot d\varepsilon_p . \quad (18)$$

Further,  $w_{\text{mech}}$  is approximated by the following relation [11] (compare Fig. 4)

$$w_{\text{mech}} = A \cdot \sigma_a \cdot \varepsilon_p , \quad (19)$$

where,  $A$  is an empirical constant describing the shape of the mechanical hysteresis loop. For the Ti-6Al-4V alloy used in the current study under LCF-conditions a narrow elliptical shape ( $A=1.57$ ) was found experimentally.

The stress-strain relationship due to a quasi-static monotonic loading in a tensile test, including both the elastic and plastic deformation, is described by the Ramberg-Osgood relation [29]. Based on this relationship the plastic deformation under low frequency loading at stress amplitudes close to the yield strength of the material can be described by

$$\varepsilon_p = \left( \frac{\varepsilon_a}{B} \right)^m \quad (20)$$

where B and m are empirical material constants.

Thus, a relationship between  $w_{\text{mech}}$  and  $\sigma_a$  can be obtained from (19) and (20). Assuming the entire hysteresis energy,  $w_{\text{mech}}$ , is converted into heat energy,  $q_{\text{diss}}$ , and applying the (7), a relationship between  $\Delta\tau_{\text{diss}}$  (temperature change per single hysteresis cycle) and  $\sigma_a$  is obtained

$$\Delta\tau_{\text{diss}} = \frac{C}{\rho \cdot c_p} \cdot \sigma_a^{m+1}, \quad (21)$$

where the constant C depends on the material and the fatigue damage state.

From the experimental results presented in Fig. 18 the exponent  $m+1$  was found equal to 3.11. This corresponds to a Ramberg Osgood Exponent of 2.11. Thus,  $\Delta\tau_{\text{diss}}$  exhibits a power law dependency on stress amplitude. The stress exponent provides insight into the mechanisms of localized microscopic heat sources in the material. These microstructural heat sources are activated disproportionately when the stress amplitude is increased. Prior studies have shown that the relationship between excitation stress amplitude and the temperature increase can be used as an indicator to microplasticity and inhomogeneous fatigue cracking [20, 31].

In a tensile test microplasticity appears at stresses significantly below the yield strength of the material [11]. Nucleation sites for the microplasticity might be weak bonding conditions within the material at inclusions or precipitations. Also locally reduced yield strength due to differing chemical composition or differing grain orientation relative to the stress loading are possible reasons. Another very important reason for microplastic deformations is the local increase of stresses due to stress concentrations at grain boundaries or microcracks. At these stress concentrations the material yield strength can be reached locally. Detailed studies of irreversible submicrostructural changes in Ti-6Al-4V that occur during cyclic mechanical loading have been conducted using transmission electron microscopy and positron annihilation methods (generation of dislocations and point defects). These results are discussed in chapter 13. A statistical evaluation of micro-crack concentration within the surface and near surface regions was conducted using High Frequency – Scanning Acoustic Microscopy (HF-SAM). Using HF-SAM early microcrack formation in Ti-6Al-4V was identified after less than 40% of consumed lifetime. These micro-fatigue cracks contribute to locally increased mechanical damping. Thus, the increase in  $\Delta\tau_{\text{diss}}$  with increasing excitation stress amplitude can be attributed to an increased number and volume of heat sources.

### 9.5.5 Fatigue Characterization by Mechanically Induced Dissipated Heat Analysis (MIDA) – Ultrasonic Excitation

#### ***Ultrasonic Excitation Compared to Low Frequency Excitation***

The NDE methodology discussed above can now be generalized to include excitation of the heat dissipation effects using ultra-high frequency (ultrasonic)

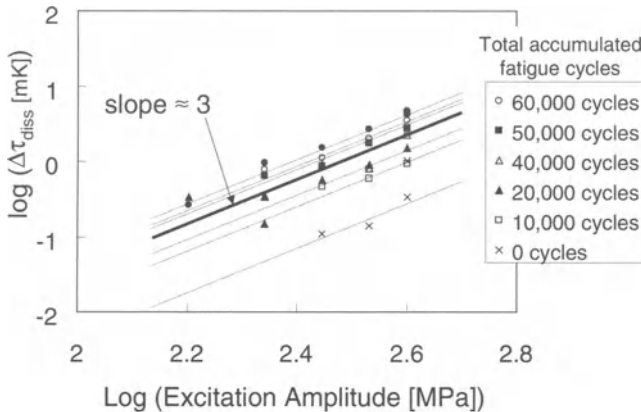


**Fig. 19.** Logarithmic plot of  $\Delta\tau_{\text{diss}}$  as a function of excitation loading amplitude for each step in fatigue life. Fatigue loading conditions:  $f = 30 \text{ Hz}$ ,  $\sigma_a = 400 \text{ MPa}$ ,  $\sigma_m = 467.5 \text{ MPa}$

loading. The total temperature increase due to dissipated heat depends on the loading frequency and amplitude, and the time duration of the excitation cycles. Figure 14 showed that for mid-range frequencies (10–60 Hz) cycling with the same mean load and amplitude resulted in values for  $\Delta\tau_{\text{diss}}$  (temperature due to heat dissipation per loading cycle) that were independent of frequency. However, cycling at the same frequency resulted in decreasing values of  $\Delta\tau_{\text{diss}}$  with decreasing stress amplitude (Fig. 18). By plotting the results in Fig. 18 on a logarithmic scale the functional relationship between excitation load amplitude and temperature increase can be examined. Figure 19 shows that independent of the number of accumulated fatigue cycles  $N$ , a curve fit to the data results in a slope  $\approx 3$ , thus  $\Delta\tau_{\text{diss}} \propto \sigma_a^3$ . As previously discussed, this third power relationship is reasonable based on the mechanical hysteresis origin of the heat dissipation. Using the average results from all of the curves in Fig. 19 a functional relationship between stress amplitude and  $\Delta\tau_{\text{diss}}$  was obtained [33]

$$\Delta\tau_{\text{diss}} [\text{mK}] = (4.5 \cdot 10^{-9} + 9 \cdot 10^{-13}N) \cdot (\sigma_a [\text{MPa}])^3. \quad (22)$$

For ultrasonic loading the mean stress is zero, and the stress amplitude is necessarily small. Applying (22) to ultrasonic excitation requires an estimation of the stress amplitude. The stress amplitude,  $\sigma_a$ , for ultrasonic loading can be calculated from the sound intensity generated by the ultrasonic device.

### Experimental Setup

The high frequency excitation in the current study was generated using a commercially available ultrasonic polymer welding system, produced by Branson Ultrasonics. The resonant system consists of a 20 kHz power supply, piezoelectric

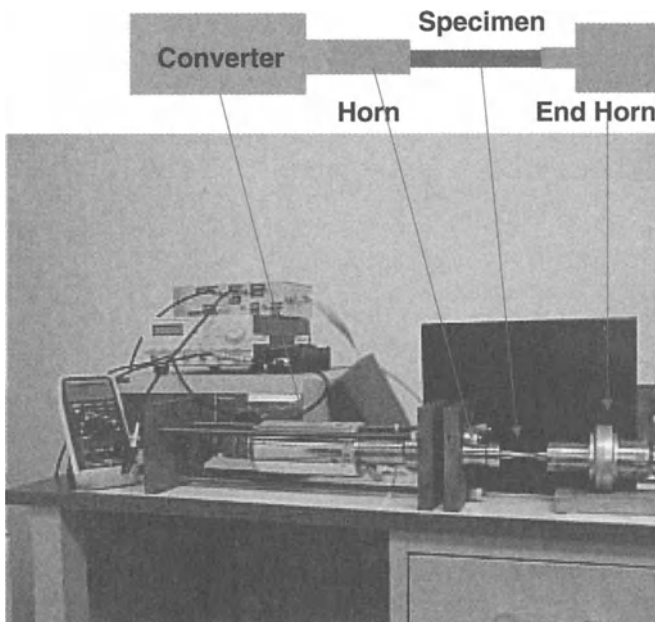


**Fig. 20.** Ultrasonic stimulation of fatigue specimen

converter, and booster horns. The system design provides high strain amplitude in the gage section of the specially designed cylindrical dogbone specimens during resonant conditions [32]. For the specimens used in this study (diameter = 4 mm) a maximum power output of 1 kW results in a maximum sound intensity in the gage section of  $80 \text{ W/mm}^2$  (Fig. 20). Measurements of the thermal parameter were conducted with an approximate power output of 50% of maximum; therefore, the sound intensity during testing was  $\approx 40 \text{ W/mm}^2$ .

### ***Experimental Results***

The applicability of ultrasonic excitation for measurement of  $\Delta\tau_{\text{diss}}$  was examined on commercial grade Ti-6Al-4V specimens. Similar to the experiments performed using low frequency thermal excitation,  $\Delta\tau_{\text{diss}}$  was measured as a function of the number of fatigue cycles. The fatigue test parameters were the same as that used with low frequency excitation, namely sinusoidal loading at 30 Hz,  $\sigma_m = 467.5 \text{ MPa}$ ,  $\sigma_a = 400 \text{ MPa}$ . The fatigue tests were interrupted after each block of 5,000 fatigue cycles for measurement of  $\Delta\tau_{\text{diss}}$ . Excitation of the thermal effects using ultrasonic frequencies required removing the specimen from the fatigue test machine and placing the specimen in the Branson ultrasonic excitation

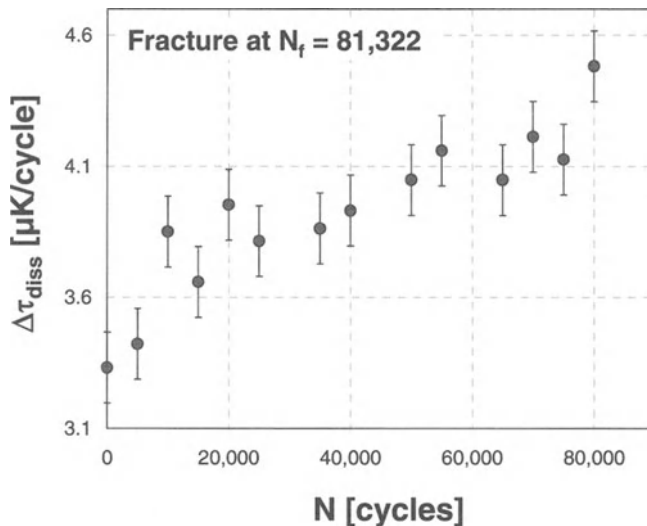


**Fig. 21.** Variation in the thermal parameter,  $\Delta\tau_{\text{diss}}$ , as a function of accumulated fatigue cycles in Ti-6Al-4V specimen ( $N_f = 81,065$ ). Thermal excitation at  $f = 20$  kHz,  $\sigma_a = 47$  MPa,  $\sigma_m = 0$  MPa. Fatigue loading conditions:  $f = 30$  Hz,  $\sigma_m = 467.5$  MPa,  $\sigma_a = 400$  MPa

device. After the thermal measurements, the specimen was placed back into the fatigue test machine and fatigue cycling resumed. The iterative process of fatigue cycles followed by thermal measurements was repeated until specimen failure in the fatigue machine.

Similar to the thermal measurements made using low frequency excitation, the temperature distributions were recorded during the ultrasonic excitation for approximately 3 to 12 seconds. The temperature measurements were made using the same infrared camera and data analysis procedure as discussed previously for the low frequency excitation experiments.

The variation in  $\Delta\tau_{\text{diss}}$  as a function of fatigue cycles is shown in Fig. 21. As previously discussed the lower stress amplitudes under ultrasonic loading result in significantly lower values for  $\Delta\tau_{\text{diss}}$ . The figure shows that ultrasonic excitation at a frequency of 20 kHz resulted in typical values for  $\Delta\tau_{\text{diss}}$  on the order of  $\approx 0.004$  mK/cycle. By comparison, using low frequency, high stress amplitude excitation  $\Delta\tau_{\text{diss}}$  was 2 to 3 orders of magnitude higher, on the order of 4 mK/cycle (Fig. 17). However, because of the comparatively high frequency (20,000 Hz), loading for at least 3 seconds resulted in sufficient dissipated heat accumulation to produce a significant temperature enhancement. The resulting total temperature increase ( $\Delta T_{\text{diss}}$ ) was similar to that obtained using high amplitude low frequency loading. The results in Fig. 20 show however that the scatter in the values of  $\Delta\tau_{\text{diss}}$  is higher with ultrasonic excitation. A possible reason is that the attachment of the fatigue specimen to the ultrasonic horn was not constant after every new measurement cycle, causing higher scattering in the measured parameter. Thus,

the excitation conditions had a larger scatter in comparison to the experiments at high mechanical loading excitation done in the fatigue machine.

The applied maximum stress for ultrasonic excitation was approximately 50 MPa. This follows from measurements using strain gages and theoretical considerations. By comparing the data calculated using (22) to the experimental results it should be considered, that the formula was established for low frequency loading (1 to 50 Hz). Excitation of the thermo-mechanical effects using ultrasonic frequencies results in different damping mechanisms. Nevertheless, (22) gives the right order of magnitude for the temperature due to dissipated heat per cycle. However, the measured increase in  $\Delta\tau_{\text{diss}}$  during fatigue is lower than expected. In contrast, the applied low-frequency excitation at stresses close to the yield strength of the material was done at high mean stresses, which may have resulted in a more rapid increase in  $\Delta\tau_{\text{diss}}$  with fatigue cycles. Further studies currently underway have indicated that  $\Delta\tau_{\text{diss}}$  is sensitive to the mean stress during excitation.

Nevertheless, the results of the study using ultrasonic excitation for thermal NDE show that a clear correlation exists between the values of  $\Delta\tau_{\text{diss}}$  and accumulated fatigue cycles. The quasi-adiabatic time interval for the thermal measurements depends on the thermal diffusivity of the material, and is a constant independent of the excitation frequency and mechanical loading. For the titanium alloy tested in the current study, the mechanical loading during the time interval ensuring quasi-adiabatic conditions resulted in a measurable temperature increase during ultrasonic excitation comparable to that during high amplitude, low frequency excitation. Analysis of the temperature distribution within the specimen showed that the magnitude of  $\Delta T_{\text{diss}}$  was significant, and well within the sensitivity of the IR camera. Further development of the thermal NDE methodology using low amplitude, high frequency cyclic ultrasonic excitation can be highly advantageous since it offers a chance for development of a nondestructive, in field inspection technique for components.

### **9.5.6 Thermographic NDE Based on Heat Dissipation – Summary and Conclusion**

#### ***Thermographic NDE Using $\Delta\tau_{\text{diss}}$***

The applicability of  $\Delta\tau_{\text{diss}}$  as a thermal NDE parameter is summarized in Fig. 22. The figure shows a logarithmic plot of the approximate temperature change expected as a function of the excitation stress amplitude for various cyclic loading conditions. Material characterization based on heat dissipation relies on measurements of the net temperature increase per excitation cycle,  $\Delta\tau_{\text{diss}}$ . Results of the current study in Ti-6Al-4V showed that low frequency excitation with a stress amplitude range of 100–400 MPa, resulted in  $\Delta\tau_{\text{diss}}$  of approximately 1 to 10 mK/cycle. Excitation of less than 50 loading cycles was already sufficient to generate a temperature change that was within the sensitivity of the IR camera

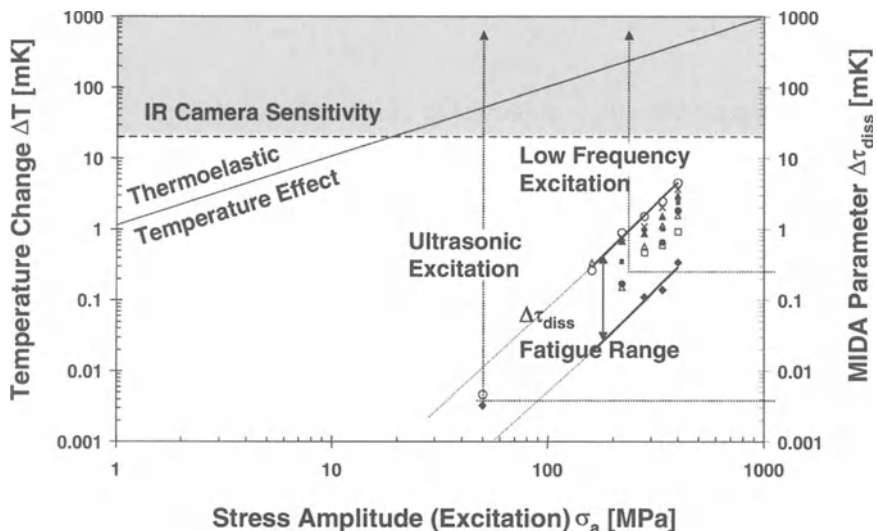


**Fig. 22.** Comparison between the thermal effects due to mechanical loading (thermoelastic temperature variation  $\Delta T_{el}$ , temperature due to dissipated heat per cycle  $\Delta\tau_{diss}$ ) as a function of excitation stress amplitude, excitation principle, fatigue damage and IR camera sensitivity [33]

(200 mK; enhanced by a factor of at least 10 through time and local temperature averaging). By comparison, ultrasonic loading with approximate stress amplitude of 50 MPa resulted in a lower value of  $\Delta\tau_{diss}$  (approximately 0.001 to 0.01 mK/cycle). The higher loading frequency however, resulted in a measurable temperature enhancement within the same quasi-adiabatic time interval of approximately 7 seconds estimated for the material under investigations (see Paragraph 9.6.2).

The stress dependence of dissipated heat effects can be compared to that of thermoelastic effects in Fig. 22. Stress measurements based on thermoelastic effects rely on the linear proportionality between temperature variation,  $\Delta T_{el}$ , and applied stress. In contrast, the heat dissipation effects are due to micro and sub-microstructural plastic deformations which are proportional to  $\Delta\tau_{diss} \propto \sigma_a^3$  (Fig. 19). The differences in stress behavior between the thermoelastic and heat dissipation effects over the entire range of measured values for  $\Delta\tau_{diss}$  show that the temperature effects are clearly separated.

The variation in  $\Delta\tau_{diss}$  due to fatigue damage state is shown in Fig. 22 for low frequency excitation (see Figs. 17 and 21). For the Ti-6Al-4V material examined it was found that stress amplitudes of  $\approx 50$  MPa were required to generate enough heat energy accumulation during short-term ultrasonic loading to measure the temperature increase. For materials with higher stress dependence (higher Ramberg-Osgood-Exponent) such as stainless steel the excitation stress dependence will be significantly higher. In addition, these results indicate that at

local stress concentrations (e.g. crack tips) much higher temperatures are generated.

### **NDE Based on Mechanical Damping and Nonlinear Effects**

NDE methodologies based on heat dissipative effects can be applied to defect detection and material characterization. For the detection of defects, e.g. cracks or delaminations, high power ultrasound is usually applied to excite local heat dissipation in the vicinity of the crack. Mechanical damping (ultrasound absorption) is enhanced due to the local increase of mechanical stresses ("notch-effect") in front of cracks or friction of surfaces (crack edges) causing a locally increased mechanical hysteresis. Microplasticity, anelasticity and viscoelasticity can be assumed as the reason for mechanical damping. The local increase in temperature due to heat dissipation enables the visualization of the defects on the material surface using infrared thermography. A sufficient heat power rating is required and the thermal effects need to be locally resolved by the infrared camera optics. Loss Angle Thermography, Vibro-Thermography and the Thermosonic methods are based on this physical principle [34, 35]. These methods are considered to be nondestructive because the internal irreversible changes within the microstructure are assumed to be negligible. Figure 23 shows fatigue cracks on a steel metal sheet imaged with ultrasonic excitation (Thermosonics). Standing wave patterns that are visible due to heat dissipation are shown as well.

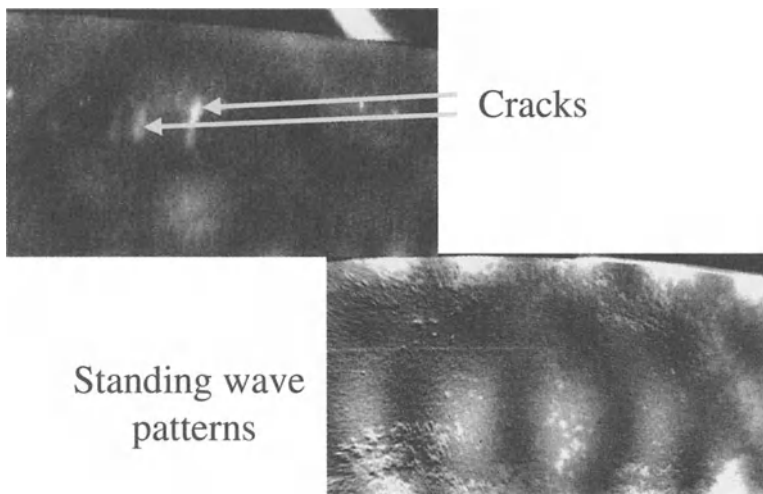


**Fig. 23.** Thermosonic images of fatigued metal sheets (experiments at Wayne State University, Detroit)

Traditionally, material characterization based on heat dissipative effects (in particular fatigue damage characterization) was limited to measurements made in-situ during the fatigue experiment. During cyclic mechanical fatigue loading, the mechanical hysteresis is generated by micro-plastic fatigue damage processes [12, 24, 25]. The mechanical loading excites internal heat sources, which are characteristic for the microstructure. Thus, the corresponding thermal effects are correlated to material properties, which are determined by the microstructure. Knowledge about the material and fatigue conditions is required for the interpretation of the microscopic processes. The most important reason for the temperature increase or decrease during fatigue is the material strengthening or softening in response to the change in mechanical hysteresis area. Analysis of the mechanical hysteresis and heat generation during cyclic loading showed that the thermal measurements were significantly more sensitive to fatigue damage accumulation than direct hysteresis measurements. Extensive examinations on steel materials showed that the temperature increase due to heat dissipation correlates to the plastic strain amplitude  $\varepsilon_p$ . Thus, the relation between strain amplitude and the number of cycles until fracture (Coffin-Manson relation) can be transferred to thermal parameters [30–31]. Further, an estimate of the fatigue limit can be obtained from the thermal parameters [11, 36, 37].

The NDE method presented in paragraphs 9.5.4 and 9.5.5 does not monitor a fatigue process continuously. A short mechanical loading pulse of 3 to 5 seconds duration is used to stimulate a thermal response of the test specimen. The measured parameter  $\Delta\tau_{diss}$  is the temperature increment per hysteresis cycle. It can be related to the damping coefficient  $\eta'$  measured by internal friction experiments. This damping coefficient  $\eta'$  is the energy generated per hysteresis cycle  $q_{diss}$ , divided by the maximum work to elongate the specimen  $w_{max}$

$$\eta' = \frac{q_{diss}}{2\pi \cdot w_{max}} \quad (23)$$

with

$$q_{diss} = c_p \cdot m \cdot \Delta\tau_{diss}. \quad (24)$$

$c_p$  is the specific heat at constant pressure and  $m$  is the mass. It follows from (23) and (24) that

$$\eta' = \frac{c_p \cdot m}{2\pi \cdot w_{max}} \cdot \Delta\tau_{diss}. \quad (25)$$

Thermographic results using high stress low frequency loading have been discussed under paragraph 9.5.4. The experimental procedure and data analysis were similar as outlined above (paragraph 9.5.5) for ultrasonic loading but the loading frequency was only 30 Hz (compared to 20 kHz used for the above experiments). The thermal parameter  $\Delta\tau_{diss}$  for the temperature increment generated per hysteresis cycle was 3 orders of magnitude larger compared to high power ultrasonic excitation and showed a linear increase with fatigue life similar to high power ultrasonic (see Fig. 17).

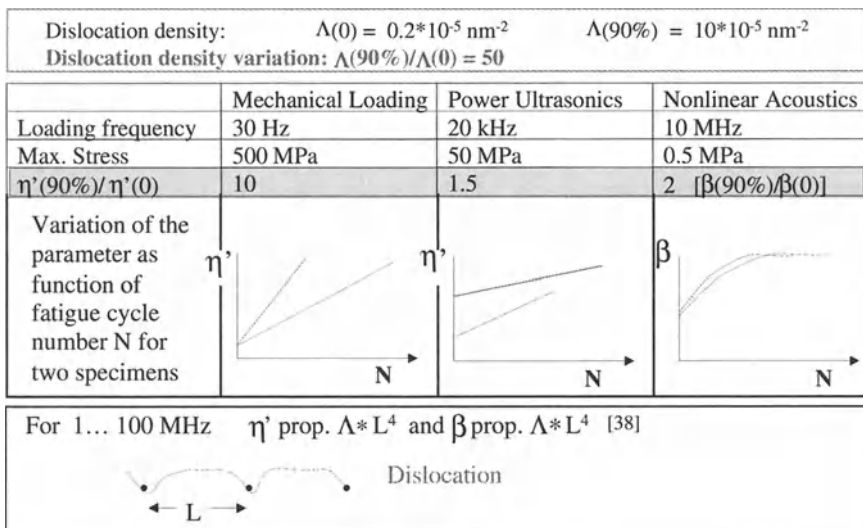


**Fig. 24.** Comparison of experimental results (schematic) for fatigued Ti-6Al-4V specimens. (0) means virgin specimen, (90%) means specimen after 90% of fatigue life [42]

$w_{max}$  is the maximum work to elongate the specimen (tensile experiment) as defined above. It does not include hysteresis loss. The elastic modulus does not significantly change during fatigue life (see chapter 7). It follows that also  $w_{max}$  does not significantly change and  $\eta'$  is almost proportional to  $\Delta\tau_{diss}$ .

Figure 24 shows a schematic which compares the internal damping determined from the thermographic results to the nonlinear acoustic experiments described in chapter 7. In contrast to the temperature increment measured for low cycle or ultrasonic loading the acoustic nonlinearity parameter  $\beta$  cannot be compared directly to the internal friction parameter  $\eta'$ . However, it can be found from the literature that the contribution of the dislocations to  $\beta$  is proportional to the dislocation density  $\Lambda$  multiplied by  $L^4$  where  $L$  is the loop length [38]. A similar relation for the ultrasonic absorption follows from the Koehler-Granato-Luecke theory and has been experimentally verified for the 1 to 100 MHz frequency range [39, 40]. Ultrasonic absorption means the transfer of ultrasonic energy into heat. Therefore  $\beta$  is compared to  $\eta'$  in Fig. 24.

The nonlinear acoustic parameter  $\beta$  was measured at the frequency of 10 MHz with transducers mounted on top and bottom of the fatigue specimen. The results illustrated schematically in Fig. 24 indicate an increase of the nonlinearity parameter with fatigue life. However, saturation was found for a high numbers of fatigue cycles.

Fig. 24 compares the damping parameter  $\eta'$  and the nonlinear acoustic parameter  $\beta$  for experiments with loading frequencies that differ with orders of magnitude. Comparison of results achieved by low frequency excitation (30 Hz), power ultrasonic loading (20 kHz) and nonlinear acoustics (10 MHz) for the same

material and fatigue conditions allow discussing different microstructural mechanisms that are responsible for the observed effects. In addition the microstructure was examined for similar materials and fatigue parameters using Transmission Electron Microscopy (TEM).

While the dislocation density increases by a factor of 50 from the virgin to the 90 percent fatigued specimen, the damping parameter increases by a factor of 10 for experiments with a low frequency mechanical loading (30 Hz). In comparison the increase in damping parameter for power ultrasonic loading (20 kHz) was only by a factor of 1.5. A relatively high offset was found in these experiments. This offset varied significantly between different test specimens. This was not highlighted in the discussion under paragraph 9.5.5. The nonlinear acoustics parameter (10 MHz) shows a slightly larger increase but saturates for about 50% of life.

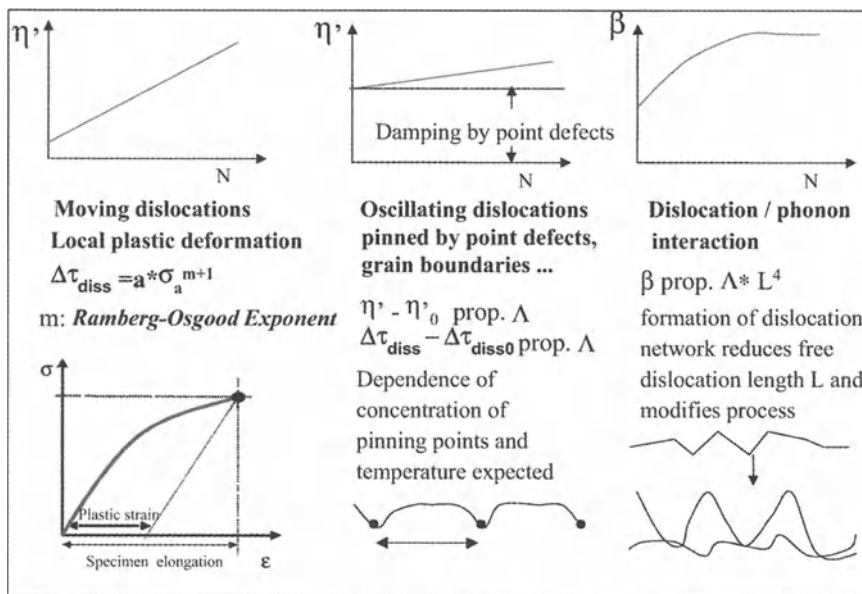


**Fig. 25.** Schematic variation of damping coefficient (from temperature increment per cycle) and nonlinearly parameter  $\beta$  as function of fatigue life of Ti-6Al-4V specimens. Microscopic explanations for low frequency (30 Hz) loading (left), power ultrasonic (20 kHz) loading (center), and nonlinear acoustic (10 MHz) experiments [42]

During an increasing number of fatigue cycles an increasing number of dislocations are generated. Dislocations form dislocation patterns and subgrain structures. This results in a decrease of the loop length  $L$  and an increase of contributions from dislocation dipole pairs. This might explain the saturation of  $\beta$  for higher fatigue cycle numbers.

An explanation for the differences in results obtained at various loading frequencies could be found in the different dissipation mechanisms (Fig. 25). As discussed in paragraph 9.5.4 microplastic deformations are dominant for very low frequencies and high stress amplitudes. Here dissipated heat could be related to the mechanical hysteresis that results from the nonlinearity of the stress-strain relation. The temperature increment is a function of the applied stress with an exponent that can be explained by the Ramberg–Osgood relation.

The dominant damping effect for the high frequencies used in nonlinear acoustic experiments is dislocation-phonon interaction, which should result in a higher damping compared to the medium stimulation frequencies (20 kHz).

The main source for heat dissipated by the power ultrasonic loading with 20 kHz should be the oscillation of dislocations that are pinned at grain boundaries and point defects. A damping parameter proportional to dislocation density is expected. However, in this frequency range, also reorientation or vibration of point defects will significantly contribute due to the internal damping. Snoek effect is one of the most common effects of this type (for carbon in iron). This damping effect should be responsible for the high offset, which was found for this type of loading [42].

## Acknowledgements

The authors would like to acknowledge the scientific and technical support of the AFRL/MLLP-Nondestructive Evaluation Branch, Materials and Manufacturing Directorate, Air Force Research Laboratory, Wright-Patterson Air Force Base, OH. We especially thank James Blackshire for providing the corrosion standard specimens examined in Fig. 10 and Dr. Joel Johnson (AFRL/MLBT) for preparing the coating specimens.

## References

1. Almond DP, Patel PM (1996) Photothermal Science and Techniques, Chapman & Hall, London
2. Bennett CA, Patty RR (1982) *Appl Opt* 21:49–54
3. Balageas DL, Krapez JC, Cielo P (1986) Pulsed photothermal modeling of layered materials. *J Appl Phys* 59:348
4. Harwood N, Cummings WM (1991) Thermoelastic Stress Analysis. Adam Hilger, Bristol, pp. 35–43
5. Monchalin JP, Bussière JF (1984) Measurement of near-surface ultrasonics by thermo-emissivity. Nondestructive methods for material property determination. Plenum Press, New York
6. Enke NF (1989) Thermographic stress analysis of isotropic materials. Ph.D. thesis, University of Wisconsin – Madison
7. Thomson W (Lord Kelvin) (1857) On the thermo-elastic and thermomagnetic properties of matter. *Quart. J of Pure & Appl Math* 1:57–77
8. Vollertsen F, Vogler S (1989) Werkstoffeigenschaften und Mikrostruktur. Carl Hanser, München Wien
9. Bratina WJ (1966) Internal friction and basic fatigue mechanisms in body-centered cubic metals, mainly iron and carbon steels. Physical acoustics: principles and methods IIIA. Academic Press, New York
10. Nowick AS, Berry BS (1972) Anelastic relaxation in crystalline solids. Academic Press, New York
11. Puskar A, Golovin SA (1985) Fatigue in materials: cumulative damage processes. Elsevier, New York
12. Harig H, Middeldorf K, Müller K (1986) Overview on thermometric investigations of fatigue behavior in steels (in German). *HTM* 41 5:286–296
13. Bratina WJ (1966) Internal Friction and Basic Fatigue Mechanisms in Body-Centered Cubic Metals, Mainly Iron and Carbon Steels. In: Warren PM (ed) Physical Acoustics: Principles and Methods. volume III, Part A: The Effect of Imperfections, Academic Press, New York, pp. 223–285
14. Meyendorf N, Ehrlich S, Nitzsche R (1992) Thermografische Ueberwachung von Schweißprozessen. *Bild und Ton* 45 3/4:55
15. Lipetzky LG, Novak MR, Perez I, Davis WR (2001) Development of Innovative Nondestructive Evaluation Technologies for the Inspection of Cracking & Corrosion Under Coatings. Technical Report NSWCCD-61-TR-2001/21, Naval Surface Warfare Center
16. Meyendorf N, Netzelmann U, Vetterlein T, Walle G (1998) Non-Contact Characterization of Layers by Thermographic Methods on Examples of Testing Problems from Aircraft and Aerospace Technology. Proceedings of Materials Week, Symposium 2b. München
17. Walle G, Karpen W, Netzelmann U, Rösner H, Meyendorf N (1999) Nondestructive Testing with Thermographic Techniques. *Technisches Messen*, vol. 66, 9:312–321
18. Hoffmann JP, Matikas TE, Sathish S, Khobaib M, Meyendorf N, Netzelmann U (1999) Nondestructive Characterization of Organic Corrosion Protective Coatings on Aluminum Alloy Substrates. 3rd Annual Report for DARPA-MURI, Grant Number F49620-96-1-0442, Dayton, OH

19. Walle G, Karpen W, Netzelmann U, Rösner H, Meyendorf N (1999) Nondestructive Testing with Thermographic Techniques. *Technisches Messen ATM*, TM 66 9:312–321
20. Busse G, Wu D, Karpen W (1992) Thermal wave imaging with phase sensitive modulated thermography. *J Appl Phys* 71:3962–3965
21. Burgschweiger J (1993) Simulation von Temperaturfeldern bei der zerstörungsfreien Werkstoffprüfung mittels der Impuls-Video-Thermographie. Master Thesis, University Magdeburg
22. Moore PO, McIntire P (1995) Nondestructive Testing Handbook, ed. 2, vol. 9, Special Nondestructive Testing Methods, ASNT
23. Mende D, Simon G (1971) Physik Gleichungen und Tabellen. Fachbuchverlag, Leipzig
24. Harig H (1975) Zur Bedeutung der Thermometrie bei der Prüfung metallischer Werkstoffe. Habilitation thesis, Technical University Berlin
25. Liaw PK, Wang H, Jiang L, Yang B, Huang JY, Kuo RC, Huang JG (2000) Thermographic detection of fatigue damage of pressure vessel steels at 1,000 Hz and 20 Hz. *Scripta Mater* 42:389–395
26. Rösner H, Meyendorf N, Karpen W, Matikas TE (1999) Nondestructive Evaluation of Fatigue in Titanium Alloys with Thermography, Development of Enabling Methodologies for Detection and Characterization of Early Stages of Damage in Aerospace Materials. Third Annual Report by the University of Dayton, DARPA NDE-MURI, AFOSR Grant No F49620-96-1-0442
27. Holman JP (1997) Heat Transfer. McGraw-Hill, New York
28. Carslaw HS, Jäger JC (1959) Conduction of heat in solids. Clarendon Press, Oxford
29. Schatt W, Worch H (1996) Werkstoffwissenschaft. Deutscher Verlag für Grundstoffindustrie, Stuttgart
30. Ballas G, Piotrowski A, Eifler D (1995) Cyclic stress-strain, stress-temperature and stress-electrical resistance response of NiCuMo alloyed sintered steel. *Fatigue Fract Eng Mat Struct* 18 No 5:605–615
31. Ballas G (1996) Cyclic deformation behavior and microstructure of sintered iron and selected sintered steels. Ph.D. thesis, University GH Essen
32. Matikas T (1998) LCF/HCF Interaction Studies Using a HCF Cell Operating in the 10–40 kHz Frequency Range, Development of Enabling Methodologies for Detection and Characterization of Early Stages of Damage in Aerospace Materials. Second Annual Report for DARPA-MURI under Air Force Office of Scientific Research, Grant Number F49620-96-1-0442
33. Meyendorf N, Rösner H, Kramb V, Sathish S (2001) Thermo-Acoustic Fatigue Characterization. To be published in *J. Ultrasonics* (2002)
34. Rantala J, Wu D, Salerno A, Busse G (1997) Lock-in-thermography with mechanical loss angle heating at ultrasonic frequencies. In: Busse G, Balageas D, Carluomagno GM (eds) Quantitative infrared thermography QIRT 96, Edizione ETS, Pisa, pp. 389–393
35. Favro LD, Han X, Li L, Ouyang Z, Sun G, Thomas RL, Richards A (2000) Thermosonic imaging for NDE. In: Thompson DO, Chimenti DE (eds) Review of progress in quantitative nondestructive evaluation 20A. AIP Conference Proceedings 557, Melville New York, pp. 478–482

36. Luong MP (1998) Nondestructive evaluation of fatigue limit of metals using infrared thermography. In: Achenbach J et al. (eds) Nondestructive characterization of materials in aging systems. MRS Symposium Proceedings, vol 503, Pittsburgh, pp. 275–280
37. Wong AK, Kirby GC (1990) A hybrid numerical/experimental technique for determining the heat dissipated during low cycle fatigue. Engn Frac Mech 37 Nr. 3:493–504
38. Canterell JH, Yost WT (1994) Phil Mag 69:315
39. Kaufmann HR, Lemz D, Luecke K (1975) Internal Friction and Ultrasonic Attenuation in Crystalline Solids, vol. II Springer, Berlin, p. 177
40. Akune K, Mondino M, Vittoz B (1975) Internal Friction and Ultrasonic Attenuation in Crystalline Solids vol. II, Springer, Berlin, p. 211
41. Maurer J (2002) Characterization of Accumulated Fatigue Damage in Ti-6Al-4V Plate Material Using Transmission Electron Microscopy and Nonlinear Acoustics. Ph.D. Thesis, University of Dayton
42. Meyendorf N, Roesner H, Frouin J, Maurer J, Sathish S (2003) Acousto-Thermal Microstructure Characterization. To be published in Rev of Progress in QNDE 2003

# **10 Scanning Vibrating Electrode Technique as a Benchmark for NDE of Corrosion**

M. Khobaib, A. Buchanan, M. Donley

## **10.1 Introduction**

One of the main purposes for aircraft coatings is to provide corrosion protection to Al-skinned structures. Polymer coatings offer an excellent corrosion barrier to these structures. Aircraft coatings provide such protection through a complex mechanism of inhibition and barrier functionality. In this scheme of corrosion prevention, the surface pretreatment (chromate conversion coating) passivates the metal surface, incorporates corrosion inhibitor, and creates a surface topography for maximum primer coating adhesion. The organic primer coating (mainly epoxies pigmented with chromates) also incorporates corrosion inhibitors and serves as an adhesive layer between the metal substrate and the topcoat layers. The surface treatment/primer coatings are intended to remain intact. The other factors contributing to corrosion initiation under the coatings include defects, pores in the primer coating, polymer degradation, and resulting changes in the transport properties of primer coatings. This allows ingress of the environment to the substrate and of course, a corrosion-prone multicomponent metallic surface. All these factors can be in a broader sense classified under loss of adhesion or open substrate at the primer/surface pretreatment interface.

Nondestructive characterization of corrosion protective coatings is of exceptional importance to enhance the usability of coating systems and thus, to reduce the costs of aircraft maintenance and to avoid extensive environmental pollution. The possible failure of the coating leads to insufficient corrosion protection and finally to the failure of the Al alloy structure. Determination of the mechanical and physical properties of the coating and the condition of the interface are required, both under different types of load and environmental exposure. Furthermore, it is necessary to detect corrosion damage in the aluminum alloy below the coating. To achieve this, the employment of state-of-the-art electrochemical techniques and high-resolution nondestructive evaluation (NDE) is necessary.

Several NDE methods for characterizing protective coatings and detecting corrosion below coatings can be found in the literature [1–6]. The following chapters of this book will describe some methods in detail. This chapter will briefly introduce an electrochemical method that will be used as a benchmark for NDE results in the following chapters.

Electrochemical techniques such as electrochemical impedance spectroscopy (EIS) and electrochemical noise methods (ENM) provide insight into the global properties of a coating system, and both techniques are being used on a limited

basis [7–11]. However, there is a need to investigate corrosion with greater spatial resolution under coatings at the metal/coating interface. Such corrosion may be related to coating defects and variations in the surface chemistry of the underlying metal. The scanning vibrating electrode technique (SVET) has been developed to allow investigating localized corrosion with high spatial resolution [12–15]. Such activity may be associated with coating defects that can be detected nondestructively. SVET has been used successfully as a benchmark for NDE to characterize coupons that have been investigated later by acoustic or thermal techniques (see chapters 9 and 11).

## 10.2 Background

One of the most common methods to prevent corrosion damage of metallic structures is through the application of organic coating systems. However, even under the best circumstances, it is impossible to completely prevent the access of water and oxygen to the metal substrate. Pinholes and other coating defects as well as the general coating film continuum allow the transport of oxygen and moisture [16]. Over time, these discontinuities grow with coating degradation and additional conductive pathways are created through the presence of electrolyte moisture etc. Once the circuit is complete, i.e., the anodic and cathodic sites connected through an electrolyte, a corrosion cell is developed resulting in corrosion current. This DC is a measure of corrosion activity under the coating and SVET only offers the capability of monitoring such currents close to the coated surface.

SVET was the primary tool used in this study to investigate corrosion initiation and its progress under coating. On a freely corroding surface, DC corrosion

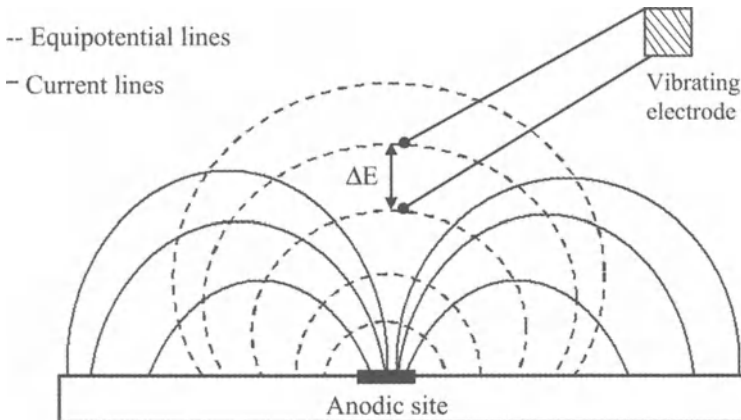


**Fig. 1.** Schematic of vibrating probe for DC current density mapping [11]

currents flow due to the presence of anodic and cathodic areas. SVET has been developed to allow in-situ examination of these DC currents associated with localized corrosion activity. The technique offers high resolution in current measurements of the order of  $0.5 \mu\text{A}/\text{cm}^2$  and is able to detect the initiation and progression of corrosion activity under a protective coating. SVET current density maps are derived from measurements of potential gradients in solution [12]. In Fig. 1, a schematic of the vibrating probe for DC current density mapping is shown. A single electrode vibrates between two points in solution and measures the changes in potential differences in the solution due to the flow of corrosion currents between the points of vibration excursion. The potential gradient is equal to the voltage difference divided by the distance between the two points of measurement. The current density in the direction of vibration is calculated according to Ohm's Law, knowing the potential gradient and the solution resistivity [12].

## 10.3 Instrumentation

SVET was the main equipment used for studying the corrosion under polymeric coatings. A schematic of the SVET system is shown in Fig. 2. The equipment was purchased from Applicable Electronics, Incorporated [13]. Periphery equipment includes a Potentiostat/Galvanostat (Model 263A) and a Frequency Response Detector (FRD) (Model 1025) manufactured by EG&G Princeton Applied Research.

The sample is placed on the stage below the video camera and zoom lens. The graphics monitor projects the image captured by the video camera and allows the user to view the sample, properly position the probe, and establish scan boundaries. The video camera can be raised or lowered to focus on the sample surface using keyboard controls. The probe is generally maintained at an approximate distance of  $75 \mu\text{m}$  above the surface. The probe vibrates in two orthogonal directions at the same time, with a different frequency of vibration in each direction. These probes are made up of platinum blackened wire with a spherical tip to provide maximum surface area. A workable probe must have a capacitance of at least  $2 \text{nF}$ . One wire serves as a ground while the other wire is a reference for the SVET. Automated Scanning Electrode Technique (ASET) software, manufactured by Applicable Electronics [13], is used to program the desired scan parameters. Commonly a grid of  $20 \times 20$  data points is chosen for current density mapping.

Calibration of the equipment is the key to obtaining reliable data. It is necessary to calibrate the probe in the solution intended for actual testing. If a different solution is used, a re-calibration step must be performed. Calibration allows the measured potentials to be converted into accurate current densities. A proper calibration method is detailed in reference [10]. Before each scan, a reference measurement is taken at a user-specified location where no corrosion currents

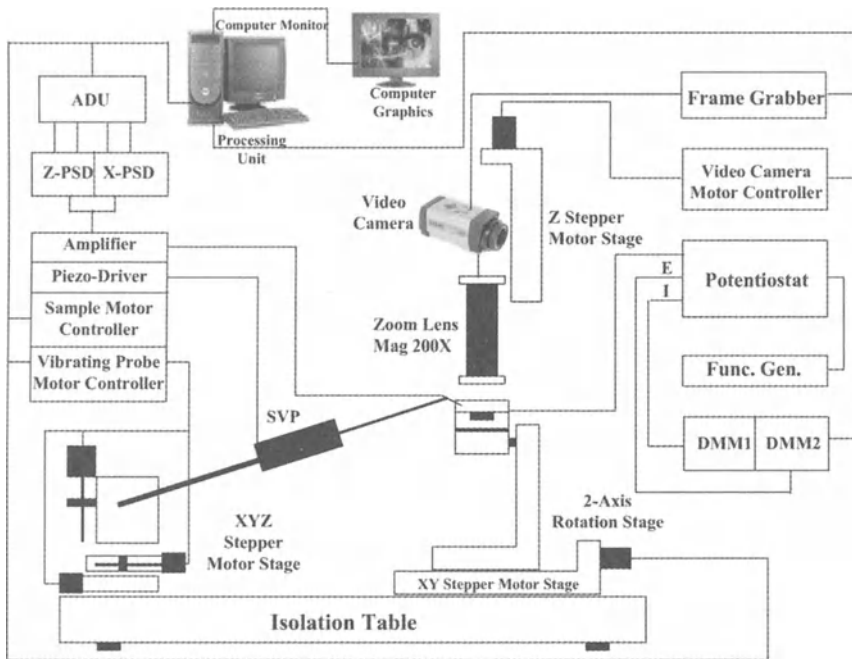


**Fig. 2.** Schematic of SVET system

is flowing, normally over a completely insulated area such as the masking tape, to obtain a baseline. Following each scan, a video image of the sample is acquired so a vector overlay plot can be created using the ASET software. A video image of the sample, captured after each scan, pinpoints the site of corrosion initiation, and calculated current density vectors can be superimposed on the video image to determine the precise location of a corrosion current source. A repeat scan function quantifies corrosion progression with time by allowing the user to choose multiple consecutive scans and observe the growth or repassivation of corrosion sites. The difference in initial corrosion activity under various coatings can be correlated to the failure life of the coatings.

Additionally, an EG&G potentiostat was used for those experiments in which external potential was imposed. In this case, an Ag/AgCl reference consisting of a silver wire in a 3M KCl solution saturated with AgCl is placed in the bath to serve as the reference electrode. A platinum wire ring, which serves as the counter electrode, is affixed to the sample cell and placed in the bath. The coated aluminum sample is the working electrode. The desired potential is set using the potentiostat front-panel controls. The camera height is adjusted to focus on the sample, the focus is raised approximately 75  $\mu\text{m}$  above the surface, and the probe is then lowered to that position which is 75  $\mu\text{m}$  above the sample. Measurements are then taken after specifying the desired scan parameters.

## 10.4 Applications

The SVET Instrument from Applicable Electronics, Inc. was used for local current density mapping of a large number of coatings systems starting from simple epoxy to advanced E-coat coating systems. Detailed results can be found in [17]. The following example was chosen to illustrate SVET results

The method was initially tested by scanning a scribed coated panel, which had gone through a 2000 hours Prohesion cycle that had produced a visible delaminated area also. The area selected for SVET scan on this epoxy coated panel was away from the scribe but included a small section of known delaminated area [18]. The probe was positioned in such a way that approximately half of the scanned region contained delaminated coating and the remaining half contained intact coating.

Figure 3 shows the current density map of the sample surface. The x- and y-axes represent locations in microns of the surface area scanned, while the z-axis represents current density ( $\mu\text{A}/\text{cm}^2$ ). Here, the convention of anodic current density showing positive current density is chosen, which is indicative of corrosion active site. From the pseudo three-dimensional map anodic current density was observed to occur in approximately half of the sample (x- and y-coordinates capture the scanner location of the area while the z-axis represents the current density).

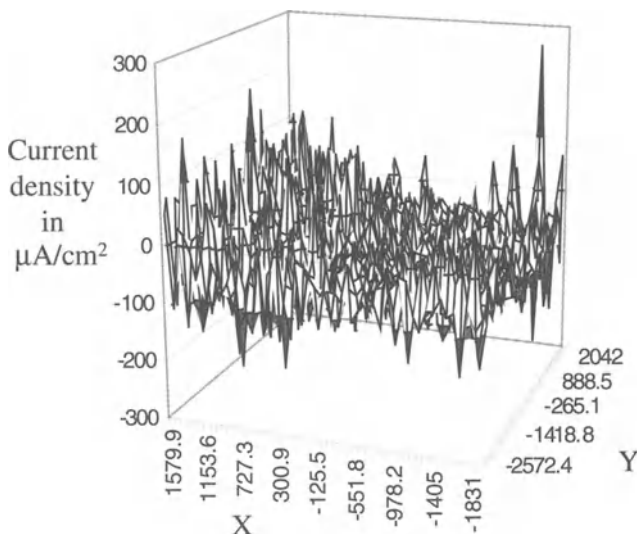


**Fig. 3.** Three-dimensional current density map of the delaminated area (the units of x and y are in micrometers)

In order to establish a one-to-one correspondence with the corrosion current measurement and the active sites in the coating, the three-dimensional surface plot was transformed into a two-dimensional plot and placed in 1:1 correspondence next to the video image of the sample captured immediately following the scan. Figures 4a and 4b compares the two-dimensional current density map with the video image of the area scanned, as indicated. In the center of the in situ video image as shown in Fig. 4b, a ridge is apparent. The delaminated portion is located to the left of the ridge, while the intact coating is located to the right of the ridge. When compared with the two-dimensional plot as shown in Fig. 4a, anodic current shows up in the delaminated region only. These data suggest that conductive pathways were present mainly in the delaminated region. This coating system appears to provide effective barrier to corrosion attack only in the absence of scratches or nicks.

EIS Bode plots were obtained from these two different locations (intact and delaminated) to analyze the status of the coatings. The difference in the video image of the scanned surface barrier resistance extrapolated from the low frequency value showed 4 to 5 orders of magnitude difference in impedance values [19]. These data also confirm the difference in corrosion activities between intact and delaminated areas. EIS was just used as a tool to obtain confidence in SVET measurement. EIS data represents global activity and lacks the ability to map corrosion current.

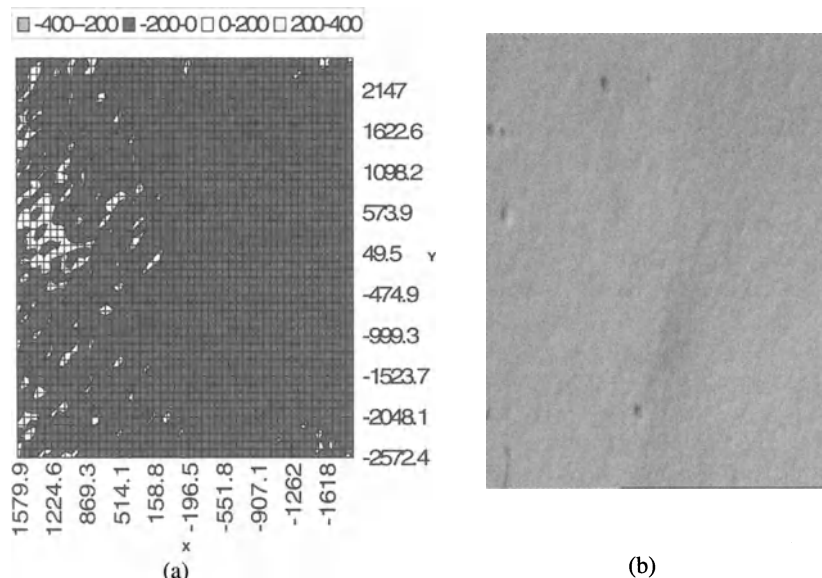


**Fig. 4.** (a) Two-dimensional current density map, units of x-and y-axes are in micrometers, current density (gray scale) is in  $\mu\text{A}/\text{cm}^2$ ; (b) video image of the scanned surface

## References

1. Li D, Ma YP, Flanagan WF, Lichter BD, Wikswo JP Jr. (1996) Applications of superconducting magnetometry to aircraft aluminium alloy corrosion. *Corrosion* 52:219–231
2. Li D, Ma YP, Lichter BD, Flanagan WF, Wikswo JP Jr. (1997) Detection of hidden corrosion of aircraft aluminium alloys using SQUID magnetometry. *Corrosion* 53:93–98
3. Andrieu C, Dalard F, Rameau J, Alcouffe F, Reboul M (1998) Aluminium alloy corrosion detection by magnetic measurements. *J Mater Sci* 33:3177–3188
4. Bellingham JG, McVicar MLA, Nisenoff M, Searson (1986) Detection of magnetic fields generated by electrochemical corrosion. *J Electrochem Soc* 133:1753–1754
5. Bellingham JG, McVicar MLA, Nisenoff M (1987) SQUID technology applied to the study of electrochemical corrosion. *IEEE transactions of Magnetics* 23:477–499
6. Murphy JC, Hartong C, Cohn RF, Moran PJ, Bundy K, Scully JR (1988) Magnetic field measurements of corrosion processes. *J Electrochem Soc* 135:310–313
7. Taylor SR (1989) Assessing the Moisture Barrier Properties of Polymer coatings Using Electrical and Electrochemical Methods. *IEEE Transactions on Electrical Insulation*, vol. 24, No. 5
8. Mansfeld F (1993) Analysis and Interpretation of EIS Data for Metals and Alloys. Issue AA Schlumberger Technologies, Billerica, MA
9. Jeffcoate CS, Wocken TL, Bierwagen GP (1997) Electrochemical Assessment of Spray-Applied Thermoplastic Coating Barrier Properties. *J Materials Eng & Performance* 6:417–420
10. Amirudi A, Thiery (1995) Application of Electrochemical Impedance Spectroscopy to Study the Degradation of Polymer-Coated Metals. *Progress in Organic Coatings*, 26:1–28
11. Macdonald JR (1987) Impedance Spectroscopy. Wiley, New York
12. Isaacs HS, Aldykiewicz Jr. AJ, Thierry D, Simpson TC (1996) Measurements of Corrosion at Defects in Painted Zinc and Zinc Alloy Coated Steels Using Current Density Mapping. *Corrosion*, vol. 52, No. 3:163–168
13. Applicable Electronics, Inc., 22 Buckingham Drive, Sandwich, MA 02563
14. Aldykiewicz Jr. AJ, Isaacs HS, Davenport AJ (1995) The Investigation of Cerium as a Cathodic Inhibitor for Aluminum-Copper Alloys. *Journal of the Electrochemical Society*, vol. 142, No. 10:3342–3350
15. Isaacs HS, Davenport AJ, Shipley A (1991) The Electrochemical Response of Steel to the Presence of Dissolved Cerium. *Journal of the Electrochemical Society*, vol. 138, No. 2:391
16. Buchanan A (1999) Masters Thesis. University of Dayton, Dayton
17. Khoabib M, Buchanan A, Donley M (2002) Characcterization of Corrosion under Protective Coatings. In: Meyendorf N (ed) Final Report: Development of Enabling Methodologies for Detection and Characterization of Early Stages of Damage in Aerospace Materials. AFOSR Grant Number F49620-96-1-0442

18. Khobaib M, Rensi A, Matikas T, Donley M (2001) Real Time Mapping of Corrosion Activity Under Coatings. *Progress in Organic Coatings* 41:266–272
19. Buchanan A, Khobaib M, Matikas T, Donley M (1999) Characterization of Advanced Coating Systems Used for Corrosion Protection of Aging Aircraft Structural Components. Proceedings of 1999 Advisory Group for Aerospace Research and Development. Corfu, Greece

# **11 Acoustic Imaging Techniques for Characterization of Corrosion, Corrosion Protective Coatings, and Surface Cracks**

J. Hoffmann, S. Sathish, E.B. Shell, S. Fassbender, N. Meyendorf

## **11.1 Introduction**

Acoustic (ultrasonic) inspection is among the most widely used NDE techniques. Ultrasonic techniques have proven to foster early detection of defects and enhance the understanding of failure processes. Acoustic imaging techniques and for instance Scanning Acoustic Microscopy (SAM) provides very detailed information about material defects with high spatial and depth resolution. It enables studying elastic properties, characterization of interfaces and detecting small defects, for instance, cracks in metals, polymers and ceramics. This chapter will consider some special applications of acoustic imaging techniques concerning recent aging aircraft problems. Characterization of corrosion, corrosion protective coatings, as well as fatigue damage are in the scope of the research reported here.

A series of excellent publications concerning ultrasonic testing of materials and acoustic microscopy are available. Among these we recommend [1] for a general introduction into ultrasonic testing and [2, 3] as excellent books for a broader view on acoustic microscopy.

## **11.2 Background**

Acoustic testing of materials in general and acoustic microscopy as a high resolution imaging technique are performed by time-of-flight spectroscopy in the pulsed regime [4, 5]. An electronic clock triggers at regular time intervals a signal generator (pulser) to send a high-voltage spike pulse to an ultrasonic transducer causing vibrations of its piezoelectric unit. Pulse repetition rate can be as high as 2000 pulses per second. The clock also controls a time measuring circuit that operates simultaneously with the signal measurement. The transducer generates short, broadband ultrasonic pulses that are sent into the test material. If operated in reflection mode, the same probe detects the reflected waves, working alternately as sending and receiving unit. In transmission mode, a second probe can be exactly positioned on the specimen backside to detect the acoustic waves. Instead of wave pulses, acoustic microscopes can be used in connection with a burst generator. A burst consists of a given number of wave cycles within a narrow frequency band. One can sweep the measuring frequency band over a frequency

range of interest. Thus, the good time resolution of a short pulse is leveraged with the good frequency resolution of a burst.

The frequency of acoustic waves highly influences ultrasonic inspection performance. For different applications, one has to find an optimal frequency band. Higher frequencies result in shorter wavelengths; thus, lateral and depth (time) resolution can be enhanced. However, high frequency waves undergo increased attenuation. These waves are more likely to interact with small sized material discontinuities (scattering). Furthermore, they experience wave energy transformation into heat energy (absorption). Eventually, the signal weakens, i.e., the signal-to-noise ratio deteriorates.

SAM transducers are focused, i.e., they include a focusing lens (Fig. 1). It is advisable to adjust the probe/sample-distance such that the sample part of interest (e.g., a coating substrate interface) is at the focal length distance. For a plane surface perpendicular to the sound beam this will be indicated by maximal reflection since all incident waves are reflected backward to the lens if and only if the reflection occurs at focal length. Focused transducers provide improved lateral resolution. However, the intensity of reflected signals can decrease fast outside focal length distance. Thus, for inspection of thick material or for detection of deeply located voids, transducers with long focal length are better suited. The low frequency is often necessary to enhance the signal-to-noise ratio, since the waves undergo higher attenuation if they travel longer distances through the test material.

For inspection of near surface material, highly focused transducers are able to utilize their advantage of improved resolution. High frequencies also improve the ability to inspect near surface material by improving both the lateral and depth resolution. The smallest possible lateral resolution is equal to the wavelength in the coupling medium (Fig. 1). For example, in the case of water ( $v_L=1500$  m/s) and a 50 MHz transducer, 30  $\mu$ m resolution can be achieved.

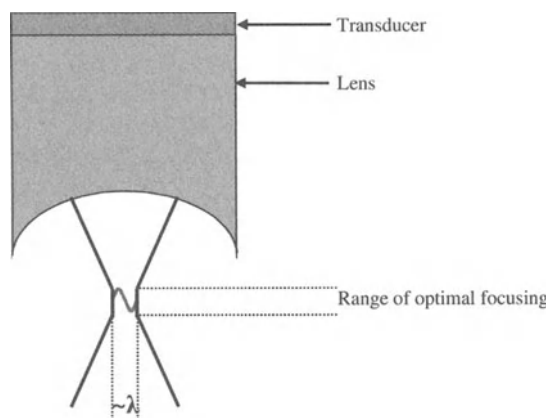


**Fig. 1.** Focusing schematic; approximately one wavelength is the smallest possible focal spot

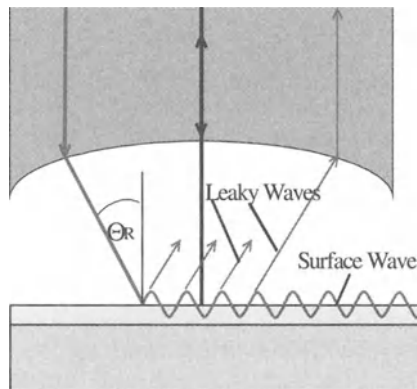


**Fig. 2.** Scheme of surface wave generation and detection

Besides longitudinal and shear wave inspection, acoustic microscopy can be used for generating and detecting surface waves. There are many different types; the most common are Rayleigh waves that occur at interfaces between a solid (strong elastic forces) and a non-solid (weak elastic forces). Rayleigh waves are generated due to incident waves at the Rayleigh angle  $\theta_R$ . They consist of longitudinal and shear components, creating elliptical particle displacement. These displacements cause longitudinal leaky waves to penetrate back into the non-solid medium. Leaky waves can be detected, if their incident angle towards the lens is such that normal incidence towards the transducer is achieved. Figure 2 illustrates the generation, propagation and detection of a surface wave. Leaky Rayleigh waves have narrow penetration depth and travel only short distances. Their velocity is slightly below the shear wave velocity. Rayleigh waves enable high-resolution inspection of near surface material [4].

### 11.3 Instrumentation

Different types of acoustic microscopes can be distinguished. The Scanning Acoustic Microscope (SAM) typically operates in a frequency range between 10–100 MHz. To enhance resolution for surface and near surface evaluation, High Frequency Scanning Acoustic Microscopy (HF-SAM) is employed [3] that operates at frequencies up to 1 GHz and above. However, very careful surface preparation is necessary for successful measurements, whereas SAM enables high-resolution ultrasonic inspection of large components that do not have to undergo a specific pretreatment.

### 11.3.1 Scanning Acoustic Microscope (SAM)

The coupling between transducer and sample is achieved by submerging both in a water bath. Since probe and sample are not in contact, the transducer can be moved with a multi-axis manipulator system. Among other parameters, the operator can control pulse repetition or sampling rate, frequency bandwidth and electronic amplification of the received signals (Fig. 3).

It is crucial to choose a suitable ultrasonic transducer for each specific application. The importance of wave frequency has already been discussed. In fact, the nominal resonance frequency of a transducer can be considered to be its most important specification. The core of a transducer is a piezoelectric crystal. The electric voltages from the pulser cause fast vibrations of the crystal along the preferable-orientated crystalline axis. This movement generates acoustic waves. These waves can leave the transducer only in one direction because of the backing material that surrounds the crystal.

If an electric pulse is imposed on the transducer, the piezoelectric crystal usually does not generate a pulse of a single cycle. Rather, it ‘rings’ until the imposed energy is dissipated. Deconvolution techniques to the digital RF signal can be used to reduce misinterpretations of the reflection patterns. To obtain short (single-cycle) pulses one has to choose probe materials that provides proper damping. However, damping will reduce the overall possible acoustic pressure, resulting in important reflections being too weak.

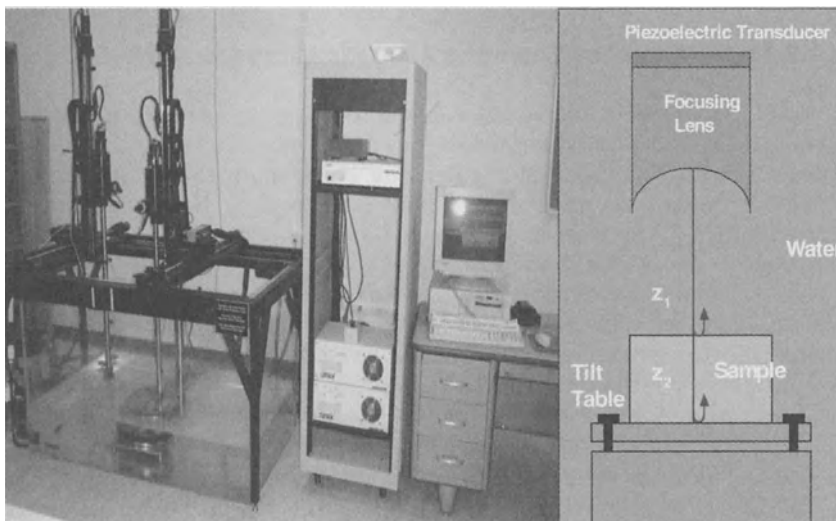


**Fig. 3.** Scanning acoustic microscope (*left*) and principle of acoustic coupling in water



**Fig. 4.** HF-SAM working in the Frequency range 5 to 400 MHz. Acoustic lenses generating Raleigh waves up to 400 MHz can be used with the microscopy, thus larger scanning areas up to 300 mm can be investigated (courtesy KSI Kramer Scientific Instruments)

### 11.3.2 High Frequency Scanning Acoustic Microscopy (HF-SAM)

The heart of a HF-SAM is a piezoelectric transducer mounted on the backside of a sapphire delay rod that is part of the acoustic lens. The acoustic lens has a spherical curvature that focuses the ultrasonic beam on the sample surface [6]. A droplet of distilled water usually achieves acoustic coupling. No immersion tank is required for HF-SAM depending on the test material, other fluids are possible as well. Figure 4 shows a HF-SAM instrument.

The resolution of the microscope is determined by the refractive index  $n$  of the sapphire delay rod and the used coupling medium. In addition the HF-SAM requires defocusing to achieve a sufficient contrast. This is a limiting factor for the resolution, as well. The refractive index is given by the ratio of the longitudinal sound velocities of both materials. For distilled water, the ultrasound is focussed to nearly one point, resulting in a resolution of approximately  $\lambda$ , the wavelength in the coupling medium. At 1 GHz, the wavelength  $\lambda$  is 1.5  $\mu\text{m}$ . The opening angle of the acoustic lens is 100°, enclosing the Rayleigh angle  $\theta_{\text{R}}$  for most of the materials. Rayleigh wave penetration depth is approximately one wavelength, a few microns, at 1 GHz. Due to this small penetration depth, investigation of near surface material becomes possible.

## 11.4 Methods

### 11.4.1 Acoustic Imaging

#### **Types of Images**

To display pulse-echo data, A-scan, B-scan and C-scan formats are possible. An A-scan basically plots the amplitude of the reflected signals over time. This is the rectified and smoothed HF-signal (Fig. 5). Amplitude and time-of-flight (the time difference between two echoes) are the main parameters taken from an A-scan. This format easily shows the depth location of the interface or discontinuity that caused the reflection. The amplitude is a function of the reflection coefficient,  $R$ , and can carry information about the type and size of a reflector (for a plain surface and perpendicular incidence of the ultrasonic wave).  $R$  increases with increasing acoustic impedance mismatch between two adjacent materials, as shown in (1). The acoustic impedance  $Z$  itself is a function of several material properties: density  $\rho$ , elastic modulus  $E$  and Poisson's ratio  $v$ . Thus, the amplitude can be evaluated for material characterization. The time-of-flight data mainly provide information about flaw depth location or specimen thickness. However, since the time-of-flight depends on sound velocity as well, further information about material properties can be obtained

$$R = \frac{Z_2 - Z_1}{Z_2 + Z_1} \quad \text{with} \quad Z = f(\rho, E, v), \quad (1)$$

where  $Z_i$  is the acoustic impedance of the material "i".

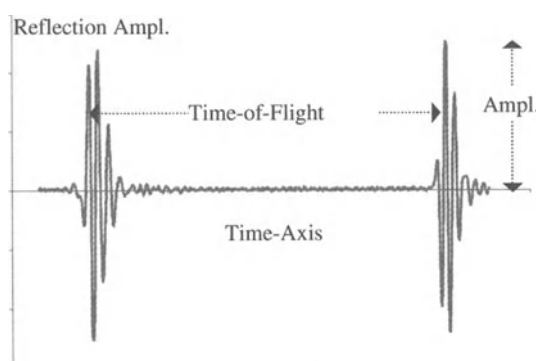


**Fig. 5.** HF signal detected by the probe. The rectified, smoothed signal is called A-scan

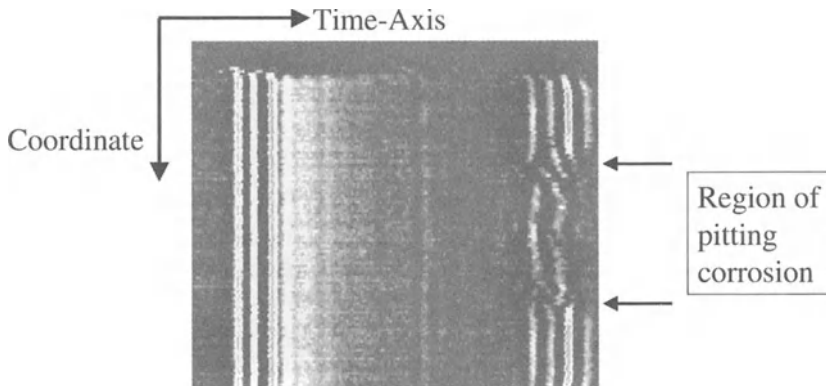


**Fig. 6.** B-scan example

A B-scan is carried out along one plane coordinate. The resulting image shows the amplitude of the reflected wave coded as different level of brightness or different color along this coordinate as a function of time. One can understand a B-scan as a specimen cross-section that images, for instance, thickness variation or flaw length along the chosen coordinate. The example in Fig. 6 shows pitting corrosion at the back surface of an Al 2024-T3 sample.

To obtain a C-scan, the transducer is moved with a given stepwidth over a given area of the sample surface plane. At each measuring position the amplitude of a reflection of interest or the time-of-flight between two reflections is recorded. These values are displayed in an image.

Figure 7 (left) shows a C-scan of exfoliation corrosion in an aluminum plate around steel fasteners. The bright spots, corresponding to increased reflection amplitude, indicate the corroded areas. The reflection has increased because the material separation due to corrosion causes internal interfaces that reflect the acoustic waves.

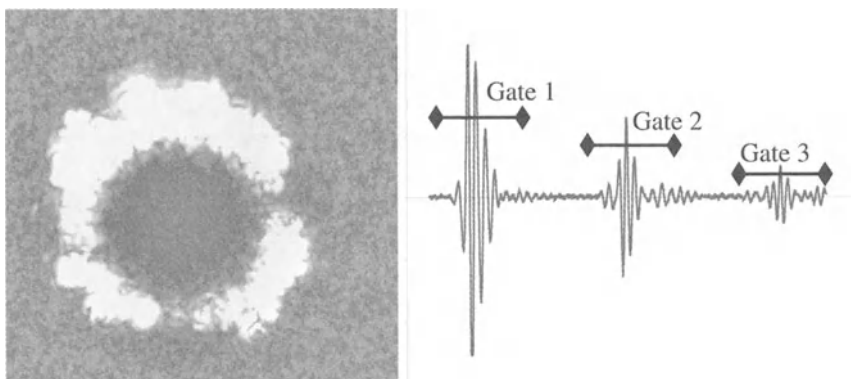


**Fig. 7.** Amplitude C-scan of exfoliation (*left*) and gating of reflections in A-scan (*right*)

The most common tool that is used to select a certain reflection for a C-scan is gating. As illustrated in Fig. 7 (right), a gate represents a time-interval over the position of the selected reflection in an A-scan. The system software will then pick the maximum amplitude within this gate to be recorded in a C-scan. For a time-of-flight C-scan, the time difference between the maxima of two successive gates is taken.

Identification of the different reflections and correlating them to sample properties is difficult. A wave that is reflected several times between two defects or inner surfaces can cause multiple reflection signals. In the case of complex time-domain signals, frequency-domain analysis might be favorable. To evaluate the frequency response of the system, Fourier transformed functions (Fast Fourier Transforms, FFT) for A-scans can be calculated. This analysis finds the corresponding frequency spectra of time-domain reflections. Different reflected waves can be distinguished and a better understanding of wave/sample interaction can be achieved.

### **High Frequency Scanning Acoustic Microscopy**

HF-SAM is used for flaw detection at or near the surface. The acoustic lens is scanned in the x- and y-directions parallel to the sample surface. Reflected ultrasonic waves are detected by the same transducer and converted into electrical signals. After amplification, the signal amplitude is shown as gray level in the acoustic image. The time required to obtain an acoustic image depends on the scan dimensions, scan speed, number of signals averaged, and the used repetition frequency.

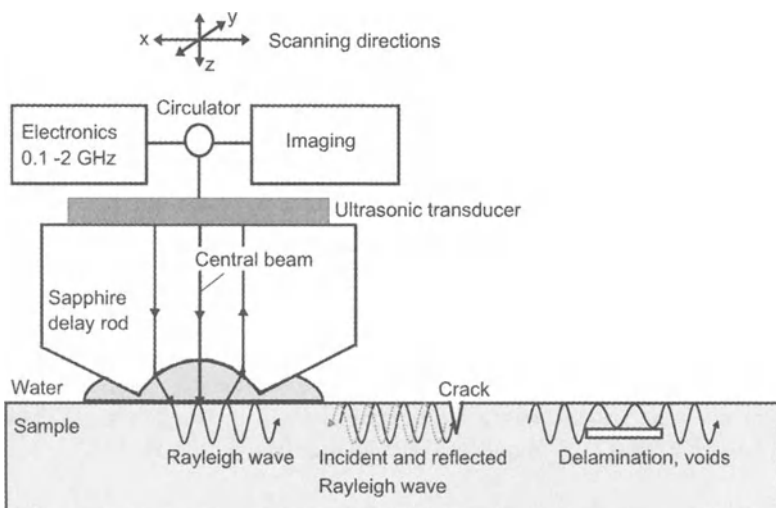


**Fig. 8.** Principle of HF-SAM, generation of Rayleigh waves and interaction of Rayleigh waves with surface near materials discontinuities

Near-surface inhomogeneities like cracks, delaminations, voids, or inclusions are disturbances for the ultrasonic wave. For example, the ultrasonic wave is reflected at open cracks, where the crack walls are not in contact (Fig. 8). The reflected ultrasonic wave interferes with the incident ultrasonic wave resulting in interference fringes around the crack. Cracks with an opening smaller than the microscope resolution can still be detected, as long as the crack length or depth is larger than the resolution [4, 7]. Therefore, the HF-SAM has a higher sensitivity for surface cracks compared to dye penetration test, replica technique or optical microscopy.

However, topographic structures like steps or general roughness dramatically disturb the measurements. The distinction between topographic features or defects is difficult. Careful surface preparation is crucial, especially, for measurements at high frequencies. An ideal surface is flat and has a mirror finish with no plastically deformed layer at the surface. Therefore, the grinding and polishing of the surface has to be done almost without pressure. It is a rule of thumb that the surface roughness should be much smaller or much larger than the used wavelength. In the first case, the surface wave is not affected by the small roughness. In the second case, one can find plain places between the roughness peaks where the Rayleigh wave can travel without disturbances. Furthermore, the shape of the roughness peaks is important. It is more difficult for Rayleigh waves to pass sharp steps than smooth peaks.

#### 11.4.2 Determination of Elastic Properties

HF-SAM has the ability to determine sound velocities of surface waves correlating with the elastic properties (Young's modulus, shear modulus, Poisson's ratio) and the density of the material. The Rayleigh wave velocity  $c_R$  can be determined from  $V(z)$ -curves with very high local resolution [8].  $V$  is the voltage measured at the transducer and  $z$  is the defocus distance between the focal point of the acoustic lens and the sample surface.  $V(z)$ -curves are evaluated by moving the acoustic lens in  $z$ -direction (parallel to the surface normal) towards the sample surface. The phases of the reflected ultrasonic waves interfere with each other; especially, the central beam interferes with the reflection component due to Rayleigh waves (Fig. 8). These interferences can be constructive and destructive depending on the defocus distance  $z$  (Fig. 9).

The central beam is reflected at the surface. The material itself does not influence its wavelength. Therefore, the central beam can be taken as the reference beam. However, the wavelength of the Rayleigh waves are material dependent. From the distance  $\Delta z$  between two minima or maxima, the Rayleigh wave velocity  $c_R$  can be estimated ((2),  $f$ : frequency) with an accuracy within 1% [5].

$$c_R = \Delta z \cdot 2f \cdot (1 - \cos \theta_R) \quad (2)$$

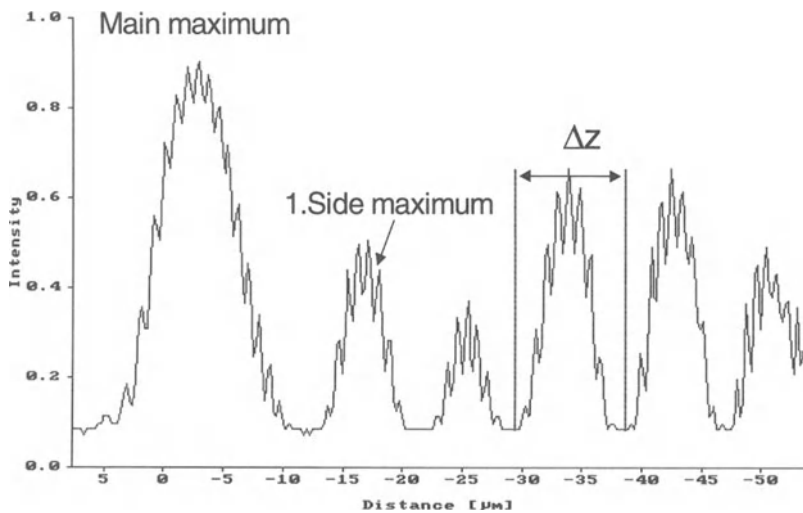


**Fig. 9.**  $V(z)$ -curve of aluminum (“Intensity” in  $V$ , defocus “Distance”:  $z$ )

For a test frequency the probed volume is between 1,000 and 10,000  $\mu\text{m}^3$  depending on the material. Equation 2 can not be used for materials with a Rayleigh wave velocity over 3500 m/s, such as ceramics. Here, the Rayleigh wave velocity has to be determined from the distance between the main maximum and first side maximum [8]. From Bergmann’s formula, the transversal shear velocity can be determined for isotropic material. Here,  $\nu$  is Poisson’s ratio,  $c_T$  the shear wave velocity and  $c_R$  the Rayleigh wave velocity.

$$c_R \approx \frac{0.87 + 1.12 \cdot \nu}{1 + \nu} \cdot c_T \quad (3)$$

Young’s modulus and shear modulus can be calculated, if Poisson’s ratio  $\nu$  and density  $\rho$  are known ((4) and (5)).

$$G = \rho \cdot c_T^2 \quad (4)$$

$$E = 2G \cdot (\nu + 1) \quad (5)$$

$V(z)$ -curves might be a powerful tool to detect defects like closed cracks, which cannot be detected in the acoustic image, but result in reduction of Rayleigh wave velocity [8]. However, the material should have a low anisotropy to avoid large differences of Rayleigh wave velocity between different grain orientations. Furthermore, the grain size should be smaller than the acoustic wavelength to enable averaging over different grain orientations.

## 11.5 Applications

To illustrate the capabilities of SAM and HF-SAM, some examples are presented. Among the most severe problems of aging aircraft are corrosion and proper protection of the aluminum alloy airframe structures. This protection is usually provided by polymeric multi-layer coating systems. Coating failure could leave the aluminum surface exposed to the environment and endanger the structural integrity of the airframe.

### 11.5.1 Characterization of Corrosion

The following paragraph describes experiments to apply the SAM to detect and quantify different types of corrosion in aluminum aircraft structures. The complete results along with surface profilometric and x-ray results have been used to develop a life prediction model based on artificial neural network and multi parameter regression algorithms in [9].

#### ***Material and Specimen Preparation***

Flat, dogbone specimens (Fig. 10) were cut by EDM from 2-mm thick Al 2024 sheet material (Fig. 11) in the as-received T3 temper and from material that was artificially aged to the peak T6 condition. Most of the specimens were cut so that the loading direction would be along the rolling (L) direction of the material. However, six T3-temper specimens were cut along the long transverse (T) direction to study the effect of orientation.

Specimens were ground down to a near-mirror finish using SiC papers up to 800 grit. All steps up to and including 600 grit were prepared using water as the lubricant. The 800 grit finish was conducted with acetone as the lubricant to avoid any pre-existing corrosion and obtain a smoother starting surface. Specimens were then ultrasonically cleaned in an acetone bath to remove grinding debris from the surface.

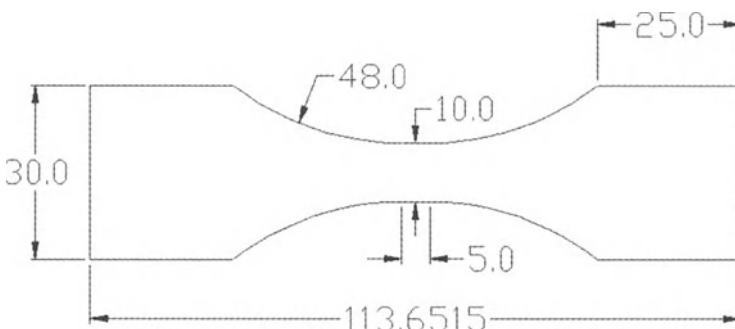


**Fig. 10.** Dogbone specimen used in study (dimensions in mm, thickness is 2mm)

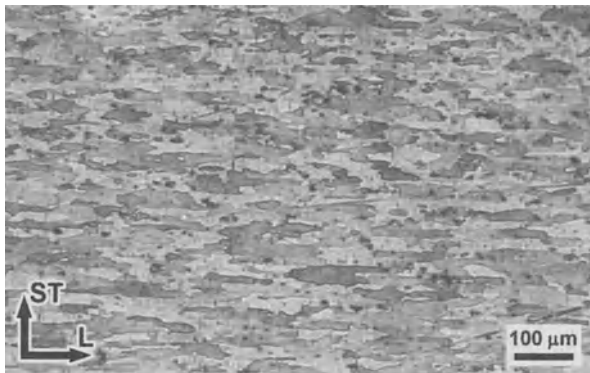


**Fig. 11.** Microstructure of the 2024-T3 sheet material

### **Corrosion of Specimens**

The gage sections of the specimens were masked using a waterproof polymer tape. One portion of the tape was removed using a 6-mm diameter hole punch. This piece was placed at the center of the gage section to leave a 0.283-cm<sup>2</sup> area unmasked. The specimen was then placed as the working electrode in an electrochemical cell. A saturated calomel electrode was used as the reference electrode, while the counter electrode was a platinum mesh. The experiment was controlled by a model EG&G Princeton Applied Research 263A potentiostat/galvanostat.

A large variety of corrosion conditions were used to provide a range of damage extents and corrosion morphologies. Variables in the corrosion process included: the solution, the exposure time, and the imposed current, in addition to the effect of the material temper and orientation. This provided a wide range of damage levels and types, from light, localized pitting or intergranular attack to deep general material removal with rough pitting attack or grain pullout.

Three different solutions were used in corroding the specimens. Two concentrations of salt solution were used, 0.5 M NaCl and 1.0 M NaCl. These solutions led to primarily pitting attack. A third solution, 1.0 M NaCl + 0.3% H<sub>2</sub>O<sub>2</sub>, was used to obtain IG corrosion. These solutions resulted in mild pitting, moderate pitting, and IG attack with possible grain pullout, respectively, under open circuit (OC) conditions. However, the attack rate, especially, with the first two electrolytes, was slow.

To expedite the corrosion process, about 2/3 of the tested specimens had some current imposed for the testing duration. This resulted in a much faster corrosion process, but also likely changed the attack mechanism and the resulting corrosion morphology. A few specimens had a current applied at the start of the test, to initiate pits, but then were left at their OC corrosion potential to grow the pits naturally.

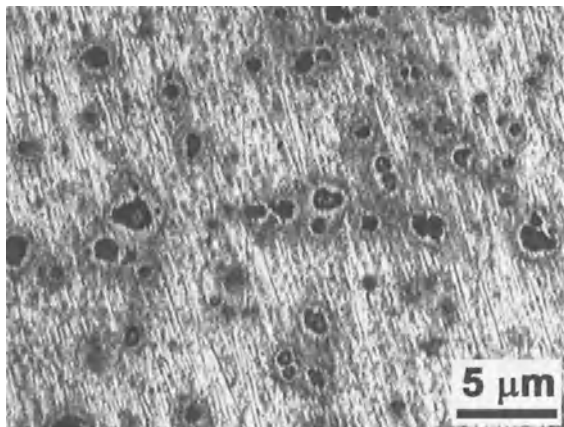


**Fig. 12.** Optical micrograph of surface pitting in Al 2024-T3

Following corrosion, the tape was removed and the specimens were cleaned in a de-oxidizing solution (30 g/L Sanchem 1000, 72 mL/L  $\text{HNO}_3$ ) at 55°C for 3 minutes to remove corrosion byproducts. This is a step that is often conducted prior to chromate conversion coating application to remove oxides from the surface and enhance adhesion of following coating layers [10].

The resulting corrosion morphology was a combination of various degrees of pitting damage (Fig. 12), intergranular damage (Fig. 13), and generalized corrosion damage (Fig. 14).

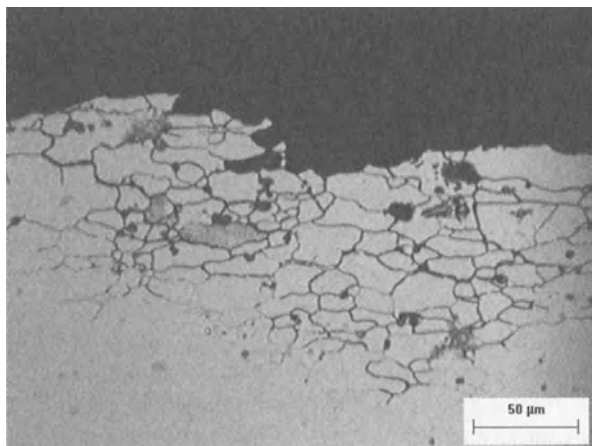


**Fig. 13.** Optical micrograph of intergranular corrosion damage in Al 2024-T3 from cross-sectional view

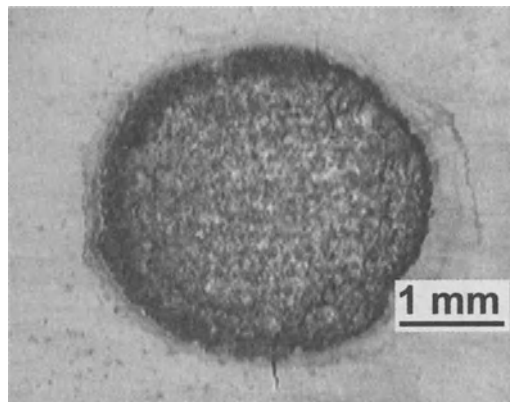


**Fig. 14.** Optical image of generalized corrosion damage in Al 2024-T3 taken a few cycles prior to final fracture

### ***Ultrasonic Measurements***

Ultrasonic measurements were obtained by transmitting the acoustic signal through the uncorroded face and measuring the reflection from the corroded (back wall) face (Fig. 15). The beam is scanned in the x- and y-directions to obtain C-scan images. In addition, the A-scan for each scan point is recorded for later analysis. A slightly focused, 50 MHz transducer (Panametrics V3193) was used, with a data collection rate of 400 MHz (Msample/s). This is performed using a Panametrics imaging system. A scan area of approximately 5 x 5 mm was examined at a step size of 75  $\mu$ m. Features of a size below this step size can be detected. However, due to averaging over the width of the acoustic beam, some intermediate reflection amplitude will be seen by the transducer. This transducer choice provides a good compromise between high depth and lateral resolution with low attenuation and scattering. The C-scan was recorded by triggering on the front wall reflection, utilizing a time delay of -0.07  $\mu$ s, and recording MultiScan (full waveform) data over 0.855  $\mu$ s, which includes the back wall reflection. Panametrics ScanView software was then used to examine C-scans for any time gating desired.

Ultrasonic inspection requires an effort to ensure that there is no inspection variation from specimen to specimen. Steps were taken to minimize this variation between measurements. Among the variables that can potentially adversely affect the quality and the magnitude of the reflected signal are: the focus, whether the beam is normal to the surface, the surface conditions (particularly the oxide layer limiting the transmission of the beam), and the sensitivity of the detection equipment.

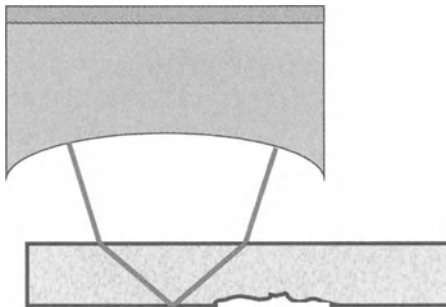


**Fig. 15.** UT inspection of corroded specimens

Because a focused transducer was used, the resolution and amplitude of the signal was sensitive to the distance between the transducer and the specimen. The particular transducer used in this study was only slightly focused, so the acoustic depth of field was relatively long. The working distance was fixed so that the beam was focused on the corroded face of the specimen.

The primary signal being measured is the reflection of longitudinal waves. Any shear waves in the material would complicate analysis of the measurements. So, it is important to ensure that the acoustic beam is normal to the surface before each measurement. This also maximizes the transference of the signal into the medium, giving a better back wall reflection signal to compare among specimens.

One variation between specimens that is difficult to avoid is the quality of the surface following the de-oxidation step. This solution is somewhat aggressive to the uncorroded surface, leaving a very thin oxidized layer over the surface. The thickness of this layer varied from specimen to specimen depending on the freshness of the solution, temperature fluctuations in the bath, small time of immersion differences, etc. For the majority of the specimens, the surface condition did not affect the measurement. However, for a couple of specimens, there was less transference of the acoustic signal into the material, resulting in very noisy signals from the back wall reflection. This is compensated by adjusting the electronic attenuation of the receiver so that the back wall reflection peak has the same amplitude for each specimen.

Three metrics were extracted from the UT data. First, a damage depth was determined by measuring the arrival time of the first signal in the material from A-scans of the specimen (Fig. 16). This can be expressed as a damage depth using (6), where  $d$  is the depth of damage,  $\Delta t$  is the time difference between the surface reflection and the defect reflection, and  $v_L$  is the longitudinal sound wave velocity. This metric is controlled by the speed of the recording equipment. In this case, data was collected at 400 MHz using a 50 MHz transducer. With this collection rate, the smallest time step would relate to a depth of about 8  $\mu\text{m}$ . However, realistically, a few time steps would be needed to notice a real change in the time of the signal. The actual depth resolution then falls to about 30  $\mu\text{m}$ .

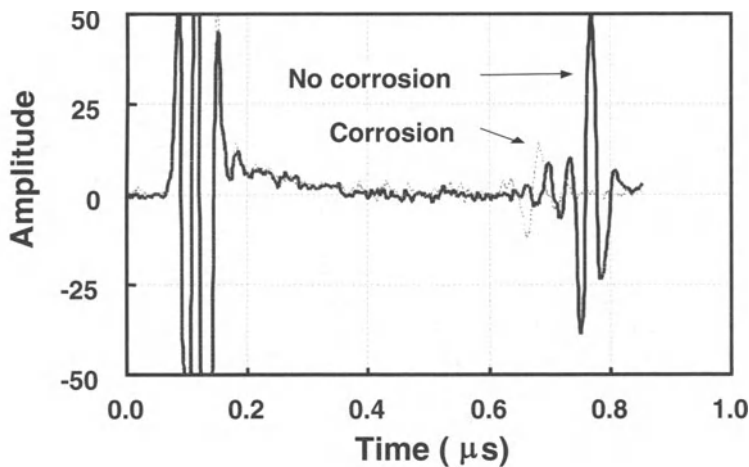


**Fig. 16.** A-scans from corroded and uncorroded areas

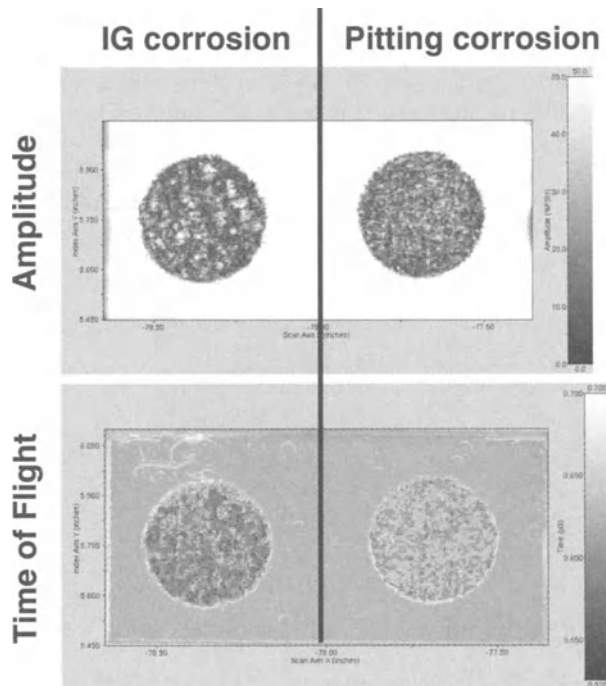


**Fig. 17.** Ultrasonic amplitude and time of flight C-scans for different types of corrosion

$$d = \frac{\Delta t \cdot v_L}{2} \quad (6)$$

More effective metrics obtained from UT involve those related to the amplitude of the signal that is reflected. In this case, C-scans from the back wall reflection were used. Figure 17 shows reflection amplitude C-scan along with time of flight c-scans. Different types of corrosion result in different “features” in the ultrasonic images. These images were normalized so that an amplitude of 1.0 was seen from an uncorroded surface, while an amplitude of 0.0 meant that there was no reflected signal at all at the back wall surface (often the case with general corrosion or IG corrosion). A reduction in the amplitude can be related to the roughness of the corroded surface or internal corrosion damage, which increase the likelihood of early crack initiation. The other metric calculated from the UT data is the maximum attenuation over the specimen. This parameter would describe the location with the most severe damage, corresponding to the area most likely to initiate the crack leading to final failure.

### **Comparison to Other NDE Techniques**

The key to achieving a better empirical relation lies in obtaining data from numerous complementary techniques. For instance, profilometric data obtained by white light interference microscopy (WLIM) contains much valuable and useful information about the surface and stress risers that are a result of pitting damage. However, by itself, it tells nothing about any damage that occurs just beneath the surface, such as intergranular (IG) corrosion, exfoliation, or torturous pitting such as seen in anisotropic materials. Likewise, a technique like microradiography will give information on general material/thickness loss and severe pitting damage, but would not be able to resolve the material loss due to IG corrosion and highly localized corrosion. Acoustic inspection, eddy current, and surface acoustic wave techniques would give information about internal and near-surface flows, crevices, cracks, and IG corrosion.

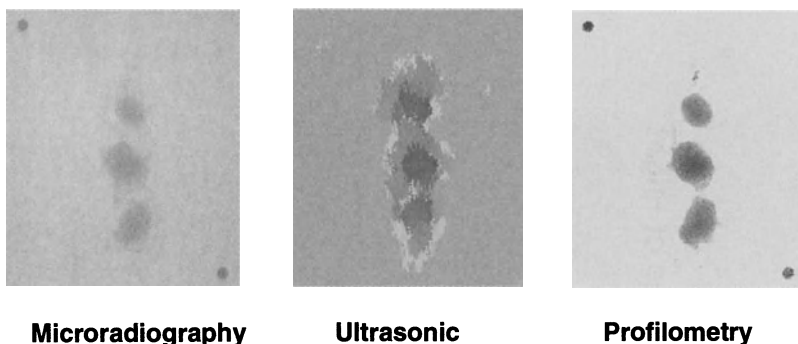
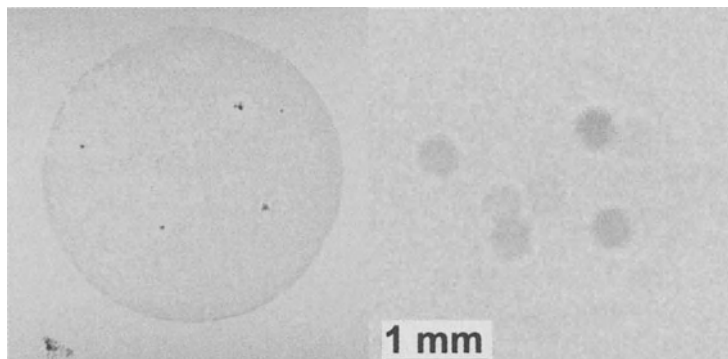
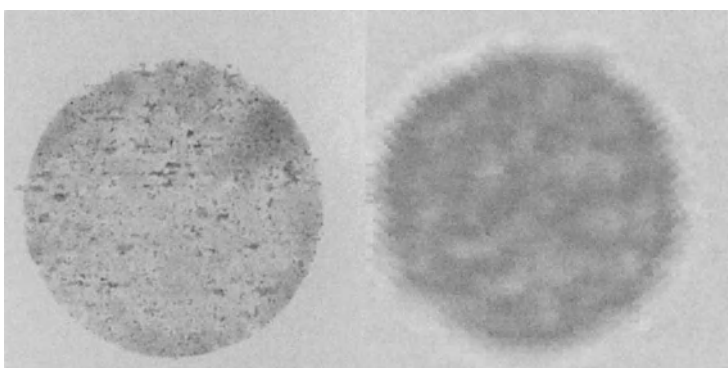


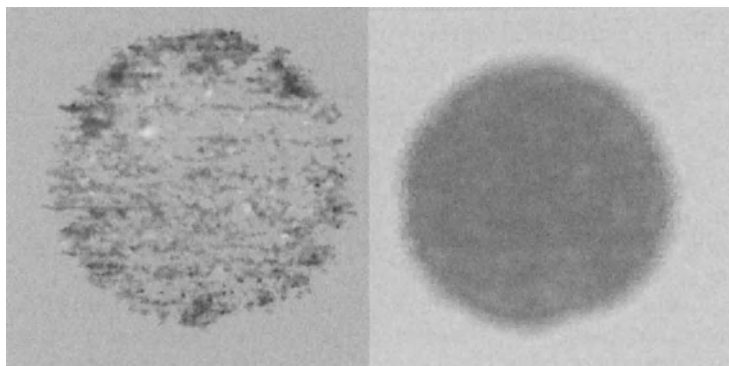
**Fig. 18.** Comparison of images from several NDE techniques



(a)



(b)



(c)

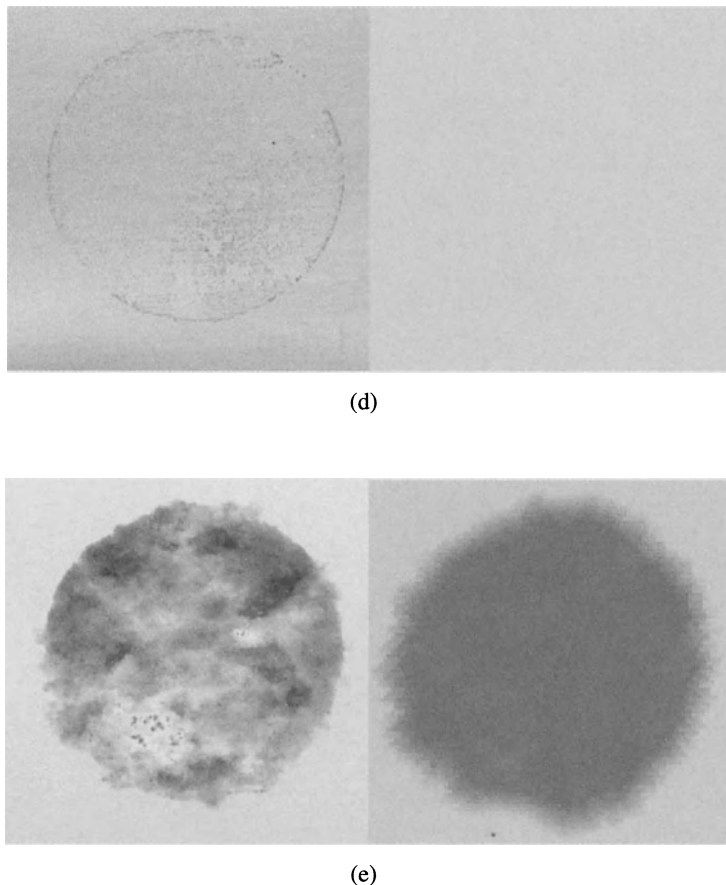


**Fig. 19.** NDE images from the fatigue specimens showing discrete pitting (a), intergranular (b), texture-oriented (c), cosmetic (d), and general (e) corrosion attack. The images are from white light interference microscopy (*left*) and ultrasonic microscopy (*right*)

Figure 18 compares ultrasonic images to x-ray images (see Chapter 3) and optical profilometric results (Chapter 2) of the same specimen. Figure 19 gives a comparison for ultrasonic and profilometric image data for different types of corrosion.

While the high resolution of white light interference microscopy allows crack initiation-related metrics to be measured, the method underestimates the damage of more advanced corrosion. This is the area that ultrasonic techniques have the greatest success in due to their ability to measure larger subsurface flaws, which may greatly reduce the structural integrity of the material. As a result, there is less prediction error for ultrasonic techniques in the low residual life range.

### 11.5.2 Characterization of Corrosion Protective Coatings

Polymeric aerospace coating systems are subject to environmental degradation from ultraviolet light, water exposure and thermal cycling. The exposure of polymer coatings to environmental conditions can cause several changes in the coating chemistry and physical properties (elastic modulus and density). This is interesting for the employment of acoustic inspection. Acoustic wave reflection at surfaces and interfaces is determined by the elastic moduli and the densities of the media that form the interface. Acoustic waves are sensitive to delaminations and other interface disturbances. The following paragraph will give some examples.

#### ***Coating Delamination due to Water Exposure***

2024-T3 substrates with a single layer epoxy/polyamine primer coating were examined. The substrate was highly polished to simplify the interface response to incoming acoustic waves. The additives allowed within the epoxy matrix were some agents to obtain a smooth surface and nearly uniform coating thickness. Within the general sample parameters, the exact formulation of the epoxy/polyamine primer was varied for different sets of samples. For example, an experiment was planned to observe the development and growth of delamination. The coating formulation was chosen to minimize the number of hydrogen bonds to the substrate and to be highly hydrophilic. SAM C-scans were performed with the transducer in front of the coating (Fig. 20).

Ultrasonic reflections that characterize the coating/substrate interface were emphasized during evaluation. Since the SAM measurements involve water exposure of the samples, water was expected to diffuse easily in the polymer matrix and, eventually, to the substrate/coating interface. The C-scans enabled monitoring the development of micro-scale delamination that accumulates over time (Fig. 20).

Eventually, the coating lost contact with the substrate. This experiment helped to identify delamination defects and distinguish them from corrosion defects.

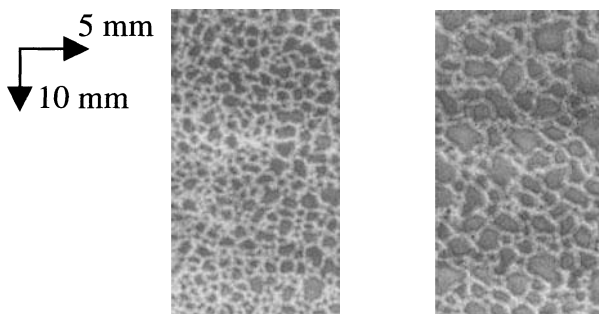


**Fig. 20.** Formation of micro-delamination at epoxy coating/ 2024-T3 interface due to water exposure; right scan is measured 3 hours after left scan

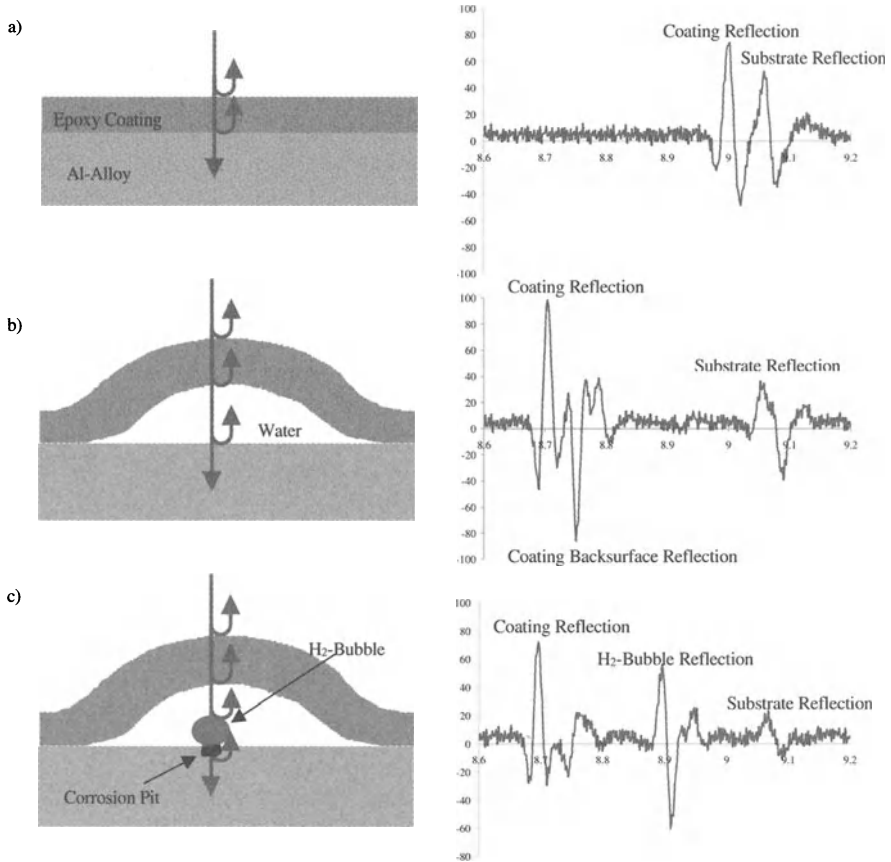


**Fig. 21.** A-scans and schemes for different positions on epoxy coating sample; a) undamaged region; b) delaminated region; c)  $H_2$ -bubble above corrosion pit

### ***Detection of Delamination Sites of Coatings***

Delaminated regions are usually filled with environmental fluids (e.g., water or acidic solutions) that act as electrolytes. This will, eventually, lead to corrosion damage at the metal substrate surface. Examination of the coating and substrate reflections allows the identification of corrosion damage sites.

In the substrate reflection C-scan, additional bright spots are observed within the possible delaminated region. It was assumed that these spots indicate a corrosion damage feature. In addition, A-scans were recorded at an undamaged position, a site of delamination and a suspected corrosion spot. At the undamaged position, only the reflections from either the coating or substrate occur (Fig. 21a).

At a delaminated position, these two reflections are more separated in time as the distance between the two surfaces increases. An additional reflection from the coating backsurface/solution interface is observed (Fig. 21b). Apparently, the water has penetrated into the open (delaminated) region separating the two materials. This reflection reveals negative amplitude, because the change of acoustic impedance from coating to water is negative as well.

The additional bright spots in the C-scans correspond to large reflections caused by a large acoustic impedance change. This happens when the acoustic wave has to propagate from water into a hydrogen gas ( $H_2$ ) bubble. This  $H_2$  bubble, generated during active dissolution, indicates the presence of a corrosion pit underneath (Fig. 21c). These findings strengthen the argument to establish clear understanding of acoustic wave interaction with the coating sample. The identification of the  $H_2$  bubble would have been impossible without knowing the source of the different reflections.

### ***Nondestructive Evaluation of Corrosion Protection with SNAP Coatings***

Representative C-scans and corresponding electrochemical scans (Scanning Vibration Electrode Technique SVET, see previous Chapter 10) for a 38  $\mu m$  thick coating (90 hours exposure to acidic solution) are presented in Figs. 22 and 23. The coating formulation used provided reasonably good water resistance and adhesion capability. Thus, exposure to a corrosive environment was considered the main cause for the coating degradation observed. The difference between the two samples is the application of a newly developed thin sol-gel initial layer prior to coating the epoxy primer. The sol-gel layer includes pre-formed, self-assembled nano-phase silane particles (SNAP). These SNAP coatings are considered to enhance corrosion resistance and adhesion to the substrate.

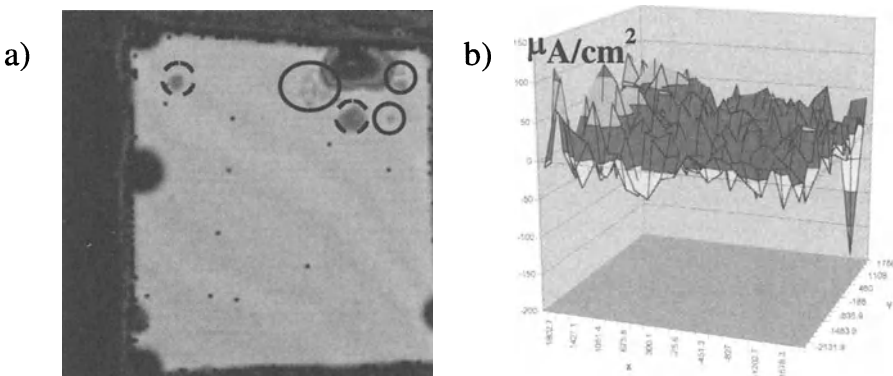


**Fig. 22.** Epoxy coating, no SNAP layer; a) SAM C-scan: scan area:  $6 \times 6 mm^2$ , b) mapping of corrosion activity with SVET (scan area:  $5 \times 5 mm^2$ )

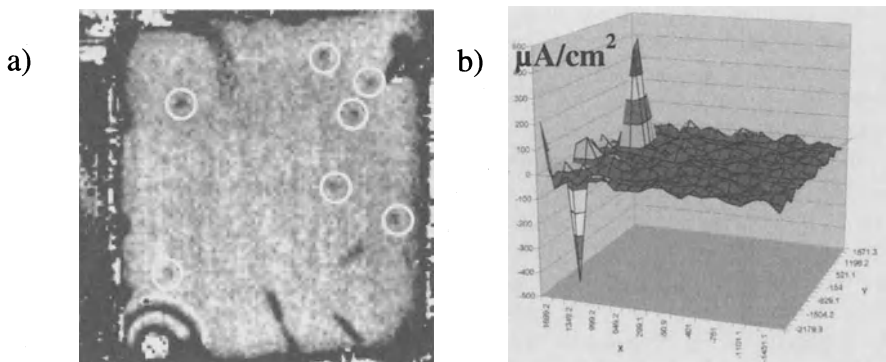


**Fig. 23.** Epoxy coating, with SNAP layer; a) SAM C-scan: scan area:  $6 \times 6 \text{ mm}^2$ ; b) mapping of corrosion activity with SVET (scan area:  $5 \times 5 \text{ mm}^2$ ). In comparison to Fig. 22 more image enhancement was required to visualize the small defects

The results indicate that the SNAP-coatings basically improve adhesion. Figure 22a presents a C-scan over a sample without additional SNAP layer. Several spots of delamination can be observed, which eventually led to some severe accumulated corrosion activity (full line circles: hidden corrosion, dashed circles: hidden delamination, large visible delamination in upper right corner). However, the measured current density does not show high peaks (maximum approximately  $100 \mu\text{A}/\text{cm}^2$ ) and is rather homogeneously distributed (Fig. 22b).

In comparison, the SVET scan for the sample with additional SNAP layer shows no significant current density over almost the complete scan-area, except one negative (cathodic) peak (approx.  $-500 \mu\text{A}/\text{cm}^2$ ) and one positive (anodic) peak (approx.  $400 \mu\text{A}/\text{cm}^2$ ) (Fig. 23b). The SAM C-scan also detects these spots, but also several additional sites (Fig. 23a; white circles: hidden corrosion). SVET does not indicate corrosion activity for these sites.

The sample without SNAP pretreatment shown in Fig. 22 is more severely damaged. Enhanced image processing needed to be performed to visualize the minute detections in Fig. 23a. These results indicate that SNAP pretreatment definitely improves adhesion capability and generally the corrosion resistance. However, if the primer coating fails, highly localized corrosion activity can lead to component failure, by promoting localized pitting rather than uniform corrosion.

### **Coating Weathering Evaluation**

Acoustic weathering inspection takes advantage of the accompanying mechanical changes the degraded coating materials undergo. According to (1), acoustic reflectivity evaluation can provide direct information about the mechanical properties. The measurement parameter that indicates coating reflectivity is the maximal amplitude  $A_c$  of the reflected ultrasonic pulse. The reflection coefficient  $R_c$  is the ratio of the sound pressure of the incident and the reflected wave. If the

signal amplitude of the A-scan is scaled proportionally to the sound pressure, this amplitude is proportional to the reflection coefficient  $R_c$  for the water-to-coating interface. For the calculation of the acoustic impedance  $Z_c$ , it is required to compare the measured reflectivity to a known reference reflection. Obvious choices are the water/Al-substrate interface or water/pristine coating condition interface. The respective acoustic impedances of water ( $Z_w$ ) and Al 2024-T3 ( $Z_A$ ) are known, as well as the reflection coefficient  $R_A$  at this interface. The maximal reflection amplitude  $A_A$  can be measured easily. Assuming that the ratios  $A_c/A_A$  and  $R_c/R_A$  are equal it is possible to calculate  $Z_c$  as shown in (7)

$$Z_c = Z_w \frac{1 + R_c}{1 - R_c} \quad \text{with} \quad R_c = \frac{A_c}{A_A} R_A. \quad (7)$$

First results were obtained for PUR topcoat specimens that were exposed to either continuous condensation, continuous UV exposure, or alternating condensation/UV exposure [11, 12]. The surface roughness of the investigated topcoats had an influence on the reflection amplitude. Thus, it was necessary to scan each coating specimen over a sufficient area to evaluate an average reflection. These average values were than considered to be the reflection amplitudes for the respective specimens. These data are essentially gray scale values. For further analysis it becomes necessary to normalize them to a reference measurement; here, the results are normalized to the value obtained from a pristine condition specimen. The C-scans were recorded over an area of 8 mm x 8 mm with a stepwidth of 50 •m (25600 points). C-scans from as-received and exposed specimens are shown in Fig. 24. Darker gray values correspond with lower  $R_c$  values.

Representative samples from different exposure cycles were measured. Figure 25 shows the results obtained for continuous *humidity* exposure. With increasing exposure time, the reflectivity of the coating decreases indicating softening of the material as expected. Humidity exposure leads to absorption of water molecules within the polymer matrix. Depending upon the molecular architecture of the polymer, hydrolysis of susceptible linkages can lead to chain scission and leaching of material from the film. As a result, water is able to penetrate the film more easily due to the hydrophilic degradation byproducts, resulting in further softening via water plasticization [13].

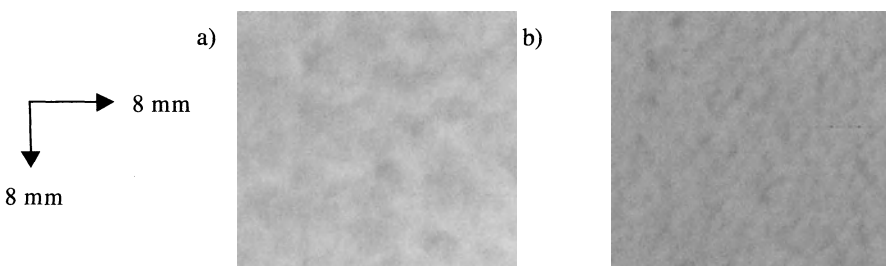


**Fig. 24.** Amplitude C-scans of a) no exposure and b) 2352 hours humidity exposure

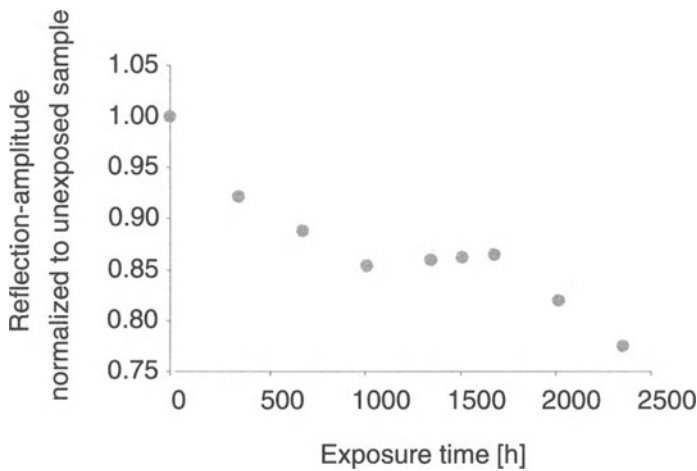


**Fig. 25.** Relative Reflection Amplitude as a function of continuous *humidity* exposure

The results for continuous *UV exposure* are shown in Fig. 26. Initially the reflection amplitude decreases. However, after approximately 1000 hours of exposure the trend is reversed and the amplitude increases rapidly. Absorption of UV initiates a series of chemical reactions that lead to the destruction of the long, flexible polymer chains. The reduction of molecular weight results in an initial softening of the coating [14]. Under low or no humidity condition, the softening

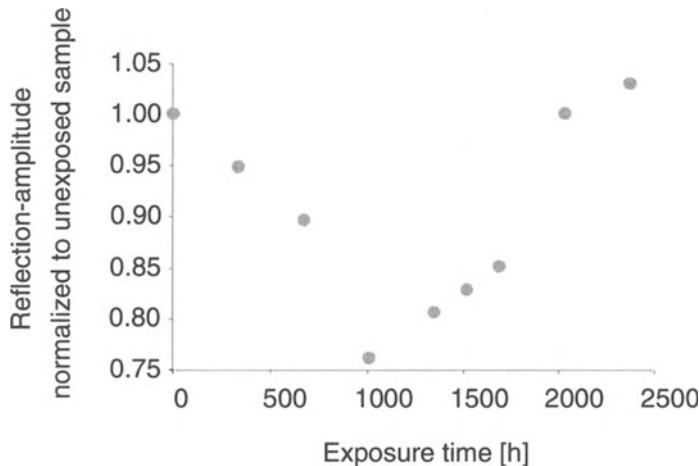


**Fig. 26.** Relative Reflection Amplitude as a function of exposure time for continuous UV exposure

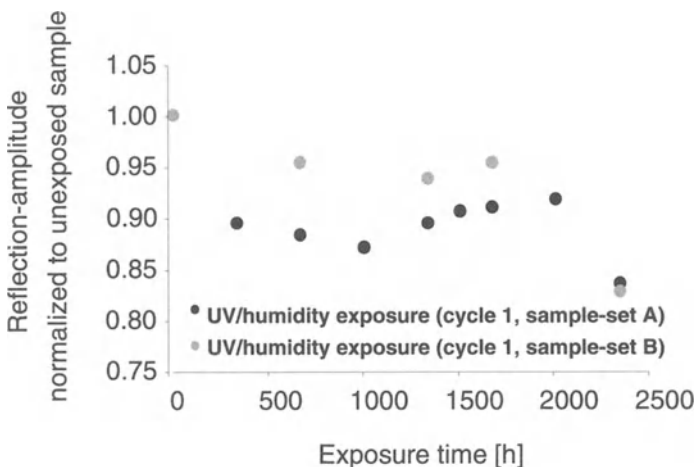


**Fig. 27.** Relative Reflection Amplitude as a function of exposure time for alternating *UV and humidity* exposure

influence of water plasticization is not effective and the small chains produced during degradation may entangle with each other, leading to an overall embrittlement and hardening [15]. The low reflectivity for this specimen at 1000 h exposure is probably not only due to its chemical/mechanical condition, but also the unusually high roughness of the surface

The results for a cycle with alternating *UV and humidity* exposure (Fig. 27) seem to illustrate that the mechanisms described above are counteracting processes: the reflection amplitude does not change significantly within approximately 300–2000 hours exposure time. Eventually the chain scission, accompanied by the water plasticization will be dominant and the coating material will soften.

### 11.5.3 Microcrack Detection of Fatigued Material Using HF SAM

#### **Test Specimens**

Two different materials, annealed, isotropic austenitic steel X6 CrNiNb18 and Ti-6Al-4V, were chosen for this study. Dogbone-shaped specimens with a rectangular cross-section (5 mm x 5 mm) were prepared. The specimens were polished with silicon carbide abrasives of reducing grit sizes. A final polish was performed with suspended colloidal silica (0.05 µm) without pressure in order to reduce micro-plastic deformation of the surface.

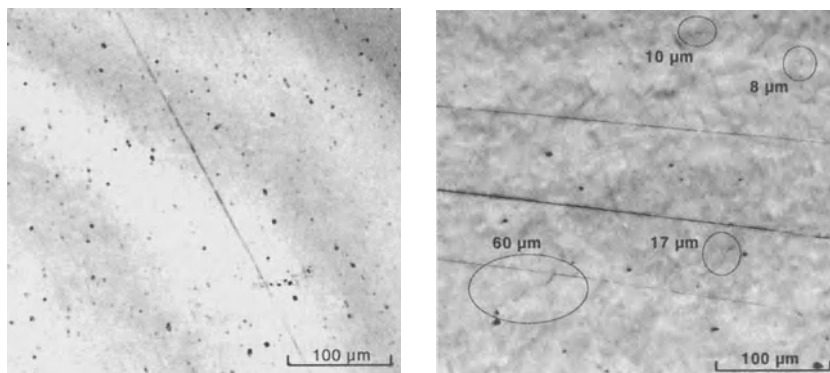


**Fig. 28.** Acoustic images in Ti-6Al-4V for a pristine dogbone specimen (*left*) and after 6000 fatigue cycles (*right*). Indications for microcracks are circled. The dark horizontal lines are surface scratches (Picture taken by Caron, IZFP)

### Imaging

HF-SAM enabled the characterization of the onset of microcracks and slip bands on the material surface due to fatigue damage. As can be seen from the acoustic images taken with 1.5 GHz (Fig. 28), microcracks were found on the Ti-6Al-4V specimen after 6,000 cycles under LCF conditions. Under these LCF conditions the expected lifetime is approximately 20,000 cycles.

Many more microcracks are generated in stainless steel during fatigue. In several fatigued stainless steel specimens, slip bands, as well as microcracks were detected [16]. Two tensile test samples were fatigued with different strain amplitudes. Since microcracks influence the topography, optimal contrast for microcrack detection was found for acoustic images with the lens in focus. Slip bands, on the other hand, are characteristics of the microstructure. For slip band detection, it is necessary to employ defocused images. The first slip band appears at 1 cycle (Fig. 29). Their number has strong local differences. The first microcracks are detected at 20 cycles (Fig. 29). Their length corresponds to the length of a grain boundary. Strong local differences in the number of generated microcracks are found. With increasing cycle number, the amount of slip bands and microcracks, as well as the mean microcrack length, increases. Above approximately 80% lifetime, no more changes in the damage structure could be found. Here, the largest microcracks are about 150 μm long. It seems that starting at this stage of fatigue, one microcrack grows until catastrophic failure occurs.

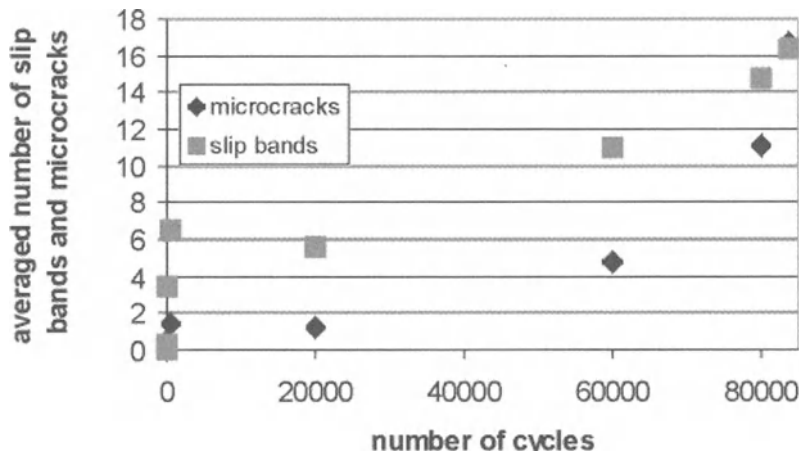


**Fig. 29.** Number of slip bands and microcracks per  $\text{mm}^2$  as function of number of cycles for X6 CrNiNb18 [17]

However, the local microcrack concentration corresponds to the local slip band concentration. With increasing cycle number, the microcrack length increases faster in areas with large slip band density compared to areas with low slip band density.

In some cases, it could be shown that the micocracks prefer to grow at slip bands generated by local stresses (Fig. 30). In most of the cases, the detection of microcracks at slip bands is difficult because the microcrack walls are tilted. This topography results in a disappearance of the slip bands.

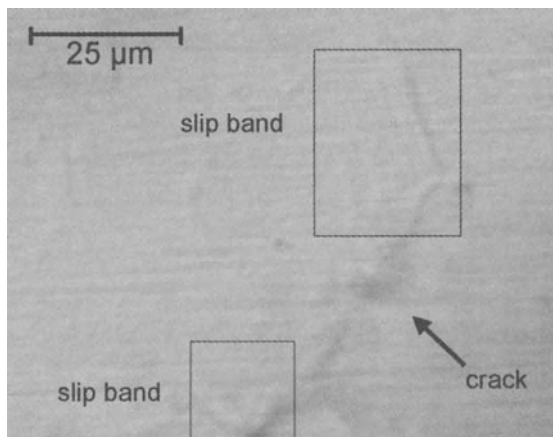


**Fig. 30.** Crack grown along slip bands, marked by rectangles. Frequency: 1 GHz, defocus distance:  $-6 \mu\text{m}$ , Material: X6 CrNiNb18

## References

1. Krautkrämer J, Krautkrämer H (1990) Ultrasonic Testing of Materials. 4th Rev. Edition, Springer-Verlag, Berlin, New York, Heidelberg
2. Briggs A (1995) Advances in Acoustic Microscopy, vol. 1, Kluwer Academic/Plenum Publishers, New York, NY
3. Briggs A, Arnold W (1996) Advances in Acoustic Microscopy, vol. 2, Kluwer Academic/Plenum Publishers, New York, NY
4. Kirra VK, Iyer VR (1995) Ultrasonics, vol. 33: 95–109
5. Briggs A (1992) Acoustic Microscopy, Oxford University Press, New York
6. NN, (2000) SAM 2000, KSI, Herborn, Germany
7. Yamanaka K, Enomoto Y, Tsuya Y (1985) IEEE Trans Sonics Ultrasonics SU-32:313
8. Hirsekorn S, Pangraz S, Weides G, Arnold W (1995) Appl Phys Lett 67:745
9. Shell E (2002) Prediction of Residual Fatigue Life from NDE of Corroded Components. Ph.D. thesis, University of Dayton
10. NN, (2000) Sanchem Inc, 8/20/02
11. [http://www.sanchem.com/safegard\\_cc\\_seals.html](http://www.sanchem.com/safegard_cc_seals.html)
12. Ullett J (2002) Corrosion Prediction: Assessing the Effect of Corrosion Protection System Aging. SBIR Report, Contract F33615-01-M-5609, Dayton, USA
13. Ullett J, Hoffmann J, Dietsch B, Peeler D (2002) Degradation Metrics for Air Force Coating Failure Assessment Model. Proc. 6th Joint FAA/DoD/NASA Conference on Aging Aircraft, (to be published) San Francisco, CA
14. Xiao GZ, Shanahan ME (1997) Water Absorption and Desorption in an Epoxy Resin with Degradation. Journal of Polymer Science Part B: Polymer Physics; vol. 35:2659–2670
15. Wicks ZW (1992) Organic Coatings: Science and Technology. John Wiley and Sons, New York
16. Bartolomeo P et al. (2000) Dynamical Mechanical Analysis and Vickers Micro Hardness Correlation for Polymer Coating UV Aging Characterization; Polymer Degradation and Stability; vol. 72:63–68
17. Fassbender SU, Karpen W, Sourkov A, Sathish S, Rösner H, Meyendorf N (2000) NDE of Fatigue on Metals Thermography, Acoustic Microscopy and Positron Annihilation Method, Proc. 15th WCNDE, Rome (on CD)

# **12 Scanning Probe Microscopy: Ultrasonic Force<sup>1</sup> and Scanning Kelvin Probe Force<sup>2</sup> Microscopy**

<sup>1</sup>C. Druffner, E. Schumaker, S. Sathish

<sup>2</sup>G.S. Frankel, P. Leblanc

## **12.1 Introduction**

In 1981, Gerd Binning and Heinrich Rohrer at IBM Zurich developed the first generation of the scanning probe microscope, the scanning tunneling microscope for which they received the Nobel Prize in physics. The Scanning Tunneling Microscope (STM) was a fantastic breakthrough with its capability to image atoms with angstrom precision. The physical operating principle of the STM is that when a bias voltage is applied between a sharp tip and a sample, a tunneling current is produced as electrons travel from one material to the other. This tunneling current is an exponential function of the distance between the tip and the sample and is responsible for the angstrom precision of the STM [1]. Wide use of the STM however was constrained by the requirement that the scanning tip and the sample must be conductive. The Atomic Force Microscope (AFM) was developed from the STM system and overcame the necessity of conductivity that accompanied STM imaging. The AFM sacrifices some of the atomic resolution of the STM as a trade off for imaging both nonconductors and conductors. The AFM resolution is classified as near atomic for topographic images.

## **12.2 Background and Instrumentation**

A basic AFM system consists of a scanning system, probe, probe motion sensor, electronics, vibration isolation system, and a computer [2]. Figure 1 shows a general schematic of an AFM system. The scanning system is the most fundamental component. In order to achieve high-resolution, a piezoelectric tube scanner capable of sub-angstrom increments is most often used. The scanner motion system comes in two designs. AFM systems can have the scanning piezoelectric installed in the AFM head unit that holds the probe or below the sample stage.

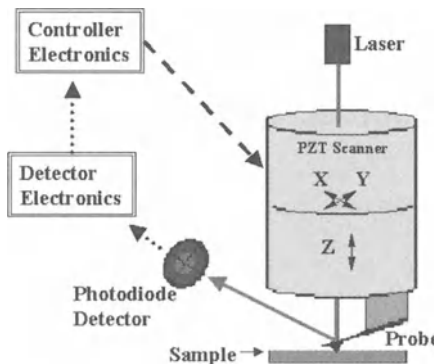


**Fig. 1.** Schematic Diagram of Atomic Force Microscope

Depending on the location of the scanner, either the sample or the probe head will be raster scanned during data acquisition. The piezoelectric scanning system motion is controlled via the computer software in order to precisely position the sample for a scan. Piezo material allows precise control of the motion of the tip in the x-, y-, and z-directions across the sample. All piezo materials exhibit some nonlinearity and hysteresis, but these effects can be compensated for through the electronics and calibration of the scanning device.

The next important AFM component is the probe. Different tips and cantilevers are available to be used with an AFM depending on the property measurement being performed. The probe consists of two sections – the cantilever and the atomically sharp tip. The cantilever provides a support onto which the probe tip is attached. The cantilever and tip can be manufactured from several different materials with various cantilever dimensions, tip shapes, and spring constants depending on the intended material property or the integrity of the sample to be examined. The cantilever can even possess a spring constant weaker than the atomic bonds of the sample material so that the tip can lightly trace and not damage the sample surface. Typical commercially manufactured cantilevers are made from either silicon or silicon nitride. Reference [3] gives further details on AFM probe tips and the internet websites of most AFM manufacturers are also excellent sources for information.

Monitoring the cantilever deflection is how the AFM measures the surface height or forces. As the tip engages the sample surface, the cantilever will deflect based on the forces acting on the tip. There are several different methods for measuring the deflection of the cantilever. Typically most AFM systems now measure the amount of cantilever deflection by reflecting a laser beam off of the cantilever's back surface into a four-quadrant laser diode detector. The position sensitive photodiode detector, itself is capable of measuring changes in light as small as 10 angstroms. A mechanical amplification of the signal gain is provided by the optical path length ratio between the cantilever's length and the light path, which allows the measurement system to detect sub-angstrom vertical changes in the cantilever position [1].

The probe sensor detection system has several auxiliary elements. A video camera is used to position the sample area for the scan. The camera is used by the operator for aligning the laser beam off the back of the cantilever and into the photodiode detector. The tip sample engagement is software controlled. Since the scanning distances involved are on the order of nanometers to a hundred microns, the scanner motion is also computer controlled. The system electronics control the scan operation based on user-selected inputs, such as the scan area size, scan rate, etc. The system electronics also include a feedback loop to monitor the position of the cantilever and the deflection force on the cantilever. The final system component is vibration isolation hardware that shields the scanning system from interference caused by external vibrations.

The AFM can be operated in three basic operational modes: contact, intermittent, or tapping mode. Contact mode can be operated in either constant height or constant force mode. In constant force mode, the surface topography is measured, while in constant height mode the interaction forces (repulsive/attractive) between the sample and tip are measured. In constant force contact mode operation, the feedback electronics maintain a set force between the sample and the tip (i.e. same cantilever deflection). The AFM feels the topography of the sample surface under the sharp probe tip. When the tip encounters a high surface asperity, the cantilever deflection will increase, so the feedback electronics will raise the Z height to return the cantilever deflection back to the preset point. The system electronics use a feedback loop to maintain the cantilever deflection by continually adjusting the Z height as the sample is scanned in the x- and y-direction. A surface topography image is outputted by correlating, point by point, the X and Y scan position of the tip with the Z height measurement of the scanner.

The lateral resolution of atomic force microscope and all scanning probe microscopes is based on the probe tip diameter which is in the nanometer range. By manufacturing a smaller, sharper tip, the resolution can be increased. This allows AFM's to maintain their spatial resolution at extreme magnifications ranging from  $10^3$  to  $10^9$  times in the x-, y-, and z-directions. This magnification ability can surpasses the Scanning Electron Microscope (SEM) and Transmission Electron Microscope (TEM) that have  $10^7$  magnification levels [3].

### 12.3 Methods

Since the discovery of atomic force microscopy [4], this methodology has evolved into one of the most powerful experimental tools for surface characterization of materials. Although the initial development was focused on near-atomic resolution surface topography measurements, later developments have proven the power of the technique to measure surface physical properties of materials [5–6]. The basic principle of the use of AFM for surface physical property measurement is the force-displacement curve [7–8]. This curve is obtained by examining the force experienced by the cantilever as the tip is brought closer to the surface of the sample. Based on the distance between the tip and the sample surface, the AFM

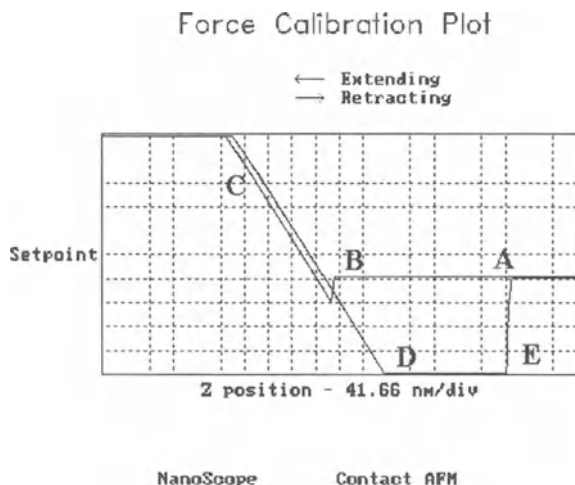


**Fig. 2.** Force Versus Displacement Plot Obtained from Contact Mode AFM

can be operated either in contact or non-contact mode. For most of the surface property measurements, the AFM is operated in the contact mode in the repulsive force region of the force-displacement curve.

Figure 2 shows a typical force versus displacement curve. In region A, the tip is brought toward the surface and maintains a constant force versus displacement due to the reference force level. As the tip approaches point B, the tip jumps to the surface because of the attractive forces. Since the tip is now contacting the surface, the force increases linearly with z-axis displacement due to the increased cantilever deflection as indicated in region C. Next, when the tip is moved away from the sample, the adhesion forces trap the tip and cause the bending direction to reverse and the force to drop below the starting value (region D). Finally, the cantilever snaps off the surface causing the sudden return to the original force (region E).

Several modifications to the standard AFM have led to various microscope systems capable of measuring different material properties [1–2, 9–10]. Some of these modified systems are Force Modulation Microscopy (FMM), Magnetic Force Microscopy (MFM), Electric Force Microscopy (EFM), Lateral Force Microscopy (LFM), Ultrasonic Force Microscopy (UFM), and Scanning Kelvin Probe Force Microscopy (SKPFM). With these developments, SPM's can measure both physical and mechanical material properties. Some of the possible properties include surface topography and conductivity, static charge distribution, localized friction, magnetic fields, and elastic moduli.

## 12.4 Application of the Methods

### 12.4.1 Imaging of Elastic Properties

#### Overview

One of the physical properties of interest is the elastic property of the surface. A variety of operation methods have been developed to image the elastic properties of the surface using the AFM [11–15]. One of the earliest versions designed for this is the Force Modulation (FM) technique [11]. In this technique, the piezo-tube utilized for the Z-positioning is supplied with a low-frequency sinusoidal signal, which makes the sample move up and down against the tip and will respond to the stiffness of the surface of the sample. This technique has been very useful in imaging soft materials like polymers and biomaterials [16]. One of the drawbacks of this method is that during scanning, the soft material can be damaged by the sharp tip. In many situations, this will damage the sample and reduce the measurement resolution. The FM technique is also not very sensitive when the specimen is relatively stiff. In order to overcome the limitations, the tapping mode [17] approach was developed. In tapping mode methodology, a cantilever having a high spring constant is oscillated near its resonant frequency. The oscillating tip is moved to approach the sample until it contacts the surface. The tip makes contact with the surface only once during the oscillation. Since the methodology reduces the shear forces during scanning, it can be used for investigation of delicate samples. The changes in the amplitude and the phase of the oscillating cantilever are affected by the stiffness of the material [18–19]. These properties have been used for studying the visco-elastic properties of the material. Although the tapping mode has become the standard methodology for imaging elastic and visco-elastic properties, imaging the adhesive potential between the tip and the sample complicates the image interpretation [18–20]. While the technique is extremely useful for soft materials, it is not suitable for stiffer materials.

An alternative method to overcome some limitations of the tapping mode is to use Pulse-Force Modulation (PFM) [21]. In PFM operation, the Z-offset is modulated by a triangular or sinusoidal voltage in the frequency range of 100 Hz to 5 kHz. The frequency is chosen such that it is lower than the resonant frequency of the tip-cantilever system. The amplitude is adjusted such that the tip jumps in and out of contact during each cycle. This allows the cantilever to display a complete force displacement curve during each cycle. By examining the waveform displayed on an oscilloscope, different parts of the force displacement curve can be examined. By measuring the amplitudes using sample-and-hold circuits at different locations on the waveform, elastic and adhesive properties of the surface can be imaged [22–24]. Although this methodology can produce simultaneous elastic and adhesive property images, eliminating the influence of the surface topography is very difficult. Since the oscillation frequency is close to the frequency of the signal produced from the surface topography variations, the images acquired are convoluted images of the properties and the surface topography.

Other approaches can also be found in the literature for imaging elastic stiffness mapping using AFM. One methodology for Ultrasonic Force Microscopy (UFM) uses a piezoelectric transducer under the sample to induce acoustic vibration [12–15]. The acoustic waves propagating through the sample are detected by the AFM tip on the opposite face of the sample. The frequency of excitation can be chosen to be anywhere in the range of a few hundred kHz to several MHz. Depending on the frequency of excitation, the detection electronics have to be changed. One of the simplest of the excitation techniques is the continuous wave (CW). In this mode, a continuous wave signal excites the transducer. The amplitude of excitation is kept very low and the frequency is chosen to be in the range of 100 kHz to about 700 kHz. This maximum frequency is probably close to the second or third harmonic of the resonant frequency of the cantilever. Since the excitation amplitude is very low and the frequency is chosen such that the tip can follow the surface displacement, the amplitude detected by the AFM tip has been shown to be directly proportional to the elastic stiffness of the material [25]. This simplified approach allows easy interpretation of the images. The continuous wave UFM has been utilized effectively to investigate elastic properties of materials and has been shown to be a very useful tool in nano-NDE applications as detailed below.

When the frequency of excitation is high (a few MHz), the tip-cantilever system cannot follow the surface displacement. In such situations, it is necessary to utilize nonlinear detection electronics [12]. This technique has proved to be very useful in the early development of UFM and the nonlinear detection can be performed at very high frequencies. The interpretation of the images involves not only elastic properties of the sample, but includes the adhesive force between the tip and the sample.

### ***Principle of Ultrasonic Force Microscopy on Nanomaterials***

A UFM system entails propagating an ultrasonic signal either through the cantilever or through the sample to investigate elasticity properties [11, 26–27]. The first technique discussed in this chapter deals with the through sample UFM operational mode. UFM combines the principles of acoustic microscopy with the resolution of the AFM operating in contact mode to generate elasticity map images for a variety of applications. As mentioned earlier, the principle of contact mode consists of applying a constant force to the cantilever during the data acquisition. The cantilever will then deflect based on surface variations. Any cantilever deflection changes the force on the tip/cantilever system. The feedback loop uses the amount of the deflection to generate a voltage to move the Z piezo-scanner in order to change the force back to the original level. The change in Z position is then used to create an image of the surface variations. The Z sensitivity of the image depends on how well the feedback loop tracks the surface as well as the cantilever spring constant. The user has to determine which spring constant is

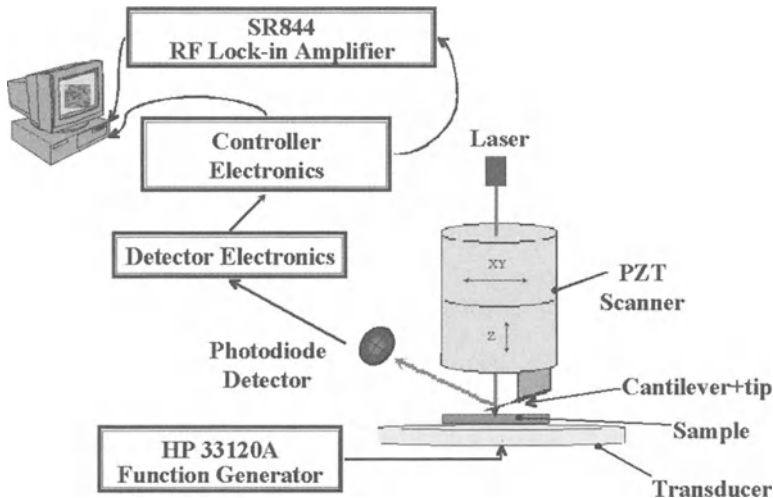


**Fig. 3.** Schematic Diagram of CW Mode UFM

better. For soft samples, lower spring constants are recommended [26]. During UFM operation, the cantilever has to stay in contact with the sample's surface and have a fast response to changes in the surface deflections caused by the acoustic wave propagating through the sample. But at the same time, the cantilever sensitivity to these surface deflections should not be compromised. Hence, we typically use a low spring constant combined with low amplitude of the detected signal and excitation frequencies in the kHz range. The principle of operation and modifications to the AFM are shown in Fig. 3.

A Hewlett Packard function generator is employed to drive a piezoelectric transducer in continuous wave mode. A Stanford Research Systems lock-in amplifier measures the magnitude of the detected signal and its phase with respect to the signal from the function generator. The UFM measurements can be related to the elastic properties of the material in contact with the tip.

### ***A Simplistic View of the Elasticity Contrast in UFM at Nanoscales***

There are two primary ways that material property data can be collected from the tip-sample interaction with the AFM. One way is a quasi-static data acquisition where a force curve is recorded at a single point. The data is a plot of the tip-sample interaction forces as a function of the tip height position. This method is time consuming and requires large data storage. The second method collects

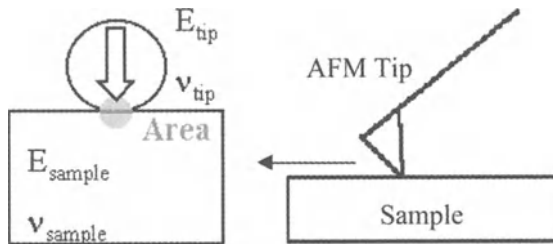


**Fig. 4.** Interaction Stiffness Defined with a Hertzian Contact

material property data using a modulation technique. The image is generated from the cantilever's amplitude or phase motion, while either the distance between the cantilever and sample or the force applied to the sample is modulated. Penetration depth is the tip-sample separation distance. The cantilever's amplitude response at a specific penetration depth is proportional to the slope of the force penetration depth curve at that particular depth. The power of the second method is in the ease with which an image of inhomogeneous materials is acquired.

In scanning probe microscopy techniques, contact can be defined as the point on the force distance curve at which there is a detectable repulsive component to the tip-sample interaction. In contact with the sample, both attractive and repulsive forces contribute to the interaction force between the tip and the sample. The interaction stiffness  $k_i$  is a force gradient. It can be measured at any penetration depth. If the sample is strongly loaded or if the attractive forces are negligible then the role of the attractive force can be ignored in the value of  $k_i$  (it is mainly repulsive force – the sample pushing back on the tip).

The local surface topography as well as the probe tip's size and shape strongly influence the contact stiffness measurements. The tip-sample interaction can be modeled by a simple Hertzian contact as shown in Fig. 4. The interaction stiffness can be related to material properties such as Young's modulus. In the limit of negligible adhesion and if a spherical probe tip is employed, the  $k_i$  can be defined as in (1) [28]. The Poisson ratio  $\nu$  and Young's modulus  $E$  are used to define the reduced elastic modulus  $K$  given in (2).

$$k_i = \frac{3 * a * K}{2}, \quad (1)$$

where  $a$  is the contact radius between the tip and sample.

$$\frac{1}{K} = \frac{3}{4} \left[ \left( \frac{1 - \nu_{tip}^2}{E_{tip}} \right) + \left( \frac{1 - \nu_{sample}^2}{E_{sample}} \right) \right] \quad (2)$$

Assuming that the Young's modulus of the tip and the Poisson ratio are constant during scanning, variations in the modulus of the sample can be imaged. While imaging, the AFM feedback seeks to maintain a constant minimal force on the surface. With the tip force on the sample being maintained constant, the Poisson ratio of the tip as a consequence should not change. The Poisson's ratio

for the sample may be changing slightly since it is a function of the sample elasticity. So in the reduced modulus equation for the tip and sample, the only factor changing significantly is the  $E_{\text{sample}}$ , that is, in the right hand term in (2). Thus, the interaction stiffness changes in the image can be attributed to the changes in the stiffness of the sample.

For the duration of one data scan, it is assumed that the tip contact area is maintained constant and that the probe tip is not degrading. To validate the assumption that the tip diameter is constant during the scan, repetitive images should be collected. The structure resolution is checked to make sure that the contact area is not changing from scan to scan. A change in feature size on repetitive scanning can be an indication that the contact area is changing during the scan. Dust, debris, or dirt from the sample surface can accumulate on the probe tip resulting in an increased contact area or force input and cause streaks or blurred lines in the image. Assuming that the tip diameter, tip elasticity, and Poisson ratio are maintained constant during the data scan collection, the only variable significantly changing in the contact stiffness equation is sample elasticity. So the UFM image can be considered a map of the elastic stiffness of the material directly under the tip. The change in contrast in the UFM image is directly caused by these elastic modulus variations in the sample below the tip. It is also believed that the depth sensitivity of the UFM is several times the diameter of the tip [25]. The information contained in the UFM image is an averaged value from the top layers of the surface over a thickness of several times the tip diameter. For low amplitude ultrasonic excitation, the AFM tip is expected to be

### System model

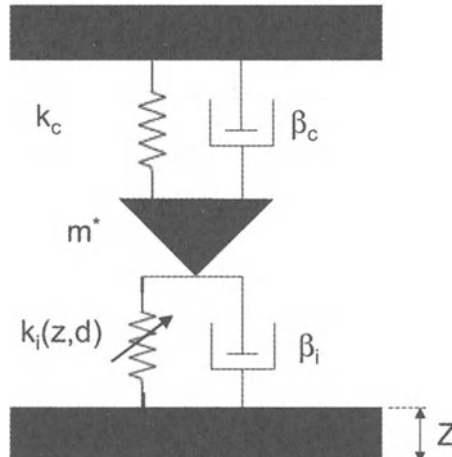


**Fig. 5.** Rheological Model of Tip-Sample Interactions

in contact with the surface and the surface displacements detected by the AFM tip are directly proportional to the stiffness of the material under the tip [25, 29].

The discussion presented above is qualitative in nature, but provides a simple physical explanation of the contrast in the UFM images. Burnham et al. has developed a more elaborate rheological model for Ultrasonic Force Microscopy. Burnham's rheological model of the transducer-sample-cantilever system for contact mode UFM that shows the elastic modulus of the material is proportional to the amplitude of the tip displacement. This model is shown in Fig. 5 [29], where  $d$  is the cantilever position and  $z$  is the transducer position. A spring with stiffness  $k_c$ , a dashpot with damping  $\beta_c$ , and an effective mass  $m^*$  represent the cantilever. The tip sample interaction is represented by a spring  $k_i(z,d)$  and a dashpot  $\beta_i(z,d)$ .

### ***Applications of the UFM Method in Nanoscale NDE***

Copper nanograins were investigated to demonstrate the feasibility of UFM to provide qualitative elasticity information on the grain structure in the nanometer regime. A copper thin film was deposited on a 1 mm thick fused quartz substrate using focused ion beam cluster deposition [30]. The thin film density varies due to the nature of the deposition process. A region in the middle of the film was found to be uniform and was chosen to be studied using AFM and UFM. A PZT transducer operating in the frequency range of a few kHz to 1 MHz was bonded to the non-deposited face of the substrate. The excitation frequency was varied to show contrast reversal in the grains. This contrast reversal has been seen in acoustic microscopy and is attributed to the large elastic anisotropy of copper [31]. Figure 6 shows both the sample's AFM topography images and the corresponding UFM amplitude images at various frequencies ( $f = 312$  kHz,  $f = 675$  kHz,  $f = 714$  kHz). [32–33]. The scan area is  $1 \mu\text{m} \times 1 \mu\text{m}$ .

The range of contrast in the surface topography images varies from –100 to 100 nm. The contrast is not very clear, making it difficult to identify individual grains in the topography scans. The grain boundaries cannot be determined and appear hazy.

On the other hand, the UFM amplitude images show very good contrast from grain to grain (almost black to white) and the grain boundaries are clearly observable. The smallest grain that can be identified has an approximate size of 20 nm. By comparing the UFM amplitude images taken at different frequencies, it can be seen that the contrast has reversed in some of the grains. Such a contrast reversal has been predicted by Burnham et. al. [25] based on a rheological model for the transducer-sample-cantilever system and has been observed in a composite sample consisting of large elastic modulus differences between the fibers and the matrix. However, we have observed contrast reversal in copper nanograins despite the elastic modulus variations being considerably less than the variation observed in the composite sample.

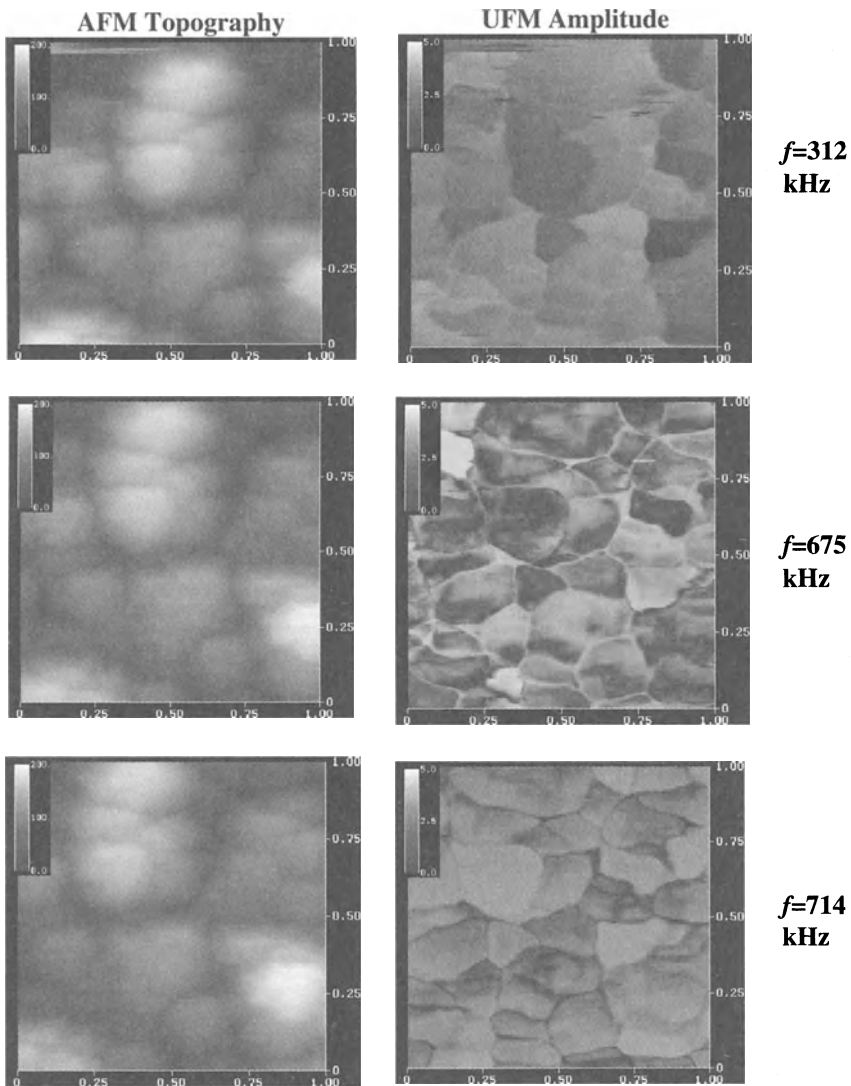


**Fig. 6.** AFM and UFM Images of the High-Density Region on a Copper Thin Film at Various Frequencies (Scan Area is  $1 \mu\text{m} \times 1 \mu\text{m}$ )

It has been shown in an acoustic microscopic study of polycrystalline copper that the grain structure can be observed and the contrast is attributed to the large elastic anisotropy of copper [31]. Following a similar argument, the contrast in the UFM images can be explained through the example of the variation in the Young's modulus of individual grains. In the case of a thin film on an elastically isotropic substrate, the variation in the elastic modulus is solely due to the thin

film. Copper has elastic constants of  $C_{11} = 168.4$  GPa,  $C_{12} = 121.4$  GPa, and  $C_{44} = 75.4$  GPa [34], which results in a large elastic anisotropy  $\eta$  ( $\eta = 2C_{44}/(C_{11} - C_{12})$ ) of 3.21. Considering the prominent three crystallographic orientations (111), (100), and (110), the respective Young's moduli are 191.15 GPa, 130.34 GPa, and 66.7 GPa. The variation in the Young's modulus for these three orientations should produce significantly different surface displacements. These different displacements account for the grain structure contrast observed in the UFM images.

A quantitative measurement of elastic modulus on a nanometer scale will be very useful. At present, several attempts for quantification can be found in literature [12–15, 35–37]. Some of the important input parameters for an exact evaluation of elastic modulus – like forces between the tip and the sample, radius of the tip, etc. – cannot be determined accurately.

It has been shown that UFM can be used for observation of copper thin films with nanograin structures. The image contrast is directly related to the elastic modulus variations from grain to grain. UFM can be applied to investigate subsurface defects on the nanometer scale due to changes in the elasticity caused by the defects. This is another extension of ultrasonic nondestructive evaluation of materials on the nanometer scale.

Figures 7–16 show other applications of the UFM ranging from hard to soft materials that we have done in our research. Figure 7 shows the grain structure of  $\text{Al}_2\text{O}_3$ -TiC raw material wafers that are used in the microelectronics industry. The  $\text{Al}_2\text{O}_3$ -TiC wafers were being investigated to determine the reason for grain bodies pulling out from the surface during manufacturing [38]. Specifically, it was desired to analyze the grain boundary itself, a very small part of the overall structure. Samples of varying composition were analyzed to try to find the origin of the grain pullout. Differences in the average grain size ranging from 1.0–1.8 microns were observed. A difference in the ultrasonic response of the grain boundary was also observed. It was thought that the difference in response at the grain boundaries between different samples is an indicator of which samples may be more susceptible to grain pullout. A three-dimensional image of the UFM amplitude results in Fig. 7 are shown in Fig. 8 in order to highlights some of the grain boundary differences.

With state of the art components being manufactured in smaller dimensions with increasingly more intricate details, there are many applications where nanoscale imaging of a device can provide insightful and key information to the manufacturer about the state and operation of the material. Characterization techniques that give high-resolution nanoscale imaging of defects, micro- and nanocracks, nanograins, or grain boundary interactions are an increasingly important aid as device miniaturization occurs. Another application, which was proved successful with AFM-UFM, was detecting microcracking in laser tooled ceramics [39–40].

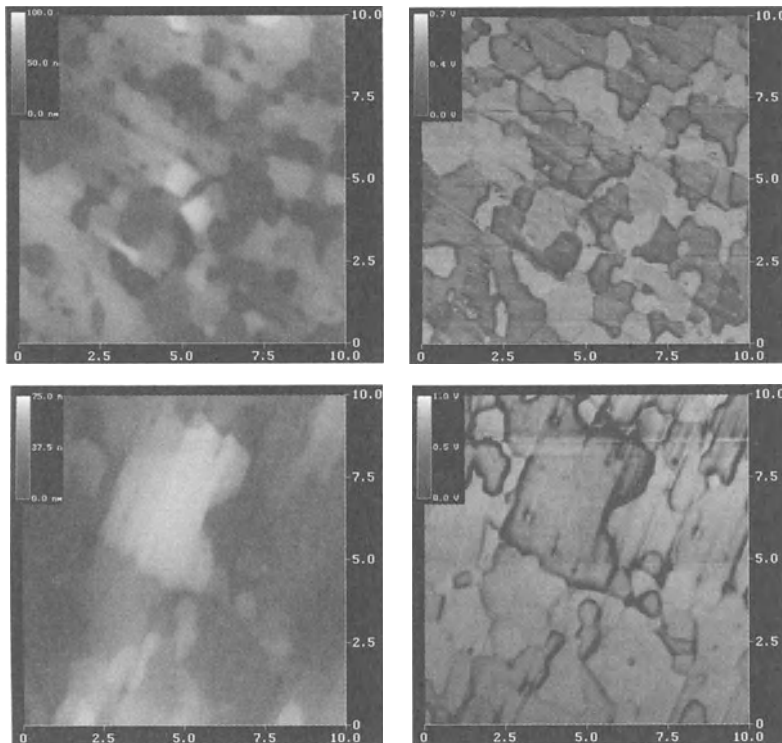


**Fig. 7.** AFM and UFM Images of Differently Prepared Samples of  $\text{Al}_2\text{O}_3$ -TiC, exhibiting the difference in material grains. (Scan Area  $10 \mu\text{m} \times 10 \mu\text{m}$ )

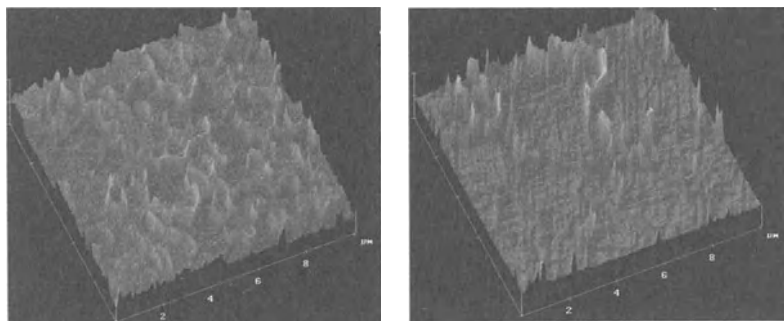


**Fig. 8.** A three-dimensional Image of the UFM Amplitude Images from Fig. 7, Highlights the Response at the Grain Boundaries in the UFM image. (Scan Area is  $10 \mu\text{m} \times 10 \mu\text{m}$ )

The head slider is the read/write chip in a computer hard drive. The slider's surface structure is specially designed and is critical to ensure that it has a stable flying height above the hard disc in operation. The head slider's body is typically

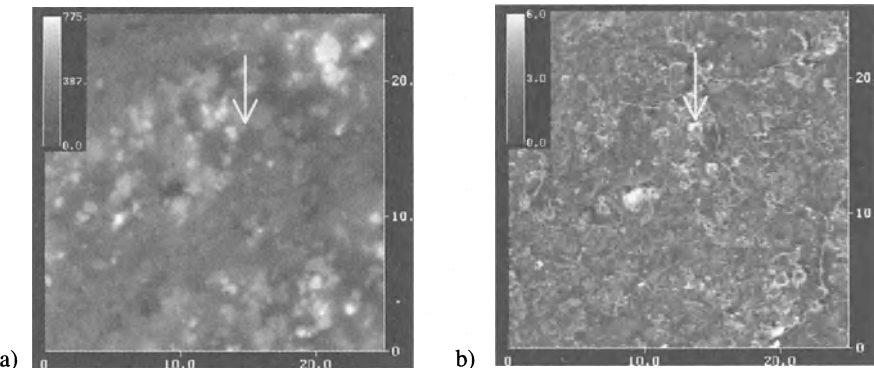


**Fig. 9.** Cracking in Laser Treated Surface Section of a Head Slider; a) AFM Surface Topography Image; b) UFM Amplitude Image (Scan Area is  $25\text{ }\mu\text{m} \times 25\text{ }\mu\text{m}$ )

made from  $\text{Al}_2\text{O}_3\text{-TiC}$  ceramics and the device is extremely small  $1\text{ mm} \times 1\text{ mm} \times 0.3\text{ mm}$ . Since the device material is very hard and combined with the device's small size, mechanical processing methods are difficult. Laser curvature adjustment technique has been shown to be very promising method for modifying the surface structure of microdevices like a head slider [41–43]. However, laser cutting can produce high temperature gradients within the material and cause stress cracking. So it is important to characterize the laser treated surface in order to optimize the laser tooling techniques for micro devices. The characterization technique of UFM allows microcracks to be clearly distinguished. These micro- and nanocracks have been imaged on the head slider as shown in Fig. 9 [39–40].

Images at higher magnification of the same cracks seen in the lower right side of the UFM image in Fig. 9 are presented in Fig. 10.

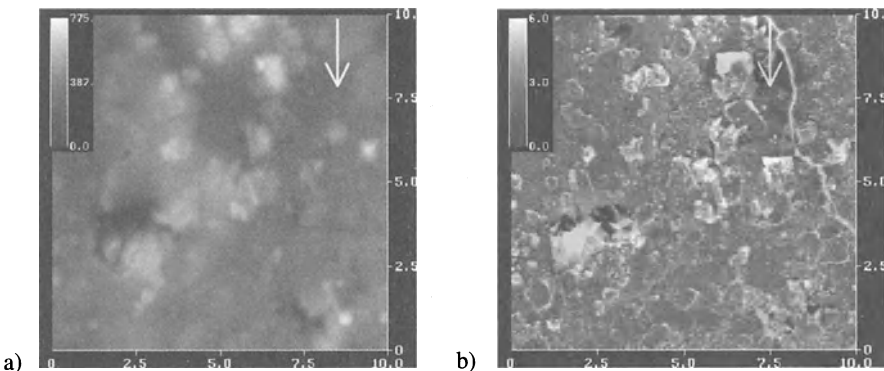


**Fig. 10.** Close up Image of Crack from Fig. 9; a) AFM Topography Image; b) UFM Amplitude Image (Scan Area is  $10\text{ }\mu\text{m} \times 10\text{ }\mu\text{m}$ )

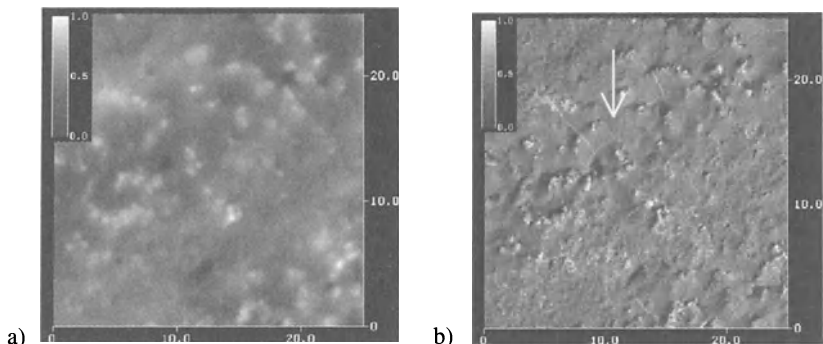


**Fig. 11.** Second Scan Location on the Laser Treated Surface on Slider #1; a) AFM Topography Image; b) UFM Amplitude Image (Scan Area is  $25 \mu\text{m} \times 25 \mu\text{m}$ )

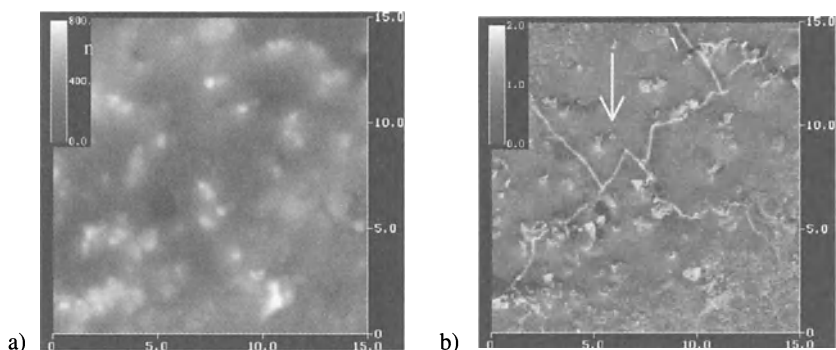


**Fig. 12.** Higher Magnification Image of the Crack in Fig. 11 on Slider #1; a) AFM Surface Topography Image; b) UFM Amplitude Image (Scan Area is  $15 \mu\text{m} \times 15 \mu\text{m}$ )

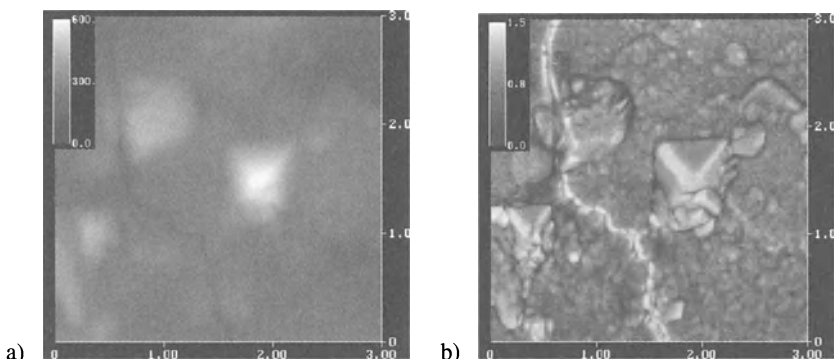


**Fig. 13.** Nanodroplets and Surface Asperities found in the Laser Treated Section; a) AFM Surface Topography Image; b) UFM Amplitude Image (Scan Area is  $3 \mu\text{m}$ )

Figure 11 to 13 show images from other sections of laser treatment as further examples where cracking occurred in the material and it is easier to detect the crack in the UFM image as opposed to the AFM.

In the laser treated region just in the immediate vicinity of the cracks, the ultrasonic displacement is much different from the rest of the matrix. One of the possible reasons for the enhanced ultrasonic displacement is the free boundary condition along the crack flanks. A crack has a gap between its two flanks. The amplitude of the cantilever oscillation near the crack flank is expected to be larger due to the freeness of the boundary compared to the regions away from the flank of the crack. Because of the stress free boundary, the ultrasonic displacement will be different than compared to other surface regions. This feature enhances the visibility of the crack. Due to the increased amplitude in the immediate vicinity of the cracks, the cracks in the UFM images appear brighter than the other regions. This enhanced amplitude helps in detecting the microcracks in the UFM.

As the electronics industry progresses to increasingly smaller wire technology, the ability to image a wire's grain structure can become especially challenging without the aid of chemically etching the surface. It is in nanograin imaging that the ability of the UFM to sense the changes in the materials elasticity can be used to provide insight about the grain structure. The grain orientation and stability achieved in a microwire is very important in regards to having the device work properly and at its peak efficiency [44]. Microwires in the copper coil of the head slider were imaged [39–40, 45]. The microwires were imaged in order to look for changes occurring in the copper nanograins caused by different processing conditions and from actual environmental use conditions. Figure 14 show images of the copper microwires where the nanograins would be very difficult or too small to image by conventional acoustic methods. The average grain size obtained using an analysis of the UFM image was found to be 150 nm.

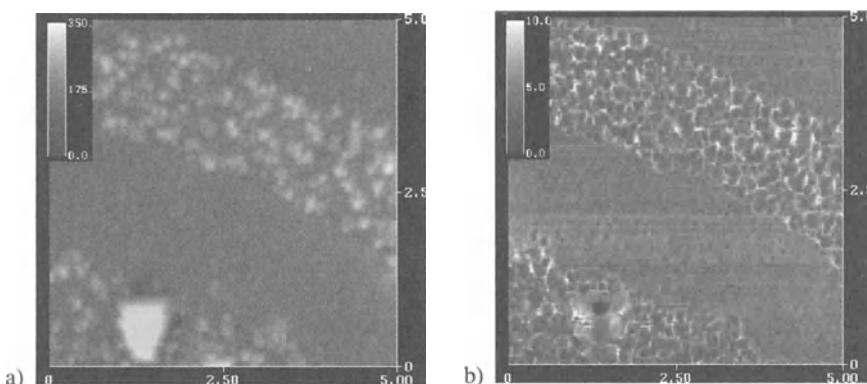


**Fig. 14.** Microstructure of Copper Grains in 2  $\mu\text{m}$  Wide Wires; a) AFM Topography Image; b) UFM Amplitude Image (Scan Area is 5  $\mu\text{m} \times 5 \mu\text{m}$ )

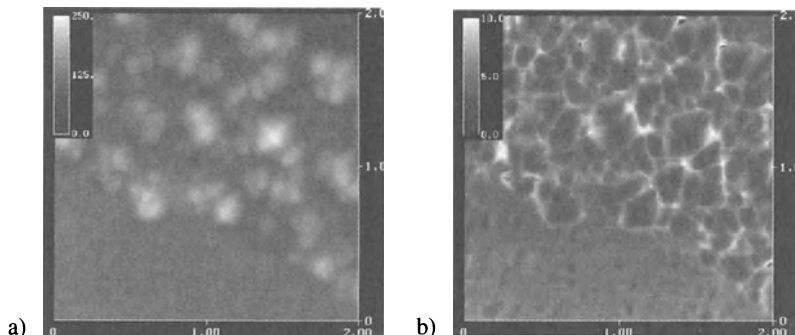


**Fig. 15.** Smaller Scanned Area from Fig. 14; a) AFM Surface Topography Image; b) UFM Amplitude Image (Scan Area is  $2 \mu\text{m} \times 2 \mu\text{m}$ )

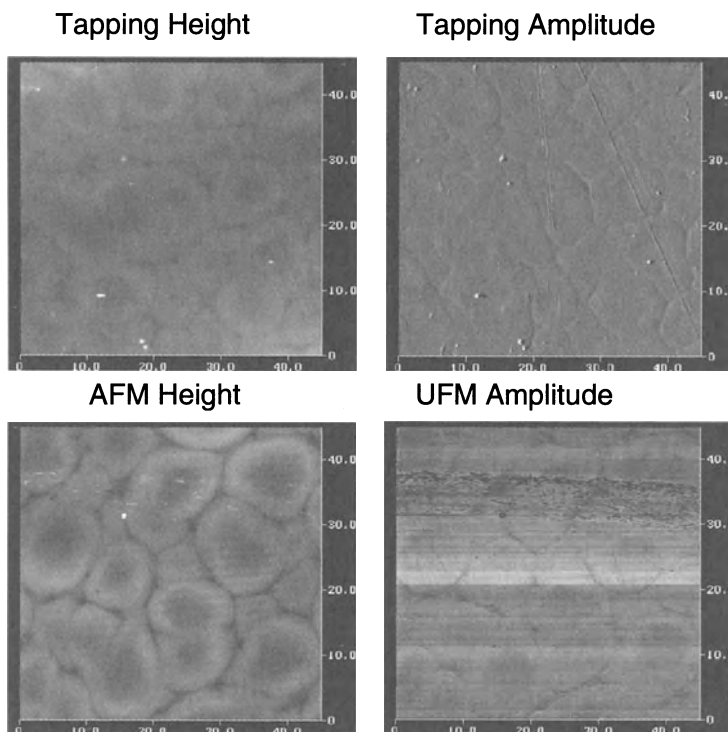


**Fig. 16.** Epoxy coating on Aluminum Substrate (Scan Area is  $45 \mu\text{m} \times 45 \mu\text{m}$ )

Soft materials were also imaged using this technique. An epoxy coating on aluminum was investigated to look at the coating degradation in a high UV environment. The images show surface effects that occurred during curing between the polymer and aluminum substrate. Tapping mode was done in order to

ensure that these interface effects were not a remnant of the imaging method. Both tapping mode and UFM images were acquired from the same sample although due to the changing the tip (each method uses a different cantilever spring constant), the scan locations are not exactly matched. An interesting note is that the interface effects were different from the edge to the center of the coating. The images are shown in Fig. 16.

### ***Conclusion on Future Trends in AFM-UFM Microscopy***

The future trends in the AFM-UFM are to apply the near field microscope to new applications in material characterization of nanoscale devices. The AFM-UFM allows high-resolution nanometer imaging that can be very useful in understanding material interactions in many small high technology devices. With the size of electronic devices constantly shrinking, new nondestructive evaluation methods need to be developed that are capable of meeting the new size requirement of these new devices. The combination of AFM-UFM allows quick imaging of nano-sized grains with little sample preparation on a scale that is not possible by conventional acoustic microscopy. Other development avenues for the AFM-UFM are to construct a system that can give a fast quantitative measure of elasticity whereas the current system is being applied to qualitative mapping of the samples for quick sample turn around time. A fast quantitative method would require the development of more precise cantilevers and probes along with the separation of sample surface adhesion effects from the elasticity information that is presently very elaborate and time consuming.

#### **12.4.2 Scanning Kelvin Probe Force Microscopy and AFM Scratching for Studies of Corrosion**

Pitting corrosion is usually driven by microstructural heterogeneities [46]. For instance, in Al alloys, alloying elements added for increased strength are often segregated to and enriched in intermetallic particles [47, 48]. Such particles can be large constituent phases on the order of tens of microns in size, or precipitated hardening particles nm in size. Localized corrosion typically initiates at the larger particles (micron size or larger), but the role of the particle in the localized corrosion process depends on the particle type. In Al 2024-T3, there exist two primary types of large intermetallic particles: AlCuFeMn particles and S phase Al<sub>2</sub>CuMg particles [47, 48]. The FeMn-containing particles have a range of composition and are often themselves heterogeneous. These particles are typically considered to be cathodic to the matrix [49]. The S phase particles are more homogeneous, and are thought to be active relative to the matrix owing to the high Mg concentration. It has been suggested that Mg and Al can dealloy from S phase particles, leaving a porous Cu-rich residue that might break apart and redistribute Cu across the sample surface, providing a large active cathode [47].

Clearly, it is of interest to be able to understand the exact role of these intermetallic particles in the localized corrosion process on Al alloys. Owing to their small size, techniques with high spatial resolution are required to do so. A number of standard techniques with sub-micron resolution exist, such as SEM, EDS, AES, and TEM. This paragraph will summarize recent work utilizing atomic force microscopy (AFM) based methods. The advantages of AFM include the ability to provide quantitative information regarding the topography of a surface and to perform those measurements *in situ*. However, perhaps the real power of AFM is that it forms the basis for associated techniques that provide enhanced capabilities. Scanning Kelvin Probe Force Microscopy (SKPFM) is one such technique, which has only recently been applied to corrosion studies [50–54]. SKPFM is an AFM-based technique with sub-micron resolution, and it is a robust technique that is relatively quick and simple to perform. It simultaneously provides topographic and potential maps of a region of a sample surface. Findings from a number of recent publications are summarized below. The nature of the potential measured by SKPFM will be discussed and it will be shown that the overall nature justifies the description of it as the Volta potential difference and the use of the name Kelvin Probe.

*In situ* scratching of a passive metal with a sharp stylus has been used by several investigators, G.T. Burstein and colleagues in particular, to assess repassivation behavior by localized removal of the passive film [55–57]. These and other studies with related methods of depassivation [58–64] have provided considerable insight into the nature of passivity and the kinetics of repassivation. Most of these repassivation studies measured current transients generated under potential control. The influence of local heterogeneities cannot be studied by most scratching methods because they have no control over the placement of the scratch relative to the microstructure. Pressure applied by an AFM tip on the surface of a sample during *in situ* contact mode rastering is a form of scratching on the micro scale. An AFM tip can be placed directly on a feature of interest as determined by the topography or by *ex situ* SKPFM and the use of fiducial marks. Furthermore, the force applied by a tip can be controlled exactly. Recent studies utilizing so called AFM scratching will also be reviewed below.

### ***Principle of Scanning Kelvin Probe Force Microscopy***

Scanning Kelvin Probe Force Microscopy was performed with commercial AFMs (Nanoscope IIIa or Dimension 3100, both from Veeco/Digital Instruments). These instruments can measure the surface topography and potential distribution simultaneously on a line-by-line basis using metal-coated silicon cantilevers that are electrically conducting. The cantilevers were also obtained from Digital Instruments. The principle and details of the SKPFM measurement have been previously described [52, 53]. In short, it involves scanning the surface in tapping mode to determine the topography on a line-by-line basis. The cantilever is then lifted a fixed distance from the surface, typically 100 nm, and the tip is rescanned at this height in “lift mode”. On the rescan, an AC voltage is applied to the tip, which stimulates oscillations of the cantilever in the presence of an electric field.

The magnitude of the oscillations at the stimulating frequency, monitored by the AFM detection scheme, is nulled on a point-by-point basis during the lift mode reread by adding a DC voltage that balances the field. This approach to potential distribution measurement is not possible in an aqueous solution because the large voltages applied to the tip would result in faradaic reactions. In this study, all potential mapping was performed in air. Since this technique is a nulling method, the output signal from the Nanoscope IIIa was inverted; it has been shown previously that inversion of the signal is needed to obtain the expected polarity of the potential measurements. The Dimension 3100 outputs the signal with the correct polarity. The values obtained are relative to the potential of the tip. The tips are only pseudo-references since their potential may vary with changes in the surface oxide. In order to avoid errors associated with variations in the tips or instabilities in the instrument electronics, the potential measurements were calibrated by comparison to the potential measured on a pure Ni surface after immersion in DI H<sub>2</sub>O. Ni was chosen as a reference because it was found to have a stable potential. All potential measurements are reported relative to that of a Ni sample. Consecutive measurements in air on a stable reference sample using different tips coated with the same metal showed potential difference of less than 50 mV, giving an indication of the reproducibility of this method.

### ***Scratching Experiments***

Scratching experiments were performed in a fluid cell with the Nanoscope IIIa using commercially available Si tips. In situ contact mode rastering was performed for varying periods of time. The effect of tip pressure during in situ contact rastering was determined by changing the setpoint voltage on the photodetector sensor that monitors the cantilever deflection. Areas were rastered at setpoints ranging from 0.2 to 8 V. The effect of high-force rastering on the surface topography was determined by subsequently reducing the setpoint to 0.2 V and increasing the scanned area size. Applied setpoint is used instead of tip pressure because the relation between the two is not straightforward and dependent on changes in tip shape that might occur during the experiment.

Samples were cut from an Al 2024-T3 sheet (nominal composition 3.8–4.9% Cu, 1.2–1.8% Mg, 0.3–0.9% Mn, 0.5% Fe, 0.5% Si, 0.25% Zn, 0.1% Cr, 0.05% Ti, balance Al). A non-aqueous lubricating slurry (Blue Lube by Struers) was used during the surface preparation (grinding and polishing). The Al 2024-T3 disks were mechanically ground with successively finer SiC paper through 1200 grit and polished with 6, 3, and 1 μm diamond paste. Prior to study, samples were cleaned ultrasonically with ethyl alcohol. The pure metal samples were polished through 1200 grit SiC paper in water and ultrasonically cleaned in distilled water. The open circuit potential was measured versus a standard calomel electrode (SCE).

### Experiments on Pure Metals

In order to calibrate and to determine the usefulness of the scanning Kelvin probe force microscopy technique, Volta measurements were made on a number of pure metal samples. The samples were exposed to DI water or aqueous solutions at open circuit for 30 min, removed, rinsed, and dried prior to measurement of the Volta potential in air. The values were compared to the open circuit potential (OCP) values measured on those samples prior to removal from solution. Volta potentials are reported vs. the potential measured on a pure Ni sample, which served as a calibration standard. Ni was chosen as a reference because it was found to have a stable Volta potential. Figure 17 shows the relationship of OCP for different metals in deionized water, 0.5 M NaCl, and 0.1 M  $\text{Na}_2\text{SO}_4$  to the Volta potential obtained in air with the Kelvin probe force microscope [50, 52]. The potential measured by SKPFM is seen to correlate directly with the OCP measured in solution for metals with a wide range of practical nobility. This signal is thus a measure of practical nobility, with the advantage that it can be mapped over a surface with high spatial resolution. This correlation between measured Volta potential and OCP also holds for a single metal exposed to different solutions in which it exhibits different open circuit potentials. For samples exposed to the chloride and sulfate solutions, both the open circuit potential in solution and the Volta potential difference in air after solution exposure were shifted in the active direction by around 150 mV relative to the values measured in and following DI water exposure. This suggests that adsorption of charged species at the electrode surface in chloride or in sulfate changed the dipole structure in the double layer and influenced the measured Volta potential measured in air by the same value.

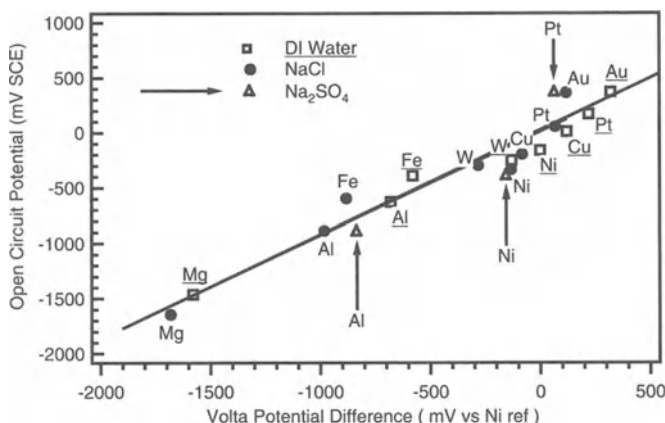


**Fig. 17.** Comparison of the potential measured in air by Scanning Kelvin Probe Force Microscopy with open circuit measured in solution: in DI water (squares and underlined elemental symbols), in 0.5 M NaCl solution (filled dots) and in 0.1M  $\text{Na}_2\text{SO}_4$  (triangles and indicated with an arrow) [50]

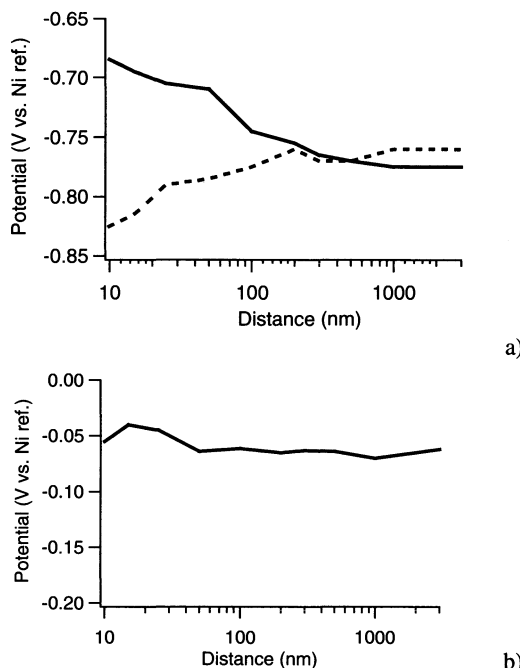


**Fig. 18.** Potential measured as a function of tip-sample distance for a) pure Al after 30 min at OCP. Solid line, directly after removal from DI water, dashed line, 1 week later; b) pure Ni after 30 min of immersion in DI water at OCP [50]

To distinguish the various components of the potential, Ni and Pt samples were held at an applied cathodic potential in sulfate solution and then withdrawn from solution under potential control [50]. For Ni, the measured Volta potential exhibited a slow decay in air associated with discharge of the oxide and a more permanent component associated with adsorbed species. This more permanent component was similar in magnitude (~150 mV) to the difference in Volta potential observed after OCP immersion in the sulfate solution relative to the value after immersion in DI water. The decay was much faster for a Pt electrode, because it does not carry an oxide layer. However, the same permanent offset was observed. These studies validate the use of SKPFM, which must be applied ex situ, for relating the potential distribution across metal alloy surfaces to their corrosion behavior, particularly for oxide-covered metals, such as are often of interest in corrosion studies. As will be shown below, the corrosion behavior of alloys can be related to the Volta potential distribution.

According to theoretical considerations, the measured potential should vary with tip-sample separation distances below 100 nm owing to the influence of image or dipole charges at the electrode surface [65]. Figure 18a shows the effect of tip-sample separation on the measured potential for pure Al directly after 30 min of immersion in DI water at OCP and one week later after storage in lab air [50]. At separation distances greater than about 100 nm, the potential is similar

for the two cases, and independent of distance. This distance dependence of the potential with a constant domain above 100 nm is in good agreement with the literature [65]. It should be mentioned that this distance between the tip and the sample is not an absolute value because, during the tapping mode scan, the tip is already at a few tens of nm from the surface. In any case, it seems that above 100 nm the measured potential is constant and can be assumed to be the Volta potential difference. However, close to the surface, the measured potential changes with tip-sample separation, and the trend is different at the two times. Adsorption phenomena might be responsible for this difference. Indeed, after one week of storage in air, the surface might dehydrate, which could change the dipole structure. The influence of the adsorbed layer on the potential/distance relationship varies considerably for different metals. Ni shows almost no distance dependence over the full range of separation distances, Fig. 18b [50]. The potential on Ni is also independent of the time in air. This suggests the nickel oxide surface is very stable, and is the reason why Ni was chosen as a reference for the Volta potential difference measurements.

The fact that the potential measured by SKPFM for distances greater than 100 nm from the surface is constant corresponds to the conceptual definition of the Volta potential difference for a metal-solution interface. However, the separation between the influence of the surface dipoles and free charges contribution on the measured potential is theoretical and does not exist as such for a real solid-liquid interface. The influence of adsorbed dipoles dominates closer to the surface, but also influences the potential measured at distances equal to or greater than 100 nm. Nonetheless, the overall nature of the potential measured by SKPFM justifies the description of it as the Volta potential difference. It should be mentioned that, although the measured potential for most materials is independent of tip-sample separation for distances above 100 nm, the lateral resolution degrades as this distance increases.



**Fig. 19.** AFM image of intermetallic particles in AA2024-T3. Both images are 80 x 80  $\mu\text{m}$ , *left*, topographical map with 100 nm z scale, *right*, Volta potential map with 1.5 V z scale [52]

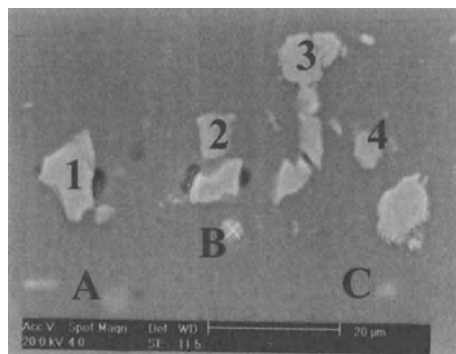


**Fig. 20.** SEM image of the same region of the same sample as shown in Fig. 3 [52]

### ***Spatial Resolution***

The advantage of the SKPFM over standard Scanning Kelvin Probes [67, 68] is the improved spatial resolution owing to the small size of the probe and the separation of the probe from the sample surface. Figure 19 shows topographic and potential maps for a region of an as-polished sample of Al 2024-T3 [52]. Considerable debris resulting from the non-aqueous polishing and rinsing of the sample is visible in the topographic image on the left. Also visible are scratches and some holes that might have resulted from corrosion or particle pull-out. Finally, there are some raised regions associated with intermetallic particles that are harder than the alloy matrix and polish slower. On the right is the Volta potential map of the same region. The intermetallic particles are clearly evident with high contrast. Figure 20 shows an SEM image of the same area [52]. The bright spots in the SEM image were found by EDS analysis to be intermetallic particles. They match up perfectly with the high potential features in the potential map of Fig. 19. The large, blocky particles are the AlCuFeMn type and the three round particles, which are barely visible in the SEM image, are S phase particles. The secondary electron intensity in the SEM image is a convolution of topographic and chemical (z-number) effects. In contrast, the topographic and potential maps produced by the SKPFM separate these effects.

The limits of the spatial resolution capability of the SKPFM have not been fully investigated. Figure 21 shows an example of a small scan taken at the edge of an AlCuFeMn particle after exposure of the sample to 0.5 M NaCl for 10 min [53]. Trenching of the matrix around the cathodic particle was observed as well as some attack within the particle. The region shown in Fig. 21 is the trench along the side of the particle, which is in the bottom left part of the figure. The trench is seen to be associated with a high potential, likely as a result of Cu enrichment. Potential and topographic features smaller than 100 nm can be seen in the images. It is likely that smaller features can be resolved by this technique if a scanner with improved resolution were used.

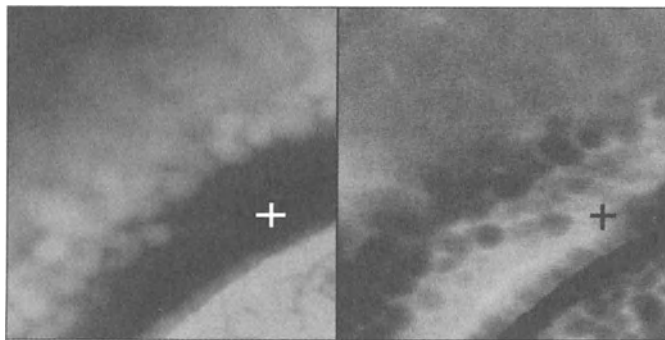


**Fig. 21.** Topographic (left, z scale 600 nm) and Volta potential (right, z scale 0.5 V) maps of a region of AA2024-T3 sample exposed to 0.5 M NaCl for 10 min. The area of both maps is 1x1  $\mu\text{m}$ . An AlCuFeMn particle is located at the bottom right of the images [53]

### Behavior of Particles in Al 2024-T3

The high Volta potential exhibited by the S phase particles in the as-polished condition relative to the matrix (Fig. 3) is opposite of what would be expected given the relatively low potential reported for grains of S phase in a bulk fabricated analog sample [49] and the correlation presented above relating Volta potential measured by the SKPFM to corrosion potential. Figure 22 shows Auger depth profiles of the matrix,  $\text{Al}_2\text{CuMg}$  and  $\text{AlCuFeMn}$  particles collected simultaneously on a sample of AA2024-T3 directly after polishing in a non-aqueous polishing slurry. The surface of the intermetallic particles was covered with Al-Mg oxide (or hydroxide); Cu was depleted on the surface of both kinds of particles relative to the concentration beneath the surface. This measurement indicates that the noble potentials observed on these types of particles after polishing using SKPFM are not caused by surface enrichment of copper as might be expected. A more complex behavior has to be considered.

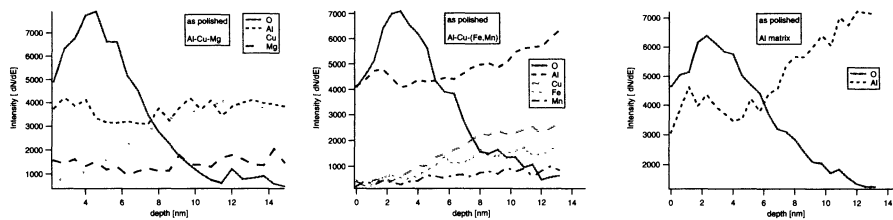


**Fig. 22.** AES depth profile of an AA2024-T3 sample after polishing in non aqueous solution: (a) S phase  $\text{Al}_2\text{CuMg}$  particle; (b)  $\text{AlCuFeMn}$  particle and (c) Al matrix

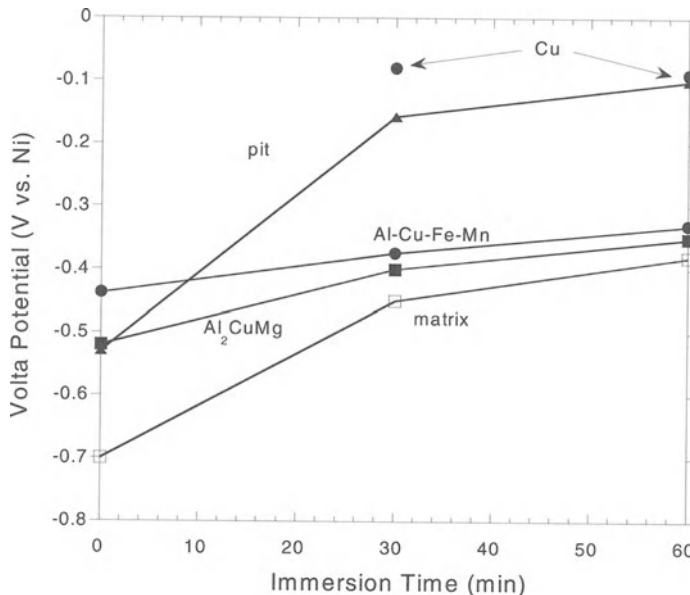


**Fig. 23.** Volta potential change of pits, uncorroded matrix and uncorroded intermetallic particles in AA2024-T3 following immersion in 0.5 M NaCl for different periods of time. Volta potential of Cu given for comparison [51]

The oxide film formed on the reactive S phase particles during non-aqueous polishing provides some protectiveness to the surface. It has been shown that S-phase particles do not dissolve immediately upon exposure to 0.1 or 0.5 M NaCl [51, 52]. The Volta potential of the different regions on the surface start out quite different, as evidenced by the contrast shown in potential map of the as polished sample. With time, these potentials merge to a single value and the contrast in the potential map decreases. This is shown in Fig. 23 for various regions of samples exposed to 0.5 M NaCl [51]. Regions that are active pits go to a high potential similar in value to pure Cu exposed to the same solution. It was shown that S-phase particles not associated with a pit in the as-polished condition are eventually attacked when their potential reaches a value similar to that of the matrix. At this point, the protectiveness of the oxide film on the particle is reduced and localized attack at the particle can commence.

### **Composition – Volta Potential Correlation**

Figure 17 shows that the Volta potential measured by SKPFM varies for different metals, and Fig. 19 shows that the Volta potential varies across the surface of a heterogeneous alloy. However, the Volta potential measured by SKPFM is not a measure of the composition of the alloy or surface oxide, and there is not necessarily a relationship between the two. For instance, a difference in Volta potential was observed for different grains of sputter-etched Mg (99.95%), even

though the composition of the surface oxide should be essentially identical from grain to grain [50]. Another example involves a sample of AA2024-T3 that was treated in  $0.5\text{ M NaCl} + 1 \times 10^{-4}\text{ M Na}_2\text{Cr}_2\text{O}_7$  [50]. The oxide formed on  $\text{Al}_2\text{CuMg}$  S-phase particles was found to contain a higher concentration of Cr than that on the matrix phase. However, despite this difference in composition, the Volta potential on the particles was found to be essentially identical to that of the matrix.

A final example also involves the S-phase particles in Al 2024-T3, which were shown to have a high potential relative to the matrix in the as-polished condition in Fig. 3. Partial removal of the oxide from an as-polished surface by sputter etching results in the reversal in contrast for some, but not all, of the S-phase particles at the surface [50, 51]. After sputter etching and subsequent exposure to air, a select number of these particles have a Volta potential lower than that of the matrix. There was difference in oxide composition of the sputtered regions, based on the Auger Electron Spectroscopic analysis of the sample surface prior to air exposure (the sputtering was performed in a Scanning Auger Microscope). Subsequent exposure of the sputter etched sample to air and then  $0.5\text{ M NaCl}$  for 30 min resulted in dissolution of some, but not all, of the particles that had exhibited a low potential after sputter etching [51]. None of the particles that exhibited an unchanged Volta potential corroded during solution exposure.

These examples, along with the observations of Al2024-T3 corrosion described above indicate that the Volta potential measured by SKPFM relates strongly to corrosion behavior, though not always to surface composition. Certain investigators in the field of corrosion have placed considerable emphasis on surface analysis and the surface composition. However, the Volta potential distribution seems to be a more important property when it comes to predicting and understanding the corrosion behavior.

### ***Small Exposed Areas***

It is possible to expose small areas of a sample by coating the sample with a thin layer of a protective polymeric film and then scratching through the film at selected regions in air [51]. In this fashion, it is possible to expose regions containing only certain microstructural features or ratios of such features that are different than that given by the alloy microstructure.

A window exposing an area containing only a portion of an  $\text{AlCuFeMn}$  particle exhibited no corrosion upon 2 h exposure to  $0.5\text{ M NaCl}$ . When such a particle was exposed with some surrounding matrix (but no large S-phase particles), considerable attack was found, and the extent of the attack increased as the fraction of the exposed area taken up by the  $\text{AlCuFeMn}$  particle increased, Fig. 24 [51]. This is what might be expected by simple galvanic corrosion considerations.  $\text{AlCuFeMn}$  inclusions are efficient cathodic regions and can drive corrosion reactions, not only at active S-phase particles but also in the matrix.

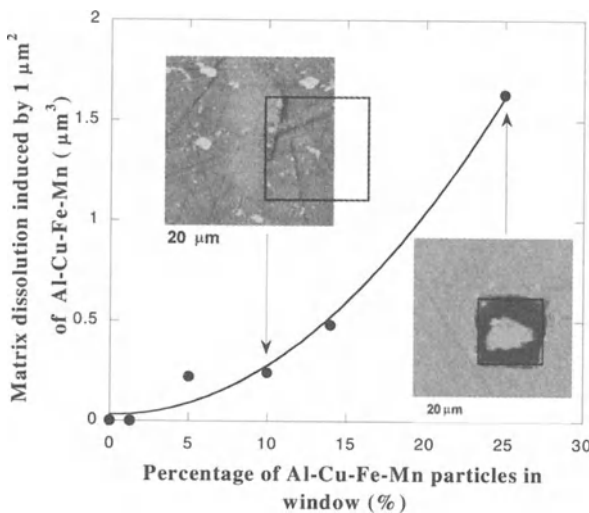


**Fig. 24.** Effect of area fraction of Al-Cu-Fe-Mn in exposed window on matrix dissolution after 60 min exposure to 0.5 M NaCl [51]

Interestingly, when an area containing typical S phase particles and matrix (no AlCuFeMn particles) was exposed to 0.5 M NaCl, no attack was seen after 120 min. This is the same as was observed when a region was exposed containing only a part of an AlCuFeMn and no matrix. Clearly, localized corrosion only initiates in this system if there is simultaneous exposure of both active cathodes (AlCuFeMn particles) and anodic sites (S-phase particle or matrix). The absence of either anode or cathode prevents local attack. It should be noted that some S-phase particles were attacked when exposed to solution in a window that did not contain an AlCuFeMn particle. These reactive S-phase particles were typically larger than average, and exhibited a lower Volta potential in the as-polished condition.

### AFM Scratching

In situ AFM scratching has been used to probe a number of different aspects of the protectiveness of the oxide film formed on Al and on different particles in the microstructure of Al alloys [51, 53, 54]. A wide range of behavior was observed depending on the sample and the environment. Scratching of 99.99% Al or Al 1100 with a Si tip in the Nanoscope III environmental cell resulted in the formation of a smooth bottomed trench, Fig. 25 [53, 54]. The depth of the trench depended on the AFM photodiode setpoint voltage, which is a measure of the scratching force. It is interesting that scratching of pure Al in 0.5 M concentrated NaCl resulted in uniform dissolution at a high rate and not in the formation of pits, even though Al might not be expected to repassivate spontaneously in this solution.

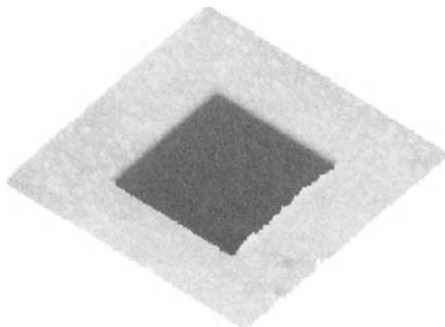


**Fig. 25.** In situ topographic map of a 15  $\mu\text{m}$  square hole in Al 99.99% obtained by contact mode scratching of the AFM tip in 0.5 M NaCl. Trench depth 75 nm, area of image 30 $\times$ 30  $\mu\text{m}$  [53]

An explanation for this behavior can be given based on the concept that a critical current density is necessary to sustain pitting and prevent repassivation [64]. The rate of dissolution in a pit is on the order of  $\text{A}/\text{cm}^2$  over the first fractions of a second following breakdown. At open circuit, the high dissolution rate must be accompanied by an equally high rate of cathodic reaction, which in aerated 0.5 M NaCl is primarily oxygen reduction. Since the volume of electrolyte in the AFM cell was rather small (about 0.1 ml) and the cell was sealed, the supply of oxygen was finite and it quickly dropped to a level insufficient to maintain the required rate of anodic reaction. The result of continual film breakdown, accelerated dissolution and repassivation was the formation of a uniform trough. This is essentially erosion corrosion. This interpretation is supported by an experiment in which the 0.5 M NaCl solution was continually pumped through the AFM cell during scratching. Instead of accelerated uniform corrosion resulting in the formation of a flat-bottomed trough, scratching with solution flow at open circuit tended to result in sustained pitting [54].

AFM scratching of AA2024-T3 in a more dilute chloride solution, 0.01 M NaCl, resulted in immediate dissolution of the S-phase particles [53], even in a stagnant cell without pumping of the solution. The AlCuMnFe particles are apparently sufficiently catalytic to support enough cathodic reaction to sustain the localized attack even with a limited supply of oxygen.

### **Conclusions**

Scanning Kelvin Probe Force Microscopy and in situ AFM scratching were shown to be useful techniques for the study of localized corrosion:

SKPFM provides a potential map, which can be considered to be a map of the Volta potential difference, and represents the practical nobility of the surface. The Volta potential measured by SKPFM on pure samples in air following immersion in solution varies approximately linearly with the corrosion potential measured in that solution. It is sensitive to the excess charge and adsorbed dipoles.

SKPFM provides clear visualization of the intermetallic particles in high strength Al alloys. The potential on the various particles and matrix changes with exposure and is related to the corrosion processes.

The use of small exposure areas created by scratching through a thin protective polymeric film allowed the investigation of individual components of the microstructure in AA2024-T3. Both an active anode and cathode are required for localized corrosion, and the extent of attack depended on the area ratios of the anodes and cathodes.

In situ AFM scratching provides information on the stability of the passive film and the ability of the system to stabilize localized attack.

### Acknowledgements

The results presented in paragraph 12.3.1 were supported by grants from the National Science Foundation under Grant CMS-9905394 and by DARPA NDE-MURI under grant F49620-96-1-0442. Additional funding and support was given by the Center for Materials Diagnostics at the University of Dayton Research Institute and by the University of Dayton through the Department of Materials Engineering. The authors would like to thank Dr. Daniel Eylon, Dr. Norbert Meyendorf, Dr. Mark Ruddell, Dr. Liming Shen, Dr. A. Brar and the personnel who provided materials, insight and help.

This work presented in paragraph 12.3.2 was supported by the United States Air Force Office of Scientific Research under contract No F49620-96-1-0479. The authors gratefully acknowledge the contributions of Dr. Patrick Schmutz, who was intimately involved with much of the work during his tenure at OSU.

## References

1. Park Scientific Instruments (1997) A Practical Guide to Scanning Probe Microscopy
2. Digital Instruments (1996) Dimension™ 3000 Scanning Probe Microscope Instruction Manual
3. Bhushan et al. (1995) Handbook of Micro/ Nano Tribology: CRC Series Mechanics and Material Science, CRC Press, New York
4. Binning G C.F. Quate CF, Gerber Ch (1986) *Phys Rev Lett* 56:930
5. Sarid D (1991) Scanning Force Microscopy. Oxford University Press, New York
6. Wiesendanger R (1994) Scanning Probe Microscopy and Spectroscopy. Cambridge Press, Cambridge
7. Burnham NA, Colton RJ, Pollock HM (1993) *Nanotechnology* 4:64
8. Burnham NA, Kulik AJ (1997) Surface Forces and Adhesion. In: Bushan B (ed) Handbook of Micro/Nanotribology, CRC Press, Boca Raton
9. Meyer G, Amer NM (1990) Simultaneous of lateral and normal forces with an optical-beam-deflection atomic force microscope. *Appl Phys Lett* 57 (20):2089–2091
10. Cohen S, Bray M, Lightbody M (eds) (1994) Atomic Force Microscopy / Scanning Tunneling Microscopy. Plenum Press, New York, pp. 217–299
11. Maivald P, Butt HJ, Gould SAC, Prater CB, Drake B, Gurley JA, Elings VB, Hansma PK (1991) *Nanotechnology* 2:103
12. Kolosov O, Yamanaka K (1993) *Jpn J Appl Phys* 32:L1095
13. Rabe U, Arnold W (1994) *Appl Phys Lett* 64:1493
14. Kulik A, Wuthrich C, Gremaud G (1995) Acoustical Imaging vol. 21, pp. 581
15. Oulevey F, Gremaud G, Semoroz A, Kulik AJ, Burnham NA, Dupas E, Gourdon D (1998) *Rev Sci Instru* 69:2085
16. Radmacher M, Tillman R, Gaub HE (1993) *Biophysical Society* 65:735
17. Zhong Q, Inniss D, Kjoller K, Ellings VB (1996) *Surf Sci* 290:L688
18. Hansma PK (1994) *Appl Phys Lett* 64:2454
19. Magonov SN, Elings V, Whangbo MH (1997) *Surf Sci Lett* 375:L385
20. Magonov SN, Reneker D (1997) *Ann Revs Mater Sci* 27:175
21. Rosa A, Weiland E, Hild S, Marti O (1997) *Meas. Sci Technol* 8:1333
22. Miyatani T, Okamoto S, Rosa A, Marti O, Fujihara M (1997) *Appl Phys Lett* 71:2632
23. Krotil HU, Stifter T, Waschipky H, Weishaupt K, Hil S, Marti O (1999) *Surf Interface Anal* 27:336
24. Okabe Y, Furugori M, Tani Y, Akiba U, Fujihara M (2000) *Ultramicroscopy* 82:203
25. Burnham NA, Gremaud G, Kulik AJ, Gallo PJ, Oulevey F (1996) *J Vac Sci Technol B14:794*
26. Hoummady M, Farnault E (1998) Enhanced sensitivity to force gradients by using higher flexural modes of the atomic force microscope cantilever. *Appl Phys A66:361–64*
27. Volodin A, Van Haesendonck C (1998) Low temperature force microscopy based on piezoresistive cantilevers operating at a higher flexural mode. *Appl Phys A66:305–308*
28. Burnham N, Kulik AJ, Oulevey F, Mayencourt C, Gourdon D, Dupas E, Gremaud G (1997) A Beginner's Guide to LPM Materials Properties Measurements. In: B. Bhushan, Kluwer (eds) Micro/Nanotribology and its Applications. Academic Publishers, pp. 421–438

29. Burnham NA, Gremaud G, Kulik AJ, Gallo PJ, Oulevey F (1996) Scanning local-acceleration microscopy. *J Vac Sci Technol B* 14 (2):1308–1312
30. Takagi T (1986) Ionized Cluster Beam Deposition and Epitaxy. Noyan Publishers, NY
31. Sathish S, Fossheim K, Bye T (1988) Imaging of Grain-Structure of Copper by Scanning Acoustic Microscopy. *J Mater Sci Lett* 7:735
32. Schumaker E (2000) Ultrasonic Force Microscopy for Materials Characterization. Masters Thesis, University of Dayton
33. Schumaker E, Shen L, Ruddell MJ, Sathish S, Murray PT (2000) Ultrasonic force microscopic characterization of nanosized copper particles. Nanophase and Nanocomposite Materials III. Symposium Materials Research Society Proceedings vol. 581, pp. 473–477
34. Truell R, Elbaum C, Chick B (1969) Ultrasonic Methods in Solid State Physics. Academic Press, New York, Appendix D, pp. 370
35. Yamanaka K, Noguchi A, Tsuji T, Koike T, Goto T (1999) Surf Interface Anal 27:600
36. Rabe U, Turner K, Arnold W (1988) *Appl Phys* A66:277
37. Turner JA, Hirsekorn S, Rabe U, Arnold W (1997) *J. Appl. Phys.*, 82, 966
38. Druffner CJ, Sathish S (2002) Improving Atomic Force Microscopy Images with the Adaptation of Ultrasonic Force Microscopy. SPIE's 7<sup>th</sup> Annual International Symposium on Nondestructive Evaluation and Reliability of Micro- and Nanomaterial Systems, San Diego, SPIE Proceedings, vol. 4703, pp. 105–113
39. To be published by C. Druffner, et al, Atomic Force and Ultrasonic Force Microscopic Investigation of Laser Treated Ceramic Head Sliders. accepted 11/2002 by Journal of the American Ceramic Society
40. Druffner CJ, Masters Thesis (2002) A Material Characterization Technique For Detection Of Microcracks And Grain Structures In Miniaturized Microelectric Devices. University of Dayton
41. Tam AC (2001) Laser processes for precise microfabrication of magnetic disk drive components. *Riken Review*, vol. 32, pp. 71–76
42. Chen G, Xu X, Poon C, Tam A (1998) Laser Assisted microscale deformation of stainless steel and ceramics. *Optical Engineering*, vol. 37, No. 10, pp. 2837–2842
43. Gatzén H (2000) Rigid disk slider micromachining challenges to meet microtribology needs. *Tribology International*, vol. 33, pp. 337–342
44. Singer P (2000) Copper CMP: A question of tradeoffs. *Semiconductor International*, vol. 23 No. 5, pp. 73–84
45. Druffner C, et al. to be published
46. Szklarska-Smialowska Z (1986) Pitting Corrosion of Metals, NACE, Houston
47. Buchheit RG, Grant RP, Hlava PF, McKenzie B, Zender GL (1997) *J. Electrochem. Soc.*, 144, 2621
48. Guillaumin V, Mankowski G (1999) *Corr Sci* 41:421–438
49. Buchheit RG (1995) *J Electrochem Soc* 142, 3994
50. Guillaumin V, Schmutz P, Frankel GS (2001) *J. Electrochem Soc* 148:B163
51. Leblanc P, Frankel GS (2001) *J Electrochem Soc*, accepted for publication
52. Schmutz P, Frankel GS (1998) *J Electrochem Soc* 145:2285–2294
53. Schmutz P, Frankel GS (1998) *J Electrochem Soc* 145:2298–2306
54. Schmutz P, Frankel GS (1999) *J Electrochem Soc* 146:4461
55. Burstein GT, Davies DH (1980) *Corr Sci* 20
56. Burstein GT, Newman RC (1980) *Electrochim Acta* 25:1009
57. Burstein GT, Marshall PI (1983) *Corr Sci* 23:125

58. Itagaki M, Oltra R, Vuillemin B, Keddam M, Takenouti H (1997) J Electrochem Soc 144:64
59. Oltra R, Indrianjafy GM (1992) J Electrochem Soc 139: 78
60. Oltra R, Indrianjafy GM, Keddam M, Takenouti H (1993) Corr Sci 35:827–832
61. Burstein GT, Davenport AJ (1989) J Electrochem Soc 136:936
62. Burstein GT, Cinderey RJ (1991) Corr Sci 32:1195–1211
63. Frankel GS, Rush BM, Jahnes CV, Farrell CE, Davenport AJ, Isaacs HS (1991) J Electrochem Soc 138: 643
64. Frankel GS, Scully JR, Jahnes CV (1996) J Electrochem Soc 143:1834
65. Bockris JOM, Reddy AKN (1970) Modern Electrochemistry. Plenum Press, New York
66. Yee S, Stratmann M, Oriani RA (1991) J Electrochem Soc 138:55
67. Stratmann M, Streckel H (1990) Corros Sci 30:681
68. Devecchio D, Schmutz P, Frankel GS, (2000) Electrochem. Solid-State Lett 3:90

# 13 High Resolution Microellipsometry

Q. Zhan

## 13.1 Introduction

Optical inspection and metrology are widely used in materials diagnostics and characterization. From the simple qualitative information obtained from imaging and phase contrast optics to the highly precise measurements provided by interferometry, polarimetry, and ellipsometry, optical techniques have been instrumental in advancing the state-of-the-art in materials science, microelectronics, biology, and many other disciplines [1]. The non-destructive nature of most optical measurements and their inherent simplicity have made them valuable to modern research and fabrication.

Thin film structures are commonly involved in the materials systems for optics, semiconductor, and data storage industries and biological sciences. New concepts for surface treatments, corrosion protection, improvement of mechanical surface properties and smart materials with integrated sensor and actuator functions for aircraft are based on thin film technologies. The accurate characterization of the topography and properties of surfaces and thin films plays a critical role in development and modern fabrication of these materials and structures. Due to the tremendous advances in nanolithography and micro-fabrication, the ever-decreasing feature sizes in industrial fabrication severely stretches the capabilities of optical characterization techniques and put a strong requirement on characterizing patterned structures.

In this chapter, microellipsometry techniques that can perform high spatial resolution materials characterization are presented. Applications of these techniques to characterize patterned surface structures, unresolved surface features, residual axial birefringence and micro-optical components will also be discussed.

## 13.2 Background

Ellipsometry is one of the most powerful optical metrological techniques of measuring thin films properties. It allows simultaneous determination of film thickness and index of refraction in an accurate and non-destructive manner [2–4]. Optical ellipsometry can be generally defined as the measurement of the state of polarization of the light wave. This technique is based on exploiting the polarization modification that occurs as polarized light is transmitted through or reflected from the interfaces of thin films. By measuring this modification, one

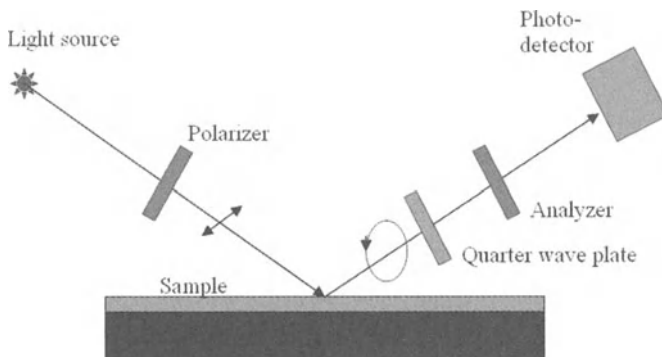


**Fig. 1.** Conceptual diagram of nulling ellipsometer

can extract the information about the coating, such as the thickness of the film, the refraction index of the material, the roughness of the interface, etc. As illustrated in Fig. 1, nulling ellipsometry involves illuminating the surface of a sample with monochromatic light with a known and controllable state of polarization at a fairly large angle. The polarization of the reflected light is then analyzed through adjusting a quarter-wave plate and an analyzer to achieve a null signal on the detector. From the angular positions of the quarter-wave plate and analyzer at the null condition, one can calculate the fundamental quantities of ellipsometry ( $\Psi$ ,  $\Delta$ ) pair given by

$$\frac{r_p}{r_s} = \tan \Psi \cdot e^{j\Delta}, \quad (1)$$

where the  $r_p$  and  $r_s$  are the complex reflection coefficients for TM (polarization in the incident plane) and TE (polarization perpendicular to the incident plane) polarized light. From the ( $\Psi$ ,  $\Delta$ ) pair, information about the sample can be deduced with proper optical modeling and numerical regression.

Owing to its astonishing accuracy and sensitivity, ellipsometry has been widely used in many thin films related disciplines, including materials characterization and diagnostics, semiconductor industry, photonics industry, and biological science. However, the spatial resolution of a standard ellipsometer, limited by the spot size, is usually on the order of hundreds of micrometers. Thus the application of conventional ellipsometry is severely hampered by its poor spatial resolution if the sample contains fine features. Spatially resolved ellipsometry is very desirable for characterization and diagnostics of patterned thin films and surfaces.

Objective lenses can be used to improve the spatial resolution of the ellipsometer. One method is to modify the standard ellipsometer setup by inserting an objective lens in the incident arm [5–8]. However, the slant angle between the objective and the sample limits the highest available numerical aperture (NA, measurement of the focusing power of an objective lens) before the lens collides with the sample. This approach only provides moderate improvement of spatial resolution. Another technique uses normal incidence and large NA objective lens

to provide high spatial resolution [9–11]. In this approach, the incident light is focused to a diffraction-limited spot and reflected by the sample surface. The alteration of the state of light polarization at the sample is then analyzed at the back focal plane of the objective lens. Since the field at the back focal plane and the field at the sample plane are related through a Fourier transform in this technique, each angle of incidence is mapped to a specific position in the back focal plane. Through analyzing the state of polarization at the back focal plane, one can infer the properties of the sample within the focus. This technique often suffers from a low signal-to-noise ratio (SNR) due to the small detector pixel size required for good ellipsometric performance.

In the following, two new microellipsometric techniques that use high NA objective lens and normal incidence are presented. The high NA lens contains more oblique rays to increase the ellipsometric signal. At the same time, the high numerical aperture serves to increase the spatial resolution in these techniques. An imaging microellipsometer is introduced at first. This imaging microellipsometer can characterize the sample with high resolution and form an image of the sample in a parallel fashion. Compared to existing techniques, this microellipsometer can perform accurate measurements with higher speed and higher resolution with a very simple setup, thereby making the ellipsometer a very powerful tool for industrial and scientific research. In another microellipsometer design, a rotational symmetry concept is applied to enhance to SNR of the microellipsometry. This rotationally symmetric scanning microellipsometer can provide high spatial resolution characterization capability with high SNR and the best ellipsometric performance.

## 13.3 Instrumentation

### 13.3.1 Imaging Microellipsometer

The imaging microellipsometer is schematically illustrated in Fig. 2. A high numerical aperture objective is used in the setup. The transmission axes of the polarizer and the analyzer are aligned with the x-axis and y-axis, respectively. The sample is placed at the focal plane of the objective lens. A fiber bundle with a narrow band filter is used as the illumination source to form an image on the CCD. The condenser collimates the light from each point from the source. Since individual points from the source in the field-of-view of the condenser subtend very small angles with respect to the optical axis, we can analyze each image point in the same way as the on-axis point. A geometric optics model is developed in [12] to give an intuitive description of the setup.

The experimental setup of our imaging ellipsometer is shown in Fig. 3. This setup uses a fiber bundle illuminator (Dolan-Jenner Fiber-Lite MI-150) as an

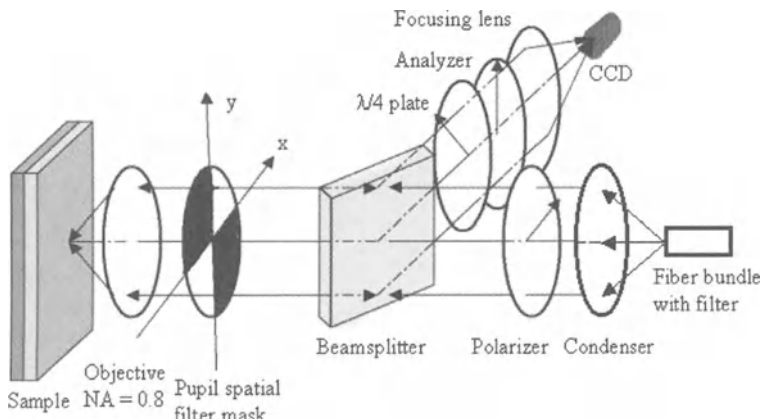


**Fig. 2.** Schematic illustration of the imaging microellipsometer

extended source to form an image of the object and permit analysis of each sample point in parallel. A diffuser is placed against the fiber bundle to homogenize the light. A Corion 10 nm interference bandpass filter with central wavelength at 633 nm is placed after the diffuser. Lens1 and lens 2 are used to collimate the light from each point of the source and project the quadrant spatial filter to the pupil plane of the objective. A Nikon CF Plan EPI objective ( $50\times/\text{NA}=0.8$ ) with 4 mm focal length is used to focus the linearly polarized incident light onto the sample. After reflection from the sample, the light is collected by the objective and steered to the analyzer arm by the beamsplitter. In general, the reflectivity of the beamsplitter for s and p polarized light is different. This difference introduces an extra ellipsometric rotation to the signal, thus it has to be included in the model in order to generate an accurate lookup table. For the beamsplitter we used,  $r_p/r_s = 0.6378 - 0.1125 j$  is determined experimentally and included in our optical model. A zero-order polymer  $\lambda/4$  plate with  $\pm 9^\circ$  angular acceptance is used in the analyzer arm. An analyzer is placed after the  $\lambda/4$  plate and aligned at a crossed position with respect to the polarizer. Lens 3 is a 40-cm-focal-length doublet that images the object onto the CCD camera. The magnification of the imaging system is 100. A PULNIX TM-7CN CCD camera is used to capture the image. The pixel size of the camera is 9.8  $\mu\text{m}$ . This pixel size corresponds to about 0.1  $\mu\text{m}$  on the object plane. The resolution of the system is  $1.22\lambda/2\text{NA} \approx 0.48 \mu\text{m}$ ; thus each resolution spot is over-sampled by a factor of five. A 10-bit A/D converter (Spiricon) is used as an interface between the camera and computer. The image size is  $512 \times 480$ , which approximately corresponds to an area of 51.2  $\mu\text{m}$  by 48  $\mu\text{m}$  on the sample. To lower the temporal noise, 64 frames are averaged. Two images for the two orthogonal orientations of the  $\lambda/4$  plate are captured for processing. A ratio of the two images is then calculated to normalize the non-uniformity of the source. Finally, the ratio signal from each point is converted into

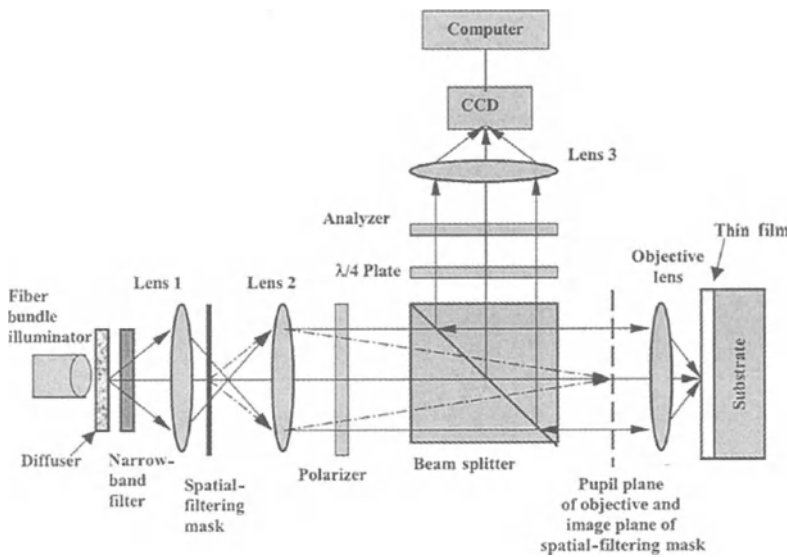


**Fig. 3.** Experimental setup of the imaging microellipsometer

thickness by utilizing a theoretical curve generated according to the optical models described above.

### 13.3.2 Rotationally Symmetric Scanning Microellipsometer

In the imaging microellipsometer technique described above, integration over a cone of angles of incidence is used to achieve high signal level at the cost of compromised ellipsometric sensitivity. The illumination non-uniformity at the pupil also affects the accuracy of the system. These drawbacks can be overcome by a microellipsometer using a rotational symmetry concept. The idea is illustrated in Fig. 4. A standard ellipsometer is illustrated in Fig. 4a. In Fig. 4b, an incident beam is normal to the sample initially. A high NA objective lens is then inserted in the optical path to focus the beam to a tight spot on the sample. Each ray path in Fig. 4b acts just like a standard ellipsometer. If we use the rotating analyzer technique to detect this channel, we will observe a sinusoidal signal on the detector and obtain the ellipsometric information carried by this ray [2]. Considering one ray as a standard rotating analyzer ellipsometric “channel”, we can repeat this channel in a rotationally symmetric manner such that the microellipsometer acts like a multi-channel conventional ellipsometer (Fig. 4c). Every individual channel located at a different angular location inside a common annular region will be designed to give the identical sinusoidal signal on the detector. The high numerical aperture illumination allows a high spatial resolution

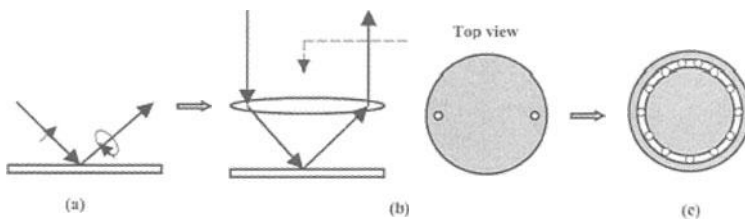


**Fig. 4.** Design principle. (a) Standard ellipsometer; (b) Insertion of lens. A single ray path represents a conventional rotating analyzer ellipsometer “channel”; (c) A microellipsometer by continuously repeating the single “channel” of (b) in a rotationally symmetric manner

and an ellipsometric measurement of the sample. Due to the symmetry, each channel contributes to the signal collaboratively and a single large-area detector can be used to capture the total power from all the channels for subsequent analysis. Consequently, the SNR of the system is improved.

To carry out this idea, the rotational symmetry has to be maintained throughout the optical system. Several tricks are played in the design of such a rotationally symmetric microellipsometer. As shown in a conceptual setup illustrated in Fig. 5, a collimated laser beam goes through a polarizer, a quarter-wave plate and beam-splitter 1. The polarizer and quarter-wave plate are adjusted such that the beam illuminating the objective pupil is circularly polarized. Due to this circular state of polarization, the illumination for each channel is equivalent except for a geometric projection phase difference (Berry’s phase) [13, 14]. Since we will detect the power on the detector, this phase has no significance in this microellipsometer design. The high NA objective lens focuses the circularly polarized beam down to a small spot on the sample and collects the reflected light. The state of polarization of each channel is modified by the Fresnel reflection at the sample interface and becomes elliptically polarized. Up to this point, the rotational symmetry has been maintained. Two identical beamsplitters are used to steer the reflected light to the analyzer arm. The two beamsplitters are aligned such that the s-polarization for the first beamsplitter becomes the p-polarization for the second beamsplitter and vice versa. In this way, the state of polarization and the rotational symmetry of the reflected beam are maintained. If only one beamsplitter is used, the difference of the reflectivity for the s and p polarizations will introduce distortion to the state of polarization and consequently destroy the symmetry.

In the analyzer arm, a variable circular retarder consisting of two half-wave plates is used to introduce a spatially invariant polarization rotation [14, 15] (Fig. 5). It can be shown that the Jones matrix for this device is

$$T = \begin{pmatrix} \cos(2\Delta\phi) & -\sin(2\Delta\phi) \\ \sin(2\Delta\phi) & \cos(2\Delta\phi) \end{pmatrix} = R(-2\Delta\phi), \quad (2)$$

where  $\Delta\phi$  is the angle between the fast axes of the two half-wave plates. This is a rotation operator with the amount of rotation independent of the initial state of polarization. Thus, the rotational symmetry of the polarization is still maintained.

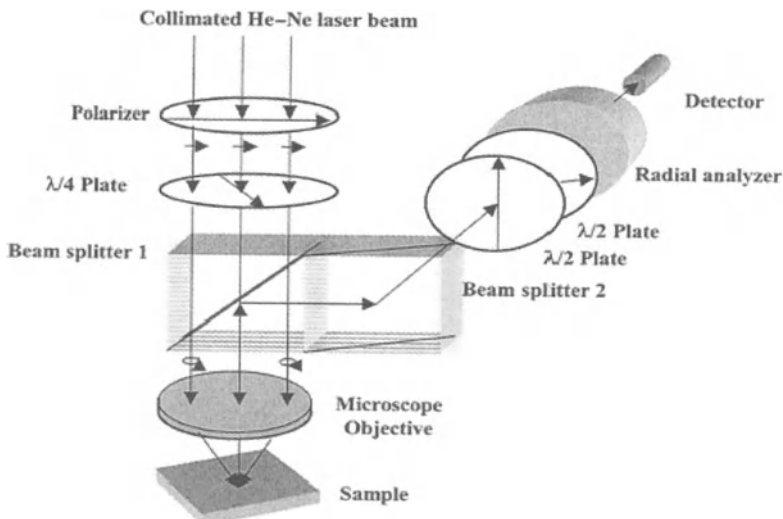


**Fig. 5.** Diagram of a rotationally symmetric microellipsometer design

The beam then passes through a radial analyzer with its transmission axis pointing in the radial direction.

The experimental setup is illustrated in Fig. 6. In the signal path, a high NA lens ( $NA=0.8$ ) focuses the circularly polarized incident light onto the sample and collects the reflected light. The reflected light passes through the coupled beamsplitter pair, variable circular retarder, radial analyzer and is brought to focus on the photodiode PD1. A motor is used to drive the first half-wave plate at a constant speed in the variable circular retarder. The radial analyzer module consists of two lenses and a c-cut calcite cube. A pre-amp is used to amplify the signal. Besides the signal path, another laser was used to generate the reference signal for synchronous detection. This He-Ne laser beam passes through a polarizer, the circularly variable retarder, another polarizer and is brought to focus on the photodiode PD2. An identical pre-amp is used to amplify the reference signal. In order to detect the modulation in the signal, a multiplier is used to mix the signal and the reference such that the dc term is raised to the first harmonic and the ac term is raised to the second harmonic [14]. The output of the multiplier is connected to the signal input of a lock-in amplifier (EG&G 7265 DSP) running at dual-harmonics mode. The reference signal is also connected to the reference input of the lock-in amplifier. The lock-in returns both the phase and amplitude of the first and the second harmonics simultaneously. With the above measured results, one can calculate the  $(\epsilon, \theta_0)$  pair that describe the state of polarization of the reflected light and further derive the refractive index and thickness of the thin film through regression models used in standard ellipsometry.

The sample is mounted on a translation stage with electro-strictive actuators. Ellipsometric images of the sample can be obtained through scanning. To facilitate

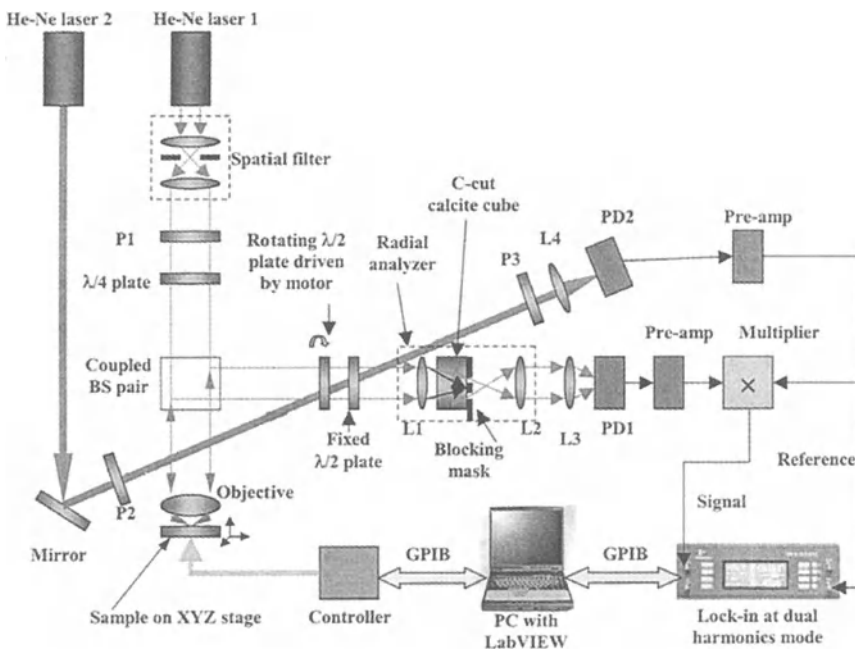


**Fig. 6.** Experimental setup for the rotationally symmetric microellipsometer

the data acquisition, the experimental setup is fully automated. A LabVIEW program in a laptop computer is used to control the scanning, collect and process measurement data, and display the captured ellipsometric images.

## 13.4 Applications

### 13.4.1 Measurement of Resolved Features

#### **Surface Topology Measurement**

The imaging microellipsometer is applied to measure a 50 nm-deep PMMA (polymethyl methacrylate) grating fabricated on top of a 100 nm  $\text{SiO}_2$  thin film with a silicon wafer as a substrate (Fig. 7). Ellipsometric images were generated at two different  $\lambda/4$  plate angles ( $+\pi/4$  and  $-\pi/4$ ), and the ratio signal was displayed. The results (see Fig. 8) clearly show the existence of distinct polarization effects for different regions. Figure 8a shows the two-dimensional

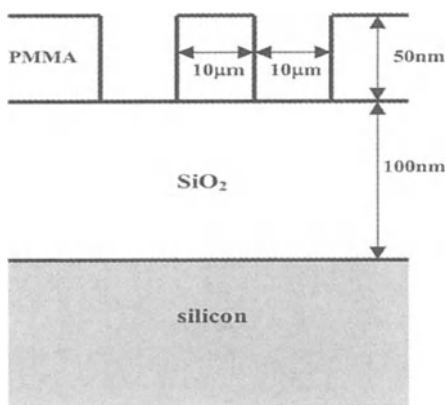


**Fig. 7.** Illustration of the PMMA grating sample

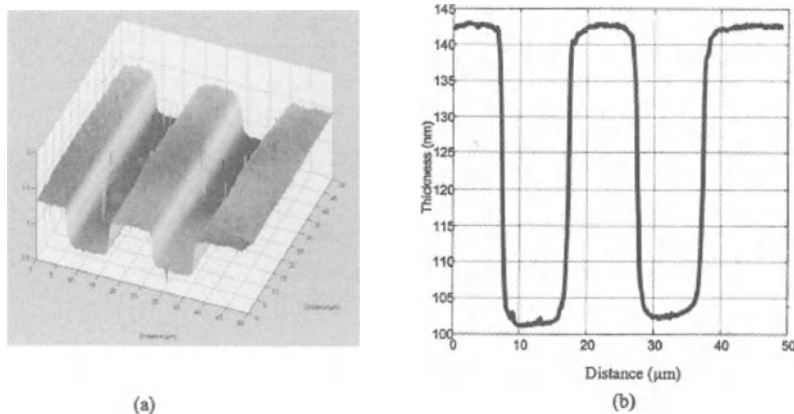


**Fig. 8.** Experimental results of the PMMA grating measurement; (a) Ellipsometric ratio image; (b) Line scan of (a) after converted into thickness

imaging ellipsometric result of the PMMA grating. A cross section of the image is shown in Fig. 8b. The mesa corresponds to a structure of PMMA(50 nm)/ $\text{SiO}_2$ (100 nm)/silicon and the trench corresponds to a structure of  $\text{SiO}_2$ (100 nm)/silicon. From the ellipsometric signal, the thickness of each region was found by looking up the measured ratio signal in a theoretical lookup table generated by the Richards-Wolf model. From the signal, the sensitivity can be determined to be approximately 5 Å. The measured thickness is within  $+/-5\%$  of the actual thickness. Several factors could contribute errors to the absolute measurement. One possible error source is the assumed index of refraction. The imaging ellipsometer should be able to measure the thickness and refractive index using the two independent intensity measurements obtained at orthogonal  $\lambda/4$  plate angles.

However, we have chosen to use the ratio of these two intensities as the analysis parameter to eliminate the effect of source non-uniformities and sample reflectance variations. From this ratio signal, only one parameter can be measured given the knowledge of the other parameter. Thus, in order to model the structure more accurately, the exact refractive index of each layer needs to be known. Other possible factors that could cause the deviation of experimental data are the residual birefringence of the lens and inaccuracies in modeling the beamsplitter. The non-uniformity of illumination at the pupil gives another possible source of error. However, a calibration procedure can be utilized to compensate the last three factors and thus improve the measurement accuracy.

### **Refractive Index Variation Measurement**

A sample with index of refraction variation has also been measured with the imaging microellipsometer. We prepared the sample by depositing 6  $\mu\text{m}$  of  $\text{SiO}_2$  on a silicon substrate. Then we polished this sample from the side and deposited 0.115  $\mu\text{m}$  of  $\text{Si}_3\text{N}_4$  on the polished side. The refractive index and thickness of the  $\text{Si}_3\text{N}_4$  layer were determined with a conventional ellipsometer by measuring a reference silicon substrate placed beside the sample during the deposition. The cross section of this sample is illustrated in Fig. 9. The ellipsometric image and its cross section obtained by our imaging ellipsometer are shown in Fig. 10. The polarization contrast obtained in this case comes from the index of refraction variations beneath the  $\text{Si}_3\text{N}_4$  layer. From the result, it is clear that the response for different refractive index regions is distinct. However, we were not able to accurately determine the index of refraction from the ratio signal. This is due to the fact that measured properties of the  $\text{Si}_3\text{N}_4$  on the reference silicon wafer do not represent the true properties of the  $\text{Si}_3\text{N}_4$  on the sample. To estimate the accuracy of the index of refraction measurement, we measured the index of refraction of the  $\text{Si}_3\text{N}_4$  on the reference sample using the imaging ellipsometer. Given the thickness, the index of refraction was determined to be 1.992, compared to 1.932 measured by conventional ellipsometer. The imperfection of polish and the low reflectivity in this experiment are the major sources of noise. From Fig. 10b, the noise level

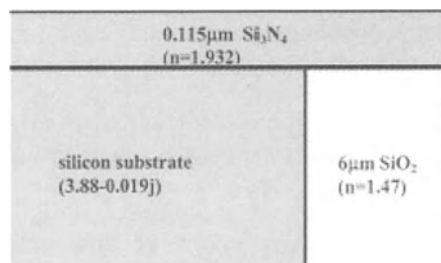


**Fig. 9.** Cross section of the sample for refractive index measurement

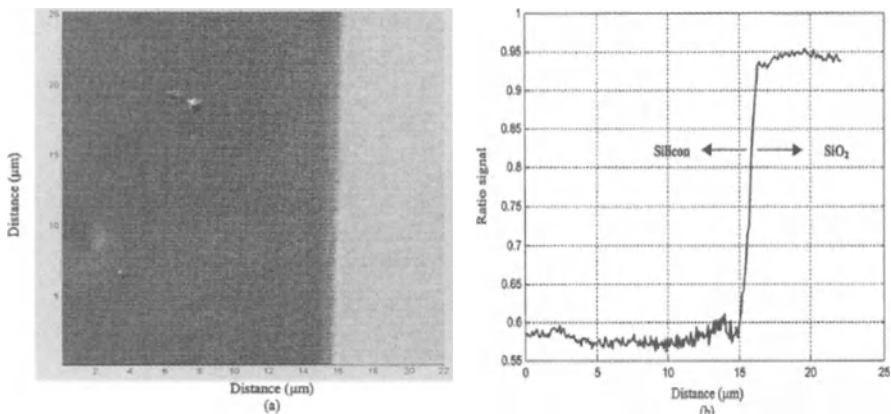


**Fig. 10.** Experimental results of index measurement; (a) Ellipsometric ratio image; (b) Line scan of (a)

of the ratio signal is determined to be  $+/-0.005$ . Based on this noise level, the sensitivity to the index of refraction is estimated to be  $+/-0.03$ . With a brighter source and better polish, a sensitivity much better than  $+/-0.01$  is expected.

### 13.4.2 Measurement of Surface Features beyond Diffraction Limit

Optical characterization techniques have long been indispensable tools for advanced micro-fabrication. However, the ever-decreasing minimum feature size has pushed many optical techniques to the limit of their capabilities. Owing to the diffraction phenomena, optical techniques have difficulties resolving features with sub-wavelength lateral dimensions. Near-field techniques, such as near-field scanning optical microscopy (NSOM) and photon tunneling microscopy (PTM), have been investigated to improve the resolution of optical systems. However, it is also possible to characterize sub-wavelength features using far-field techniques without actually resolving them. Provided with certain a priori information, which is often available in modern micro-fabrication, characterization of sub-wavelength structures can be performed through parametric model fitting. For example, scatterometry has been used to characterize periodic sub-wavelength structures by studying the far-field scattering signature [16]. It is well known that sub-wavelength structures can modify the polarization of incident light. In optical metrology applications, this effect can be used as a sensitive measure of the sub-wavelength structures, which has been demonstrated in periodic structure characterization [16] and isolated trench measurement [17]. Using the imaging microellipsometer, we extend the application of this polarization effects to characterize isolated sub-wavelength structures in a parallel fashion [18, 19].

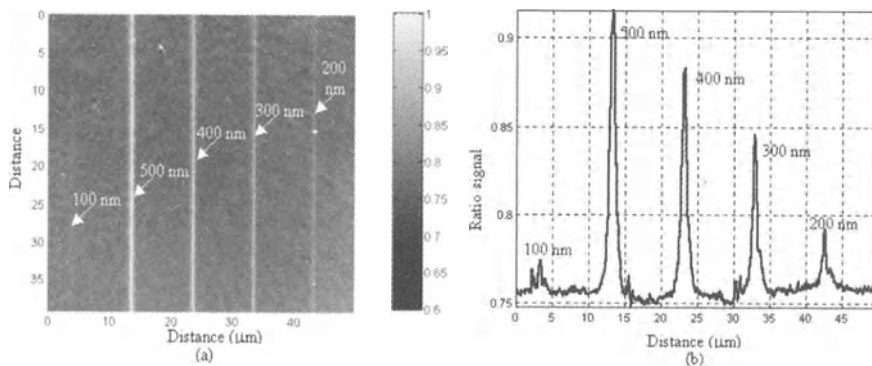


**Fig. 11.** Imaging ellipsometric measurement of sub-micron PMMA lines; (a) Ratio signal image; (b) Line scan of (a)

To demonstrate the polarization effects from sub-wavelength structures and their application to characterize unresolved features, we measured the imaging ellipsometric signals of a sample containing sub-micron lines. The sample is prepared with e-beam lithography. A 105 nm SiO<sub>2</sub> layer was deposited on a silicon wafer followed by a 50 nm layer of PMMA. The PMMA was removed by e-beam lithography to form lines with 100, 200, 300, 400 and 500 nm width. Figure 11a shows the experimental measurement of the ratio image along with a line scan of the ellipsometric image shown in Fig. 11b. The experimental result clearly shows the polarization effect from sub-wavelength features. Different linewidths give different polarization ratio signals. This polarization ratio signal can be used as a sensitive signature of linewidth. We repeated the measurement on similar test lines and used the previously obtained ratio signals as calibrated signals to calculate the linewidths. From the results, the accuracy of the measurement has been determined to be about 10 nm for lines that are broader than 100 nm. The signal for 100 nm line is more susceptible to noise, but the signal has been clearly observed. To verify that the signal indeed comes from the polarization effect, the exact same procedures were performed without polarizers in the setup. The ratio image obtained in this manner was essentially unity and the signatures of the sub-micron lines disappeared.

A focused beam rigorous coupled wave analysis (FB-RCWA) [20] has been developed to study the polarization effects from non-periodic sub-wavelength structures. The RCWA method is inherently designed for periodic structures [21, 22]. However, if we choose the period of the structure large enough and synthesize a small spot illumination with multiple plane waves, the optical response from a non-periodic structure can be obtained. FB-RCWA simulations of these sub-wavelength structures were performed and the corresponding ratio signals were calculated and shown in Fig. 12 along with the experimental data. Despite a small discrepancy between theoretical and experimental data, the tendency of experimental signals is consistent with the simulation. The

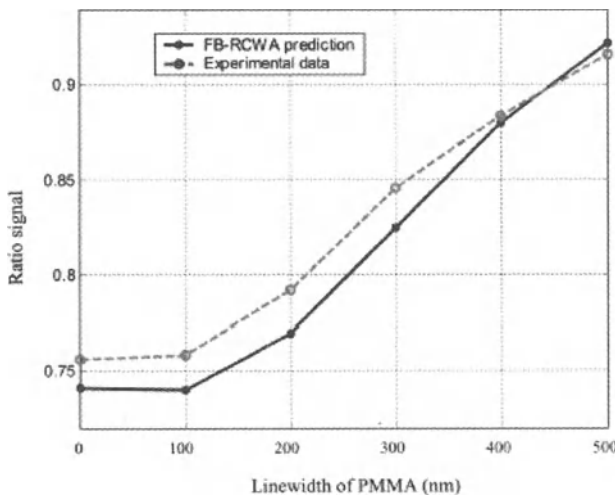


**Fig. 12.** Theoretical and experimental imaging microellipsometric signals for unresolved lines

FB-RCWA simulation also predicts the dip at the center of 100 nm line shown in Fig. 11b [23]. Considering the complex physics that governs this problem, the match between the experimental curve and theoretical curve calculated by our simple optical model is remarkably good. The theoretical calculations are sensitive to many other parameters, such as residual birefringence of the objective lens, the retardation from the wave plate, the index of refraction of each layer, the thickness of the film, and so on. In practice, it is unnecessary to obtain an exact match between the two curves in Fig. 12. The accuracy of an actual measurement tool would be improved substantially by compensating for these effects through a calibration procedure.

### 13.4.3 Measurement of Axial Birefringence

Axial birefringence is birefringence distribution that obeys rotational symmetry. This birefringence often occurs in an objective lens due to optical coating and stress. This birefringence causes polarization aberrations that degrade the performance of the optical devices [24]. Accurate characterization of this axial birefringence is very important for the applications of these optical devices to photolithography and optical data storage. The rotationally symmetric microellipsometer can be used to accurately characterize the axial birefringence in optical systems and devices. In this experiment, a series of  $\text{SiO}_2$  thin films on silicon with different thickness were used. The  $\text{SiO}_2$  was deposited onto silicon substrates by use of PECVD (Plasma Enhanced Chemical Vapor Deposition) and the thickness and refractive index were measured with a spectroscopic

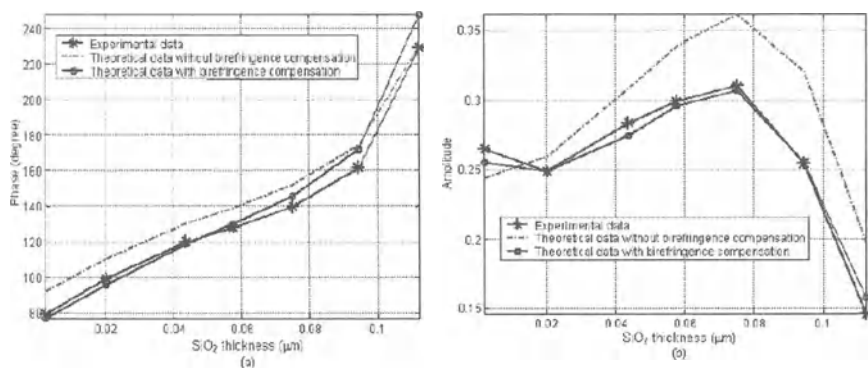


**Fig. 13.** Comparison of experimental and theoretical data for a series of  $\text{SiO}_2$  thin films on silicon substrate; (a) Phase; (b) Amplitude

ellipsometer. The measured thickness and index were then used in the optics model to calculate the amplitude ( $\cos 2\epsilon$ ) and phase ( $2\theta_0$ ) of the signal. The calculated values were then compared with the experimental results. An appreciable discrepancy between the experimental and the theoretical data was found if we assumed that the objective lens was perfect. A small amount of residual axial birefringence was discovered in the objective we used. After we included this residual birefringence ( $2^\circ$  retardation) from the objective lens in the optical model, very good agreement between the theoretical and experimental curves was obtained. The experimental and theoretical data are shown in Fig. 13. The measured amount of axial birefringence is comparable to those reported in literature [25].

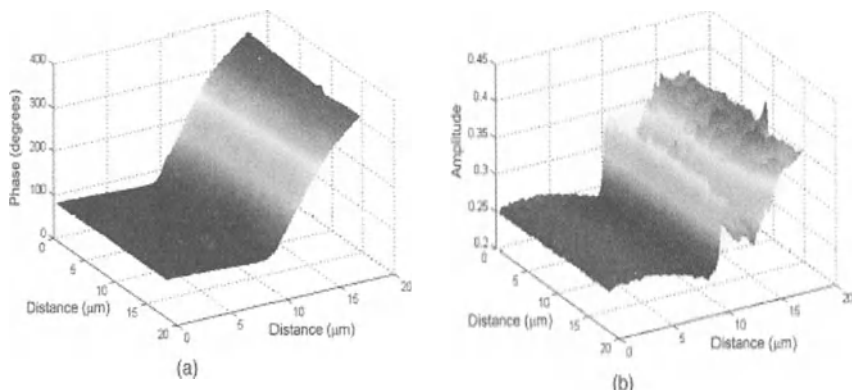


**Fig. 14.** Phase and amplitude images of a photoresist microp prism measured by the rotationally symmetric microellipsometer; (a) Phase; (b) Amplitude

### 13.4.4 Measurement of Micro-Optical Components

Recently, micro-optical components became increasingly important due to their wide applications in communications and information technology. Accurate characterization of these devices plays critical role in successful mass production of such devices. The rotationally symmetric microellipsometer can be used to characterize micro-optical components. A photoresist micro-prism is fabricated with gray scale mask technique. Ellipsometric images of this micro-prism are obtained through scanning in two dimensions (see Fig. 14). The image size is  $18 \mu\text{m} \times 18 \mu\text{m}$  with  $0.2 \mu\text{m}$  scanning step size. A resolution of  $0.5 \mu\text{m}$  can be estimated from the illumination wavelength and numerical aperture. The integration time of the lock-in was set to be 100 ms. Due to the vibration caused by the motor, the amplitude data was relatively noisy compared to the phase data. We measured the refractive index of photoresist with a standard ellipsometer and used this index of refraction and the phase data to calculate the thickness of the photoresist microstructure. A line scan is shown in Fig. 15. Despite some deviations, this result was in good agreement with a profiler measurement. The deviations could be caused by the fact that the two instruments did not measure the exact same location of the sample. In addition, it is noteworthy that the profiler measurements showed a slight increase in thickness for the leftmost part of the line scan, while the microellipsometer data showed a slight decrease of thickness for the same region. We believe this is due to the large stylus size ( $\sim 5 \mu\text{m}$  radius) and the leveling error of the profiler. The comparison clearly demonstrates the advantages of the microellipsometer over a stylus profiler. Besides the non-contact and non-destructive characteristics, the microellipsometer measurement gives the absolute thickness of the sample, instead of the topology, with higher spatial

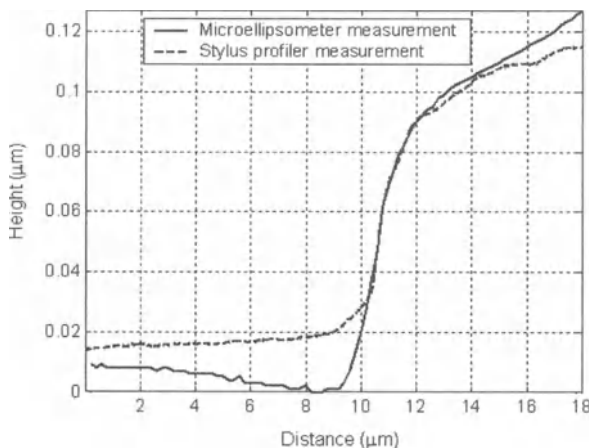


**Fig. 15.** Comparison of surface profile measured by the microellipsometer and a stylus profiler

resolution. It is necessary to point out that, although only the thickness was measured in this experiment, simultaneous determination of thickness and refractive index of sample is possible with less noisy amplitude data, which is another advantage of the microellipsometer.

## 13.5 Future Trends

We have described two high resolution microellipsometry techniques and their applications in characterization of patterned surface structures. These techniques have wide applications in aerospace materials research, semiconductor industry, photonics industry, and many other disciplines. Based on the microellipsometry techniques described above, current research is going on to design spectroscopic microellipsometer and generalized microellipsometer. These techniques will significantly expand the capabilities of microellipsometry and enable accurate characterization and diagnostics of more complicated materials. The resolution of microellipsometry can be further increased by incorporating near-field optical techniques (such as NSOM and SIL [26]). Cylindrical vector beams may also be incorporated in the rotationally symmetric microellipsometer to further increase its spatial resolution [14, 27]. Another trend is to integrate other optical and non-optical techniques (such as reflectometry, opto-thermal technique, acoustics, etc.) with the microellipsometry. This integration can provide more information about the sample and more data to analyze, allowing more accurate diagnostics and characterization of the material structures.

Coating structures are extensively used in modern aerospace engineering for multiple purposes. For example, polymeric coating systems have been widely used in corrosion protection for aircrafts. Failure of these coatings will leave the metallic structures underneath exposed to harmful environmental conditions, which will further cause the mechanical structure to degrade and fail to function well before the original design life. Thus maintaining and monitoring the integrity of the protective coating is very critical for the proper performance and the lifetime extension of the mechanical structure. The high-resolution microellipsometry we developed will be applied to inspect the coating integrity and study the corrosion mechanism for aerospace materials research.

## Acknowledgement

A large part of this work was performed when the author was with Prof. James Leger's research group at the University of Minnesota-Twin Cities. The research was supported by the CyberOptics Corp., Minneapolis, MN. The author's current research efforts in the microellipsometry lab are supported by the Center for Electro-Optics of University of Dayton and the Center for Materials Diagnostics, University of Dayton Research Institute. The author is thankful for their support.

## References

1. Herman P (1996) Optical diagnostics for thin film processing. Academic Press, San Diego
2. Azam RMA, Bashara NM (1977) Ellipsometry and polarized light. North Holland Publishing Company, New York
3. Tompkins HG (1993) A users' guide to ellipsometry, Academic Press
4. Tompkins HG, McGahan WA (1999) Spectroscopic ellipsometry and reflectometry: a user's guide. Wiley, New York
5. Erman M, Theeten JB (1986) Spatially resolved ellipsometry. *J Appl Phys* 60:859–873
6. Liu AH, Wayner PC Jr, Plawsky JL (1994) Image scanning ellipsometry for measuring nonuniform film thickness profiles. *Appl Opt* 33:1223–1229
7. Albersdörfer A, Elander G, Mathe G, Neumaier KR, Paduscheck P, Sackmann E (1998) High resolution imaging microellipsometry of soft surfaces at  $3\mu\text{m}$  and  $5\text{\AA}$  normal resolution. *App Phys Lett* 72:2930–2932
8. Jin G, Jansson R, Arwin H (1996) Imaging ellipsometry revisited: Development for visualization of thin transparent layers on silicon substrates. *Rev Sci Instrum* 67:2930–2935
9. Gold N, Willenborg DL, Opsal J, Rosencwaig A. High resolution ellipsometric apparatus. US patent, #5042951
10. Leng JM, Chen J, Fanton J, Senko M, Ritz K, Opsal J (1998) Characterization of titanium nitride (TiN) films on various substrates using spectrophotometry, beam profile reflectometry, beam profile ellipsometry and spectroscopic beam profile ellipsometry. *Thin Solid Films* 313–314:308–313
11. See W, Somekh MG, Holmes RD (1996) Scanning optical microellipsometer for pure surface profiling. *Appl Opt* 35:6663–6668
12. Zhan Q, Leger JR (2002) A high resolution imaging ellipsometer. *Appl Opt* 41:4443–4450
13. Zhan Q, Leger JR (2002) Interferometric measurement of Berry's phase in space-variant polarization manipulations. *Opt Commun* 213:241–245
14. Zhan Q, Leger JR (2002) Microellipsometer with radial symmetry. *Appl Opt* 41:4630–4637
15. Zhan Q, Leger JR (2002) Focus shaping using cylindrical vector beams. *Optics Express* 10:324–331
16. Minhas BK, Coulombe SA, Naqvi SSH McNeil JR (1998) Ellipsometric scatterometry for the metrology of sub- $0.1\text{-}\mu\text{m}$ -linewidth structures. *Appl Opt* 37:5112–5115
17. Wang X, Mason J, Latta M, Strand T, Marx D, Psaltis D (2001) Measuring and modeling optical diffraction from subwavelength features. *J Opt Soc Am A* 18:565–572
18. Zhan Q, Leger JR (2002) Measurement of surface features beyond the diffraction limit using an imaging ellipsometer. *Opt Lett* 47:821–823
19. Zhan Q, Leger JR (2001) Imaging ellipsometry for high-spatial-resolution metrology. Invited paper, SPIE proceedings vol. 4435, Wave Optics and VLSI photonic devices for information processing, pp. 65–76
20. Otaki K, Osawa H, Ooki H, Saito J (2000) Polarization effect on signal from optical ROM using solid immersion lens. *Jpn J Appl Phys* 39:698–706

21. Moharam MG, Grann EB, Pommert DA, Gaylord TK (1995) Formulation for stable and efficient implementation of the rigorous coupled-wave analysis of binary gratings. *J Opt Soc Am A* 12:1068–1076
22. Moharam MG, Grann EB, Pommert DA, Gaylord TK (1995) Stable implementation of the rigorous coupled-wave analysis for surface-relief gratings: enhanced transmittance matrix approach. *J Opt Soc Am A* 12:1077–1086
23. Zhan Q and Leger RJ (2002) Measuring unresolved surface features using imaging ellipsometric polarization signatures. In: DOMO technical digest, Diffractive-Optics Micro-Optics (DOMO) Topical Meeting, Tucson AZ, pp. 101–103
24. Stallinga S (2001) Axial birefringence in high-numerical-aperture optical systems and the light distribution close to focus. *J Opt Soc Am A* 18:2846–2859
25. Shribak M, Inoué S, Oldenbourg R (2002) Polarization aberrations caused by differential transmission and phase shift in high-numerical-aperture lenses: theory, measurement, and rectification. *Opt Eng* 41:943–954
26. Zhan Q, Leger JR (2003) Near-field nano-ellipsometer for ultrathin film characterization. accepted by the Journal of Microscopy
27. Quabis S, Dorn R, Eberler M, Glöckl O, Leuchs G (2000) Focusing light into a tighter spot. *Optics Commun* 179:1–7

# 14 Positron Annihilation Spectroscopy (PAS)

G. Dlubek, N. Meyendorf

## 14.1 Introduction

Positron annihilation spectroscopy (PAS) was established in the early 70's as a laboratory method with high sensitivity to measure and distinguish between thermally generated single and divacancies in pure metals. From there, PAS has been developed to investigate many kinds of open volume defects in metals, semiconductors, ceramics, and polymers. Recently it has been demonstrated that PAS is able to analyze layered structures up to approximately  $2 \mu\text{m}$  non-destructively, and even determine chemical properties of the outmost surface-layer, undetectable by any other spectroscopic method. Unlike many other methods of material analysis, internal stresses or textures do not effect positron spectroscopy.

Most applications of PAS are still focussed on materials research in the laboratory for studying structural defects such as dislocations, vacancies, vacancy cluster, microvoids, and microbubbles in metals but also in all other kinds of solid materials. In decomposed alloys positrons may detect atomic clusters, coherent zones, semicoherent precipitates and incoherent nanometer size particles [1–8]. Because of its nondestructive nature and the ability to be applied to large components PAS attracts more and more attention for technical applications as a nondestructive method for materials characterization [9].

This chapter will introduce the reader to the very basics of positron annihilation spectroscopy (PAS). Applications concerning the characterization of the plastic deformation of steel, fatigue of titanium alloys, decomposition in aluminum alloys, and degradation of polymer coatings will demonstrate the potential of the method.

## 14.2 Background and Instrumentation

### 14.2.1 Basis of the Method

#### *Preparation of Positron Sources*

Gamma rays are emitted if a positron annihilates with an electron. Several experimental techniques are used to detect and analyze this radiation [1–4]. The most important are the positron annihilation lifetime spectroscopy (PALS) and the

measurements of the Doppler-broadened annihilation radiation (DBAR). Positrons are emitted by radioactive sources such as  $^{22}\text{Na}$ ,  $^{64}\text{Cu}$ , or  $^{58}\text{Co}$ . For PALS and DBAR measurements usually  $^{22}\text{Na}$  sources with a typical strength of  $1\times 10^5$  to  $10\times 10^5$  Bq are employed.  $^{22}\text{Na}$  has a half-life of 2.6 years. Commercial suppliers deliver aqueous solutions of  $^{22}\text{NaCl}$  with high specific activity. A source is prepared by dripping a small amount of the solution onto a thin ( $\sim 5\ \mu\text{m}$ ) foil of aluminum, nickel or Kapton. A small grain of  $^{22}\text{NaCl}$  salt remains after the water solvent has been evaporated. The source is then covered by a second sheet of the foil. For conventional laboratory experiment this weak source is sandwiched between two identical test coupons to guarantee that no positrons annihilate outside the sample source system. Other sample source configurations have been considered for NDE applications. One option is to place the source at the surface of the test specimen and cover the source by a known reference material [9].

### **Principle of the Method**

Positrons are emitted by  $^{22}\text{Na}$  with kinetic energies up to  $E_{\max} = 0.54$  MeV. The maximum of the energy distribution is located at 0.20 MeV. The stopping profile (distribution of penetration depths of particles in a material) of positrons emitted from a radioactive source is a decreasing exponential

$$P(x) = \alpha \exp(-\alpha x), \quad \alpha [\text{cm}^{-1}] = 38.6 \rho [\text{g/cm}^3], \quad (1)$$

where  $\rho$  is the density of the solid and  $x$  is the penetration depth of the positron [1]. The characteristic penetration depth,  $1/\alpha$  (63% positron absorption), is 288  $\mu\text{m}$  in polyethylene, 96  $\mu\text{m}$  in Al or Ti, 33  $\mu\text{m}$  in Fe, and 12  $\mu\text{m}$  in Pt. Test coupon thickness of 1.99, 0.66, 0.23, and 0.083 mm, respectively are required for absorption of 99% of all positrons.

In a solid, energetic positrons rapidly lose their energy via ionization and excitation of atoms, excitation of plasmons, and finally creation of electron-hole pairs and phonons. After a few picoseconds the positrons are in thermal equilibrium with the material within. During their life of 100–400 ps these thermalized positrons migrate over a mean distance of typically 100 nm before annihilating with an electron of the material. During annihilation energy, momentum and spin are conserved. This leads to the emission of two  $\gamma$ -rays (photons), each with the energy of  $mc^2 = 0.51$  MeV ( $m$  – mass of the electron,  $c$  – vacuum velocity of light), in almost collinear directions.

Due to the conservation of energy, momentum and spin during annihilation the emitted annihilation photons carry information about the properties of electrons that participated in the annihilation process. Conclusions on the type and properties of annihilating electrons can be drawn from the analysis of the spectroscopic properties of annihilation photons with respect to their energy, angular distribution, and moment of emission [1–7]. Figure 1 shows the principle of a positron annihilation experiment.  $^{22}\text{Na}$  emits a 1.28 MeV photon almost simultaneously with the positron. This indicates the birth of the positron. The 0.51 MeV-photons appear if the positron annihilates. The lifetime of an individual positron can be measured by detecting of the time delay between the emission

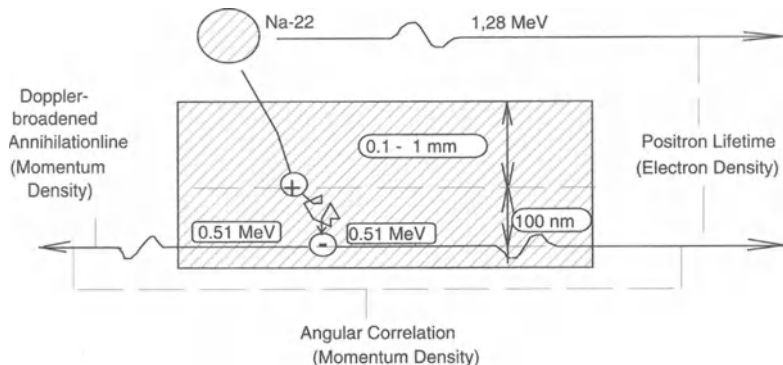


**Fig. 1.** The positron experiments

of the 1.28 MeV “birth” photon and the 0.51 MeV “death” photon. The mean lifetime of an ensemble of positrons responds inversely to the density of electrons at the site of the annihilating positrons.

The momentum  $p$  of the annihilating electron-positron pair leads to two observable effects. The first is that the angle of emission of two annihilation photons deviates from the collinearity by a value of  $\varphi \approx \tan\varphi = p_z/m_0c$ , where  $p_z$  is the momentum component perpendicular to the original direction of photon emission. Two scintillation detectors operating in coincidence are used to measure the angular correlation of annihilation radiation (ACAR). The counting rate of annihilation photons coming from the same annihilation event is determined as a function of the angle between both photons. This angular correlation curve corresponds to the one-dimensional momentum density of annihilation electron-positron pairs (1D-ACAR). The two-dimensional momentum density can be measured by using position-sensitive detectors (2D-ACAR).

The second effect is a deviation of the energy of the annihilation photons from  $E_0 = m_0c^2$  ( $m_0$  – rest mass of an electron) by  $+ \delta E$  and  $- \delta E$  where  $\delta E = p_y c/2$ .  $p_y$  is the momentum component of the annihilating electron-positron pair parallel to the original direction of the photon emission.

### 14.2.2 Positron Annihilation Lifetime Spectroscopy (PALS)

#### Experimental Setup

Figure 2 shows a schematic of a lifetime spectrometer. It is a fast-fast coincidence system conventionally used in nuclear spectroscopy [1–4]. As described above the  $^{22}\text{NaCl}$  source covered by thin foils is sandwiched between two identical test coupons. The detectors consist of fast plastic scintillators coupled to fast photomultiplier tubes. Nowadays, the more efficient  $\text{BaF}_2$  scintillators are typically used.

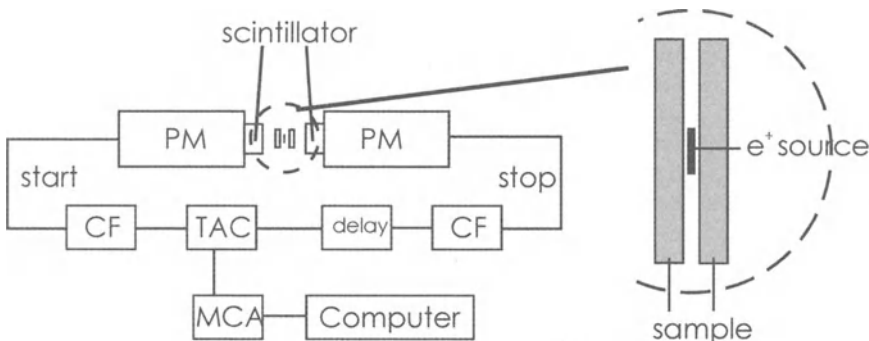


**Fig. 2.** Scheme of a fast-fast positron lifetime spectrometer, PM – photomultiplier, CF – constant fraction discriminator, TAC – time amplitude converter, MCA – multi channel analyzer [8]

This, however, requires infrared sensitive photomultiplier tubes. The energy window of one of the constant fraction discriminators (CF) is adjusted to detect 1.27 MeV photon. This indicates the decay of a  $^{22}\text{Na}$  atom and the emission of a positron. This detector starts a clock. The second discriminator accepts photons of the energy of 0.511 MeV. This photon is generated by the annihilation of a positron with an electron and stops the clock. A time-to-amplitude converter (TAC) is used as a clock. The TAC transforms the time delay between the “birth” and the “death” photons into a proportional pulse amplitude. So, the distribution of delay times between the emissions of “birth” and “death” photons, indicating the distribution of individual positron lifetimes, is transferred into a pulse amplitude spectrum. A multi channel analyzer (MCA) evaluates and stores the positron lifetime spectra.

The setup in Fig. 2 shows the typical PALS device used in solid state physics and materials research. The conventional sample-source-sample sandwiches are, however, not useful for in-the-field mapping of NDT. Therefore, an arrangement with detectors placed in right-angle to each other was suggested and applied for NDT [9]. The positron source is prepared and applied as described above but a reference material is placed on the opposite side of the source (compare Fig. 4). However, the reference material is responsible for an additional component in the lifetime spectrum. Its lifetime value and intensity must be determined by a separate experiment. The application of PALS and DBAR for NDT is discussed in detail by Allen et al. [10]. These authors showed that local plastic damage variations in the vicinity of a crack could be detected using a point-like positron source.

Recently, the prototype of a novel positron lifetime spectrometer has been developed [11]. The detector pulses are directly digitized using a fast digital oscilloscope or a digitizer PCI-card. The subsequent analysis with signal processing software replaces the conventional analog electronics chain (CF, TAC, and MCA). This setup is cost efficient and easier to handle than the conventional hardware.

When using a conventional  $^{22}\text{Na}$  positron source, the information depth is typically 0.1 mm. Activation of material by neutrons or high energy radiation can generate a positron source deep inside a material. Thus, an *in situ*  $^{58}\text{Co}$  source

useful for annihilation line studies (see the next chapter) can be produced by irradiation of nickel or nickel containing material with reactor neutrons [12]. A method applicable for many materials has been developed recently [13]. Positron emitting nuclei are induced through photo-neutron excitation deep within the test object itself. The high-energy (15 to 25 MeV) bremsstrahlung photons (“breaking” photons are caused by sharp deceleration of charge carriers) are generated by a small electron accelerator (LINAC) such as those used medically for radiological therapy. High energy x-rays generate positrons inside the material by pair production. These sources are useful for annihilation line studies.

### ***Analysis of Positron Lifetime Spectra***

The positron lifetime spectrum has to be analyzed (by assuming a certain model spectrum) in order to obtain information about the properties of the inspected material. Positrons can annihilate in a crystal lattice in defect-free regions or from several states after being trapped at defects. Each of which gives a characteristic annihilation rate  $\lambda_i$  and characteristic lifetime  $\tau_i = 1/\lambda_i$ , respectively. The positron lifetime spectrum  $s(t)$ , i.e. the probability of an annihilation at the time  $t$  after the birth of the positron, is a sum of the exponential decay components [1–4]

$$s(t) = -\frac{dn(t)}{dt} = \sum_i I_i \lambda_i \exp[-\lambda_i t], \quad \sum_i I_i = 1, \quad (2)$$

with the relative intensities  $I_i$  and the decay constants  $\lambda_i$ . Here  $n(t)$  is the probability that a positron is still alive at the time  $t$  after its birth. The average lifetime of the ensemble of positrons,  $\tau_{av}$ , can be calculated from the first momentum of the spectrum, or from the sum of the characteristic lifetimes weighted with their intensities  $I_i$

$$\tau_{av} = \int_0^\infty ts(t)dt = \sum_i I_i \tau_i. \quad (3)$$

For data analysis, the lifetime spectrum  $s(t)$  is convoluted with the resolution function of the spectrometer which is assumed to be a single Gaussian or a sum of two or three Gaussian functions. The convoluted spectrum is fitted to the experimental lifetime spectrum by means of standard non-linear fitting procedures. Different analysis routines which assume either a sum of discrete exponential components (PATFIT [14], LIFSPECFIT [15], LT7.0 [16]) or a continuos lifetime distribution (CONTIN [17], MELT [18], LT7.0 [16]) are currently under use. The fitting delivers the characteristic lifetimes  $\tau_i = 1/\lambda_i$  and their intensities  $I_i$ , the time zero  $t_0$ , and the background due to random coincidences of “birth” and “death” photons coming not from the same annihilation event (typically  $\leq 1\%$ ). Before applying this procedure, the annihilation events from the  $^{22}\text{NaCl}$  source, and covering foil, have to be subtracted. These components as well as the resolution function are estimated

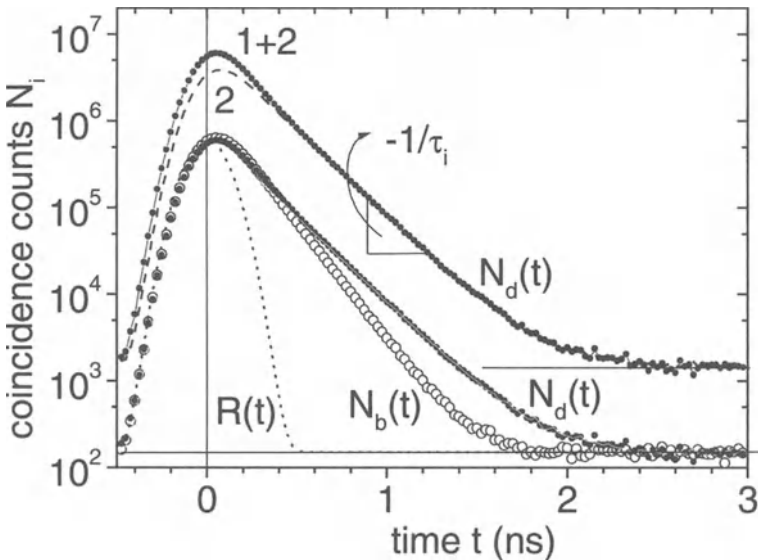


**Fig. 3.** The resolution function of the spectrometer,  $R(t)$ , and positron lifetime spectra of defect-free,  $N_b(t)$  ( $\tau = \tau_b = 160$  ps), and 10% cold-rolled,  $N_d(t)$ , aluminum. The upper plot of  $N_d(t)$  shows the two exponential components (1, 2) which have slopes of  $-1/\tau_1$  and  $-1/\tau_2$ . The parameters of this spectrum are  $\tau_1 = 98$  ps,  $\tau_2 = 220$  ps,  $I_2 = 70\%$  (compare (5))

from measurements of a reference material (well annealed aluminum, for example) with a well known, single positron lifetime.

In Fig. 3 typical positron lifetime spectra for defect free and cold rolled aluminum are displayed. Shown is the number of 1.27 MeV  $\gamma$ (start) to 0.51 MeV  $\gamma$ (stop)-coincidence events  $N_i$  as a function of the channel number  $i$  which is calibrated in time units. The resolution function  $R(t)$  is a Gaussian with a full width at half maximum of FWHM = 250 ps.  $N_b(t) = N_0 s_b(t)$  denotes the spectrum of the well annealed aluminum where  $N_0 = 5 \times 10^6$  is the total number of annihilation events in the sample and  $s_b(t)$  is given by (2). All positrons annihilate in the bulk of the metal with a lifetime of  $\tau_1 = \tau_b = 160$  ps and an intensity of  $I_1 = 100\%$ . After cold rolling with a thickness reduction of 10%, a second component with a lifetime of  $\tau_2 = \tau_d = 220$  ps and an intensity of  $I_2 = 70\%$  appears that originates from positrons which are trapped at dislocations.  $\tau_1$  has now a value of 98 ps. This spectrum is denoted by  $N_d(t) = N_0 s_d(t)$ . We will see later that  $\tau_2$  characterizes the type of defects where positrons are trapped, while  $I_2$  contains information's on the positron trapping rate  $\kappa_d$ , which determines the defect density.

#### 14.2.3 Doppler-Broadening of Annihilation Radiation (DBAR)

The Doppler shift of the energy of annihilation photons by  $\pm \delta E = p_y c/2$  leads to a broadening of the annihilation line centered at  $E_0 = m_0 c^2 = 511$  keV. The

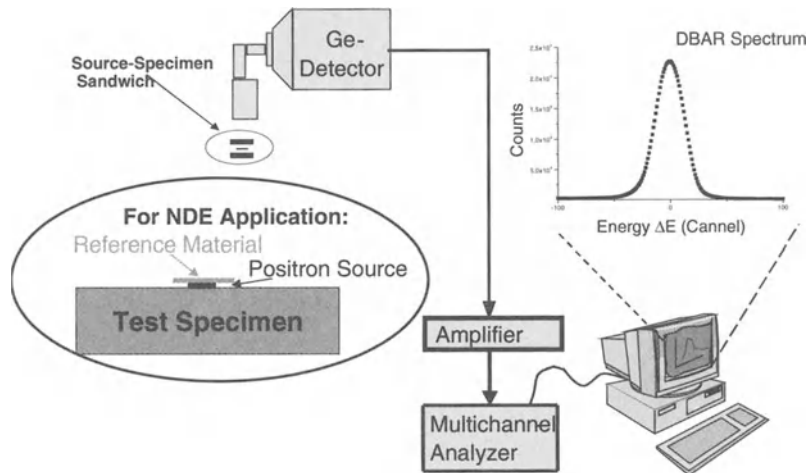


**Fig. 4.** Typical setup for DBAR spectroscopy. For NDE applications with one side access the source is covered by a reference material (as shown in the schematic)

broadened curve shows the one-dimensional momentum density of annihilation electron positron pairs. Since the momentum of the thermalized positron is neglectable, the electron momentum determines the momentum of the electron-positron pair  $p$ .

For measuring the Doppler-broadened annihilation radiation (DBAR), a conventional  $\gamma$ -spectrometer with a high resolution Ge-detector is used [1–4]. Figure 4 illustrates a typical setup using sandwich specimens (left upper corner). A schematic of the sample source arrangement for NDE applications with one side access to the test specimen is shown in the encircled lower left corner of Fig. 4 .

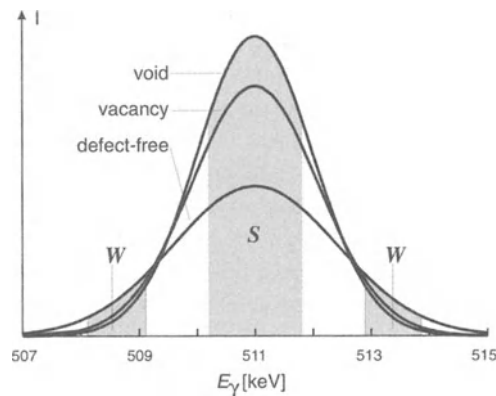


**Fig. 5.** Doppler-broadened annihilation lines the perfect lattice, vacancies and microvoids in nickel. Shown is the rate of detected photons as a function of their energy  $E_\gamma$  [8]. Grey areas are used to calculate the shape parameters  $S$  and wing parameter  $W$  by dividing these areas by the area under the full line

Typical annihilation  $\gamma$ -spectra are shown in Fig. 5. The Doppler-broadened annihilation lines have a typical width of  $\text{FWHM} = 2\text{--}3 \text{ keV}$  while the internal resolution of the spectrometer leads to a  $\gamma$ -line width of  $\text{FWHM} = 1.1\text{--}1.3 \text{ keV}$ .

In defect-free metals positrons annihilate in the bulk with free and core electrons the latter one has a rather broad distribution of momentum. In vacancy-type defects the annihilation with core electrons is reduced which results in a narrowing of the momentum distributions and therefore of the Doppler-broadened curve. The larger the open volume of the defect, the stronger the narrowing of the curve. This effect may be used to identify the type of defect that trapped the positron.

For the analysis of experiments, typically, two parameters, denoted by  $S$  and  $W$ , are extracted from the annihilation line shown in Fig. 5. The line shape parameter  $S$  is calculated by dividing the marked central area under the line (highlighted in grey) by the entire area under the curve. The window (energy range) for  $S$  is chosen so that the defined area covers about 50% of the total area of the annihilation line ( $S \sim 0.5$ ). To facilitate the comparisons between various experiments, frequently relative values like  $S/S_{\text{ref}}$  are reported where a good reference is the defect-free bulk of the same material.  $S$  mirrors the probability of positrons to annihilate with low-momentum electrons. Complementary, the wing parameter  $W$  is the grey marked area under the wings of the line divided by the total area under the curve. It shows the probability of annihilations with high-momentum (core) electrons. Figure 5 shows schematically how those parameters change when vacancies and microvoids trap positrons.

#### 14.2.4 Slow Positron Beam Techniques

For the study of near surface properties of bulk materials, coatings and thin films monoenergetic positrons with a small kinetic energy are required. By accelerating the slow positrons to defined energies, the penetration depth may be changed systematically between a few nanometers to several microns. These requirements fulfill the slow positron beam techniques which have been developed during the past two decades [19, 20] (and see Refs. [4, 7] and references given therein).

In Fig. 6 a view of a slow-positron-beam system is shown. The first step is the generation of slow monoenergetic positrons. This is accomplished by a “moderator”, which is a material with a positive positron workfunction that spontaneously emits thermalized positrons with a typically energy at  $\sim 1 \text{ eV}$ . Moderators operating in the transmission mode may be made from a thin ( $2 \mu\text{m}$ ) tungsten foil, a stack of foils, or a fine network. Thick moderator plates may be used in a reflection geometry setup. Fast positrons emitted by a conventional  $^{22}\text{Na}$  source or produced via pair-production from high-energy photons penetrate the thin moderator film. A small fraction are slowed down inside the film. The thermalized positrons may migrate to the opposite surface and be spontaneously emitted. Typically a moderation efficiency of the order of  $10^{-3}$  to  $10^{-4}$  can be achieved. The slow positrons are magnetically or electrically guided via a drift tube to the  $\mathbf{E} \times \mathbf{B}$  filter. This filter separates the slow and the fast positrons (the latter have been transmitted through the moderator film without moderation).

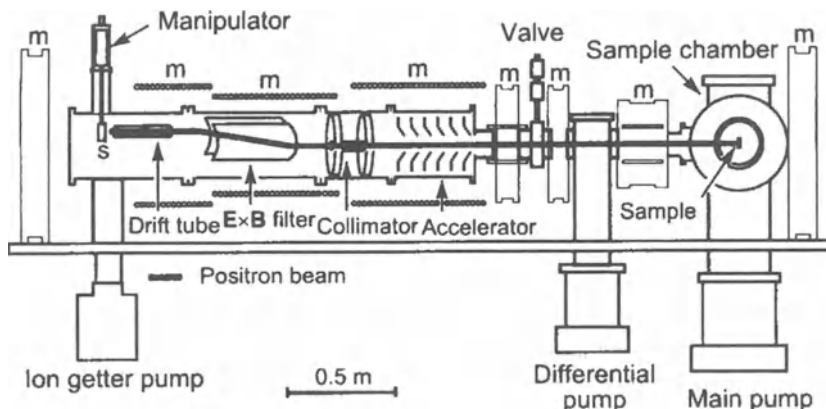


**Fig. 6.** Section view of a typical slow-positron-beam system [4]. Positrons emitted from the source-moderator arrangement (s) are fed through the collimator by the  $E \times B$  filter and accelerated to the sample. The overall longitudinal magnetic field is generated by the guidance coils (m). The vacuum is in the  $10^{-6}$  Pa range at the source side and  $10^{-9}$  Pa in the specimen chamber

Thereafter, the collimated slow positron beam is accelerated toward the sample with an energy that may range from a few eV to a maximum of 40 keV. A longitudinal magnetic field along the whole beam system, forces the positrons onto a helical trace. This ensures that all moderated slow positrons reach the target.

Usually a positron beam system is equipped with a Ge-detector for DBAR measurements [4, 19, 20]. For positron lifetime measurements a pulsed positron beam may supply the start pulse for the clock. Such PALS have been utilized in only a few laboratories (for example see Ref. [21] and articles published in Ref. [7]).

Monoenergetic positron beams are applied for monitoring defects as a function of depth (defect profiling) [4, 19, 20, 7]. For example structural defects and chemical modifications generated by irradiation of materials with high-energy ions can be investigated. Interesting applications are the study of the incorporation of nitrogen into the surface of stainless steel by plasma immersion ion implantation and the corrosion of metals. Some new fast growing applications for positron beams include studying of the durability of polymeric coatings during mechanical loading and analyzing natural or artificial weathering. Some groups are developing reemission positron microscopes and scanning positron probes. One way to accomplish this is to equip a conventional scanning electron microscope with a slow positron source [22, 23] (for all these applications see Refs. [1] to [7] and original papers therein).

## 14.3 Interaction of Positrons with Lattice Defects and Precipitates

### 14.3.1 Change of the Annihilation Parameters Due to Positron Trapping at Defects

In metals the thermalized positrons may migrate over a mean diffusion length of  $\Lambda_+ = 100 - 200$  nm until being annihilated. Before annihilation, vacancy-type structural defects such as vacancies, small vacancy agglomerates, voids, bubbles and dislocations may trap positrons. Trapped positions localize at vacancy-type defects due to energy state reductions caused by the absence of repulsive atomic cores present in the materials bulk [24]. Positrons do not sense lattice defects with a higher local atom density than in the bulk, such as interstitials. In Fig. 7 the structure of typical positron traps in metals, their potential to be sensed by the positron,  $V(r)$ , and the density distribution of the localized positron,  $n_+(r)$ , are shown. Monovacancies (a), vacancy agglomerates (d), and (internal or external) surfaces (c) form deep positron traps with binding energies of  $E_b \geq 1$  eV. Small substitutional atoms such as H, He, N, and C, (b) form shallow positron traps with  $E_b \leq 1$  eV. At elevated temperate positrons may escape from these traps.

Single, foreign atoms are usually not able to hold a positron. However, they may have an attractive interaction (affinity) to positrons which leads to a slightly preferred annihilation at these atoms. But when an alloy decomposes, chemically inhomogeneities are formed which may hold positrons [25, 26]. Coherent clusters or precipitates that are enriched with the kind of atoms that have the higher positron affinity (e) may trap positrons without the support of lattice defects.

In the case of semi-coherent or incoherent precipitates misfit dislocations (f) or the incoherent particle-matrix interfaces are responsible for positron localization. In case of dislocations, the trapped positron moves along the dislocation line until it becomes held at a jog or a vacancy.

When positrons annihilate from a state localized at a defect, the annihilation parameters show characteristics associated with a certain defect, which is different than the bulk values as well [24]. The density of the trapped positron is enhanced at the center of the defect (see Fig. 7) where the electron density has its minimum. This leads to an increase of the corresponding lifetime  $\tau_d$  compared with the bulk value  $\tau_b$ . As can be observed in Fig. 8, the larger the open volume of the defect the higher the increase in  $\tau_d$ . The same behavior is true for the DBAR curve-shape parameter  $S_d$  while the wing parameter  $W_d$  changes in the opposite direction (see Fig. 5).

As shown in Table 1,  $\tau_d / \tau_b$  increases by a factor of 1.2 to 1.5 in case of monovacancies, and by a factor of 4 for microvoids and surfaces. The positron lifetime for microbubbles is decreased compared with empty voids (Fig. 8). From its value the gas pressure inside the bubble can be estimated. In case of coherent precipitates the change of  $\tau_d / \tau_b$  may be larger (Mg in Al) or smaller (Zn in Al)

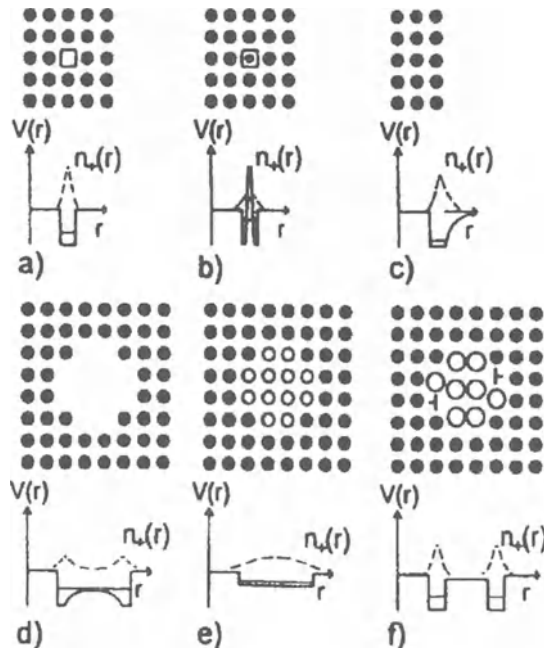


**Fig. 7.** The structure of typical positron traps in metals, their potential sensed by the positron,  $V(r)$ , and the density distribution of the localized positron,  $n_s(r)$ ; a) monovacancy; b) substitutional small atom (H, He, N, or C); c) surface; d) void or bubble; e) small coherent atom cluster (Guinier-Preston zone); f) partially coherent or incoherent precipitate

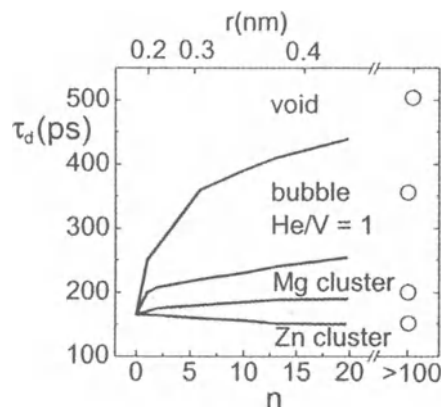


**Fig. 8.** Variation of the trapped positron lifetime  $\tau_d$  for different types of defects in aluminum. The positron traps are: voids, He filled bubbles (He/V – helium/vacancy ratio = 1), and coherent clusters of Mg or Zn.  $n$  denotes the number of vacancies and atoms, respectively, in the agglomerate,  $r$  is the corresponding radius of the spherical agglomerate

than unity depending on the host and precipitate material. Jogs and vacancies on dislocation lines exhibit positron lifetimes and  $S$  parameters somewhat smaller than those of monovacancies in the bulk (Table 1).

**Table 1.** Experimental lifetimes  $\tau$  (in ps) of positrons trapped at different defects in metals

$\tau$	Annihilation at:	Al	Cu	Fe	Ni	Mo
$\tau_b$	bulk	165	120	110	110	120
$\tau_d$	dislocation	230	150	165	150	150
$\tau_v$	(mono)vacancy	245	180	175	180	180
$\tau_c$	large vacancy cluster	540	500	450	500	465

### 14.3.2 Kinetics of Positron Trapping

The kinetics of positron trapping by defects is described by the so-called trapping model [24]. It assumes that at time  $t = 0$  all positrons are thermalized and freely mobile in the bulk. The positrons may annihilate with a rate characteristic for the bulk,  $\lambda_b$ , or be trapped at defects with a rate  $\kappa_d$ . Once trapped, the positrons will annihilate with a rate  $\lambda_d$  characteristic for the defect. For simplicity we assume only one kind of defect and no detrapping of positrons from the defects. Figure 9 illustrates the situation. At time  $t \geq 0$ , the probability for the positron to be in the free state is  $n_b(t)$  and in a defect  $n_d(t)$ . The total probability for the positron to be alive is  $n = n_b + n_d$ . The positron kinetics is described by a set of combined first-order differential equations

$$\begin{aligned} \frac{dn_b}{dt} &= -(\lambda_b + \kappa_d)n_b \\ \frac{dn_d}{dt} &= -\lambda_d n_d + \kappa_d n_b. \end{aligned} \quad (4)$$

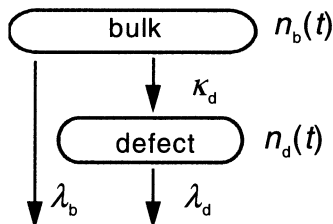


**Fig. 9.** Trapping model for positrons in crystals with one kind of defect and no de-trapping from the defect

The probability for the positron to be alive at time  $t$  follows from the solution of (4) with the initial condition  $n_b(0) = 1$  and  $n_d(0) = 0$ .

$$\begin{aligned} n_b(t) &= \exp[-(\lambda_b + \kappa_d)t] \\ n_d(t) &= \left( \frac{\kappa_d}{\lambda_b - \lambda_d + \kappa_d} \right) \{ \exp[-\lambda_d t] + \exp[-(\lambda_b + \kappa_d)t] \}. \end{aligned} \quad (5)$$

The parameters of the lifetime spectrum follow from a comparison of (5) and (2),  $s(t) = -dn/dt$

$$\begin{aligned} \tau_1 &= \frac{1}{\lambda_1} = \frac{1}{\lambda_b + \kappa_d}, \quad \tau_2 = \frac{1}{\lambda_2} = \frac{1}{\lambda_d} \\ I_1 &= 1 - I_2, \quad I_2 = \frac{\kappa_d}{\lambda_b - \lambda_d + \kappa_d} . \end{aligned} \quad (6)$$

The fraction of annihilation events from bulk,  $\eta_b$ , and from defects,  $\eta_d$  is obtained from

$$\eta_b = 1 - \eta_d, \quad \eta_d = \int_0^\infty \lambda_d n_d(t) dt = \frac{\kappa_d}{\lambda_b + \kappa_d} = \frac{\tau_b \kappa_d}{1 + \tau_b \kappa_d} . \quad (7)$$

These fractions control all time averaged parameters such as the average positron lifetime  $\tau_{av}$  and the parameters  $S$  and  $W$  of the Doppler-broadened annihilation curve

$$\begin{aligned} \tau_{av} &= (1 - \eta_d) \tau_b + \eta_d \tau_d \\ S &= (1 - \eta_d) S_b + \eta_d S_d \\ W &= (1 - \eta_d) W_b + \eta_d W_d . \end{aligned} \quad (8)$$

Here  $\tau_b$ ,  $S_b$ , and  $W_b$  are the characteristic annihilation parameters of the bulk, and  $\tau_d$ ,  $S_d$ , and  $W_d$  are those of the defect.

An additional parameter ( $R_d$ ) follows from the changes of  $S$  and  $W$

$$R_d = \left| \frac{\Delta S}{\Delta W} \right| = \left| \frac{S - S_b}{W - W_b} \right| = \left| \frac{S_d - S_b}{W_d - W_b} \right| . \quad (9)$$

$R_d$  is independent of the fraction of trapped positrons and thus characteristic for the trapping defect.  $R_d$  may be obtained as the slope of the  $S$  over  $W$  plot. With increasing value of  $\eta_d$  the points in this plot vary linearly from the point  $(S_b, W_b)$  to the point  $(S_d, W_d)$ . A bend in this plot indicates the appearance of a new type of defect with different values of  $S_d$  and  $W_d$  [24].

The trapping rate  $\kappa_d$  that is related to concentration of the positron trapping lattice defect may be estimated from experimental data (for example  $I_2$  or  $\eta_d$ ) by using (6) to (8). The trapping model assumes that the defects are homogeneously distributed and that the trapping rate  $\kappa_d$  is proportional to the defect concentration  $C_d$ ,

$$\kappa_d = \mu C_d. \quad (10)$$

The specific trapping rate,  $\mu$ , is determined by both the diffusion of the positron to the defect and its transition from the free to the localized state. In case of small defects like monovacancies, small vacancy clusters and dislocations the transition is distinctly slower than the diffusion. This means the trapping is transition-limited and  $\mu \approx \mu_t$ . Since  $\kappa_d$  has the unit  $s^{-1}$ ,  $\mu$  must be given in units of ( $s^{-1}$ atom) if  $C_d$  is given in atomic concentration (defects per host atoms). When  $C_d$  is the volume concentration ( $cm^{-3}$ ), the unit for  $\mu$  must be ( $s^{-1}cm^3$ ). The relation between both values is  $\mu_s [s^{-1}cm^3] = \mu_t [s^{-1}atom]/N_{at}[cm^{-3}]$  where  $N_{at}$  is the host atom density.

In diffusion-limited trapping the transition to the localized state is much faster than the diffusion. This is the case for extended traps like voids, bubbles, and precipitates. Then the specific trapping rate can be written in the form

$$\mu_d [s^{-1}cm^3] = 4 \pi r_d D_+, \quad (11)$$

where  $r_d[cm]$  is the radius of the spherical trap and  $D_+[cm^2s^{-1}]$  the diffusion constant of the positrons. In the case that diffusion and transition have similar importance a combined specific trapping rate can be used.

The transition limited specific trapping rate,  $\mu_t$ , can be either calculated or estimated when another technique provides the defect density in a reference sample. For monovacancies irradiation with fast electrons is usually used to introduce a defined number of vacancies. Another possibility is the differential dilatometry which allows the estimation of the absolute concentration of thermal vacancies appearing at higher temperatures. It was found that the specific trapping rate of monovacancies in metals is approximately  $\mu_{tv} = 1$  to  $10 \times 10^{14} s^{-1}$ . It might change when impurities or alloy atoms are bound to these vacancies. For small vacancy agglomerates containing not more than  $n = 10$  vacancies the specific trapping rate increases linearly with  $n$ ,  $\mu_{nv} = n \mu_{tv}$ . For larger agglomerates  $\mu_{nv}$  initially increases proportionally to  $n^{1/2}$  and decreases to  $n^{1/3}$  at later stages meaning the trapping is now diffusion limited and follows (11). The trapping of positrons by clusters of atoms follows similar rules. For larger microvoids and precipitates the trapping is diffusion limited where the positron diffusion constant is typically around  $D_+ = 1 - 2 cm^2/s$ . For dislocations specific trapping rates of  $0.1 - 1 cm^2/s$  were estimated.

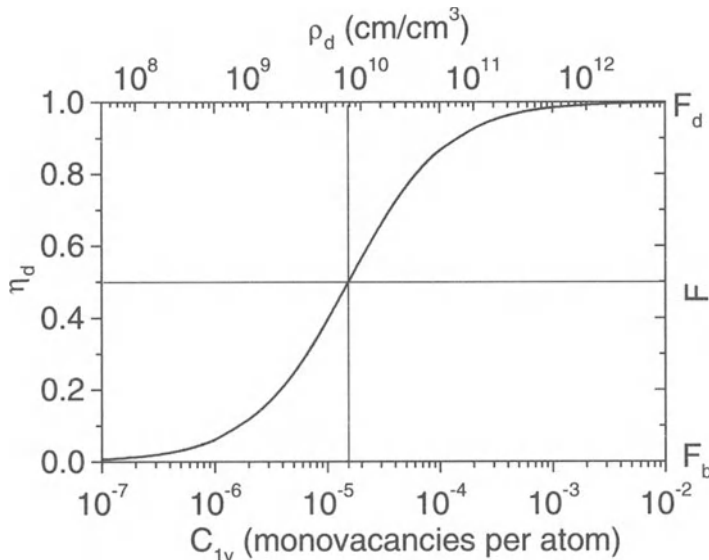


**Fig. 10.** Fraction of annihilation events from defects,  $\eta_d$ , and the annihilation parameters  $F (= S, W, \tau_{av})$  as a function of the density of monovacancies  $C_{1v}$  and dislocations  $\rho_d$

Both,  $I_2$  and  $\eta_d$  show a sigmoidal behavior when being plotted as a function of trapping rate or defect density, respectively. Figure 10 shows  $\eta_d$  as a function of the vacancy concentration  $C_{1v}$  ( $\mu_{1v} = 5 \times 10^{14}$  s<sup>-1</sup>at.,  $\tau_b = 130$  ps) as well as the dislocation density  $\rho_d$  (cm/cm<sup>3</sup>) ( $\mu_d = 1$  cm<sup>2</sup>s<sup>-1</sup>). The sensitivity of positron annihilation for vacancies ranges from  $5 \times 10^{-7}$  per atom to  $10^{-3}$  per atom. For dislocations the corresponding range is from  $\rho_d = 10^8$  to  $5 \times 10^{11}$  cm/cm<sup>3</sup>. That means that the sensitivity is below the detection limit for well annealed metals. The bulk parameters  $\tau_b$ ,  $S_b$ , and  $W_b$ , can be determined for these materials. At high defect densities positron trapping is saturated and the experimental parameters are identical to those characteristic for the trapping defect type ( $\tau_d$ ,  $S_d$ , and  $W_d$ ). In the intermediate range the annihilation parameters are determined by both the defect concentration and the characteristic annihilation parameters. Defect concentration may be estimated if bulk and saturation parameters and specific trapping rates are known. In case of fine-grained materials or compacted powders, positron trapping at grain boundaries or internal surfaces may become important. The trapping rate at internal surfaces can be estimated from  $\kappa_S = \pi^2 D_+ / R^2 = (\pi^2 / 2 \tau_b) (\Lambda_+/R)^2$  where  $R$  is the grain radius and  $\Lambda_+ = (2 \tau_b D_+)^{0.5} \approx 100$  nm the mean positron diffusion length. The lifetimes of trapped positrons correspond to those of vacancy clusters. This effect can be used to study sintering processes and other similar procedures [27].

## 14.4. Applications

Positron annihilation has shown its ability to solve a wide variety of characterization tasks for different classes of materials. Metals, semiconductors, ceramics and polymers were under consideration. The following paragraph will discuss topics like plastic deformation and fatigue of metals and weathering of polymer coatings that are of importance for aircraft applications.

### 14.4.1 Characterization of Plastic Deformation of Stainless Steel

The following experiments demonstrate the ability of positron annihilation spectroscopy (PAS) to characterize plastic deformation of metals. Densities of defects such as dislocations, vacancies and vacancy agglomerates that are formed during tensile tests have been correlated to the degree of plastic deformation. Tensile test specimens of stainless steel X6 CrNiNb 18 10 with a gauge length of 30 mm were produced and then annealed at 1050 °C for 110 min and subsequently water-quenched. The composition of the steel is: Cr 18.45, Ni 10.80, Mn 1.88, Nb 0.35, Si 0.22, C 0.026, P 0.009, and S 0.001, leaving the balance Fe (in weight-%). The specimens were repeatedly tensile strained in a testing machine. After each loading step positron annihilation measurements were taken at various stress ( $\sigma$ ) strain ( $\varepsilon$ ) intervals. The strain in the following figures is normalized to the fracture strain as illustrated in Fig. 11.

DBAR and PALS have been measured simultaneously. On a logarithmic scale the S-parameter increases almost linear for strains larger than 1% (Fig. 12). The initial 1% of strain might be elastic and do not generate plastic deformation. The average positron lifetime shows a similar behavior as the S-parameter. However, a change in slope was found for strains larger than 20%.

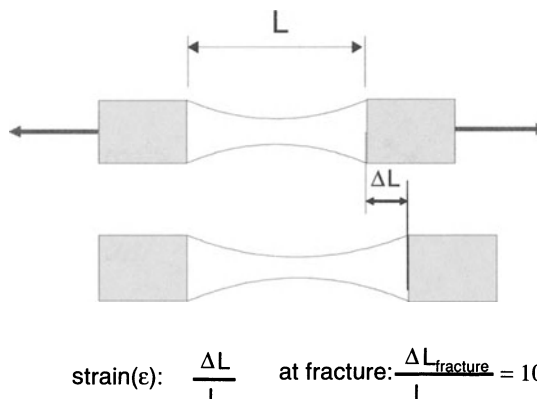


**Fig. 11.** Calculation of normalized strain values as given below in Figs. 12 and 13

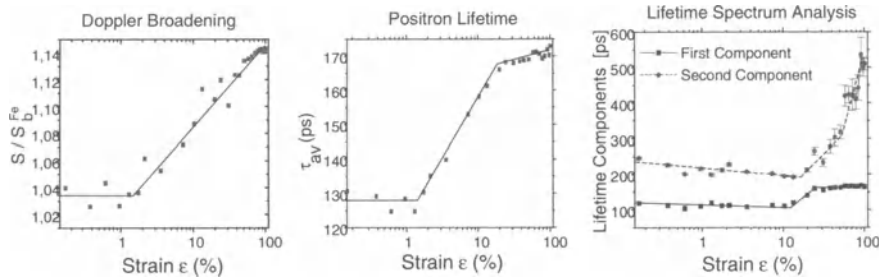


**Fig. 12.** PAS parameters of stainless steel as function of normalized strain

The positron lifetime spectra were decomposed into two discrete exponential components with the lifetimes  $\tau_{1,exp}$ ,  $\tau_{2,exp}$  and the intensities  $I_{2,exp}$ ,  $I_{1,exp} = 1 - I_{2,exp}$ . The time components can be compared to the average lifetime in Fig. 12. The following discussion will show that analysis of the lifetime spectra separates the information about different types of lattice defects and estimates the defect concentrations. Figure 13 shows the average positron lifetime  $\tau_{av}$  and the applied stress  $\sigma$  as a function of the normalized strain  $\epsilon = (\Delta L/L) / (\Delta L_{fracture}/L) * 100\%$  on a linear scale. The individual lifetimes  $\tau_{1,exp}$  and  $\tau_{2,exp}$  and the intensity  $I_{2,exp}$  are shown in Fig. 14a. For  $\epsilon = 0$ ,  $\tau_{av}$  amounts to 128 ps. This is larger than the pure iron bulk value,  $\tau_b = 105$  ps that can be attributed to positron trapping at defects. The value of  $\tau_{2,exp}$  of approximately 220 ps corresponds to annihilation of positrons at open-volume defects. These open volume defects have a size of approximately a

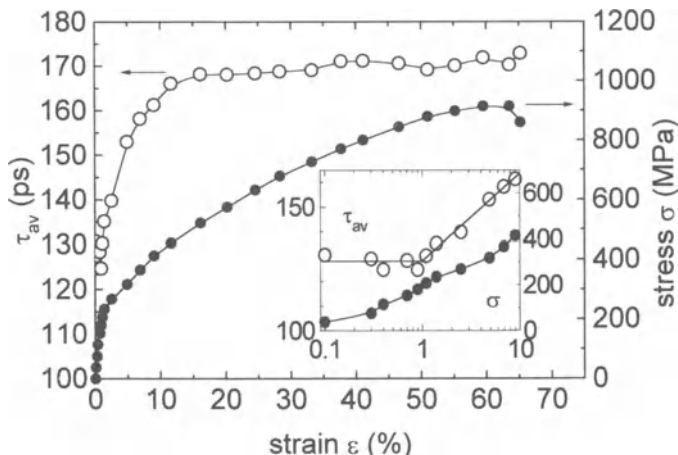


**Fig. 13.** Average positron lifetime  $\tau_{av}$  and stress  $\sigma$  as a function of the normalized strain  $\epsilon$  due to tensile straining of the stainless steel X6 CrNiNb

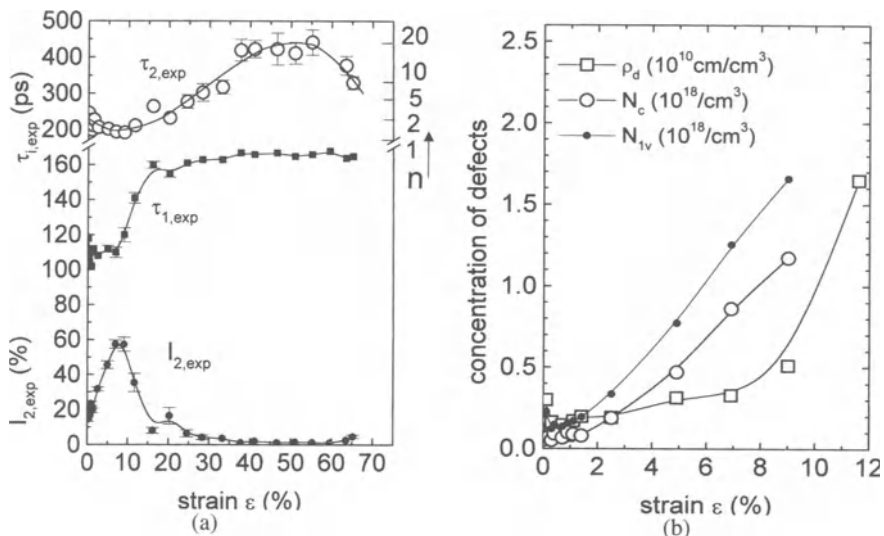


**Fig. 14.** (a) Lifetime parameters  $\tau_{1,\text{exp}}$ ,  $\tau_{2,\text{exp}}$ , and  $I_{2,\text{exp}}$  and, (b) defect densities as a function of the normalized strain  $\varepsilon$  due to tensile straining of the stainless steel X6 CrNiNb.  $n$  is the average number of vacancies contained in one vacancy cluster.  $\rho_d$  is the dislocation density,  $N_c$  is the concentration of vacancy clusters and  $N_{\text{lv}}$  denotes the total concentration of vacancies contained in the clusters.

divacancy. This effect is probably due to positron trapping at grain boundaries, interfaces of incoherent precipitates and at vacancy-impurity complexes.

The value of  $\tau_{1,\text{exp}}$  is 110 ps. This is somewhat larger than  $\tau_b$ . For strains higher than 8%,  $\tau_{1,\text{exp}}$  increases significantly. We assume that this increase is due to positron trapping by dislocations.  $\tau_{2,\text{exp}}$  reflects positrons annihilating at incoherent interfaces and small vacancy clusters (for instance for larger strain).

With these assumptions the positron trapping rates may be estimated from an extension of the one trap model (as discussed in the last paragraph) into a two-trap model (three-stages: bulk – b, dislocations – d, vacancy cluster – c). Three lifetime components appear as solution of the differential equations. However due to small separation between  $\tau_b = 105$  ps and  $\tau_d = 155$  ps these lifetimes merge into a single, mean value, while the larger lifetime can be separated from the experimental data ( $\tau_c = \tau_{2,\text{exp}}$ ). The trapping rate of dislocations,  $\kappa_d$ , and vacancy clusters,  $\kappa_c$ , can be calculated from the analyzed lifetime parameters.  $\kappa_c$  is required to calculate the number of vacancy clusters per  $\text{cm}^3$  by  $N_c = (\kappa_c N_a)/(n \mu_{\text{lv}})$ ,  $\mu_{\text{lv}} = 10^{15} \text{ s}^{-1}$ .  $N_a$  is the number of atoms in a  $\text{cm}^3$ . The average number of vacancies in a cluster ( $n$ ) (Fig. 14a) may be estimated from  $\tau_{2,\text{exp}}$  using the lifetime for trapped positrons. This was calculated for iron by Hautojärvi and Corbel 1995 as a function of the number of vacancies agglomerated in a cluster,  $\tau_c = f(n)$  [24]. The calculated variation of the defect concentration as a function of strain  $\varepsilon$  is shown in Fig. 14b. Here  $N_{\text{lv}}$  is the total number of vacancies in the clusters,  $N_{\text{lv}} = n N_c$ . The dislocation density was estimated from  $\rho_d = \kappa_d / \mu_d$ ,  $\mu_d = 0.1 \text{ cm}^2 \text{s}^{-1}$ .

### 14.4.2 Characterization of Fatigue in Ti-6Al-4V

#### ***Materials and Fatigue Conditions***

The material selected for this study is a forged Ti-6Al-4V plate. The microstructure that has been studied in this work was a duplex microstructure. This material has been very carefully prepared and processed. Precautions were taken to provide conditions which are as close as possible to the microstructure found in forged titanium alloy fan blades [28]. This duplex microstructure has about 50% equiaxed primary alpha phase and 50% fine lamellar transformed alpha plates.

In the case of Low Cycle Fatigue (LCF), the material was cycled well into the plastic zone to result in a fatigue life of 10,000–50,000 cycles [29]. This represents loading take-off conditions of jet engines that are typically at 100% engine output. The relatively low number of life cycles is compatible with the service life of both military and civilian turbojet engines. During such cycles, the material is undergoing plastic deformation that leads to generation, motion, and rearrangement of dislocations [30]. A maximum stress level of 850 MPa produced an average fatigue life of 34,545 cycles. The 850 MPa stress level was selected as the “working condition” for all LCF experiments.

For the fatigue damage generation, a Servo-hydraulic machine with capability of cycling at frequencies up to 100 Hz has been utilized. Fatigue specimens are cylindrical smooth samples with a grip diameter of 14mm and a gauge diameter of 7.5 mm.

#### ***Experiment***

A fatigued and cracked dogbone specimen of Ti-6Al-4V was cut into 1.5 mm slices. Spark cutting was used to obtain good surface quality (Fig. 15). For each measurement step the  $^{22}\text{Na}$  source was placed between two slices to obtain a sandwich arrangement. Positron lifetime spectra and Doppler broadening line width was measured simultaneously. Two time components were separated from lifetime spectrum. For slices with numbers higher than 10 the two component fit of the spectrum was not stable. This data might have large errors. Figure 16 summarizes the results [8, 31].

Positron lifetimes of about 150 to 160 ps are expected for annihilation in dislocations and lifetimes above 180 ps should indicate trapping in vacancy type defects.

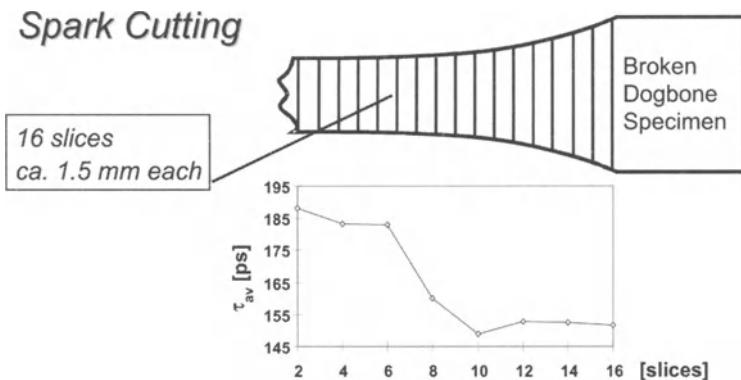


**Fig. 15.** Positron lifetime measurement at a sliced dogbone specimen

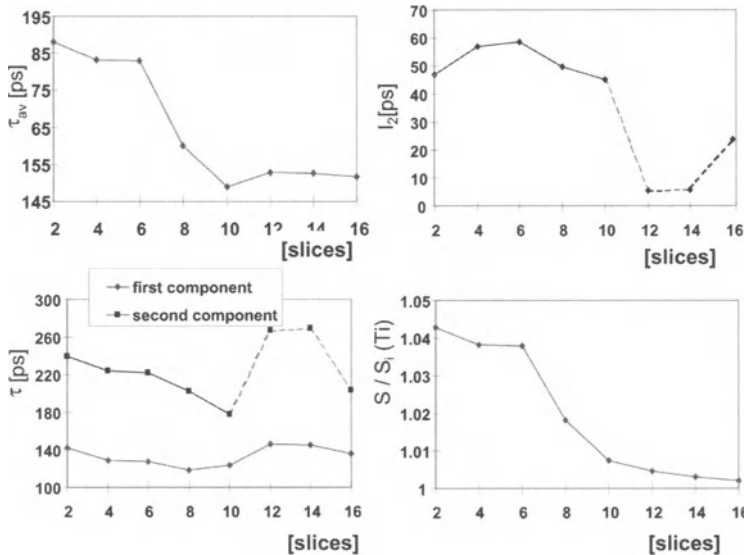


**Fig. 16.** Average positron lifetime (*upper left*) and Doppler broadening lineshape parameter "S" (*bottom right*) of a fatigued dog bone specimen of Ti-6Al-4V. Separation of two lifetime components (*bottom left*) and intensity of the longer component (*upper right*)

Close to the fracture (slices 1–7) the average positron lifetime was above 175 ps. For slices 9 and higher the average lifetime is lower than the lifetime for positrons annihilating in dislocations (155 ps). This indicates that not all positrons are trapped by lattice defects in these slices. This result corresponds to the expected fatigue damage within the length of the specimen. Vacancies or vacancy type clusters and dislocations are responsible for the high values of  $\tau_{av}$  in the most fatigued area close to the crack. There was no significant damage close to the grip section.

### Comparison of TEM and PAS

Transmission electron microscopy (TEM) was conducted on fractured fatigue samples to characterize the types and amounts of damage occurring in the material during the fatigue experiments (for details of the experiments see Ref. [32]). A LCF sample (which failed at 32,589 cycles) was sectioned into 2 mm slices up the gauge length away from the fracture surface thus providing graded imaging of the internal damage. The dislocation densities determined for the different sections of the fatigued specimen are shown in Fig. 17. They show a dramatic decrease away from the fracture surface. TEM photomicrographs taken of the fracture surface itself reveal extremely high levels of internal damage, such as extensive dislocation tangles in an equiaxed alpha region and dislocation buildup in a lamellar region of the material.

Figure 17 shows the result for a second PAS experiment with enhanced accuracy and smaller slices. The average positron lifetime  $\tau_{av}$  is compared to the dislocation density calculated from TEM results of a specimen that was fatigued under similar conditions.  $\tau_{av}$  follows closely the TEM results for medium deformation and can be used to calculate the dislocation density as long as positron trapping is not saturated. Larger dislocation density variations are not mirrored in  $\tau_{av}$ . This result establishes the finding in [33, 34] that the positron annihilation technique saturates for low amounts of fatigue damage. Therefore this technique is capable to characterize the very early stages of fatigue.

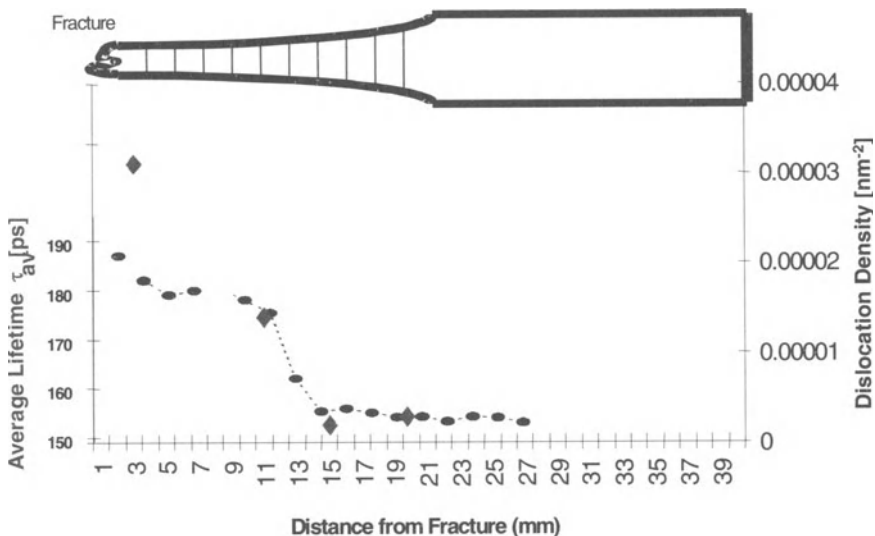


**Fig. 17.** Average positron lifetime (ellipses) in comparison to dislocation density determined by TEM (diamonds)

### 14.4.3 Precipitation Phenomena in Aluminum Alloys

PAS is an important non-destructive method for studying vacancies and dislocations in metals. In decomposed alloys positrons may be trapped by coherent zones, semicoherent precipitates and incoherent particles [25, 26]. The annihilation parameters describe the type of positron traps.

In Table 2 a collection of positron lifetimes  $\tau_i$  and DBAR curves shape parameters  $S_t$  for positrons trapped in aluminum alloys are shown [25, 37].  $\tau_i$  and  $S_i$  are specific for the type of positron traps and for the material. The electron density at a vacancy-type defect sensed by a positron is smaller than the average electron density in the bulk. This leads to an increase of the lifetime  $\tau_i$  of positrons trapped at vacancies or dislocations compared with their lifetime in the metal bulk  $\tau_b$ . Due to similar reasons the S-parameter increases. In case of coherent particles (e.g. Guinier-Preston zones)  $\tau_i$  and  $S_i$  depend on the type of precipitated metal and on the composition of the particle. Depending on the type of the precipitated metal, the annihilation parameters may increase or decrease when compared with pure Al. Coherent particles may contain vacancies in their interface or in interior regions. Positrons trapped first by the coherent particle get localized finally at the vacancy. The annihilation parameters mirror the open volume of the vacancy as well as its chemical surroundings. Positrons are localized at misfit dislocations of semicoherent precipitates and at the particle-matrix interface of incoherent particles.

**Table 2.** The characteristic positron lifetimes  $\tau_i$  and curve shape parameters  $S_i/S_{Al}$  of the Doppler-broadened annihilation line, which were normalized to the value of pure Al bulk, for various positron traps. a) pure metals: b – bulk, v – vacancy, d – dislocation; b) coherent and c) semi- and incoherent precipitates in Al alloys.

Metal	Al	b	v	d	Ag	b	v	Zn	b	v	Cu	b	v	Mg	b	v	Li	b	Si	b
$\tau_i$ (ps)	157	240	235	147	220	152		220	120	180	150	225	253	293		312	222		230	
$S_i/S_{Al}$	1	1.04	1.035	0.83	0.93	0.89		0.966	0.80	0.90		1.10	1.13				0.98		0.99	

Type of Particle	Coherent particle without vacancies				Coherent particle associated with vacancies			
Alloy	Al-Zn	Al-Ag	Al-Li		Al-Zn-Mg	Al-Sc	Al-Li-Sc	
Particle	GPZ	$\eta$ -GPZ	$\epsilon$ -GPZ	$\delta$ (Al,Li)	GPZ2	Al,Sc	$\delta$ (Al,Li)/Al,Sc	$\delta$ (Al,Li)/ $\beta$ (Al,Zr)
$\tau_i$ (ps)	155	146	156	185	220	225	225	245
$S_i/S_{Al}$	0.911	0.872	0.940		1.010			

Type of Particle	Semic coherent Precipitate						Incoherent precipitate		
Alloy	Al-Zn	Al-Ag	Al-Cu	Al-Cu-Mg	Al-Zn-Mg	Al-Li-Cu	Al-Li-Mg	Al-Si	Al-Ge
Particle	$\alpha'_R$	$\gamma'$ Ag, Al	$\Theta'$ Al,Cu	S' Al,CuMg	$\eta'$ Zn,Mg	T, Al,LiCu	Al,LiMg	Si	Ge
$\tau_i$ (ps)	240	225	192	240	240	255	235	230	225
$S_i/S_{Al}$	0.997	0.94	0.965	1.02	1.05			1.02	1.01

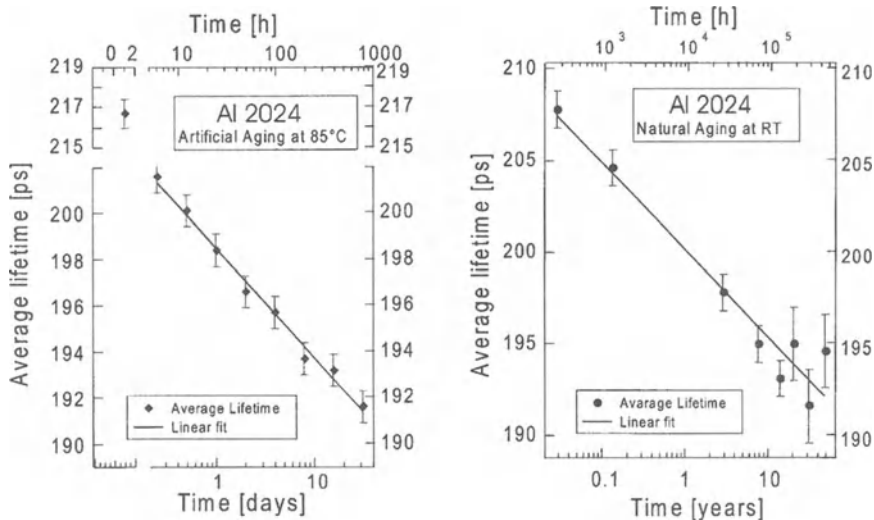


**Fig. 18.** Positron lifetime of artificially and naturally aged Al 2024 [35]

Again, the annihilation parameters reflect the dislocation-type of trap as well as its chemical surroundings. Generally, the lifetime  $\tau$  is more sensitive to the size of the open volume of a trap, while the parameter  $S$ , mirrors sensitively the chemical nature of the positron trap.

### Aging

Figure 18 shows results from Staab et al. for Al 2024 [35]. The specimens were homogenized at 550°C and then quenched. Aging causes coherent Guinier-Preston (GP) zones that are responsible for the excellent mechanical properties. Their large stress fields are barriers for dislocation movement and thus responsible for the high hardness. The positron lifetime varies almost exponentially with aging time (time scale in Fig. 18 is logarithmic) for both artificial aging at 85 °C or natural aging at room temperature. The average lifetime of 210 ps for the quenched specimens is close to the value for vacancies in Al. In accordance with the explanation given for Fig. 20 this might be caused by Cu stabilized vacancies. (Vacancies in pure Al disappear below room temperature.). The decrease of the positron lifetime can be explained by disappearance of the vacancies while Cu agglomerates in GP zones (also called  $\theta''$ -phase).

### **Heat Treatment of Al Alloys**

The following discussion will demonstrate that PAS is a powerful tool to analyze heat treatment processes in aluminum. This might be of importance for the development of aging and special heat treatment processes.

The variation in the average positron lifetime during decomposition of various aluminum alloys is shown in Fig. 19. We studied (i) the commercial alloys Al 2024 (impurities: Mn 0.3; Fe 0.3; Si 0.5; Cr 0.06 at.-%) and Al 7010 (impurities: Zr 0.03; Mn 0.05; Fe 0.05 at.-%), and (ii) some laboratory alloys prepared from aluminum 5N and 4N purity (Table 3). Each sample was solution treated at 500 °C for 3 hours and water-quenched. Following isothermal annealing treatments (1 hour each) positron annihilation (PALS and DBAR) measurements were conducted at room temperature [31].

**Table 3.** Composition (in atomic-%, balance Al) of the alloys under investigation

Notation	Zn	Cu	Mg
AlZn	4.5	—	—
AlZnMg	4.5	—	2.5
AlCu	—	1.9	—
Al 2024	—	2.0	1.7
Al 7010	2.7	1.0	2.7

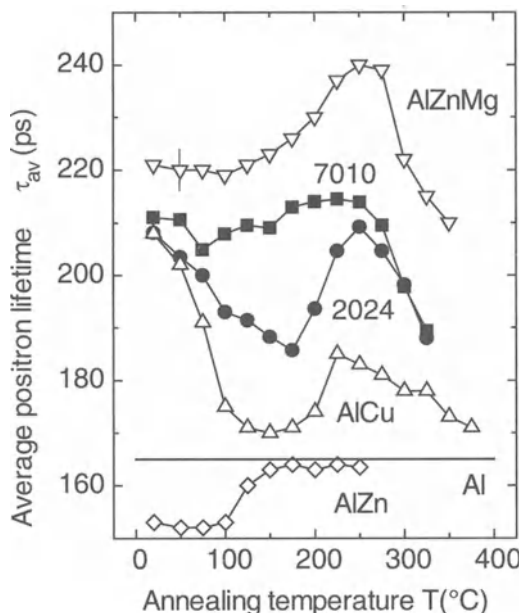


**Fig. 19.** Average positron lifetime versus the isothermal annealing temperature

**Al-Cu laboratory alloy:** The decomposition sequence in binary Al-Cu alloy is supersaturated solid solution  $\rightarrow$  Guinier-Preston (GP) zone  $\rightarrow \theta'' \rightarrow \theta' \rightarrow \theta$ . From atomprobe field ion microscopic studies (APFIM, see references given in Dlubek et al. 1998) it was concluded that the GP zones consist of several layers lying parallel on a {200} plane with compositions varying from 25 to 45 at.-% Cu. During aging the GP zones transform to  $\theta''$  particles which have nearly the same composition as the GP zones, but consist of Al-rich layers separated by Cu-rich layers.

In Fig. 20 the average positron lifetime  $\tau_{av}$ , the trapped positron lifetime  $\tau_t = \tau_2$  estimated from the two-exponential decomposition of spectra, the S-parameter, and the curve-shape parameter of trapped positrons,  $S_t$ , are shown.  $S_t$  was calculated from  $\eta_t$  according to (8) – second line, (*index d*  $\equiv$  *t*).  $\eta_t$  was estimated from the lifetime data via (8) – first line. The annihilation parameters of the as-quenched Al-Cu alloy are consistent with an almost complete positron trapping by quenched-in vacancies which are stabilized by single Cu atoms or by small clusters of Cu atoms,  $I_2 = 90\%$ . The positron lifetime of these vacancies ( $\tau_v = 204$  ps) are smaller than in pure Al,  $\tau_v(\text{Al}) = 240$  ps, due to the presence of Cu atoms in their surroundings,  $\tau_v(\text{Cu}) = 180$  ps (Table 2). This interpretation is confirmed by the value of  $S_t$  which is smaller than  $S_v^{\text{Al}}$  as well as the S-parameter of Al bulk ( $S_b^{\text{Al}} = S_{\text{Al}}$ ) due to the presence of Cu atoms (Table 2).

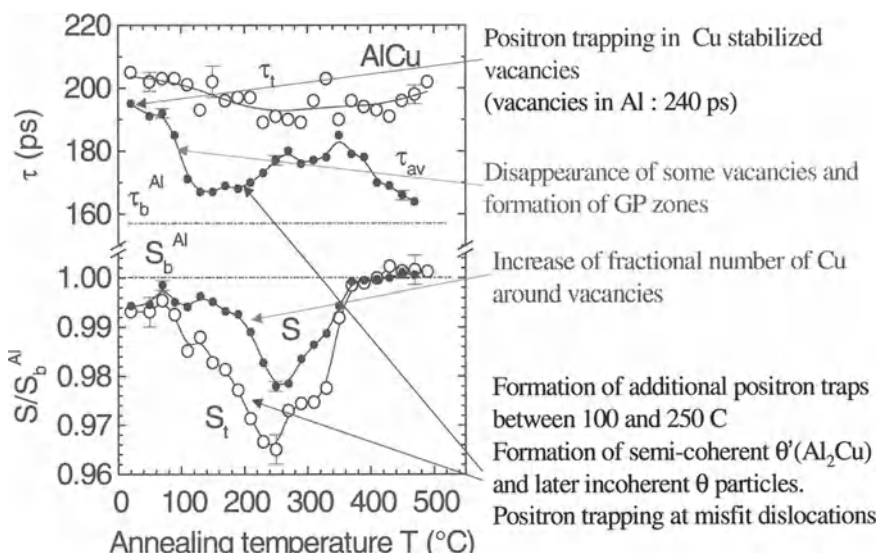


**Fig. 20.** Average positron lifetime  $\tau_{av}$  and S-parameter during aging of AlCu1.9 at. %. Shown are also the parameters of trapped positrons  $\tau_t$  and  $S_t$  and the bulk parameters  $\tau_b$  and  $S_b$

The explanations given in Fig. 20 for the variations of the measured and calculated PAS parameters are based on the comparison of both lifetimes and S-parameters to the values in Table 2. For details see [36]. The curves shown in Fig. 19 are there discussed in detail.

#### 14.4.4 Characterization of Polymers and Polymer Composites

##### ***Introduction***

Improvements in aircraft performance transpose into lighter, higher performance materials to reduce structural mass and to allow higher temperature capabilities. Presently, polymer composites reinforced with carbon, glass, or boron fibers are used in aircraft structures. High performance composites for the aircraft fuselage are under development. Monolithical polymers, polymer composites and polymers foams find wide application in secondary structures where low weight, toughness and durability have been the key issues. Currently used thermosetting epoxy and semi-thermoplastic polyimide materials have maximum operating temperature in excess of 200 °C.

There are many methods to test the characteristics of polymeric materials. To determine the microscopic structure of polymers PAS has been applied in the last decade to examine intermolecular-space characteristics. Polymers contain cavities or holes of atomic and molecular dimension which arise from irregular molecular packing in the amorphous phase (static and pre-existing holes) and molecular relaxation among the molecular chains and terminal ends (dynamic and transient holes). The appearance of holes lowers the density of the amorphous polymer by about 10% compared with the crystalline state of the same material. The holes form a (excess) free volume which effects thermal, mechanical and relaxation properties of polymers. The diffusion of small molecules (gases, organic and inorganic liquids, humidity) in polymers occurs through local free volumes [38].

Positron annihilation lifetime spectroscopy (PALS) is a well-established and very sensitive technique for probing sub-nanometer sized local free volumes in solids. In molecular materials such as polymers, a fraction of the injected positrons will form a bound state called positronium (Ps) [3]. The Ps appears either as a para-positronium (p-Ps, singlet spin state) or as a ortho-positronium (o-Ps, triplet spin state), with a relative abundance of 1:3. In vacuum, an o-Ps has a relatively long lifetime of 142 ns. When injected into matter, the positron of the Ps may collide with atoms or molecules and annihilate with an electron other than its bound partner that has opposite spin (pick-off annihilation). The result is a sharply reduced o-Ps lifetime depending on the collision frequency. Given a sufficiently large concentration of cavities in the sample, the Ps density is largely restricted to these open volumes. The o-Ps pick-off lifetimes, which are typically in the nanosecond range and can be evaluated to estimate the size of the cavities [39–44].

A simple model incorporating quantum-mechanical and empirical considerations provides an analytic expression relating the radius  $r$  of the hole (assumed to be spherical) to the observed o-Ps pick-off lifetime  $\tau_s = \tau_{po}$  [42–44],

$$\tau_3 = \tau_{\text{o-Ps}} = 0.5 \left[ 1 - \frac{r}{r + \delta r} + \frac{1}{2 \pi} \sin \left( \frac{2 \pi r}{r + \delta r} \right) \right]^{-1}. \quad (12)$$

The factor of 0.5 ns is the inverse of the spin-averaged Ps annihilation rate which is also observed in densely packed molecular crystals.  $\delta r$  represents the depth of the penetration of the Ps-wave function into the walls of the hole. This is modeled by a square-well potential of infinite depth and radius  $r+\delta r$ . A widely used value of  $\delta r = 0.166$  nm is obtained by fitting (12) to the observed o-Ps lifetime of known mean hole radii in porous materials [42–44]. Using (12), the mean hole radius  $r$  and the mean hole volume  $v_h = (4/3\pi)r^3$  can be extracted using  $\tau_3$  obtained from the lifetime analysis.

Some examples are given below for testing the polymer microstructure employing PALS.

### **Characterization of the Hole Volume in Epoxy Resin**

Epoxies are thermoset materials. They require polymerization to be generated in the base material by addition of a curing agent and, usually, application of an elevated temperature [45]. The material formed is set in its final shape. The properties of thermoset materials are profoundly affected by changes in the chemical structure and cure temperature. Variations in the glass transition temperature and in the specific volume may be related to differences in the type of the network generated during the cure.

In Fig. 21 the hole volume  $v_h$  of two different type of resins, dian diglycidyl ether (DDGE) and tetramethyl biphenol diglycidyl ether (TMDGE) cured with 4,4'-dihydroxybiphenol (BP) is shown as a function of the mole content  $x$  of curing agent [46]. The material was cured at 100 °C for 4 h. For low values of  $x$ , the mean hole sizes are in the range of 0.076 to 0.081 nm<sup>3</sup>. The hole sizes decrease with increasing  $x$  from 0.076 to 0.071 nm<sup>3</sup> in DDGE and from 0.081 to 0.065 nm<sup>3</sup> in TMDGE. The fractional hole volume,  $h = v_h N_h$ , may be estimated from the comparison of  $v_h$  with the macroscopic specific volume, this comparison delivers the number density of holes,  $N_h = 0.4$  nm<sup>-3</sup>. The  $h$  values are shown on the right wing y-scale of Fig. 21. With increasing content of curing agent the free (hole) volume decreases, the glass transition temperature decreases, and the hardness and the temperature capability increase.

The addition of modifier allows the controlled variation in the epoxy properties. When mixing the resin with a polymer before curing, an interpenetrating network will be formed. DDGE- polycaprolactone (PCL) mixtures were cured at 150 °C for 4 h. In Fig. 22 the elasticity modulus  $E$ , mass density  $\rho$ , and hole volume  $v_h$  are shown as a function of the content  $x$  of the PCL modifier [46].

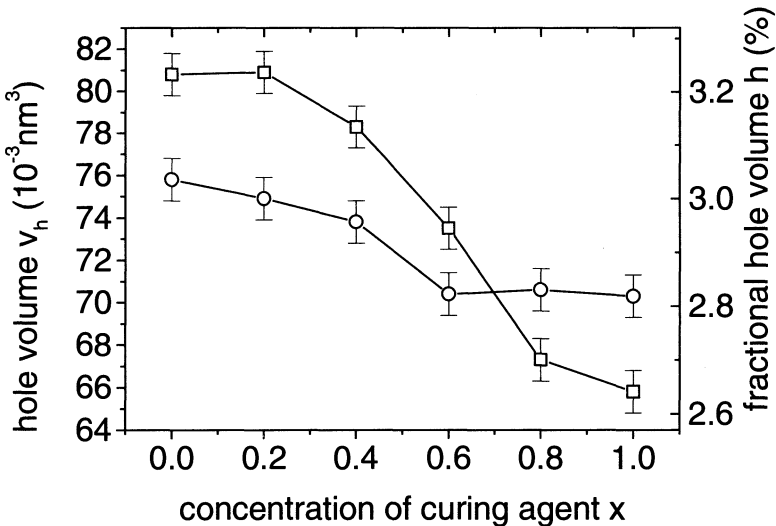


**Fig. 21.** Hole volume  $v_h$  and the corresponding fractional free (hole) volume  $h$  of two different type of epoxy resins (DDGE – circles, and TMDGE – squares) as a function of the concentration of the curing agent (BP). Composition: resin/curing agent/accelerator (2-methylimidazol) = 1:x:0.05 [46]

Increasing  $x$  will increase the mean hole volume resulting in a reduction in the mass density. Parallel to this, the glass transition temperature  $T_g$  decreases from 100 °C to 20 °C. The resulting effect is an increase in elasticity (decreasing elasticity modulus  $E$ ) as well as toughness. Depending on the use of the epoxy its properties are adjusted by mixing the resin with controlled amounts of modifier, hardener, and accelerator and by setting the curing time and temperature. All of these parameters have a distinct effect on the free volume hole size tested in PALS experiments [47–49].

Epoxyes are widely applied as adhesives, coatings, and in microelectronics as packaging components like glob top encapsulations, underfill materials, attachments and substrates. Optimizing the coefficient of thermal expansion, Young's modulus and other mechanical properties can minimize thermal stress and avoid package cracking during manufacturing and service conditions [50]. For this optimization, polymers can be mixed with filler of different thermal and mechanical properties. Typically, a powder of silica, which exhibits a very small coefficient of thermal expansion, is used as filler material of polymers for optimization of the coefficient of thermal expansion. To optimize the polymer-filler composite it is necessary to understand the thermal behavior of the free volume of the components forming the system and how the components interact with each other.

In Fig. 23 the mean o-Ps lifetime  $\tau_3$  and the average hole volume  $v_h$  estimated from  $\tau_3$  in differently filled epoxy materials are shown as a function of the ambient temperature [46]. The same epoxy was studied in an unmodified state as well as

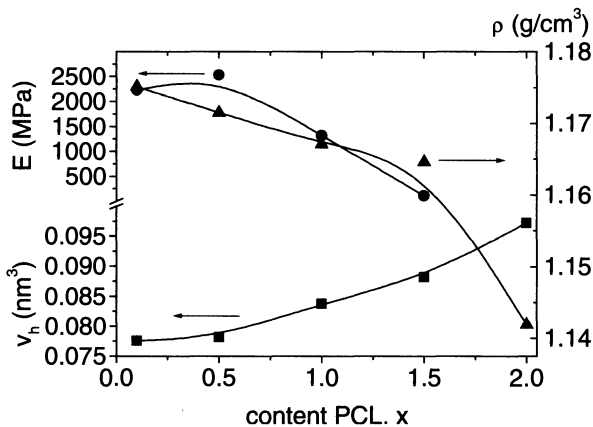


**Fig. 22.** Elasticity modulus  $E$ , mass density  $\rho$ , and hole volume  $v_h$  as a function of the mole content  $x$  of the modifier polycaprolactone (PCL). Composition: resin/ PCL/curing agent (2,4,6-DMP) = 1: $x$ :0.05 [46]

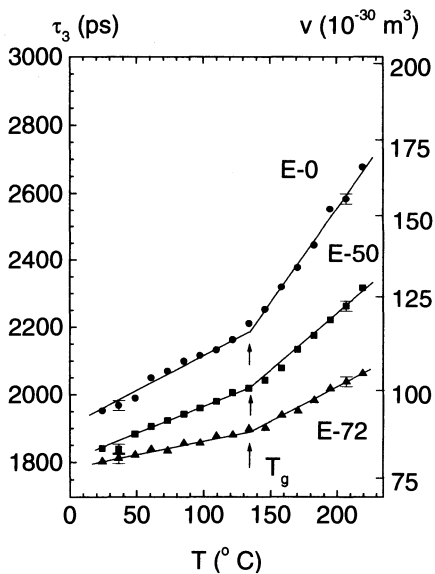


**Fig. 23.** The mean o-Ps lifetime  $\tau_3$  and the average hole volume  $v_h$  in epoxy filled with 50 wt-% (E-50) and 72 wt-% (E-72) silica and in the unmodified resin (E-0) as a function of the ambient temperature [46]

filled with two different contents of filler. A filler silica powder of a mean size of 50  $\mu\text{m}$  was used, and the samples will be referred by their filler content (in weight-%) as E-0, E-50, and E-72). The hole size shows a slight increase at temperatures below the glass transition temperature  $T_g = 135 (\pm 3)$  °C followed. There is a sharper increase in hole size above  $T_g$ .  $T_g$  can be estimated from the

intersection of two straight lines fitted to the data below and above  $T_g$ . Above  $T_g$ , the molecular and segmental motion increase and the free-volume holes obtain a dynamic character resulting in a more distinct increase of the holes size  $v_h$  with temperature  $T$  than below  $T_g$ .

The addition of silica powder to the epoxy reduces the thermal expansion in both the glassy ( $\alpha_g$ ) and rubbery ( $\alpha_r$ ) state of the polymer. Thermal-mechanical analysis shows that the coefficient of thermal expansion of macroscopic volume changes from  $\alpha_g/\alpha_r = 2.04 \times 10^{-4} \text{ K}^{-1}/5.46 \times 10^{-4} \text{ K}^{-1}$  for E-0 to  $1.16 \times 10^{-4} \text{ K}^{-1}/3.25 \times 10^{-4} \text{ K}^{-1}$  in E-50 and  $0.76 \times 10^{-4} \text{ K}^{-1}/2.20 \times 10^{-4} \text{ K}^{-1}$  in E-72. The coefficient of thermal expansion of the average hole volume,  $\alpha_{hg}$  and  $\alpha_{hr}$ , show a similar variation. However, they are by about one order of magnitude larger than  $\alpha_g$  and  $\alpha_r$ . This indicates that the fractional free (hole) volume(h) has a value of approximately  $h = 1/10$ . The decreases in these coefficients are due to the mixture of the epoxy with the glass. The glass has a disappearing coefficient of thermal expansion. The interesting question arises whether there is an interaction between the two phases of the filled epoxy. Other than dilatation experiments, PAS allows to separate the o-Ps lifetimes of the silica filler ( $\tau_{3,s}$ ) and the epoxy ( $\tau_{3,e}$ ). The results of this separation (four-term analysis of positron lifetime spectra) are shown in Fig. 24.

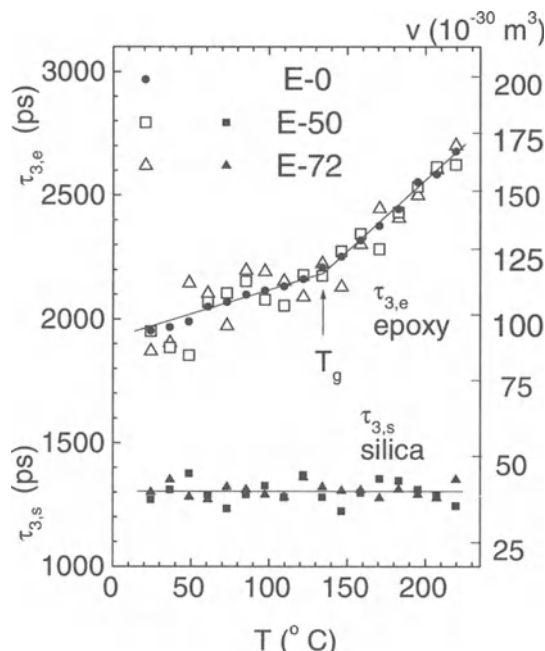


**Fig. 24.** As in Fig. 3, but the o-Ps lifetimes of the epoxy matrix,  $\tau_{3,e}$ , and the silica filler,  $\tau_{3,s}$ , separated via a constrained four-exponential fit of the lifetime spectra [46]

In all of the epoxies  $\tau_{3,s}$  has a value of 1.30 ns ( $v_h = 0.040 \text{ nm}^{-3}$ ) while  $\tau_{3,e}$  shows a variation between 2.0 to 2.7 ns ( $v_h = 0.10 - 0.17 \text{ nm}^{-3}$ ). The results show that in this case there is no interaction between two phases and no effect of interfaces on the thermal properties of the filled epoxies. A similar result was found for carbon-fiber-filled epoxy resins [51]. However, in nano-sized silica dispersed epoxy, an increase of the o-Ps lifetime with content of silica and a decrease with content of particle-matrix coupling agent has been observed [52]. This indicates the sensitivity of o-Ps annihilation to interface-related free volumes in very finely dispersed systems.

### **Characterization of Humidity Sorption of Polyimides**

Polyimides have found widespread application in different fields owing to their superior mechanical and dielectric properties, coupled with excellent thermal stability and chemical resistance, [53]. For aircraft construction the maximum operating temperature in excess of 200 °C is of special interest. Other important applications are as insulating layers in microelectronic device fabrication. A major drawback of these polymers is their hygroscopic nature, which results in the absorption of up to 5% moisture under ordinary environmental conditions. The moisture absorption leads to swelling of the material, thus degrading its mechanical and insulating properties. The exact mechanisms that govern humidity induced water uptake and diffusion of water molecules within the material are still unclear. It is generally assumed that both sorption and swelling behavior are closely related to the free-volume properties of the polyimide which can be studied by PALS.

The following example shows a study of the humidity sorption from the ambient atmosphere of the polyimide 6FDA-ODA (hexafluoropropane dianhydride-diaminodiphenyl ether, the Pyralin series from DuPont®) [54]. It has been observed that the o-Ps lifetime  $\tau_3$  and intensity  $I_3$  decrease with increasing humidity of the ambient atmosphere. This was interpreted as trapping of water molecules by holes of the free volume and blocking of these holes for Ps formation. PALS results correlated with humidity-induced mass uptake and volume expansion support a model according to which water absorption in polyimides occurs in two stages.

At relative humidity smaller than about 30%, water is absorbed mostly in large, pre-existing holes, with each hole typically occupied by a single water molecule. Increasing the humidity increases the fraction of the sorbed water molecules will occupy sites other than pre-existing empty holes.

When the polyimide samples are exposed to an atmosphere of given humidity, the PALS parameters  $\tau_3$  and  $I_3$  change as a function of exposure time. In Fig. 25 the average positron lifetime  $\tau_{av}$  which is controlled by the term  $I_3\tau_3$  is plotted as a function of the square root of measurement time in the ambient atmosphere,  $\sqrt{t_m}$ . Before measurements, the samples were exposed over a period of one month to an atmosphere of controlled humidity RH.

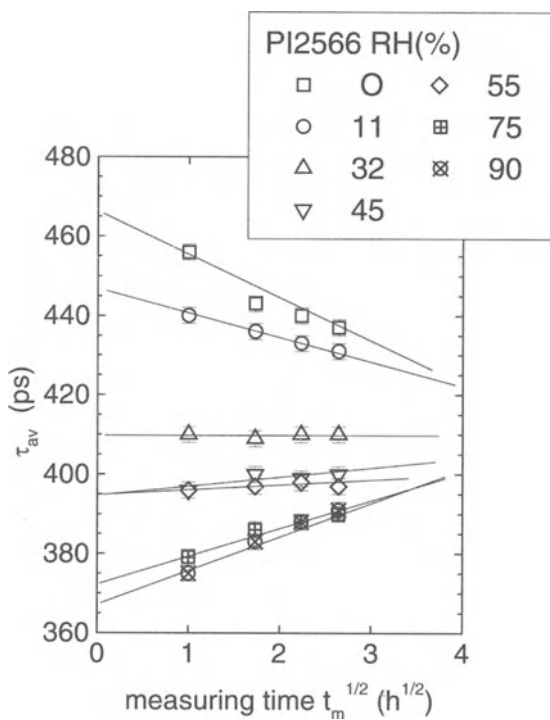


**Fig. 25.** Average positron lifetime  $\tau_{av}$  in polyimide PI2566 samples exposed to different RH before measurements as a function of the square-root of measuring time  $\sqrt{t_m}$  in ambient atmosphere

The observed behavior of  $\tau_{av}$  is attributed to water desorption from the samples (RH > 30%) and water sorption into the samples (RH < 30%) during the measurement. Only those samples that are exposed to a humidity equal to that of the laboratory atmosphere (~30%RH, 25 °C) are in a steady state condition during the measurement.  $\tau_{av}$  decreases or increases linearly with  $\sqrt{t_m}$  which serves as evidence for the validity of Fick's law of diffusion. In general, the results show that PALS may be used as detector for the amount of humidity absorbed by a polymer and for detecting structural changes caused by the humidity sorption.

#### 14.4.5 Characterization of Polymer Coatings

The durability of protective polymer coatings is of primary concern for their structural applications [55]. Environmental degradation from moisture, light, weather, fluids and mechanical processes reduces the service life of coatings. It has been recently shown that slow positron beam techniques are very successful

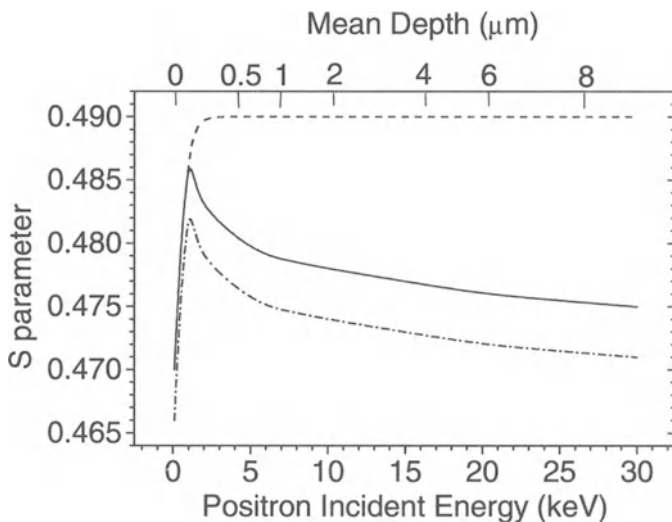


**Fig. 26.** Illustration of typical  $S$  parameter depth profiles for a pure polymer (dashed line), a polymer with  $\text{TiO}_2$  pigments (solid line) and the latter one after cyclic loading with more than 5 million cycles (dot-dashed line)

in monitoring the early stages of degradation of polymer coatings caused by artificial [56–59] and natural [60] weathering. Slow positron beam techniques have been used to track the degradation of polyurethane films due to UV radiation [57, 58] and xenon light radiation [59, 61]. It has been shown that the depth profiling ability of the slow positron beam on the polymer coatings allows the determination of kinetic data of the degradation process as a function of both time and depth from the surface. This is achieved by the correlation of the parameters of positron lifetime spectra (PALS) or of the  $S$  parameter of the Doppler-broadened annihilation radiation (DBAR), as a function of time and depth. The positron results show that sub-nanometer parameters, such as free hole volumes provide important information about the physical and chemical origins of deteriorations [56–63].

Figure 26 illustrates the changes of DBAR  $S$  parameter as function of the incident positron energy. These relations are typically observed for polymers without pigments and with  $\text{TiO}_2$  pigments and the latter one after mechanical loading [56–63]. The initial increase in the  $S$  parameter close to the surface of the pure polymer is due to back scattering and diffusion of the positrons and Ps (positronium) to the surface at very small implantation depths. Positron- and Ps-annihilation at the surface leads to a small  $S$  parameter value. With increasing positron energy this fraction decreases and annihilation in the polymer layer dominates. The result is the observed increase of the  $S$  parameter and leveling-off of  $S$ . However, this depends on the chemistry of polymer. While an increase of  $S$  has been observed for polyurethanes and epoxies, the  $S$  parameter of other polymers may be constant (polyimides) or decrease (polytetrafluoroethylene) [61].

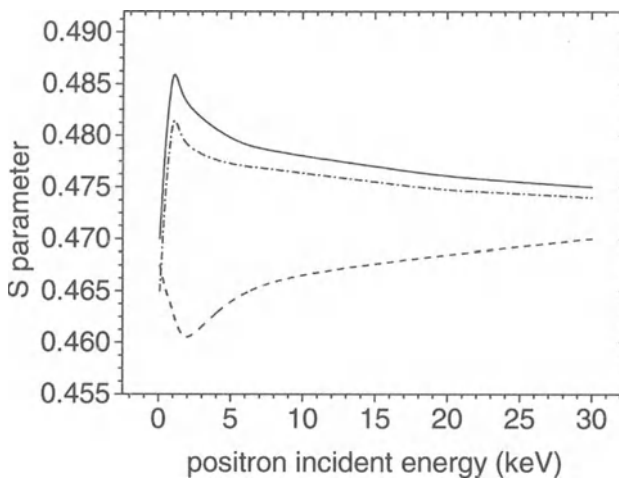


**Fig. 27.** Illustration of typical  $S$  parameter depth profiles for a polymer with  $\text{TiO}_2$  pigments without (solid line) and after natural weathering for 6–8 weeks (dash-dotted line) and 16 weeks (dashed line)

The variation of the  $S$  parameter for the polymer containing  $\text{TiO}_2$  pigments is strongly affected by the pigments.  $\text{TiO}_2$  leads to inhibition of Ps formation resulting in the observed reduction of  $S$ . Evidence for this was found in slow positron beam experiments combined with PALS [57]. The variation of  $S$  is attributed to a concentration gradient of the pigments from the surface toward the bulk. Aircraft and bridge coatings are multi-layered systems. Each layer is a complex mixture of polymers, solvents, pigments, stabilizers, binding agents, and other additives used to achieve desired properties. Cao et al. [57] observed a three-layer depth profile of the  $S$  parameter in the aircraft topcoat MIL-C-85285-B: a surface polymer skin layer, an intermediate layer and the bulk.

Figure 26 illustrates that the cyclic loading of polymer- $\text{TiO}_2$  topcoats leads to a lowering of the  $S$  parameter [63]. The lowering increases with the number of cycles, but is almost independent of the incident positron energy (independent of the depth from where the signal comes from). The lowering is interpreted as due to a loss of free volume during cyclic loading of the coating. Polymer molecules tend to align under tensile stress as end chains move to fill some available free volumes. The decrease of the free volume of the coatings leads to a loss in its viscoelastic properties and an increase in brittleness of the material. Eventually, coatings lose their durability and protective functions for structural applications.

In Fig. 27 typical changes in the  $S$  parameter of polymer- $\text{TiO}_2$  topcoats due to artificial or natural weathering are shown [60]. Natural weathering leads to a decrease of the  $S$  parameter. The decrease is attributed to a loss of free volume due to degradation of the coatings. In the case of polyurethanes loss of free volume due to increasing cross-linking of the polymer during irradiation with UV radiation and xenon light radiation has been observed [62]. The decrease progresses with increasing exposure time to the natural weathering (for 1 to 8 weeks). Different than for cyclic loading the decrease in  $S$  now depends upon the

depth below the surface. The degradation is most pronounced near the surface and decreases progressively inside the bulk. This behavior can be used for studying kinetic data of the degradation as function of the depth below the surface [59]. For long-term weathering the depth profile of the  $S$  parameter may show at the beginning a strong decrease followed by a moderate increase (Fig. 27).

In conclusion, slow positron beam techniques are able to detect the very early stages of degradation of polymer coatings. For example for natural weathering, significant changes are observed as early as one week after starting the weathering procedure. Another application of the techniques is the study of microstructural modifications of polymers and metals due to various surface treatments. Examples of this are, the modification of near surface regions in polyimides by ion radiation [64] and of X6CrNiTi1810 stainless steel nitrided by plasma immersion ion implantation [65]. Other groups studied the changes of a polymer/metal interfaces under stress [66], the corrosive breakdown of passive films on titanium [67], and the pore formation in anodic layers on aluminum [68].

## References

1. Dupasquier A, Mills AP Jr. (eds) (1995) *Positron Spectroscopy of Solids*. Proc. of the Int. School of Physics "Enrico Fermi", Course CXXV, Varenna 6–16 July 1993, Amsterdam: IOS Press
2. van Veen A, Corbel C, Mijnarends PE (eds) (1995) *Europhysics Industrial Workshop EIW-12, Industrial Applications of Positron Annihilation*. Oisterwijk, The Netherlands 10–12 March 1994, *J de Physique IV*, vol 5, Colloque C1, Supplementa No 1
3. Mogensen O E (1995) *Positron Annihilation in Chemistry*. Springer-Verlag: Berlin, Heidelberg
4. Krause-Rehberg R, Leipner HS (1999) *Positron Annihilation in Semiconductors*. Springer Verlag: Heidelberg
5. Ito Y, Suzuki T, Kobayashi Y (eds) (2000) Proc of the 6th Int. Workshop on Positron and Positronium Chemistry (PPC-6), *Radiat Phys and Chem* 58:401–795
6. Triftshäuser W, Kögel G, Sperr P, (eds.) (2001) Proc 12th Int Conf on Positron Annihilation, *Mat Sci Forum* 363–365:1
7. Brauer G, Awand W (2002) SLOPOS-9, Proc. of the 9th Int. Workshop on Slow-Positron Baam Techniques for Solids and Surfaces, Dresden, *Appl. Surface Science* 194:1
8. Somieski B, Sourkov A, Maurer JL, Meyendorf N (2002) *Positron Annihilation Spectroscopy and Transmission Electron Microscopy for Characterization of Lattice Defects in Fatigued Metals*. In: Meyendorf N (ed) Final Report: Development of Enabling Methodologies for Detection and Characterization of Early Stages of Damage in Aerospace Materials. AFOSR Grant No F49620-96-1-0442 pp. 286–298
9. Somieski B, Krause-Rehberg R, Salz H, Meyendorf N (1995) In: *J de Physique IV*, vol 5, Colloque C1, Supplementa No 1:C1–127
10. Allen AJ, Coleman CF, Conchie SJ, Smith FA, Holbrook J, Bussière J (eds) In: *Nondestructive Monitoring of Materials Properties*, Symposium Proceedings, vol 142, Materials Research Society, p. 131
11. Rytölä K, Nissilä J, Kokkonen J, Laasko A, Aavikko R, Saarinen K (2002) *Appl Surface Science* 194:260
12. Drubek G, Brümmer O, Meyendorf N (1979) *Vacancy Impurity Binding Enthalpy in NiSb by Means of Positron Annihilation*. *phys stat sol (a)* 53:K157–160
13. Akers DW, Denison AB, Harmon F (2002) *Appl Surface Science* 194:245
14. Kirkegaard P, Pedersen NJ, Eldrup M (1989) Report RISØ-M-2740, Riso Mational Laboratory, Roskilde, Denmark
15. LIFSPECFIT 5.1, Lifetime spectrum fit version 5.1, Technical University of Helsinki, Laboratory of Physics, 1992
16. Kansy J (1996) *Nucl Instr and Meth A*:374, 235
17. GREGORY RB, Y. ZHU Y (1990) *Nucl Instr and Meth A* 290:172
18. SHUKLA A, PETER M, HOFFMANN L (1993) *Nucl Instr and Meth A* 335:310
19. Schultz PJ, Lynn KG (1988) *Rev Mod Phys* 60:701
20. Vehanen A (1989) In: Dorikens-Vanpraet L, Dorikens M, Segers D (eds.) *Positron Annihilation*. Proc. 8th Int. Conf., Gent, Belgium, World Scientific, Singapore, p. 39
21. Sperr P, Kögel G (1987) *Mater Sci Forum* 255–257, 109
22. Greif H, Haaks M, Holzwarth U, Männig U, Tongbhoyai M, Wider R, Maier K, Bihl J, Huber B (1997) *Appl Phys Lett* 71:2125
23. Kögel GI (2002) *Appl Surface Science* 194:200.
24. Hautojärvi P Corbel C (1995) *Positron Spectroscopy of Defects in Metals and Semiconductors*. In: Dupasquier A, Mills AP Jr. (eds.) *Positron Spectroscopy of Solids*. Proc. of the Int. School of Physics "Enrico Fermi", Course CXXV, Varenna 6–16 July 1993, Amsterdam: IOS Press, pp. 491

25. Dlubek G (1987) Positron Studies of Decomposition Phenomena in Al Alloys. In: Proc. 4th Int. Conf. on Age-hardenable Aluminium Alloys, Balatonfüre, Hungary, 26–30 May, 1986, Mat. Sci. Forum 13/14, p. 15
26. Dupasquier A, Folegati P, de Diego N, Somoza A (1998) J Phys: Condens. Matter 10: 10409
27. Staab TEM, Krause-Rehberg R, Kieback B (1999) J Mat Sci 34:3822
28. Eylon D (1998) Summary of the Available Information on the Processing of the Ti-6Al-4V HCF/LCF Program Plates. Report prepared for the PRDA V Meeting, San Antonio, TX
29. Eylon D, Bartel TL, Rosenblum ME (1980) High Temperature Low Cycle Fatigue in Beta Processed Ti-5Al-5Sn-2Zr-2Mo-0.25Si. Metallurgical Transactions A 11A: 361–1367
30. Eylon D, Bania PJ (1978) Fatigue Cracking Characteristics of Beta-Annealed Large colony Ti-11 Alloy. Metallurgical Transactions A, 9A:1273–1279
31. Depetasse S, Meyendorf N, Dlubek G, Krause-Rehberg R, Sourkov A (1999) Positron Annihilation as a New Method to Characterize Different Heat Treated Aluminum Alloys such as the Deformation and Fatigue States of Austenitic Steels (German) Proceedings of DACH Annual Conference 1999, Celle
32. Maurer JL (2002) Characterization of Accumulated Fatigue Damage in Ti-6Al-4V Plate Material Using Transmission Electron Microscopy and Nonlinear Acoustics. Ph.D. theses, University of Dayton
33. Somiesky B (1997) Positron Annihilation as Method for Nondestructive Testing. Ph.D. Theses, Universitaet des Saarlandes
34. Depetasse S (1999) Studium der Entmischungsvorgänge in ausgewählten Aluminiumlegierungen mit der Positronenannihilationsmethode. Master Thesis, IZFP Saarbruecken
35. Staab TEM, Zschech E, Krause-Rehberg R, Positron lifetime measurements for characterization of nano-structural changes in the age hardenable AlCuMg 2024 alloy, Journal of materials science 35(2000):4667–4672.
36. Dlubek G, Depetasse S, Sourkov A, Meyendorf N (1999) Positron Annihilation Studies of Precipitation in Aluminum Alloys. 20th Riso Interantional Symposium on Materials Science, Roskilde, Denmark, pp. 313–319
37. Dlubek G, Lademann P, Krause H, Krause S, Unger R (1998) Positron lifetime studies of decomposition in 2024 and 7010 alloys. Scripta Mater 39: 893–899.
38. Prez J (1998) Physics and Mechanics of Amorphous Polymers. Balkema AA, Rotterdamm, Brookfield
39. Jean YC (1990) Microchem J 42:72
40. Jean YC (1995) Positron Annihilation, Proc. 10th Int Conf He YJ, Cao BS, Jean YC (eds) Mat Sci Forum 175–178, Trans Tech Publ :59.
41. Pethrick R A (1997) Progr Polym Sci 22: 1.
42. Tao SJ (1972) J Chem Phys 56:5499
43. Eldrup M, Lightbody D, Sherwood JN (1981) Chem Phys 63:51
44. Nakanishi H; Jean YC (1988) In: Schrader DM, Jean YC (eds.) Positron and Positronium Chemistry, studies in physical and theoretical chemistry. 57, Elsevier Sci. Publ. Amsterdam, p. 159
45. Ellis B (1993) Chemistry and Technology of Epoxy Resins, Chapman & Hall,
46. Dlubek G private communication.
47. Deng Q, Zandiehnadem F, Jean YC (1992) Macromolecules 25:1090
48. Ueda E, Uedono A, Ajiihira Y, Yamashita S, Naito T, Horie K (1992) In: Positron Annihilation, Proc. 9th. Int. Conf., Kajcsos Zs, Szeles C (eds.) Mat Sci Forum :105–110;1745
49. Suzuki T, Oki Y, Numajiri M, Mira T, Kondo K, Ito Y. Polymer 1993;34:1361
50. Lupinski JH, Moore RS (1988) Polymeric Materials for Electronics Packaging and Interconnection, ACS Symposium Series 407, California

51. Dale JM, Hulett LD, Rosseel TM (1987) *J Appl Polym Sci* 33:3055
52. Nishijima S, Honda Y, Tagawa S, Okada T (1996) *J Radioanal & Nucl Chem* 211; No. 1:93
53. Ghosh K; Mittal KL (1996) *Polyimides, Fundamentals and Application.* Marcel Dekker, Inc.: New York
54. Dlubek G, Buchhold R, Hübner CH, Nakladal A (1999) *Macromolecules* 32:2348
55. Clough RL, Billingham NC, Gillen KT (eds) (1996) *Polymer Durability: Degradation, Stabilization and Lifetime Predictions.* *Adv Chem Ser* 349, Am Chem Soc, Washington, DC
56. Hulett LD Jr., Wallace S, Xu J, Nielsen B, Scales CS, Lynn KG, Pfau J, Schaub A (1995) *Appl Surf Sci* 85:234
57. Cao H, Zhang R, Sundar CS, Yuan JP, He Y, Sandreczki TC, Jean YC (1998) *Macromolecules* 31:6627
58. Cao H, Yuan JP, Zhang R, Huang CM, He Y, Sandreczki TC, Jean YC, Nielsen B, Suzuki R, Ohdaira T (1999) *Macromolecules* 32:5925
59. Cao H, He Y, Zhang R, Yuan JP, Sandreczki TC, Jean YC, Nielsen B (1999) *J Polym Sci Part B: Polym Phys* 37:1289
60. Mallon PE, Li Y, Zhang R, Chen H, Wu Y, Sanreczki TC, Jean YC, Suzuki R, Ohdaira T (2002) *Appl Surf Sc* 194:176
61. Zhang R, Cao H, Chen HM, Mallon P, Sandreczki TC, Richardson JR, Jean YC, Nielsen B, Suzuki R, Ohdaira T (2000) *Radiat Phys Chem* 58:639
62. Zhang R, Mallon PE, Chen H, Huang CM, Zhang J, Li Y, Wu Y, Sandreczki TC, Jean YC (2001) *Prog Org Coat* 42:244
63. Chen H, Peng Q, Huang YY, Zhang R, Mallon PE, Zhang J, Li Y, Wu Y, Richardson JR, Sandreczki TC, Jean YC, Suzuki R, Ohdaira T (2002) *Appl Surf Sc* 194:168
64. Dlubek G, Börner F, Buchhold R, Sahre K, Krause-Rehberg R, Eichhorn KJ (2000) *J Polym Sci Part B: Polym Phys* 38:3062
65. Jirásková Y, Brauer G, Schneeweiss O, Blawert C, Anward W, Coleman PG (2002) *Appl Surf Sc* 194:145
66. Escoba Galindo R, van Veen A, Alba Garcia A, Schut H, DE Hosson JM (2001) In: Triftshäuser W, Kögel G, Sperr P (eds) (2001) *Proc 12th Int Conf on Positron Annihilation, Mat Sci Forum* 363–365:1, p. 499
67. Dull TL, Frieze WE, Gidley DW, Scherer GB, Ellerbrock DJ, Macdonald DD (1997) *Mater Sci Forum* 255–257:671
68. van Hoecke T, Segers D, Schut H, Dauwe C, van Veen A, van Waeyenberge B, Palfy L (1997) *Mater Sci Forum* 255–257:724

# Index

- Absolute Nonlinearity Parameter, 229
- Absorption Bands, 251
- Absorption Measurement, 238
- Acoustic
  - Absorption, 2
  - Imaging, 294
  - Impedance, 299
  - Microscopy, 8, 14
  - Reflectivity, 8
  - Testing, 294
  - Waves, 295
- Active Thermal NDE, 253
- AFM Scratching, 341, 350
- Aging, 396
- Aircraft Coatings, 286
- Al 2024, 396
- Al 2024-T3, 342, 346, 347
- Al–Cu Laboratory Alloy, 398
- Aluminum Alloys, 395
- Amplitude and Phase Images, 253
- Amplitude Ratio, 220
- Artificial Neural Networks, 4
- A-Scan, 235
- Asynchronous Time-Averaging, 185
- Atmospheric Windows, 251
- Atomic Force Microscope, 323, 324
- Atomic Force Microscopy, 2
- Attenuation, 218, 225, 228, 234
- Automated Scanning Electrode Technique, 288
- Axial Birefringence, 368
- Backscattered Ultrasonic Echo, 194
- Brightness, 69
- B-Scan, 300
- Cantilever, 324
- Cantilever Deflection, 324
- Capacitive Detector, 210
- CCD Cameras, 252
- Characterization of Corrosion, 304
- Characterization of Fatigue, 392
- Coating Substrate Interface, 8
- Coating Thickness, 8
- Coating Weathering Evaluation, 316
- Coffin–Manson Relation, 279
- Coherent Zones, 395
- Constructive Superposition, 123
- Contrast Sensitivity, 73
- Copper Grains, 338
- Copper Thin Film, 333
- Corner Crack Model, 148
- Corrosion, 9, 29, 294
  - Fatigue, 12
  - Growth, 105
  - Pits, 2, 38
  - Protection, 286
  - Protective Coatings, 5, 7, 297, 313
- Crack
  - Closure, 164
  - Damage, 47
  - Growth, 18, 46
  - Initiation, 17
  - Nucleation, 16
  - Propagation Model, 151
  - Size Determination, 170
  - Tip, 47
- Crack-Closure, 182
- Crack-Depth Determination, 133
- Crevice Corrosion, 9
- Critical Crack Length, 16
- C-Scan, 300
  - Images, 307
- Cyclic Mechanical Loading, 206
- Damping Coefficient, 279, 281
- DBAR Spectroscopy, 380
- Deformation Field, 29
- Degradation, 5, 7
- Delamination, 6, 8, 313
- Depth Profiling, 8
- Detectability, 69
- Diffraction Limit, 366
- Dislocation, 391
  - Density, 2
- Dissipated Heat, 250, 262, 277
- Dogbone Specimen, 216
- Doppler-Broadened Annihilation Radiation, 375, 380
- Dye Penetrant Testing, 2
- E×B Filter, 381
- Elastic Modulus, 299
- Elastic Properties, 327
- Elasticity Contrast, 329

- Electrochemical Impedance Spectroscopy, 286  
 Electrochemical Techniques, 286  
 Epoxy Coating, 339  
 Exfoliation, 14
- Fan Thermography, 7, 257, 258, 259  
 Fast-Fast Positron Lifetime Spectrometer, 377  
 Fatigue, 2, 15, 206  
 – Characterization, 269, 272  
 – Crack, 13, 91  
 – Crack Generation, 41  
 – Crack Growth, 147  
 – Damage, 206, 209  
 – Life, 18, 58, 70, 174, 281  
 – Life Prediction, 172  
 – Tests, 145  
 Film Density, 60  
 Focal Plane Array Cameras, 252  
 Focused Transducers, 295  
 Focusing, 295  
 Foil Penetration Method, 99  
 Force vs. Displacement Curve, 326  
 Foreign Object Damage, 15  
 Fracture, 18  
 Fracture Toughness, 16  
 Free-Boundary Reflection, 124  
 Frequency Translated Holography, 4, 126, 128  
 Fretting, 15, 21  
 – Fatigue, 21, 29  
 – Fatigue Damage, 22, 30  
 – Wear, 29
- General Corrosion, 9  
 Generalized Corrosion, 307
- Head Slider, 335  
 Heat Dissipation, 251  
 Heat Treatment, 397  
 Hertzian Contact, 330  
 Heterodyne Interferometry, 125  
 HF Signal, 299  
 HF Ultrasound, 14  
 HF-SAM, 301, 320  
 Hidden Corrosion, 14, 71  
 Hidden Pitting Corrosion, 90  
 High Cycle Fatigue, 15, 206, 227  
 High Frequency Scanning Acoustic Microscope, 298
- High Frequency Scanning Acoustic Microscopy, 296, 301  
 Hole Volume, 401  
 Hole Volume in Epoxy Resin, 400  
 Holography, 125  
 Humidity Exposure, 318
- Imaging Microellipsometer, 359  
 Imaging of Surface Waves, 130  
 Imaging Techniques, 2  
 Incoherent Particles, 395  
 Infrared Cameras, 251  
 Infrared Imaging, 255  
 In Situ Monitoring, 143  
 In Situ Ultrasonic Measurement, 146, 214  
 Insufficient Curing, 6  
 Intergranular Corrosion, 306  
 Internal Friction Parameter, 280  
 Interrupted Fatigue Measurements, 217  
 IR Camera, 252  
 – Sensitivity, 277
- Laser Treated Surface, 336  
 Laser Ultrasound, 237  
 Laser-Generation of Ultrasound, 236  
 Laser-Induced Crack-Closure, 195  
 Laser-Ultrasonic Measurement, 237  
 Lateral Resolution, 295, 325  
 Lattice Defects, 383  
 Leaky Waves, 296  
 Line Shape Parameter, 381  
 Linear Acoustic Measurements, 207, 218  
 Linear Fracture Mechanics, 142  
 Local Damage Measurements, 224  
 Local Ultrasonic Scattering, 122, 131  
 Localized Corrosion, 37, 101  
 Lock-In Thermography, 253  
 Longitudinal Sound Velocity, 218, 221  
 Low Cycle Fatigue, 15, 206
- Magnetic Particle Techniques, 2  
 Maintenance, 1  
 Mechanical Damping, 278  
 Mechanical Hysteresis, 251  
 Mechanically Induced Dissipated Heat Analysis, 261, 272  
 Mechanically Induced Heat, 249  
 Microbolometer Cameras, 252  
 Microcrack Concentration, 321  
 Microcrack Detection, 319

- Microcracks, 2, 321  
Microellipsometer, 358  
Microellipsometry, 356  
Microfabrication, 356  
Micro Focus X-ray Techniques, 14  
Micro-Optical Components, 370  
Microplastic Fatigue Damage Processes, 279  
Microradiographic Detectability, 66  
Microradiographic System, 61  
Microradiography, 3, 74  
Microstructure, 2  
Microwires, 338  
Monoenergetic Positron Beam, 382  
Monovacancies, 383  
  
Nanodroplets, 337  
Nanograin Imaging, 338  
Nanolithography, 356  
Nanomaterials, 328  
Nanoscale Imaging, 334  
Near-Field Scanning Interferometry, 127  
Nondestructive Evaluation, 1  
Nonlinear Acoustic Measurements, 207, 213, 219  
Nonlinear Acoustic Parameter, 210, 226, 228, 280  
Nonlinear Acoustics, 2, 19, 207  
Nonlinear Effects, 278  
Nonlinear Parameter, 281  
Nulling Ellipsometer, 357  
  
Object-to-Film Distance, 98  
Optical  
– Absorption Spectra, 189  
– Interferometry, 125  
– Profilometry, 14, 88  
– Surface Characterization, 31  
Organic Coatings, 254  
  
Paris Law, 147  
Passive Infrared Imaging, 254  
Phase Shift Interferometry, 27  
Phase-Contrast, 95  
Phase-Locked Synchronous Detection, 184  
Photoresist, 369  
Piezoelectric Method, 213  
Pit Depth, 44, 58, 69, 76, 79  
Pit Size, 41  
Pit Size Measurements, 157  
Pitting Corrosion, 12  
  
Plastic Deformation, 389  
Poisson Ratio, 302, 330  
Polyimides, 404  
Polymer, 399  
– Coatings, 225, 405  
– Composites, 399  
– Degradation, 8  
Positron, 375  
– Annihilation, 2, 20  
– Annihilation Lifetime Spectroscopy, 374  
– Annihilation Lifetime Spectroscopy, 376  
– Annihilation Spectroscopy, 374  
– Experiment, 376  
– Lifetime, 383, 384, 393  
– Lifetime Spectra, 378, 379  
– Traps, 383, 384  
Power Spectral Density, 32  
Profilometer Images, 50  
Projection Magnification, 67, 75, 97  
Protective Coatings, 286  
Pulsed Thermography, 253, 256  
Pulse-Force Modulation, 327  
  
Quantum Well Infrared Photon Detectors, 252  
Quasi-Adiabatic Conditions, 265  
  
Radiography, 59  
Rayleigh Angle, 296  
Rayleigh Wave, 116, 118, 296, 302  
Rayleigh Wave Velocity, 302, 303  
Real Time Holography, 132  
Reflection, 119  
– Coefficient, 299, 317  
– of Surface Wave, 160, 164  
Refractive Index, 365  
– Measurement, 365  
Reliability, 1  
Reverberation Experiment, 235  
Reverberation Technique, 234  
Rheological Model, 331  
Rotationally Symmetric  
– Microellipsometer, 362, 363  
Rotationally Symmetric Scanning  
– Microellipsometer, 360  
  
Scanning  
– Acoustic Microscope, 296  
– Acoustic Microscopy, 3, 7, 294  
– Electron Microscopy, 37

- Interferometry, 132
- Kelvin Probe Force Microscopy, 326, 341
- Probe Microscopy, 2
- Tunneling Microscope, 323
- Vibrating Electrode Technique, 4, 8, 287
- Scattering, 119
  - of Ultrasonic Energy, 115
  - Theory, 152
- Scratching Experiments, 342
- Second Harmonic Signal, 219
- Self-Assembled Nano-Phase Silane Particles, 315
- Semicoherent Precipitates, 395
- Sizing of Crack, 160
- Slip Bands, 321
- Slow-Positron-Beam System, 381
- SNAP Coatings, 315
- Sound Velocity, 218
- Stiffness, 330
- Stress Corrosion, 12
  - Crack, 136
- Stress Intensity Factor, 44, 46, 150, 154
- Subsurface Corrosion, 260
- Subsurface Defects, 256
- Surface
  - Acoustic Waves, 116, 117
  - Acoustic Wave Monitoring, 146
  - Damage, 26, 29
  - Deformation, 47
  - Features, 366
  - Pitting, 306
  - Topography, 325
  - Topology Measurement, 363
  - Treatment, 286
  - Wave Generation, 296
  - Wave Scattering, 152
- Temperature Contrast, 257
- Temperature Decay Curve, 249
- Thermal
  - Conductivity, 247
  - Diffusion Techniques, 246
  - Diffusivity, 187, 247
  - NDE Parameter, 263
  - Pulse, 248
  - Wave, 246, 247, 253
- Thermoacoustic Characterization, 19
- Thermodynamic Effect, 249
- Thermoelastic Temperature Variation, 277
- Thermoelectric Power, 19
- Thermography, 7, 14
- Thermo-Optical Modulation, 185, 192, 193, 198
- Thermophysical Parameters, 248
- Thickness Loss, 14
- Through-Thickness Crack Model, 149
- Ti-6Al-4V, 48
- Transducers, 295
- Transmission Electron Microscopy, 207, 394
- Trapping Model, 385
- Ultrasonic
  - Absorption, 234, 239
  - Excitation, 272
  - Force Microscopy, 3, 326, 328
  - Loading, 273, 279
  - Measurements, 158
  - Nondestructive Evaluation, 114
  - Reflections, 120
  - Scattering, 116
  - Wave Propagation, 115
- Ultrasonics, 2
- Ultrasound, 14
- Unsharpness, 69
- UV Exposure, 318
- V(z)-curve, 302, 303
- Vacancy Agglomerates, 383
- Vertical Scanning Interferometry, 27
- Volta Potential, 341, 344, 345, 348
- Water Exposure, 313
- Weak Bonding, 6
- Weathering, 6
- White Light Interference Microscopy, 3, 14, 20, 26, 39
- Wing Parameter, 381
- X-Ray
  - Microfocal Techniques, 4
  - Microfocal Tubes, 59
  - Source, 59
  - Techniques, 2
- Young's Modulus, 303, 330

# Springer Series in MATERIALS SCIENCE

---

*Editors:* R. Hull    R. M. Osgood, Jr.    J. Parisi    H. Warlimont

- 10 Computer Simulation of Ion-Solid Interactions  
By W. Eckstein
  - 11 Mechanisms of High Temperature Superconductivity  
Editors: H. Kamimura and A. Oshiyama
  - 12 Dislocation Dynamics and Plasticity  
By T. Suzuki, S. Takeuchi, and H. Yoshinaga
  - 13 Semiconductor Silicon  
Materials Science and Technology  
Editors: G. Harbeke and M. J. Schulz
  - 14 Graphite Intercalation Compounds I  
Structure and Dynamics  
Editors: H. Zabel and S. A. Solin
  - 15 Crystal Chemistry of High-T<sub>c</sub> Superconducting Copper Oxides  
By B. Raveau, C. Michel, M. Hervieu, and D. Groutt
  - 16 Hydrogen in Semiconductors  
By S. J. Pearton, M. Stavola, and J. W. Corbett
  - 17 Ordering at Surfaces and Interfaces  
Editors: A. Yoshimori, T. Shinjo, and H. Watanabe
  - 18 Graphite Intercalation Compounds II  
Editors: S. A. Solin and H. Zabel
  - 19 Laser-Assisted Microtechnology  
By S. M. Metev and V. P. Veiko  
2nd Edition
  - 20 Microcluster Physics  
By S. Sugano and H. Koizumi  
2nd Edition
  - 21 The Metal-Hydrogen System  
By Y. Fukai
  - 22 Ion Implantation in Diamond, Graphite and Related Materials  
By M. S. Dresselhaus and R. Kalish
  - 23 The Real Structure of High-T<sub>c</sub> Superconductors  
Editor: V. Sh. Shekhtman
  - 24 Metal Impurities in Silicon-Device Fabrication  
By K. Graff 2nd Edition
  - 25 Optical Properties of Metal Clusters  
By U. Kreibig and M. Vollmer
  - 26 Gas Source Molecular Beam Epitaxy  
Growth and Properties of Phosphorus Containing III-V Heterostructures  
By M. B. Panish and H. Temkin
  - 27 Physics of New Materials  
Editor: F. E. Fujita 2nd Edition
  - 28 Laser Ablation  
Principles and Applications  
Editor: J. C. Miller
  - 29 Elements of Rapid Solidification  
Fundamentals and Applications  
Editor: M. A. Otooni
  - 30 Process Technology for Semiconductor Lasers  
Crystal Growth and Microprocesses  
By K. Iga and S. Kinoshita
  - 31 Nanostructures and Quantum Effects  
By H. Sakaki and H. Noge
  - 32 Nitride Semiconductors and Devices  
By H. Morkoç
  - 33 Supercarbon  
Synthesis, Properties and Applications  
Editors: S. Yoshimura and R. P. H. Chang
  - 34 Computational Materials Design  
Editor: T. Saito
  - 35 Macromolecular Science and Engineering  
New Aspects  
Editor: Y. Tanabe
  - 36 Ceramics  
Mechanical Properties, Failure Behaviour, Materials Selection  
By D. Munz and T. Fett
  - 37 Technology and Applications of Amorphous Silicon  
Editor: R. A. Street
  - 38 Fullerene Polymers and Fullerene Polymer Composites  
Editors: P. C. Eklund and A. M. Rao
-

Springer Series in  
**MATERIALS SCIENCE**

---

*Editors:* R. Hull    R. M. Osgood, Jr.    J. Parisi    H. Warlimont

- 39 **Semiconducting Silicides**  
Editor: V. E. Borisenko
- 40 **Reference Materials  
in Analytical Chemistry**  
A Guide for Selection and Use  
Editor: A. Zschunke
- 41 **Organic Electronic Materials**  
Conjugated Polymers and Low  
Molecular Weight Organic Solids  
Editors: R. Farchioni and G. Grossos
- 42 **Raman Scattering  
in Materials Science**  
Editors: W. H. Weber and R. Merlin
- 43 **The Atomistic Nature  
of Crystal Growth**  
By B. Mutaftschiev
- 44 **Thermodynamic Basis  
of Crystal Growth**  
*P-T-X* Phase Equilibrium  
and Non-Stoichiometry  
By J. Greenberg
- 45 **Thermoelectrics**  
Basic Principles  
and New Materials Developments  
By G. S. Nolas, J. Sharp,  
and H. J. Goldsmid
- 46 **Fundamental Aspects  
of Silicon Oxidation**  
Editor: Y. J. Chabal
- 47 **Disorder and Order  
in Strongly  
Nonstoichiometric Compounds**  
Transition Metal Carbides,  
Nitrides and Oxides  
By A. I. Gusev, A. A. Rempel,  
and A. J. Magerl
- 48 **The Glass Transition**  
Relaxation Dynamics  
in Liquids and Disordered Materials  
By E. Donth
- 49 **Alkali Halides**  
A Handbook of Physical Properties  
By D. B. Sirdeshmukh, L. Sirdeshmukh,  
and K. G. Subhadra
- 50 **High-Resolution Imaging  
and Spectrometry of Materials**  
Editors: F. Ernst and M. Rühle
- 51 **Point Defects in Semiconductors  
and Insulators**  
Determination of Atomic  
and Electronic Structure  
from Paramagnetic Hyperfine  
Interactions  
By J.-M. Spaeth and H. Overhof
- 52 **Polymer Films  
with Embedded Metal Nanoparticles**  
By A. Heilmann
- 53 **Nanocrystalline Ceramics**  
Synthesis and Structure  
By M. Winterer
- 54 **Electronic Structure and Magnetism  
of Complex Materials**  
Editors: D.J. Singh and  
D. A. Papaconstantopoulos
- 55 **Quasicrystals**  
An Introduction to Structure,  
Physical Properties and Applications  
Editors: J.-B. Suck, M. Schreiber,  
and P. Häussler
- 56 **SiO<sub>2</sub> in Si Microdevices**  
By M. Itsumi
- 57 **Radiation Effects  
in Advanced Semiconductor Materials  
and Devices**  
By C. Claeys and E. Simoen
- 58 **Functional Thin Films  
and Functional Materials**  
New Concepts and Technologies  
Editor: D. Shi
- 59 **Dielectric Properties of Porous Media**  
By S.O. Gladkov
- 60 **Organic Photovoltaics**  
Concepts and Realization  
Editors: C. Brabec, V. Dyakonov, J. Parisi and  
N. Sariciftci